University of Newcastle upon Tyne

Department of Civil Engineering

A Numerical and Experimental Study of Open-Channel Flow in a Pipe of Circular Cross-Section With a Flat Bed

by

CHANGELA HOOHLO

Thesis submitted in fulfilment of the requirements for the degree of Doctor of Philosophy

November 1994

ABSTRACT

Uniform open-channel flow in a pipe of circular cross-section with a flat bed, is studied by experiment and numerical modelling. A pipe of diameter D = 305 mm, and mild bed slopes S_o = 4.63 x 10^{-4} and 9.27 x 10^{-4} was studied - the former slope only by experiment. The bed thicknesses (e), e/D = 0.141, and 0.285 were studied experimentally and numerically, with e/D = 0.020, studied only numerically. Five flow depths (Y_o) were studied; (Y_o+e)/D = 0.3, 0.4 (and 0.416), 0.5, 0.667, and 0.751. A smooth bed and bed roughnesses d_{50} = 0.93, 4.20, and 1.71 mm were also used.

Mono-chromatic Laser Doppler Anemometry (LDA) was used to measure the local mean longitudinal (primary), and vertical velocities, and their respective turbulence intensities. The primary velocity contours display dipped maxima and bulging towards the corner. The inwardly-curving side-walls slightly modify these contours. In each channel half there is a surface cell and a bottom cell. These move high momentum fluid away from the centreline towards the corner zone. The primary and secondary flows are largely similar to those in rectangular channels. The wall shear force ratios obtained by the Vanoni-Brooks separation technique follow the empirical trend from various channel types. Similarity laws for the longitudinal mean velocity in the corner-influenced zones are proposed.

The numerical model is based on the SIMPLE technique, and computes the flow on a Cartesian grid, using a non-linear k-ε turbulence model with wall functions. The model boundary conditions were modified to reflect the effects of the corners, the curved side-wall, and a roughened bed. Model predictions of the primary mean velocities, and centreline turbulence intensities, are close to the experimental and empirical distributions. Primary velocity predictions for e/D = 0.020 compare well to the case of a clear pipe flowing part-full. The predicted secondary flows are largely similar to the experimental patterns. Usage of a small mesh size (e.g. when (Y_o + e)/D < 0.5) results in side-wall points lying within the laminar sub-layer, leading to inaccurate secondary flow prediction by the k-ε model. As in rectangular channels, the predicted local boundary shear stress decreases from the centreline along the bed and minimises at the corner. On the side-walls, the model overpredicts the local boundary shear stresses. Nonetheless, computed wall shear force ratio values follow the empirical trend.

ACKNOWLEDGEMENTS

I wish to thank my supervisor, Dr C. Nalluri MICE, for his invaluable assistance and guidance throughout the study. His advice and support were truly helpful indeed. Due gratitude is also expressed to Professor P. Novak for his valuable comments and suggestions.

I also wish to thank Messrs Peter Dawber and Alan Jefferson, technicians in the Hydraulics Laboratory, for their unstinting support and efficiency in the laboratory.

I am indebted to the Lesotho Highlands Development Authority for the financial support which enabled me to conduct the various parts of the study, and present the results at the 8th International Conference on Numerical Methods in Laminar and Turbulent Flow, at Swansea.

Finally, sincere gratitude is extended to my entire family for their strong support and patience, without which this study could not have been possible.

TABLE OF CONTENTS

NOMENCLATURE

A	flow area
a	coefficients in SIMPLE
a, b, c	empirical constant for the corner symmetry law (Eqn 7.7)
b	constant term in SIMPLE
C_k	empirical constant for turbulent intensity distributions
$c_{1\varepsilon}$, $c_{2\varepsilon}$	empirical k-ε model constants
c_μ	empirical shear layer constant = 0.09
D	pipe diameter
D_u, D_v, D_w	empirical constants for turbulent intensity distributions
d	sand roughness diameter e.g. d_{50}
e	thickness of the rigid bed
F	body force
Fr	Froude number
f	frequency; f_d shift frequency; Δf Doppler shift by Bragg cell
g	gravitational acceleration
h	channel flow depth
h_{weir}	flow depth over measurement weir
k	turbulent kinetic energy
k_s	equivalent sand roughness
l	mixing length
m	index of refraction
P	pressure; wetted perimeter: bed P_b, wall P_w
P_k	production term for turbulent kinetic energy
Pe	Peclet number

Q	bulk flow rate
R	hydraulic radius
r, r_o	pipe radius
Re	Reynolds number; Re_m , Re_*
S	slope: bed S_o; energy gradient S_f
S_{ij}	mean rate of strain (Chapts 2, 3, and 6)
S_ϕ	integrated volumetric source (Chapt. 4)
SF	side-wall shear force ratio; shear force: components SF_w, SF_b
T	water surface width
T'	temperature
t	time
U	longitudinal local mean velocity
U_m	bulk mean velocity
U_{max}	maximum local velocity
U_*	shear velocity
U, V, W	mean velocity components
U_{rms}, V_{rms}, W_{rms}	turbulence intensities
u, v, w	instantaneous velocity components
u', v', w'	velocity fluctuations
V_n	Vedernikov number
Vol	volume
X_m	inlet distance for the experimental measurement section
x	axial/longitudinal Cartesian co-ordinate; inlet distance
Y_o	uniform flow depth
y	vertical Cartesian co-ordinate
y_p	perpendicular distance to the wall
z	transverse/lateral Cartesian co-ordinate

α	aspect ratio = B/h; $= 2Z_o/Y_o$
α_ε	empirical constant = 0.18 (Eqn 3.36)
Δ	change
δ	boundary layer thickness; difference; Kronecker delta function
ε	rate of turbulent kinetic energy dissipation
Φ	time-mean of fluctuating scalar ϕ
ϕ	scalar quantity
Γ	diffusive constant
κ	von Karman constant = 0.412 in open channels
λ	Darcy-Weisbach friction factor; light frequency
μ	dynamic/molecular viscosity
ν	kinematic viscosity; turbulent eddy viscosity (ν_t)
Π	wake parameter (= 0.2)
π	pi
τ	stress tensor; shear stress
ς	wake function; Eqn 2.26b
Ω	mean vorticity
ω	fluctuating vorticity
θ	angle subtended at the centre by bed or free surface
ρ	density
σ	Prandtl numbers

SUBSCRIPTS

ave	spatial average
b	pertaining to the channel bed
cn	of the corner
E, W, N, S, T	at the neighbour nodes (Chapt. 4)
e, w, n, s, t	at the centre of cell face (Chapt. 4)

eff	effective
f	friction
i, j, k	coordinate directions; tensor indices
K, k	pertaining to the turbulent kinetic energy
l	of the laminar sublayer
norm	the norm of two variables
o	bed values; wall condition; pertaining to uniform flow
rms	root mean squared
sec	of secondary flow
T	total
t	turbulent
U	pertaining to U
V	pertaining to V
W	of the wall or channel side-wall; pertaining to W
x, y, z	pertaining to coordinate directions
γ	index for refractive indices
ε	of the turbulent dissipation rate
ϕ	pertaining to scalar quantity ϕ
1, 2, 3	coordinate directions
2D	two-dimensional
*	of the wall shear; based on U_*

SUPERSCRIPTS

k	iteration number
C	convection
D	diffusion
*	predictor stage in the SIMPLE method
**	from the previous iteration in the SIMPLE method

$'$	fluctuating component
$+$	normalised wall quantity
$\overline{\quad}$	(overbar) time mean

LIST OF FIGURES

PLATE

LIST OF TABLES

CHAPTER 1: INTRODUCTION

1.1 Background

Open channel flows in engineering applications are mainly turbulent. These include flows in rectangular channels, and circular channels flowing part-full. In pipe sewers, deposition of sediments during low flows leads to the modification of the channel cross-section. The circular channel develops a flat bed. The present work is aimed at studying the effects of this altered shape on the turbulent flow characteristics.

Previous studies, e.g. Manning and Chezy, were based on the bulk flow characteristics of fully-rough open channel turbulent flow - e.g. the cross-sectional mean velocity and the channel's resistance to the flow. However, unwanted sedimentation within channels, or the destructive erosion of channel walls, showed the need for detailed measurements. Velocity distributions across the channel cross-section were then studied. Direct measurement of the boundary shear stresses using the Preston tube, were also carried out. In fact the shapes of channels were optimised so as to minimise the localised effects and aid flow through the channels. The high cost of these experimental studies limited the number of channel shapes and flows that could be studied.

Although the Navier - Stokes equations had been known to govern open channel flow, their solution could not be achieved by methods other than that of numerical computation. Computational methods were first applied to boundary layer flows in the 1960s. These were only adopted for open-channel flows in the late 1970s. Numerical computation is often called refined flow modelling in civil engineering applications.

1.2 Aims and Objectives of the Present Study

The aim of the present study is to enable the prediction of velocity and boundary shear distributions in open channels by numerical computation. The case of the pipe-section of circular cross-section with a modifying flat bed is studied.

The important flow characteristics were firstly identified. These were (i) the longitudinal local mean velocity (U); (ii) the secondary mean flow in the plane of the cross-section (present in flows with a non-circular cross-section); (iii) the turbulence intensities in all the three directions: and (iv) the boundary shear stress. Their accurate prediction constitutes the accurate prediction of the flow.

1.3 Route of Examination

Unlike with other channel shapes (e.g. circular and rectangular), the present uniquely-shaped channel has not been extensively studied. As such there is no data against which comparisons with numerical results may be made. An extensive experimental study was undertaken to collect information on items (i), (ii) and (iii) in Section 1.2 above. This will provide a database for flows in the present cross-section. The Laser Doppler Anemometry (LDA) technique was used to measure the said quantities. To enable automated measurement in future studies, a computer-controlled mounting for the LDA apparatus was also customised.

Uniform flow was studied in two mild bed slopes 4.63×10^{-4}, and 9.27×10^{-4}. The bed thickness ratio (e/D), where e is the bed thickness and D = the pipe diameter, was varied. Two ratios e/D = 0.141 and 0.285, were studied. Measurements in channels with a smooth bed and roughened beds using three different roughnesses d_{50} = 0.93mm, 1.71mm, and 4.2mm, were taken.

The numerical study of the present cross-section involved (i) adopting the turbulence model to be used - the k-ε model; (ii) selecting the appropriate numerical scheme for the present flow - the SIMPLE technique; (iii) selecting the co-ordinate system to be used - the Cartesian system; (iv) writing a computer program - in FORTRAN computer code. Also, (v), the modified non-linear k-ε turbulence model was used in order to enable the prediction of secondary flows which cannot be predicted by use of the standard k-ε model. Lastly, (vi), the standard boundary conditions derived for two-dimensional flow, were modified to account for the side-wall curvature, the channel corners, and the effect of a roughened bed.

1.4 Contents of the Thesis

In Chapter 2 the adoption of the Navier-Stokes equations for turbulent flow description through the use of Reynolds averaging is reviewed. Boussinesq's eddy viscosity hypothesis, which links the resulting unknown Reynolds stresses to the mean flow field, is introduced. In Sections 2.4 the application of turbulent boundary layer theory to open-channel flow is reviewed. This involves the use of universal velocity laws to describe flows bounded by rigid boundaries. Lastly in Chapter 2, past treatment of boundary shear stress characteristics in channels is reviewed and given relevance to the present study.

With the governing equations introduced, Chapter 3 discusses the models used to describe the turbulence and resolve the unknown Reynolds stresses. The standard zero- and one-equation models are introduced. The more complex, albeit flawed, full Reynolds Stress Models (RSMs) are introduced as a reference. Their similarities with the k-ε are pointed out, and the reasons for the choice of the k-ε over them are given. The modified non-linear k-ε model is presented in Section 3.4. It enables the computation of secondary flow, which can not be achieved by the standard k-ε model. Finally, the treatment (the physics) of the variables at the rigid, and free-surface boundaries is presented in Section 3.5.

The *S*emi-*I*mplicit *M*ethod for *P*ressure-*L*inked *E*quations (SIMPLE) for numerical computation of parabolic flows is described in Chapter 4. The discretisation of the governing equations, the Cartesian grid generation, the staggered variable arrangement, and the solution for the pressure are discussed in Sections 4.2 - 4.4. The implementation of the boundary conditions of Section 3.5 is treated in Section 4.5. The solution algorithm is then presented in Section 4.6, along with a discussion of the stability and convergence of the numerical method.

The experimental procedures taken to collect experimental data in the present channel, for the channel configurations mentioned above, are detailed in Chapter 5. Section 5.2 deals with the establishment of the fully-developed uniform turbulent flow. Section 5.3 describes the procedure adopted in roughening the bed. The theory and practice of the LDA technique is presented in Section 5.4. This includes its adaptation to the present channel. Lastly, an analysis of the errors in the measured variables is presented in Section 5.5.

On the numerical front, the adaptation of the numerical scheme to the present channel is presented in Chapter 6. Section 6.2 describes the numerical treatment of the rigid and free-surface boundaries, and the sloping side-wall in the Cartesian co-ordinate system. How the marching procedure of SIMPLE is adopted to save computation storage is also presented. The inclusion of the physical effects of the side-wall curvature, the presence of the corners, and the bed roughness into the numerical model, is treated in Sections 6.3-6.6 respectively.

In Chapter 7 the results of the experimental investigation are presented in Sections 7.2 - 7.4. Comparisons with equivalent existing data are made. Friction parameters derived from the measurements are also presented. The similarity laws to account for the corner effect are analysed in Section 7.5.

Chapter 8 follows the form of Chapter 7 in presenting the results of the numerical computation. The computed flow variables are presented in Sections 8.2 - 8.4, with similarity laws discussed in Section 8.5.

The main conclusions of the study are noted in Chapter 9, Section 9.1. Recommendations for future studies in the present channel shape, and in general open channel flow are also listed in Section 9.2.

CHAPTER 2: GOVERNING EQUATIONS - A REVIEW

2.1 Introduction

When investigating flow mechanisms and the effects of the flow, it is necessary to describe the flow in formal terms. This chapter reviews the usage of the Navier-Stokes equations in describing turbulent fluid flow. In Sections 2.2 and 2.3 illustrates how these equations are adapted to describe general turbulent flow.

The application of turbulent boundary layer theory to open-channel flow is introduced in Section 2.4. In this section the universal velocity distribution laws, and the secondary flow phenomenon, are discussed. This section points out the main flow features to be studied.

Finally, boundary shear stress treatment in open-channels is discussed in Section 2.5 with reference to its application in the present cross-section.

2.2 Basic Navier-Stokes Equations

The basic Navier-Stokes equations are quoted in most standard texts (Tennekes and Lumley 1972, Hinze 1975, and McComb 1990). They follow from Newton's Second Law and portray the conservation of momentum per unit mass of fluid. For an instantaneous flow-field these equations take the form:

$$\frac{\partial u}{\partial t}+u\frac{\partial u}{\partial x}+v\frac{\partial u}{\partial y}+w\frac{\partial u}{\partial z}=-\frac{1}{\rho}\frac{\partial p}{\partial x}+\nu\nabla^2 u+F_x \qquad (2.1a)$$

$$\frac{\partial v}{\partial t}+u\frac{\partial v}{\partial x}+v\frac{\partial v}{\partial y}+w\frac{\partial v}{\partial z}=-\frac{1}{\rho}\frac{\partial p}{\partial y}+\nu\nabla^2 u+F_y \qquad (2.1b)$$

$$\frac{\partial w}{\partial t}+u\frac{\partial w}{\partial x}+v\frac{\partial w}{\partial y}+w\frac{\partial w}{\partial z}=-\frac{1}{\rho}\frac{\partial p}{\partial z}+\nu\nabla^2 u+F_z \qquad (2.1c).$$

for the three space directions (x, y, z) in a Cartesian co-ordinate system. u, v, w are the velocity components in the x- (longitudinal), y- (vertical), and z- (transverse) directions respectively; with p the pressure; ρ the density of the fluid; and ν the kinematic viscosity of the fluid. The first term on the left-hand side of each equation is the time-change term; the next three are the convective momentum transport terms. The first term on the right-hand side is the gradient of the pressure (p); followed by the divergence of the viscous stresses; and lastly, the body force per unit mass (F) exerted by external influences on the fluid.

A further consideration is the conservation of mass in fluid flow. In the absence of sources or sinks of the fluid, and taking mass to be a transferable property, the equation of mass conservation (the continuity equation) results:

$$\frac{\partial \rho}{\partial t} + \frac{\partial \rho \mathrm{u}}{\partial \mathrm{x}} + \frac{\partial \rho \mathrm{v}}{\partial \mathrm{y}} + \frac{\partial \rho \mathrm{w}}{\partial \mathrm{z}} = 0 \qquad (2.2)$$

Eqns 2.1 and 2.2 are deemed to govern Newtonian fluid flow and form the basis on which transport properties of flows may be investigated. Since most engineering flows are turbulent, the form of the equations that govern turbulent flow is next considered.

2.3 Turbulent Flow

The flow is said to be turbulent (rather than laminar) when the Reynolds number (Re) is greater than a critical value. The Reynolds number is defined as $\mathrm{Re} = \mathrm{U}_{\mathrm{scale}} l_{\mathrm{scale}} / \nu$ where $\mathrm{U}_{\mathrm{scale}}$ is the characteristic velocity scale of a flow, and l_{scale} is the characteristic length scale.

2.3.1 Reynolds Equations

Osborne Reynolds (1894) proposed that in turbulent flow, the instantaneous velocity at a point, u be expressed as a sum of the turbulent fluctuation of the velocity u' and the time-mean velocity U such that $u = U + u'$. This expression pertains to other quantities (ϕ) (e.g. pressure, temperature and heat flux) affected by the turbulent flow field whereupon $\phi = \Phi + \phi'$. Substituting the expression for u into Eqn 2.1 and taking the time-average, the Reynolds equations result

$$\frac{\partial U}{\partial t}+U\frac{\partial U}{\partial x}+V\frac{\partial U}{\partial y}+W\frac{\partial U}{\partial z}=-\frac{1}{\rho}\frac{\partial P}{\partial x}+\nu\nabla^2 U-\frac{\partial \overline{u'u'}}{\partial x}-\frac{\partial \overline{u'v'}}{\partial y}-\frac{\partial \overline{u'w'}}{\partial z}+F_x$$

(2.3a)

$$\frac{\partial V}{\partial t}+U\frac{\partial V}{\partial x}+V\frac{\partial V}{\partial y}+W\frac{\partial V}{\partial z}=-\frac{1}{\rho}\frac{\partial P}{\partial y}+\nu\nabla^2 V-\frac{\partial \overline{v'u'}}{\partial x}-\frac{\partial \overline{v'v'}}{\partial y}-\frac{\partial \overline{v'w'}}{\partial z}+F_y$$

(2.3b)

$$\frac{\partial W}{\partial t}+U\frac{\partial W}{\partial x}+V\frac{\partial W}{\partial y}+W\frac{\partial W}{\partial z}=-\frac{1}{\rho}\frac{\partial P}{\partial z}+\nu\nabla^2 W-\frac{\partial \overline{w'u'}}{\partial x}-\frac{\partial \overline{w'v'}}{\partial y}-\frac{\partial \overline{w'w'}}{\partial z}+F_z$$

(2.3c)

The overbar symbolises the time-mean of the quantity. The time-averaged quantities are often referred to as Reynolds-averaged. P is the time average of the pressure (mean pressure).

For economy of space, and the ease with which the terms of compact form may be analysed Eqn 2.3 can be written in a more compact tensor form:

$$\frac{\partial U_i}{\partial t}+U_j\frac{\partial U_i}{\partial x_j}=-\frac{1}{\rho}\frac{\partial P}{\partial x_i}+\nu\frac{\partial^2 U_i}{\partial x_j \partial x_j}-\frac{\partial \overline{u_i'u_j'}}{\partial x_j}+F_i \qquad (2.4)$$

I II III IV V VI

Einstein's summation notation is used. The terms are as in Eqn 2.1 although the instantaneous velocities of Eqn 2.1 have been replaced by mean velocities. Also, in the case of steady(time-invariant or stationary) flow, term (I) is discarded. Finally, an additional term (term V), results from the presence of velocity fluctuations (u'_i) in turbulent flow. The interpretation of this term follows.

2.3.2 The Stress Tensor

The term $-\rho\,\overline{u_i'u_j'}$ is called the Reynolds stress, so called because the resulting transfer of momentum from one part of fluid to the other due to turbulent fluctuations u'_i and u'_j, has a net diffusive effect on the flow - akin to the mean viscous stresses expressed by term (IV) of Eqn 2.4. The total stress (τ), which includes the viscous and turbulent Reynolds stresses, can be expressed in a tensorial form τ_{ij} - which means τ_{ij} is the stress acting in the x_j-direction in the plane perpendicular to the x_i-axis. It is worth noting from this notation that the normal stresses $\tau_{\alpha\alpha}$ (the Greek subscripts are used to indicate that there is no summing) act in the same physical sense as pressure, and can thus be lumped together with the pressure.

As a second-order tensor, τ_{ij} comprises a spherically symmetrical part equal to $\tau_{ii}/3$ and an anti-symmetrical part (τ_{ij}^*) that is traceless ($\tau_{ii}^*=0$). The latter part gives rise to the deformation of the fluid. Spatial variations in the velocity field $\partial U_i/\partial x_j$ can also be broken down into its symmetrical part $\overline{S_{ij}}$, (the mean strain rate); and anti-symmetrical part $\frac{1}{2}\Omega_k\varepsilon_{ijk}$ (in which Ω_k is the rotation tensor without deformation, and ε_{ijk} is the cyclic third-order tensor), where

$$\overline{S_{ij}} = \frac{1}{2}\left(\frac{\partial U_i}{\partial x_j} + \frac{\partial U_j}{\partial x_i}\right). \tag{2.5}$$

With Newtonian fluids, the relationship between $\overline{S_{ij}}$ and τ_{ij}^* is linear, with the dynamic viscosity $\mu = \rho\nu$ as the constant of proportionality. Therefore if the pressure (P) is incorporated as a form of the symmetrical part of τ_{ij}, the expression

$$\tau_{ij} = -P\delta_{ij} + 2\rho\nu\overline{S_{ij}} \tag{2.6}$$

results. δ_{ij} = Kronecker delta function equals unity if i = j, and equals 0 otherwise. With the presence of turbulence, the Reynolds stresses $-\rho\overline{u_i'u_j'}$ have to be added to Eqn 2.6, giving

$$\tau_{ij} = -P\delta_{ij} + 2\rho\nu\overline{S_{ij}} - \rho\overline{u'_iu'_j} \tag{2.7}$$

It is apparent from Eqn 2.4 that to compute the flow, the Reynolds stresses need to be determined. It is the determination of these stresses, termed modelling, which constitutes the

bulk of the effort in turbulent flow computation. The eddy viscosity concept of Boussinesq (Hinze 1975) and the full Reynolds stress transport model of Launder *et al* (1975) are the two most popular methods of computing Reynolds stresses. These will be introduced and reviewed in full in Chapter 3.

Boussinesq's concept of the eddy viscosity assumes that Reynolds stresses can be linearly related to the mean strain rate in analogy to viscous stresses. Hence by introducing a scalar eddy viscosity (ν_t), Eqn 2.7 becomes

$$\tau_{ij} = -P\delta_{ij} + 2\rho(\nu + \nu_t)\,\overline{S_{ij}} \tag{2.8a}$$

when viscous stresses are taken into account. In high Reynolds number flows viscosity effects decrease and the stress relation becomes

$$\tau_{ij} = -P\delta_{ij} + 2\rho\nu_t\,\overline{S_{ij}} \tag{2.8b}$$

Unlike the kinematic viscosity, ν_t is a property of the turbulence rather than that of the fluid and it may vary from flow to flow, and from point to point within one flow. Turbulence models that result from this concept are the most widely used (Rodi 1980). However, it is worth mentioning that although Boussinesq proposed a constant eddy viscosity, this can be realised only in homogeneous flows. In flows bounded by a rigid and impervious wall: open-channel, closed-duct, and free boundary-layer, the flow is not homogeneous in that zone of the domain where the wall exerts an influence - the boundary layer. Therefore a non-constant eddy viscosity has to be specified at points in the flow domain. In fact the above flow examples are of a class termed turbulent shear flow. This type of flow is marked by the presence of a substantial gradient of the predominant velocity U_i, in the direction perpendicular to the x_i-axis. The present case of open-channel flow falls into this category U_i being U_1.

Before considering turbulent shear flows, it is worth introducing a useful quantity called the turbulent kinetic energy ($k = \frac{1}{2}\overline{u_i'u_i'}$). The derivation of its governing transport equation is straight-forward but lengthy, and is given in detail in Hinze (1975) and Townsend (1976). For steady flow, and by neglecting the buoyancy-driven transport of k, this transport equation is given in tensor notation as

$$U_j \frac{\partial k}{\partial x_j} + \frac{\partial}{\partial x_j}(\overline{p'u' + u_i'u_i'u_j'}) + \overline{u_i'u_j'} \frac{\partial U_i}{\partial x_j} = \nu \overline{u' \frac{\partial^2 u_i'}{\partial x_j^2}}. \qquad (2.9)$$

I II III IV

Terms I to IV of Eqn. 2.9 are similar to those of the momentum equations 2.4. Term I represents convective transport of k; term II the diffusive transport by velocity and pressure fluctuations; term III the production of k by the action of the mean velocity gradients on the Reynolds stresses; and lastly, term IV, the viscous term, which comprises the action of viscous stresses on the turbulent motion, and the dissipation (conversion into heat) of k by the velocity fluctuations. Term IV is often written in its isotropic form ε. It can be seen that third-order correlations of the pressure and velocity, term II, emerge from the derivation of Eqn 2.9. The significance of these third and higher-order correlations in turbulent flow computation will be discussed further in Chapter 3. Presently, turbulent shear flow is examined.

2.3.3 Turbulent Shear Flow

Townsend (1976) notes that this class of turbulent flow is characterised by the inhomogeneity of the flow field and thus includes free turbulent flows like jets and wakes. He notes that the main difference between these free shear flows and wall-bounded flows (wall turbulence) is that free flows are governed by their spreading into the surrounding non-turbulent field, whereas wall turbulence is strongly influenced by the proximity of the wall. As Hinze (1975) notes, this is a small difference as their similarity is in the way they maintain their turbulence - by the action of the velocity gradients mentioned in section 2.3.2. Therefore, some results from studies of free turbulent flow (e.g. Rodi 1972) have been cited herein. Fundamental analysis of wall-bounded flows was carried out on the two-dimensional boundary layer in the early 20th century by Prandtl (Schlichting 1968). His work has since been extended in application to closed-duct and open-channel flow.

Prandtl proposed that Eqns 2.3 and 2.4 can be approximated for use in boundary layers. The main approximations are that the longitudinal (x-direction) length and velocity scales are much larger than the transverse (y-direction) ones. Eqn 2.3(a) reduces to

$$U\frac{\partial U}{\partial x}+V\frac{\partial U}{\partial y}+W\frac{\partial U}{\partial z}=-\frac{1}{\rho}\frac{\partial P}{\partial x}+\nu\frac{\partial^2 U}{\partial y^2}-\frac{\partial\overline{v'u'}}{\partial y}+F_x. \qquad (2.10)$$

Similar approximations for Eqns 2.3(b) and 2.3(c) can be obtained. These approximate expressions, together with Eqn. 2.9 form the basis for the analysis of wall-bounded turbulent shear flow.

2.4 Turbulent Open-Channel Flow

Ever since Nikuradse's experiments in pipe flow, the apparent complexity of the flow mechanisms has indicated that studies of wall turbulent flow should lean heavily on experimental evidence - rendering them semi-empirical. Boundary layer analysis therefore reflects theoretical arguments based on empirical data (i.e. semi-empirical). Most of the development of turbulent boundary layer theory was derived in two-dimensional boundary layers, but the theory can be applied with guarded confidence to open-channel and several other types of flow. Indeed for such flows, Eqns 2.3(a), 2.3(b), and 2.3(c) can further be respectively approximated to

$$\frac{\partial\overline{u'v'}}{\partial y}=-\frac{1}{\rho}\frac{\partial P}{\partial x}+\nu\frac{\partial^2 U}{\partial y^2} \qquad (2.11a)$$

$$\frac{\partial\overline{v'^2}}{\partial y}=-\frac{1}{\rho}\frac{\partial P}{\partial y} \qquad (2.11b)$$

$$0=-\frac{1}{\rho}\frac{\partial P}{\partial z}. \qquad (2.11c)$$

Integration of Eqn 2.11(a) yields a linear shear stress distribution

$$\tau=\mu\frac{\partial U}{\partial y}-\rho\overline{u'v'}=\tau_o+\frac{dP_o}{dx}y \qquad (2.12)$$

where, τ_o = boundary shear stress (the shear stress at the wall y = 0), and P_o = time-mean pressure at the wall. This also shows that the shear stress comprises the viscous, and turbulent components.

2.4.1 Universal Velocity Distribution Laws

Wall-bounded turbulent shear flows (wall flows) are primarily distinguished by the presence of high mean velocity gradients near the wall. Within the wall area, as Laufer (1954) found, and Townsend (1961, 1976) noted, the production and dissipation rates of the turbulent kinetic energy are much higher than at other zones of the flow further from the wall. This was corroborated by Kline *et al* (1967), using the hydrogen bubble technique. Since the production and dissipation rates are much higher than the convective, diffusive, and viscous transfer rates, the turbulent kinetic energy is said to be in equilibrium. This equilibrium determines the nature of the flow within and outwith these wall regions.

In the near-wall zone (the inner region) the characteristic length and velocity scales are given as ν/U_* and U_* respectively. $U_* = \sqrt{(\tau_o/\rho)}$ is the shear velocity and τ_o = boundary shear stress as before. Near the wall, where the turbulent fluctuations decrease, the viscous stress term (in Eqn. 2.12) becomes relatively larger than the Reynolds stress term. The layer of flow adjacent to the wall is thus called the viscous sub-layer, and has the linear profile $U/U_* = y\,U_*/\,\nu$ (see Figure 2.1).

Similarity laws (Yaglom 1979) are used to describe the velocity in the fully turbulent zones of the flow: Reynolds similarity, and wall similarity. Reynolds number similarity follows from this dependence of the flow (even farther from the wall) on the fluid viscosity. If the ratio of the viscous sub-layer thickness (δ_l) to flow depth (h) is small, the defining parameters for the turbulent region are h, the wall shear stress (τ_o), the velocity scale U_*. This leads to the velocity distribution

$$U = U_t + U_* F\,(y/h) \tag{2.13}$$

where U = mean longitudinal velocity; U_t = velocity of translation dependent on the flow type (= maximum velocity in open-channel flow). Eqn 2.13 can then be expressed as the defect law

$$\frac{U_{max} - U}{U_*} = F\,(y/h) \tag{2.14}$$

which is valid for both smooth and rough flows. The nature of the function F(y/h) can be determined by looking at the velocity distribution in the fully turbulent region of the wall zone - beyond the viscous sub-layer. It is instructive to note that this can be obtained by several means.

Firstly, in the near-wall zone the velocity distribution depends on fluid molecular viscosity (μ), density (ρ), distance from the wall (y), the flow depth (h), wall shear stress τ_o, characteristic height of the wall roughness elements (k_s), and dimensionless parameters that describe the shape and distribution effects of the wall roughness (α, β...):

$$U = f\,(\mu,\rho,y,h,\tau_o,k_s,\alpha,\beta.....) \tag{2.15}$$

which can be made dimensionless

$$\frac{U}{U_*} = f\,(\frac{U_*y}{\nu},\frac{k_s}{h},\frac{y}{h},\alpha,\beta....) \tag{2.16}$$

and in smooth flow becomes

$$\frac{U}{U_*} = f(\frac{U_*y}{\nu}) \tag{2.17}$$

where $U_*y/\nu = y^+$ = local turbulence Reynolds number Re_* (also referred to as the normalised wall distance y^+). Since Eqn 2.14 applies in the outer region of flow, Millikan proposed in the 1930s that there exists a region wherein Eqns 2.14 and 2.17 equally apply for flows of moderately high Reynolds number ($U_{max}h/\nu$). Matching the two functions F(y/h) and f (U_*y/ν) leads to the expression

$$U_*f\,(\frac{U_*y}{\nu}) = U_*F\,(\frac{y}{h}) + U_t \tag{2.18}$$

Bearing in mind the dependence of U on the Reynolds number and k_s in the inner zone, the only possible forms of F(y/h) and $f\,(U_*y/\nu)$ are the logarithmic functions

$$F\left(\frac{U_* y}{\nu}\right) = \frac{1}{\kappa}\ln\left(\frac{U_* y}{\nu}\right) + A \tag{2.19}$$

$$f\left(\frac{y}{h}\right) = \frac{1}{\kappa}\ln\left(\frac{y}{h}\right) + A' \tag{2.20}$$

in which κ = von Karman's universal constant (~ 0.4), and A (~ 5.0 - 5.3), and A' are empirical constants. Equilibrium layers (Townsend 1961) have a region within which the shear stress changes only slightly from the wall shear stress τ_0 and can effectively be considered constant. When this region of constant stress is taken into account for the fully turbulent part of the flow, the expression for U becomes

$$\frac{U}{U_*} = \frac{1}{\kappa}\ln\left(\frac{U_* y}{\nu}\right) + A \tag{2.21}$$

This is known as the law of the wall for the fully turbulent regions of wall flows. Grass (1967, 1971) further notes that this law is strongly dependent on Reynolds number similarity and applies to where the constant stress layer can be distinguished.

We can, secondly, derive the U velocity distribution of Eqn 2.21 by analysing the terms of the turbulent energy equation (Eqn 2.9) using experimental results of Kline *et al* (1967) and Perry *et al* (1969), and Townsend (1976). Noting the existence of an equilibrium layer, wherein terms III and IV of Eqn 2.9, are of the same order of magnitude and much larger terms I and II the equation

$$-\overline{u_i' u_j'}\frac{\partial U_i}{\partial x_j} = \varepsilon \tag{2.22}$$

results. It shows the relationship of the mean and fluctuating flow fields. Assuming that the region of equilibrium is small compared to h, and that the primary shear stress ($-\overline{u_i' u_j'} = -\overline{u'v'}$) is almost constant and equal to wall shear stress τ_0, it can be concluded that production and dissipation processes depend on U_*, y and ν. By dimensional analysis the resulting functions are

$$\frac{\partial U}{\partial y} = \frac{U_*}{\kappa y} f\left(\frac{U_* y}{\nu}\right) \tag{2.23a}$$

$$-\overline{u'v'} = U_*^2 g\left(\frac{U_* y}{\nu}\right) \tag{2.23b}$$

$$\varepsilon = \frac{U_*^3}{\kappa y} G\left(\frac{U_* y}{\nu}\right) \tag{2.23c}$$

Eqn 2.23(a) is equivalent to Eqn 2.17. Beyond the viscous sub-layer(at large $U_* y/\nu$), ε becomes solely a cubic function of U_* and y. Therefore, within the constant stress layer, the energy equation shows that

$$\frac{\partial U}{\partial y} = \frac{U_*}{\kappa y} \tag{2.24}$$

Integration of Eqn 2.24 yields Eqn 2.21.

Thirdly, Prandtl's mixing length hypothesis (also see Eqn 3.3), in which the turbulent shear stress is linked to the mean velocity field by an equivalent eddy viscosity as in Eqn. 2.8

$$-\overline{u'v'} = l^2 \frac{\partial U}{\partial y}\left|\frac{\partial U}{\partial y}\right| \tag{2.25a}$$

$$= \nu_t \frac{\partial U}{\partial y} \tag{2.25b}$$

(where l = mixing length = κy near the wall) can be used to derive the velocity distribution by setting $-\overline{u'v'} = \tau_o$ and integrating Eqn 2.25. l is assumed to be small compared to the scale of the mean flow (the macroscale) - typified by h. The resulting U distribution obtained by integration, is identical to Eqn 2.21.

One last method of deriving Eqn 2.21 makes use of von Karman's similarity theory, in which the mixing length (l) is taken to depend on local values of U, dU/dy, d^2U/dy^2 ... -leading to a dimensionless group $\varphi(l\ (d^2U/dy^2)/(dU/dy))$. Assuming that vertical and horizontal velocity fluctuations are equal, Prandlt's expression, Eqn 2.25(a), can be derived (see Schlichting 1958, p. 551). Again, integration of Eqn 2.25, with the assumption of the constant stress layer yields the law of the wall of Eqn 2.21.

Millikan's assumption, in the first of the derivations of Eqn. 2.21, of the overlap region for inner and outer flow regimes neglects the fact that Eqn 2.14 is dependent on upstream conditions by virtue of the large outer eddies' longer lifetime, whereas Eqn. 2.17 is not. This shows their incompatibility and hence the invalidity of the first derivation based on the 'region of overlap' concept. Bradshaw and Huang (1994) expound on this, and further note the unrestricted applicability of Eqn 2.21 when Eqns 2.17 and 2.23(a) are used in its derivation. Next, questions on the 'smallness' of l (Grass 1967) have been raised by Batchelor for the plane-wall boundary layer and pipe flows. So have points questioning the validity of the local turbulent kinetic energy equilibrium - in which diffusion is negligible - as the results of Kline *et al* (1967) show substantial diffusion in the near-wall region. Furthermore the thickness of the layer of constant stress may not be small relative to the depth of flow (h) as in the corner region (Bragg 1969). These questions, coupled with the fact that original derivation of the law was for two-dimensional boundary layer flows, mean that Eqn 2.21 has to be modified to be applicable for open-channel flow in which three-dimensional effects are not insignificant (further analysis of this is given in Chapter 7). Despite all these misgivings, Eqn 2.21 accurately predicts mean velocity distributions (Townsend 1976, and Bradshaw and Huang 1994) in the turbulent wall zone.

Coles (1956) noted that flow structure farther from the wall, in the outer zone, was similar to that in wakes. He proceeded to fit data to Eqn 2.14 by including a function of the wake parameter (Π) such that Eqn 2.14 becomes 'the defect law of the wake'

$$\frac{U_{max}-U}{U_*} = -\frac{1}{\kappa}\ln\left(\frac{y}{h}\right) + \frac{2\Pi}{\kappa}\cos^2\left(\frac{\pi}{2}\frac{y}{h}\right) \qquad (2.26a)$$

$$\zeta(y/h) = \frac{2\Pi}{\kappa}\sin^2\left(\frac{\pi y}{2h}\right) \qquad (2.26b)$$

where ζ(y/h) is the 'wake function'. Steffler *et al* (1985), Nezu and Rodi (1986) and Cardoso *et al* (1989) experimentally verified the validity of Eqn 2.26(a) in open channel flows by fitting their data to it. They found that the semi-empirical parameter $\prod$ is a function of the Reynolds number .($Re_m = 4hU_m/\nu$) up to Re_m = 200 000. Beyond this, $\prod$ is constant and equals 0.2.

The form of the wake term of Eqn 2.26(a) is obtained by comparing the trigonometric function $1+\sin[(2y/h-1)\pi/2]$ to an experimentally determined function in a typical wake. This yielded the wake function, Eqn 2.26(b). By assuming that U_{max} occurs at y = h and subtracting the U/U_*- from the U_{max}/U_*-equation, Eqn 2.26(a) is obtained. Bradshaw (1974) quotes a function of $\prod$ that gives a more realistic result of $\partial U/\partial y = 0$ at y = h, unlike $\partial U/\partial y \neq 0$ when the trigonometric Eqn 2.26(b) is used. It is emphasised that $\prod$ is a semi-empirical parameter which does not necessarily give Eqn 2.26(a) the universality of Eqn 2.21.

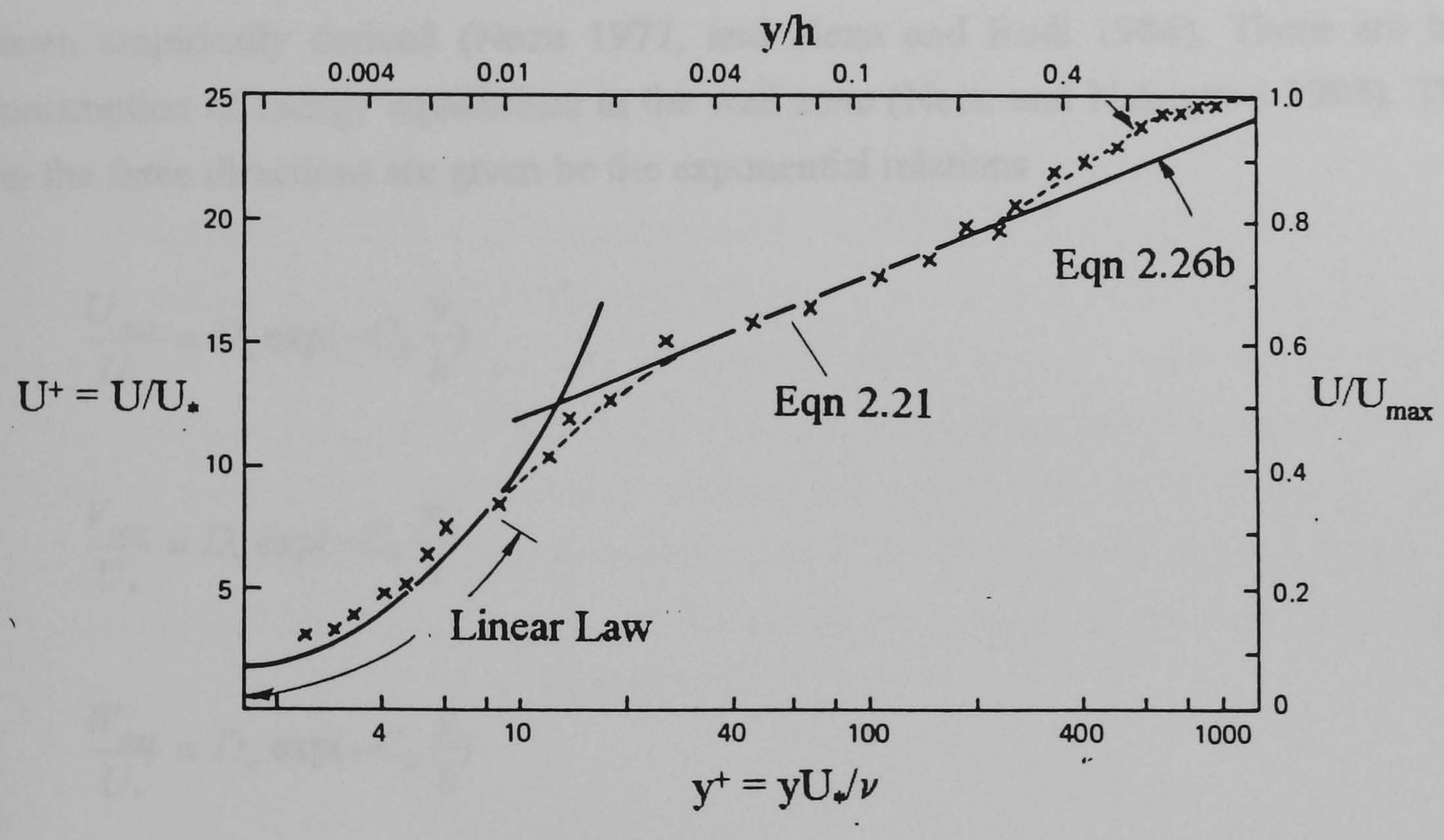

Figure 2.1 A Typical Mean Velocity Profile: $Re_m = 9.2 \times 10^4$ (After Tritton 1988)

Figure 2.1 illustrates the mean velocity distribution over in a boundary layer. It shows the linear distribution in the viscous sublayer, the logarithmic law (Eqn 2.21), and the outer region wake law (Eqn 2.26b).

2.4.2 Turbulence Intensity Distributions

Turbulence intensity is defined as the root mean squared (rms) value of the velocity fluctuation (u_i'), i.e. $U_{rms} = \sqrt{\overline{u'^2}}$; $V_{rms} = \sqrt{\overline{v'^2}}$; $W_{rms} = \sqrt{\overline{w'^2}}$. It is thus linked to the normal Reynolds stresses. Most of the first turbulence intensity measurements were in pipes (Laufer 1954), and closed ducts (Laufer 1951, MacQuivey and Richardson 1969, and Hussain and Reynolds 1975) by hot-wire anemometry. In open channels measurements have been undertaken using the hydrogen bubble technique Grass (1971), and by hot-film anemometry, Nezu (1977). Laser Doppler Anemometry (LDA) was used by Steffler *et al* (1985), Nezu and Rodi (1986), and Cardoso *et al* (1989), and the effect of roughness on turbulence intensities was investigated by Wang *et al* (1993). Hoohlo (1991) took LDA measurements for smooth flow in the present cross-section.

Universal laws for turbulence intensity distributions in the fully turbulent wall zone have been empirically derived (Nezu 1977, and Nezu and Rodi 1986). These are based on the assumption of energy equilibrium in the wall zone (Nezu and Nakagawa 1993). The intensities in the three directions are given be the exponential relations

$$\frac{U_{rms}}{U_*} = D_u \exp(-C_k \frac{y}{h}) \qquad (2.27\ a)$$

$$\frac{V_{rms}}{U_*} = D_v \exp(-C_k \frac{y}{h}) \qquad (2.27b)$$

$$\frac{W_{rms}}{U_*} = D_w \exp(-C_k \frac{y}{h}) \qquad (2.27c)$$

where D_u, D_v, D_w, and C_k are empirical constants derived from measurements in two-dimensional ducts in the depth range $0.1 < y/h < 0.6$. Using pipe flow data of Laufer (1954) the constants were evaluated as $D_u = 2.30$, $D_v = 1.27$, $D_w = 1.63$, and $C_k = 1.0$. They have proved to be independent of the Reynolds and Froude numbers.

2.4.3 The Effect of Wall Roughness

To account for surface roughness, Prandtl's original functional (Eqn 2.16) is recalled. In the near-wall zone, the flow is determined by parameters U_*, y/k_s, α, β, etc.. Since the effect of roughness is dependent on whether the roughness elements protrude into the flow, beyond the viscous sub-layer, a local Reynolds number ($U_* k_s / \nu$) indicates the extent to which flows are affected by the roughness - and hence which parameters characterise the mean near-wall flow (see Schlichting 1968). For $U_* k_s / \nu < 5$ the surface is hydraulically smooth and Eqn 2.17 applies. For $U_* k_s / \nu > 70$, the surface is hydraulically rough and $U/U_* = f(y/k_s, \alpha, \beta....)$. Lastly, when $5 \leq U_* k_s / \nu \leq 70$, the flow is in the transitional regime between smooth and rough flow and $U/U_* = f(U_* y/\nu, y/k_s, \alpha, \beta....)$. Therefore, by eliminating the effect of viscosity in rough flow, whence $U/U_* = f(y/k_s, \alpha, \beta....)$, and using the arguments used to derive Eqn 2.21, the mean flow distribution becomes

$$\frac{U}{U_*} = \frac{1}{\kappa} \ln\left(\frac{y}{k_s}\right) + B_s. \qquad (2.28)$$

B_S is a universal function of roughness shape and distribution parameters α and β. Perry *et al* (1969) classified boundary roughness into two types 'k'-type (e.g. sand roughness) and 'd'-type (e.g. regular roughness strips). In the present study, 'k'-type roughness is examined, and the roughness length k_S is often called the sand roughness. For a given roughness, this is the size of uniform sand-grains which would induce the same wall shear stress under similar flow conditions. Figure 2.2 shows Nikuradse's (see Yalin 1977) plot of B_S as a function of ($U_* k_s / \nu$) indicating the dependence of B_S on the roughness regime of the flow. For fully rough flow when $U_* k_s / \nu > 70$, B_S has a constant value ~ 8.5.

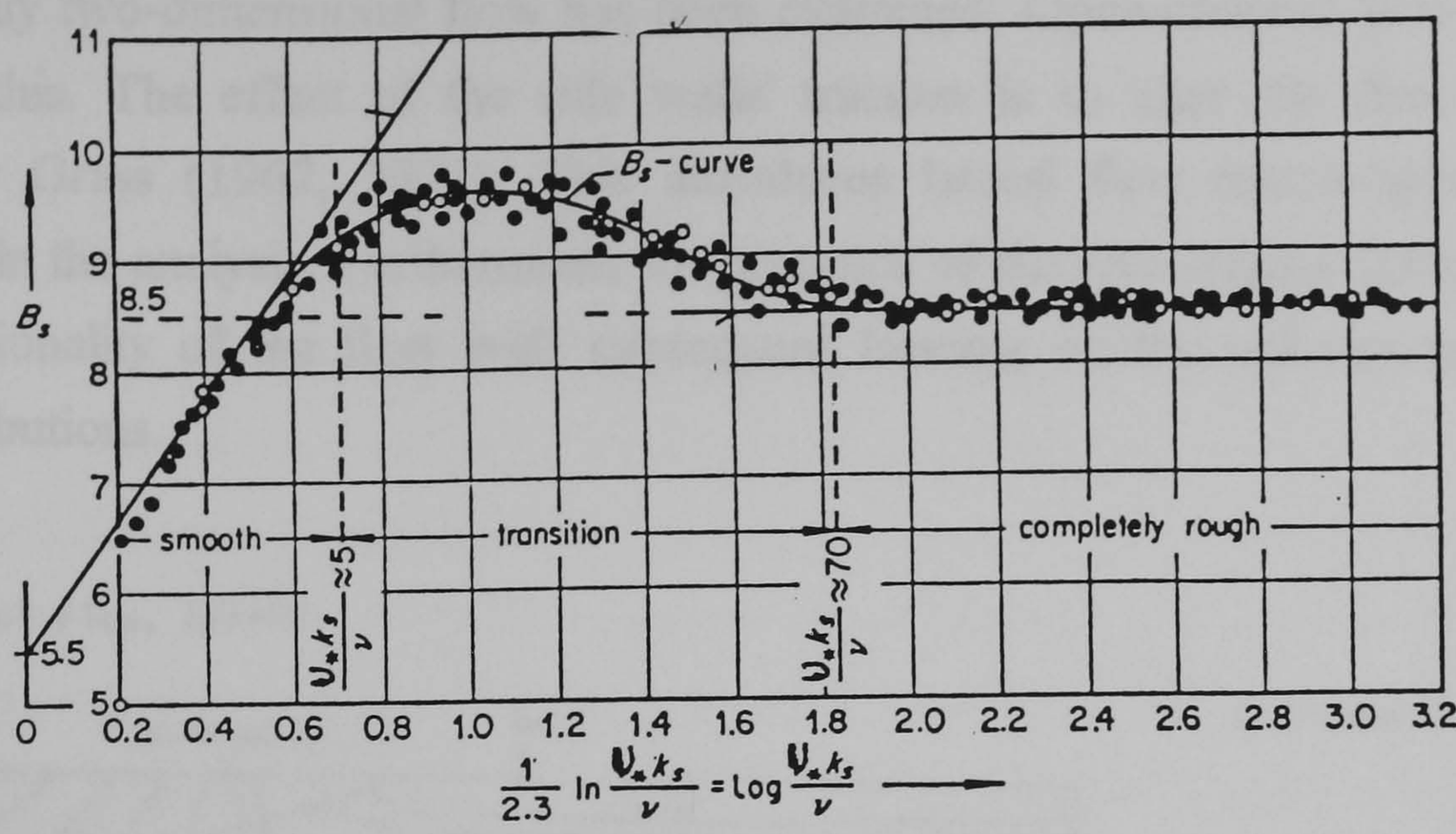

Figure 2.2 B_S versus ($U*k_S/\nu$) (After Yalin 1977)

The problem of determining the origin (y = 0) for the velocity profile (at which U = 0) has been studied extensively, most notably by Perry *et al* (1969), Grass (1971) Kamphuis (1974), and Jackson (1981). By noting that the presence of roughness leads to a displacement of the velocity profile, y in Eqn 2.28 is then replaced by (y - Δy), where Δy is the displacement thickness - the amount of shift the velocity profile undergoes due to the roughness (see Figure 2.3). It is equivalent to the height at which the mean drag of the roughness elements equals the wall shear stress. Although strongly dependent on the density of the roughness elements' distribution, Δy is usually taken to be 0.3 times the roughness height.

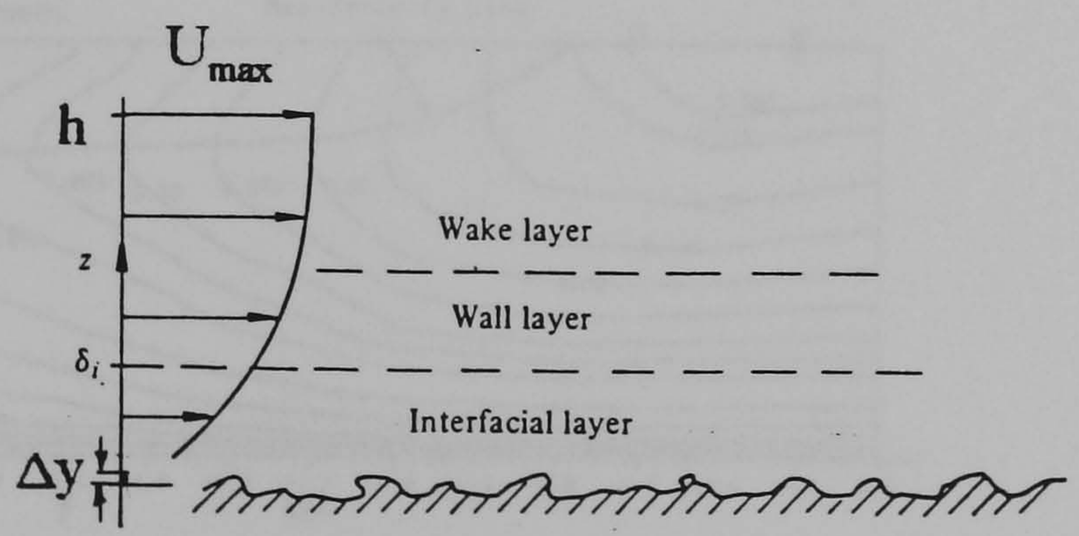

Figure 2.3 Regions of the Rough Wall Flow (not to scale).

Thus far, only two-dimensional flow has been examined. Open-channel flow represents a departure from this. The effect of the side walls' traction is to alter the flow structure as demonstrated by Grass (1967, 1971). This introduces lateral flow inhomogeneity hitherto unaccounted for in the analysis. Furthermore, the presence of the free surface further reinforces the three-dimensionality of the flow with subsequent bearing on the velocity and boundary shear stress distributions.

(a) Open Channel Flow, B/h=10

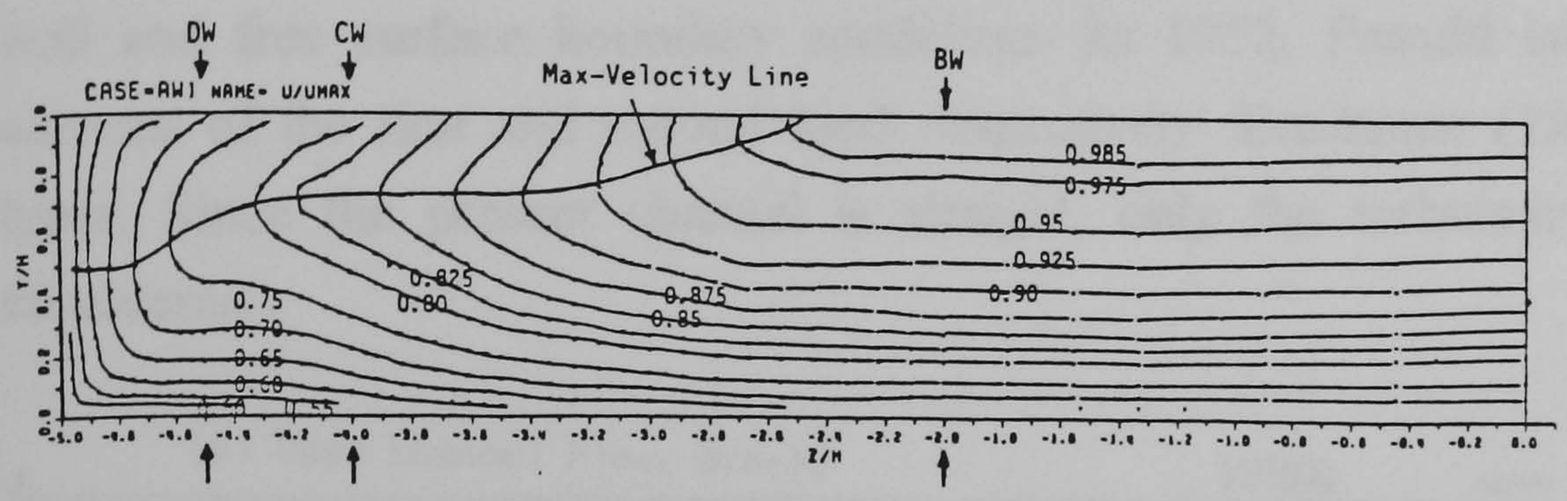

(a') Duct Flow, B/h=10

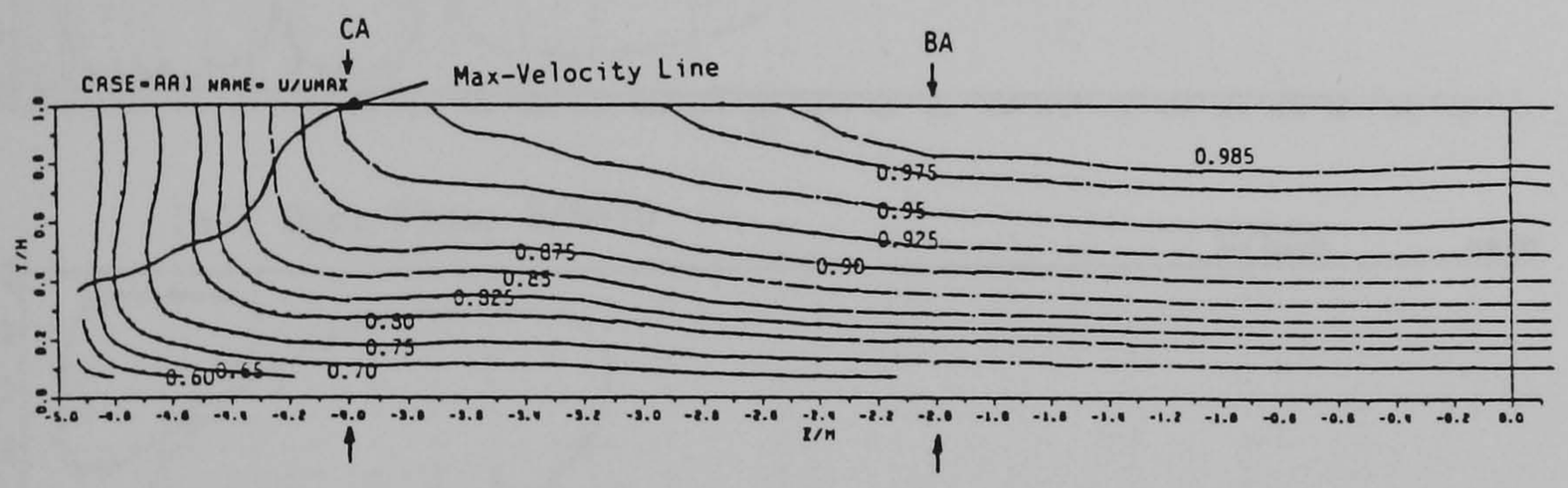

(b) Open Channel Flow, B/h=6

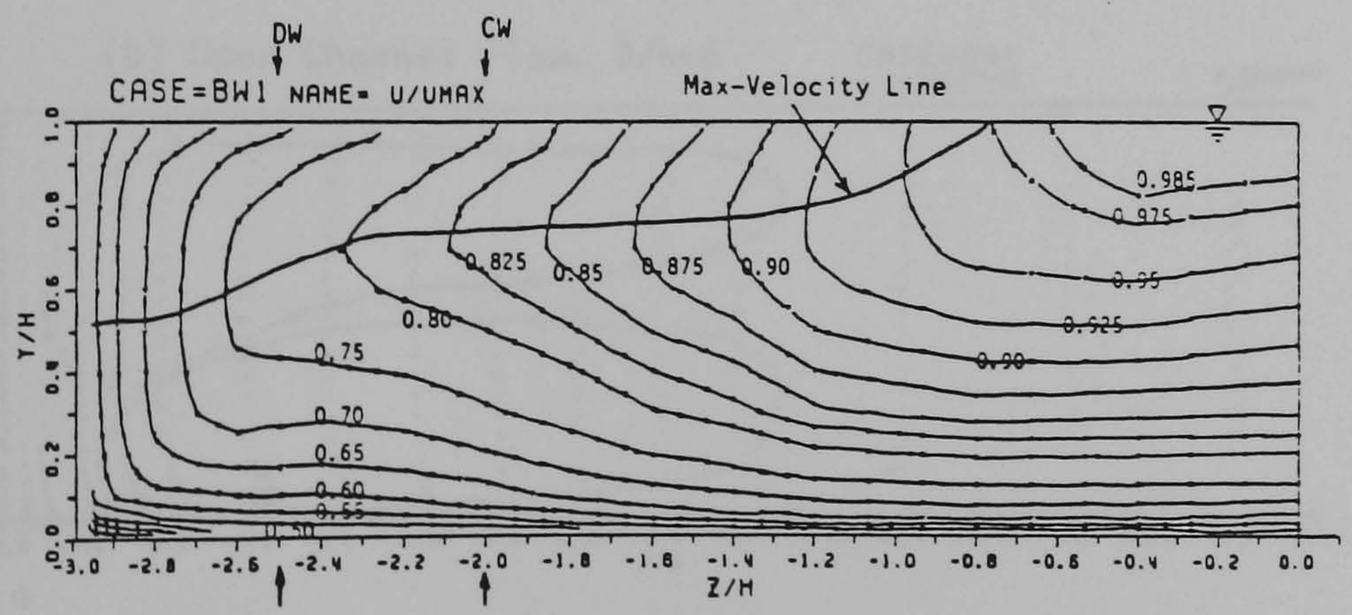

(c) Open Channel, B/h=2

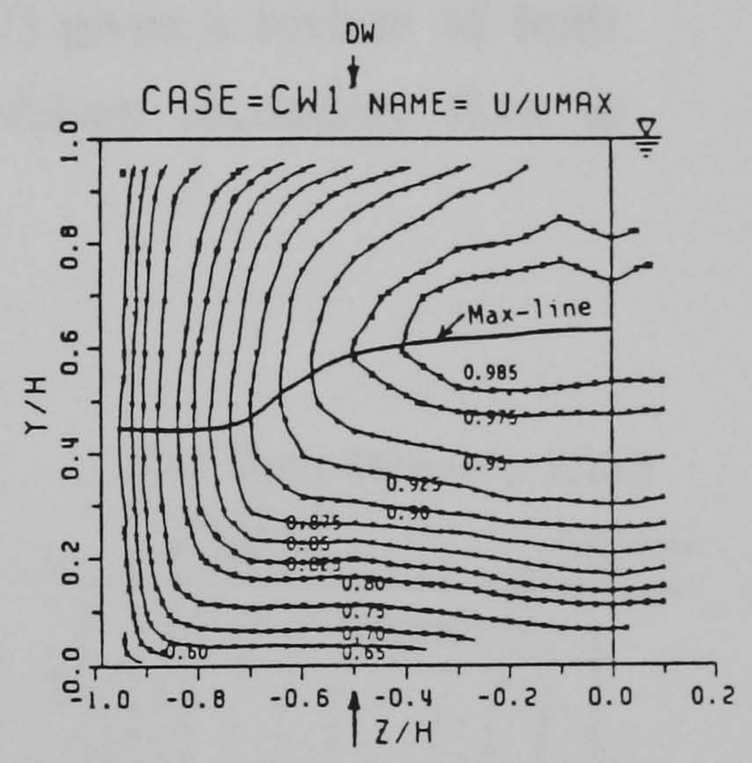

(d) Open Channel, B/h=1

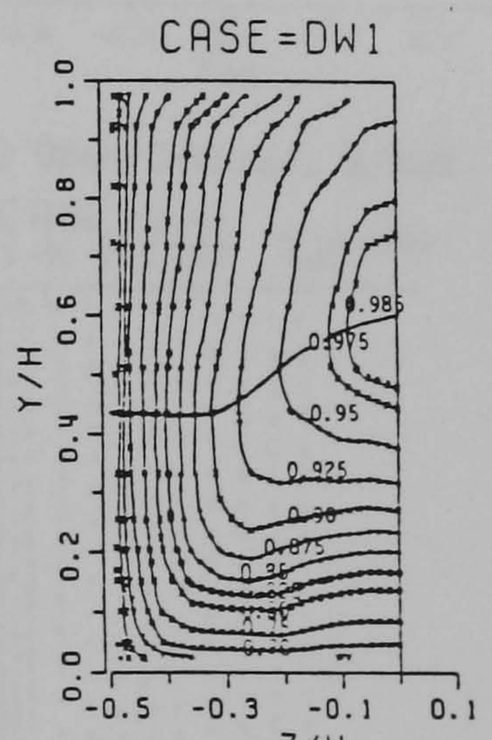

Figure 2.4 (a-d) Mean Velocity Distributions (U/U_{max}): Duct and Open Channel Flow (Nezu and Rodi 1985)

2.4.4 Secondary Flow

Secondary flow is the additional mean flow in the plane perpendicular to the primary longitudinal (x_1 or x) direction whose existence was first noted by Nikuradse. He predicted - and was subsequently proved right (e.g. Einstein and Li 1958, and Leutheusser 1963) - that this flow seems to have a substantial effect on the mean longitudinal flow and the boundary shear stresses. Secondary flow results, firstly, from the action of centrifugal forces in curved channels and meandering rivers; and secondly, from anisotropy of the turbulence imposed by the rigid wall and free surface boundary conditions. In 1952, Prandtl labelled these 'the secondary currents of the first and second kind' respectively. Bradshaw (1987) gives a review of both types. Since the present channel is straight, only the turbulence-driven secondary flow is considered.

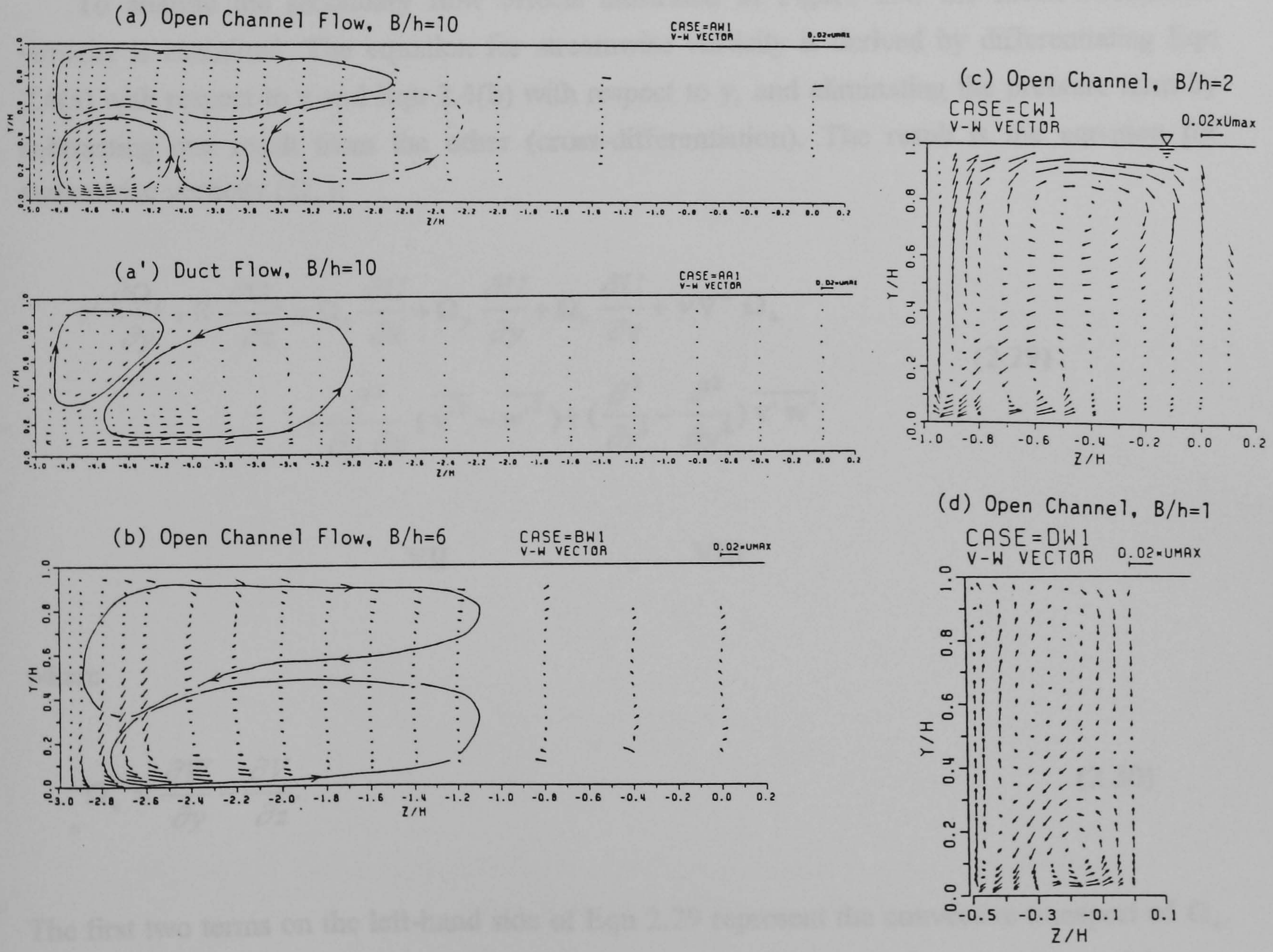

Figure 2.5 (a-d) Secondary Currents: Duct and Open Channel Flow - As in Fig. 2.4 (Nezu and Rodi 1985)

Figures 2.4(a-d) illustrate the effect of the secondary flow on primary mean velocity in open channels due to Nezu and Rodi (1985). In these figures, the contour lines join points of equal velocity. The contours bulge towards the side-walls and corner zone. This is due to the movement of high-momentum fluid from the channel centre towards the corner. The plotted secondary flow vectors in Figures 2.5(a-d) do indeed show a general movement of fluid into the corners.

The general lowering of the velocity maximum away from the free surface is due to the presence of the free surface itself. Comparisons with the duct flow contours illustrates this. This velocity 'dip' is also indirectly caused by the secondary flow - as illustrated in the flow chart of Figure 2.6.

To analyse the secondary flow effects illustrated in Figure 2.4, the mean streamwise vorticity is examined. The equation for streamwise vorticity is derived by differentiating Eqn 2.4(a) with respect to z and Eqn 2.4(b) with respect to y, and eliminating the pressure term by subtracting one result from the other (cross-differentiation). The result is the equation for streamwise vorticity (Ω_x):

$$V\frac{\partial \Omega_x}{\partial y}+W\frac{\partial \Omega_x}{\partial z}=\Omega_x\frac{\partial U}{\partial x}+\Omega_y\frac{\partial U}{\partial y}+\Omega_z\frac{\partial U}{\partial z}+\nu\nabla^2\,\Omega_x$$
$$+\frac{\partial^2}{\partial y\,\partial z}(\overline{v'^2}-\overline{w'^2})+(\frac{\partial^2}{\partial z^2}-\frac{\partial^2}{\partial y^2})\overline{v'w'} \qquad (2.29)$$

VII VIII

where

$$\Omega_x=\frac{\partial W}{\partial y}-\frac{\partial V}{\partial z}. \qquad (2.30)$$

The first two terms on the left-hand side of Eqn 2.29 represent the convective transport of Ω_x. The first three terms on the right-hand side represent the generation of streamwise vorticity as a result of curved longitudinal mean streamlines. They are usually found in both laminar and turbulent flows in flows with longitudinal curvature, and are thus neglected in the present

production of Ω_x by the anisotropy of the normal Reynolds stresses in the plane perpendicular to the longitudinal direction (x). Term VIII suppresses the generation of secondary flows. Nezu and Nakagawa (1984) experimentally verified the roles of terms VII and VIII, whilst Demuren and Rodi (1984) verified them numerically.

By noting that the terms of Eqn 2.29 are at least and order of magnitude smaller than terms in equations for Ω_y and Ω_z, Gessner (1973) deduced that the anisotrpoy of the normal Reynolds stresses ($\overline{v'^2} - \overline{w'^2}$) does not greatly affect secondary flow generation. Generation, he inferred, must depend on the transverse gradients of the Reynolds stresses. Gessner's analysis, while accurate, is only part of the description of the secondary flow generation mechanism. Figure 2.6, due to Nezu and Nakagawa (1993), illustrates the complexity of the various processes associated with secondary flow. It shows that the anisotropy ($\overline{v'^2} - \overline{w'^2}$) affects the Reynolds stress $\overline{v'w'}$ which leads to secondary flow according to Eqn 2.29. As the secondary

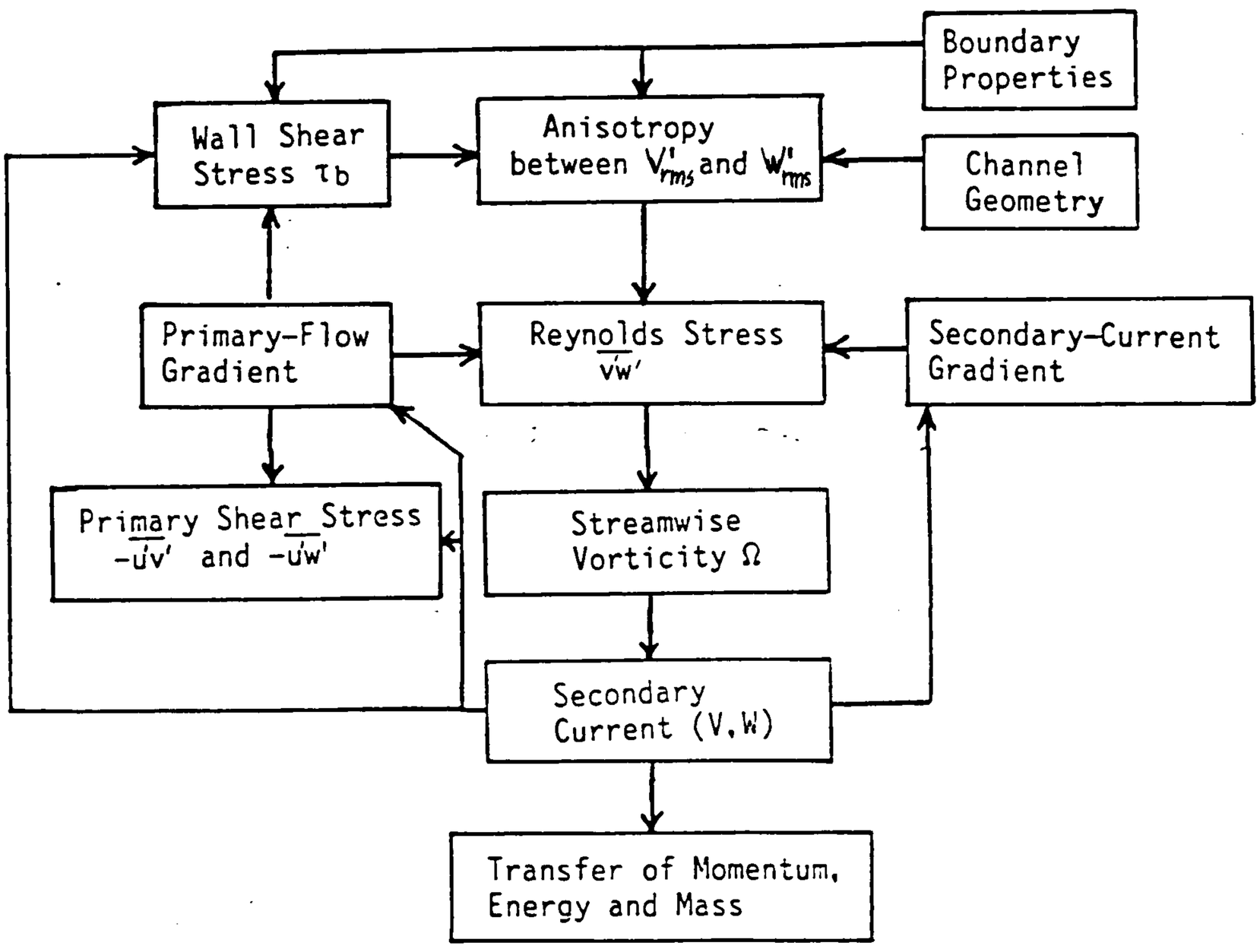

Figure 2.6 Generation Mechanism of Turbulence-driven Secondary Flow (After Nezu and Nakagawa 1993)

currents become established, they extract momentum from the primary mean velocity U and affect its distribution. This in turn directly influences the shear stress distribution at the bed (τ_b). Indeed variations in τ_b are known (Columbini 1993) to increase the anisotropy ($\overline{v'^2} - \overline{w'^2}$) and

thus further increase secondary flow generation. Launder and Ying (1972) noted that the magnitude of $(\overline{v'^2} - \overline{w'^2})$ normalised with U_* is constant for different flow types.

The complex inter-dependence of secondary flow and boundary shear stress distribution has been analysed in phenomenological models of Eqn 2.29, starting with Perkins (1970). His work, followed on by Townsend (1976) and Gerard (1978), was aimed at deriving a universal function for the vorticity generation term $(\overline{v'^2} - \overline{w'^2})$ in the form

$$\frac{\overline{w'^2} - \overline{v'^2}}{U_*^2} = \text{fun.}(y/L) \sim \alpha_I \frac{\overline{-u'v'}}{U_*^2} \qquad (2.31)$$

where L is a characteristic length at which $\overline{v'^2} = \overline{w'^2}$, and is approximately equal to the flow depth (h). α_I = an empirical constant ~ 1. U_* is the local shear velocity at the point of the wall nearest to the point of consideration. Perkins concluded that any lateral perturbations of L or U_* affect the production term VII of Eqn 2.29. Therefore any perturbation of L, such as the lateral variation of the geometry, results in the production of secondary flow. This is the self-perpetuating mechanism by which sand ridges are formed in channels with mobile beds.

On the other hand, Gerard (1978) also derived an expression for $(\overline{v'^2} - \overline{w'^2})/U_*^2$ by assuming, *a priori*, a sinusoidal lateral variation of τ_b (or U_*). It follows from the results of Perkins (1970) and Townsend (1976) in which the boundary shear stress increases in the region of secondary currents' downflow and decrease in the region of upflow. Knight and Patel's (1985) results and analysis also show this relationship. However, this is an inadequate model since its derivation does not take into account the effects of the side wall, the free-surface, and bed roughness. It is purely empirical, and has to be applied with caution to other cross-sectional shapes.

The present study seeks to investigate the type of link between boundary shear and the secondary flow pattern without *a priori* assumptions. The geometry effect on the generation mechanism, as shown in Figure 2.6, is accounted for by analysing the effect of lateral wall curvature, and the presence of the bed/wall corner on the mean and turbulence quantities. The role of the free-surface and bed roughness on secondary flow (and hence boundary shear), is also accounted for. The generation term $(\overline{v'^2} - \overline{w'^2})$ is computed accurately by direct computation of all the Reynolds stress components, τ_{ij} using a non-linear form of τ_{ij} (Eqn 2.8) in the two-equation k-ε model (Baker and Orzechowski 1983, Speziale 1987, 1991) - see Section 3.4. Naot and Rodi (1982), and Demuren and Rodi (1984) used more complex Reynolds closures to compute the components. Nonetheless, it is apparent that the secondary flow patterns of open-channel flow need to be modelled accurately in order to produce a realistic distribution of the primary velocity, and the boundary shear stress.

2.4.4 Coherent Structures

Experimental studies (e.g. Grass 1967, 1971, Kline *et al* 1967, Saga *et al* 1991) have revealed the existence of large eddy structures termed coherent structures. In his 'Attached Eddy Hypothesis', Townsend (1976) refers to them as energy-carrying eddies attached to the wall. They are thought to originate from the instabilities of the viscous sub-layer (Robinson 1991), and develop into large eddies spanning and affecting the whole depth of the boundary layer (Perry and Chong 1982) as they are swept along by the burst-cycles generation mechanisms of the inner wall zone (Nezu 1977, Smith *et al* 1991, Nezu and Nakagawa 1993). Their life-span is thought to approach that of the large energy-carrying eddies of the turbulence.

Several investigators have linked the production of Reynolds stresses in the near-wall zone to the varying stages of their existence (Robinson 1991). However how the burst sequence and evolution of these structures lead to the logarithmic mean profile is not known (Perry and Chong 1982, Smith *et al* 1991). This has lead to a number of imperfect models (e.g. Perry *et al* 1991), which attempt to use coherent structures to model the near wall mean flow.

It is clear that the coherent structure approach to flow modelling is more relevant to modelling flows where geometric effects are substantial than existing Reynolds-averaged turbulence models (see Section 3.2). However, for the present study, it is felt that they are not sufficiently developed enough to enable quantitative predictions of the near-wall zone. They can only be used to qualitatively describe the flow structure near the wall (e.g. Saga *et al* 1991) as in Chapter 6.

2.5 Boundary Shear Stress

To complete this review of the governing laws for open-channel flow, it is appropriate to review previous methods of determining local boundary shear stresses to be compared to the average shear stress value given by

$$\overline{\tau_o} = \rho g R S_f \qquad (2.32)$$

where g = gravitational acceleration, R = the hydraulic radius = the ratio of the cross-sectional area (A) to the wetted perimeter (P); and S_f = energy gradient which equals the bed slope (S_o) in uniform flow. The slope S_f reflects the loss of mean fluid energy to friction induced by the channel boundary. Eqn 2.32 is obtained by balancing the net effect of gravity on the fluid with an equal and opposite 'tractive force' exerted by the fluid at the channel boundary. Chow (1959) notes that du Boys was the first to derive this concept.

Replogle (1964), and Hoohlo (1991) give a detailed review of methods based on the usage of universal velocity distributions Eqns 2.14, 2.21 and 2.26 to determine the local boundary shear stresses. These will hereafter be called velocity gradient methods because they rely on calculating the velocity gradient near the wall from measured profiles. They are semi-empirical in nature. Direct experimental measurement of boundary shear stresses have been undertaken by practitioners such as Ghosh and Roy (1970), Knight (1981), Knight *et al.*(1984), and Knight *et al.*(1994).

2.5.1 Boundary Shear from Velocity Distribution

Of the velocity gradient methods, the most prominent is that of using Eqn 2.21 for the smooth boundary - and Eqn 2.27 for rough boundaries - at two distances from the wall to obtain the shear velocity at that cross-section from the relation (also see El-Zaemey 1991)

$$\frac{U_1 - U_2}{U_*} = \frac{1}{\kappa}\ln(\frac{y_1}{y_2}). \qquad (2.33)$$

Several difficulties with using Eqn 2.33 have to be pointed out. Its usage relies on the accurate determination of the measurement points which is difficult when the boundary is rough - as mentioned in the discussion of Eqn 2.28. Secondly, the validity of applying the inner law to flow points that probably fall into the outer-zone, as can often be the case since U_* is unknown, is questionable. Furthermore, Eqns 2.21 and 2.28 have been shown to be strictly applicable to two-dimensional boundary layers whereas open channel flow is inherently three-dimensional. It is thus no surprise that there is a wide discrepancy in boundary shear values calculated by gradient methods akin to Eqn 2.33 as concluded by Hoohlo (1991). Therefore, Eqn 2.33-type formulae may be used merely to indicate the level of boundary shear stresses.

2.5.2 Friction Laws in Open-Channel Flow

As a result of the inapplicability of velocity gradient methods, validation of the boundary shear stress results of the numerical model of Chapter 7 will lean on comparing computed and experimentally-determined values of two coefficients of friction C_f, and λ. Validation also uses what is termed the shear force.

Friction Factors

Firstly, C_f, the ratio of the boundary shear stress and the maximum dynamic pressure, is given by

$$C_f = \frac{\tau_o}{1/2\,\rho U_{max}^2} = 2(\frac{U_*}{U_{max}^2})^2 \qquad (2.34)$$

where, from Eqn 2.32,

$$\tau_o = \rho U_*^2, \qquad (2.35)$$

and that U_{max} is the maximum velocity (on the profile) at the point of consideration. This definition of C_f follows from that derived for two-dimensional boundary layers. It thus poses the question of whether it is truly applicable to open channel flows.

The Darcy-Weisbach friction factor (λ) is the constant of proportionality that links the energy slope (S_f) to the bulk mean (i.e. averaged over the cross-section) velocity head ($U_m^2/2g$) such that

$$\lambda = \frac{8gRS_f}{U_m^2}. \tag{2.36}$$

Eqn 2.36 defines λ as a bulk flow parameter which cannot be used to determine detailed shear stress distribution across the boundary. However, in channels with a roughened bed, the Vanoni-Brooks separation technique, detailed by Alvarez-Hernandez (1990), is used to determine values of λ for the bed and wall - λ_b and λ_w respectively. This is done by assuming that in a channel there are independent zones, some in which the bed's traction acts, and others in which the traction of the wall acts. These zones all move at the bulk velocity U_m to avoid shearing between them, and have respective friction factors λ_b and λ_w. The equivalent sand friction factor (λ_s) is given by the relation

$$\lambda_s = \frac{P_b\lambda_b + P_w\lambda_w}{P_b + P_w}, \tag{2.37}$$

where P_b = wetted perimeter for the bed, and P_w = wetted perimeter for the side-walls. Comparisons of these factors in flows studied by experimental measurement, with those of computed flows, will be made in Chapters 6 and 8 in order to indicate the accuracy of the computational model.

Shear Force

The shear force for a given section of the boundary is the traction exerted by the said boundary section on the fluid. In open-channel flow, it is used to determine the relative contributions of the bed and walls to the total traction - SF_b and SF_w respectively. Gosh and Roy (1970), Knight (1981), and Knight *et al.*(1984) studied friction laws in rectangular

channels, and Knight *et al.*(1994) in trapezoidal channels. Their studies concentrated mainly on the direct measurement of boundary shear using Preston tubes (Knight and Patel 1985).

The studies are aimed at deriving semi-empirical laws of how the total boundary shear force is separated into its wall and bed components

$$\tau_s = \frac{P_b \tau_b + P_w \tau_w}{P_b + P_w}, \tag{2.38}$$

where τ_b = average boundary shear over the bed, and τ_w = average boundary shear for the side-walls. τ_s is the cross-sectional average boundary shear stress, Eqn 2.35, for channels with rough beds. Based on this relation, the separation of shear forces leads to the expression

$$SF_T = SF_b + SF_w. \tag{2.39}$$

where SF_T is the total tractive force per unit length of the channel.

Figure 2.7 gives the lateral boundary distribution measured by various practitioners quoted by Nezu and Nakagawa (1993). Nezu and Rodi (1985), and Steffler *et al* (1985) presented similar measured open-channel distributions. It shows a clear difference in boundary shear distributions ($\tau_b / \overline{\tau_o}$) in open- and closed-channel flows. The maximum shear stress in open channel flow occurs at or near the channel centre. Also, for open-channel flow, a local minimum and maximum occur before the stress dips to a minimum ($\tau_b / \overline{\tau_o} \sim 0.8$) near the corner. This distribution can be accounted for by noting the coincidence of $\tau_b / \overline{\tau_o}$ minima and maxima respectively with upflow and downflow regions of secondary flow cells. Although, unlike with rectangular ducts, the present channel does not have a right-angled corner, a stress distribution similar to that Figure 2.7 is to be expected. This is tested in computations presented in Chapter 8.

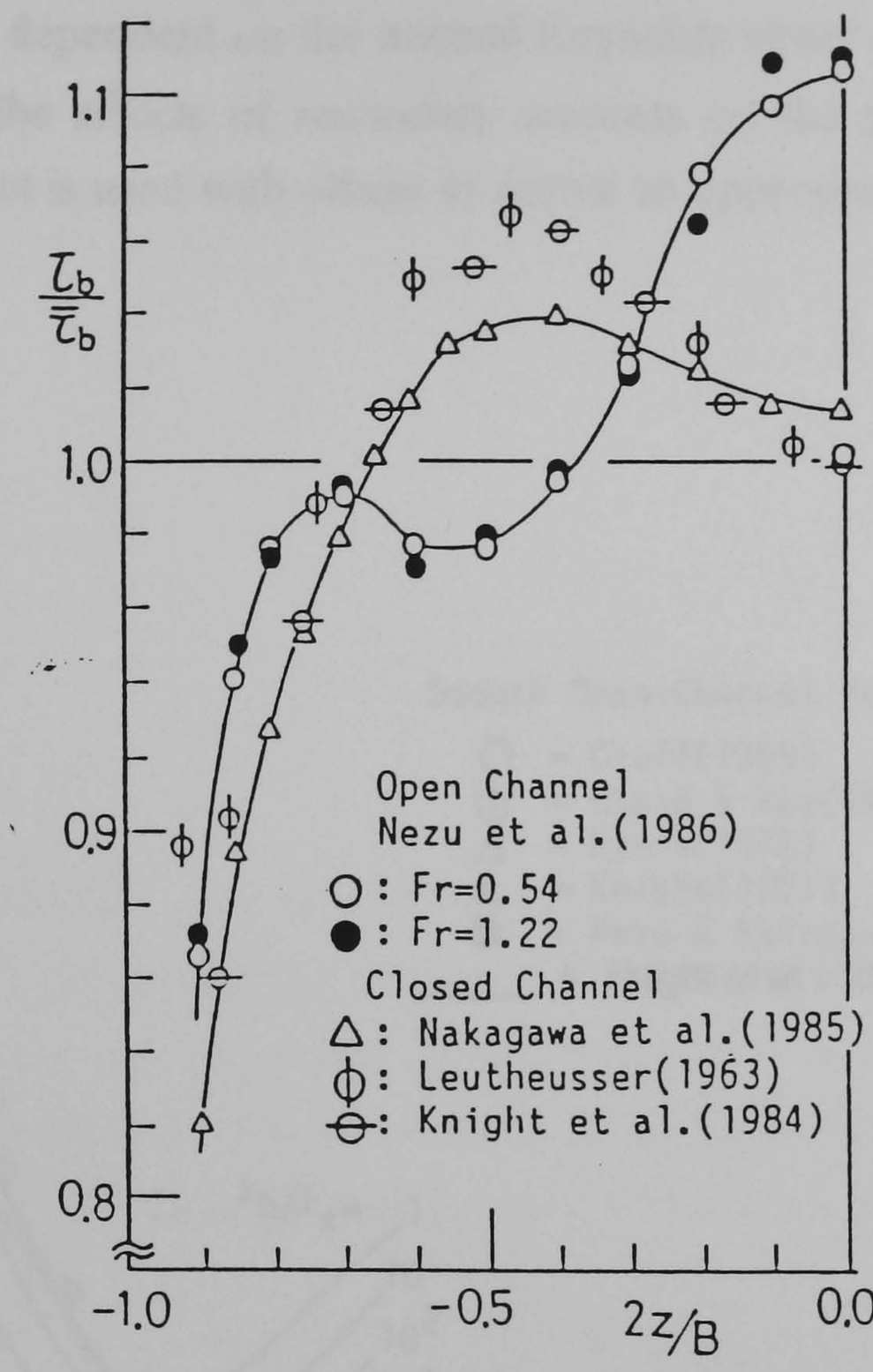

Figure 2.7. Boundary Shear Distribution. Open-Channel and Closed Rectangular Ducts (After Nezu and Nakagawa 1993)

Lastly, the separation of the side-wall and bed friction forces by integrating local shear distributions like those of Figure 2.7 for the wall and for beds gives a clear indication of the role of shape in the form of aspect ratio (α = B/h). Figure 2.8, due to Knight *et al* (1984), indicates this. A channel is said to be narrow if α is less than a critical value (approximately 5.0; Nezu and Nakagawa 1993), and wide otherwise. However a further problem is that the aspect ratio for the present channel can not be easily specified due to the curvature of the side walls. The results of the experimental study are, therefore, used in Chapter 8 to indicate the appropriate definition of α.

Nonetheless it is notable that, however defined, α indicates the nett effect of the rigid boundaries on the flow, through the boundary's influence on the normal shear stresses. As secondary flows are dependent on the normal Reynolds stress anisotropy (of Eqn 2.31), Figure 2.8 indirectly links the effects of secondary currents on the general distribution of boundary shear forces. This fact is used with others to derive an appropriate definition of α.

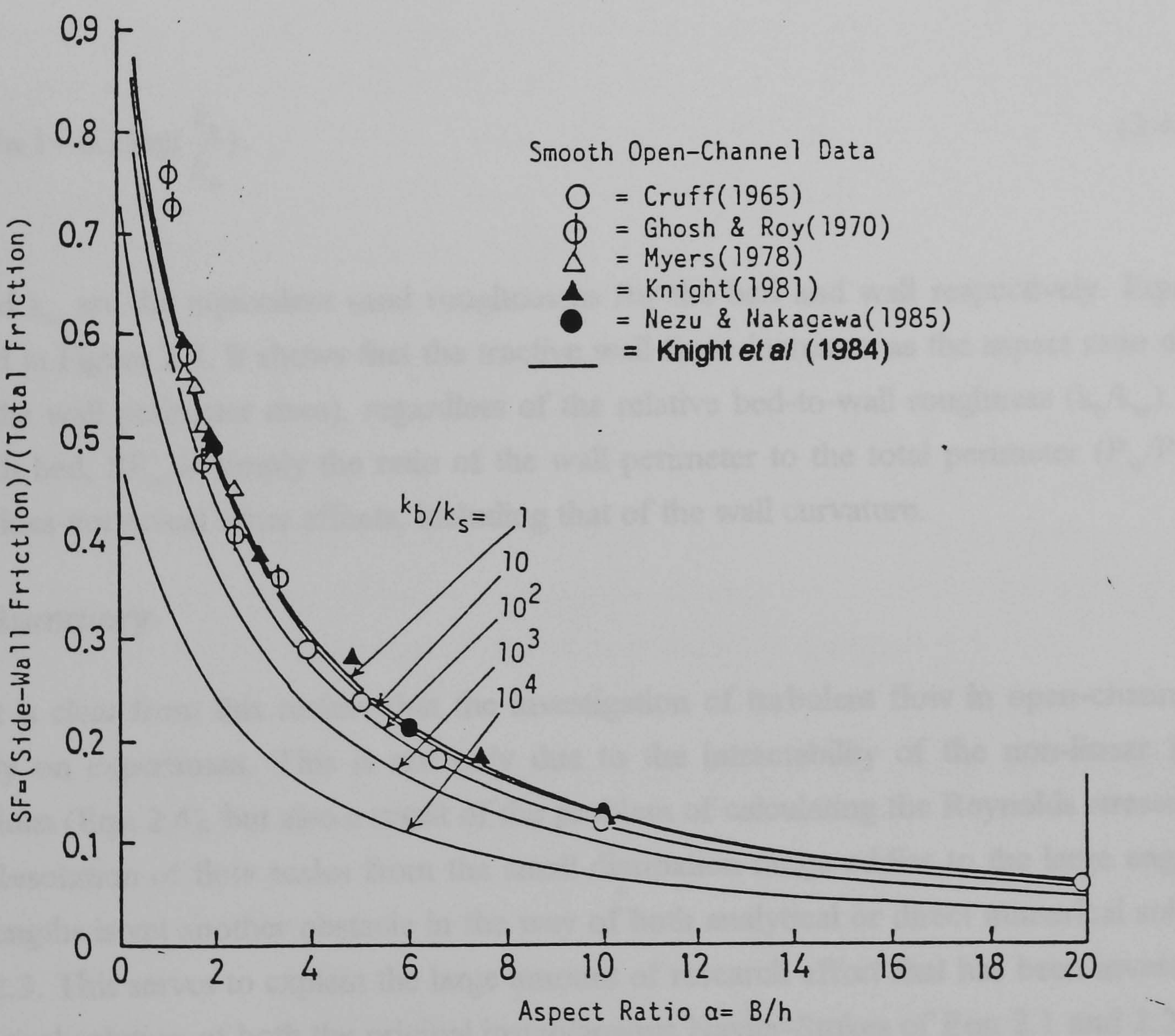

Figure 2.8 Side-Wall Friction Force *versus* Aspect Ratio(α = B/h). (After Knight *et al* 1984)

The empirical function, SF, expresses SF_w as a function of α given by Knight *et al* (1984). It is expressed as

$$SF = \frac{SF_w}{SF_T} = 0.01\exp(-3.23\log(\alpha+3)+6.146)\cdot E(\beta), \tag{2.40}$$

where

$$E(\beta) = \tanh(\pi\beta) - \frac{(\tanh(\pi\beta)-\beta)^2}{2}, \tag{2.41}$$

and

$$\beta \equiv 1 - 0.2\log(\frac{k_b}{k_w}). \tag{2.42}$$

k_b, and k_w are the equivalent sand roughnesses for the bed and wall respectively. Eqn 2.40 is plotted in Figure 2.8. It shows that the tractive wall force increases as the aspect ratio decreases (and the wall perimeter rises), regardless of the relative bed-to-wall roughness (k_b/k_w). For the smooth bed, SF_w is simply the ratio of the wall perimeter to the total perimeter (P_w/P) and as such does not reveal other effects, including that of the wall curvature.

2.6 Summary

It is clear from this review that the investigation of turbulent flow in open-channels leans heavily on experiment. This is not only due to the intractability of the non-linear Reynolds equations (Eqn 2.4), but also a result of the problem of calculating the Reynolds stresses in Eqn 2.3. Resolution of flow scales from the small dissipation-range eddies to the large engineering-size lengths is yet another obstacle in the way of both analytical or direct numerical solutions of Eqn 2.3. This serves to explain the large amount of research effort that has been invested in the numerical solution of both the original instantaneous Navier-Stokes of Eqn 2.1 and 2.2, and the Reynolds-averaged equations 2.3. These methods are reviewed in full in Chapter 3.

CHAPTER 3: MODELLING OF TURBULENT FLOW

3.1 Introduction

As stated in Chapter 2 the present flow is fully turbulent and the governing equations (Eqns 2.1 and 2.3) are non-linear and difficult to solve analytically. Recourse is then made to the modelling of the flow. Modelling falls into two categories: (a) direct solution with resolution of all the scales of flow; and (b) Reynolds-averaged modelling. Direct solution involves two routes; one which involves the solution of the instantaneous velocity field - termed Direct Numerical Simulation (DNS). Present computer capabilities imply that only low Reynolds number flows can be computed in this manner. With Large Eddy Simulations (LES), the second route, only the large scales of the flow (which require less spatial resolution) are solved, and the smaller scales are modelled by subgrid scale models. LES also require large amounts of resources, and can thus not be easily used in engineering-scale flows.

Rodi (1980), and Speziale (1991) give authoritative reviews of turbulence modelling based on Reynolds-averaging. Reynolds-stress closure, as this modelling is also called, is aimed at evaluating the Reynolds stresses which appear in Eqn 2.3. Numerous popular models are based on Boussinesq's eddy viscosity concept (introduced in sub-section 2.3.2). However, there is a second class of models in which the Reynolds stresses are evaluated by solving transport equations for the Reynolds stresses. These are introduced in sub-section 3.3.2.

The chosen turbulence model for the present study is the non-linear two-equation k-ε model. It is explained in Sections 3.3 and 3.4.

3.2 General Reynolds-Stress Closures

It is appropriate to introduce the concept of eddy-diffusivity at this stage. As with the eddy-viscosity concept, in which the transport of momentum by the turbulent fluctuations is assumed proportional to the velocity gradient (see Eqn 2.8), it is assumed that the diffusive transport of any quantity ϕ (e.g. heat, enthalpy, mass, turbulent kinetic energy, or other turbulence species) occurs down the spatial gradient of ϕ. This is termed the gradient diffusion hypothesis and is expressed as

$$-\overline{u_j'\phi} = \Gamma_\phi \frac{\partial \phi}{\partial x_j} \tag{3.1}$$

where Γ_ϕ is the turbulent diffusivity of the quantity ϕ. The diffusivity is linked analogously to the eddy viscosity (ν_t) by the expression

$$\Gamma_\phi = \frac{\nu_t}{\sigma_t} \tag{3.2}$$

in which σ_t = the Prandtl number in heat and turbulence transport; and the Schmidt number for mass transport. This formulation simplifies the expression for the diffusive properties of the turbulence, and will be seen to be quite amenable to numerical formulation and computation in Chapter 4.

3.2.1 Zero-Equation Models

Zero-equation models are those in which closure is achieved without the solution of transport equations. Prandtl's mixing length hypothesis, alluded to in Eqn 2.25, is based on the assumption that a velocity fluctuation υ is proportional to the gradient $\partial U/\partial y$ (in two-dimensional flow) such that: $\upsilon = l\, \partial U/\partial y$, where l = the mixing length over which a pocket of fluid does not loose momentum. It is thus a characteristic length of the large scale flow at a point; in as much as υ is the velocity scale. The eddy viscosity of the flow is equal to the product of υ and l :

$$\nu_t = l^2 \left| \frac{\partial U}{\partial y} \right|. \tag{3.3}$$

Therefore, closure for primary Reynolds stress $\overline{u'v'}$ (= $\nu_t\, \partial U/\partial y$) is achieved, as in Eqn 2.25, through the expression

$$-\overline{u'v'} = l^2 \left| \frac{\partial U}{\partial y} \right| \frac{\partial U}{\partial y}. \tag{2.25a}$$

The problem now becomes that of specifying l. Firstly, Prandtl specified that $l = \kappa y$ (κ = von Karman constant = 0.4) near the wall for flows bounded by a rigid boundary, where y is the distance to the wall. Nikuradse (Schlichting 1968) later derived an empirical relation

$$\frac{l}{h} = 0.14 - 0.08(1-\frac{y}{h})^2 - 0.06(1-\frac{y}{h})^4 \qquad (3.4)$$

which can be approximated to κy in the fully turbulent zone near the wall (y/h < 0.2). Closer to the wall where viscous effects dominate, Van Driest applied a damping of l such that

$$l = \kappa y[1-\exp(-\frac{yU_*}{\nu A})] \qquad (3.5)$$

where A = empirical constant = 26, and U_* = the shear velocity.

Prandtl's expression for l, together with Eqns 3.4 and 3.5, were derived for two-dimensional boundary layer flow and are thus unsuitable for flows in more complex geometries. For example, in Eqn 3.5 U_* cannot be easily specified in flows near corners where more than one wall influences the flow. Therefore, in general, mixing length models are not suitable for layers with high convective-diffusive transport, and flows wherein the mixing length is difficult to specify. Instead their role is limited to that of checking predicted flow in zones away from the corners.

3.2.2 One-Equation Models

To account for the transport of turbulent quantities, a model which determines the fluctuating velocity scale from a transport equation is employed. The eddy-viscosity concept was invoked such that ν_t is expressed as a product of the large-scale turbulent motion velocity scale (typified by $\sqrt{k}$), and the corresponding length scale (L):

$$\nu_t = c_\mu' \sqrt{k} L \qquad (3.6)$$

where c_μ' is an empirical constant. The turbulent kinetic energy, k, is determined by solving its transport equation, Eqn 2.9,

$$U_i \frac{\partial k}{\partial x_i} = \frac{\partial}{\partial x_i}[\overline{u_i' (\frac{u_j' u_j'}{2} + \frac{p'}{\rho})}] - \overline{u_i' u_j'} \frac{\partial U_i}{\partial x_j} - \nu \overline{\frac{\partial u_i'}{\partial x_j} \frac{\partial u_i'}{\partial x_j}} \qquad (2.9)$$

I II III IV

in its modelled form

$$U_i \frac{\partial k}{\partial x_i} = \frac{\partial}{\partial x_i}(\frac{\nu_t}{\sigma_k} \frac{\partial k}{\partial x_i}) - \nu_t (\frac{\partial U_i}{\partial x_j} + \frac{\partial U_j}{\partial x_i}) \frac{\partial U_i}{\partial x_j} - c_D \frac{k^{3/2}}{L}. \qquad (3.7)$$

I II III IV

In Eqn 3.7 term I represents the convective transport of k, term II is the gradient diffusion model of the diffusive term in Eqn 2.9 (based on the eddy diffusivity concept of Eqns 3.1 and 3.2), term III is the production term of k (the modelled form in Eqn 3.7 based on the eddy viscosity concept), and term IV represents the isotropic dissipation rate of k - discussed further in sub-section 3.2.2 below. c_D is an empirical constant linked to c_μ' by the expression $c_D\ c_\mu' = 0.3$ for most shear flows.

Eqns 3.6 and 3.7 lead to the specification of the Reynolds stresses if the length scale, L, is known. In fact we are justified to use a macro-scale L to model the dissipation ε (which occurs at the small flow scales) purely on the assumption that the dissipated energy originates from the large scales and cascades down the eddy sizes, and is therefore determined by the macro-length scale. Semi-empirical methods of determining L (see Rodi 1980) suffer from being complex, and non-reflective of the convective and diffusive flow processes. For example in zones of high dissipation, small-scale eddies are destroyed, which implies an increase in the eddy size (and L itself). Semi-empirical models cannot predict this effect. A transport model for L is thus the next best solution.

The two equation k-ε model solves a second transport equation (Eqn 3.18, discussed later in Section 3.3.1) for the rate of dissipation

$$\varepsilon = c_D \frac{k^{3/2}}{L} \tag{3.8}$$

from which the eddy viscosity is determined (according to Eqns 3.6 and 3.8)

$$\nu_t = c_\mu \frac{k^2}{\varepsilon}. \tag{3.9}$$

The empirical constant c_μ is taken as 0.09. This is the preferred turbulence model in the present study. It is introduced in full in Sections 3.3 and 3.4. However, prior to that, the closures based on the full transport equations for the Reynolds stresses, also called second-order models, are introduced.

3.2.2 Second-Order Models

In 1951 Rotta attempted a statistical treatment of turbulent shear flow. By mainly using Kolmogorov's statistical ideas from the 1940s, he proposed the now familiar transport equations for the Reynolds stress ($\tau_{ij} = \overline{u_i' u_j'}$) (see Daly and Harlow 1970, Hinze 1975, and Launder *et al* 1975).

Full Reynolds Stress Model (RSM)

The full Reynolds stress transport equation is given by (see Hinze 1975, Daly and Harlow 1970, and Speziale 1991)

$$\frac{\partial \tau_{ij}}{\partial t} + U_k \frac{\partial \tau_{ij}}{\partial x_k} = -\tau_{ik} \frac{\partial U_j}{\partial x_k} - \tau_{jk} \frac{\partial U_i}{\partial x_k} - \frac{\partial C_{ijk}}{\partial x_k} + P_{ij} - \varepsilon_{ij} + \nu \left(\frac{\partial^2 \tau_{ij}}{\partial x_k^2}\right) \tag{3.10}$$

where P_{ij} = the pressure-strain correlation, and C_{ijk}= the diffusion correlation (incorporating the diffusive transport by both the velocity and pressure fluctuations), both given respectively as

$$P_{ij} = \overline{p'(\frac{\partial u_i'}{\partial x_j} + \frac{\partial u_j'}{\partial x_i})} \tag{3.11}$$

$$C_{ijk} = \overline{u_i' u_j' u_k'} + \overline{p' u_i'} \delta_{jk} + \overline{p' u_i'} \delta_{ik}. \tag{3.12}$$

The terms on the left-hand side of Eqn 3.10 are the familiar rate of change, and convection respectively. The first two terms on the right-hand side are the Reynolds stress production terms; and the last represents the viscous destruction of the Reynolds stresses.

The dissipation rate of the turbulent kinetic energy, ε_{ij}, is embedded in Term IV of the kinetic energy transport equation (Eqn 2.9)

$$\overline{\nu u_i' \frac{\partial^2 u_i'}{\partial x_j^2}}.$$

It is given by

$$\varepsilon_{ij} = 2\nu \overline{\frac{\partial u_i'}{\partial x_k} \frac{\partial u_i'}{\partial x_k}}. \tag{3.13}$$

Its isotropic form, ε, is used in high turbulence Reynolds number flows, and is expressed as

$$\varepsilon = \frac{1}{2}\varepsilon_{ii} = \nu \overline{\frac{\partial u_i'}{\partial x_k} \frac{\partial u_i'}{\partial x_k}}. \tag{3.14}$$

This is achieved by assuming homogeneity and expanding Term IV of Eqn 2.9:

$$\overline{\nu u_i' \frac{\partial^2 u_i'}{\partial x_j^2}} = \nu \frac{\partial^2}{\partial x_j^2}\left(\frac{1}{2}\overline{u_i' u_i'}\right) - \nu \overline{\frac{\partial u_i}{\partial x_j}\frac{\partial u_i}{\partial x_j}} \tag{3.15}$$

Because it is simpler to use than the true form ε_{ij}, the scalar form is often preferred. Bradshaw and Perot (1993) used direct simulation data for the viscous sub-layer to show that the difference between the two is indeed negligibly small and ε can safely be used. As previously mentioned, ε is obtained from its transport equation given by

$$\begin{aligned}\frac{\partial \varepsilon}{\partial t} + U_k \frac{\partial \varepsilon}{\partial x_k} = {} & \nu \frac{\partial^2 \varepsilon}{\partial x_k \partial x_k} - 2\nu \frac{\partial U_i}{\partial x_k}\overline{\frac{\partial u_j'}{\partial x_j}\frac{\partial u_k'}{\partial x_j}} - 2\nu \frac{\partial U_i}{\partial x_k}\overline{\frac{\partial u_j'}{\partial x_i}\frac{\partial u_j'}{\partial x_k}} - 2\nu \frac{\partial^2 U_i}{\partial x_j \partial x_k}\overline{u_k' \frac{\partial u_i'}{\partial x_j}} \\ & - 2\nu \overline{\frac{\partial u_i'}{\partial x_k}\frac{\partial u_i'}{\partial x_m}\frac{\partial u_k'}{\partial x_m}} - \nu \frac{\partial}{\partial x_k}\overline{u_k' \frac{\partial u_i'}{\partial x_m}\frac{\partial u_i'}{\partial x_m}} - 2\nu \frac{\partial}{\partial x_k}\left(\overline{\frac{\partial p'}{\partial x_m}\frac{\partial u_k'}{\partial x_m}}\right) \\ & - 2\nu^2 \overline{\frac{\partial^2 u_i'}{\partial x_k \partial x_m}\frac{\partial^2 u_i'}{\partial x_k \partial x_m}}\end{aligned} \tag{3.16}$$

where the seven higher-order correlations on the right-hand side of Eqn 3.16 represent three physical phenomena. The first four terms indicate the production of ε, the next two terms give rise to the turbulent diffusion of ε, and the last term represents the turbulent destruction of ε. Eqn 3.16 was derived from the fluctuating vorticity transport equation since, in homogenous turbulence, the isotropic dissipation rate is equal to the square of the fluctuating vorticity (see Tennekes and Lumley 1970).

It is clear from Eqns 3.10 - 3.12, and 3.16 that solving for a second-order correlation (the Reynolds stress) yields third-order correlations which then need to be specified. Deriving and solving the transport equations for these third-order correlations would in turn give yet higher-order correlation terms - in an unending spiral. In response to this, modelled forms of Eqns 3.10 - 3.12 have been developed (Launder and Li 1994). Rodi (1976) also took the route towards simplifying the differential transport equations, Eqns. 3.10 - 3.12, into algebraic expressions - the Algebraic Stress Model (ASM).

The complexity of the stress and dissipation rate transport equations renders their solution expensive in computer resource terms. Furthermore, the unknown nature of the pressure-strain terms (Launder *et al* 1975, Lumley 1978), the inaccuracy of the diffusion term near solid walls (Launder and Tselepidakis 1988), and the need to specify the wall proximity functions (Launder and Li 1994) complicate the models still further. On the basis of these difficulties, the k-ε model is used in the present study.

3.3 The Standard Two-Equation k-ε Turbulence Model

It is worth noting at the outset that the standard two-equation k-ε turbulence model is limited by (a) their implicit assumption of the separation of flow scales as in molecular dynamics; (b) their neglect of non-local effects; (c) their inability to account for longitudinal streamline curvature; and (d) their inability to predict the anisotropy of the turbulence. Second-order models are able to predict (b) - (d). However, the computational effort required to solve the six stress-transport equations (of the second-order model), together with the momentum equations (Eqn 2.3), and the transport equation for the dissipation rate, is large. The k-ε model offers a cheaper alternative, especially since the non-local effects, and the anisotropy of the turbulence (in b and d above), can be accounted for by the use of non-linear k-ε models described in Section 3.4 below.

3.3.1 High Reynolds Number k-ε Models

The k-ε model was developed for zones of high Reynolds number, and was first developed by Kolmogorov in the 1940s. As Launder and Spalding (1974), Rodi (1980), and Bradshaw (1991) point out, the k-ε model belongs to a class of transport equations in which the transport equations for a general variable (Z)

$$Z = k^m L^n \tag{3.17}$$

is solved. Since k is known from its transport equation, L can be determined from Eqn 3.17. Several authors, (Bradshaw 1991), give examples of models with various m and n exponents. From Eqns 3.8 and 3.9, m = 3/2 and n = -1. As before, ε is determined from the modelled form of its transport equation Eqn 3.16

$$U_i \frac{\partial \varepsilon}{\partial x_i} = \frac{\partial}{\partial x_i}(\frac{\nu_t}{\sigma_\varepsilon} \frac{\partial \varepsilon}{\partial x_i}) + c_{1\varepsilon} \frac{\varepsilon}{k} P_K - c_{2\varepsilon} \frac{\varepsilon^2}{k} \qquad (3.18)$$

I II III IV

where, for the case of steady flow, the ∂/∂t term is omitted. Term I represents convective transport of ε; term II is the diffusion term represented by the gradient diffusion hypothesis of Eqn 3.1. In term III, P_k represents the kinetic energy production term of Eqns 2.9 and 3.7

$$P_K = \nu_t (\frac{\partial U_i}{\partial x_j} + \frac{\partial U_j}{\partial x_i}) \frac{\partial U_i}{\partial x_j}. \qquad (3.19)$$

Terms III and IV together represent the nett production of ε and have to be modelled together. The empirical constants $c_{1\varepsilon} = 1.44$, $c_{2\varepsilon} = 1.92$, and $\sigma_\varepsilon = 1.30$ have been determined from comparisons between numerical computation and grid turbulence results (Rodi 1980).

The complete k-ε model is thus expressed as

$$U_i \frac{\partial k}{\partial x_i} = \frac{\partial}{\partial x_i}(\frac{\nu_t}{\sigma_k} \frac{\partial k}{\partial x_i}) + \nu_t (\frac{\partial U_i}{\partial x_j} + \frac{\partial U_j}{\partial x_i}) \frac{\partial U_i}{\partial x_j} - \varepsilon \qquad (3.7)$$

$$U_i \frac{\partial \varepsilon}{\partial x_i} = \frac{\partial}{\partial x_i}(\frac{\nu_t}{\sigma_\varepsilon} \frac{\partial \varepsilon}{\partial x_i}) + c_{1\varepsilon} \frac{\varepsilon}{k} P_K - c_{2\varepsilon} \frac{\varepsilon^2}{k} \qquad (3.18)$$

$$\nu_t = c_\mu \frac{k^2}{\varepsilon}. \qquad (3.9)$$

The Reynolds stress is expressed as

$$\tau_{ij} = -\rho \overline{u_i' u_j'} = \rho \nu_t (\frac{\partial U_i}{\partial x_j} + \frac{\partial U_j}{\partial x_i}) - \frac{2}{3} \rho k \delta_{ij}. \qquad (3.20)$$

The last term on the right-hand side of Eqn 3.20 is introduced in order to ensure that $k = \frac{1}{2}\overline{u_i' u_i'}$ since the first term gives k = 0 as a result of the continuity equation ($\partial U_i/\partial x_i = 0$) in incompressible flow. It is equivalent to the pressure term in Eqn 2.8(b).

Cazalbou and Bradshaw (1993) re-evaluated the model constants from direct numerical simulation data at Stanford University. They found that c_μ is nearly constant for the most part of the wall zone in channel flows. For boundary layer flows the "Prandtl numbers" σ_k and σ_ε are affected by pressure-diffusion effects across the flow depth - especially in the intermittent zone (between the viscous layer and the logarithmic zone) of a boundary layer. They then concluded that the non-constant nature of the "Prandtl numbers" shows the need for an examination of the usage of the gradient-diffusion hypothesis to model the diffusive processes.

It can be seen from Eqn 3.20 that the formulation of the stress tensor is such that all the normal stresses are equal. In non-circular channels, this is not the case. In fact normal stress inequalities lead to secondary flows as discussed in sub-Section 2.4.4. As an improvement on this, non-linear forms of Eqn 3.20, which give the required normal-stress anisotropy, have been proposed by Speziale (1982, 1987) and Baker and Orzechowski (1983). They are introduced in Section 3.4 below.

3.3.2 Low Reynolds Number k-ε Models

Patel *et al* (1985) provide a review of the of k-ε models applied to low-Reynolds number flows - in the near wall region. They are used as a bridge between the fully turbulent (high Reynolds number) zones away from the wall, and the near-wall regions where viscosity effects are substantial. This enables the integration of the transport equations to the wall. Their main premise is that the damping functions for the ε transport equation are used. However, the empirical and rather arbitrary nature of these functions (Mansour *et al* 1989, and Bernard 1986) hampers the applicability of these models. Durbin (1991) went a step further and developed a model aimed at modelling the actual damping of the velocity fluctuations normal to the wall. This too, has limited application due to its dependence on damping functions. Low-Re models also require large computing resources in order to model the high velocity gradients in close to the wall.

In the present study the integration of the momentum, kinetic energy, and ε transport equations is not carried out to the wall, but to point at a distance away from the wall, and within the fully turbulent zone. Besides avoiding the use of near-wall damping functions, this approach also saves computation effort. The boundary conditions which are thus applied at these points, are described in Section 3.5 below.

3.4 The Non-linear k-ε Model

Lumley (1970) showed that away from solid walls - which influence the flow - and in fully developed flows, the turbulence shows non-linear (non Newtonian) behaviour similar to that of viscoelastic fluids. This can be demonstrated by the need for the expression for the stress, Eqns 2.8(b) and 3.20, to satisfy two principles derived from classical solid mechanics (see Truesdell and Noll 1965, and Chung 1988): (i) Material Frame Indifference (MFI), and (ii) Determinism.

3.4.1 Material Frame Indifference (MFI)

The principle of MFI states that, as Chung (1988) put it, *the material response is independent of the spatial frame of reference used.* Therefore the constitutive equations used to describe, for example the Reynolds stress, should be invariable under transformation of the observer. Lumley (1970) invoked this principle in order to model turbulence in rapidly rotating flows, wherein the turbulence is affected by the straining imposed by the rotation. However, the principle is not lost in non-rotating flows. Speziale (1982, 1987, 1991) applied it in order to ensure the wide applicability of the k-ε model, and for the fact that it results in normal stress anisotropy in non-circular channel flows.

3.4.2 Determinism

This means that the flow field at any point in time, is dependent on the state of other points at previous times. When used in modelling the Reynolds stress, it gives the turbulence a memory - a dependence of the flow field on previous (and non-local) states of the turbulence. This is absent in the standard linear k-ε model; with its linear stress/mean-strain relationship given by Eqn 3.20.

3.4.3 The Non-Linear Shear Stress Expression

Taking into account the principles of MFI and Determinism, Speziale (1987) derived a non-linear expression for the stress, which becomes a quadratic (rather than linear) function of the mean strain rate (S_{ij})

$$\tau_{ij} = \frac{2}{3}k\delta_{ij} - 2\nu_t\overline{S_{ij}} - 4c_D c_\mu^2 \frac{k^3}{\varepsilon^2}(\overline{S_{ik}}\,\overline{S_{kj}} - \frac{1}{3}\overline{S_{mn}}\,\overline{S_{mn}}\delta_{ij}) - 4c_E c_\mu^2 \frac{k^3}{\varepsilon^2}(\overline{\overline{S_{ij}}} - \frac{1}{3}\overline{\overline{S_{mm}}}\delta_{ij}) \tag{3.21}$$

where

$$\overline{\overline{S_{ij}}} = \frac{\partial \overline{S_{ij}}}{\partial t} + U_k \frac{\partial \overline{S_{ij}}}{\partial x_k} - \frac{\partial U_i}{\partial x_k}\overline{S_{kj}} - \frac{\partial U_j}{\partial x_k}\overline{S_{ki}} \tag{3.22}$$

is called the frame-indifferent Oldoroyd derivative of $\overline{S_{ij}}$, and $c_D = c_E = 1.68$. Although theoretically quite sound, usage of this Eqn 3.21 has been found to be very unstable in flow computations (Pender and Manson 1994).

An alternative model was developed by Baker and Orzechowski (1983). It is derived from the same principles of MFI and determinism, and is an expansion of τ_{ij} (Daly and Harlow 1970) in terms of $\overline{S_{ij}}$ such that

$$\tau_{ij} = -\frac{1}{3}\overline{u_k' u_k'}\, a_i\, \delta_{ij} + c_4 \frac{k^2}{\varepsilon}\overline{S_{ij}} + c_2 c_4 \frac{k^3}{\varepsilon^2}\overline{S_{ik}}\,\overline{S_{kj}} + \ldots \tag{3.23}$$

where a_i are coefficients admitting anisotropy ($a_1 = 0.94$, $a_2 = a_3 = 0.56$). $c_2 = 0.067$, and $c_4 = c_\mu = 0.068$. The value of the empirical constant $c_\mu = 0.068$, is similar to that found by Cazalbou and Bradshaw (1993) from DNS data of the viscous sublayer. However, for more general computations (including the present), the standard value of $c_\mu = 0.09$ is used. This formulation is more numerically robust, and is easily used in computations using the k-ε model

format presented in Chapters 4 and 6. In Chapter 6 the expanded terms for each stress component are detailed.

3.5 Boundary Conditions

The momentum equations are elliptic - as defined in standard texts on numerical methods like Smith (1985). The term "boundary conditions" here includes both the inlet conditions and the prevailing conditions at the solid and free-surface boundaries throughout the channel length. With the inlet conditions, the variable (e.g. U(x, y, z)) has its value U(0, y, z) , and its derivatives normal to the inlet boundary $\partial U(0, y, z)/\partial x$. Prevailing boundary conditions during the computation are given as values U(x, y, z), OR as normal derivatives to the boundary $\partial U(x, y, z)/\partial n$. When, as in the present study, the equations are of a parabolic form and the conditions downstream of a point do not influence the flow at that point, (see Section 4.2), the types of boundary conditions required for all the variables (U, V, W, P, k and ε) remain the same. Inlet conditions, and boundary conditions within the channel are required.

3.5.1 At the Inlet and Outlet

U, V, W values may be specified at the inlet. U is derived from the flat-plate (two-dimensional) logarithmic law of Eqn 2.21, whilst V and W are set to zero. The pressure (P) cannot be specified at the inlet because the continuity equation cannot then be enforced. With the fully-developed U distribution known, linear flat-plate profiles for k and ε are derived (Alfrink and van Rijn 1983) such that

$$k_{INLET} = \frac{U_*^2}{\sqrt{c_\mu}}\left(1-\frac{y}{h}\right) \tag{3.24}$$

$$\varepsilon_{INLET} = \frac{|U_*^3|}{\kappa\, y}\left(1-\frac{y}{h}\right) \tag{3.25}$$

where y is the distance from the bed of the present cross-section. These inlet conditions do not have a large effect on the outcome of the computation (Alfrink and van Rijn, 1983, Leschziner and Rodi 1979). The three-dimesionality of the flow is accounted for in Chapter 6 wherein

modifications to the two-dimensional profiles are proposed. At the outlet, gradients of all the variables are set to zero. No flow rate or pressure is set.

3.5.2 At the Rigid Boundary

In preference to the low-Reynolds-number method of sub-section 3.3.2, the wall function approach is used. As Launder and Spalding (1974) point out, this economises on computer time and storage, and enables *ad-hoc* modifications which reflect the boundary characteristics (like roughness). This condition is often termed the free-slip condition for it allows the velocity at the computation point nearest to the wall to be non-zero. This is unlike the zero-slip condition used in low-Reynolds number and viscous flow modelling whereby the velocity at the wall is zero.

It is based on the assumption that the wall point lies within the fully turbulent zone. This is reflected by the magnitude of the local turbulent Reynolds number based on the kinetic energy (rather than the shear velocity U_*), and the distance from the wall y_w, such that $k^{1/2}y_w/\nu >> 1$. Several models have been proposed (Launder 1981) which depend on the velocity scale used to describe the momentum relation. The momentum relation used herein follows from the standard law of the wall

$$\frac{U_w}{U_*} = U_w^+ = \frac{1}{\kappa}\ln(E_s y_w \frac{U_*}{\nu}) \qquad (3.26)$$

where the subscript 'w' indicates values at the wall point. U_w is the resultant velocity parallel to the boundary, and its non-dimensional value is U_w^+. Using Eqn 3.26, Nezu and Nakagawa (1987) reproduced the standard log-law profile in their computations.

The value of E_s depends on the roughness of the boundary and equals 9.0 for a smooth boundary. With a rough boundary, an empirical expression was determined by Krishnappan and Lau (1986) based on fitting Eqn 2.28 to Figure 2.2 to get

$$E_s = \exp[\frac{B_s}{(\frac{U_* k_s}{\nu})}]. \qquad (3.27)$$

where B_s is given by the curve-fitted expression

$$B_s = \exp\{-0.217[\ln\frac{U_* k_s}{\nu}]^2\}\ [5.50 + 2.5\ln\frac{U_* k_s}{\nu}]$$
$$+ 8.5\{1 - \exp[-0.217(\ln\frac{U_* k_s}{\nu})^2]\}. \qquad (3.28)$$

k_s is the equivalent sand roughness size of Eqn 2.28 and NOT the turbulent kinetic energy (k). It is worth noting that Launder and Spalding (1974) also used an expression similar to Eqn 3.26, which uses the velocity scale $k^{1/2}$, and constants $E_s^* = 5.0$ and $\kappa^* = 0.23$

$$\frac{U_w}{U_*^2} k_w^{1/2} = \frac{1}{\kappa^*} \ln[E_s^* y_w \frac{k_w^{1/2}}{\nu}]. \qquad (3.29)$$

From the one equation model, k_w may be used as the to yield the shear velocity

$$(U_*)_1 = c_\mu^{1/4} k_w^{1/2} \qquad (3.30)$$

which can then be used in the next computation step to set U_w, (through Eqn 3.26). A second approximation for U_* can be obtained from Eqn 3.26:

$$(U_*)_2 = \frac{\kappa U_w}{\ln[E_s y_w \frac{c_\mu^{1/4} k_w^{1/2}}{\nu}]} \qquad (3.31)$$

from which the wall shear stress is determined

$$\tau_w = [-\text{sign of}\ (U_w)]\rho(U_*)_1(U_*)_2. \qquad (3.32)$$

The term [- sign of (U_w)] ensures that the shear stress acts opposite to the direction of U_w. Since there is no recirculation in the present study this term is redundant.

Within the same computation step (iteration) Eqn 3.26 is used to set the wall value of ε. This is achieved by assuming that the rate of production of turbulent kinetic energy (P_K) is equal to the dissipation rate (e.g. Rodi 1980) - the turbulence energy equilibrium. In two-dimensional flow this is expressed as

$$\varepsilon = P_K = -\overline{u'v'}\frac{\partial U}{\partial y} = U_*^2(\frac{\partial U}{\partial y})_w. \qquad (3.33)$$

Using the log-law expression for U (Eqn 3.26) and differentiating with respect to y, the resulting expression for ε_w is

$$\varepsilon_w = \frac{U_*^3}{\kappa y_w} = \frac{c_\mu^{3/4} k_w^{3/2}}{\kappa y_w}. \qquad (3.34)$$

The assumption of the presence of an equilibrium layer is discussed further in Chapter 6.

3.5.3 At the Free-surface

The rigid lid boundary condition is used for the velocities and pressure. This assumes that the water surface is not deformed even by a net transport of momentum into the surface region. Alfrink and van Rijn (1983) report that this is especially valid for low Froude number flows.

For the case of zero surface shear stress, zero gradient normal to the surface for U, W, k and ε is assumed. V, the velocity normal to the free surface, is set to zero. At the free surface, the dissipation increases with a resultant decrease of the eddy viscosity. Naot and Rodi (1982), and Gibson and Rodi (1989) developed the free-surface condition for ε:

$$\varepsilon_{fs} = \frac{1}{\kappa}(k_{fs}\, c_\mu^{1/2})^{3/2}[\frac{1}{y'} + \frac{1}{y_l}] \qquad (3.35)$$

where the subscript '*fs*' denotes the values at the free surface. y' is the distance from an imaginary origin above the free-surface = 0.07 h, and y_l is the average distance the nearest

boundary on the free surface. y_l ensures the smooth transition of ε_{fs} at the point where the free surface meets the side-wall. Celik and Rodi (1984) used the free-surface condition

$$\varepsilon_{fs} = \frac{k_{fs}}{\alpha_\varepsilon h} \tag{3.36}$$

where the empirical $\alpha_\varepsilon = 0.18$. Like Eqn 3.35, Eqn 3.36 raises the value of ε at the free surface. Eqn 3.35 is selected for use in the present study.

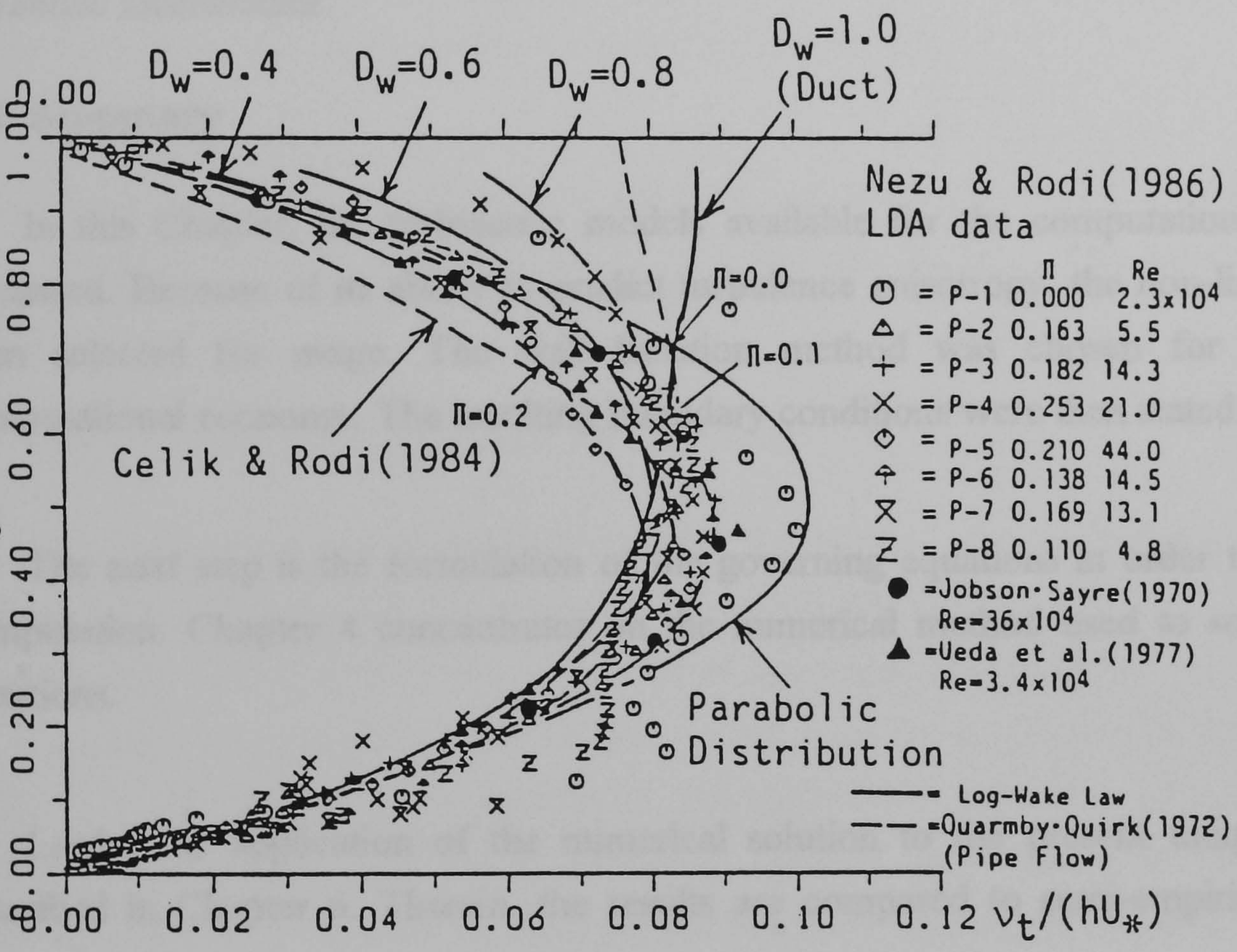

Figure 3.1 Computed and Measured Eddy Viscosity ($\nu_t/(hU_*)$)
(After Nezu and Nakagawa 1993)

Nezu and Nakagawa (1987) used a damping function, D_w, for k (i.e. decreased eddy viscosity) at the free-surface. Figure 3.1 shows the close agreement between their eddy viscosity profiles using several values of D_w, and those determined by experiment.The empirical profiles for k, ε, and the eddy (ν_t) viscosity in open-channel flow are (Nezu and Nakagawa 1993)

$$\frac{k}{U_*^2} = 4.78 \exp(-\frac{2y}{h}) \tag{3.37}$$

$$\frac{\varepsilon h}{U_*^3} = 9.8 (\frac{y}{h})^{-1/2} \exp(-\frac{3y}{h}) \tag{3.38}$$

$$\frac{\nu_t}{h U_*} = -\kappa (\frac{y}{h})^2 + \kappa \frac{y}{h} \tag{3.39}$$

respectively. Eqns 3.37 and 3.38 lead to Eqn 3.39. In Figure 3.1, Eqn 3.39 is labelled the 'Parabolic Distribution'.

3.6 Summary

In this Chapter, the turbulence models available for the computation of the flow were discussed. Because of its ability to predict turbulence anisotropy, the non-linear k-ε model has been selected for usage. The wall function method was chosen for its simplicity and computational economy. The resulting boundary conditions were then stated.

The next step is the formulation of the governing equations in order to enable numerical computation. Chapter 4 concentrates on the numerical method used to solve these transport equations.

Lastly, the application of the numerical solution to the present unique cross-section is described in Chapter 6. Therein, the results are compared to semi-empirical of Eqns 3.37 - 3.39.

CHAPTER 4: NUMERICAL METHODS

4.1 Introduction

In the previous two chapters, the governing equations of flow were adopted, and a corresponding model of the fluid turbulence was selected. The non-linear nature of the equations precludes a direct analytical solution method. The present chapter describes the method of numerical integration used to obtain the numerical solution. Section 4.2 introduces the basic finite volume technique behind the method, the discretisation procedure, and treatment of the convective, diffusion, and source terms. Sections 4.3 to 4.5 describe the interpolation schemes, grid variable arrangements, and boundary conditions used. The solution of the resulting algebraic equations is treated in Section 4.6.

Due to the expected and assumed symmetry of the flow about the channel centreline, the computation is carried out in only one half of the pipe section. This saves the computational effort.

4.2 Discretisation of Governing Equations

The finite volume technique, also called the control volume technique, is based on the weighted residuals method (Finlayson 1972). With this formulation (see Patankar 1981), the calculation domain is divided into a number of non-overlapping control volumes which contain the calculation grid points (nodes) for any solved quantity ϕ - momentum or scalar quantities. Figure 4.1 illustrates this. Integration of the differential equations occurs over the control volume. Between the grid points, piecewise profiles of ϕ define the integrals. Values of quantities ϕ are then stored at the grid points. It is clear that the technique is a direct expression of the standard discretisation principles used in the elementary derivation of the governing flow equations. As such, it inherently observes conservation principles for quantities ϕ.

4.2.1 Generalised Forms of the Equations

The momentum equations in each of the three dimensions (Eqns. 2.3), and the transport equations for the scalar quantities k and ε, (Eqns. 3.7 and 3.18), can be expressed in a generalised form:

$$U_j \frac{\partial(\rho\phi)}{\partial x_j} = \frac{\partial}{\partial x_j}(\Gamma_\phi \frac{\partial \phi}{\partial x_j}) + S_\phi \qquad (4.1)$$

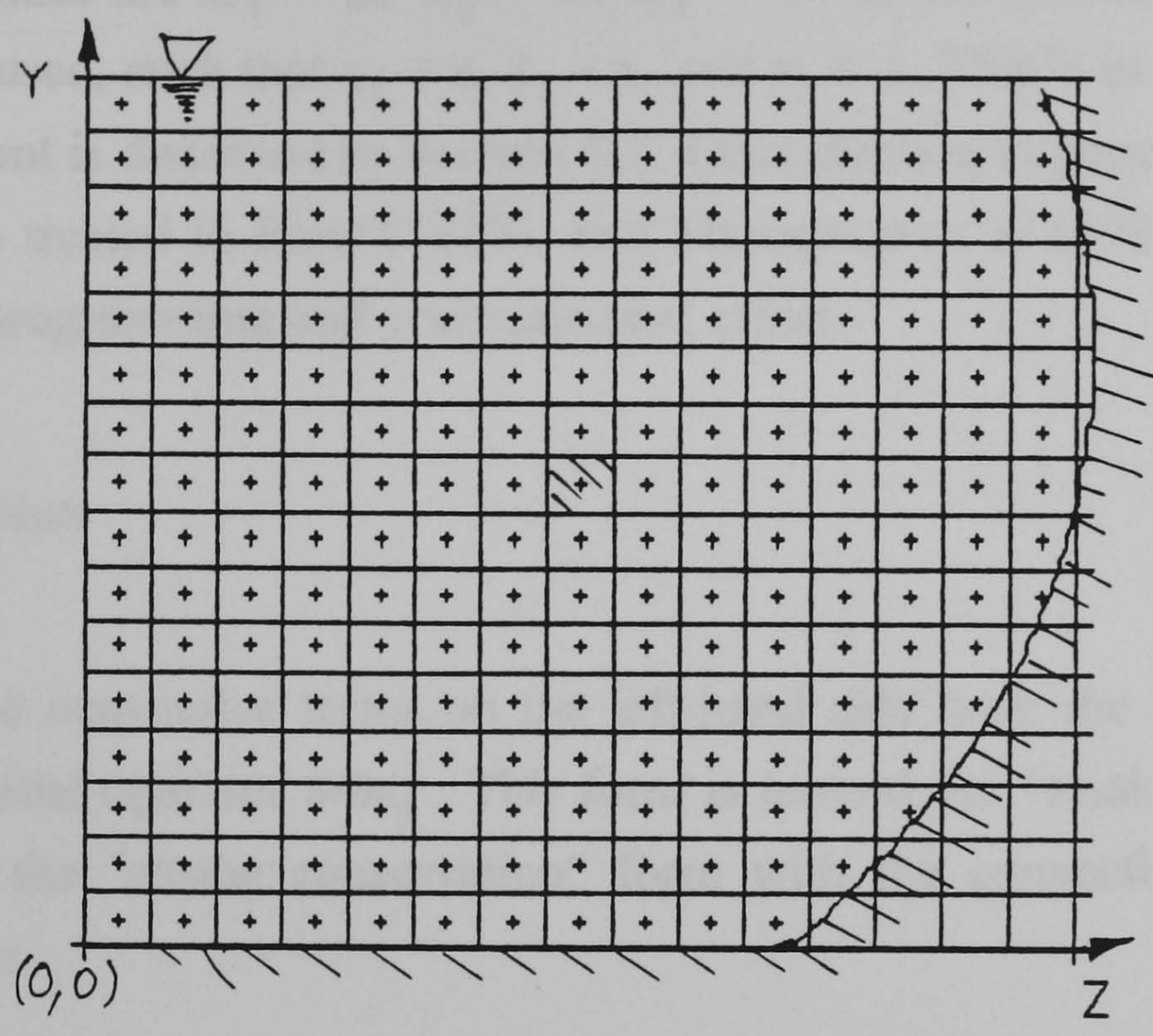

Figure 4.1 Control Volume Discretisation

On the left-hand side of Eqn 4.1 are the convective transport terms. The first term on the right-hand side represents the diffusive transport term expressed using the gradient transport hypothesis introduced in Section 3.2. The last term on the right-hand side, S_ϕ, represents the nett source of ϕ: the production less the destruction within the control volume.

Continuity Equation

The continuity equation Eqn. 2.2 is represented in tensor notation as

$$\frac{\partial(\rho U_i)}{\partial x_i} = 0, \qquad (4.2)$$

which in its full form becomes

$$\frac{\partial(\rho U_1)}{\partial x_1} + \frac{\partial(\rho U_2)}{\partial x_2} + \frac{\partial(\rho U_3)}{\partial x_3} = 0 \qquad (4.3)$$

in which the velocities are $U_1 = U$, $U_2 = V$, $U_3 = W$. In the present study, a Cartesian co-ordinate system is used, such that $x_1 = x$, $x_2 = y$, and $x_3 = z$. This is in spite of the curved side-wall whose treatment is discussed in Section 6.2. Discretisation in general (e.g. body-fitted) co-ordinate systems is treated in Peric (1985), and Thompson *et al* (1985). These, however, are costly in terms of programming and computational effort.

Momentum Equation

In Eqn 4.1 the convective terms on the left-hand side have the convecting velocities U_j outside the differential operator $\partial/\partial x_j$. This form is termed the "weak conservation". Eqn 4.4 below is given in the "strong conservation" form with the convecting velocities within the differential operator

$$\frac{\partial(\rho U_j)U_i}{\partial x_j} = \frac{\partial}{\partial x_j}\left(\frac{\rho \nu_t}{\sigma}\frac{\partial U_i}{\partial x_j}\right) + S_{U_i} \qquad (4.4)$$

This classification is due to Roache (1976). The diffusivity constant is expressed as $\Gamma_t = \nu_{eff}/\sigma$, where ν_{eff} $(= \nu_t + \nu)$, the effective viscosity, is the sum of the eddy and kinematic viscosities, and the Prandtl number, σ, is equal to unity. This term incorporates the viscous diffusion effects, and the turbulent diffusion. Although both Eqn 4.2 and 4.4 physically describe the same convective process, the difference in the two formulations has a bearing on the accuracy of the discretisation.

Over a finite number of control volumes, the integration of the differential equations - in Eqn 4.3 form leads to the bulk fluxes (over the whole domain) being satisfied at the boundaries. As Peric (1985) points out, this leads to a more realistic conservation of quantities - hence the term "strong conservation form". The continuity equation, Eqn 4.2, is also given in the "strong" conservation form.

On the other hand, the exclusion of the convective velocities from within the differential operator means that the fluxes are associated with the control volume centres, and not involved with the fluxes at the control volume faces. Therefore the bulk conservation of quantities is not easily enforceable and thus, not guaranteed. Eqn 4.2 is of the "weak conservation form".

In the "strong" conservation form, the expanded momentum conservation equations in all the three space directions are thus:

$$\frac{\partial(\rho U_1)U_1}{\partial x_1}+\frac{\partial(\rho U_2)U_1}{\partial x_2}+\frac{\partial(\rho U_3)U_1}{\partial x_3}=\frac{\partial}{\partial x_1}(\frac{\mu_{eff}}{\sigma}\frac{\partial U_1}{\partial x_1})+\frac{\partial}{\partial x_2}(\frac{\mu_{eff}}{\sigma}\frac{\partial U_1}{\partial x_2})+\frac{\partial}{\partial x_3}(\frac{\mu_{eff}}{\sigma}\frac{\partial U_1}{\partial x_3})+[-\frac{\partial P''}{\partial x_1}-gS_f]$$

(4.5)

$$\frac{\partial(\rho U_1)U_2}{\partial x_1}+\frac{\partial(\rho U_2)U_2}{\partial x_2}+\frac{\partial(\rho U_3)U_2}{\partial x_3}=\frac{\partial}{\partial x_1}(\frac{\mu_{eff}}{\sigma}\frac{\partial U_2}{\partial x_1})+\frac{\partial}{\partial x_2}(\frac{\mu_{eff}}{\sigma}\frac{\partial U_2}{\partial x_2})+\frac{\partial}{\partial x_3}(\frac{\mu_{eff}}{\sigma}\frac{\partial U_2}{\partial x_3})+[-\frac{\partial P''}{\partial x_2}-g\cos S_f]$$

(4.6)

$$\frac{\partial(\rho U_1)U_3}{\partial x_1}+\frac{\partial(\rho U_2)U_3}{\partial x_2}+\frac{\partial(\rho U_3)U_3}{\partial x_3}=\frac{\partial}{\partial x_1}(\frac{\mu_{eff}}{\sigma}\frac{\partial U_3}{\partial x_1})+\frac{\partial}{\partial x_2}(\frac{\mu_{eff}}{\sigma}\frac{\partial U_3}{\partial x_2})+\frac{\partial}{\partial x_3}(\frac{\mu_{eff}}{\sigma}\frac{\partial U_3}{\partial x_3})+[-\frac{\partial P''}{\partial x_3}]$$

(4.7)

The calculated pressure, P", is the deviation from the hydrostatic pressure distribution.

Scalar Equations

The transport equation for the turbulent kinetic energy, Eqn 3.7, is given in Eqn 4.4 form:

$$\frac{\partial(\rho U_1)k}{\partial x_1}+\frac{\partial(\rho U_2)k}{\partial x_2}+\frac{\partial(\rho U_3)k}{\partial x_3}=\frac{\partial}{\partial x_1}(\frac{\nu_{eff}}{\sigma_k}\frac{\partial k}{\partial x_1})+\frac{\partial}{\partial x_2}(\frac{\nu_{eff}}{\sigma_k}\frac{\partial k}{\partial x_2})+\frac{\partial}{\partial x_3}(\frac{\nu_{eff}}{\sigma_k}\frac{\partial k}{\partial x_3})+[P_k-\varepsilon] \tag{4.8}$$

where the diffusivity constant Γ_k has been expressed as ν_{eff}/σ_k. The production term P_k is given explicitly as

$$\begin{aligned} P_k &= \nu_t\,[\,(\frac{\partial U_1}{\partial x_2})^2+(\frac{\partial U_1}{\partial x_3})^2+2(\frac{\partial U_2}{\partial x_2})^2+2(\frac{\partial U_3}{\partial x_3})^2+(\frac{\partial U_2}{\partial x_3}+\frac{\partial U_3}{\partial x_2})] \\ &= \nu_t\,[\,\overline{D}\,]. \end{aligned} \tag{4.9}$$

Similarly the dissipation rate transport equation (Eqn 3.18) is written in the form

$$\frac{\partial(\rho U_1)\varepsilon}{\partial x_1}+\frac{\partial(\rho U_2)\varepsilon}{\partial x_2}+\frac{\partial(\rho U_3)\varepsilon}{\partial x_3}=\frac{\partial}{\partial x_1}(\frac{\nu_{eff}}{\sigma_\varepsilon}\frac{\partial k}{\partial x_1})+\frac{\partial}{\partial x_2}(\frac{\nu_{eff}}{\sigma_\varepsilon}\frac{\partial \varepsilon}{\partial x_2})+\frac{\partial}{\partial x_3}(\frac{\nu_{eff}}{\sigma_\varepsilon}\frac{\partial \varepsilon}{\partial x_3})+[c_{1\varepsilon}\frac{\varepsilon}{k}P_k-c_{2\varepsilon}\frac{\varepsilon^2}{k}] \tag{4.10}$$

in which the diffusivity constant Γ_ε is also expressed as $\nu_{eff}/\sigma_\varepsilon$.

4.2.2 Parabolic Nature of the Computation

It is worth noting that as the fluid flow is assumed to be fully developed and uniform in the longitudinal (streamwise) direction, the derivative terms $\partial/\partial x_1$ are eliminated from the preceding equations.

The boundary-layer-like behaviour of the flow (in which no longitudinal reverse flow occurs) in the present open-channel, implies that conditions downstream of a point of consideration do not affect those at the section being considered. This substantially simplifies the computation scheme as only the known upstream characteristics influence computations at each cross-section. Patankar and Spalding's (1972) computation method makes use of this nature of the flow to produce a marching type computation in which computation progresses downstream from section to section, and is dependent only on upstream conditions.

4.2.3 Discretisation Procedure

Discretisation is aimed at representing the flow fields on a grid which represents the physical domain. It is to be expected that as the number of grid points increases (the grid becomes finer) the solution to the discretised equation approaches the "exact" solution. Figure 4.2 illustrates the interconnection of the grid points. The five points P, E, W, N, and S represent the grid points, also referred to as nodes. Together, they form one computation molecule. A single control volume is also to referred to as a computation cell.

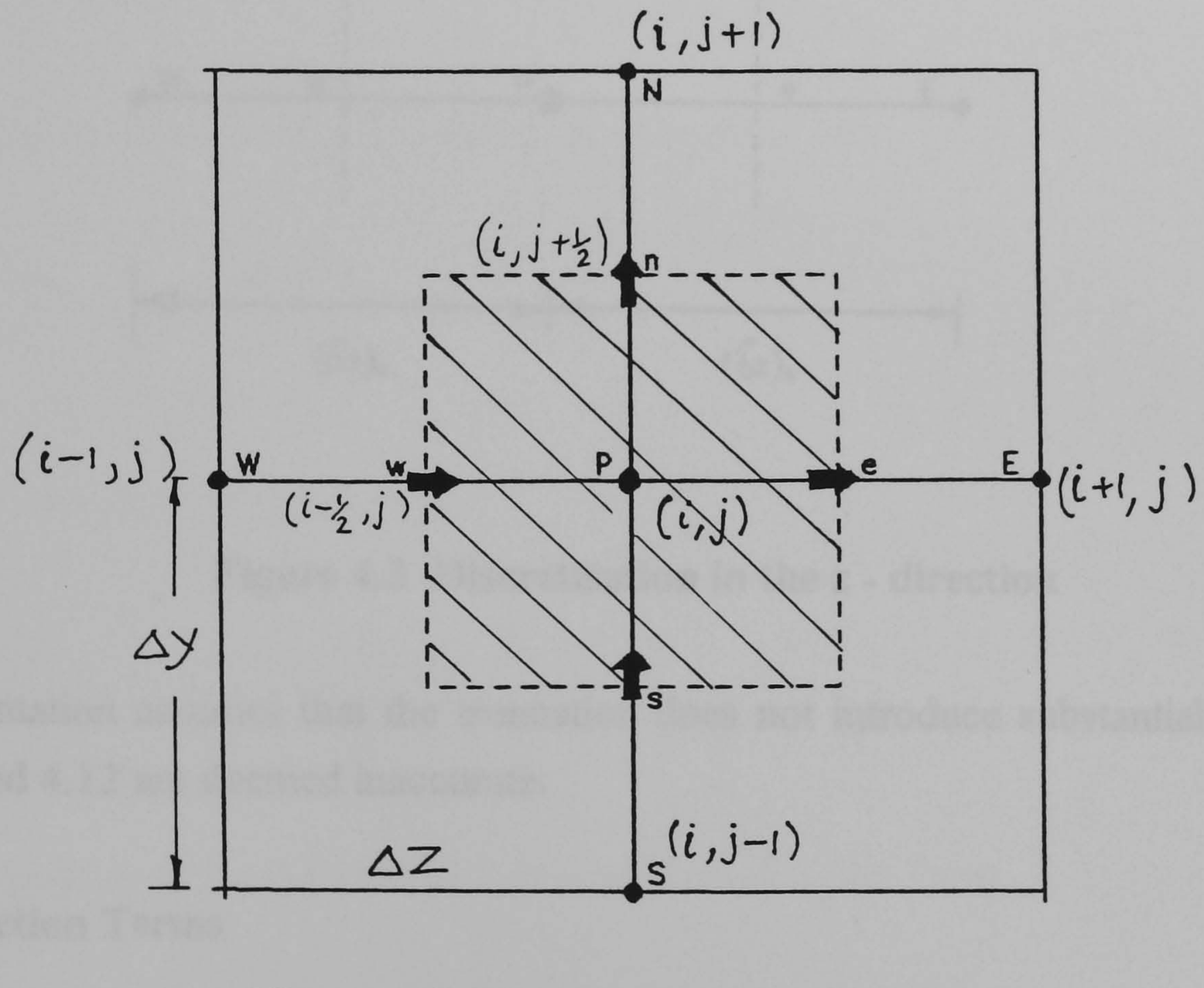

Figure 4.2 The Computational Molecule

The derivative terms in the transport Eqns 4.1 - 4.10 are usually represented by a truncated Taylor series (see Ames 1977, and Smith 1988). In the z-direction $(d\phi/dz)_p$ of Figure 4.3 becomes

$$(\frac{d\phi}{dz})_P = \frac{\phi_E - \phi_W}{2\delta z} \cong \frac{\phi_e - \phi_w}{\Delta z} \tag{4.11}$$

and the second order derivative $(d^2\phi/dz^2)_p$ is represented by

$$(\frac{d^2\phi}{dz^2})_P = [\frac{d}{dz}(\frac{d\phi}{dz})]_P = \frac{\phi_E + \phi_W - 2\phi_P}{(\delta z)^2} \tag{4.12}$$

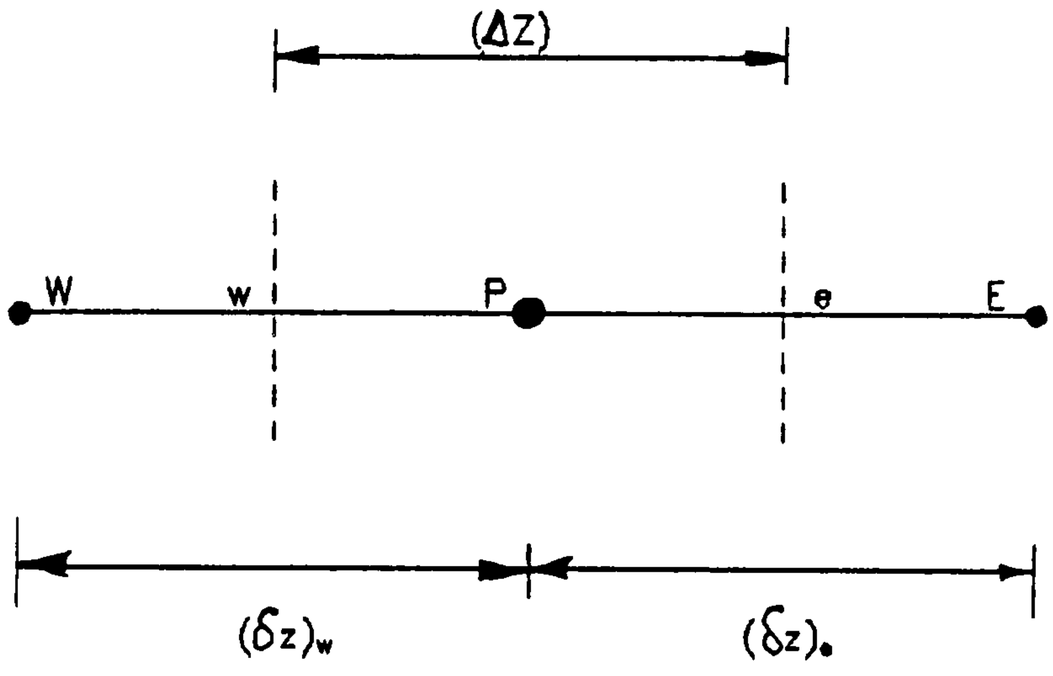

Figure 4.3 Discretisation in the z - direction

This representation assumes that the truncation does not introduce substantial error such that Eqns 4.11 and 4.12 are deemed inaccurate.

4.2.4 Convection Terms

Substitution of Eqn 4.11 into the convection terms of the z-direction momentum transport equation (Eqn 4.1) yields the discretised equation

$$\frac{\partial(\rho w)\phi}{\partial z} = \frac{(\rho w)_e \phi_e - (\rho w)_w \phi_w}{\Delta z} \tag{4.13}$$

and for the y-direction equation

$$\frac{\partial(\rho v)\phi}{\partial y} = \frac{(\rho v)_n \phi_n - (\rho v)_s \phi_s}{\Delta y} \tag{4.14}$$

where the cell-face values for ϕ can be determined from the nodal values

$$\begin{aligned} \phi_e &= fn(\phi_E, \phi_P); \qquad \phi_w = fn(\phi_W, \phi_P) \\ \phi_n &= fn(\phi_N, \phi_P); \qquad \phi_s = fn(\phi_S, \phi_P) \end{aligned} \tag{4.15}$$

wherein $fn(\phi)$ represent interpolation functions discussed in Section 4.3 below.

4.2.5 Diffusion Terms

The diffusion terms in the z-direction are discretised into

$$\frac{\partial}{\partial z}[\Gamma \frac{\partial \phi}{\partial z}] = \frac{1}{\Delta z}[\Gamma_e \frac{\phi_E - \phi_P}{(\delta z)_e} - \Gamma_w \frac{\phi_P - \phi_W}{(\delta z)_w}] \tag{4.16a}$$

and for the y-direction diffusion term

$$\frac{\partial}{\partial y}[\Gamma \frac{\partial \phi}{\partial y}] = \frac{1}{\Delta y}[\Gamma_n \frac{\phi_N - \phi_P}{(\delta y)_n} - \Gamma_s \frac{\phi_P - \phi_S}{(\delta y)_s}]. \tag{4.16b}$$

The integration of the full momentum equations takes the form

$$U_j \frac{\partial(\rho \phi)}{\partial x_j} \delta Vol = [\frac{\partial}{\partial x_j}(\Gamma_\phi \frac{\partial \phi}{\partial \phi}) + S_\phi] \delta Vol .$$

In discretised form Eqn 4.5 becomes

$$
\begin{aligned}
&[(\rho U)_P \phi_P - (\rho U)_{P,T} \phi_{P,T}]\,\Delta y\,\Delta z \\
&+[(\rho W)_e\,\phi_e - (\rho W)_w\,\phi_w]\,\Delta x\,\Delta y + [(\rho V)_n\,\phi_n - (\rho V)_s \phi_s]\,\Delta x\,\Delta z \\
&+[\Gamma_e \frac{\phi_E - \phi_P}{(\delta z)_e} - \Gamma_w \frac{\phi_P - \phi_W}{(\delta z)_w}]\,\Delta x\,\Delta y + [\Gamma_n \frac{\phi_N - \phi_P}{(\delta y)_n} - \Gamma_s \frac{\phi_P - \phi_S}{(\delta y)_s}]\,\Delta x\,\Delta z \\
&+\bar{S}\,\Delta x\,\Delta y\,\Delta z = 0
\end{aligned}
\tag{4.17}
$$

where $\bar{S}$ is the source term at P in Figure 4.2 which is assumed to apply over the whole control volume (δVol). The overbar illustrates this averaging over the control volume. The formulation of the source term is analysed next. Subscript T denotes to the upstream section. Hence the first term in Eqn 4.17 represents convection from the upstream.

4.2.6 Source Terms

The source term for certain species ϕ (e.g. k, and ε) is dependent on the value of ϕ at P, ϕ_P. To represent this dependence the S_ϕ is taken as a linear function of ϕ_P.

$$\bar{S} = S_C + S_P\,\phi_P \tag{4.18}$$

where S_C = the constant part, independent of ϕ_P, and S_P is the coefficient for ϕ_P and NOT the source term value at P.

It is best to estimate S from ϕ values from the previous computational iteration, ϕ^{**}, S^{**} (Patankar 1980) such that

$$S = S^{**} + (\frac{dS}{d\phi})^{**} (\phi_P - \phi_P^{**}). \tag{4.19}$$

The source terms for the three momentum equations are,

$$S_{U_1} = S_{U_1}^{**}; \quad (\frac{dS_{U_1}}{d\phi})^{**} = 0$$

$$S_{U_2} = S_{U_2}^{**}; \quad (\frac{dS_{U_2}}{d\phi})^{**} = 0 \qquad (4.20)$$

$$S_{U_3} = S_{U_3}^{**}; \quad (\frac{dS_{U_3}}{d\phi})^{**} = 0$$

and the k and ε sources respectively become

$$S_k = (S_C)_k + (S_P)_k \, k_P = [\rho \frac{c_\mu k_P^{**2}}{\varepsilon_P^{**}} \overline{D}] + [-\frac{\rho \varepsilon_P^{**}}{k_P^{**}}] k_P$$

$$S_\varepsilon = (S_C)_\varepsilon + (S_P)_\varepsilon \, \varepsilon_P = [\frac{c_\mu k_P^2}{\varepsilon_P^{**}} c_{1\varepsilon} \overline{D} \; \frac{\varepsilon_P^{**}}{k_P}] + [-\rho c_{2\varepsilon} \frac{\varepsilon_P^{**}}{k_P}] \varepsilon_P \qquad (4.21)$$

where $\overline{D}$ is the velocity gradient term defined in Eqn 4.9. This linearisation, fully utilises the dependence of S_ϕ on ϕ.

It is worth noting although the pressure gradients "drive" the momentum equations, they are not included in the source terms. This is because although they are linked to the velocity field, there is no explicit form of expressing them in the form of Eqn 4.19. The pressure field computation is described in Section 4.4.

4.2.7 Discretised Equations

Eqn 4.17 can thus be represented in an algebraic manner

$$a_P \phi_P = a_T \phi_T + a_E \phi_E + a_W \phi_W + a_N \phi_N + a_S \phi_S + b \qquad (4.22)$$

$$= \sum a_{nb} \phi_{nb} + b$$

where the subscript '*nb*' refers to the "neighbouring" nodes to node P. The coefficients are given by

$$a_P = a_T + a_E + a_W + a_N + a_S - S_P \, \Delta x \; \Delta y \; \Delta z \tag{4.23}$$

$$\begin{aligned} a_T &= a_T^C + a_T^D \\ &= (\rho U)_{P,T} \, g(\phi_{P,T}) + \frac{\Gamma_T}{(\delta x)} \end{aligned} \tag{4.24}$$

$$\begin{aligned} a_E &= a_E^C + a_E^D \\ &= (\rho W)_e \, g(\phi_E) + \frac{\Gamma_e}{(\delta z)_e} \end{aligned} \tag{4.25}$$

$$\begin{aligned} a_W &= a_W^C + a_W^D \\ &= (\rho W)_w \, g(\phi_W) + \frac{\Gamma_w}{(\delta z)_w} \end{aligned} \tag{4.26}$$

$$\begin{aligned} a_N &= a_N^C + a_N^D \\ &= (\rho V)_n \, g(\phi_N) + \frac{\Gamma_n}{(\delta y)_n} \end{aligned} \tag{4.27}$$

$$\begin{aligned} a_S &= a_S^C + a_S^D \\ &= (\rho V)_s \, g(\phi_S) + \frac{\Gamma_s}{(\delta y)_s} \end{aligned} \tag{4.28}$$

$$b = S_C \, \Delta x \, \Delta y \, \Delta z \tag{4.29}$$

wherein $g(\phi)$ is the "inverse" function to the interpolation function $fn(\phi)$ of Eqn 4.15. These functions are discussed next.

4.3 Interpolation Schemes

With the computational grid representing the physical space, the interpolation process should represent the ϕ field as closely as possible. Therefore the interpolation schemes have several properties which they have to satisfy, namely, numerical stability, conservativeness, boundedness, and transportiveness (Peric 1985).

Numerical stability means that the numerical solution should approach the exact solution as the grid becomes finer regardless of the interpolation function used.

With conservativeness, the nett conservation of mass, momentum, and other transported species should result from the interpolation scheme. This ensures physically realistic computed values like positive kinetic energy ($k > 0$), and non-negative density values ($\rho > 0$). Therefore in Eqn 4.17, the flux (convective transport), is represented at cell faces. Furthermore, the expression for ϕ at face 'e' is should be similar to that for ϕ at cell face 'w'.

The boundedness property of the interpolation scheme is satisfied if, within a given cell with no sources or sinks, the value of ϕ lies between the maximum and minimum boundary values ϕ_B : $\min(\phi_B) < \phi < \max(\phi_B)$. This ensures the smoothness, and physical realism of the resulting solution.

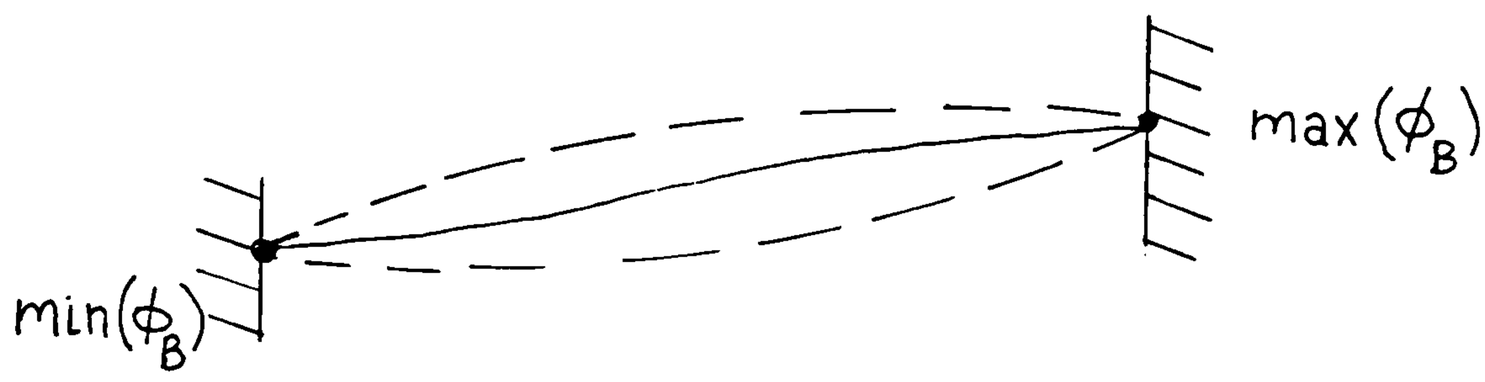

Figure 4.4 Boundedness Property

Finally, the transportiveness property is based on the ratio of convection and diffusion called the Peclet number (Pe). It is defined by

$$Pe = \frac{\rho U_c L_c}{\Gamma} \tag{4.30}$$

where U_c = a characteristic convective velocity, and L_c = a characteristic length scale. To illustrate transportiveness, a point P with a constant ϕ source in a flow field U_c is considered. When Pe = 0, the ϕ field is stagnant and all the transport is by diffusion - resulting is circular ϕ contours centred at P. As Pe increases, U_c transports ϕ downwind, with some lateral diffusion occurring to give ellipsoid ϕ contours. When Pe $\rightarrow \infty$ a streamline emanating from P flowing downwind results. There is no diffusive transport, and the convection of ϕ from the source solely affects points downwind of P. Upwind of P, no effect is registered.

These criteria are satisfied by interpolation functions based on the Taylor truncation used to derive Eqn 4.11 and 4.12.

4.3.1 Interpolation Schemes for Convection Terms

A common (Patankar 1980, and Peric 1985) interpolation scheme (or differencing scheme) is the Central Differencing Scheme (CDS). As illustrated in Figure 4.5 it is based on the assumption of a linear profile between grid nodes. From this, cell face values are determined using Eqn 4.31 below

$$\phi_e = \phi_E f_{ip} + \phi_P (1 - f_{ip}) \tag{4.31}$$

wherein f_{ip} = the linear interpolation factor based on the relative position of cell face 'e' between nodes P and E. This scheme is quite stable at low Peclet numbers, Pe < 2, (Peric 1985) but less so in strongly convective flows (Patankar 1988). Worse still, as Pe $\rightarrow \infty$ upwind propagation of ϕ is still possible - a physically unrealistic result.

With reference to Figure 4.6, the Upwind Differencing Scheme (UDS) is stated as

$$\begin{aligned} \phi_e &= \phi_P \text{ if } F_{W,e} > 0 \text{ and} \\ &= \phi_E \text{ if } F_{W,e} < 0. \end{aligned} \tag{4.32}$$

where $F_{W,e} = (\rho W)_e$. Substitution of the scheme of Eqn 4.32 into Eqns 4.24 - 4.28 defines the

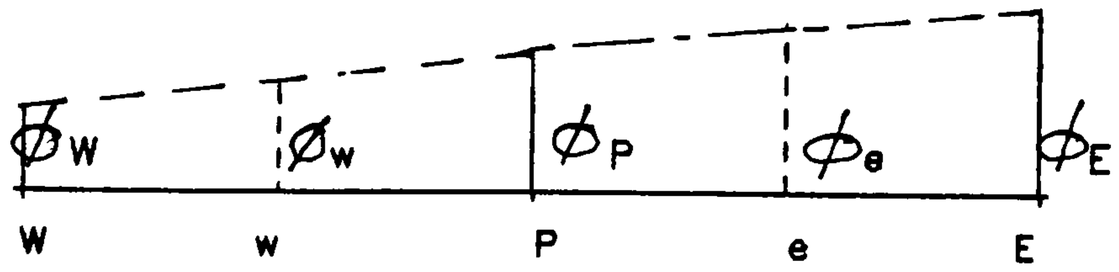

Figure 4.5 Central Differencing Scheme (CDS)

interpolation functions $g(\phi)$ such that

$$a_E^C = \max(0, -F_{W,e}); \qquad a_W^C = \max(0, F_{W,w});$$
$$a_N^C = \max(0, -F_{V,n}); \qquad a_S^C = \max(0, F_{V,s}); \tag{4.33}$$

and since the flow is parabolic, with no longitudinal upstream propagation, the coefficient for longitudinal convection is given by $a_T^C = F_{U,T}$. Eqn 4.33 is the upwind scheme for convection terms, and it is used in the present study.

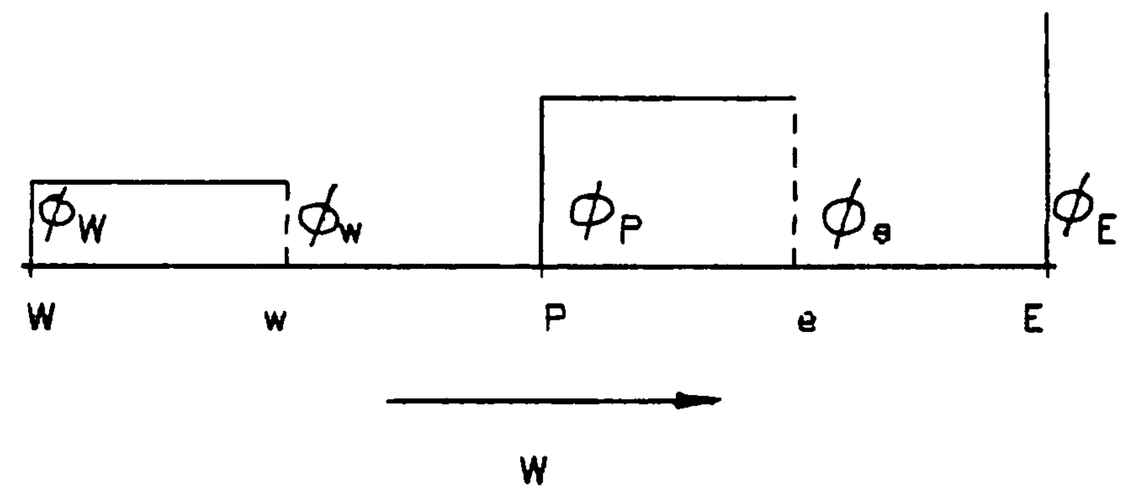

Figure 4.6 Upwind Differencing Scheme (UDS)

4.3.2 Interpolation for Diffusion Terms

A hybrid method which includes convection and diffusion terms in the form of

$$a_E^D = \max(F_{W,e}, (D - \frac{F_W}{2})_e, 0) \tag{4.34}$$

maybe used; where $D_e = [\Gamma/(\delta z)]_e$ the diffusion coefficient. Using Eqn 4.30, the Peclet number is then expressed as

$$Pe = \frac{(F_W)_e}{D_e} = \frac{(\rho W)_e (\delta z)_e}{\Gamma_e} \tag{4.35}$$

where $(\delta z)_e = \Delta z$ for a uniform grid. It has been shown by Patankar (1980) that Eqn 4.34 severely underestimates the coefficient a_E for $|Pe| > 2$ in one-dimensional heat flow. A more accurate scheme which produces results close to the exact exponential solution function (for the said flow type) is thus needed.

The Power-Law scheme of Patankar (1980, 1981) meets this criterion. It was also derived as a solution to one-dimensional heat flow, and links the convective and diffusive properties of the flow through a fifth-order function of Pe:

$$a_E^D = [\Gamma/(\delta z)]_e \max[0, (1 - 0.1|Pe|_e)^5] \tag{4.36}$$

$$a_W^D = [\Gamma/(\delta z)]_w \max[0, (1 - 0.1|Pe|_w)^5] \tag{4.37}$$

$$a_N^D = [\Gamma/(\delta y)]_n \max[0, (1 - 0.1|Pe|_n)^5] \tag{4.38}$$

$$a_S^D = [\Gamma/(\delta y)]_s \max[0, (1 - 0.1|Pe|_s)^5] \tag{4.39}$$

There is no diffusion from the upstream section (T). Unlike with the central difference scheme which gives a bad fit for $|Pe| > 2$ and requires an uneconomically fine grid in order to mimic the exponential exact solution, Eqns 4.36 - 4.39 give accurate solutions even on coarse grids.

The major weakness of the power law scheme is that it was derived from a one-dimensional solution, and, as such, cannot account for flows occurring at an angle to the grid. This lateral convective transport results in "false numerical diffusion" being introduced into the computation. Some practitioners (Peric 1985) have recommended the use of CDS as a more theoretically sound scheme although, as it has already been illustrated, the CDS gives inaccurate solutions when $|Pe| > 2$. Several schemes (Raithby 1976) aimed at eliminating false diffusion have been proposed but have been inadequately tested. Therefore, the power-law scheme is adopted despite these limitations as the nett false diffusion (in the secondary flow plane) is deemed small compared to the cost of, and uncertainty in implementing schemes which eliminate false diffusion.

4.3.3 The Full Discretisation Equations

From Eqns 4.33 and 4.35 - 4.39, the resultant coefficients are given by

$$a_{E,W,N,S,T} = a^{C}_{E,W,N,S,T} + a^{D}_{E,W,N,S}. \tag{4.40}$$

These can now be used to represent the terms of Eqns 4.5 - 4.8, and 4.10 in the discretised form of Eqns 4.22 - 4.29:

U component

$$\begin{aligned} a_P U_P &= a_T U_T + a_E U_E + a_W U_W + a_N U_N + a_S U_S + (P_{P,T} - P_P)\frac{\Delta y\,\Delta z}{\Delta x} \\ &= \sum a_{nb} U_{nb} + (P_{P,T} - P_P)\frac{\Delta y\,\Delta z}{\Delta x} \end{aligned} \tag{4.41}$$

V component

$$\begin{aligned} a_P V_P &= a_T V_T + a_E V_E + a_W V_W + a_N V_N + a_S V_S + (P_P - P_N)\,A_n \\ &= \sum a_{nb} V_{nb} + (P_P - P_N)\,A_n \end{aligned} \tag{4.42}$$

W component

$$a_P W_P = a_T W_T + a_E W_E + a_W W_W + a_N W_N + a_S W_S + (P_P - P_E) A_e$$
$$= \sum a_{nb} W_{nb} + (P_P - P_E) A_e \qquad (4.43)$$

The pressures in Eqns 4.41 - 4.43 have yet to be determined, and several arrangements for this have to be made.

4.4 Grid Arrangement of Variables and Pressure Calculation

An alternative grid arrangement to that of Figure 4.1 is given in Figure 4.7 wherein the physical space (domain) is mapped by a grid rather than the adjoining control volumes of Figure 4.1. While the gridding of Figure 4.7 is easier to generate, it often results in half cells being attached to the boundaries - an undesired property. Furthermore, unlike with the gridding

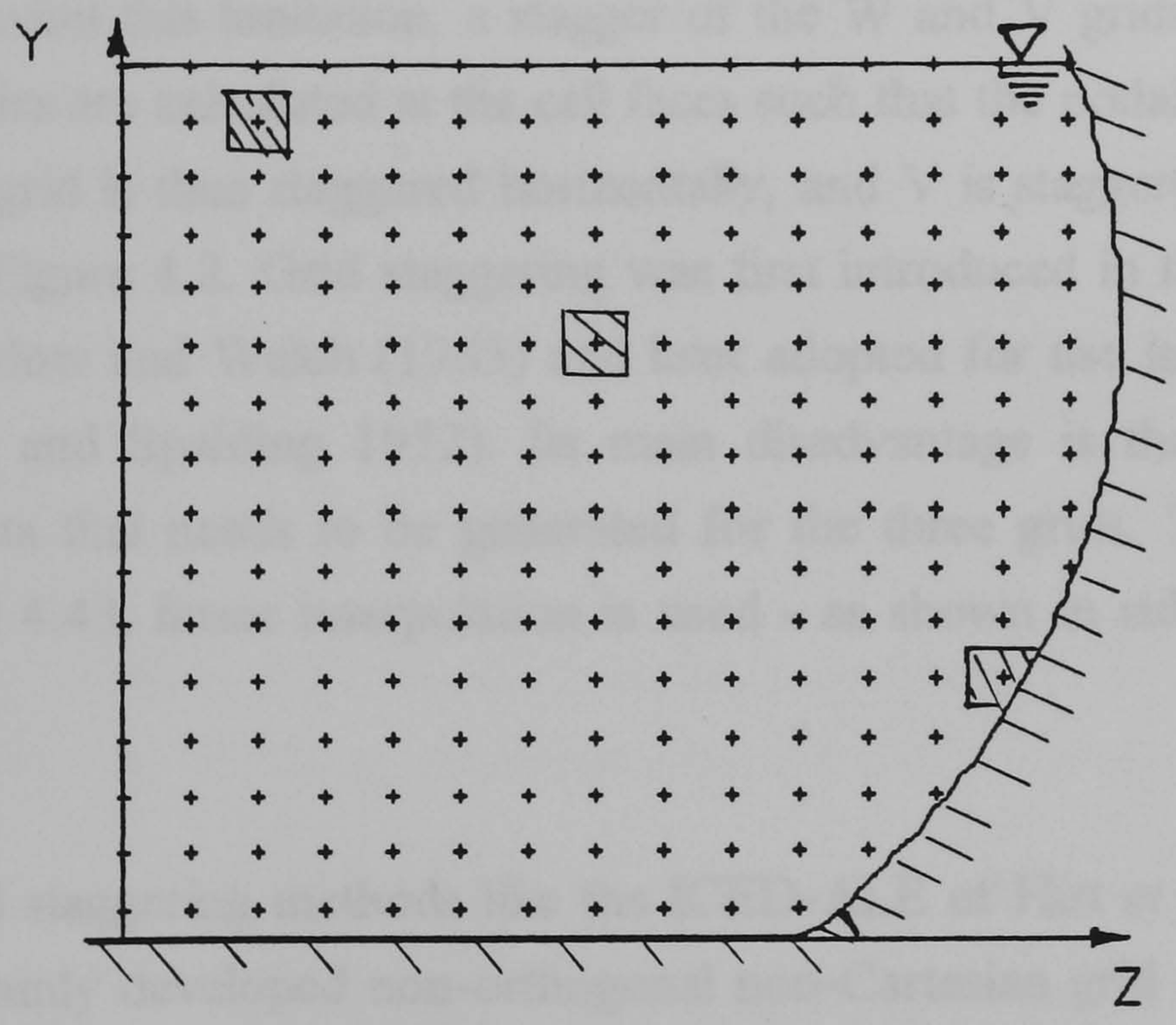

Figure 4.7 Alternative Grid Formulation

shown in Figure 4.1, grid nodes in the gridding method of Figure 4.7 do not represent the centres of the control volume which they are supposed to represent. Therefore, the control volume grid arrangement of Figure 4.1 is used for the present study.

4.4.1 Staggered Variable Arrangement

For pressure variation in the z-direction, the following difference equation results

$$P_e - P_w = \frac{P_E + P_P}{2} - \frac{P_W + P_P}{2} = \frac{-P_W + P_E}{2} \tag{4.44}$$

which expresses the pressure gradient in terms of two *alternate* grid points E and W. This may lead to an unrealistic "checkerboard" pressure distribution in which the differences between adjacent nodes do not "drive" the velocities as expected. This phenomenon is explained in detail by Patankar (1980). Rhie and Chow (1983) also note that such anomalous pressure distributions may persist and be registered in the final numerical solutions. Expressions for terms of the continuity equation are similar to that of Eqn 4.44 where the continuity at a node is expressed by velocities from two *alternate* grid points - possibly also leading to a "checkerboard" solution.

To circumvent this limitation, a stagger of the W and V grids is introduced. This ensures that the velocities are calculated at the cell faces such that the nodal pressure differences "drive" them. The W grid is thus staggered horizontally, and V is staggered vertically as illustrated by the arrows in Figure 4.2. Grid staggering was first introduced in the Marker And Cell (MAC) method of Harlow and Welch (1965) and later adopted for use in finite volume computations (e.g. Patankar and Spalding 1972). Its main disadvantage is the large amount of grid and geometrical data that needs to be generated for the three grids. To derive the coefficients of Eqns 4.42 and 4.43, linear interpolation is used - as shown in sub-Section 6.2.2, Eqns 6.14 - 6.17.

Other grid staggering methods like the ICED-ALE of Hirt *et al* (1974), and TURF (Peric 1985) were mainly developed non-orthogonal non-Cartesian grid solutions in which the MAC stagger produces poor results. Since the present co-ordinate system is Cartesian, the MAC grid stagger is adopted for use in the present study.

4.4.2 Pressure Calculation: SIMPLE

Since there is no equivalent transport equation for the pressure, an alternative solution method for P is in order. In two-dimensional flows, vorticity/stream-function methods (see Patankar 1980 for a list) have been employed to eliminate the need to directly compute the pressure field. The two-dimensionality of the methods precludes them from use in the present study, notwithstanding the need in the present study, to calculate the pressure field. An alternative is thus sought.

To calculate the pressure field, the *S*emi-*I*mplicit *M*ethod for *P*ressure-*L*inked *E*quations (SIMPLE) was first introduced by Patankar and Spalding (1972). It has been extensively used and modified (Van Doormaal and Raithby 1984, Vanka 1985, and Patankar 1988). Its basic principle is that the pressure is determined by using the continuity equation before the discretised momentum equations, Eqns 4.41 - 4.43, are solved. This is mainly a result of the exclusion of pressure gradient terms from the source terms for the momentum equations - as previously stated. Previous studies have shown the routine to be numerically robust and is quite stable (Rhie and Chow 1983, Peric 1985, and Patankar 1988).

The method is best described by expressing it in two stages: the Predictor, and the Corrector stages.

Predictor Stage

This stage involves the estimation of the pressure field in order to determine velocities using Eqns 4.41 - 4.43. Using estimated pressures, P*, Eqns 4.41 - 4.43 become: for the U component

$$a_P U_P^* = a_T U_T^* + a_E U_E^* + a_W U_W^* + a_N U_N^* + a_S U_S^* + (P_P^* - P_{P,T}^*) A_T \tag{4.45}$$

$$= \sum a_{nb} U_{nb}^* + (P_P^* - P_{P,T}^*) A_T$$

the V component

$$a_P V_n^* = \sum a_{nb} V_{nb}^* + (P_P^* - P_N^*)\, A_n \tag{4.46}$$

and for the W component

$$a_P W_e^* = \sum a_{nb} W_{nb}^* + (P_P^* - P_E^*) A_e. \tag{4.47}$$

where the superscript '*' indicates the estimated value that pertaining to the Predictor stage. Using the estimated pressure field means that an inaccurate velocity field (U*, V*, W*) is computed. These velocities do not, in general, satisfy the continuity equation (Eqn 4.3) whose discretised form is given as

$$[(\rho W)_e - (\rho W)_w]\,\Delta x\,\Delta y + [(\rho V)_n - (\rho V)_s]\,\Delta x\,\Delta z + [(\rho U)_{P,T} - (\rho U)_P]\,\Delta y\,\Delta z = 0. \tag{4.48}$$

Therefore to improve the velocities, the pressure estimates have to be improved - or "corrected".

Corrector Stage

The correct pressure (P) is assumed to be a sum of the estimated pressure (P*) and a correction P':

$$P = P^* + P'. \tag{4.49}$$

Similarly, the correction of P leads to a corresponding correction of the velocity field (U*, V*, W*) by corrections (U', V', W') such that

$$U = U^* + U'; \quad V = V^* + V'; \quad W = W^* + W'. \tag{4.50}$$

Taking V equations as an example: an implicit expression for V' is obtained by subtracting Eqn 4.46 from Eqn 4.42 to get:

$$a_P V_n' = \sum a_{nb} V_{nb}' + (P_P' - P_N')\, A_n . \tag{4.51}$$

To make Eqn 4.51 explicit in V' so as to enable the correction V' to be determined solely from P', the "neighbour" term $\sum a_{nb} V_{nb}'$ is omitted from Eqn 4.51. As extensively discussed by Patankar (1980), this omission merely serves to make Eqn 4.51 explicit in V' and does not result in an erroneous solution. Further simplification of Eqn 4.51 leads to

$$\begin{aligned} V_n' &= \frac{A_n}{a_n}(P_P' - P_N') \\ &= d_n(P_P' - P_N') \end{aligned} . \tag{4.52}$$

Substitution of Eqn 4.52 into the V correction formula of Eqn 4.50 results in the explicit correction formula

$$V_n = V_n^* + d_n(P_P' - P_N') \tag{4.53}$$

which can similarly be produced for the U and W

$$U_P = U_P^* + d_T(P_P' - P_{P,T}') \tag{4.54}$$

$$W_e = W_e^* + d_e(P_P' - P_E') . \tag{4.55}$$

Only the pressure corrections, P', are now left to be computed.

4.4.3 Pressure Correction

Substitution of the correction formulae Eqns 4.53 - 4.55 into the discretised continuity equation 4.48 yields a discretised equation for P'

$$a_P P_P' = a_E P_E' + a_W P_W' + a_N P_N' + a_S P_S' + b \tag{4.56a}$$

where

$$a_E = \rho_e d_e \, \Delta x \, \Delta y \tag{4.56b}$$

$$a_W = \rho_w d_w \, \Delta x \, \Delta y \tag{4.56c}$$

$$a_N = \rho_n d_n \, \Delta x \, \Delta z \tag{4.56d}$$

$$a_S = \rho_s d_s \, \Delta x \, \Delta z \tag{4.56e}$$

$$b = [(\rho W^*)_e - (\rho W^*)_w] \, \Delta x \, \Delta y + [(\rho V^*)_n - (\rho V^*)_s] \, \Delta x \, \Delta z + [(\rho U)_{P,T} - (\rho U^*)_P] \, \Delta y \, \Delta z . \tag{4.56f}$$

For parabolic flows (Patankar and Spalding 1972) there is no "upstream" node for Eqn 4.56(a). Eqn 4.56(f) is similar to the continuity equation, Eqn 4.48, the only slight difference being that former is based on approximated velocities. It can be seen that 'b' thus represents the mass conservation error resulting from the estimated flow field. This "mass source" is to be eliminated by the velocity corrections - which are themselves computed from P'.

The complete SIMPLE procedure is as follows.

(i) EstimatePressure field P^*;
(ii) Compute the approximate (U^*, V^*, W^*) velocity field using Eqns 4.45-4.47;
(iii) Solve for the pressure correction Eqn 4.56, through several iterations;
(iv) Correct the pressure using Eqn 4.49;
(v) Correct the velocities using Eqn 4.50;
(vi) Solve the discretised equations for k and ε;
(vii) Using the corrected pressure as the new estimate P^*, goto step (ii) and repeat the computation until a converged solution is obtained.

To aid convergence the pressure correction Eqn 4.49 needs to be under-relaxed such that

$$P = P^* + \alpha_p P' . \tag{4.57}$$

where α_p lies between zero and unity (~ 0.8).

Since the pressure correction is derived from the continuity constraint alone, it tends to force the velocities to obey the continuity constraint alone and not the momentum one. This lead Patankar (1980) to produce a *R*evised SIMPLE procedure SIMPLE*R* in which P' is used to correct the velocities only, and a separate equation is solved for P. SIMPLER yields faster convergence (Patankar 1981) than when SIMPLE is used, although its major drawback is that it involves the solution of an extra equation. Van Doormaal and Raithby (1984) developed a still faster converging *C*onsistent method: SIMPLEC. Some practitioners (e.g. Thiart 1990) have used a *N*on-staggered variable arrangement method, SIMPLEN. The SIMPLE method is used in the present study as the overriding priority is the description of the flow mechanisms rather than the perfection of the numerics of the computation.

4.5 Implementation of Boundary Conditions

The aim of numerical boundary conditions is to reproduce the physical flow boundary conditions of Section 3.5 (Roache 1976). As the domain is limited to only one half of the pipe section an additional symmetry condition at the centreline results. It is described in Sub-Section 4.5.2. Two type of conditions are possible: (i) the Dirichlet condition, where boundary values are given; and (ii) the Neumann condition, where the gradient normal to the boundary is specified. Figures 4.8 - 4.10 illustrate these conditions.

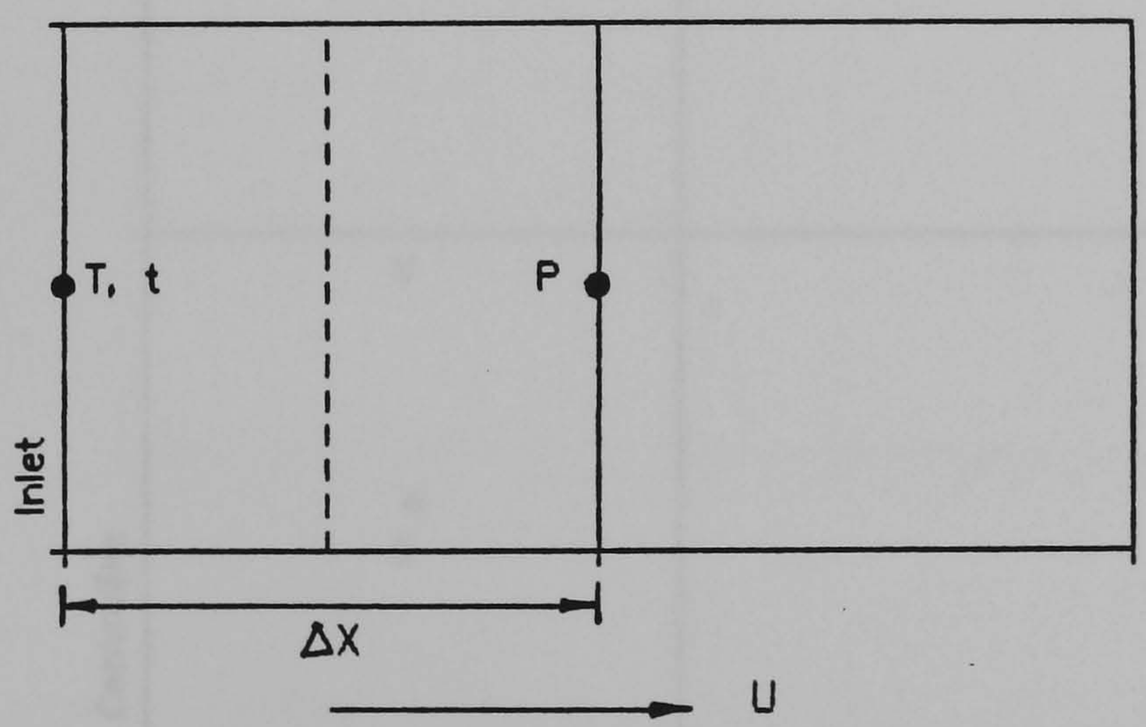

Figure 4.8 Inlet Boundary Conditions

4.5.1 Inlet and Outlet Boundaries

The flow in the present study is fully developed and uniform in the longitudinal direction. The inlet cell coincides with the inlet as shown in Figure 4.8. The initial values of Section 3.5 for U, V, W, k, ε, and P are used.

The Outlet condition is immaterial as the flow is uniform and parabolic and the downstream nodes are not included in the computation molecule of Figure 4.2.

4.5.2 Symmetry Boundaries: Centreline and Free Surface

The symmetry boundary condition is typified by zero cross flux and diffusion across the symmetry line. As shown in Figure 4.9 the centreline symmetry flux and diffusion conditions are given by

$W_w = 0$ that is $F_{w,w} = 0$, and $D_w = 0$; and $a_W = 0$. (4.58)

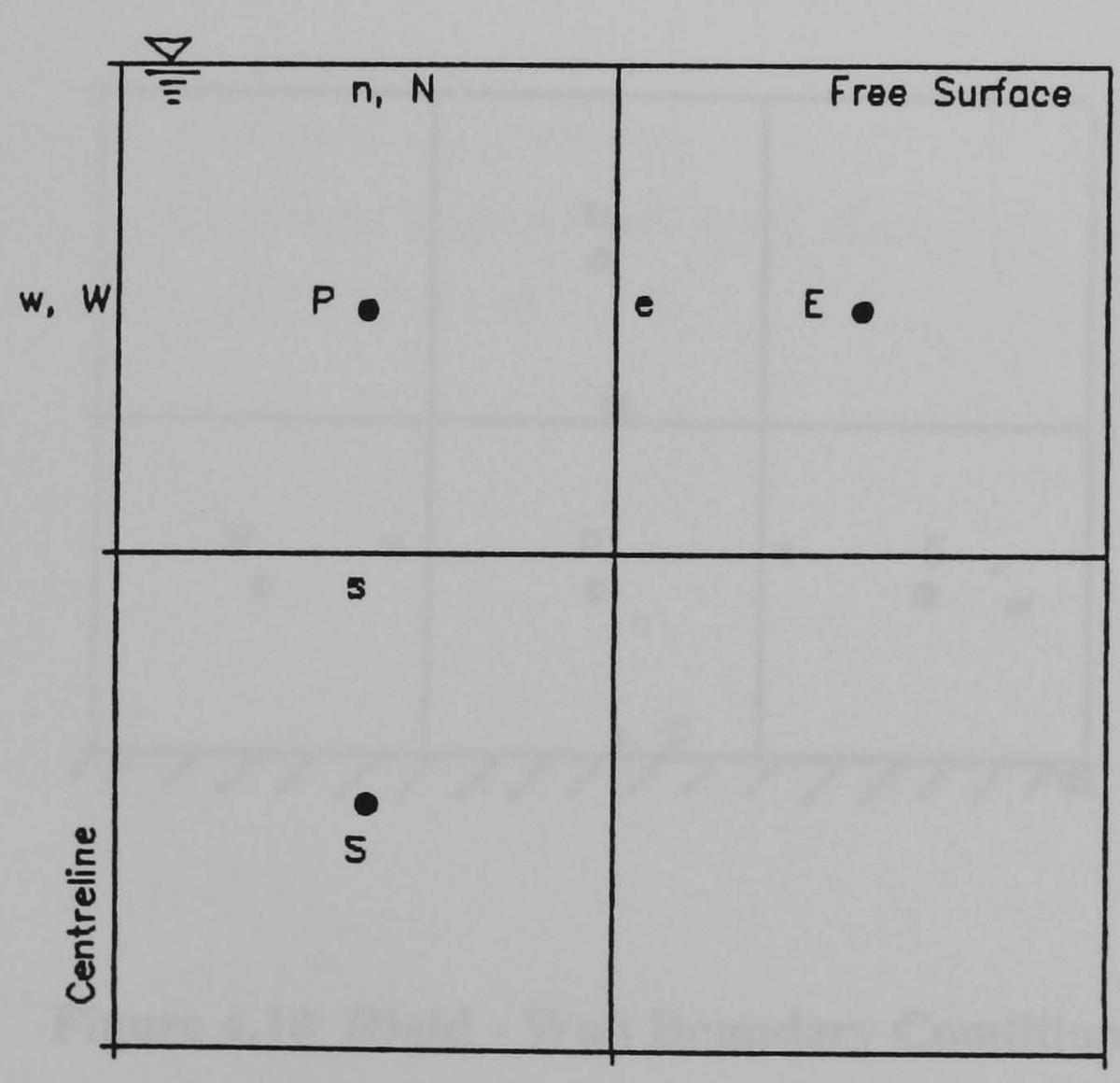

Figure 4.9 Symmetry Boundary Conditions

At the free-surface these flux conditions become

$V_n = 0$ that is $F_{V,n} = 0$, and $D_n = 0$; and $a_N = 0$. (4.59)

The symmetry of the ϕ (U, k) profile about the centreline and the free surface is expressed at both boundaries by the expression

$$\frac{\partial \phi}{\partial n_s} = 0 \tag{4.60}$$

where n_s is the normal to the symmetry boundary. This is a Neumann condition..

4.5.3 Rigid Boundaries: Bed and Side-Wall

Figures 4.1 and 4.10 illustrate the attachment of the computation grid to the bed and side boundaries. The curved side-wall is in effect represented by a stepped profile pertaining to the computational grid. This does not affect the boundary values U_{wall} and ε_{wall}, expressed is Section 3.5 (Eqns 3.26 and 3.32 respectively).

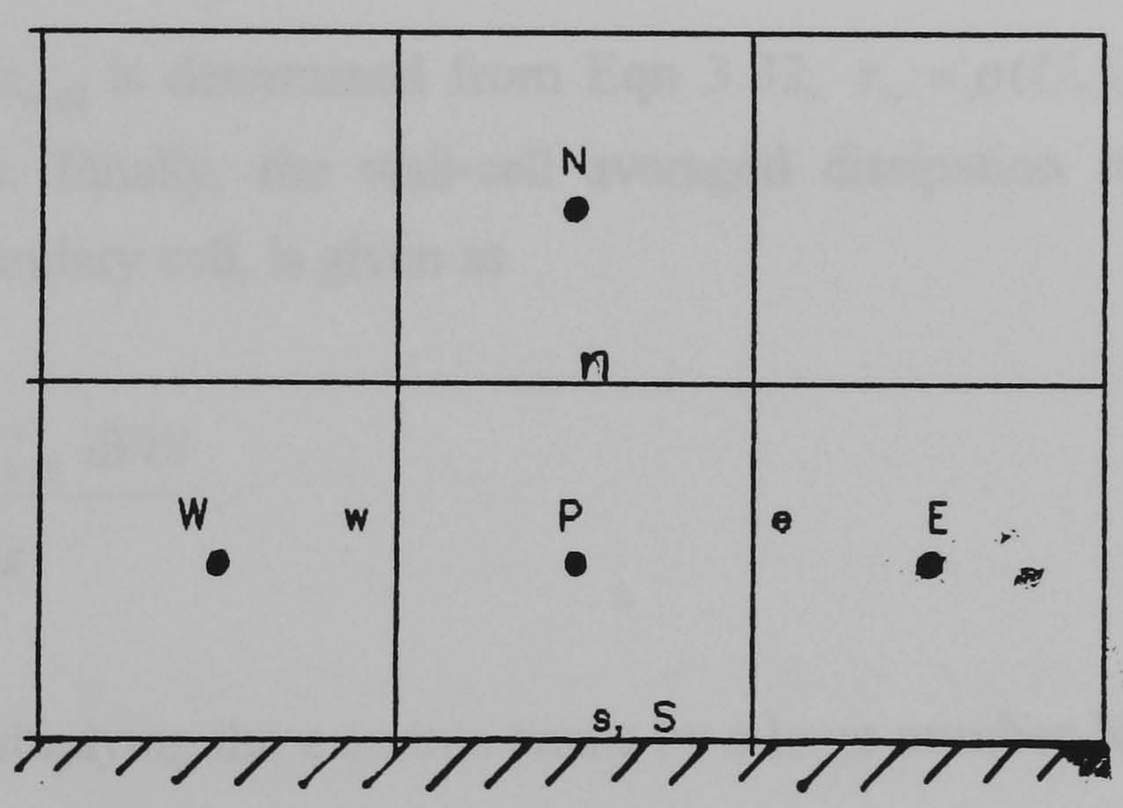

Figure 4.10 Rigid - Wall Boundary Condition

At the bed the condition is expressed as

$V_s = 0$ that is $F_{S,s} = 0$, and $D_s = 0$; and $a_S = 0$ (4.61a)

and for the side-wall the wall condition becomes

$W_e = 0$ that is $F_{W,e} = 0$, and $D_e = 0$; and $a_E = 0$. (4.61b)

Additionally, the diffusion to the wall is set to zero

$$(\frac{\partial k}{\partial n_s})_{wall} = 0; \tag{4.62}$$

the generation term for k, P_k, is modified to allow for the wall shear, and its integral average over the boundary cell becomes

$$\overline{(P_k)_{wall}} = \frac{\tau_{wall}\, U_{wall}\, \delta Vol}{y_{wall}} \tag{4.63}$$

where the wall shear τ_{wall} is determined from Eqn 3.32, $\tau_w = \rho(U_*)_1(U_*)_2$, and δVol is the boundary cell volume. Finally, the wall-cell averaged dissipation rate, where Eqn 3.34 is integrated over the boundary cell, is given as

$$\overline{\varepsilon_{wall}} = \frac{c_\mu^{3/4}\, k_{wall}^{3/2}\, U_{wall}^{+}\, \delta Vol}{y_{wall}}. \tag{4.64}$$

This is achieved by multiplying the ε source terms by a large number $N_\varepsilon \sim 10^{30}$ such that

$$S_\varepsilon = (S_C)_\varepsilon + (S_P)_\varepsilon\, \varepsilon_P = N_\varepsilon \frac{c_\mu^{3/4}\, k_P^{3/2}}{\kappa\, y_w} + N_\varepsilon\, \varepsilon_P]. \tag{4.65}$$

4.5.4 Boundary Conditions for the Pressure Correction Equation

Patankar (1980), and Van Doormaal and Raithby (1984) give a discussion on the nature of boundary conditions for P'. The main point is that these boundary conditions have to match the pressure and velocity values at the boundary. In the present section no pressure boundary specification is made. The velocities are specified at all the boundaries according to Eqns 4.58 - 4.62. At the centreline symmetry boundary (Figure 4.9), the relationship

$$W_w = BW_e + C \quad \text{and}$$
$$W_w^* = BW_e^* + C \qquad (4.66a,b)$$

is used. B is specified (B = 0) and C is the specified velocity. When Eqn 4.66(a) is substituted into continuity equation, Eqn 4.48, the resulting P' equation (similar to Eqn 4.56) has the coefficients

$$a_W = 0; \qquad a_E = (\rho Ad)_e - (\rho A)_w d_e B;$$
$$a_N = (\rho Ad)_n; \qquad a_S = (\rho Ad)_s; \qquad (4.67a,b,c,d)$$
$$a_P = a_E + a_W + a_N + a_S$$
$$b_P = (\rho W^* A)_w - (\rho W^* A)_e + (\rho V^* A)_s - (\rho V^* A)_n$$

Formulations similar to Eqns 4.66 and 4.67 are derived for the other boundaries.

4.6 Solution Algorithm

The general form of the discretised equations for all the variables including P', is given by Eqns 4.22 and 4.56. Over the whole domain these equations form a set of nominally linear algebraic equations expressed in matrix form as

$$[A]\,[\phi] = [B] \qquad (4.68)$$

where [A] is the coefficient matrix, [ϕ] the variable matrix, and [B] the constant matrix. The most cost effective type of Eqn 4.68, is the one in which matrix [A] is tridiagonal: i.e. Eqn 4.68 is of the form

$$\begin{vmatrix} a_{11} & a_{12} & 0 & 0 & 0 & 0 & 0 & 0 \\ a_{21} & a_{22} & a_{23} & 0 & 0 & 0 & 0 & 0 \\ 0 & a_{32} & a_{33} & a_{34} & 0 & 0 & 0 & 0 \\ 0 & 0 & .. & .. & .. & 0 & 0 & 0 \\ 0 & 0 & 0 & .. & .. & .. & 0 & 0 \\ 0 & 0 & 0 & 0 & .. & .. & .. & 0 \\ 0 & 0 & 0 & 0 & 0 & a_{n-1n-2} & a_{n-1n-1} & a_{n-1n} \\ 0 & 0 & 0 & 0 & 0 & 0 & a_{nn-1} & a_{nn} \end{vmatrix} \begin{vmatrix} \phi_1 \\ \phi_2 \\ \phi_3 \\ . \\ . \\ . \\ \phi_{n-1} \\ \phi_n \end{vmatrix} = \begin{vmatrix} B_1 \\ B_2 \\ B_3 \\ . \\ . \\ . \\ B_{n-1} \\ B_n \end{vmatrix} .$$

4.6.1 Tridiagonal Matrix Algorithm (TDMA)

To make [A] tridiagonal, a powerful "sweeping" procedure was developed by Patankar and Spalding (1972). It involves sweeping in the z and y directions. For the z-sweep the coefficients of the discretised equations are calculated along a line of constant y. The coefficient matrix [A] is calculated from the P, E and W coefficients whilst assuming the N and S terms are constant The constant terms are combined with the 'b' term (Eqn 4.56f) to derive the [B] matrix. With the y-sweep the E and W terms are assumed constant. Further details of using TDMA to solve Eqn 4.68, are well documented and described in standard texts on numerical analysis like Vichenevetsky (1981).

4.6.2 TDMA Applied to the Pressure Correction Equation

During a z-sweep along a constant y (the *j*th line), the best estimate for the P'_{ij+1} (P_N') value is usually that from the previous *k*-1 th iteration P'^{k-1}_{ij+1}. This leads to slowed convergence. Van Doormaal and Raithby (1984) introduced an approximation for P'_{ij+1} that makes use of the P'_{ij} (P_p') such that

$$[P'_{ij+1}]_{best\ estm.} \sim [P'_{ij+1}]^{**} + (\theta - 1)(P'_{ij} - [P'_{ij}]^{**}) \tag{4.69}$$

where θ is a relaxation parameter which lies in the range 1.85 - 1.95. The present study uses a value of θ = 1.85. The superscript '**' indicates the value from the previous iteration. When Eqn 4.69 is introduced into the P' equation, Eqn 4.56, the result is

$$[a_P - a_N(\theta - 1)]\, P'_P = a_E P'_E + a_W P'_W + a_N\{[P'_N]^{**} - (\theta - 1)[P'_P]^{**}\} + a_S P'_S + b \tag{4.70}$$

The relaxation parameter, θ, is applied to the y-sweep along lines of constant z (i lines) in a similar manner. This relaxation is used in the present study.

4.6.3 Stability and Convergence

To stabilise the computation and remove the risk of divergence, the standard discretised equation, Eqn 4.22, is under-relaxed by a factor, E, such that

$$a_P (1 + \frac{1}{E})\, \phi_P = \sum a_{nb} \phi_{nb} + b + \frac{a_P}{E} \phi_P^{**} \tag{4.71}$$

where ϕ_P^{**} is the value of ϕ_P from the previous iteration. This also improves the convergence of the computation. E is related to a relaxation parameter similar to that of Eqn 3.57, α_p, by

$$E = \frac{\alpha_\phi}{1 - \alpha_\phi} \tag{4.72}$$

and lies in the range of 4 to 10.

For all the variable computations, the convergence criterion used to terminate the computation, as stated in Section 4.6, is of the form

$$\|r_P\|^k \leq \beta \|r_P\|^0, \tag{4.73}$$

where

$$\|r_P\|^k = \{ \sum_{\text{domain}} [(a_E\phi_E + a_W\phi_W + a_N\phi_N + a_S\phi_S + b - a_P\phi_P)^{(k)}]^2 \}^{1/2} \qquad (4.74)$$

is the Euclidean norm of residuals for the k th iteration. The factor β is used to express $\|r_P\|^k$ as a fraction of $\|r_P\|^0$ (the residuals at the start of the computation), and lies in the range 0.15 - 0.25. This criterion requires less computational effort than that of attempting to drive $\|r_P\|^k$ to below a cut-off value (Van Doormaal and Raithby 1984).

4.7 Summary

In the foregoing, the momentum, and turbulence species transport equations have been discretised and presented for numerical integration. The SIMPLE method of pressure field computation, through the use of the continuity equation, was presented. These procedures will be applied to the present flow situation in Chapter 7 and the results of the numerical study presented in Chapter 8. As stated in the Introduction, the format of the computations in Chapter 7 leans on the present and past empirical data. Chapter 5, next, is devoted to the collection of this experimental data in the present cross-section.

CHAPTER 5: EXPERIMENTAL INVESTIGATION

5.1 Introduction

To experimentally determine the mean and turbulent flow fields in this study, several experimental procedures were used. This chapter describes the methods used. Section 5.2 describes the experimental set-up, and how uniform flow was established. It also explains how the development and cross-sectional symmetry of the turbulent flow at the measurement section was assured. Section 5.3 deals with the roughening of the flume bed. Finally, Section 5.4 introduces the practise of Laser Doppler Anemometry (LDA), which was used to carry-out detailed point-by-point measurements. The results of these investigations are presented in Chapter 7.

5.2 Establishment of Fully-Developed Uniform Open-Channel Flow

The experiments were conducted in the Hydraulics Laboratory of the Department of Civil Engineering, at Newcastle University.

5.2.1 The Experimental Set-Up

Figure 5.1, and Plates 5.1 and 5.2 show the set-up of the experimental rig. The cross-section of the pipe channel itself is shown in Figure 5.2. The set-up consists of a 305 mm internal diameter (D) pipe flume 12 metres long - made up of several pipe-sections. All the sections, bar three at the measurement area, were of opaque hydraulically smooth commercial Poly-Vinyl Chloride (PVC). To facilitate LDA usage, the three pipe sections near the measurement section - at $x = X_m = 6.265$m downstream of the inlet - were of transparent perspex. The flume rests on brackets placed within a rectangular glass-walled channel - and the slope of the outer channel is equal to that of the pipe flume. The flat rigid bed shown in Figure 5.2 is made-up of PVC layers and runs the whole length of the flume. A sealant was applied to the pipe-section joints, and the pipe-bed interface.

Flow is supplied by a recirculating pump delivering water from a sump up to an elevated tank which then delivers the water to the header tank of Figure 5.1. In the header tank, diffusers were designed and fitted onto to incoming conduits, and within the tank itself in order to dampen fluctuations and steady the flow. This also assured the symmetry of the flow at the inlet to the flume.

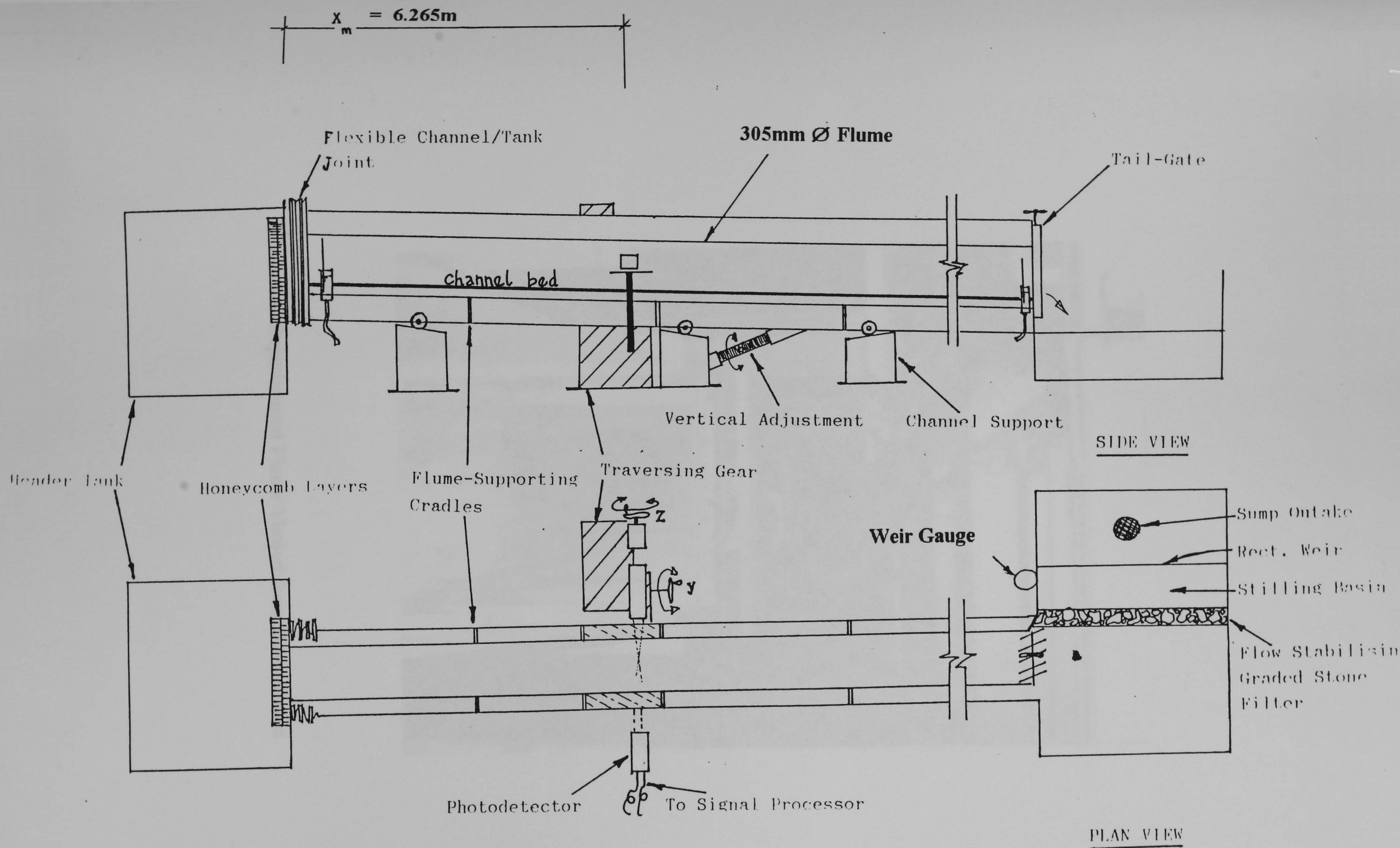

Figure 5.1 Experimental Set-Up - not to scale (Hoohlo 1991)

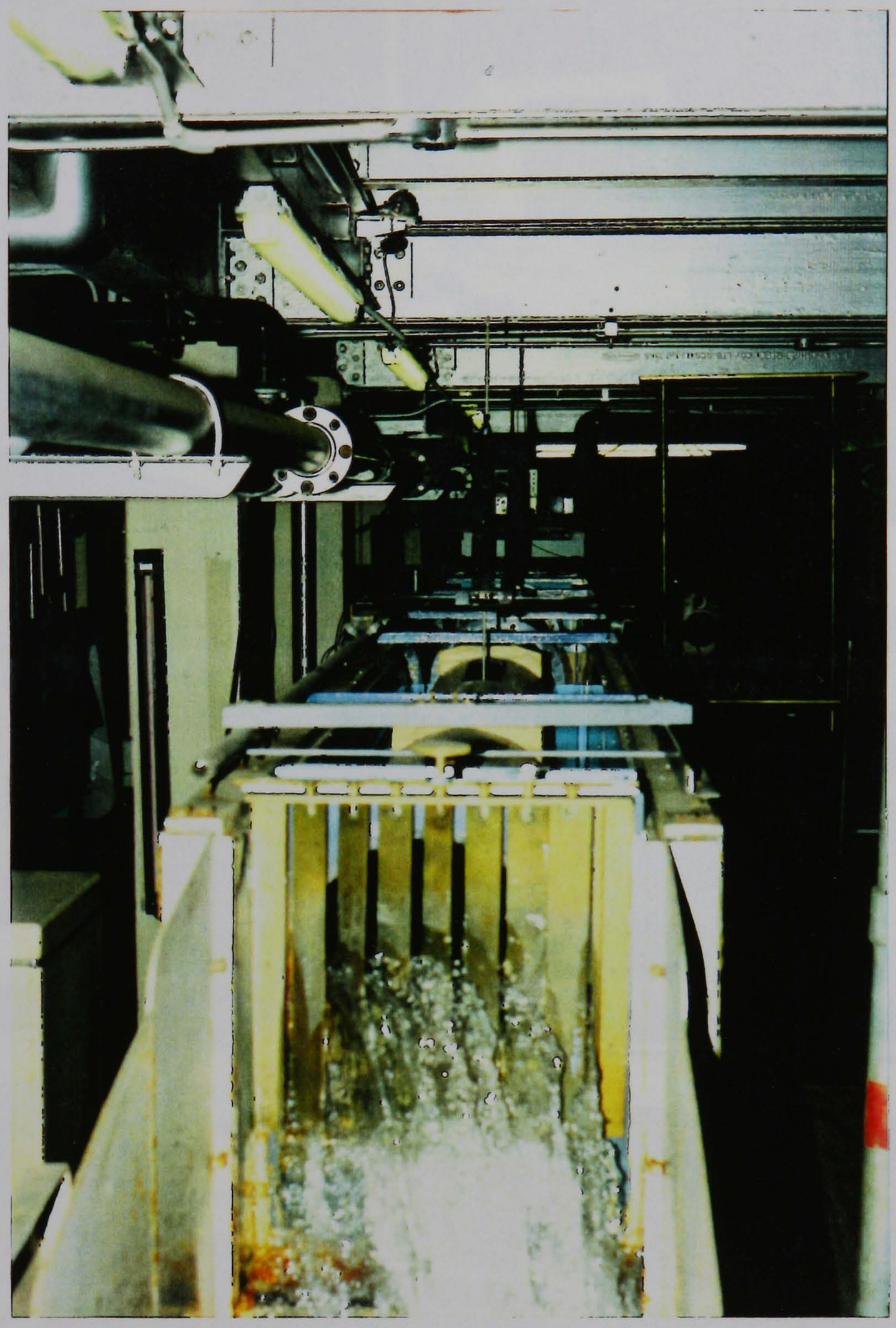

Plate 5.1 Experimental Flume Viewed from Downstream

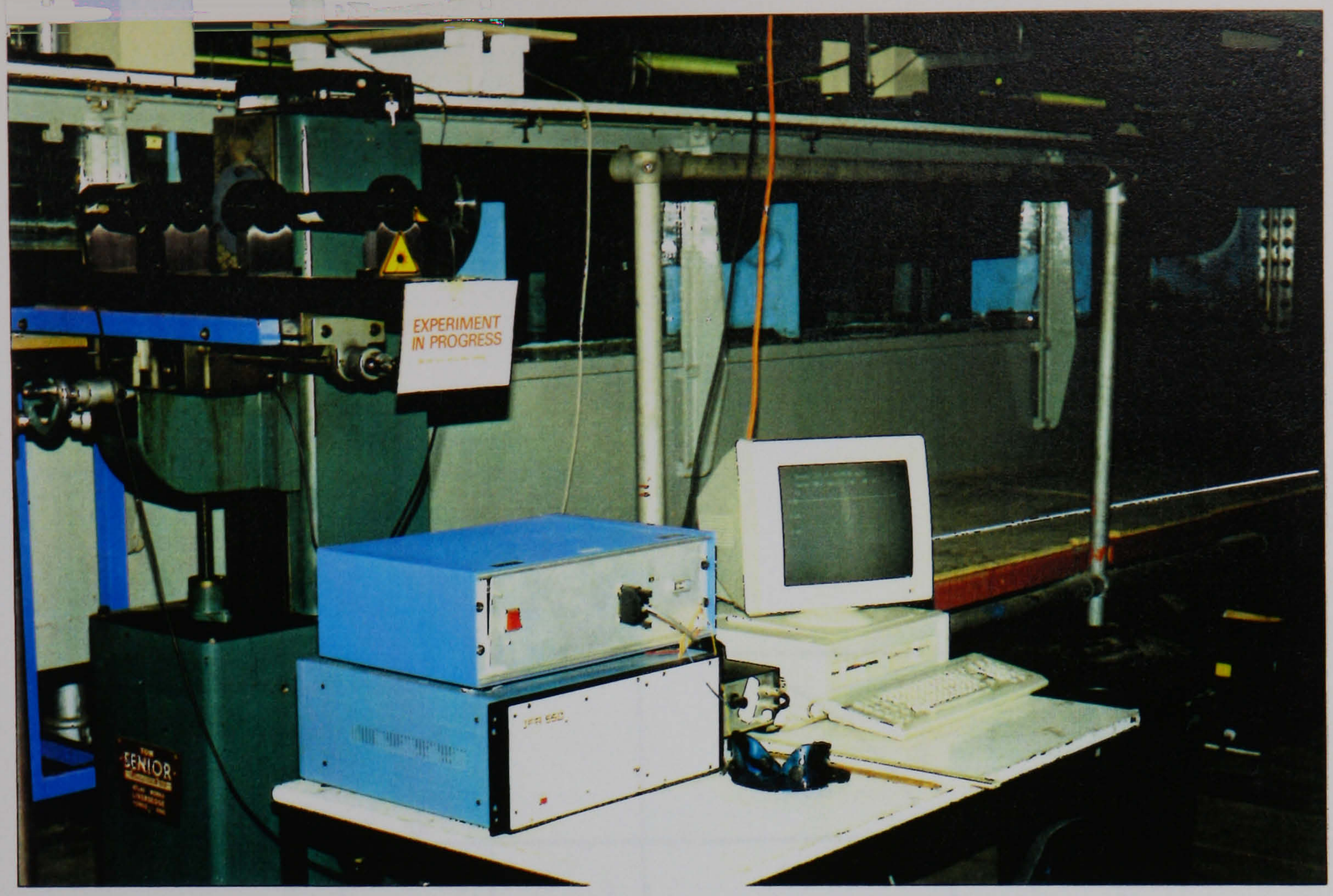

(a) Transmitting Optics, Traversing Gear, IFA 550, Computer

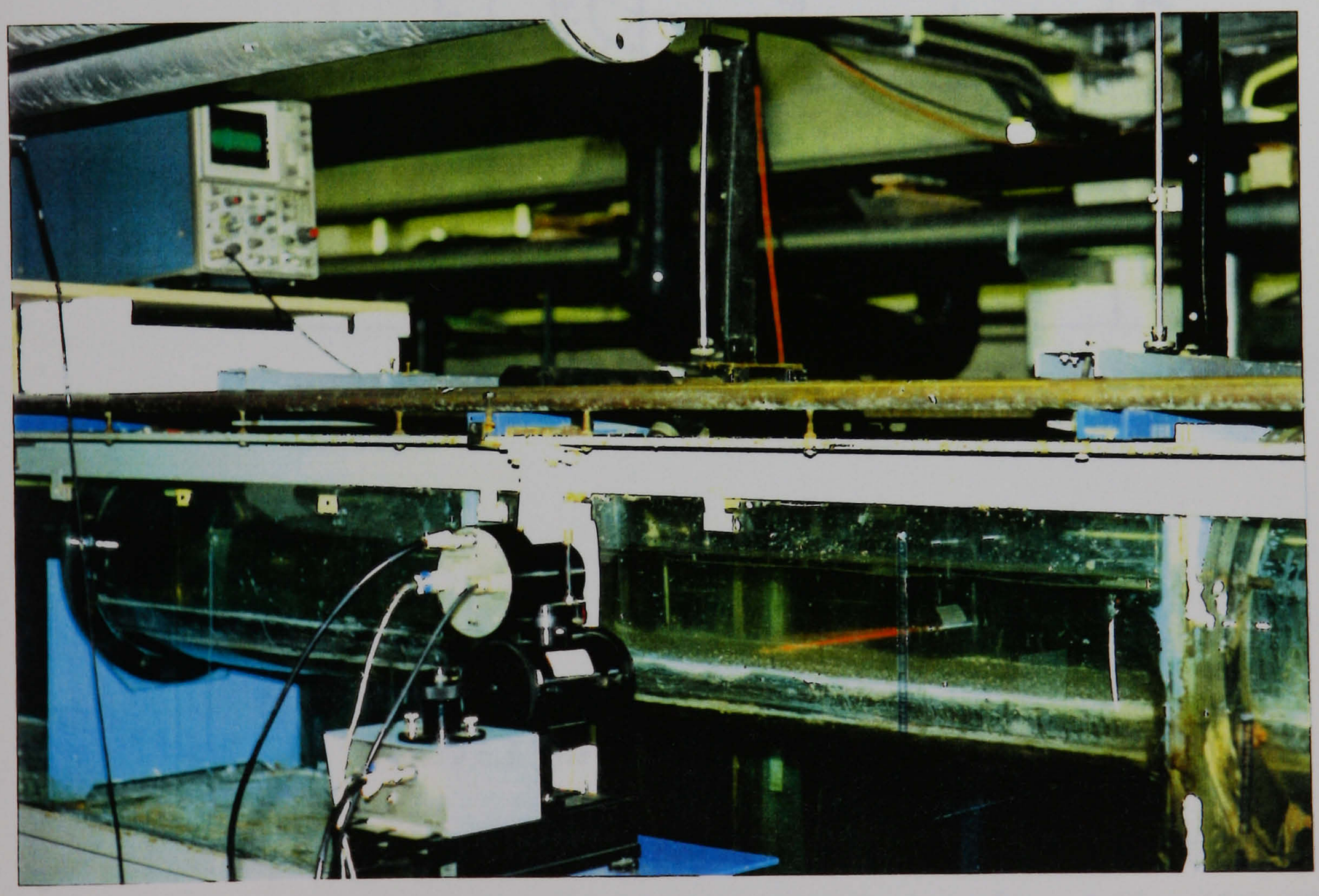

(b) Receiving Optics, Oscilloscope

Plate 5.2 LDA Apparatus

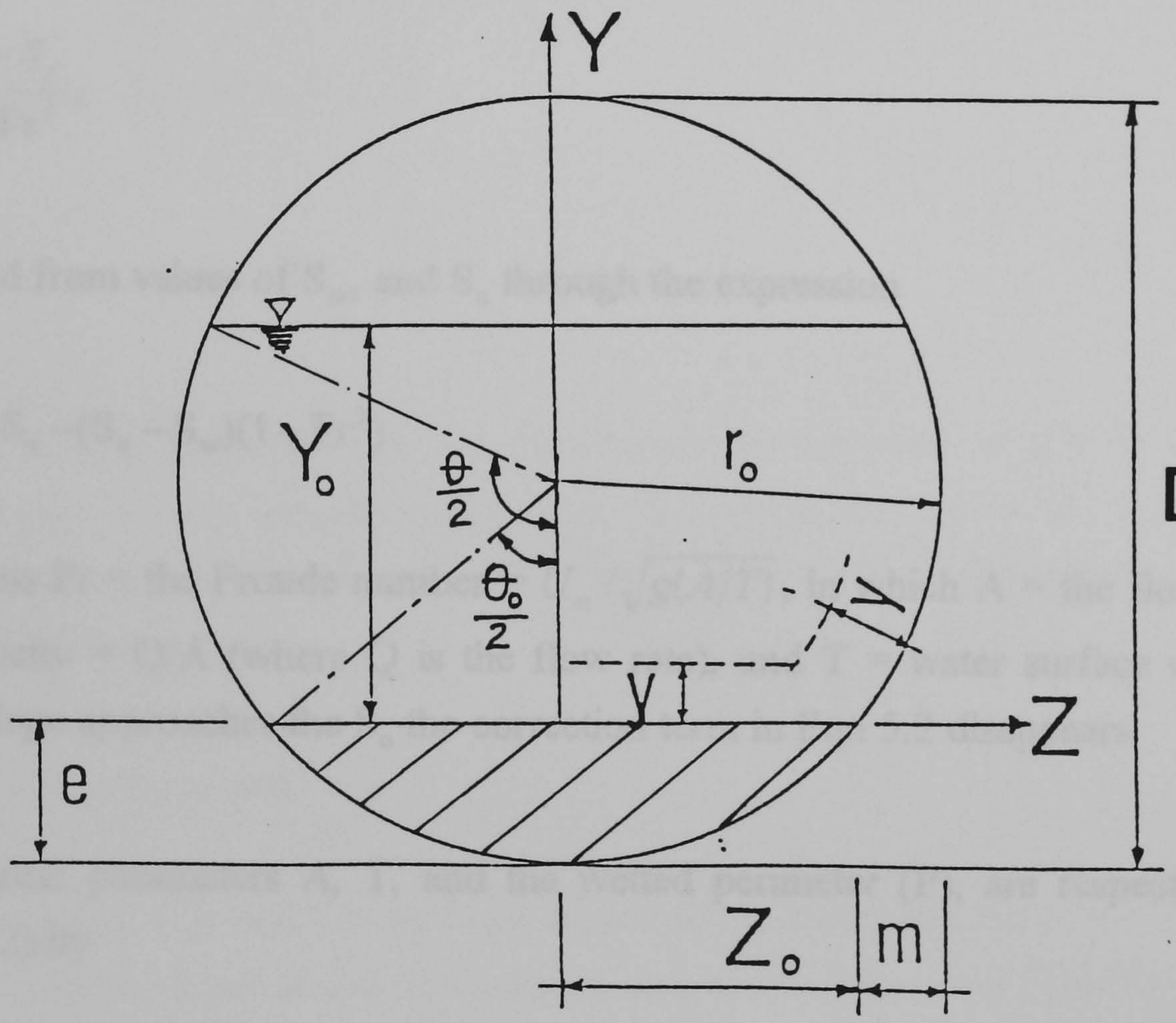

Figure 5.2 The Channel Cross-Section

The channel slope (S_o) was manually adjusted by means of the jack shown in Figure 5.1. The set-up was capable of S_o values ranging from zero (horizontal) to 4.36×10^{-3}. The maximum measurement error was of 0.002% of the smallest slope used. Measurements were carried out for two slopes 4.63×10^{-4} and 9.27×10^{-4}.

5.2.2 Uniform Flow Establishment

Uniform flow was established by the procedure explained by El-Zaemey (1991). The water surface slope (S_w) is determined by a linear regression fit of the uniform flow depths (Y_o) measured at approximately 1 m intervals. The existence of S_w means that the effective friction slope differs from both the bed slope S_o and the friction slope S_f This effective friction slope ($S_{effective}$) is derived from the standard gradually varied flow equation

$$\frac{dY_o}{dx} = \frac{S_o - S_f}{1 - \mathrm{Fr}^2}, \tag{5.1}$$

and is calculated from values of S_w, and S_o through the expression

$$S_{effective} = S_o - (S_o - S_w)(1 - \mathrm{Fr}^2). \tag{5.2}$$

In both equations Fr = the Froude number = $U_m / \sqrt{g(A/T)}$, in which A = the flow area, U_m = bulk mean velocity = Q/A (where Q is the flow rate), and T = water surface width. As the water surface slope approaches the S_o the correction term in Eqn 5.2 disappears.

The geometric parameters A, T, and the wetted perimeter (P), are respectively defined (from Figure 5.2) by

$$A = \frac{D^2}{4}\left(\theta - \frac{\sin 2\theta}{2}\right) - \frac{D^2}{4}\left(\theta_o - \frac{\sin 2\theta_o}{2}\right) \tag{5.3}$$

$$T = \frac{D}{\sqrt{2}}[1 - \cos(2\pi - \theta)]^{1/2} \tag{5.4}$$

$$P = D(\theta - \theta_o + \sin\theta)) \tag{5.5}$$

Slight mis-alignments of the pipe sections lead to the formation of cross-waves and subsequent unevenness of the water surface. To check whether these affected the uniformity and steadiness of the flow, the Vedernikov number (V_n) was used (see Chow 1959). It is defined as

$$V_n = m' \gamma \frac{U_m}{U_{crit}} = m' \gamma \mathrm{Fr} \tag{5.6}$$

where m' = 2/3, U_{crit} = the critical bulk velocity of the flow. The shape factor (γ) is defined as

$$\gamma = 1 - R\frac{dP}{dA}, \tag{5.7}$$

where R is defined as the hydraulic radius

$$R = \frac{A}{P}. \tag{5.8}$$

When the value of V_n is less than unity, the disturbances are drowned out and the flow is stable. The slopes investigated were subcritical (Fr < 1). As a result, the values of V_n were less than unity. This showed that the flow was stable, and the surface profile disturbances did not develop into unstable roll-waves.

5.2.3 Bulk Flow Measurement

The bulk flow rate (Q) was measured by means of a rectangular sharp-crested weir placed downstream of a stilling basin at the downstream end of the flume (see Figure 5.1). The weir was calibrated according to the British Standard BS 3680: Part 4A:1981 by El-Zaemey (1991). For the present study, only the datum of the weir gauge was reset and regularly checked according to BS 3680 to give a standard error of 1.5%.

The expression for Q (in m^3/s) in terms of the head over the weir (h_w) was given by El-Zaemey (1991):

$$Q = [1.777 + 0.245(\frac{h_w + 0.0012}{0.443})]0.4495(h_w + 0.0012)^{3/2} \tag{5.9}$$

in which h_w is given in metres (m).

Fluctuations of the water level inside the well gauge occurred despite the stilling basin and were of the order of 5 mm - giving an error to the value of h_w. In this study, they affect the calculated value of Q by up to 5.6% for the lowest flow. This is acceptable as the quoted value is an overestimate based on the largest fluctuations affecting the lowest flow - although the highest fluctuations occur at the higher flow cases.

5.2.4 Development of the Flow Profile

Patel (1974) quotes Coles' criterion for turbulent channel flow development: *a fully developed state is assured when all the structure related statistical quantities (velocity rms, spectra ... etc.) at a given x-station do not change with x and, in addition, do not change when the flow system's inlet conditions are altered in a significant way.* For this reason, buffers at the inlet were not used as an aid to the flow development (see Clark 1968, and Hussain and Reynolds 1975). The 'Honeycomb Layers' in Figure 5.1, are drawn-in purely for illustrative purposes. In fact, Bradshaw (1965) showed that buffer usage may affect the transverse boundary shear distribution. Only two trip wires (of 2 mm diameter), and a 25mm x 25mm wire mesh were thus used to trip the flow. This is based on the principle of the critical height (k_{crit}) of a roughness element placed across the flow such that the element aids the transition of the flow to turbulence (see Schlichting 1968) - and is given by $k_{crit} = 20\ \nu/(U_*)_{ave}$ where $(U_*)_{ave}$ is the average shear velocity. For all flows the thickness of the mesh and trip wires is above this critical thickness.

Flow development was judged from the centreline profile of the longitudinal velocity measured at approximately 1m intervals up to x = 7.120m, using an analogue propellor current meter. The velocity is calculated from the manufacturer's calibration curves (Alvarez-Hernadez 1990) based on the number of cycles per second (Hz) made by the meter's propeller. Melling (1975), and Melling and Whitelaw (1976) took measurements at the measurement distance, X_m, such that $X_m/(4R) = 36.8$. In the present study, measurements were taken at $X_m = 6.265$m which yields $19 \leq X_m/(4R) \leq 49$ depending on the flow depth. The values of $X_m/(4R)$ and the velocity profile measurements showed that the flow was sufficiently well-developed. Inlet distances were taken using a normal tape measure with 1mm gradation.

The symmetry of the flow about the channel centreline was also checked using the LDA, prior to the actual measurements being taken.

5.2.5 Kinematic Viscosity

The kinematic viscosity (in m^2/s) was determined from an empirical function of the water temperature, T', (El Zaemey 1991)

$$\nu = \frac{1.79 \times 10^{-6}}{1 + 0.03368\,T' + 0.000221\,T'^2}. \qquad (5.10)$$

During each experimental run, variations in T' were small due to the large water reservoir used. The values of T' were taken to the accuracy of 1 °C.

5.3 Roughening of the Flat Bed

Graded sand and gravel were used to roughen the pipe bed. The roughening material was graded in accordance with the British Standard BS1377: Part 2: (1990). Three roughnesses, d_{50} = 0.93mm, 4.2mm, and 1.71mm, were used (roughnesses Rough1, Rough2, and Rough3 respectively). d_{50} is the diameter at which 50 *per cent* of the grains of the graded material are smaller. It is obtained from grading curves produced according to BS 1377: Pt 2 (1990).

The grains were attached to the flat bed by (i) placing a double-sided tape onto the bed; (ii) applying oil-based paint onto this tape to act as an adhesive; (iii) evenly sprinkling the grains onto the bed by hand when the paint is sticky; (iv) and, letting the paint dry over 24 hours and removing the excess grains to form a uniform single-layered roughness. Plates 5.3 - 5.5 show the three applied roughnesses. The endurance of the roughness was tested by running the flume at flow rates higher than experimental ones. Only when no erosion occurred was the roughness adopted for experimentation. Flows over the roughened bed also have to satisfy the above criteria of uniformity and development.

The equivalent sand roughness (k_s) is determined from the method of Kamphuis (1974) such that

$$k_s \cong 2d_{90}. \qquad (5.11)$$

This uses the rough-boundary logarithmic law, Eqn 2.28, to obtain k_s from the measured velocity profile. The origin of this profile is assumed to be at $0.7d_{90}$ above the smooth surface. Kamphuis deduced Eqn 5.11 from results in which $10 < Y_o/d_{90} < 100$, (as with present flow

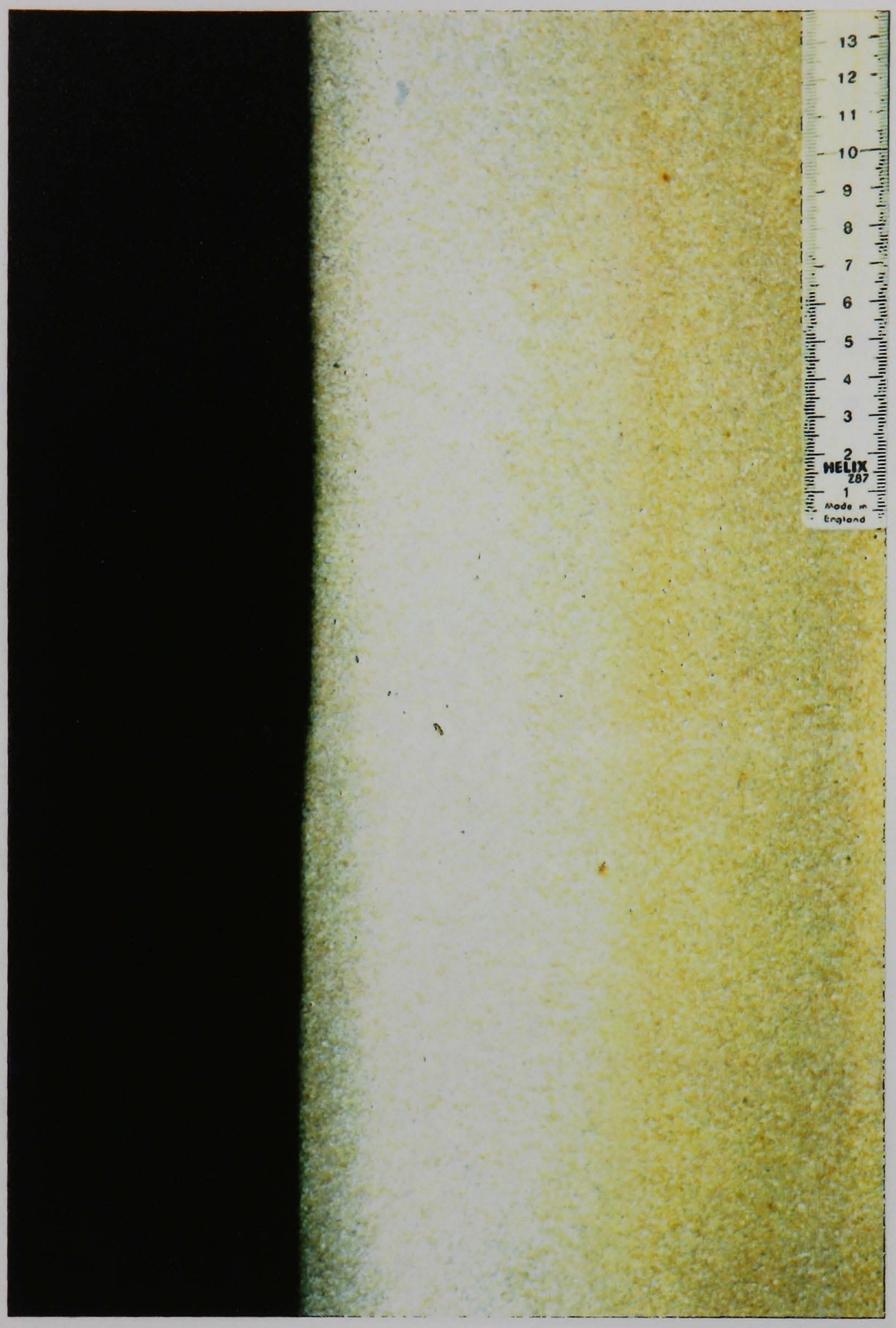

Plate 5.3 Bed Roughness (Rough1): d_{50} = 0.93 mm

Plate 5.4 Bed Roughness (Rough2): d_{50} = 4.20 mm

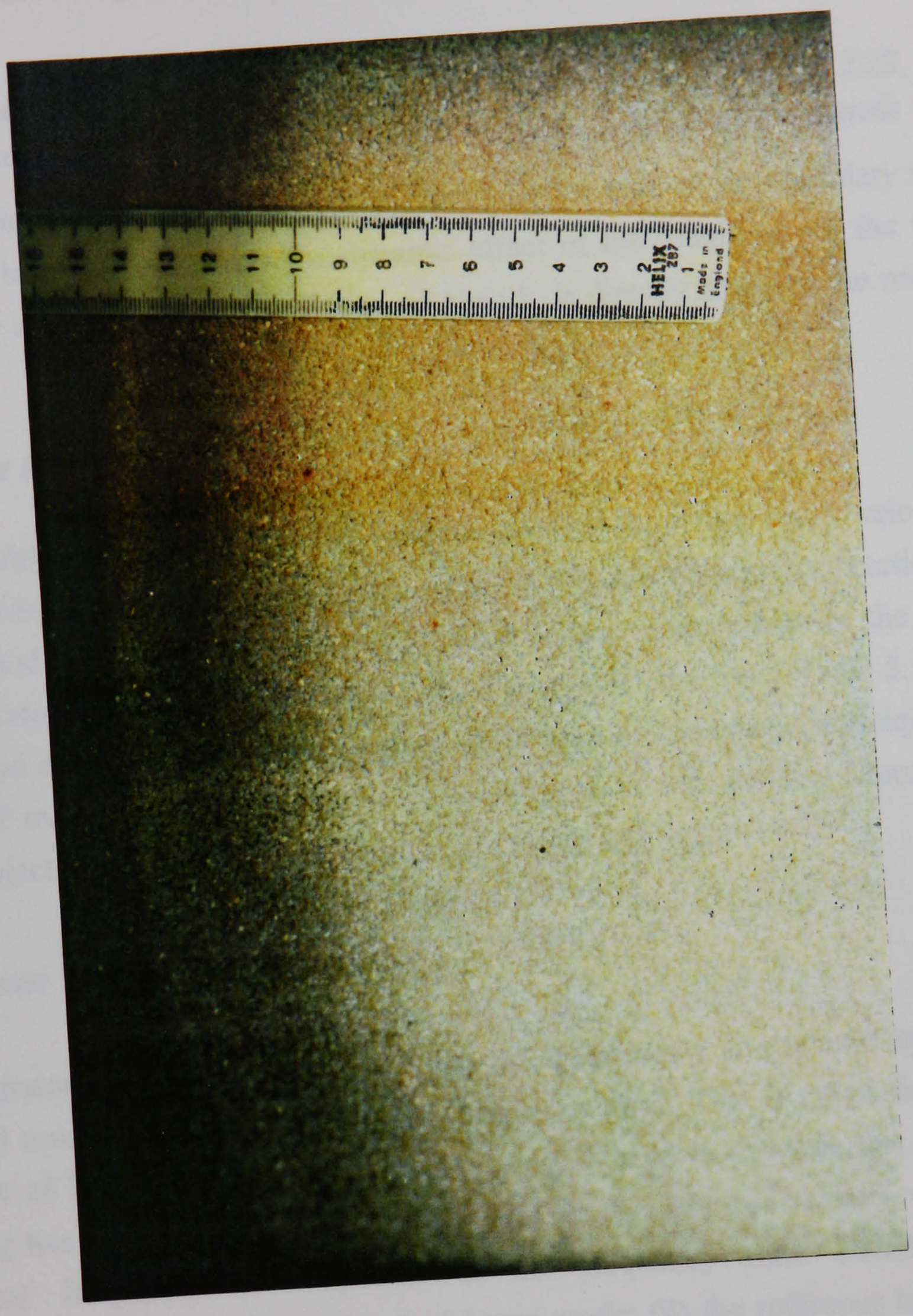

Plate 5.5 Bed Roughness (Rough3): d_{50} = 1.71 mm

cases) leading presently to its adoption as the definition of k_s. In the present study k_s = 2.36mm, 10.2mm, and 3.92mm for Rough1, Rough2, and Rough3 respectively.

The large k_s values given by Eqn 5.11 result from Kamphuis' use, in Eqn 2.28, of the friction velocity defined as $U_* = \sqrt{g\,Y_o\,S_f}$ (as opposed to $U_* = \sqrt{g\,R\,S_f}$) for channels of high bed roughness. This simplification follows from the fact that the bulk of the boundary shear is carried by the rough bed. It thus reflects the dynamic effect of the roughness on the velocity profile rather than the normal physical description wherein k_s is directly linked to the roughness size.

5.4 Laser Doppler Anemometry

Laser Doppler Anemometry (LDA) was used to measure both the mean velocity and turbulence intensities in the present study in the longitudinal (x), and vertical (y) directions. The Laser Doppler Method (developed in the1960s) is based on the measurement of the Doppler shift of laser light scattered from small particles carried along with the fluid. Table 5.1 gives a list of advantages and disadvantages of LDA - over other fluid measurement techniques, such as hot-film. A brief overview of the theory of LDA is given in this section. More detailed treatment of the subject is given in texts like Durst *et al* (1976) and Drain (1980).

5.4.1 Theory of Laser Doppler Anemometry

In typical laboratory flows, when the laser light of frequency f is scattered by particles carried in the fluid medium, it undergoes a small frequency shift. This is called the Doppler shift. The principle of heterodyning or frequency-'beating' is used to measure this shift. This involves presenting two light beams of different frequencies to a photo-detector - which then produces the 'beat' frequency or component of the frequency shift. Possible optical arrangements used to achieve this are (i) the dual beam mode; (ii) the reference beam mode; and (iii) the dual scatter mode. A dual beam forward scatter arrangement, shown in Figure 5.3(a), is used in the present study. The scattered light (from one of the beams) is heterodyned with light from the second beam which has the original frequency. Of the three above, this mode gives the best signal-to-noise ratio.

The Doppler shift frequency (f_d) is given by (Drain 1980)

$$f_d = \frac{2u}{\lambda}\sin(\frac{\phi}{2}) \qquad (5.12)$$

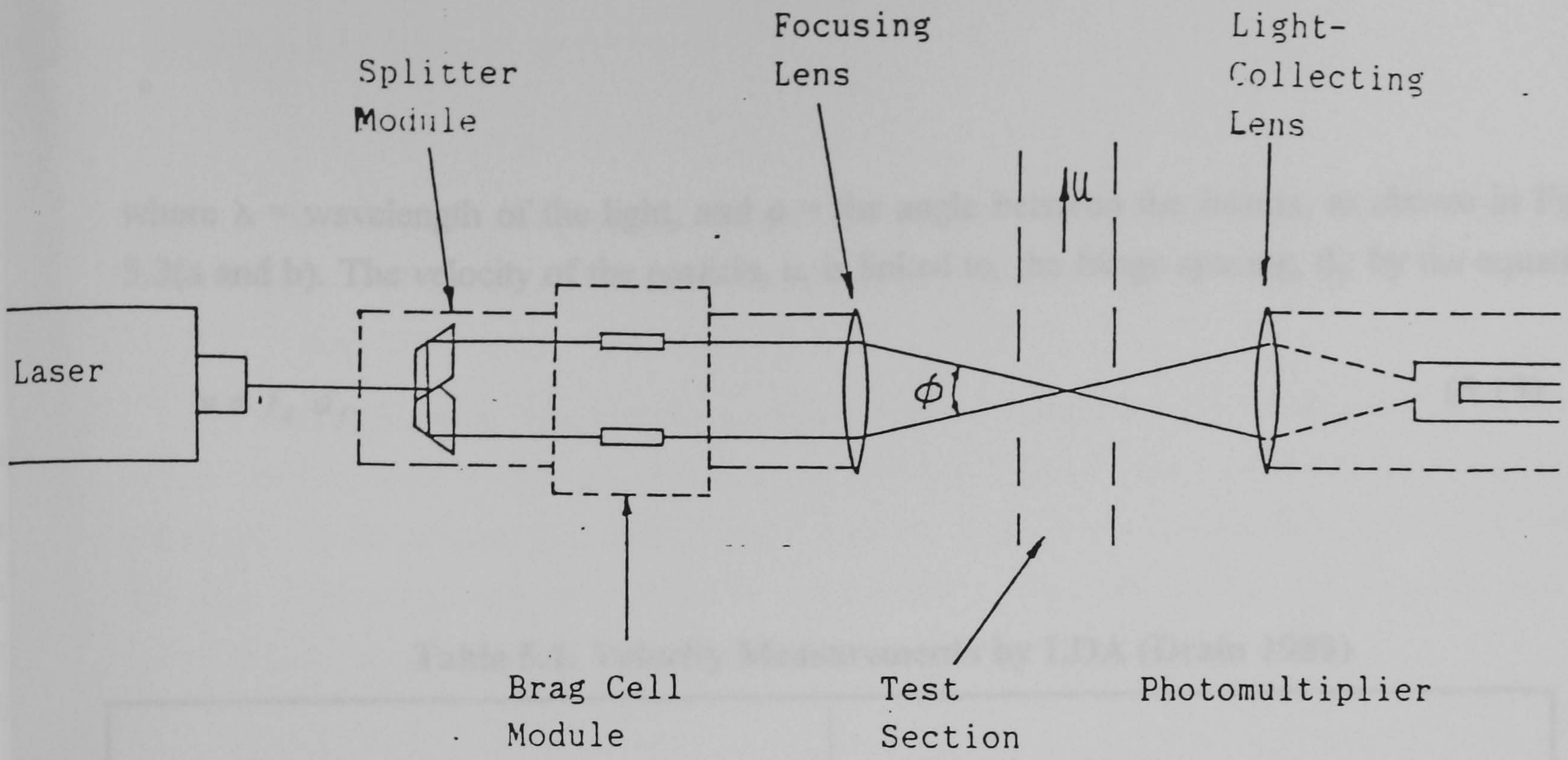

(a)

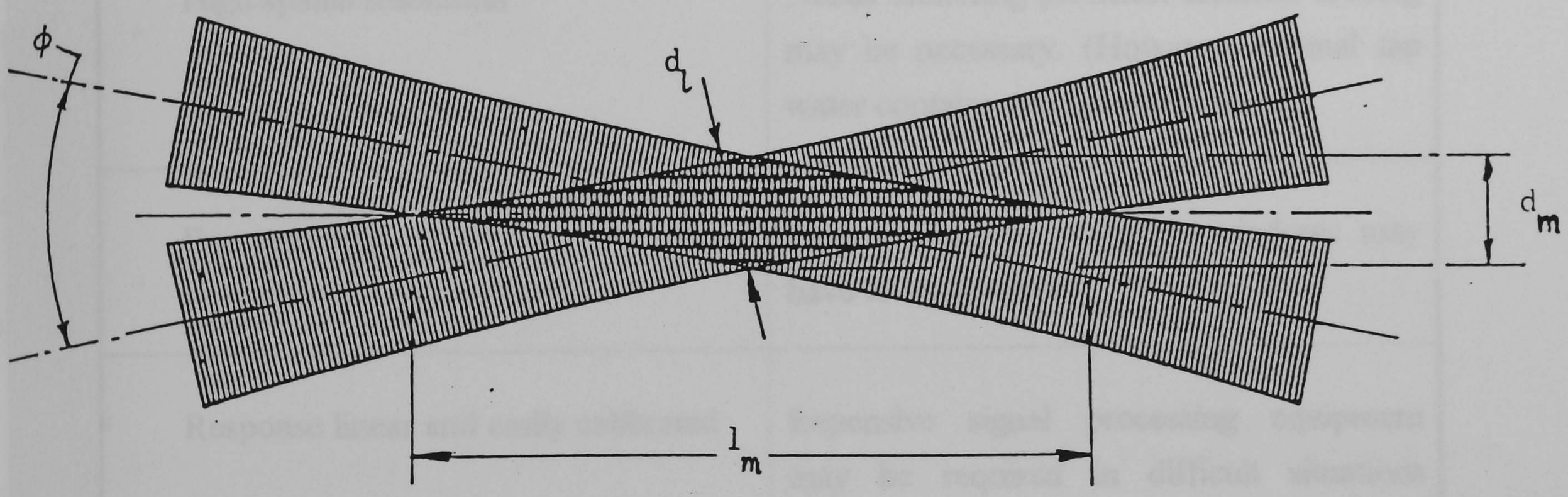

(b)

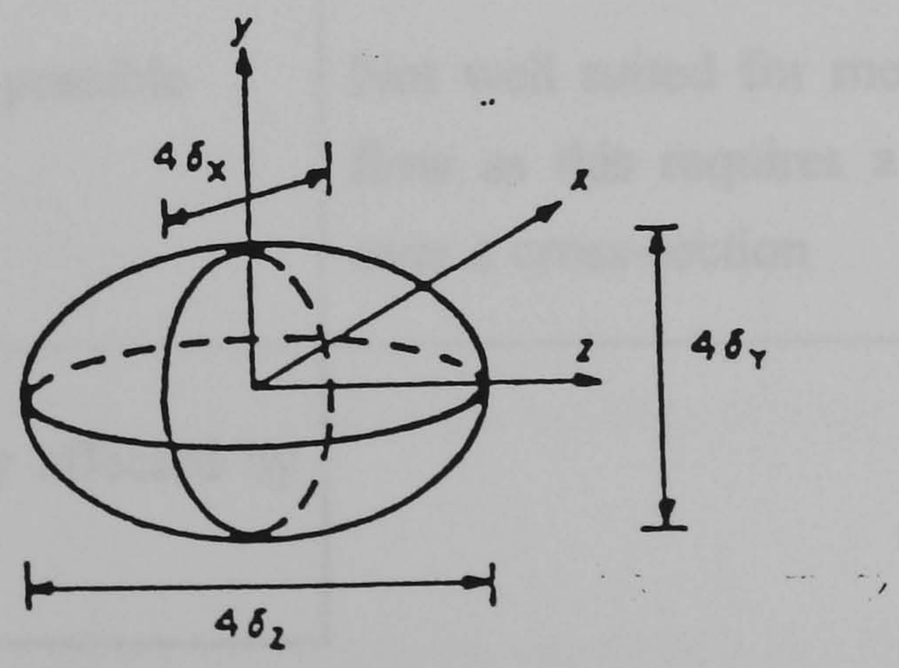

(c)

Figure 5.3 Priciples of LDA. (a) Beam Crossing; (b) Fringe Model

(c) Ellipsoid Probe Volume

where λ = wavelength of the light, and ϕ = the angle between the beams, as shown in Figure 5.3(a and b). The velocity of the particle, u, is linked to, the fringe spacing, d_f, by the equation

$$u = f_d \; d_f. \tag{5.13}$$

Table 5.1. Velocity Measurements by LDA (Drain 1980)

Advantages	Disadvantages
Does not disturb the flow	Medium must be transparent
High spatial resolution	Needs scattering particles: artificial seeding may be necessary. (However, normal tap water contains enough particulates)
Fast response	Optical access is required: windows may have to be installed
Response linear and easily calibrated	Expensive signal processing equipment may be required in difficult situations where the signal-to-noise ratio is poor
Directional discrimination possible	Not well suited for measurements of total flow as this requires a tedious integration over a cross-section
Operation not usually seriously affected by temperature	

The crossing of the two beams gives out a 'fringe' pattern of Figure 5.3(b) which is due to the light of the two beams 'beating': adding (light areas) and cancelling-out (dark areas). The intensity of the light across each beam (and the fringe pattern) follows a Gaussian distribution,

with a maximum at the centre. A particle moving perpendicularly through this fringe pattern scatters light. The intensity of the scattered signal is also Gaussian.

To obtain the dual beam mode, a single beam generated by a 20 milliwatt (mW) Helium-Neon (He-Ne) laser is split into two of equal intensity, placed at an equal distance from and on either side of the original line of the beam. A prism arrangement shown in Figure 5.3(a) is used for this. This prism unit is called the beam-splitter. The two beams are focused onto the measurement point by a lens of 243 mm focal length.

To achieve as small an intersection (measurement) volume as possible (and thus improve the spatial resolution), the angle ϕ is kept low. Presently $\phi = 5°$. The rough dimensions of this volume, shown in Figure 5.3(a and c), are

$$l_m = 4\delta_x = 4\sigma_x = \frac{d_l}{\sin \phi/2} \tag{5.14}$$

$$d_l = 4\delta_y = 4\sigma_y \tag{5.15}$$

$$d_m = 4\delta_z = 4\sigma_z = \frac{d_l}{\cos \phi/2}. \tag{5.16}$$

where σ_X, σ_Y, and σ_Z.are the standard deviations of the Gaussian intensity distribution of the beams. The quality of the signal that is given out by the particles carried in the fluid is determined by the number of fringes within the measurement volume (N_f)

$$N_f = \frac{d_m}{d_f} = \frac{2d_l}{\lambda} \tan \frac{\phi}{2} \tag{5.17}$$

following Eqns 5.12, 5.13, and 5.16. The higher the number of fringes, the higher the signal-to-noise ratio.

The flow direction of a scattering particle is distinguished by shifting the frequency of one of the light beams before crossing the two beams. Several methods used to produce the frequency shift (Δf) (Drain 1980) include reflection, diffraction gratings, and acoustic waves. Presently, (Table 5.2) an acoustic frequency shifter called the Bragg cell is used.

When the shifted and the unshifted beams cross, a moving fringe pattern similar to that of Figure 5.3(b) results. A stationary particle placed in this fringe pattern gives-out a signal of frequency Δf. Therefore, a particle traversing the pattern in the direction of the fringe 'movement' results in a signal of frequency $f - \Delta f$. A signal of frequency of $f + \Delta f$ is given out by a particle moving in the opposite direction. This enables directional discrimination. It is worth noting that shifting the beam also deflects it. A prism is incorporated near the Bragg cell to return the beam to its original direction.

Frequency shifting leads to errors in measurements near the wall, and where there is a large curvature of the wall. This is caused by the 'moving' fringe pattern, whereby stationary objects like impurities stuck onto the wall, result in a signal of frequency near Δf. The solution for this is to set the band-pass filters of the signal processors to leave out or 'drop out' signals at or near frequency Δf. This does not affect the measurements greatly (Drain 1980).

The scattered light is collected by a light detector. To improve the signal quality, it is protected by from stray light by means of lens covers with apertures large enough to allow-in light only from the measurement volume at the beam crossing point. The present detector is of the photo-multiplier type. Questions about the coherence of the scattered light and the signal thus produced, are posed by Buchhave *et al* (1979). For the present study coherence does not pose a significant problem.

Processing the signal involves (i) identifying a Doppler signal from the photo-detector; (ii) ensuring that it is 'held' long enough to produce correlations etc.; and (iii) presenting that signal for collection by computer. The TSI IFA 550 signal processor carries out these functions (Figure 5.4), which are explained further in sub-Section 5.4.2 below.

In addition to the disadvantages stated in Table 5.1, George and Lumley (1973) pointed out that other inherent errors of LDA include (i) the neglect of velocity fluctuations within the measurement volume, (ii) the neglect of mean velocity gradients within the volume, (iii) the effect of the finite transit time through the volume, and (iv) the fact that the measured velocity is that of the solid particles not of the fluid itself. In this study these problems do not significantly affect the results.

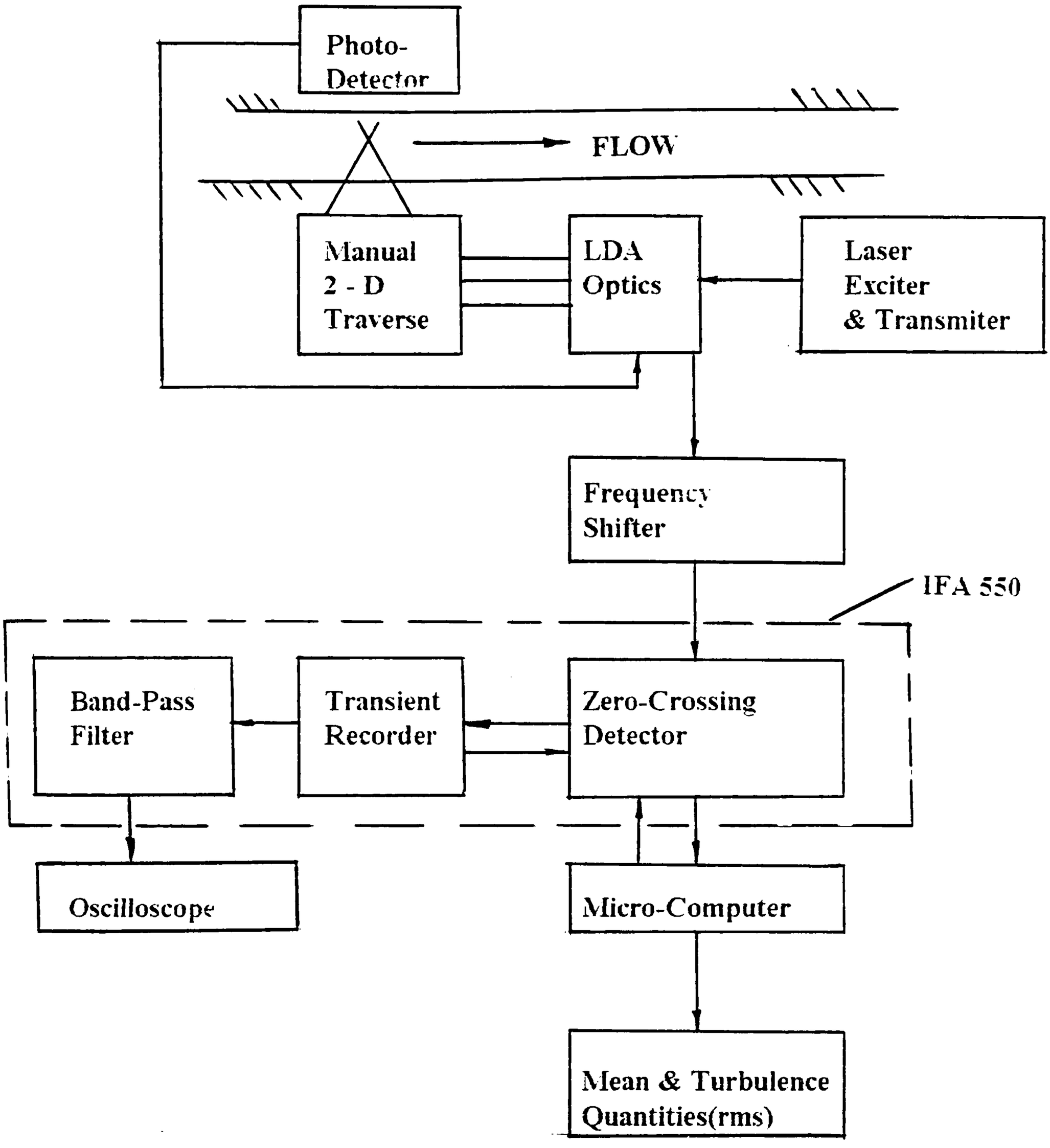

Figure 5.4 Schematic Diagram of LDA System

5.4.2 Equipment Used

Most of the LDA equipment is manufactured by Thermo-Systems Inc.(TSI). Table 5.2 summarises the details of the individual components schematically illustrated in Figure 5.4. The dual beam system is used in the forward scatter mode in which the scattered light is collected on the other side of the measurement point - aligned with the transmitting optics (Plate 5.2).

The transmitting and receiving optics are mounted on a manual traversing table which moves in the y - z plane. Positioning errors and corrections are reviewed in sub-Section 5.4.3 below. An automated y-direction traversing table controlled directly by computer was commissioned as part of the study; details are given in Appendix A. However, the manually-controlled table was used throughout the study because of its ability to move in the two directions x and y, which enabled channel-wide measurements.

5.4.3 Evaluation of Equipment

With the laser light being mono-chromatic, only one component of velocity is measured at a time. The rotation of the beam splitter is used to enable independent x- and y-direction measurements. The mean velocities U and its corresponding true 'rms' value, U_{rms}, were measured first. The beam splitter was then rotated 90° to measure V and V_{rms}. Since the flow is assumed steady and stationary, independent measurement of the two components results in little error. Nezu and Rodi (1986) also note that a two-colour system did not substantially improve the accuracy of their earlier results (Nezu and Rodi 1985) obtained with a one-color system. The ranges of the measured values were: $0.050\ m/s \leq U \leq 0.900\ m/s$: $0.010 \leq U_{rms} \leq 0.090 m/s$; $-0.040 \leq V \leq 0.040\ m/s$; and $0.000 \leq V_{rms} \leq 0.040\ m/s$.

The curvature of the pipe walls leads to positioning errors unless the beams always strike the pipe walls perpendicularly. Since the traverses are in the Cartesian x- and y-directions, the beams are not always perpendicular to the pipe wall. The curvature effect was eliminated by placing water within the rectangular channel at the measurement section (see Durst *et al* 1976). This is based on the assumption that the refractive index (m) of the rectangular glass channel is equal to that of the perspex pipe.

Table 5.2. Equipment Used.

Component	Make and Model
Laser Exciter	Spectra Physics. Model 124
Laser Generator	TSI. Model 925. 20 mW He-Ne Monochromatic. Light Wavelength = 0.6328 μm.
Beam Splitter	TSI. Model 915. 50 mm spacing of split beams.
Frequency shifter	TSI. Model 910 Bragg cell. 0.1 MHz Shift Used.
Focusing Lens	TSI. Model 918. Focal length = 243 mm.
Receiving Optics	TSI. Model 930, with Model 932 base. Model 10096 eyepiece for manual signal optimisation.
Photo detector	TSI. Model 950. Photo-diode.
Current Amplifier	TSI. Model 960.
Signal Optimisation	By eye as mentioned above. Also by optimising the trace of the signal displayed on the oscilloscope.
Signal detection, recording and processing	TSI. Intelligent Flow Analyser(IFA) Model IFA 550.

To ensure that the curvature effect has been removed, a correction of the position of the crossing point is made by using different refractive indices for glass and perspex. This is done according to Eqn 5.18:

$$z_5 = t_4\,(1-\frac{\cos\alpha_3}{\sqrt{(\frac{m_4}{m_3})^2-\sin^2\alpha_3}}) + [z_3' + t_2\,(1-\frac{\cos\alpha_1}{\sqrt{(\frac{m_2}{m_1})^2-\sin^2\alpha_1}})]\;\frac{1}{\cos\alpha_1}\sqrt{(\frac{m_3}{m_1})^2-\sin^2\alpha_1}$$

(5.18)

which is derived by treating the five layers of Figure 5.5(a) as two sets of multiple layers - the first two-layered, and the second three-layered. The known values are those of the refractive indices m_γ and layer thicknesses (t_γ), where γ = 1,2,3,4, as shown on Figure 5.5. In Figure 5.5(b), the distance z'_3 is defined by

$$z_3' = (\frac{B_L}{2} - z_B \tan\frac{\theta_L}{2})\,\tan(\frac{\pi}{2}-\alpha_1). \qquad (5.19)$$

It was found that the position corrections were small. This confirms that the placing of the water within the rectangular channel does eliminate the curvature effect. This is true for measurements in both directions.

To find the centre of the channel the beam-crossing was placed on one of the walls and the position of the traversing table recorded. The beam-crossing was then horizontally moved to the opposite wall - and the position also recorded. The centreline is half-way between the two wall points. The same procedure was used in order to determine the vertical centre point. The nominal positioning accuracy of the table is $\pm 25\ \mu$m.

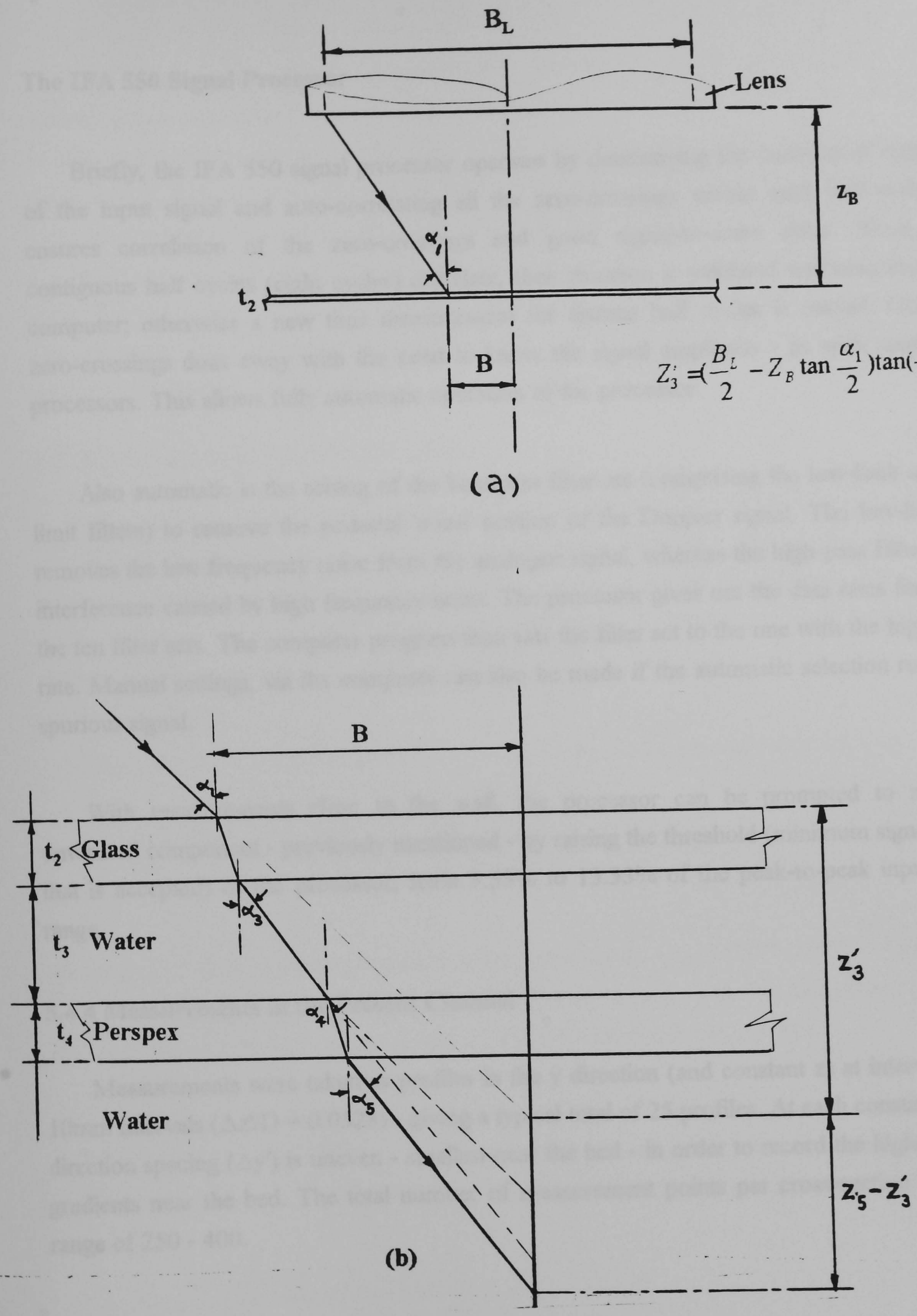

$$Z_3' = (\frac{B_L}{2} - Z_B \tan\frac{\alpha_1}{2})\tan(\frac{\pi}{2} - \alpha_1)$$

Figure 5.5 Refraction Correction: (a) From Focusing Lens; (b) Within Layers

The IFA 550 Signal Processor

Briefly, the IFA 550 signal processor operates by determining the duration of eight cycles of the input signal and auto-correlating all the zero-crossings within each half-cycles. This ensures correlation of the zero-crossings and good signal-to-noise ratio. When sixteen contiguous half cycles (eight cycles) correlate, their duration is validated and outputted to the computer; otherwise a new time measurement for sixteen half cycles is started. Correlation zero-crossings does away with the need to know the signal amplitude - as with counter-type processors. This allows fully automatic operation of the processor.

Also automatic is the setting of the bandpass filter set (comprising the low-limit and high-limit filters) to remove the pedestal 'noise' portion of the Doppler signal. The low-limit filter removes the low frequency noise from the analogue signal, whereas the high-pass filter reduces interference caused by high frequency noise. The processor gives out the data rates for each of the ten filter sets. The computer program then sets the filter set to the one with the highest data rate. Manual settings, via the computer can also be made if the automatic selection results in a spurious signal.

With measurements close to the wall, the processor can be prompted to reject the unwanted component - previously mentioned - by raising the threshold (minimum signal voltage that is accepted) of the processor; from 9.33% to 13.33% of the peak-to-peak input voltage range.

5.4.4 Measurements in the Present Channel

Measurements were taken as profiles in the y direction (and constant z) at intervals $\Delta z' =$ 10mm intervals ($\Delta z'/D = 0.0328$) - giving a typical total of 25 profiles. At each constant z, the y direction spacing ($\Delta y'$) is uneven - smallest near the bed - in order to record the higher velocity gradients near the bed. The total number of measurement points per cross-section lies in the range of 250 - 400.

Data rates were reasonable at around 100 - 300 samples per second (Hz), with the mean and rms values determined at 1000 samples intervals. The number of samples used to determine the true turbulence value varied from 6000 - 8000 for good signals, to 8000 - 18000 for poorer signal quality. At first, mean and rms values were recorded by hand in order to preserve a trace of the parameters. Time constraints meant automatic recording directly onto magnetic diskettes, was later used. The typical period for a complete traverse of the cross-section was around 22 hours. This meant more than one session was needed; although the effect of this on the results was minimised by limiting the variations of the flow rate (Q) and uniform slope from one session to the next to under 2%.

5.5 Summary of Error Calculations

There are two basic types of errors Systematic, and Random (Melling 1975). Systematic errors are a result of faulty or rigged/biased apparatus. They are often quoted to specify the level of accuracy expected from the apparatus - as noted in the preceding sections. Random errors introduce the scatter of data about a mean value. A summary of how these errors are calculated, is given herein.

The error for a calculated parameter Y, e_Y is determined from a standard formula

$$e_Y \equiv dY = \frac{\partial Y}{\partial \beta_1} de_{\beta_1} + \frac{\partial Y}{\partial \beta_2} de_{\beta_2} + \frac{\partial Y}{\partial \beta_3} de_{\beta_{31}} + \ldots \tag{5.20}$$

where β_i (i = 1,2,3...) are measured variables whose errors, $e_{\beta i}$, contribute to e_Y. Using Eqns 5.3 - 5.5, 5.8, and 5.20, the expressions for errors in the area (e_A), the wetted perimeter (e_P), the hydraulic radius (e_R), and the water surface width (e_T) respectively, become

$$e_A = \frac{D(1-\cos 2\theta)}{\sqrt{1-(\frac{r-e-Y_o}{r})^2}} e_{Y_o}, \tag{5.21}$$

$$e_P = \frac{4(1+\cos\theta)}{\sqrt{1-(\frac{r-e-Y_o}{r})^2}} e_{Y_o}, \tag{5.22}$$

$$e_R = R\,\frac{1+e_A/A}{1+e_P/P}, \tag{5.23}$$

$$e_T = -\sqrt{2}\frac{[1-\cos(2\pi-\theta)]^{-1/2}\sin(2\pi-\theta)}{\sqrt{1-(\frac{r-e-Y_o}{r})^2}}e_{Y_o}, \qquad (5.24)$$

where r = the pipe radius. The errors in the diameter (D) and bed thickness (e) specifications are considered negligible and thus do not contribute to the error expressions of Eqns 5.21 - 5.24. The resulting errors are tabled in Table 5.3.

Table 5.3. Errors in the Experimental Parameters

Parameter	Systematic Error (maximum)	Random Error
Y_o	± 0.1 mm. i.e.0.1% to 0.25%	± 0.5 mm. (0.5% to 1.25%)
S_o	±0.002% max.	±0.1%
Q	±1.5%	±5.6% max.
A (Eqn 5.3)	0.5% (Eqn 5.21)	1.25%
P (Eqn 5.5)	±1.5% (Eqn 5.22)	±1.5%
R (Eqn 5.8)	±1.5% (Eqn 5.23)	±1.5%
T (Eqn 5.4)	±1.5% (Eqn 5.24)	±1.5%
LDA positioning	±25μm	±25μm

5.6 Summary

In the foregoing, the experimental set-up was described. The equipment and procedures used to establish uniform open-channel flow were also described in Section 5.2. Flow tripping at the inlet, to aid development of the flow was introduced. It was found that the longitudinal mean velocity profile was sufficiently developed at the measurement section. The weir gauge datum was re-set and regularly checked to minimise the error in measuring the flow rate Q.

The sand and gravel materials used to roughen the bed were graded using according to BS1377: Part 2. Three roughnesses, d_{50} = 0.93mm, 4.2mm, and 1.71mm were used to roughen the bed. The corresponding equivalent sand rougheness k_s values (obtained from Kamphuis'(1974) empirical formula) were given as 2.36mm, 10.2mm and 3.92mm respectively.

In Section 5.4, the theory of Laser Doppler Anemometry was introduced. The He-Ne mono-chromatic system, including the signal processing, used in the present study was described. Mean velocities U and V, and their respective turbulence intensities were obtained by the rotation of the LDA beam-splitter.

The errors in the measured quantities, and how they affect other parameters derived from them, were assed in Section 5.5.

The results obtained from the methods described above are presented and analysed in Chapter 7. They were obtained in order to create a database for the present and future studies of turbulent flow in the present cross-section. General open-channel flow studies may also utilise these data.

CHAPTER 6: APPLICATION OF THE NUMERICAL MODEL

6.1 Introduction

Additional modifications to the non-linear k-ε turbulence model of Chapter 3, and the SIMPLE finite-volume numerical method, of Chapter 4, are required before their application to the present cross-section.

In Section 6.2, the implementation of the numerical scheme in the present cross-section is described. The effect of the side-wall curvature, on the physics of the flow, is accounted for in Section 6.3; the corner effect in Section 6.4; and the effect of the bed roughness in Section 6.5. The combined effect of the three aspects is described in Section 6.6.

Details of the computer program written to carry-out the computations are given Appendix C.

6.2 Implementation of the Numerical Scheme

From the general form of the momentum transport equations, given in Eqn 4.4,

$$U_j \frac{\partial(\rho U_i)}{\partial x_j} = \frac{\partial}{\partial x_j}(\Gamma_t \frac{\partial U_i}{\partial x_j}) + S_{U_i} \qquad (4.4)$$

extra terms arise as a result of the expression of the stress tensor. Furthermore, implementation of boundary conditions at the curved/sloping side-wall requires particular attention.

6.2.1 Source Term Dependence on the Form of the Stress Tensor

The extra terms that result from expressing momentum transport in the form of Eqn 4.4 are obtained by the following procedure. The six linear Reynolds stresses

$$-\rho\overline{u'u'} = 2\rho\, \nu_t (\frac{\partial U_1}{\partial x_1}) + \frac{2}{3}\rho k \qquad (6.1)$$

$$-\rho\overline{v'v'} = 2\rho\, \nu_t \left(\frac{\partial U_2}{\partial x_2}\right) + \frac{2}{3}\rho k \tag{6.2}$$

$$-\rho\overline{w'w'} = 2\rho\, \nu_t \left(\frac{\partial U_3}{\partial x_3}\right) + \frac{2}{3}\rho k \tag{6.3}$$

$$-\rho\overline{u'v'} = \rho\, \nu_t \left(\frac{\partial U_1}{\partial x_2} + \frac{\partial U_2}{\partial x_1}\right) \tag{6.4}$$

$$-\rho\overline{u'w'} = \rho\, \nu_t \left(\frac{\partial U_1}{\partial x_3} + \frac{\partial U_3}{\partial x_1}\right) \tag{6.5}$$

$$-\rho\overline{v'w'} = \rho\, \nu_t \left(\frac{\partial U_2}{\partial x_3} + \frac{\partial U_3}{\partial x_2}\right) \tag{6.6}$$

are substituted into the momentum transport equations based on Eqns 2.3

$$\frac{\partial(\rho U)U}{\partial x} + \frac{\partial(\rho V)U}{\partial y} + \frac{\partial(\rho W)U}{\partial z} = -\frac{\partial P}{\partial x} + \rho\,\nu\nabla^2 U - \frac{\partial \rho\overline{u'u'}}{\partial x} - \frac{\partial \rho\overline{u'v'}}{\partial y} - \frac{\partial \rho\overline{u'w'}}{\partial z} + \rho F_x$$

(6.7a)

$$\frac{\partial(\rho U)V}{\partial x} + \frac{\partial(\rho V)V}{\partial y} + \frac{\partial(\rho W)V}{\partial z} = -\frac{\partial P}{\partial y} + \rho\,\nu\nabla^2 V - \frac{\partial \rho\overline{v'u'}}{\partial x} - \frac{\partial \rho\overline{v'v'}}{\partial y} - \frac{\partial \rho\overline{v'w'}}{\partial z} + \rho F_y$$

(6.7b)

$$\frac{\partial(\rho U)W}{\partial x} + \frac{\partial(\rho V)W}{\partial y} + \frac{\partial(\rho W)W}{\partial z} = -\frac{\partial P}{\partial z} + \rho\,\nu\nabla^2 W - \frac{\partial \rho\overline{w'u'}}{\partial x} - \frac{\partial \rho\overline{w'v'}}{\partial y} - \frac{\partial \rho\overline{w'w'}}{\partial z} + \rho F_z.$$

(6.7c)

The momentum equations Eqns 4.5 - 4.7 are then subtracted from Eqns 6.7 in each of the three dimensions. The differences are the extra diffusion terms. They are, however, incorporated into the momentum source terms. This enables computation of the field described by Eqns 6.7, using the simplified form of Eqns 4.4 - 4.7.

For the non-linear k-ε model (i.e. wherein the stress is quadratic in the mean strain rate $\overline{S_{ij}}$), the Reynolds stress formulation of Eqn 3.23 leads to non-linear terms for the six stresses (Baker and Orzechowski 1983)

$$-\rho\overline{u'u'} : \rho c_1 k - \rho c_2 \nu_t \frac{k}{\varepsilon}\left[\left(\frac{\partial U_1}{\partial x_2}\right)^2 + \left(\frac{\partial U_1}{\partial x_3}\right)^2\right] \tag{6.8}$$

$$-\rho\overline{v'v'} : \rho c_3 k - \rho c_2 \nu_t \frac{k}{\varepsilon}\left[\frac{\partial U_1}{\partial x_2}\right]^2 \tag{6.9}$$

$$-\rho\overline{w'w'} : \rho c_3 k - \rho c_2 \nu_t \frac{k}{\varepsilon}\left[\frac{\partial U_1}{\partial x_3}\right]^2 \tag{6.10}$$

$$-\rho\overline{u'v'} : -\rho c_2 \nu_t \frac{k}{\varepsilon}\left[\frac{\partial U_1}{\partial x_3}\left(\frac{\partial U_2}{\partial x_3} + \frac{\partial U_3}{\partial x_2}\right) + 2\frac{\partial U_1}{\partial x_2}\left(\frac{\partial U_1}{\partial x_1} + \frac{\partial U_2}{\partial x_2}\right)\right] \tag{6.11}$$

$$-\rho\overline{u'w'} : -\rho c_2 \nu_t \frac{k}{\varepsilon}\left[\frac{\partial U_1}{\partial x_2}\left(\frac{\partial U_2}{\partial x_3} + \frac{\partial U_3}{\partial x_2}\right) + 2\frac{\partial U_1}{\partial x_3}\left(\frac{\partial U_1}{\partial x_1} + \frac{\partial U_3}{\partial x_3}\right)\right] \tag{6.12}$$

$$-\rho\overline{v'w'} : -\rho c_2 \nu_t \frac{k}{\varepsilon}\frac{\partial U_1}{\partial x_2}\left(\frac{\partial U_1}{\partial x_3}\right) \tag{6.13}$$

which are also added to the source terms together with the extra diffusion terms.

6.2.2 Treatment of the Free Surface and Sloping Side-Wall

To enforce the respective boundary conditions, the distinction between analytical and computational boundary conditions is made. Roache (1976) notes that the discretisation does not enforce a different physical domain. Rather, the discrete control volumes and boundaries represent the physical space in numerical space. The following treatment of the free surface and the curved side-wall results.

The Free Surface

The surface point is the centre of the surface cell. Therefore, the accentuation for ε, Eqn 3.35, is applied by making the assumption that the kinetic energy at the free surface acts at the surface cell centre - that is $(\varepsilon_{ij})_{surface} = \varepsilon_{fs}$ as shown in Figure 4.9. This condition is consistent with the rigid-lid assumption. Chan and Street (1970) show the surface condition specification when the free surface is deformable.

The Sloping Side-wall

Figure 6.1(a) illustrates a typical wall cell at the side-wall boundary. Attempting to derive values for the wall point (i, j) using the boundary values b_1 and b_2 leads to increased truncation errors. slowed convergence and poor relaxation at the point. and programming difficulties (Roache 1976). As a result a "stepped" wall is used in place of the curved wall (Figure 6.1b).

The conditions that are used are for a stepped wall are similar to those used at the straight rigid bed boundary. Figure 6.1(b) shows the computational molecule which pertains to the wall point. With reference to Figure 4.2 and sub-Section 4.4.1, the following standard MAC specifications (see e.g. Chan and Street 1970) apply

$$W_{ij} = \frac{1}{2}(W_{i+1/2\,j} + W_{i-1/2\,j}) \qquad (6.14)$$

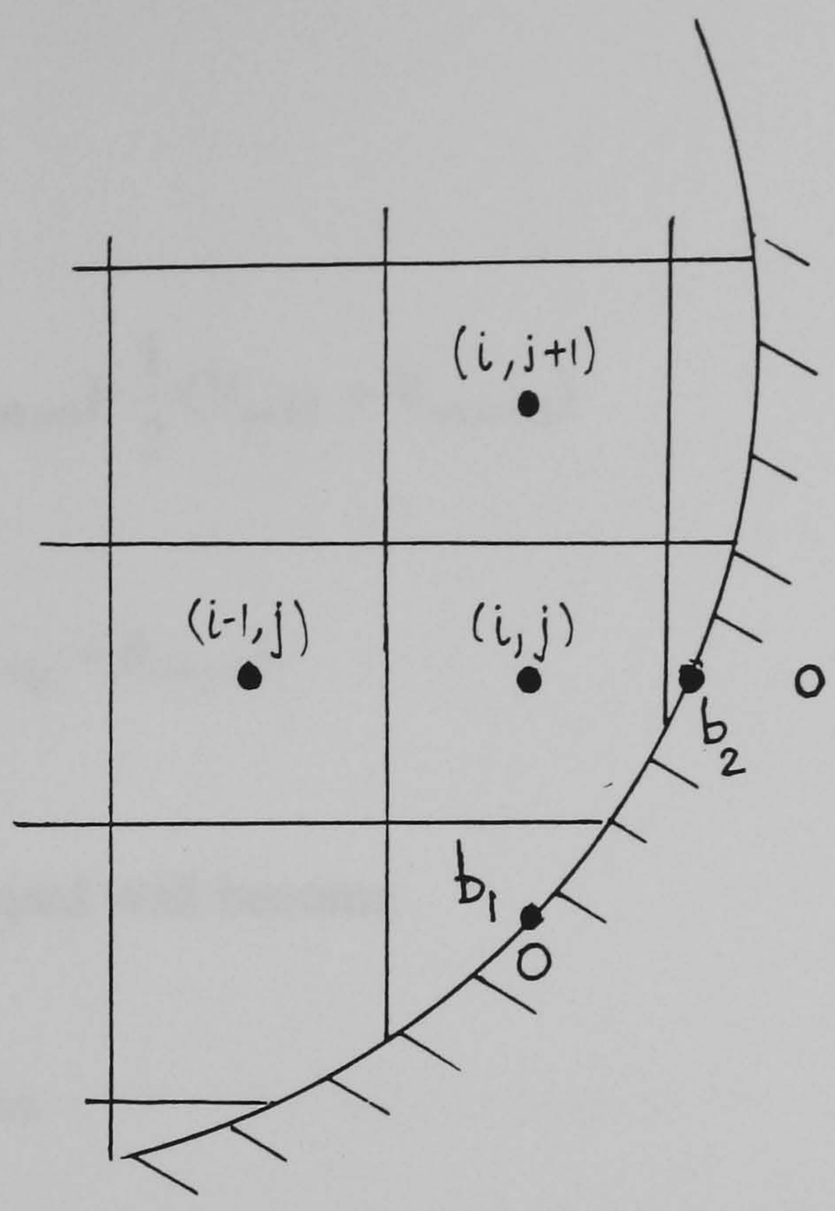

(a) Irregular

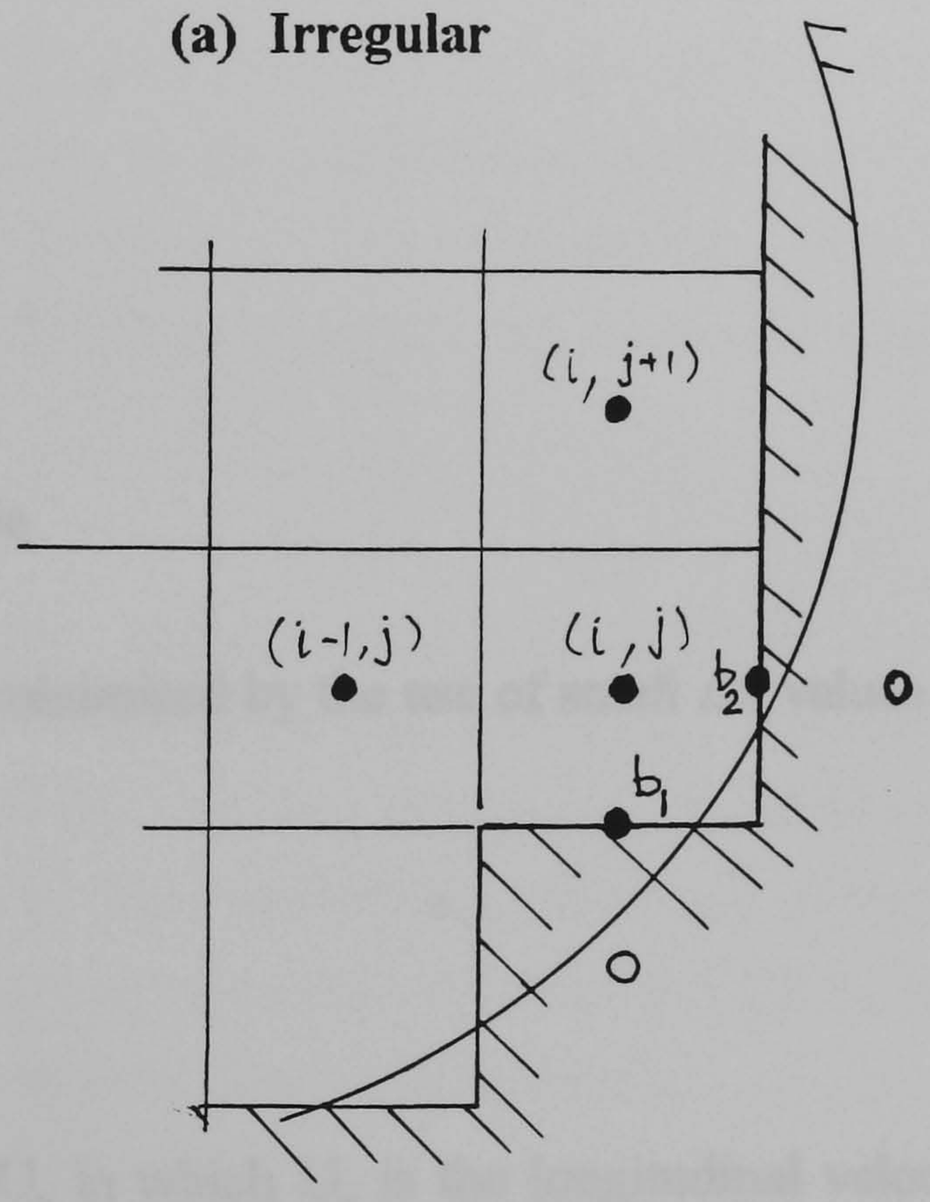

(b) Stepped Wall

Figure 6.1 Sloping Side-Wall Molecules

$$V_{ij} = \frac{1}{2}(V_{ij+1/2} + V_{ij-1/2}) \tag{6.15}$$

$$(WV)_{i+1/2\,j+1/2} = \frac{1}{2}(W_{i+1/2\,j} + W_{i+1/2\,j+1}) \cdot \frac{1}{2}(V_{ij+1/2} + V_{i+1\,j+1/2}) \tag{6.16}$$

$$\phi_{i+1/2\,j+1/2} = \frac{1}{2}(\phi_{ij} + \phi_{ij+1}) + \frac{1}{2}(\phi_{i+1\,j} + \phi_{i+1\,j+1}). \tag{6.17}$$

The boundary conditions at the stepped wall become

$$V_{i+1\,j+1/2} = V_{ij+1/2}\,; \quad V_{i+1\,j-1/2} = V_{ij-1/2} \tag{6.18a}$$

$$(VW)_{i+1/2\,j+1/2} = 0; \qquad (VW)_{i+1\,j-1/2} = 0 \tag{6.18b}$$

$$W^2_{i+1\,j} = W^2_{ij} \tag{6.18c}$$

$$W_{i+1/2\,j} = 0. \tag{6.18d}$$

6.2.3 The Marching Procedure

Formal truncation error is minimised by the use of small Δx values such that

$$\Delta t < \frac{1}{4\nu}\frac{\Delta y^2\,\Delta z^2}{(\Delta y^2 + \Delta z^2)}, \tag{6.19}$$

where the 'time step' $\Delta t = \Delta x/U_x$ in which U_x is the longitudinal velocity scale. In the present study $U_x = U_m$ for experimentally-investigated flows. Otherwise it is estimated using standard resistance formulae of Manning or Chezy (Featherstone and Nalluri 1988). ν is the kinematic viscosity. Eqn 6.19 also ensures the stability of the computation.

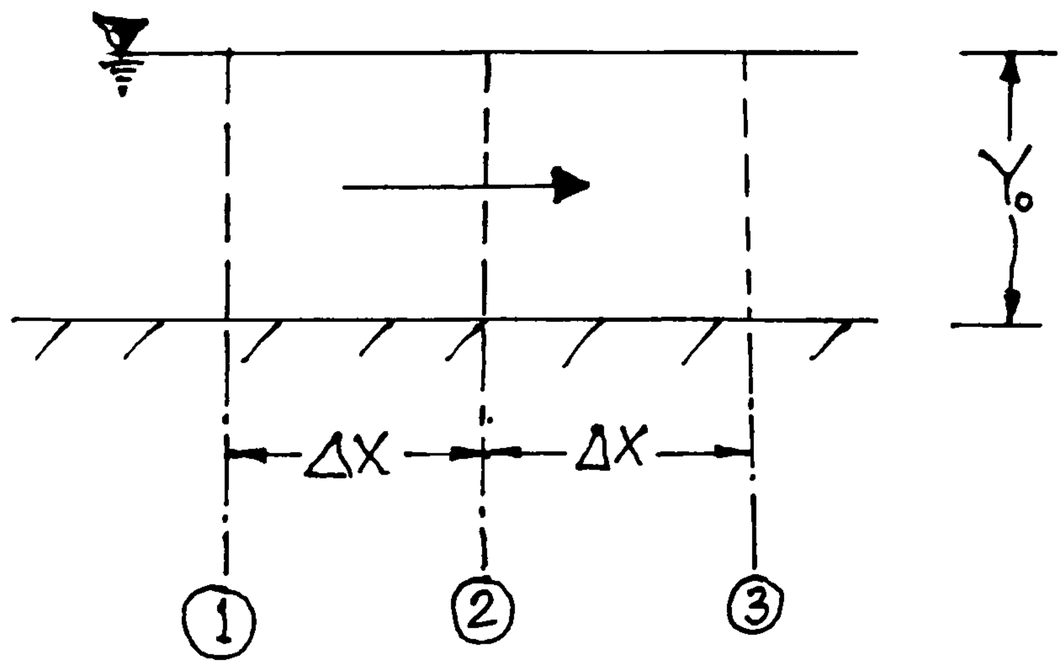

Figure 6.2 The Marching Procedure

In order to compute the flow over a sufficient 'numerical pipe length' until convergence, a large number of iterations is required. To enable this, the 'pipe' is broken into sections of length 2 Δx - Figure 6.2. Section 1 is the inlet boundary and computation occurs at sections 2 and 3 since the flow is parabolic and downstream conditions are irrelevant. The values of section 3 are then transferred to section 1 to continue the computation. This cycle is repeated until convergence is reached. This saves the computer storage required during the computation.

6.3 Wall Curvature Effect

In this and the following two Sections, modifications applied to the standard boundary conditions are presented. These are due to the wall-curvature effect, the presence of the corner, and due to the lateral variation of the boundary roughness. These three-dimensional effects are unaccounted for in the derivation of the standard logarithmic law of the wall, Eqn 2.21. As Eqn 2.21 is used to derive boundary conditions for flow parameters like ε, three-dimensional effects are thus absent from these boundary condition specifications.

6.3.1 Constant Stress Layer

Eqn 2.21, is based on the assumption that the primary shear stress is constant and equal to the boundary shear stress τ_o within the turbulent wall region - the constant stress layer. In flows over walls with lateral wall curvature, the existence of this wall region is brought into question. 'Strong' lateral curvature is given by the limit $\delta/r_o \leq 1$ (Huffman and Bradshaw 1973), where δ is the boundary layer depth and r_o is the radius of curvature of the boundary. Although the present cross-section does not strictly meet this criterion, whereby $\delta = Y_o$, and $r_o = D/2$, the following analysis equally applies. Ginevskii and Solodkin (1958) derived an expression for the normalised velocity U/U_*, by using the mixing length hypothesis. This approach is flawed in that it uses a hypothesis which was originally derived using flat-plate two-dimensional data.

Using the analysis of Richmond (1957), Rao (1967) derived an expression for U/U_* for flows over a boundary with convex curvature. Eqn 2.17,

$$\frac{U}{U_*} = f\left(\frac{U_* y}{\nu}\right) \qquad (2.17).$$

is modified to include the lateral curvature such that

$$\frac{U}{U_*} = f\left(\frac{U_* y}{\nu}, \frac{U_* r_o}{\nu}\right). \qquad (6.20)$$

y is the perpendicular wall distance (see Figure 5.2). Using the x-direction momentum, and continuity equations in polar co-ordinates, the expression for the stress very close to the wall (in the absence of any pressure gradient) is given as

$$(y + r_o)\tau = r_o\, \tau_o. \qquad (6.21)$$

This suggests the absence of the constant stress layer. From Eqn 6.21, using $\tau = \mu\, \partial U / \partial (r_o + y)$, the velocity distribution within the region of high viscous effects becomes

$$\frac{U}{U_*} = \frac{U_* r_o}{\nu} \ln \frac{y + r_o}{r_o}. \tag{6.22}$$

It is equivalent to the linear relation for U/U_* in the viscous sublayer. For the fully turbulent region, Eqn 6.20 then becomes

$$\frac{U}{U_*} = g\left(\frac{U_* r_o}{\nu} \ln \frac{y + r_o}{\nu}\right). \tag{6.23}$$

This is the logarithmic law, Eqn 2.21, modified to account for the wall curvature

$$\frac{U}{U_*} = \frac{1}{\kappa} \ln\left(\frac{U_* r_o}{\nu} \ln \frac{y + r_o}{r_o}\right) + A' \tag{6.24}$$

where A' = 5.75 for boundary layer flow, and 5.29 in open channels. Eqn 6.24 collapses to the standard flat-plate form (Eqn 2.21) when $r_o \rightarrow \infty$. For the present concave curvature of the wall, Eqn 6.24 becomes 'Rao's law'

$$\frac{U}{U_*} = \frac{1}{\kappa} \ln\left(\frac{U_* r_o}{\nu} \ln \frac{r_o}{r_o - y}\right) + A' \tag{6.25}$$

It is worth noting that Eqn 6.25 applies to flow over hydraulically smooth surfaces only. An equivalent rough surface similarity expression may be derived using Eqn 2.28. Bradshaw and Patel (1973) also note that Eqn 6.25 is not a universal similarity law similar to Eqn 2.21. It is thus only applicable to certain equilibrium layers, including the present, given in the similarity analysis of Townsend (1961).

6.3.2 Modified Boundary Conditions

The boundary condition for U in the side-wall region is then derived using Eqn 6.25, which replaces Eqn 3.26 such that

$$\frac{U_w}{U_*} = \frac{1}{\kappa} \ln[E_s \ (\frac{U_* r_o}{\nu} \ln \frac{r_o}{r_o - y_w}) \ ]. \qquad (6.26)$$

The subscript 'w' refers to the computation point near the side-wall. Along the flat bed, Eqn 3.26 applies.

Furthermore, the boundary condition for ε, ε_w, based on Eqns 3.33 and 4.64 is expressed as

$$\varepsilon_w = -\frac{c_\mu^{3/4} \ k_w^{3/2}}{\kappa[\ln(\frac{r_o - y_w}{r_o}) \ (r_o - y_w)]}. \qquad (6.27)$$

Figure 6.3 compares ε_w values derived from Eqn 6.27 for various radii of curvature, and fixed

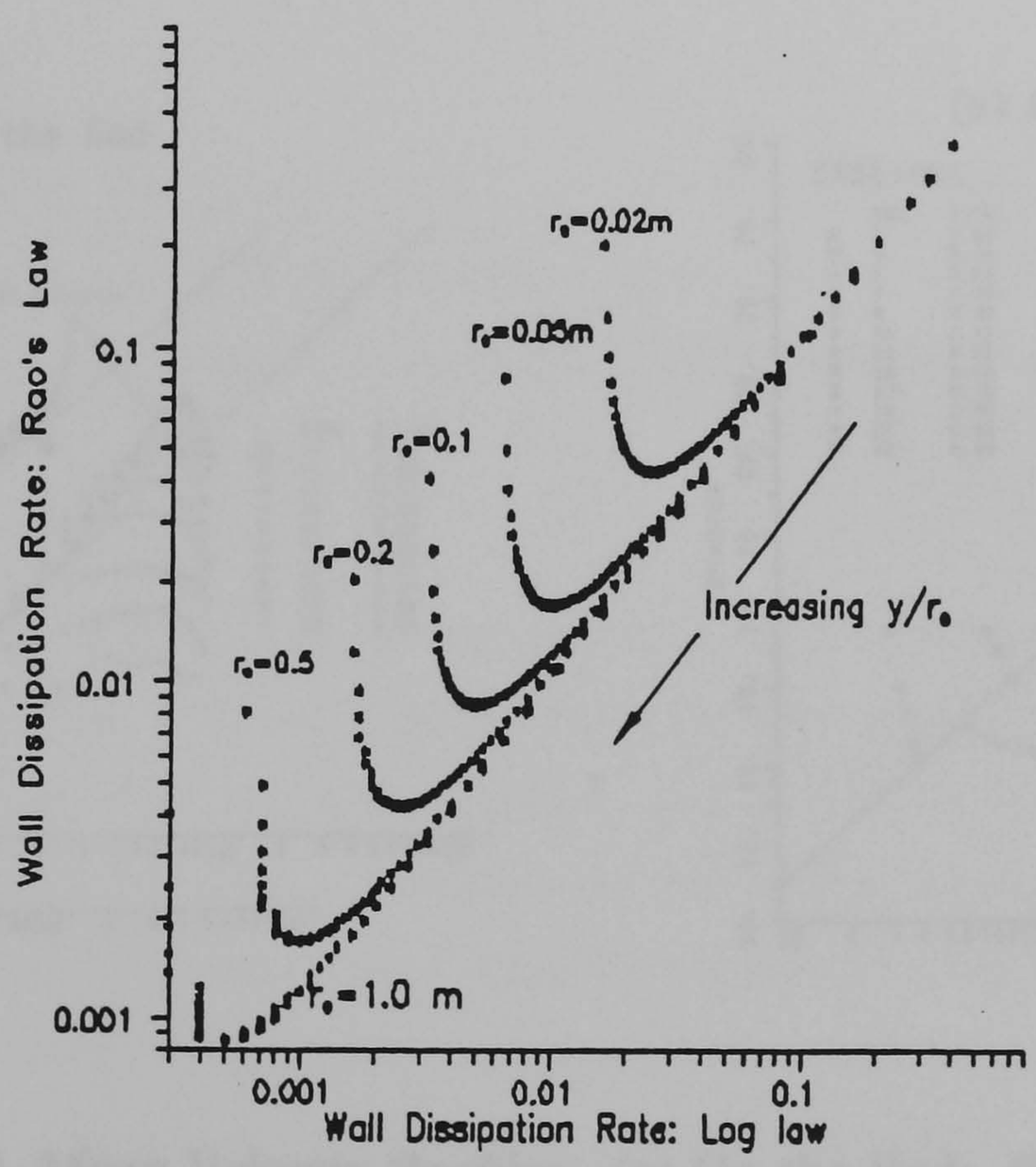

Figure 6.3 The Modified ε Boundary Condition

U_*, to those of Eqn 3.33. This shows that for the present channel, r_o = D/2 = 0.1525m, Eqn 3.33 overestimates the dissipation rate at the wall point. Indeed Hoohlo and Nalluri (1993) used

Eqns 6.26 and 6.27 to compute the present flow. Their results showed agreed well with experimental data.

6.4 Corner Effect

The corner affects the flow through the tractive action of the two adjoining walls. It also affects the shape, size, and behaviour of the coherent structures therein (Saga *et al* 1991). Since the latter effect can only be qualitatively described, it is not pursued further in the present study.

6.4.1 Derivation of Corner Similarity Laws

Figures 6.4 show Nezu and Rodi's (1985) U/U_* profiles plotted at the channel centreline and lateral sections towards the corner region in a rectangular open channel. The centreline distribution follows Eqn 2.21. However, towards the corner, U/U_* deviates substantially, decreasing to below that given by Eqn 2.21. This flattened profile illustrates the increased

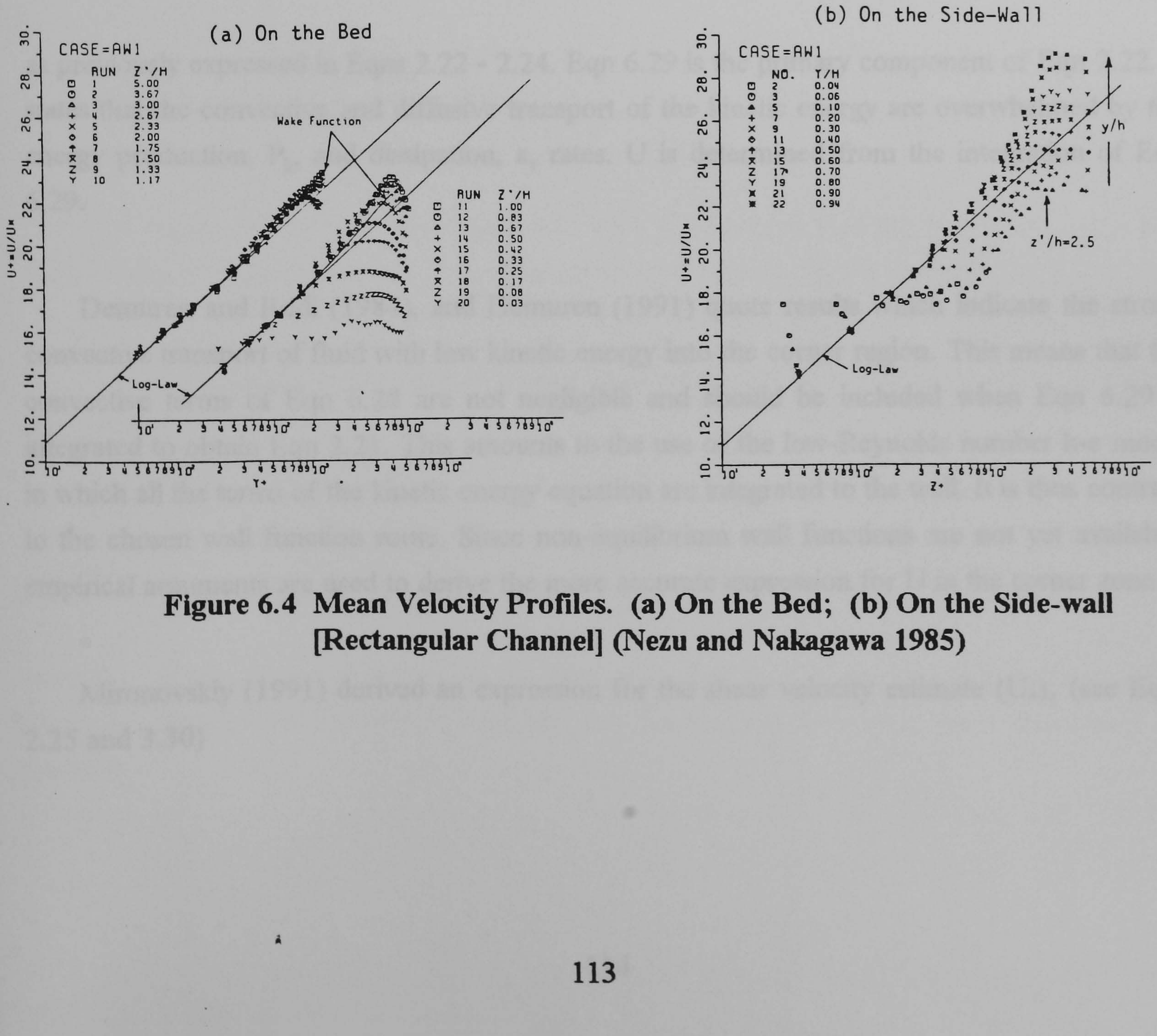

Figure 6.4 Mean Velocity Profiles. (a) On the Bed; (b) On the Side-wall [Rectangular Channel] (Nezu and Nakagawa 1985)

traction due to the two walls at the corner. It also illustrates the independence of U/U_* from the inner wall distance y^+. Therefore, y^+ is an inappropriate wall length scale for the corner region. The present study assumes that mean flow in the 'corner region' follows similarity laws similar to Eqn 2.21.

The similarity arguments used to derive Eqn 2.21, (Kline 1965, Townsend 1976, and Yaglom 1979), depend on the condition of turbulent energy equilibrium in the wall region. That is to say that, the shortened turbulent kinetic equation (see Eqn 2.9)

$$[W\frac{\partial k}{\partial z}+V\frac{\partial k}{\partial y}]-\frac{\partial}{\partial y}[\overline{u'(\frac{u_j'u_j'}{2}+\frac{p'}{\rho})}]-\overline{u'v'}\frac{\partial U}{\partial y}=\varepsilon, \tag{6.28}$$

becomes

$$-\overline{u'v'}\frac{\partial U}{\partial y}=\varepsilon \tag{6.29}$$

as previously expressed in Eqns 2.22 - 2.24. Eqn 6.29 is the primary component of Eqn 2.22. It states that the convective and diffusive transport of the kinetic energy are overwhelmed by the energy production, P_k, and dissipation, ε, rates. U is determined from the integration of Eqn 6.29.

Demuren and Rodi (1984), and Demuren (1991) quote results which indicate the strong convective transport of fluid with low kinetic energy into the corner region. This means that the convective terms of Eqn 6.28 are not negligible and should be included when Eqn 6.29 is integrated to obtain Eqn 2.21. This amounts to the use of the low-Reynolds number k-ε model in which all the terms of the kinetic energy equation are integrated to the wall. It is thus contrary to the chosen wall function route. Since non-equilibrium wall functions are not yet available, empirical arguments are used to derive the more accurate expression for U in the corner zone.

Mironovskiy (1991) derived an expression for the shear velocity estimate $(U_*)_1$ (see Eqns 2.25 and 3.30)

$$\tau_o = \rho(U_*)_1^2 = \nu_t \frac{\partial U}{\partial t'}, \tag{6.30}$$

where t' is a self-similar function of the respective bed (y), and side-wall (z' = $|Z_o - z|$) distances,

$$t' = (y^{-n} + z'^{-n})^{-1/n}. \tag{6.31}$$

The empirical exponent $n = 2$ for right-angled corners. It, however, can not be used in the present channel where the corner is not right-angled. Eqn 6.31 nonetheless illustrates the importance of using the two boundary distances in developing the expression for U.

Bragg (1969) experimentally studied the turbulent boundary layer in a right-angled corner. By comparing the U_* values 'far' from the wall, $(U_*)_{2D}$, to those within the wall, he identified the 'corner region' as the zone within which the corner exerts an effect on the distribution of the boundary shear stress along any of the two boundaries. This zone extends to a distance of

$$\frac{z'(U_*)_{2D}}{\nu} = \frac{(Z_o - z)(U_*)_{2D}}{\nu} = 2520 \tag{6.32}$$

from the corner, where z' is interchangeable with y, and Z_o is half the bed width. This is a useful check of what proportion of the channel width is affected by the corner.

The velocity in the highly viscous region, deep within the corner zone, is governed by the expression

$$\frac{U}{U_{cn}} = \left(\frac{U_{cn}\, y}{\nu}\right)\left(\frac{U_{cn}\, z'}{\nu}\right) \tag{6.33}$$

where U_{cn} is the corner velocity scale. As with method of Rao above, Eqn 6.33 is assumed to affect the form of the logarithmic similarity law for the turbulent zone, such that Eqn 2.21 becomes

$$\frac{U}{U_K} = 2\,G \ln(\frac{U_K\, y}{\nu}) + 3.0, \qquad (6.34)$$

near the corner symmetry line where y ~ z'. G = 40.0 and U_k is a velocity scale although can not be explicitly expressed in terms of $(U_*)_{2D}$.

6.4.2 Modified Boundary Conditions

The wall symmetry zone is defined by

$$\frac{|y_p - y|}{\min(\, y_p, y)} < \beta \qquad (6.34)$$

where y_p is the perpendicular distance to the side-wall. β lies in the region 0.05 - 0.25. It is set at 0.20.

Within the regions defined by Eqns 6.32 and 6.34, the boundary condition for U is then given by

$$\frac{U_w}{(U_*)_1} = \frac{1}{\kappa} \ln [\frac{(U_*)_1\ \min(y_w\,, y)}{\nu}] + 5.3. \qquad (6.35)$$

This takes account of the combined effects of the two walls within the corner symmetry zone. ε_w is expressed is terms of Eqn 6.35 as with Eqn 6.27.

6.5 Bed Roughness Effect

The roughened bed introduces a lateral variation of the boundary roughness. Hinze (1967), Hinze (1973), and Naot (1984) studied rectangular closed ducts and open channels with lateral roughness variation. Roughness discontinuities were found to cause strong convective transport of kinetic energy by secondary currents. This state of non-equilibrium again precludes the use of standard equilibrium wall functions at the roughness discontinuity.

6.5.1 Roughness-discontinuity Modification of Boundary Conditions

In the absence of the appropriate wall functions at the discontinuity, grid refinement does not lead to the solution's independence from the grid size. Indeed unreasonably high normal turbulent stress gradients were observed (Naot 1984), leading to high secondary currents not corroborated by experimental evidence.

Naot (1984) reports that physically plausible results are obtained by limiting the lateral size of the wall computation cell (Δz) by such that

$$\frac{\Delta k_s}{\Delta z} < 0.25 \qquad (6.36)$$

where Δk_s is the roughness step at the discontinuity (= k_s - k_w). Eqn 6.36 is applied to the bed cell adjacent to the side-wall.

The three present roughness steps give the lower limit for Δz as 9.44mm, 40.8mm, and 15.68mm respectively. These limits are two high and lead to numerical instability. Eqn 6.36 is relaxed (halved) to give Δz limits as 4.72mm, 20.4mm, and 7.84mm respectively. The standard roughness boundary condition, Eqns 3.26 - 3.28, applies elsewhere on the roughened bed.

6.6 Combined Effects: Curvature, Corner and Roughness

The combined effects of side-wall curvature, bed-wall corner, and the roughness discontinuity are enforced though the application of Eqns 6.26, 6.27, 6.35, and 6.36. At the corner cell, the local side-wall curvature is neglected and the corner condition, Eqn 6.35 is applied. With a roughened bed, the additional Eqn 6.36 condition is also applied. The three effects are thus applied linearly as a combination of independent effects.

The inlet conditions for k and ε are given by, Eqns 3.24 and 3.25, with the wall distance, y in y/h (= y/Y_o), is now specified as the perpendicular distance to the nearer of the two boundaries. This is consistent with the usage of Eqn 6.34 in Eqn 6.35.

Future derivation of a single expression for the three depends on the development of non-equilibrium wall functions. This would depend on the better understanding of the role of diffusive and convective transport of the kinetic energy in non-two-dimensional situations like the three above. The gradient hypothesis which dominates the present models would have to be revised or replaced by more physically realistic models. Indeed, as noted in sub-Section 3.3.1, data obtained using Direct Numerical Simulations (Cazalbou and Bradshaw 1993) question the validity of the gradient hypothesis.

6.7 Summary

In the foregoing, the numerics and the physics of the computation model were discussed. In Section 6.2, the implementation of the SIMPLE numerical scheme was introduced. The extra source terms that result from the shear stress specification, and the use of the non-linear k-ε model were presented. The numerical treatment of the free-surface and sloping side-wall boundaries was also explained. Furthermore, the streamwise marching procedure used was presented.

Section 6.3 dealt with how the side-wall curvature was incorporated into the model through the modification of the boundary conditions. The boundary conditions were also modified to account for the tractive effect of the bed-wall corner in Section 6.4. Lastly, the grid size limitation due to the difference in roughness between the bed and side-walls, was presented in Section 6.5. The combination of the three physical effects was briefly discussed in Section 6.6.

The results of the present numerical model are presented in Chapter 8. Prior to this, the results of the experimental investigation in are presented Chapter 7. These results will be used to confirm the similarity arguments used in the model above. They will also be the basis of comparison for the results of the numerical model.

CHAPTER 7: RESULTS OF THE EXPERIMENTAL INVESTIGATION

7.1 Introduction

The results of the investigations based on the experimental methods of Chapter 5 are presented in this chapter.

Section 7.2 deals with the analysis of errors derived from the investigation, and their effects on calculated parameters. The calculation of the third mean velocity component W is also covered. In Section 7.3, the data for the case of the smooth bed is presented, whereas Section 7.4 deals with the case of the roughened bed. Experimental evidence of the similarity laws based on the concepts of Chapter 6, is presented in Section 7.5.

7.2 Data Presentation and Analysis

The form of the data presentation, and the analysis undertaken to derive other parameters, is introduced in this Section. As shown in Table 7.1, thirty-three flow cases, based on the bed slope (S_o), the bed thickness (e), the uniform flow depth (Y_o), and the bed roughness, were studied. In these, the mean velocities and turbulence intensities in the x and y directions were measured. Two bed slopes $S_o = 4.63 \times 10^{-4}$, and $S_o = 9.27 \times 10^{-4}$ were used to establish the effect of Reynolds number variation on the turbulence. After establishing that this was negligible (see Sections 7.3 and 7.4), only the higher slope was then used in subsequent cases.

Two bed thicknesses e = 43 mm (e/D = 0.141), and e = 87 mm (e/D = 0.285) are used. For e/D = 0.285, only the slope $S_o = 9.27 \times 10^{-4}$ was used. To determine the effect of the cross-sectional shape, four cases of the ratio $(Y_o + e)/D$ for each roughness were used. These were $(Y_o + e)/D = 0.305$, 0.400, 0.502 and 0.666 for the e/D = 0.141 bed thickness, and $(Y_o + e)/D = 0.416$, 0.502, 0.666, and 0.751 for the e = 87 mm bed thickness.

Table 7.1 Hydraulic Parameters

Case	2	3	4	5	6	7	8
	So	Yo/D	e/D	(Yo+e)/D	Q	Qi	A
					(Eqn 3.9)	Integrtd	(Eqn 3.3)
					(cumecs)	(cumecs)	(m^2)
S1111	4.63E-04	0.164	0.141	0.305	0.00442	0.00256	0.0125741
S1211	4.63E-04	0.259	0.141	0.400	0.00904	0.00492	0.0210100
S1311	4.63E-04	0.361	0.141	0.502	0.01350	0.01339	0.0304026
S1411	4.63E-04	0.525	0.141	0.666	0.02281	0.02635	0.0453663
S2111	9.27E-04	0.164	0.141	0.305	0.00570	0.00396	0.0125741
S2211	9.27E-04	0.259	0.141	0.400	0.01148	0.00918	0.0210100
S2311	9.27E-04	0.361	0.141	0.502	0.01821	0.01491	0.0304026
S2411	9.27E-04	0.525	0.141	0.666	0.03218	0.02386	0.0453663
R1111	4.63E-04	0.164	0.141	0.305	0.00635	0.00451	0.0125741
R1211	4.63E-04	0.259	0.141	0.400	0.00724	0.00550	0.0210100
R1311	4.63E-04	0.361	0.141	0.502	0.01263	0.00995	0.0304026
R1411	4.63E-04	0.525	0.141	0.666	0.02408	0.01939	0.0453663
R2111	9.27E-04	0.164	0.141	0.305	0.00669	0.00311	0.0125741
R2211	9.27E-04	0.259	0.141	0.400	0.00847	0.00631	0.0210100
R2311	9.27E-04	0.361	0.141	0.502	0.01376	0.01141	0.0304026
R2411	9.27E-04	0.525	0.141	0.666	0.02521	0.02047	0.0453663
R1412	4.63E-04	0.525	0.141	0.666	0.01796	0.01488	0.0453663
R2112	9.27E-04	0.164	0.141	0.305	0.00314	0.00185	0.0125741
R2212	9.27E-04	0.259	0.141	0.400	0.00679	0.00511	0.0210100
R2312	9.27E-04	0.361	0.141	0.502	0.01282	0.01011	0.0304026
R2412	9.27E-04	0.525	0.141	0.666	0.02225	0.01803	0.0453663
S2121	9.27E-04	0.131	0.285	0.416	0.00322	0.00251	0.0116039
S2221	9.27E-04	0.216	0.285	0.502	0.00704	0.00584	0.0194975
S2321	9.27E-04	0.380	0.285	0.666	0.01611	0.01358	0.0344612
S2421	9.27E-04	0.466	0.285	0.751	0.02191	0.01797	0.0416582
R2123	9.27E-04	0.131	0.285	0.416	0.00248	0.00190	0.0116039
R2223	9.27E-04	0.216	0.285	0.502	0.00561	0.00462	0.0194975
R2323	9.27E-04	0.380	0.285	0.666	0.01373	0.01168	0.0344612
R2423	9.27E-04	0.466	0.285	0.751	0.01906	0.01606	0.0416582
R2122	9.27E-04	0.131	0.285	0.416	0.00231	0.00157	0.0116039
R2222	9.27E-04	0.216	0.285	0.502	0.00477	0.00395	0.0194975
R2322	9.27E-04	0.380	0.285	0.666	0.01175	0.00961	0.0344612
R2422	9.27E-04	0.466	0.285	0.751	0.01518	0.01281	0.0416582
D=	305	mm					
ro=	152.5	mm					

Table 7.1(Cont.) Hydraulic Parameters

9	10	11	12	13	14	15	16
Ai	Pb	Pw	P	R	T	Aspect	Aspect
Integrtd	(2 Zo)					Ratio	Ratio
(m^2)	(m)	(m)	(m)	(m)	(m)	(2Zo/Yo)	(T/Yo)
			(Eqn 3.5)	(Eqn 3.8)	(Eqn 3.4)		
0.0076502	0.2123	0.1220	0.3343	0.0376	0.2808	4.25	5.62
0.0152651	0.2123	0.1829	0.3952	0.0532	0.2988	2.69	3.78
0.0246102	0.2123	0.2453	0.4576	0.0664	0.3050	1.93	2.77
0.0377505	0.2123	0.3472	0.5595	0.0811	0.2878	1.33	1.80
0.0104402	0.2123	0.1220	0.3343	0.0376	0.2808	4.25	5.62
0.0177502	0.2123	0.1829	0.3952	0.0532	0.2988	2.69	3.78
0.0266504	0.2123	0.2453	0.4576	0.0664	0.3050	1.93	2.77
0.0392603	0.2123	0.3472	0.5595	0.0811	0.2878	1.33	1.80
0.0095702	0.2123	0.1220	0.3343	0.0376	0.2808	4.25	5.62
0.0176401	0.2123	0.1829	0.3952	0.0532	0.2988	2.69	3.78
0.0262602	0.2123	0.2453	0.4576	0.0664	0.3050	1.93	2.77
0.0379606	0.2123	0.3472	0.5595	0.0811	0.2878	1.33	1.80
0.0095701	0.2123	0.1220	0.3343	0.0376	0.2808	4.25	5.62
0.0170396	0.2123	0.1829	0.3952	0.0532	0.2988	2.69	3.78
0.0262604	0.2123	0.2453	0.4576	0.0664	0.3050	1.93	2.77
0.0379544	0.2123	0.3472	0.5595	0.0811	0.2878	1.33	1.80
0.0383805	0.2123	0.3472	0.5595	0.0811	0.2878	1.33	1.80
0.0088003	0.2123	0.1220	0.3343	0.0376	0.2808	4.25	5.62
0.0181990	0.2123	0.1829	0.3952	0.0532	0.2988	2.69	3.78
0.0253506	0.2123	0.2453	0.4576	0.0664	0.3050	1.93	2.77
0.0383507	0.2123	0.3472	0.5595	0.0811	0.2878	1.33	1.80
0.0098021	0.2754	0.0842	0.3596	0.0323	0.3007	6.89	7.52
0.0159902	0.2754	0.1364	0.4118	0.0473	0.3050	4.17	4.62
0.0286003	0.2754	0.2383	0.5138	0.0671	0.2878	2.37	2.48
0.0345804	0.2754	0.2957	0.5711	0.0729	0.2638	1.94	1.86
0.0091252	0.2754	0.0842	0.3596	0.0323	0.3007	6.89	7.52
0.0153403	0.2754	0.1364	0.4118	0.0473	0.3050	4.17	4.62
0.0292504	0.2754	0.2383	0.5138	0.0671	0.2878	2.37	2.48
0.0355057	0.2754	0.2957	0.5711	0.0729	0.2638	1.94	1.86
0.0069001	0.2754	0.0842	0.3596	0.0323	0.3007	6.89	7.52
0.0149501	0.2754	0.1364	0.4118	0.0473	0.3050	4.17	4.62
0.0266502	0.2754	0.2383	0.5138	0.0671	0.2878	2.37	2.48
0.0331503	0.2754	0.2957	0.5711	0.0729	0.2638	1.94	1.86

Table 7.1(Cont.) Hydraulic Parameters

17	18	19	20	21	22	23	24	25	26
Um	Umax	Re	Re	Re	Fr	d50	ks	Yo/ks	U*
		4RUm/vi	YoUm/vi	TUm/vi	Um/(gYo)				
(m/s)	(m/s)					(mm)	(mm)		(m/s)
0.352	0.413	46209	15358	86259	0.502	-	-	-	0.013
0.430	0.376	79918	29687	112299	0.489	-	-	-	0.016
0.444	0.628	103082	42665	118298	0.428	-	-	-	0.017
0.503	0.837	142410	70256	126369	0.401	-	-	-	0.019
0.454	0.487	59583	19803	111224	0.648	-	-	-	0.018
0.546	0.631	101448	37685	142552	0.621	-	-	-	0.022
0.599	0.655	138977	57522	159491	0.577	-	-	-	0.025
0.709	0.689	200874	99099	178248	0.566	-	-	-	0.027
0.505	0.618	66314	22040	123790	0.721	0.93	2.36	21	0.013
0.345	0.397	64019	23781	89957	0.392	0.93	2.36	33	0.016
0.415	0.465	96411	39904	110642	0.400	0.93	2.36	47	0.017
0.531	0.609	150316	74156	133385	0.424	0.93	2.36	68	0.019
0.532	0.410	69901	23232	130485	0.760	0.93	2.36	21	0.018
0.403	0.467	74879	27815	105217	0.458	0.93	2.36	33	0.022
0.453	0.521	105017	43466	120518	0.436	0.93	2.36	47	0.025
0.556	0.636	157389	77646	139661	0.444	0.93	2.36	68	0.027
0.396	0.473	112126	55316	99497	0.316	4.2	10.2	16	0.019
0.250	0.306	32841	10915	61306	0.357	4.2	10.2	5	0.018
0.323	0.407	60017	22294	84334	0.367	4.2	10.2	8	0.022
0.422	0.520	97828	40490	112268	0.406	4.2	10.2	11	0.025
0.490	0.593	138867	68508	123226	0.391	4.2	10.2	16	0.027
0.278	0.335	31279	9693	72871	0.443	-	-	-	0.017
0.361	0.469	59710	20810	96168	0.449	-	-	-	0.021
0.468	0.548	109533	47358	117493	0.438	-	-	-	0.025
0.526	0.600	133981	65207	121160	0.446	-	-	-	0.026
0.214	0.272	24106	7470	56159	0.341	1.71	3.92	10	0.017
0.288	0.415	47086	16411	75837	0.358	1.71	3.92	17	0.021
0.398	0.487	93796	40554	100612	0.373	1.71	3.92	30	0.025
0.457	0.560	114738	55842	103759	0.388	1.71	3.92	36	0.026
0.199	0.287	20816	6451	48495	0.318	4.2	10.2	4	0.017
0.245	0.359	38806	13525	62500	0.304	4.2	10.2	6	0.021
0.341	0.453	75979	32850	81500	0.320	4.2	10.2	11	0.025
0.364	0.473	87628	42647	79242	0.309	4.2	10.2	14	0.026

The side-walls were kept smooth to enable LDA measurements. Flows over a smooth bed were first studied. In addition three bed roughnesses, d_{50} = 0.93, 4.2, and 1.71 mm (Rough1, Rough2, and Rough3 respectively), were used. Roughnesses d_{50} = 0.93 mm and d_{50} = 4.20 mm were used for the bed thickness e/D = 0.141. For the bed thickness e/D = 0.285, the bed was roughened with d_{50} = 1.71 mm and d_{50} = 4.20 mm roughness. The increase in one of the roughnesses from 0.93 to 1.71mm, as e/D was increased, was made in order to ensure the that the beds were hydraulically rough - that the roughness elements fully penetrate the viscous sublayer of thickness δ_l for all the flows. The discussion on the determination of the roughness criteria is given below in sub-Section 7.4.1.

A five-character case-reference code is used S/R*ijkl* (e.g. S2411, R2212). The first letter refers to either a smooth (S) or a rough (R) bed. *i* indicates the first (*i* = 1) or second (*i* = 2) bed slope - $S_o = 4.63 \times 10^{-4}$, or $S_o = 9.27 \times 10^{-4}$. *j* indicates the depth ratio for the given bed thickness: for e/D = 0.141, *j* = 1, 2, 3, and 4 for $(Y_o + e)/D$ = 0.305, 0.400, 0.502 and 0.666; and *j* = 1, 2, 3, and 4 for $(Y_o + e)/D$ = 0.416, 0.502, 0.666, and 0.751 when e/D = 0.285. The bed thickness is identified by figure *k* such that *k* = 1 for e/D = 0.141, and *k* = 2 for e/D = 0.285. The roughness used is specified by *l* = 1, 2, and 3 for Rough1, Rough2, and Rough3 respectively. For smooth-bed cases, *l* = 1.

7.2.1 Hydraulic Parameters

Hydraulic parameters are given in Table 7.1, and in Table B.1 of Appendix B. Maximum errors in the calculated parameters due to the errors in the measured parameters (Y_o, S_o, h_w, and the z- and y- traverse) were given in Table 5.3.

The bulk flow rate (Q) varies from 0.00231 to 0.03218 m^3/s, well within the capacity of the experimental set-up. The integrated mean flow rate (Q_i) varies by up to 30.0% of the measured value. Correspondingly, the integrated area (A_i) calculated from the LDA traverse differs from the area calculated from Eqn 5.3 by a maximum of 30.0% (Table B.1). As the flow near the wall - especially at the points of high side-wall inclination where LDA errors would be large - is not measured, this flow is not included in the integrated value of Q leading to the error in Q. This is more pronounced in the lower $(Y_o + e)/D$ ratio cases where the un-measured near-wall flow forms a higher proportion of the total flow.

The correlation of the errors in Q and A (as included Table B.1) illustrates that the LDA measurements are accurate and would yield values integrated values close to the measured ones had the inclusion of the near-wall flow been possible. The longitudinal bulk mean velocity is thus calculated from the measured values: $U_m = Q/A$. The values of U_m for cases R1111 and R2111 are due to large errors in Q. Hydraulic parameters for which these U_m values are used are thus omitted from analyses.

Two length scales, Y_o and A/T, were used to obtain the Froude number, such that $Fr = U_m/\sqrt{(gY_o)}$, and $Fr = U_m/\sqrt{(gA/T)}$. T is the width of the free surface. All the flow cases were subcritical with, $Fr < 1$, regardless of the length scale used. Yet another important length, illustrated in Figure 5.2, is the width of the rigid bed $2Z_o$, which is equal to the bed perimeter P_b in Table 7.1. It can be used to calculate an indicative aspect ratio, $2Z_o/Y_o$, based on the corresponding ratio for rectangular channels. In Table 7.2 the two aspect ratios, $2Z_o/Y_o$ and T/Y_o, are quoted.

7.2.2 Calculation of the Transverse Velocity Component

The transverse velocity, W, is computed from the measured distribution of the vertical velocity, V. The continuity equation in the yz-plane is integrated to yield W through

$$W = -\int_0^{|z|} \frac{\partial V}{\partial y}\, dz. \qquad (7.1)$$

Firstly, the measured V values were curve-fitted, and the gradients $\partial V/\partial y$ determined using available subroutines from the Numerical Algorithms Group (NAG) FORTRAN library. These $\partial V/\partial y$ values were then numerically integrated in the z direction according Eqn 7.1 also using a NAG subroutine. The curve fitting and numerical integration using NAG routines introduces very small errors. This was verified by fitting pre-determined curves, and evaluating known integrals.

7.3 The Smooth Bed

The k_s value for the smooth bed case is taken to be zero. Ghani (1993) notes that k_s calculated through the Colebrook-White equation is highly sensitive to the (measured) values of the Darcy-Weisbach friction factor (λ).

7.3.1 Longitudinal Mean Flow Characteristics

The centreline longitudinal velocity is normalised by U_m. The development of this normalised profile is illustrated by Figures 7.1 (a-d) for typical cases. It is clear that the distance from the inlet, which is $19 \leq X_m/(4R) \leq 49$, is sufficient for a turbulent velocity profile to develop especially for the higher flow depths. For all the flows, the profiles also show the surface retardation of the mean flow, mentioned by Cardoso *et al* (1989). It is also clear that the shape of the profiles approaches that of full pipe flow as $(Y_o + e)/D > 0.5$ with the maximum occurring near $Y_o/2$.

At the measurement section, the longitudinal mean velocity is also normalised by U_m into U/U_m. Isovels for U/U_m, - which are lines that join points of equal value - are plotted in Figures 7.2. These are also referred to as velocity contours. On these and subsequent secondary flow plots, the axes are not normalised. This is to avoid the distortion of the side-wall curvature, and it thus enables the curvature effect on the flow structure to be identifiable. The horizontal axis is plotted using the variable $z' = z + D/2$, where z is defined in Figure 5.2.

For bed thickness $e/D = 0.141$, Figures 7.2 (a-e), there is a slight asymmetry of the flow illustrated by the 'skewed' location of the velocity maxima. This is in spite of the symmetry having been verified before measurements were taken. Melling and Whitelaw (1976) observed that since the flow is highly developed, a slight deviation (or asymmetry) in the z - direction is magnified on the contour plots. In this light, the observed contour asymmetry is deemed acceptable. The isovels for the bed thickness $e/D = 0.285$, Figure 7.2(f), are more symmetrical.

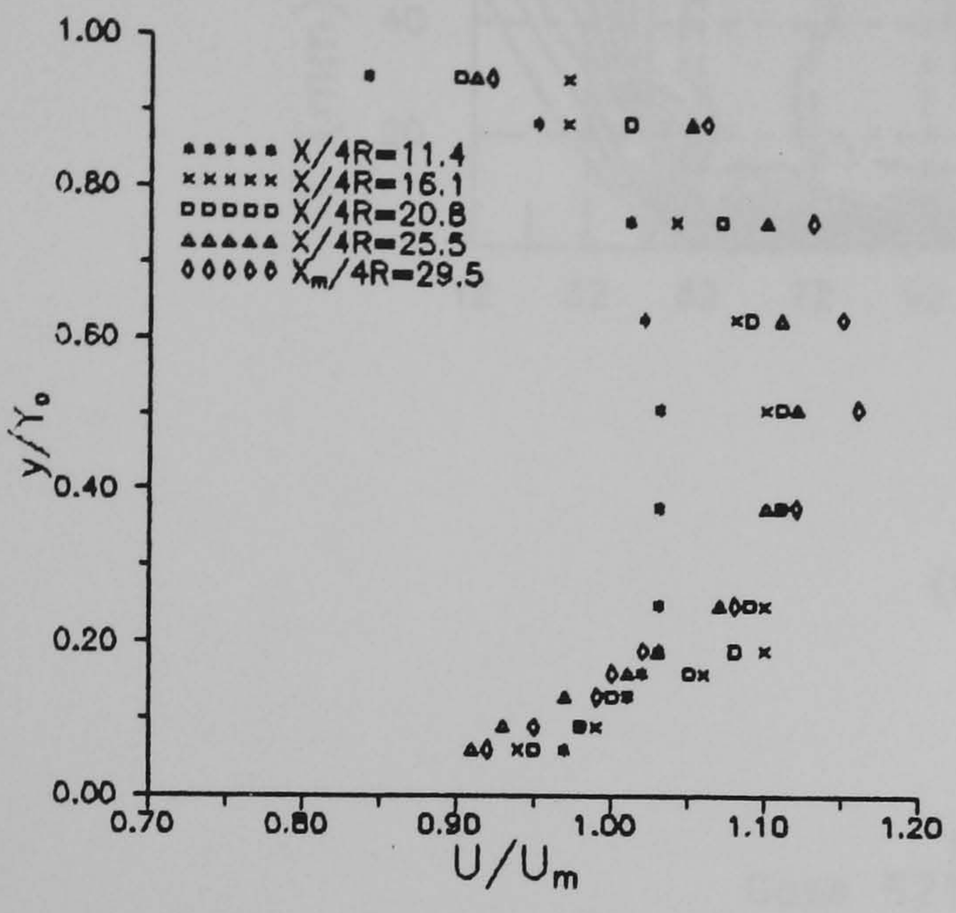

(a) Case S2211

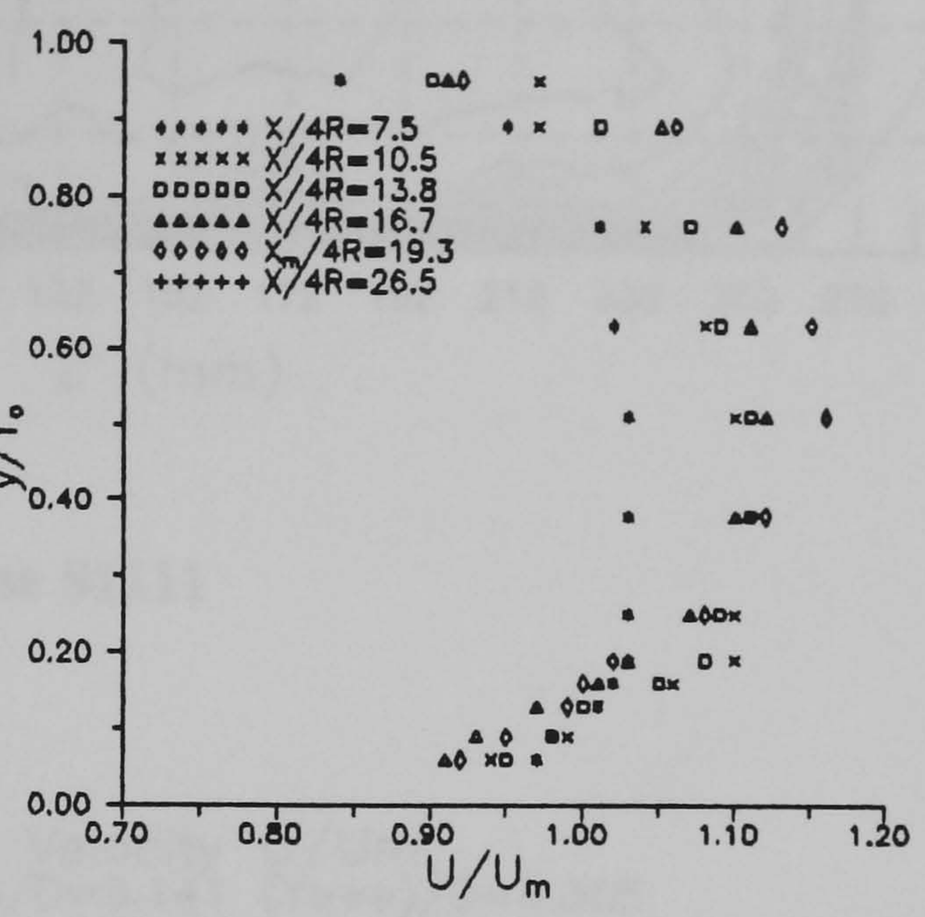

(b) Case S2411

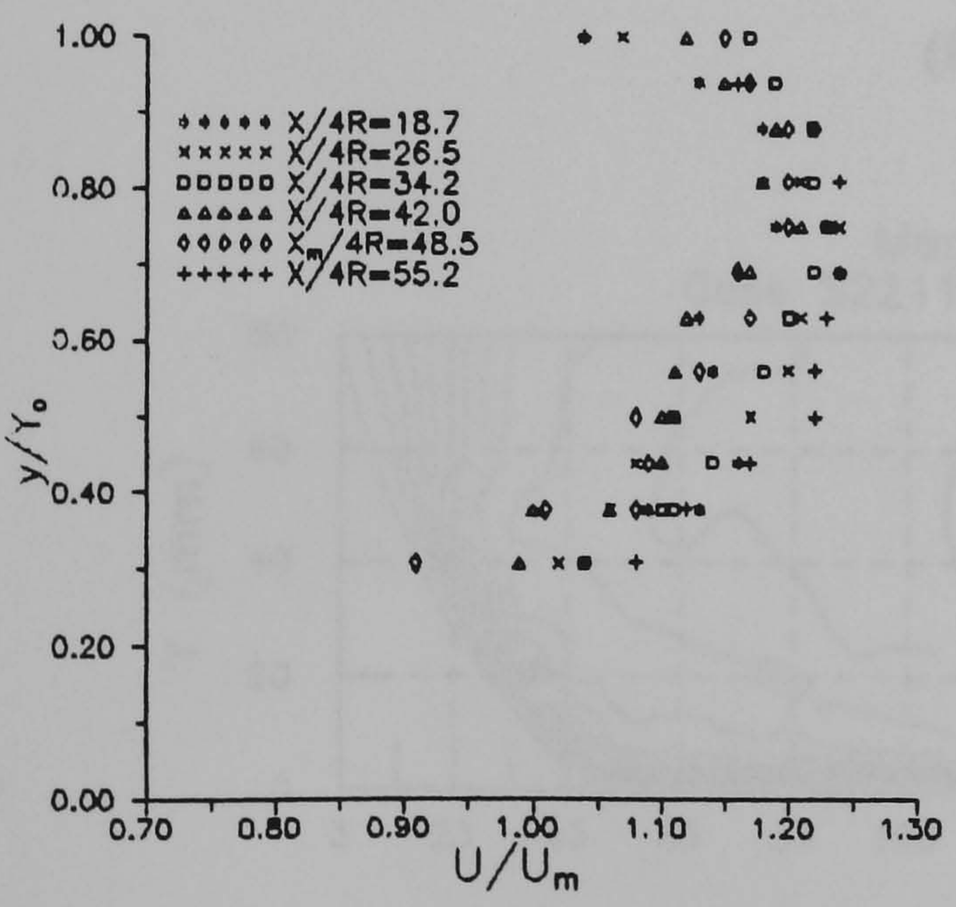

(c) Case S2121

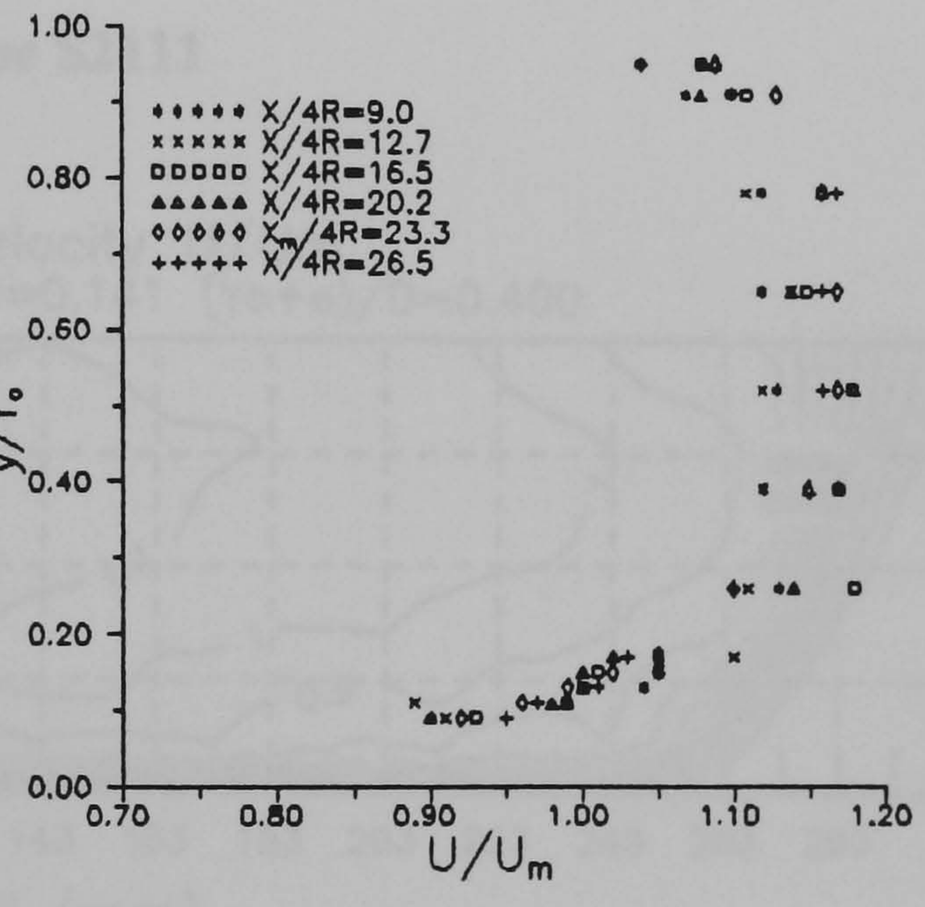

(d) Case S2321

Figure 7.1 Development of the Velocity Profile.

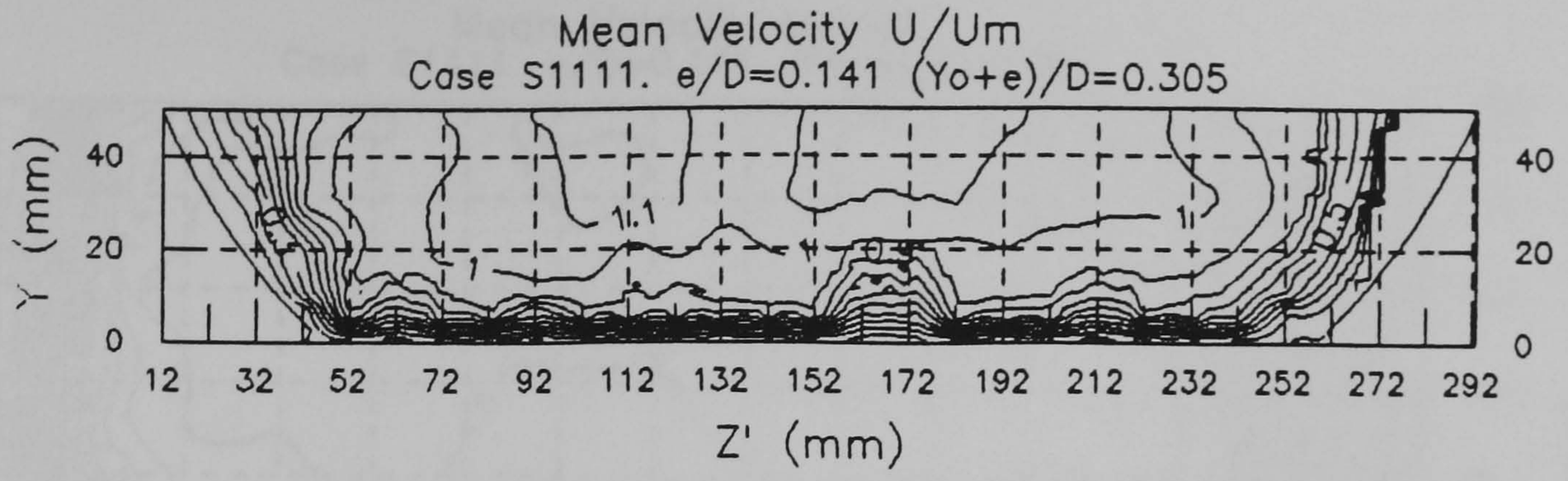

(a) Case S1111

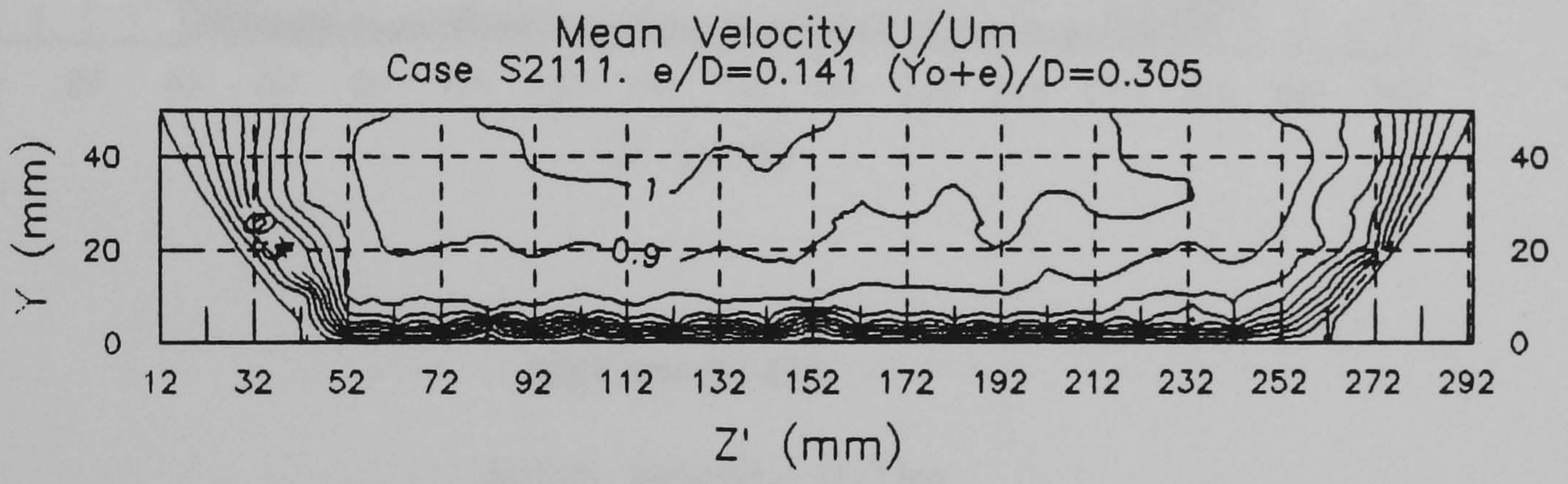

(b) Case S2111

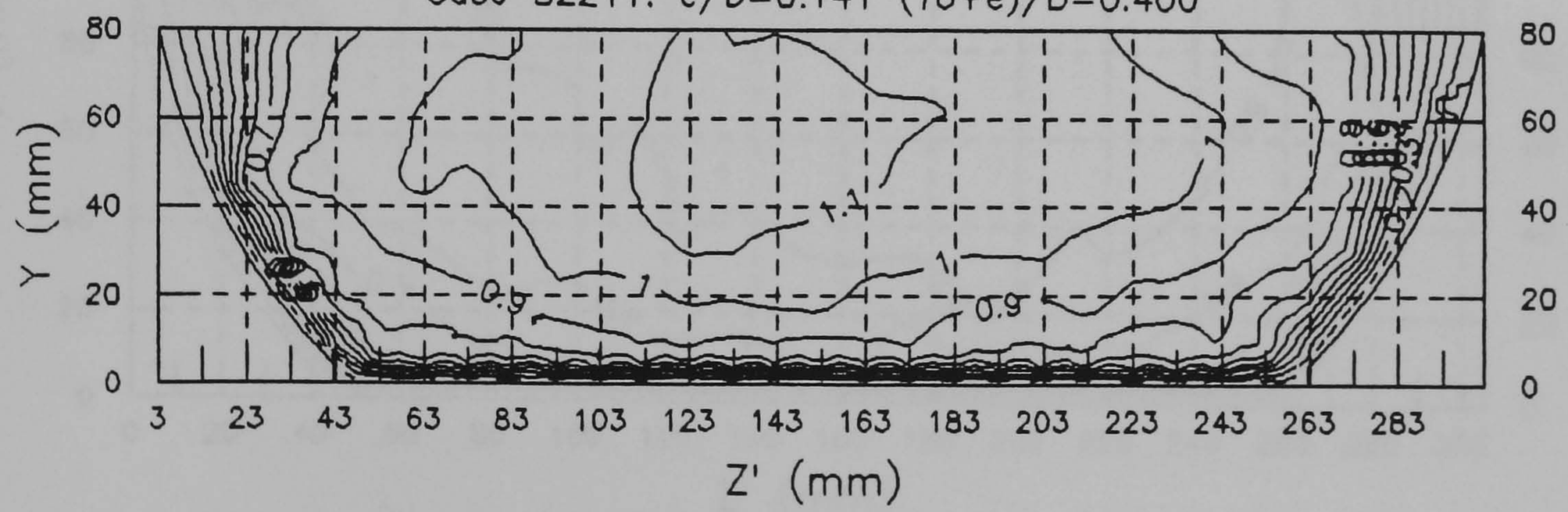

(c) Case S2211

Figure 7.2 (a - c) Mean Velocity Distribution U/U_m : Smooth Bed

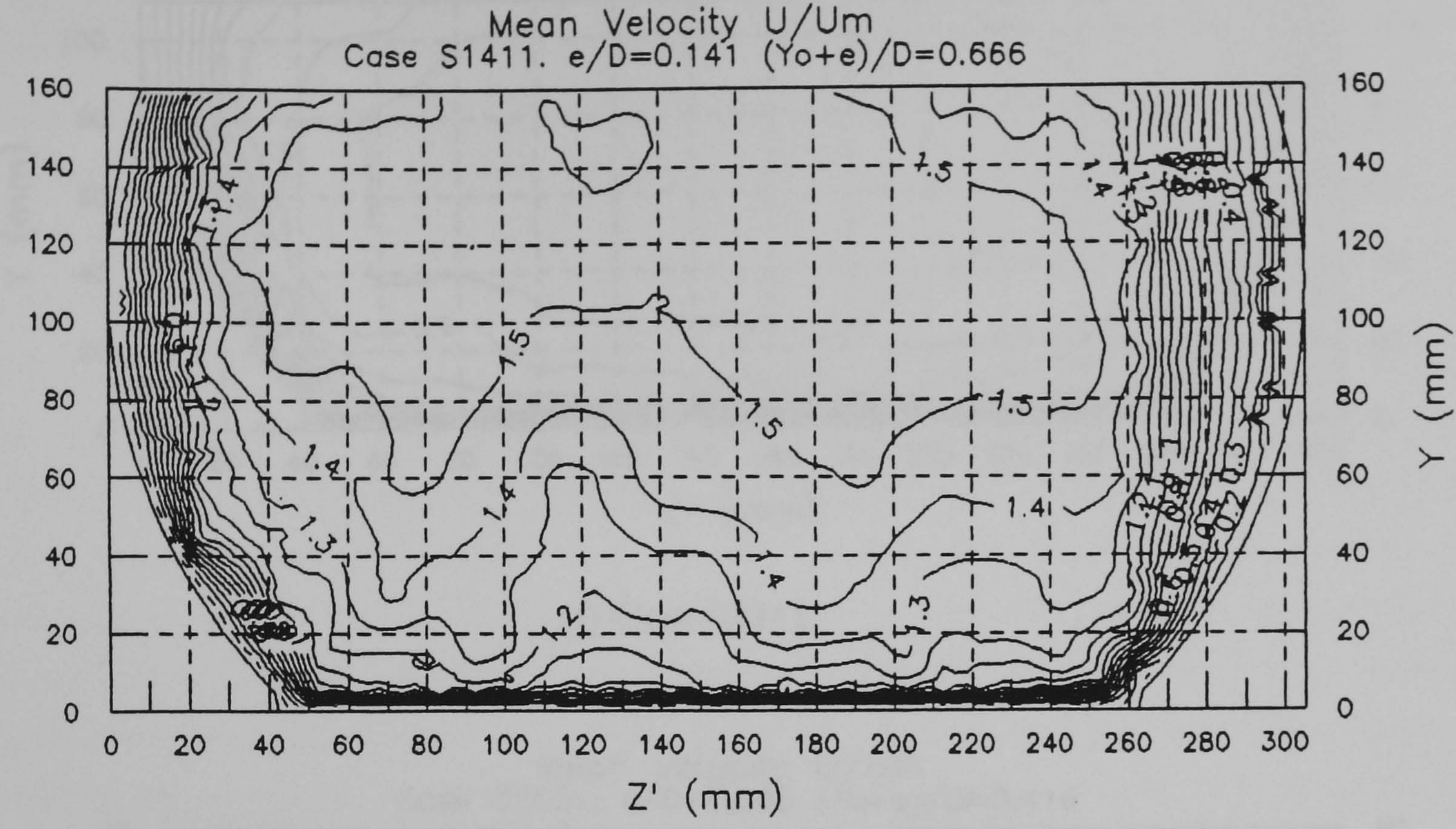

(d) Case S1411

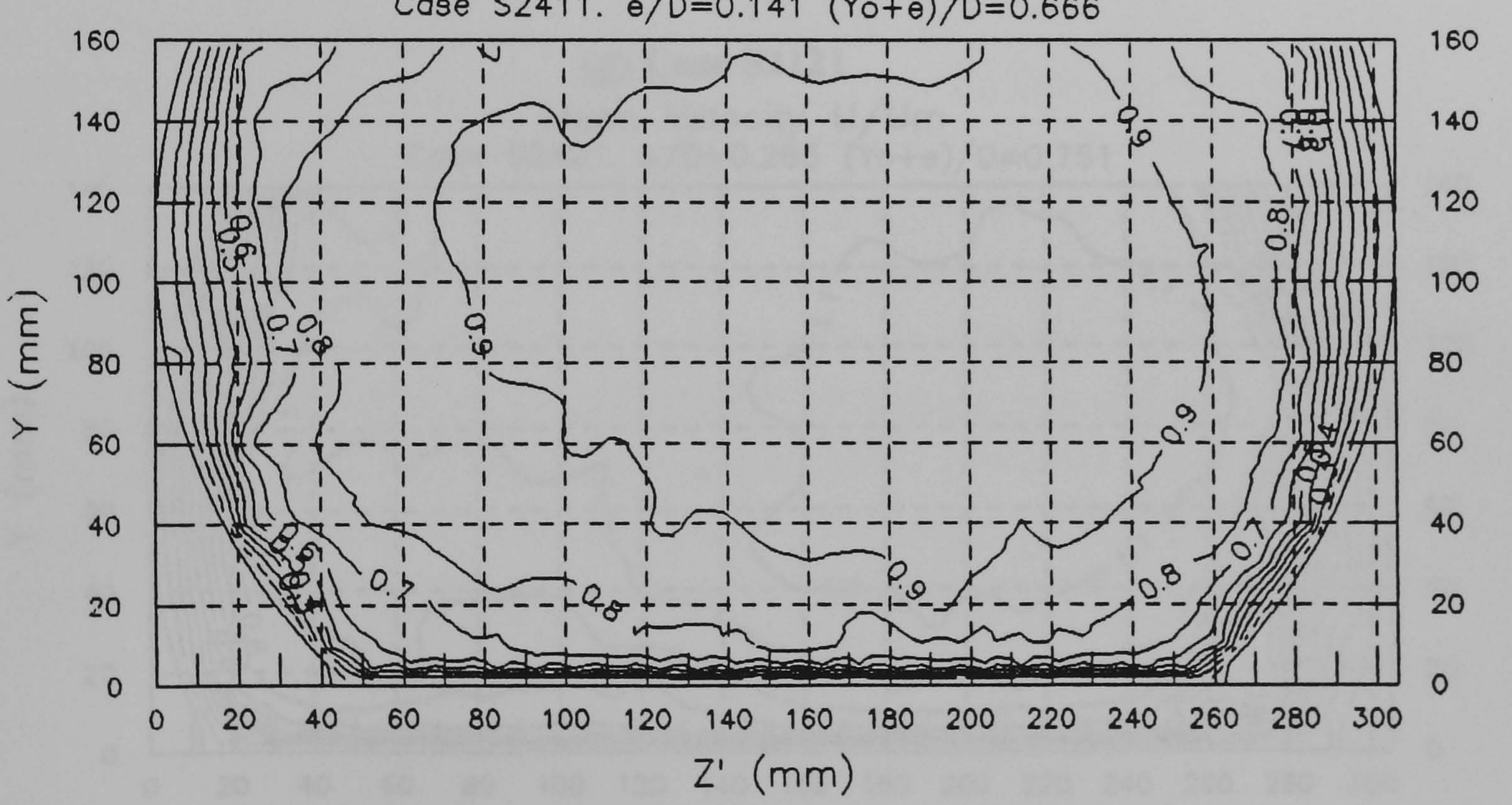

(e) Case S2411

Figure 7.2 Cont. (d -e) Mean Velocity Distribution U/U_m : Smooth Bed

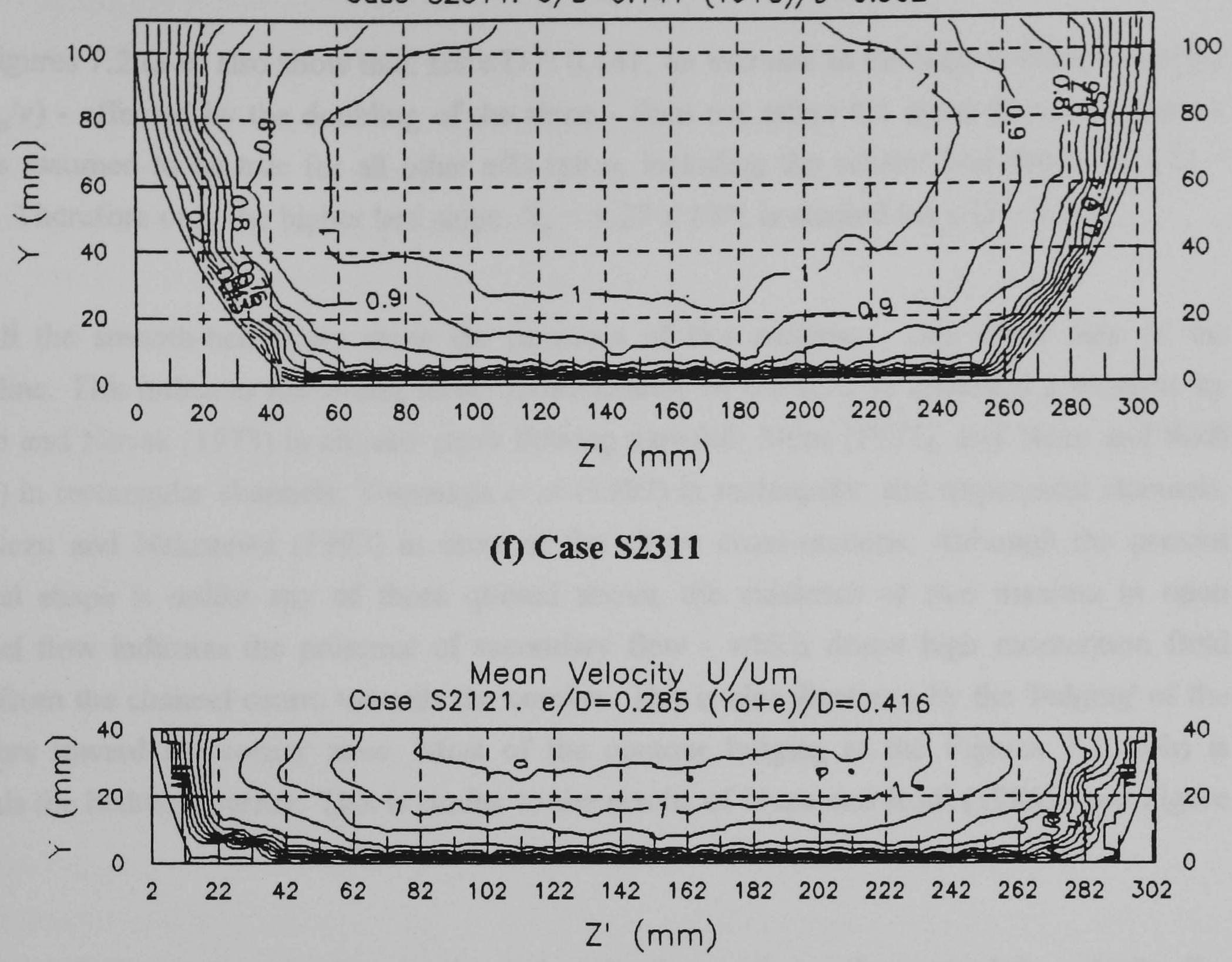

(f) Case S2311

(g) Case S2121

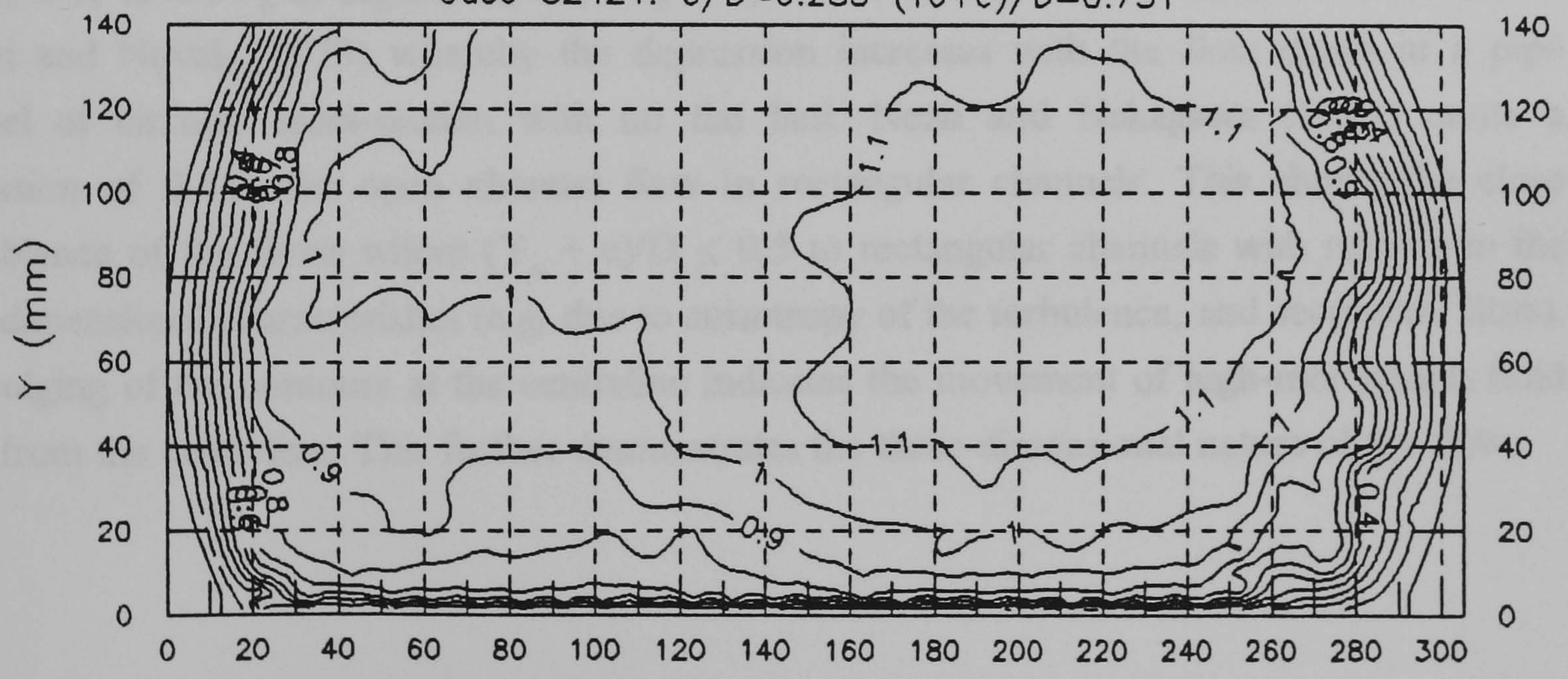

(h) Case S2421

Figure 7.2Cont. (f - h) Mean Velocity Distribution U/U_m : Smooth Bed

Figures 7.2 (a-e) also show that, for e/D = 0.141, an increase in the bulk Reynolds number ($4RU_m/\nu$) - effected by the doubling of the slope - does not affect the mean flow distribution. This is assumed to be true for all other e/D ratios, including the second bed thickness e/D = 0.285. Therefore only the higher bed slope, $S_o = 9.27 \times 10^{-4}$, is studied for e/D = 0.285.

All the smooth-bed flows show the presence of two maxima - one either side of the centreline. This indicates the strong three-dimensionality of the flow as observed previously by Nalluri and Novak (1973) in circular pipes flowing part-full; Nezu (1977), and Nezu and Rodi (1986) in rectangular channels; Tominaga *et al* (1989) in rectangular and trapezoidal channels, and Nezu and Nakagawa (1993) in most of the above cross-sections. Although the present channel shape is unlike any of those quoted above, the existence of two maxima in open channel flow indicates the presence of secondary flow - which draws high momentum fluid away from the channel centre towards the corners. This is also illustrates by the 'bulging' of the contours toward the corner zone. Most of the contour bulging in the Figures 7.2 (a-h) is towards the bed/wall corner. This is similar to the results of Nezu and Rodi (1985) - see Figure 2.4.

The velocity maxima are depressed to below the free surface - also termed the velocity dip. The extent of the depression varies from $0.25Y_o$ (i.e. $y_{max}/Y_o = 0.75$) at low flow depths, $(Y_o + e)/D \leq 0.5$, to $0.5Y_o$ at higher depths, $(Y_o + e)/D > 0.5$. This closely mimics the results of Nalluri and Novak (1973) whereby the depression increases with the flow depth in a pipe channel of circular cross-section with no flat bed. Nezu and Nakagawa (1993) quote a depression of $0.4Y_o$ for open channel flow in rectangular channels. This shows the close resemblance of the flows where $(Y_o + e)/D \leq 0.5$ to rectangular channels with respect to the three-dimensional characteristics (e.g. due to anisotropy of the turbulence, and secondary flow). The bulging of the contours at the centreline indicates the movement of high-momentum fluid away from the centreline. This further demonstrates the three-dimensional nature of the flow.

7.3.2 Normalised Turbulence Intensities

Figures 7.3 show the normalised turbulence intensity profiles at the channel centreline. They are normalised using the cross-sectional average shear velocity $(U_*)_{ave} = \sqrt{(gRS_o)}$. The use of the velocity scale, $(U_*)_{ave}$, is appropriate for smooth flows since the local value is not known and can not be accurately deduced from the local longitudinal mean velocity profile (Hoohlo 1991).

The longitudinal turbulence intensities, (Figure 7.3a), are compared to the empirical formula of Nezu and Rodi (1986),

$$\frac{U_{rms}}{U_*} = D_u \exp(-C_k \frac{y}{Y_o}), \qquad (2.27a)$$

where $D_u = 2.30$, and $C_k = 1.0$. In general the intensities show an exponential decrease with an increase in depth. The intensities for Case S1411 are up to twice the values given by Eqn 2.27(a). These high values are caused by the bulk flow rate, Q, being higher than that pertaining to the flow depth - i.e. the flow being artificially uniform. Indeed this is illustrated by the high cross-sectional maximum velocity, U_{max} (= 0.837 m/s), which is greater than the U_{max} value for Case S2411! For the rest of the smooth-bed cases the intensities are lower than Eqn 2.27(a) in the near the bed, $y/Y_o < 0.3$, and higher farther from the bed, $y/Y_o > 0.7$. This flatter distribution is due to the three-dimensional effects which enforce a uniform distribution of the turbulence. This is apparent for the higher $(Y_o + e)/D$ flows. Nonetheless the fitted profile for all flows gives the constants $D_u = 1.94$, and $C_k = 2/3$, which is close to Eqn 2.27(a).

Figure 7.3(b) shows the normalised V_{rms} profiles compared with their respective empirical profile (Nezu and Nakagawa 1986)

$$\frac{V_{rms}}{U_*} = D_v \exp(-C_k \frac{y}{Y_o}) \qquad (2.27\,b)$$

where $D_v = 1.27$, and $C_k = 1.0$. The profiles are much flatter than Eqn 2.27(b) with $D_v = 0.777$ and $C_k = 0.186$, illustrating a higher retardation near the bed than that predicted by Eqn 2.27(b). This 'retardation' of the turbulence is due to the transfer of mean flow momentum (from which the turbulence extracts its energy) away from the centreline.

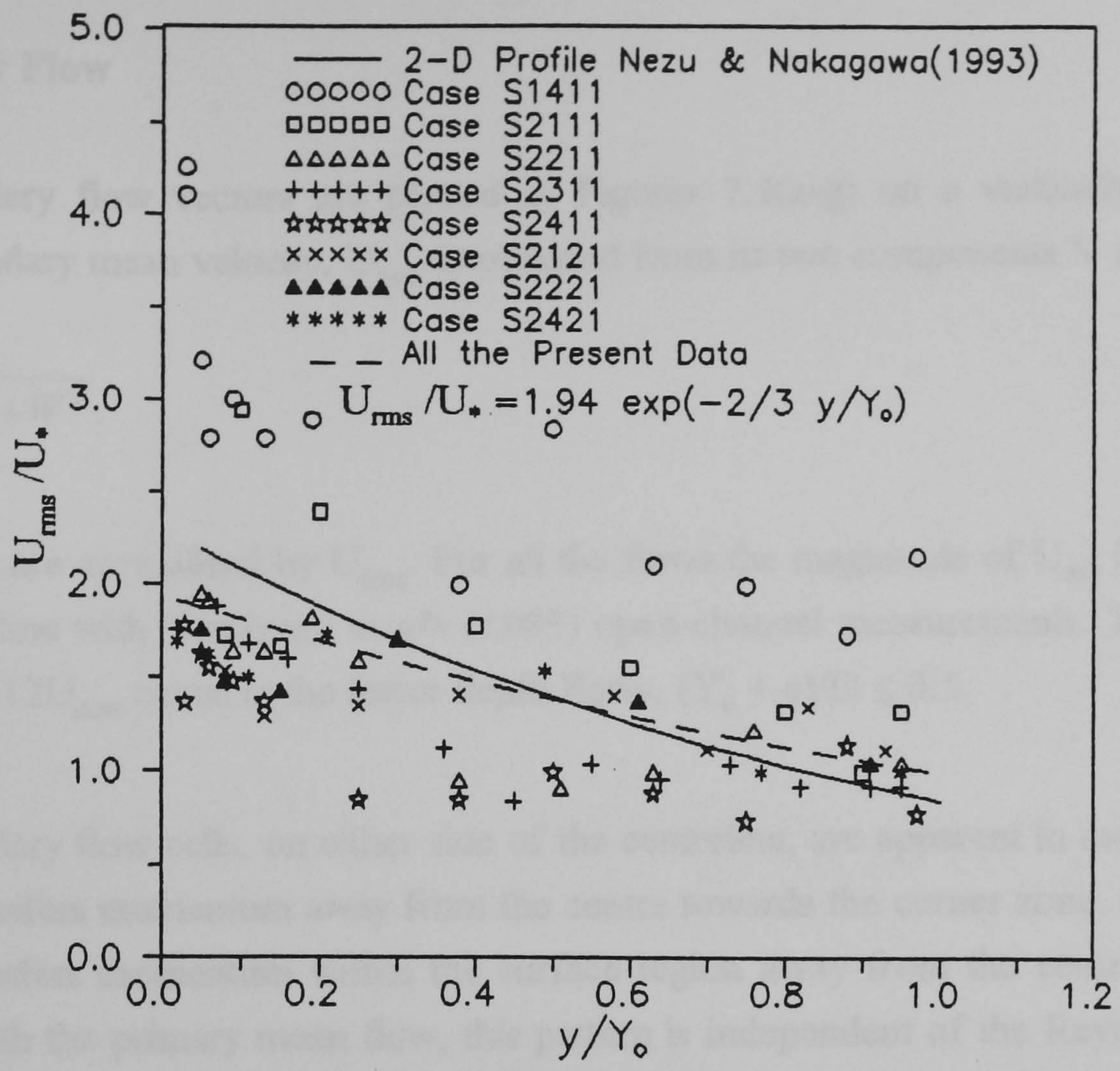

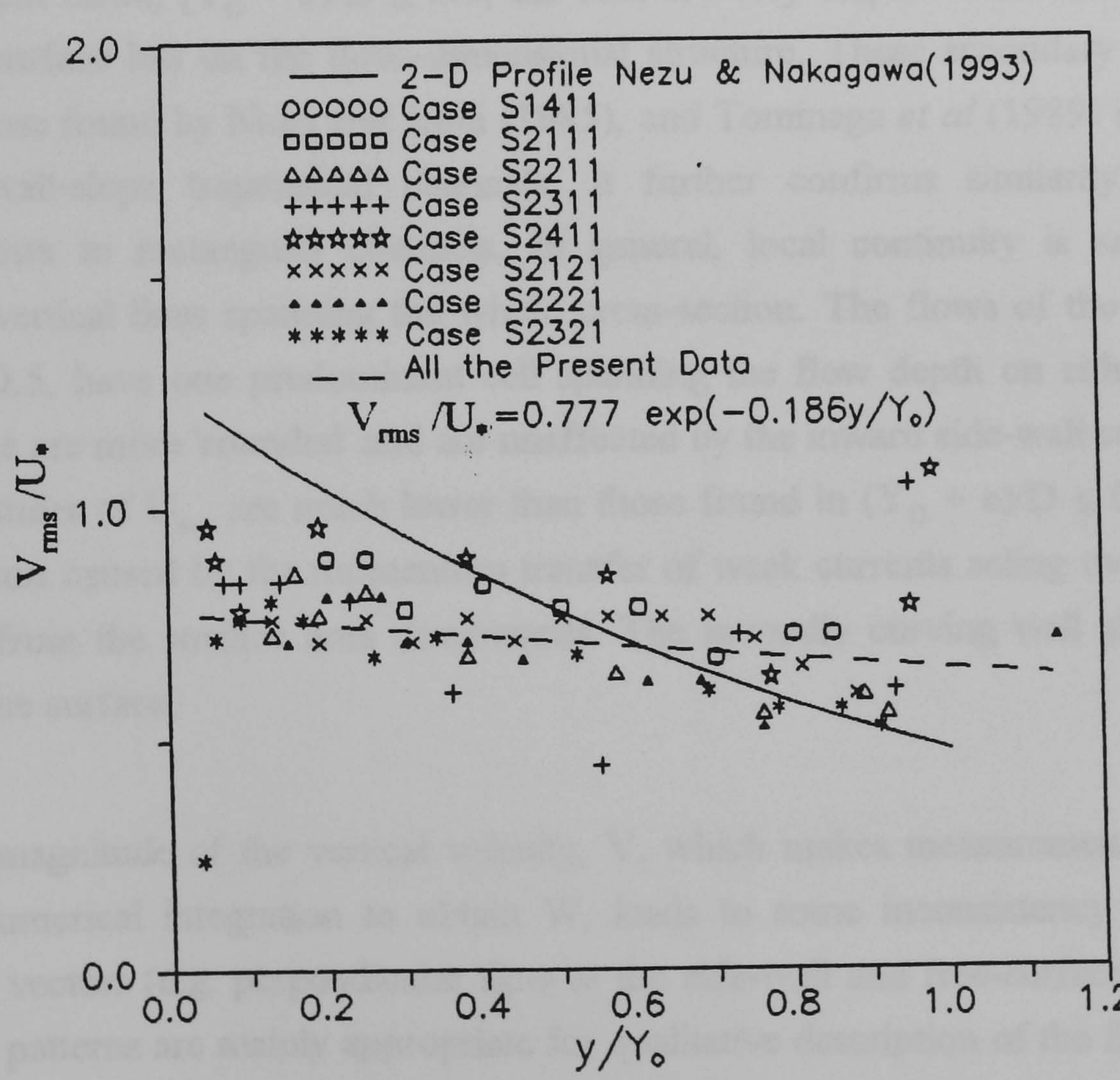

Figure 7.3 Smooth Bed Turbulence Intensities. (a) U_{rms}/U_*.; and (b) V_{rms}/U_*.

7.3.3 Secondary Flow

The secondary flow vectors are plotted in Figures 7.4(a-g) on a vertically exaggerated scale. The secondary mean velocity, U_{sec}, is obtained from its two components V and W:

$$U_{sec} = \sqrt{V^2 + W^2} \,. \tag{7.2}$$

U_{sec}, V, and W, are normalised by U_{max}. For all the flows the magnitude of U_{sec} is of the order of $0.03U_{max}$, in line with Tominaga *et al*'s (1989) open-channel measurements. The maximum U_{sec} values of $0.12U_{max}$ occur in the lower depth flows, $(Y_o + e)/D \leq 0.5$.

Two secondary flow cells, on either side of the centreline, are apparent in most flows. The 'bottom' cell transfers momentum away from the centre towards the corner zone. At the top the surface cell transfers momentum within the surface region away from the centre towards the side-wall. As with the primary mean flow, this pattern is independent of the Reynolds number. In the lower depth flows, $(Y_O + e)/D \leq 0.5$, the cells are very elliptic. This indicates the large effect the free surface has on the three-dimensional structure. These secondary flow patterns are similar to those found by Nezu and Rodi (1985), and Tominaga *et al* (1989) in rectangular, and high-side-wall-slope trapezoidal channels. It further confirms similarity of the low $(Y_O + e)/D$ flows to rectangular channels. In general, local continuity is satisfied across horizontal and vertical lines spanning the whole cross-section. The flows of the higher depth, $(Y_O + e)/D > 0.5$, have one predominant cell spanning the flow depth on either side of the centreline. These are more 'rounded' and are unaffected by the inward side-wall curvature at the top. The magnitudes of U_{sec} are much lower than those found in $(Y_O + e)/D \leq 0.5$ flows. The velocity dip is thus caused by the momentum transfer of weak currents acting over a large part of the section, from the surface area downwards. The inwardly curving wall also retards the flow near the free surface.

The small magnitude of the vertical velocity, V, which makes measurement difficult, and the need for numerical integration to obtain W, leads to some inconsistency in the plotted secondary flow vectors (e.g. perpendicular flow at the side-wall and free-surface). As such the secondary flow patterns are mainly appropriate for qualitative description of the flow.

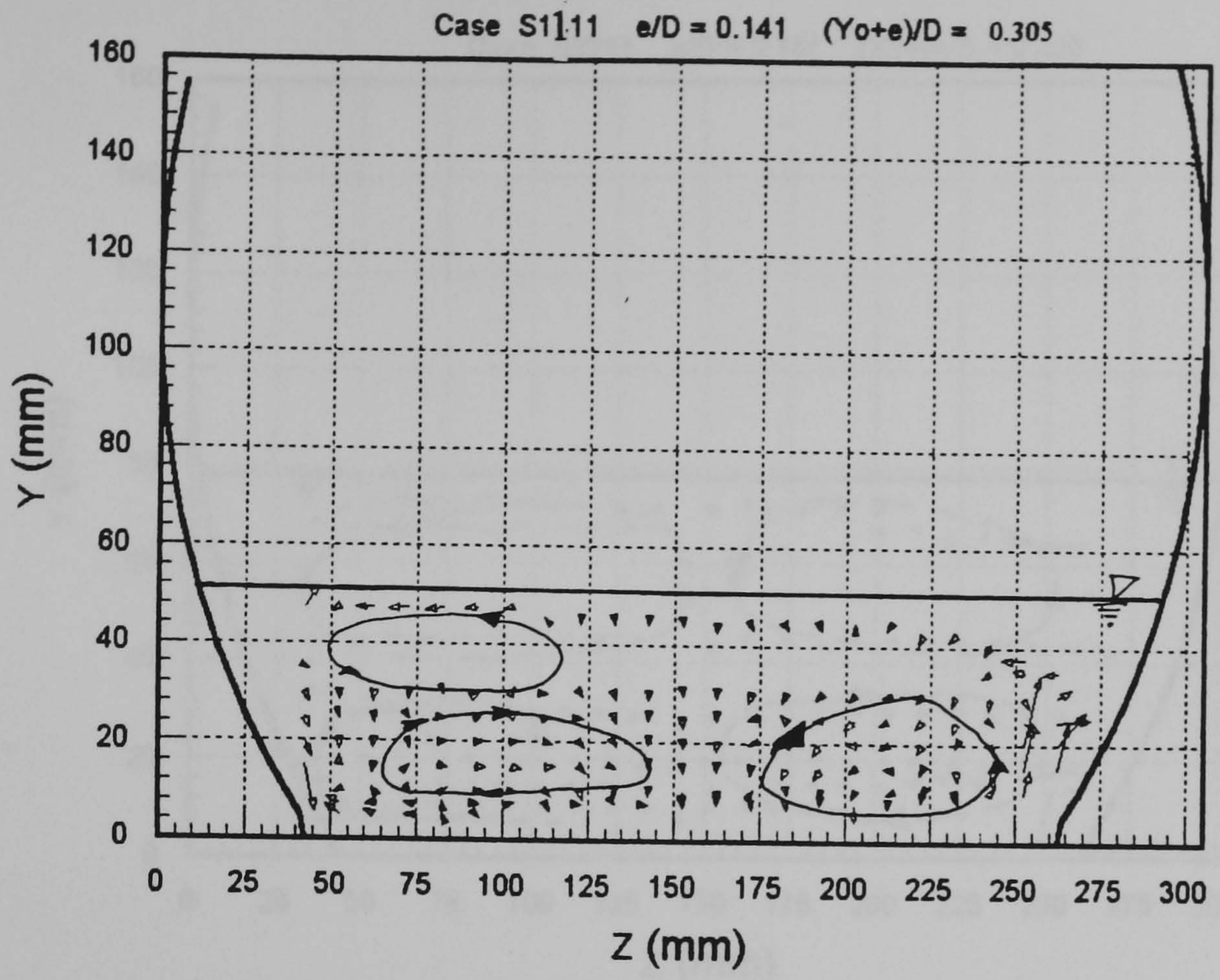

(a) Case S1111

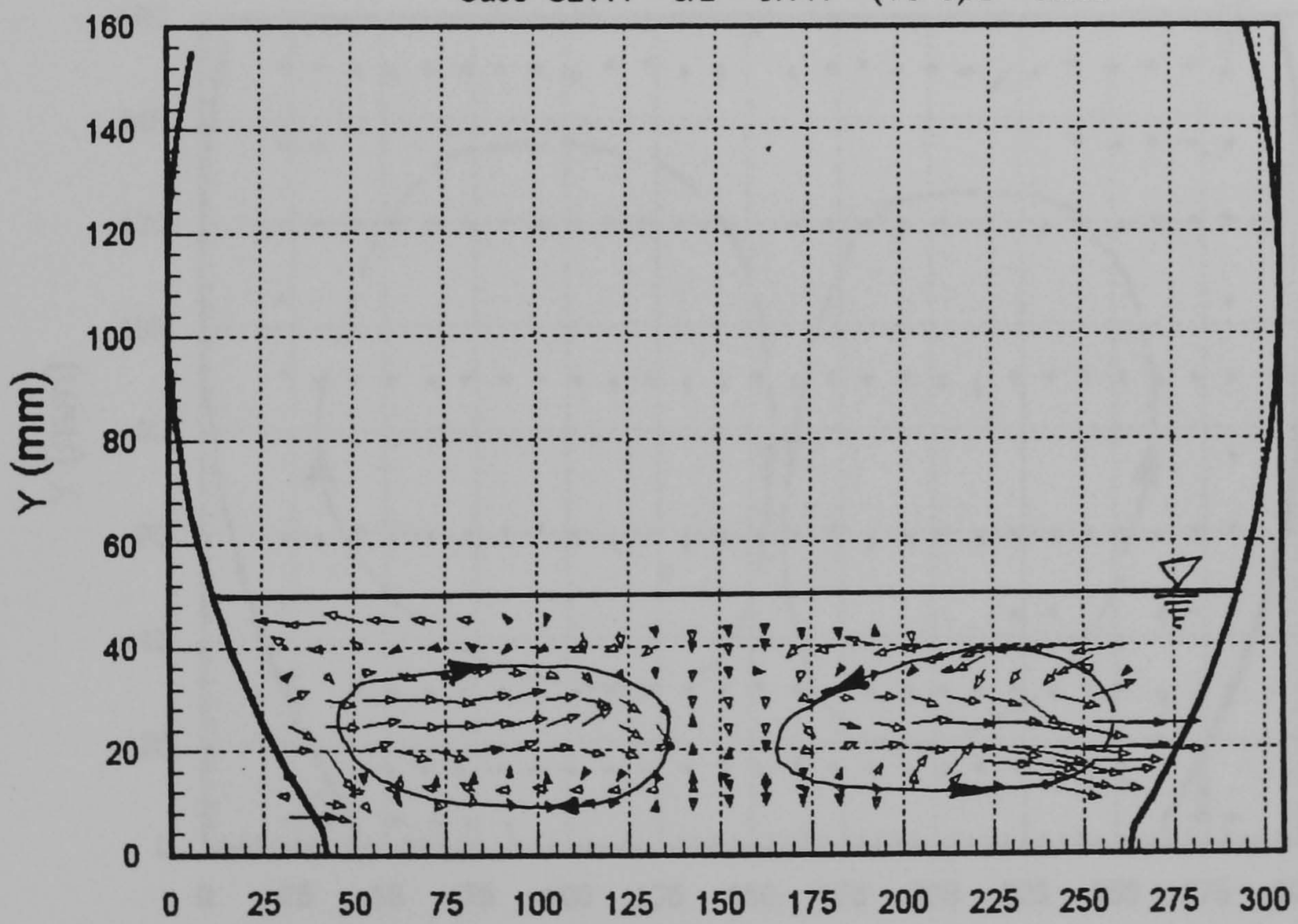

(b) Case S2111

Figure 7.4 (a - b) Secondary Flow: Smooth Bed

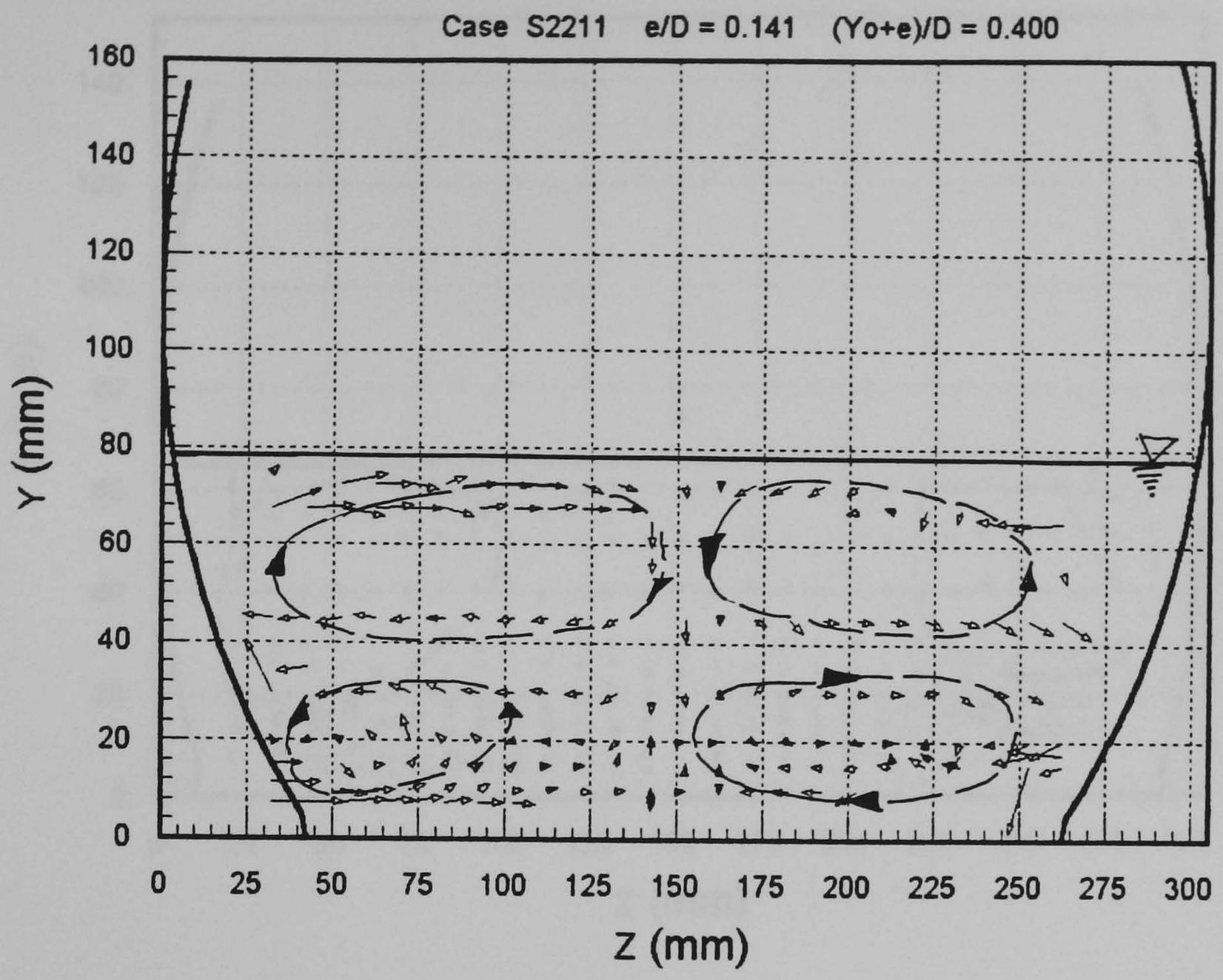

(c) Case S2211

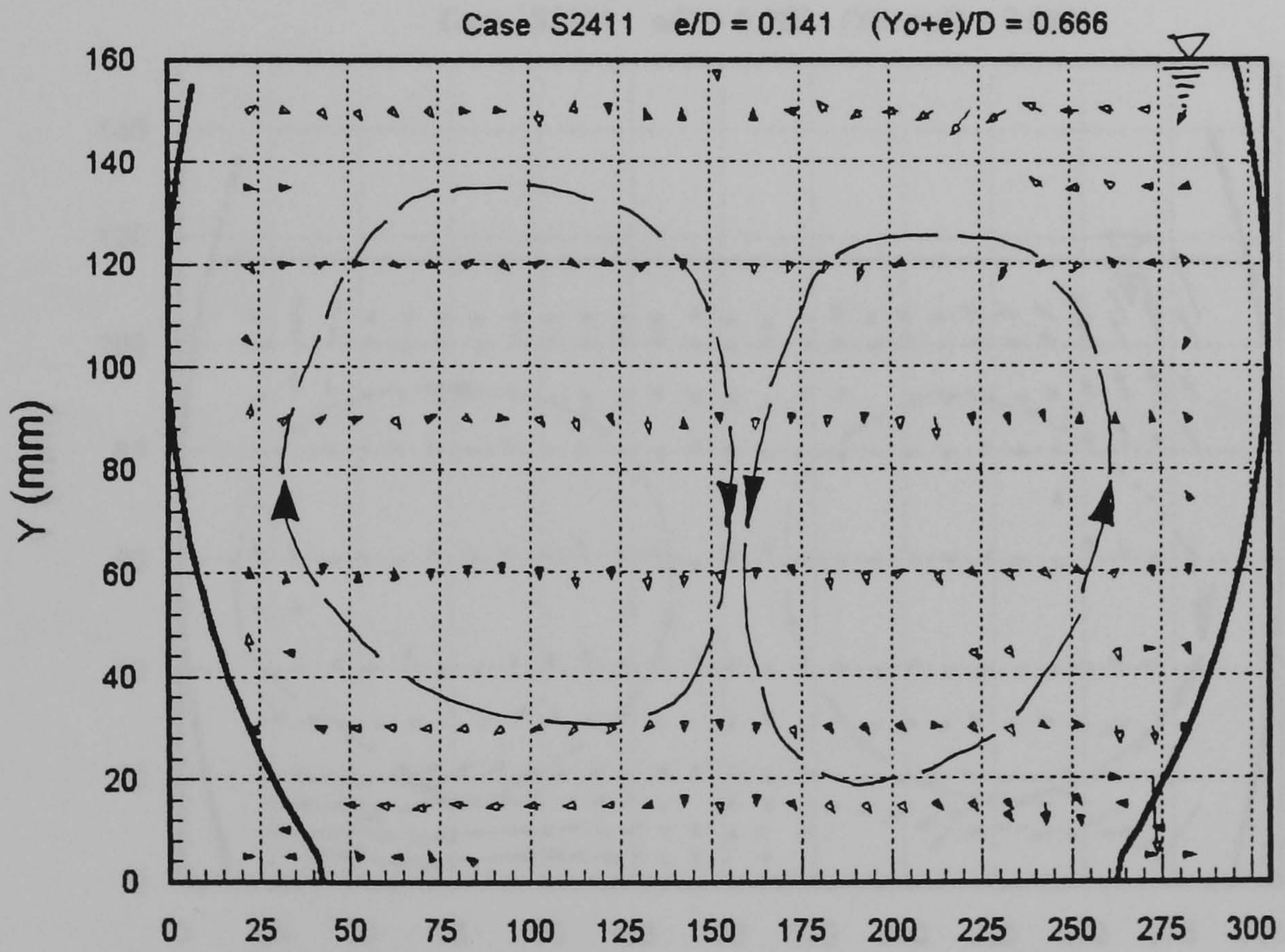

(d) Case S2411

Figure 7.4 (c - d) Secondary Flow: Smooth Bed

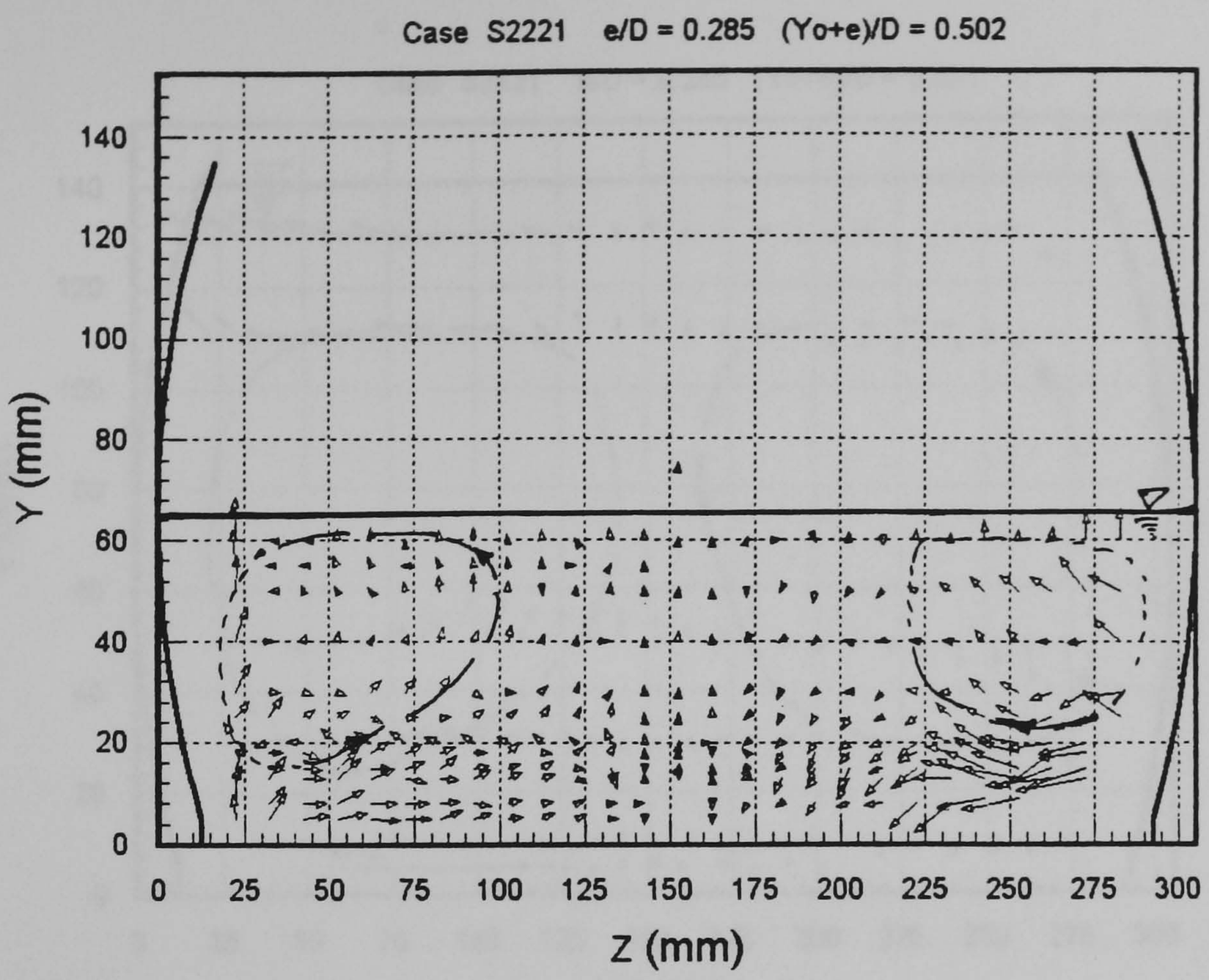

(e) Case S2221

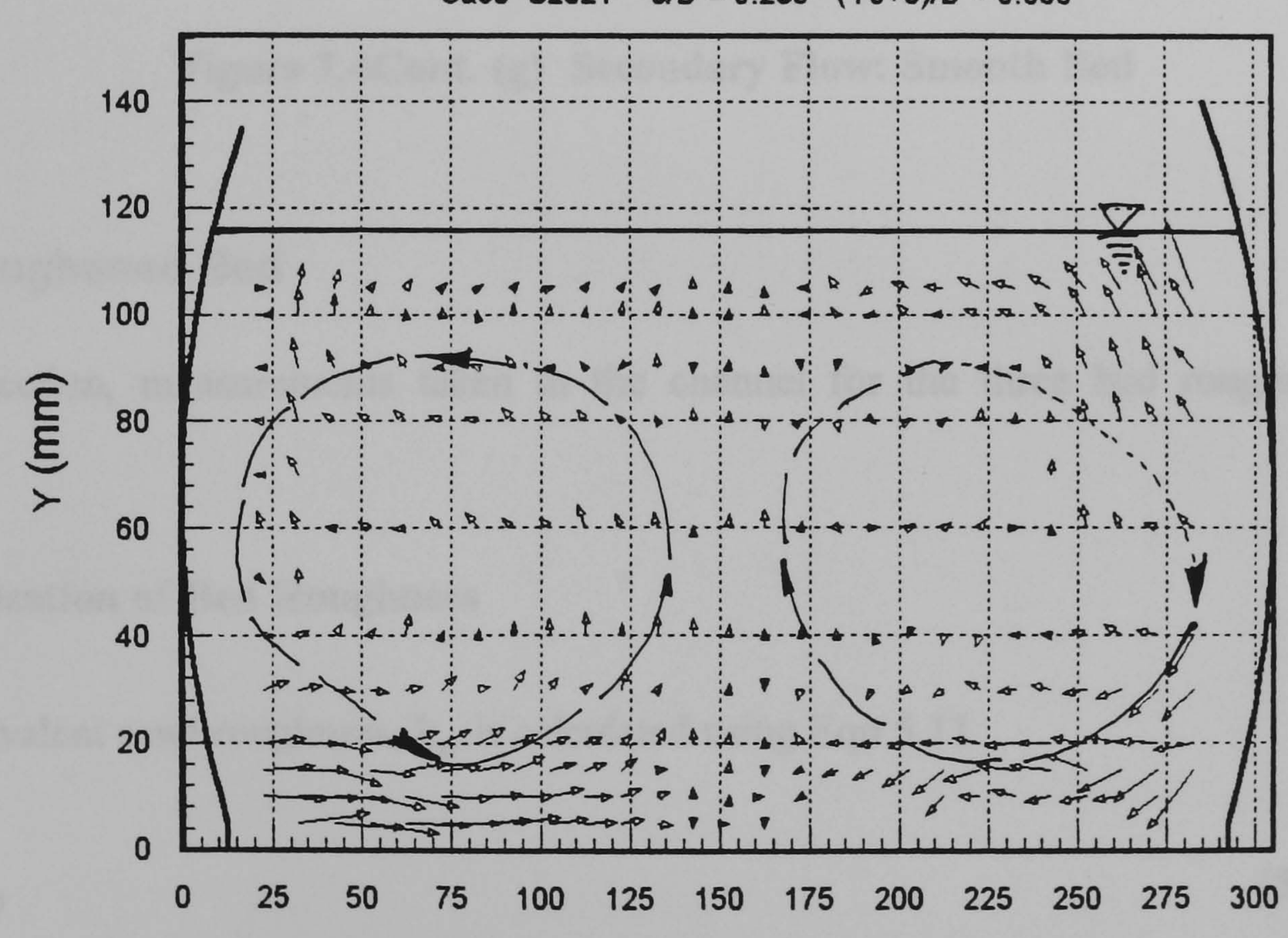

(f) Case S2321

Figure 7.4Cont. (e - f) Secondary Flow: Smooth Bed

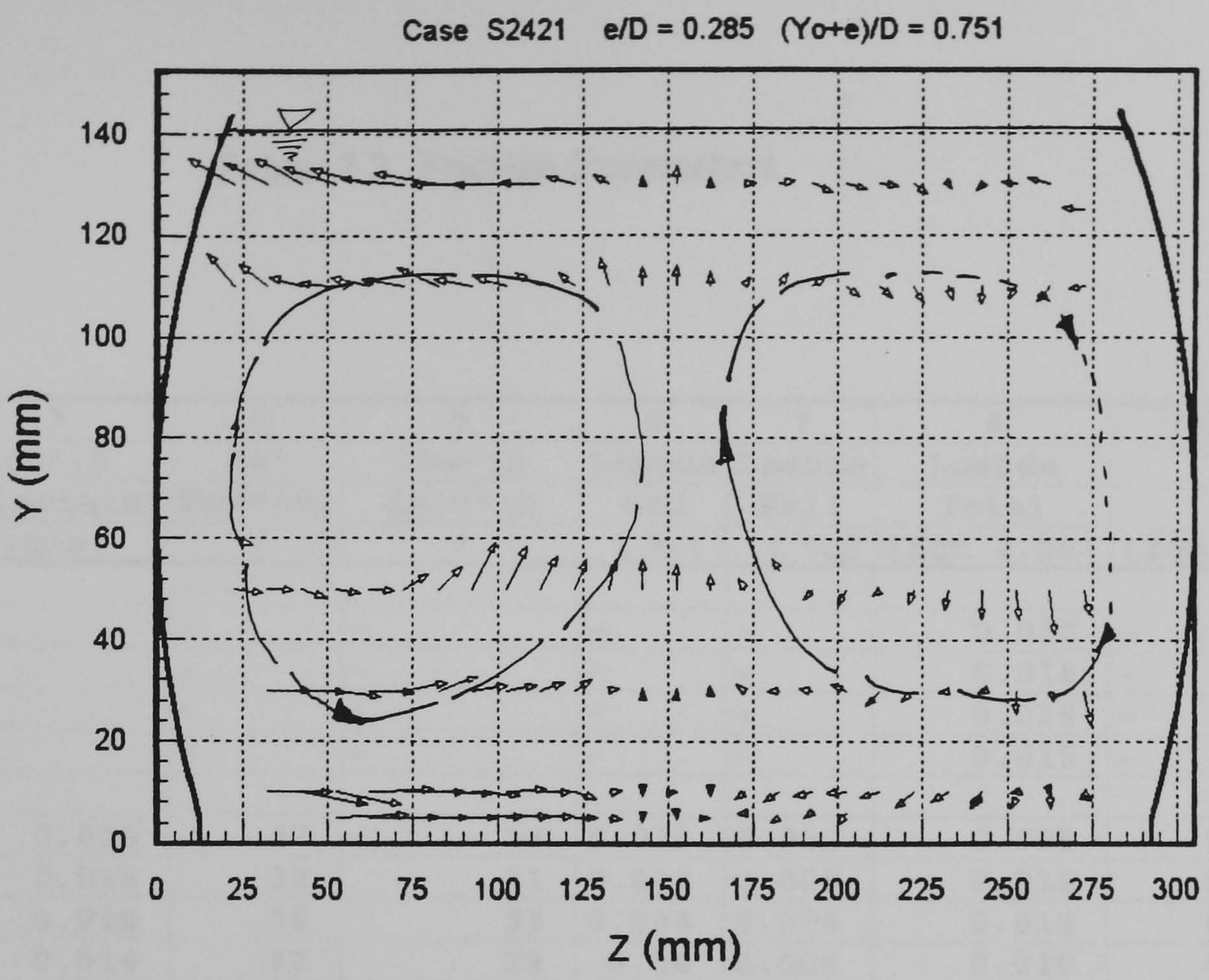

(g) Case S2421

Figure 7.4Cont. (g) Secondary Flow: Smooth Bed

7.4 The Roughened Bed

In this section, measurements taken in the channel for the three bed roughnesses are presented.

7.4.1 Classification of Bed Roughness

The equivalent sand roughness, k_s, is calculated using Eqn 5.11

$$k_s \cong 2d_{90} \qquad (5.11)$$

and is given in Table 7.1. d_{90} is derived from the grading curves for the sand roughness. The relative roughness Y_o/k_s lies in the range 3.9 - 67.8 (see Table 7.2).

Table 7.2 Friction Parameters

Case	2	3	4	5	6	7	8	9
	Yo/ks	(U*)b	Re*	(Re*)b	Lambda	Lambda	Lambda	λ_s
		(Einstein)	KsU*/vi	Ks(U*)b	Bed	Wall	Total	
		(m/s)		ν	(λ_b)	(λ_w)	(Eqn 2.36)	(Eqn 2.37)
S2111	-	-	-	-	-	-	0.020	-
S2211	-	-	-	-	-	-	0.018	-
S2311	-	-	-	-	-	-	0.016	-
S2411	-	-	-	-	-	-	0.015	-
R1111	21	0.016	27	33	0.033	0.006	0.005	0.023
R1211	33	0.015	32	31	0.032	0.006	0.016	0.025
R1311	47	0.016	36	33	0.034	0.006	0.014	0.023
R1411	68	0.014	40	29	0.04	0.006	0.010	0.022
R2111	21	0.015	38	31	0.031	0.006	0.010	0.023
R2211	33	0.024	45	49	0.03	0.006	0.024	0.027
R2311	47	0.028	51	58	0.033	0.006	0.024	0.028
R2411	68	0.031	56	64	0.037	0.006	0.019	0.026
R2112	5	0.021	165	187	0.029	0.006	0.044	0.034
R2212	8	0.026	196	232	0.028	0.006	0.037	0.032
R2312	11	0.029	219	258	0.029	0.006	0.027	0.028
R2412	16	0.033	242	294	0.032	0.006	0.025	0.027
S2121	-	-	-	-	-	-	0.024	-
S2221	-	-	-	-	-	-	0.020	-
S2321	-	-	-	-	-	-	0.017	-
S2421	-	-	-	-	-	-	0.017	-
R2123	10	0.018	59	62	0.03	0.006	0.051	0.035
R2223	17	0.023	70	78	0.029	0.006	0.042	0.033
R2323	30	0.029	85	100	0.03	0.006	0.031	0.030
R2423	36	0.030	87	101	0.031	0.006	0.025	0.028
R2122	4	0.019	142	157	0.029	0.006	0.059	0.036
R2222	6	0.024	177	205	0.028	0.006	0.057	0.038
R2322	11	0.030	209	254	0.029	0.006	0.042	0.035
R2422	14	0.032	216	269	0.029	0.006	0.040	0.035

Table 7.2(Cont.) Friction Parameters

10 λ_b / λ_s Bed	11 λ_w / λ_s Wall	12 Meantau (Eqn 2.35) (N/m^2)	13 Bed Shear (Einstein) (N/m^2)	14 $(\overline{\tau_b} / \overline{\tau_o})$ (Einstein)	15 Shear Force Ratio Wall (SF)
	-	0.3419	-	-	0.37
	-	0.4833	-	-	0.46
	-	0.6040	-	-	0.54
	-	0.7371	-	-	0.62
1.44	0.26	0.1708	0.2560	1.50	0.05
1.29	0.24	0.2414	0.2250	0.93	0.50
1.46	0.26	0.3017	0.2560	0.85	0.61
1.85	0.28	0.3681	0.1960	0.53	0.80
1.34	0.26	0.3419	0.2250	0.66	0.58
1.11	0.22	0.4833	0.5760	1.19	0.36
1.18	0.21	0.6040	0.7840	1.30	0.40
1.43	0.23	0.7371	0.9610	1.30	0.51
0.84	0.17	0.3419	0.4410	1.29	0.18
0.87	0.19	0.4833	0.6760	1.40	0.25
1.03	0.21	0.6040	0.8410	1.39	0.35
1.17	0.22	0.7371	1.0890	1.48	0.44
1.000	1.000	0.2934	-	-	0.23
1.000	1.000	0.4304	-	-	0.33
1.000	1.000	0.6098	-	-	0.46
1.000	1.000	0.6631	-	-	0.52
0.86	0.17	0.2934	0.3240	1.10	0.15
0.87	0.18	0.4304	0.5260	1.22	0.18
0.99	0.20	0.6098	0.8410	1.38	0.26
1.10	0.21	0.6631	0.9000	1.36	0.35
0.80	0.17	0.2934	0.3610	1.23	0.06
0.74	0.16	0.4304	0.5760	1.34	0.10
0.83	0.17	0.6098	0.9000	1.48	0.21
0.84	0.17	0.6631	1.0240	1.54	0.26

The thickness of the viscous sublayer, δ_l, is given by the standard Blasuis formula

$$\delta_l = \frac{32.8}{\mathrm{Re}\sqrt{\lambda}} \tag{7.3}$$

where Re is the Reynolds number (= $4RU_m/\nu$), and λ is the friction factor for an equivalent smooth flow (Eqn 2.36).

The bed roughness Reynolds number, $Re_* = (U_*)_b\ k_s/\nu$, is used to classify the hydraulic roughness of the flows. The equivalent bed shear velocity $(U_*)_b$ is obtained by using the separation technique of Einstein (sub-Section 2.5.2). Re_* values obtained in the study lie in the range of $29 \leq Re_* \leq 269$. The lower values, $Re_* \leq 70$, indicate a flow in transition from hydraulically smooth to hydraulically rough as noted in sub-Section 2.4.3 The roughness elements do not fully penetrate the viscous sublayer (i.e. $\delta_l \geq k_s$). This is true for all the Rough1 (k_s = 2.36 mm) flow cases, and generally for flows where $Y_o/k_s > 17$. The higher bed roughness cases are fully rough, with $Re_* > 70$ and $\delta_l < k_s$. It is worth noting that all the $(U_*)_b$ values are greater than the cross-sectional average shear velocity $(U_*)_{ave}$. This is expected as the roughness induces higher traction on the flow than does a smooth boundary.

7.4.2 Longitudinal Mean Flow Characteristics

Figures 7.5 (a-c) show the development of the U profile along the channel length. The turbulent flow profile is achieved sooner that in corresponding smooth bed, with Rough2 profiles developing fastest, followed by Rough3 and Rough1. The profile is very flat away from the bed. This illustrates the high level of turbulent mixing that prevail over the flow depth.

The two mean velocity contours plots, Figures 7.6 (a and b), are similar. This indicates the absence of the Reynolds number (= $4RU_m/\nu$) effect on the velocity distribution for the fully rough flows. For the rest of the roughened bed flow, Figures 7.7 - 7.8, the symmetry of the flow in the roughened bed cases, is better than that achieved for smooth-bed flow.

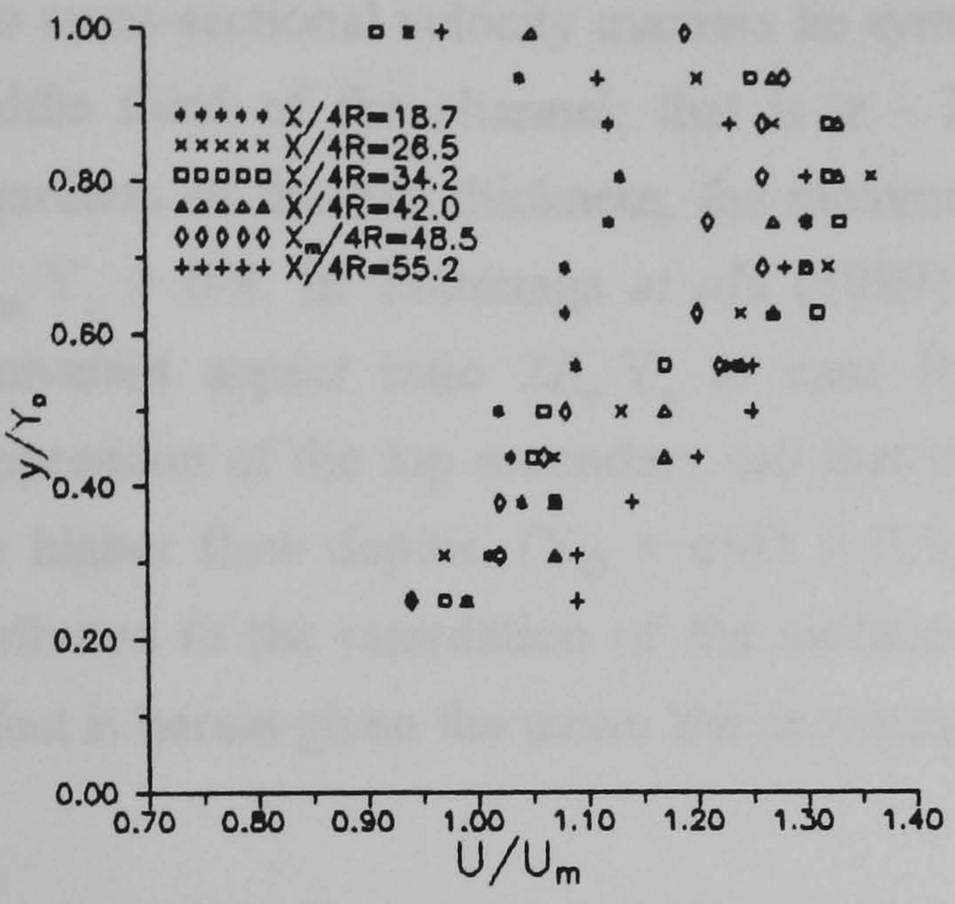

(a) Rough3: Case R2123

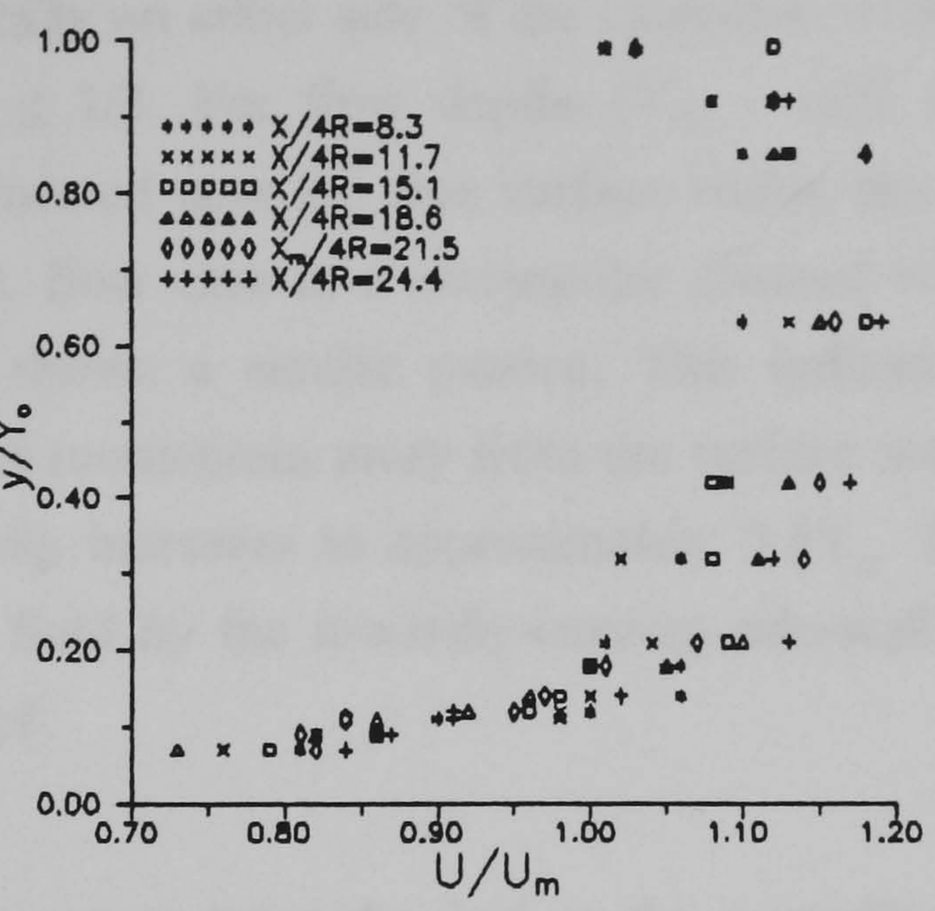

(b) Rough3: Case R2423

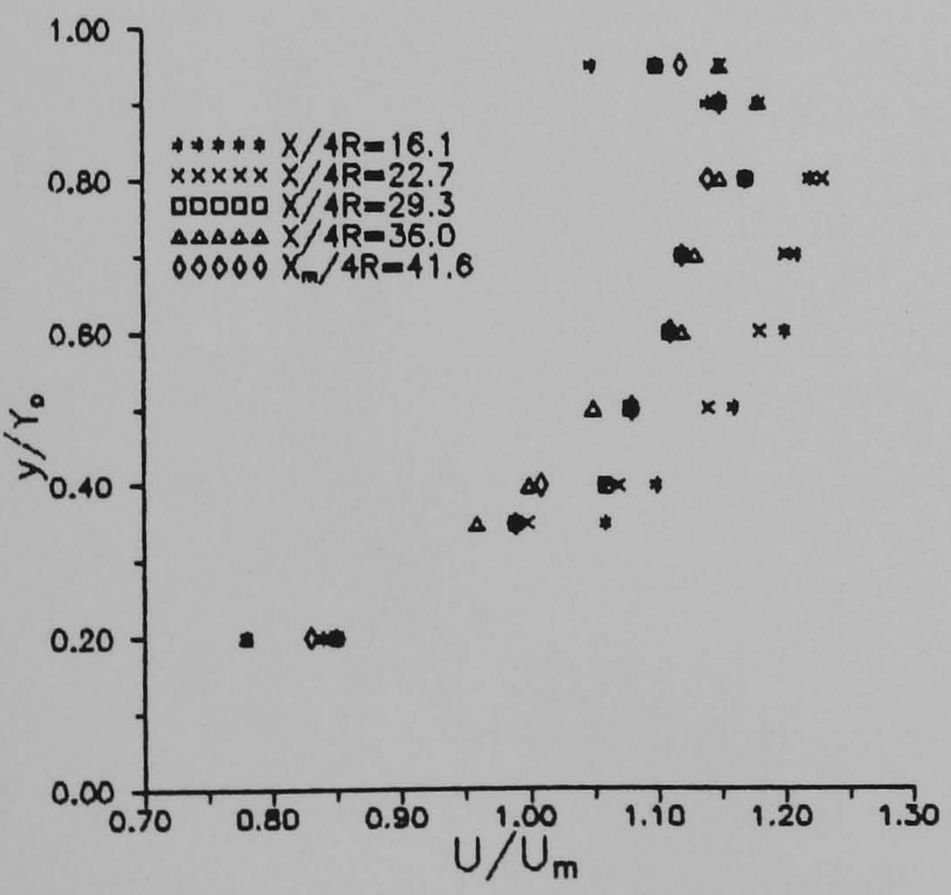

(c) Rough2: Case R2112

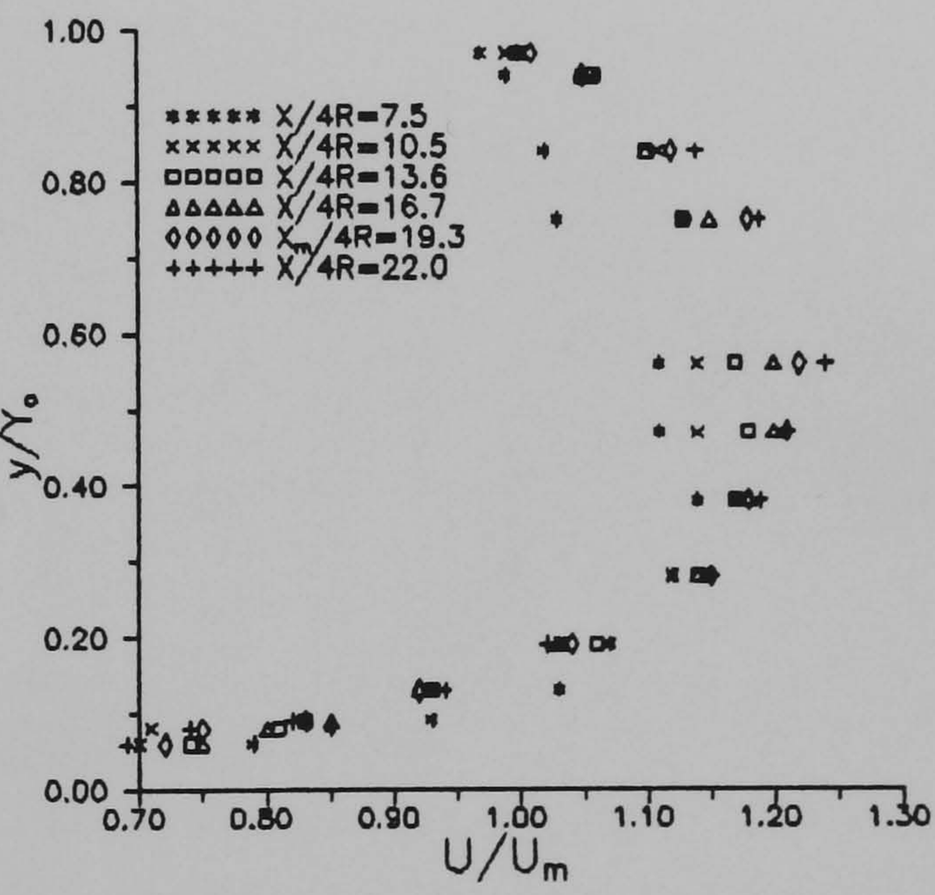

(d) Rough2: Case R2412

Figure 7.5 Development of the Velocity Profile: Rough3 and Rough2

The velocity dip is present, albeit to a lesser extent than that in the smooth-bed cases. The two cross-sectional velocity maxima lie symmetrically on either side of the centreline within the middle third of the channel; that is $|z - Z_o|/Z_o \leq 1/3$. For flow depths $(Y_o + e)/D \leq 0.5$, regardless of the bed thickness, the maxima are located near the free surface within the range $y_{max}/Y_o > 0.8$. In Tominaga *et al*'s (1989) study, flow case in a rectangular channel with an equivalent aspect ratio $2Z_o/Y_o$ to case R2122 shows a similar pattern. This indicates the suppression of the top secondary cell that transfers momentum away from the surface zone. At the higher flow depths, $(Y_o + e)/D > 0.5$, the dip increases to approximately $0.5Y_o$. This is attributed to the retardation of the surface-zone fluid by the inwardly-curving side-wall. This effect is herein given the name 'the crowning effect'.

For all bed roughnesses, the contours bulge away from the bed at the centreline, and towards the corner zone. This suggests the presence of a strong bottom cell carrying the high-momentum fluid away from the centreline towards the corner along the bed zone. The difference in roughness between the bed and the side-wall causes the lateral bulging of the contours towards the corner zone. This is due to the lower traction exerted by the side-wall on the fluid, shown by the higher momentum fluid near the wall, and thus the bulging of the contours.

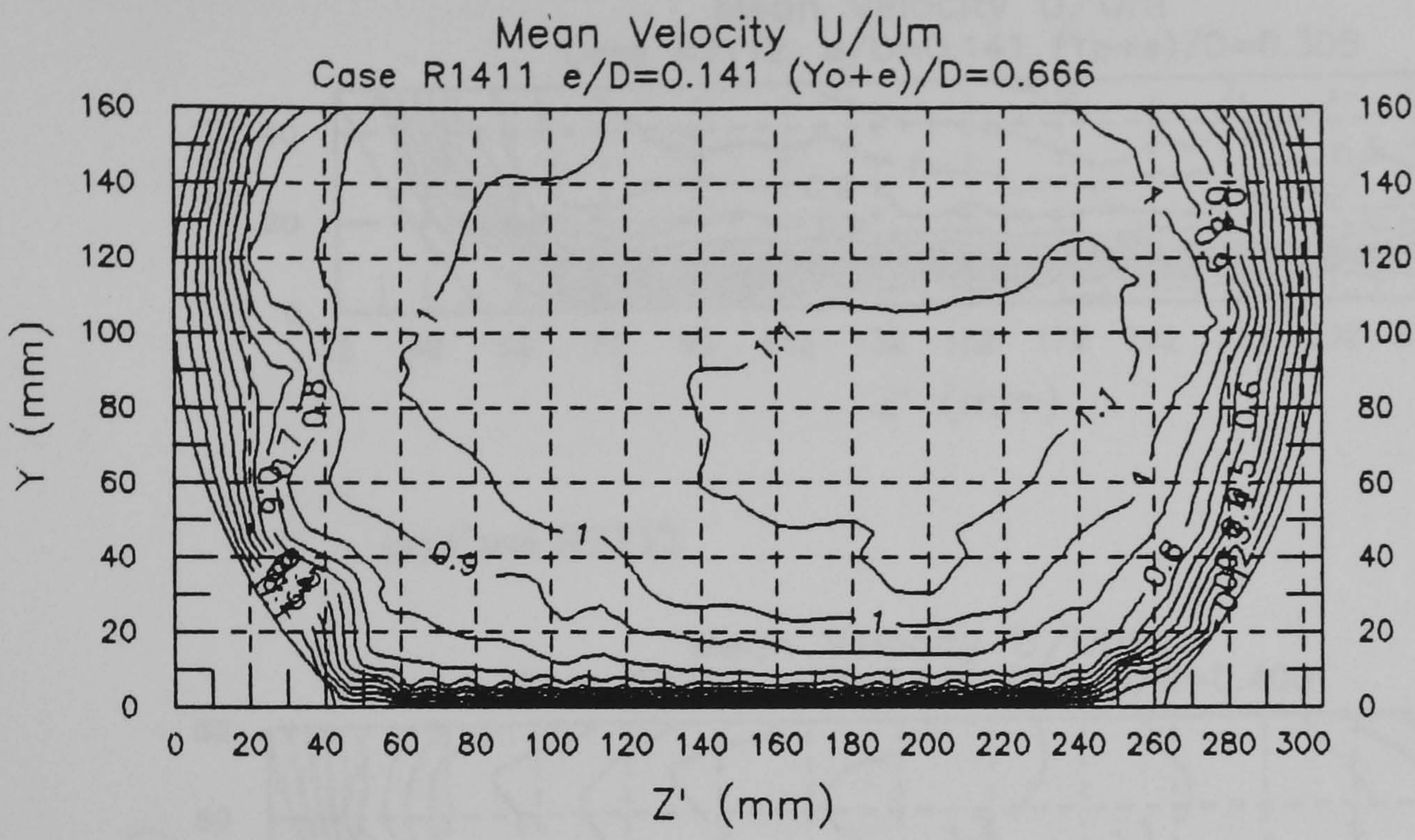

(a) Case R1411

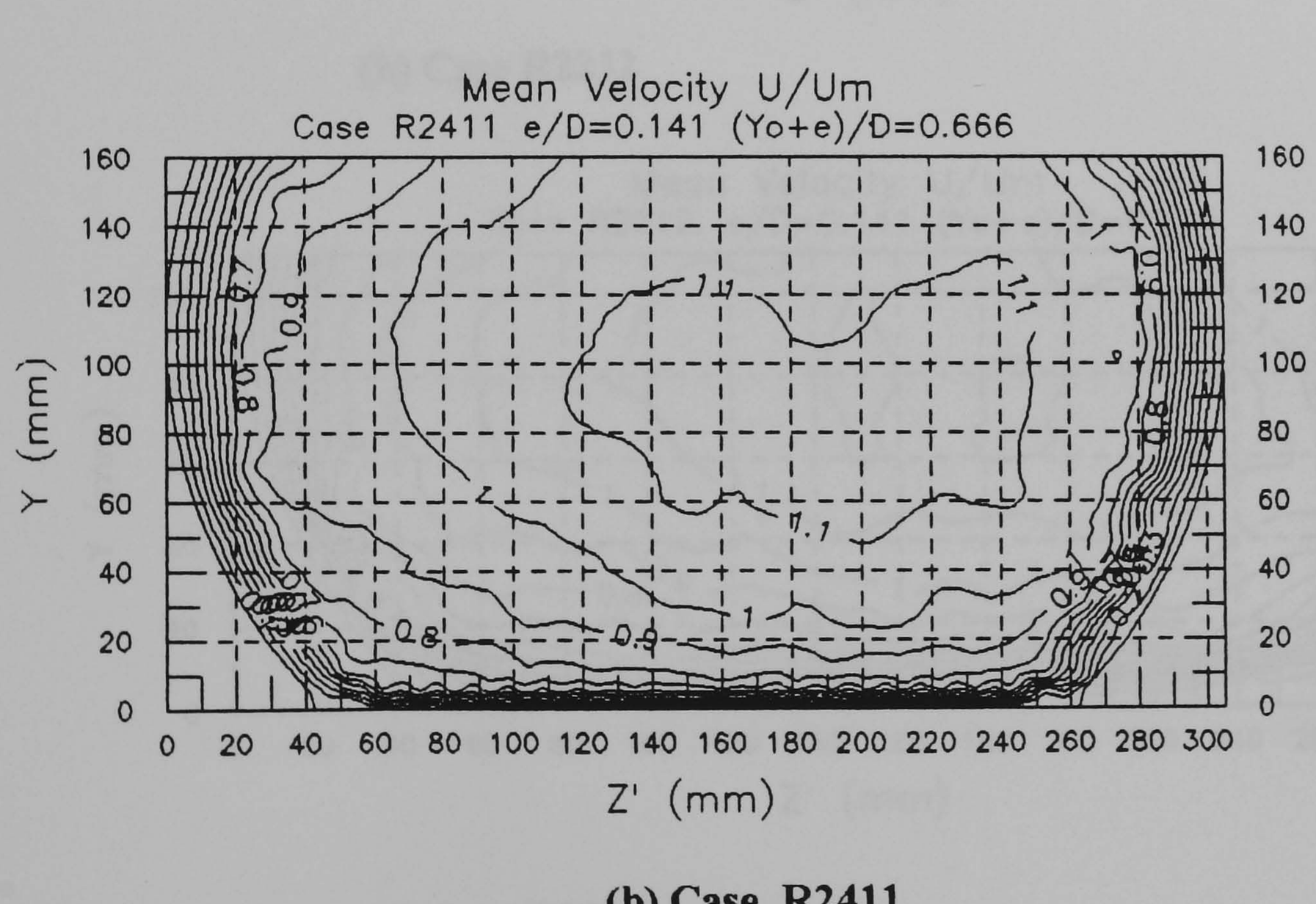

(b) Case R2411

Figure 7.6 Mean Velocity Distribution U/U_m : Rough1

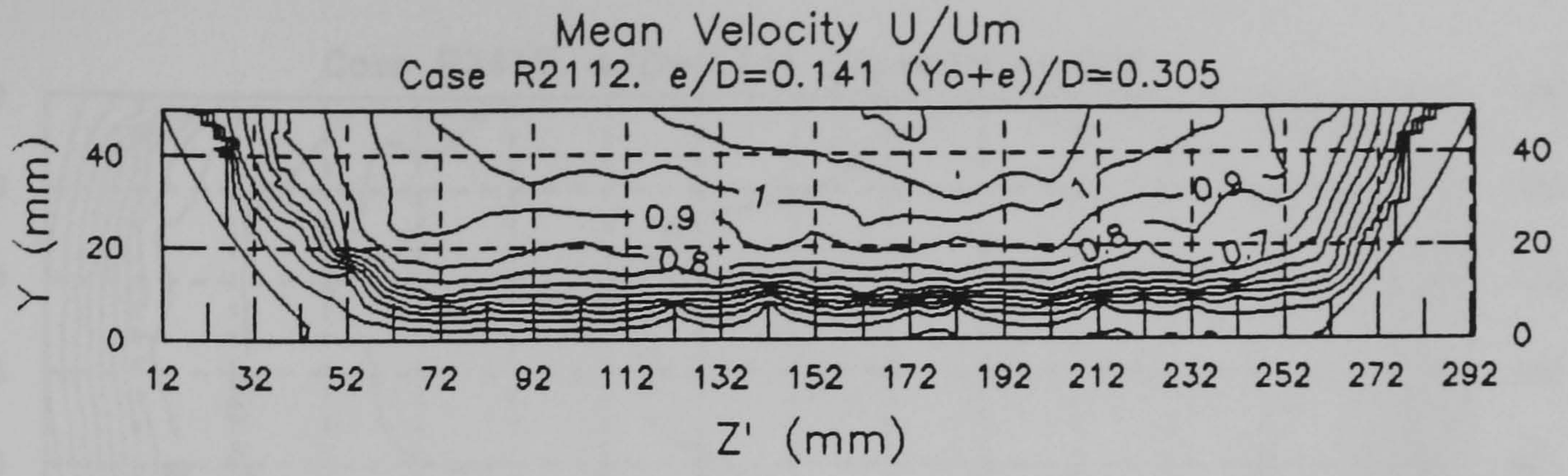

(a) Case R2112

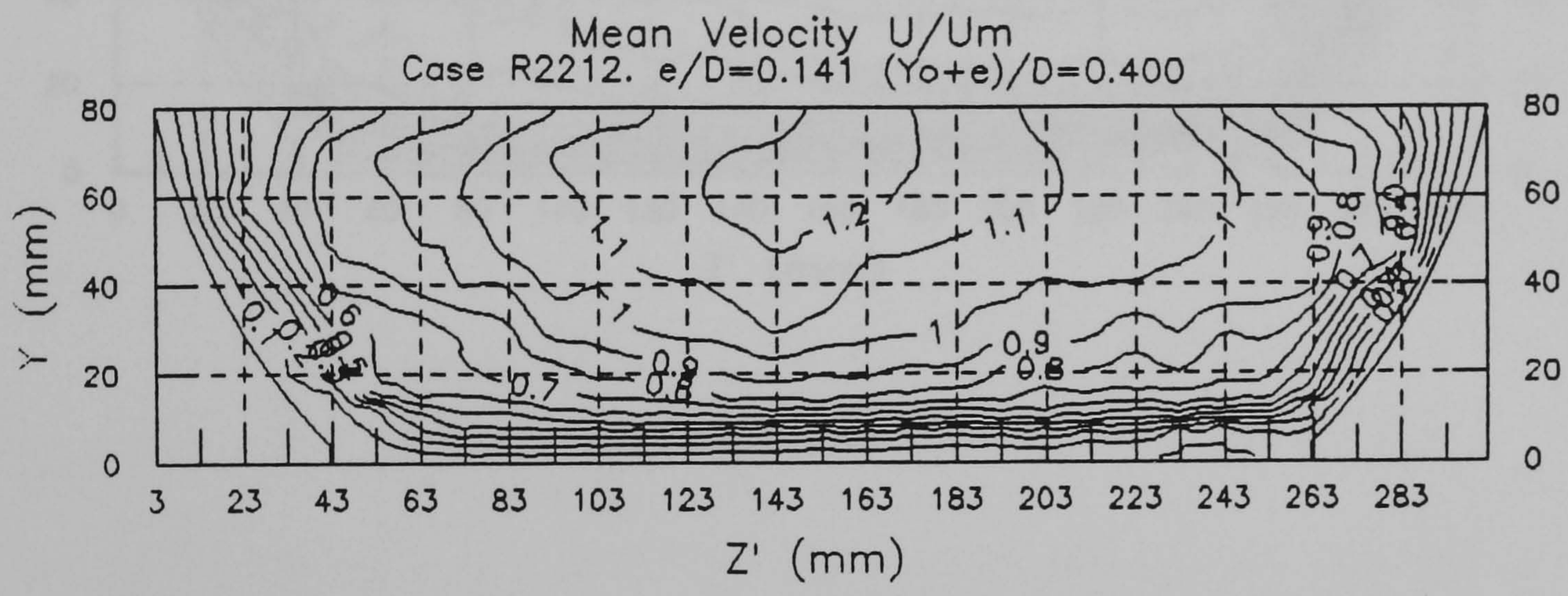

(b) Case R2212

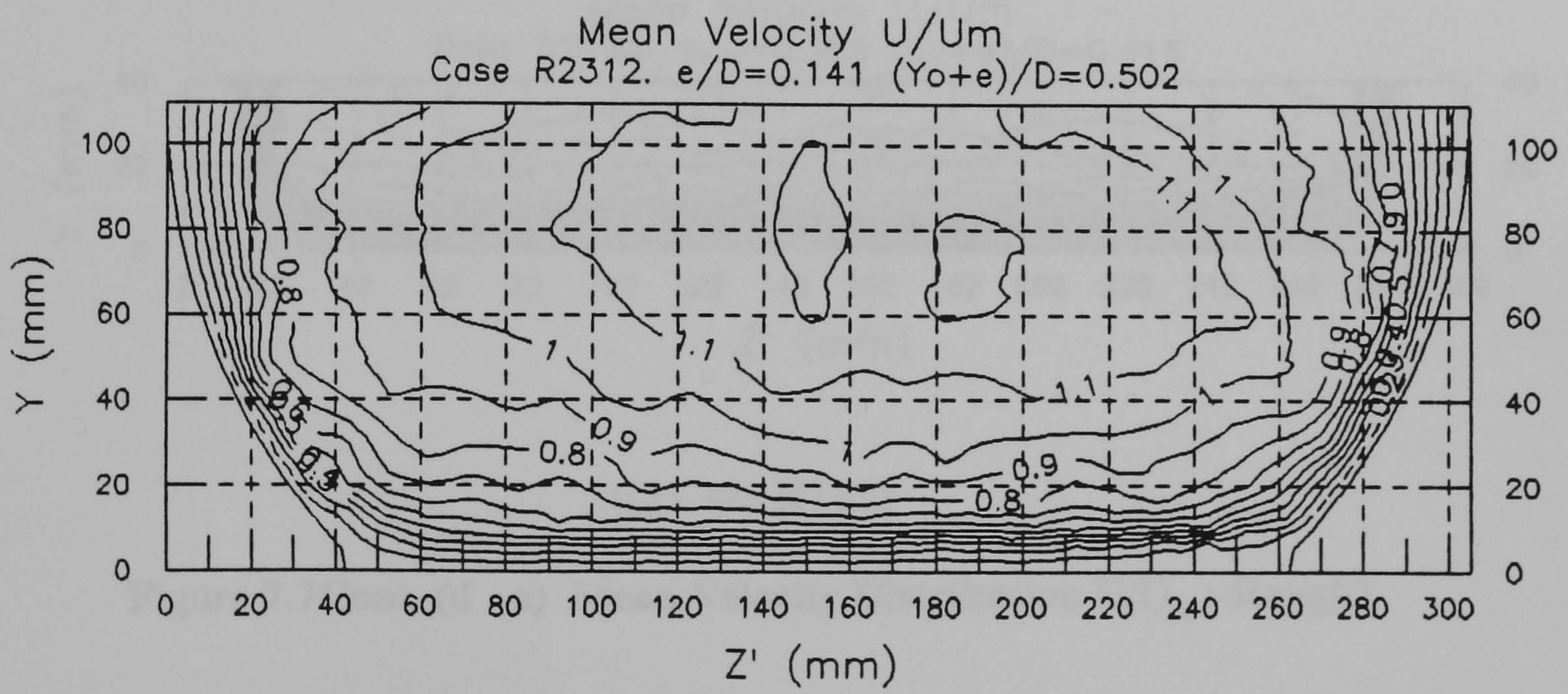

(c) Case R2312

Figure 7.7(a - c) Mean Velocity Distribution U/U_m : Rough2

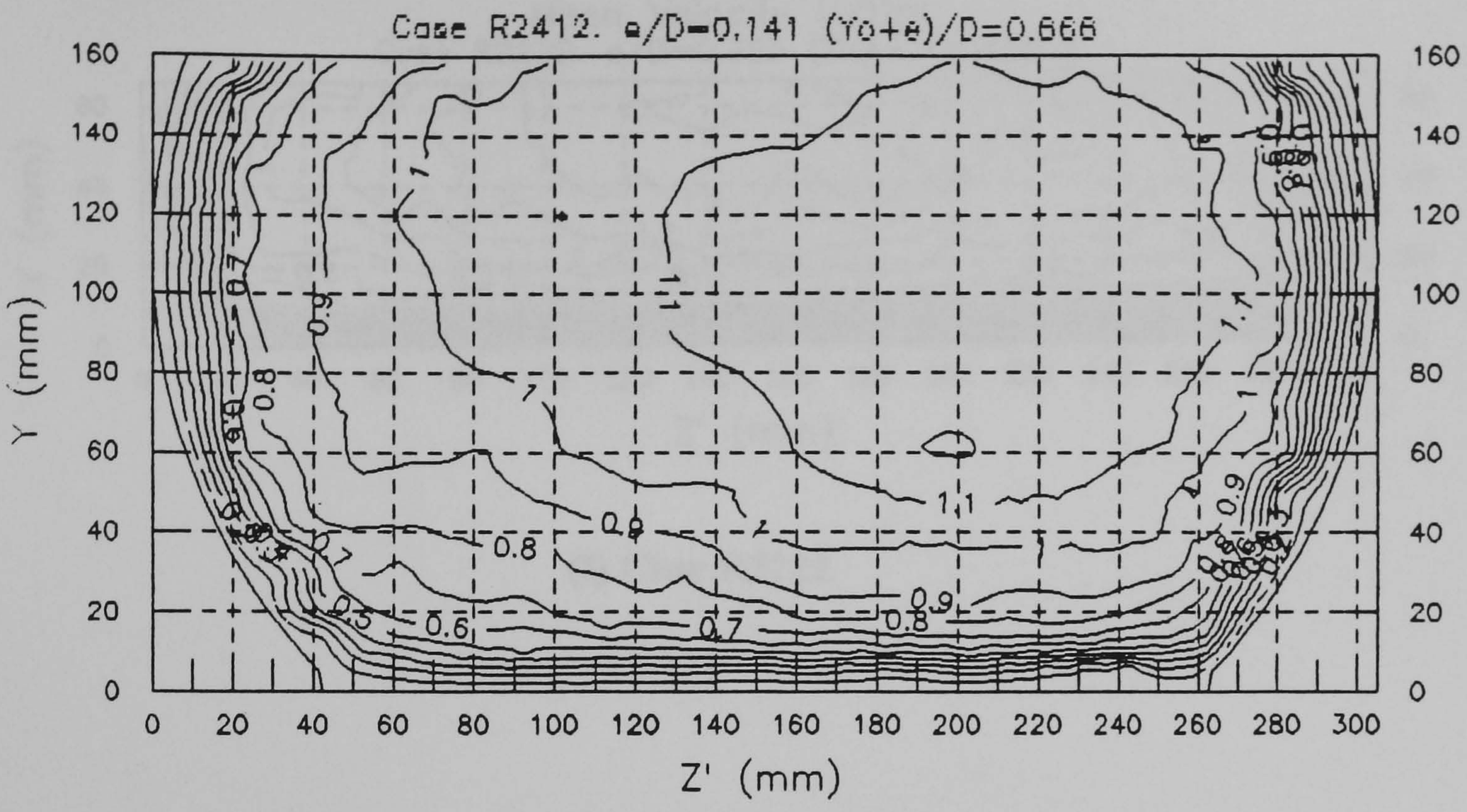

(d) Case R2412

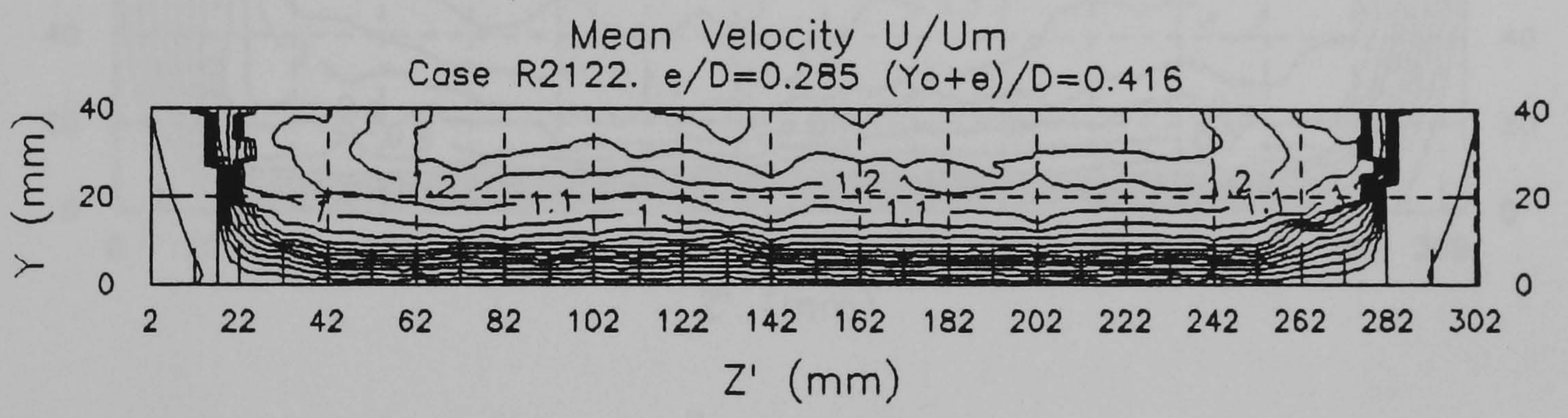

(e) Case R2122

Figure 7.7Cont. (d - e) Mean Velocity Distribution U/U_m : Rough2

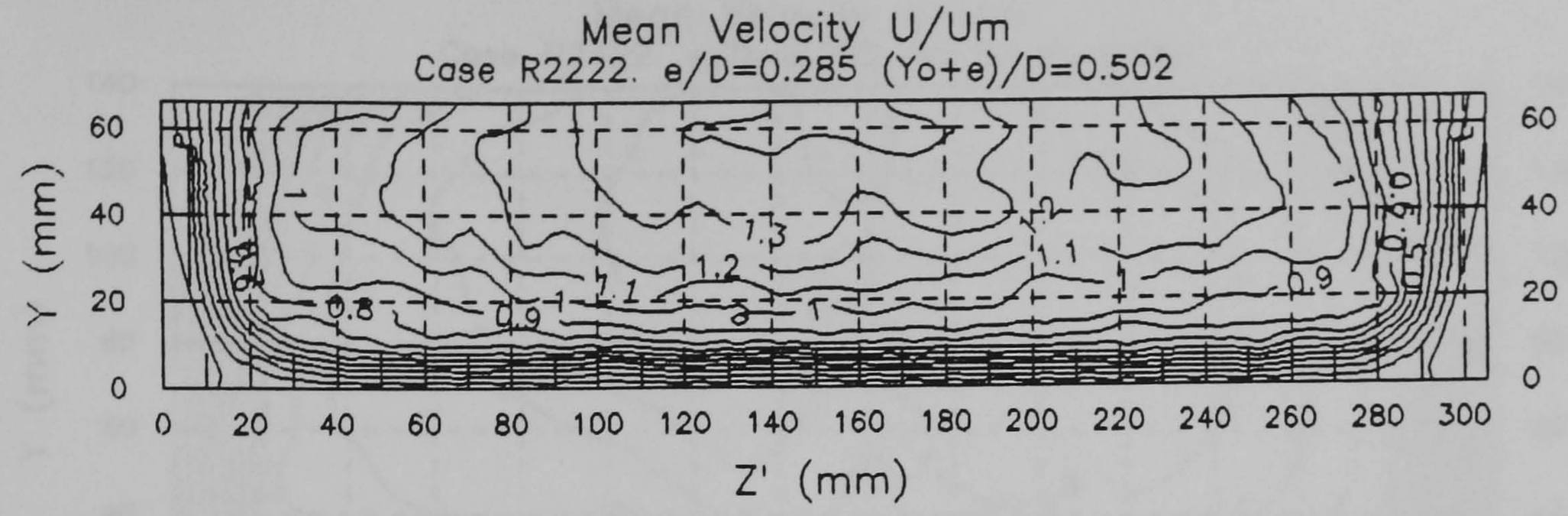

(f) Case R2222

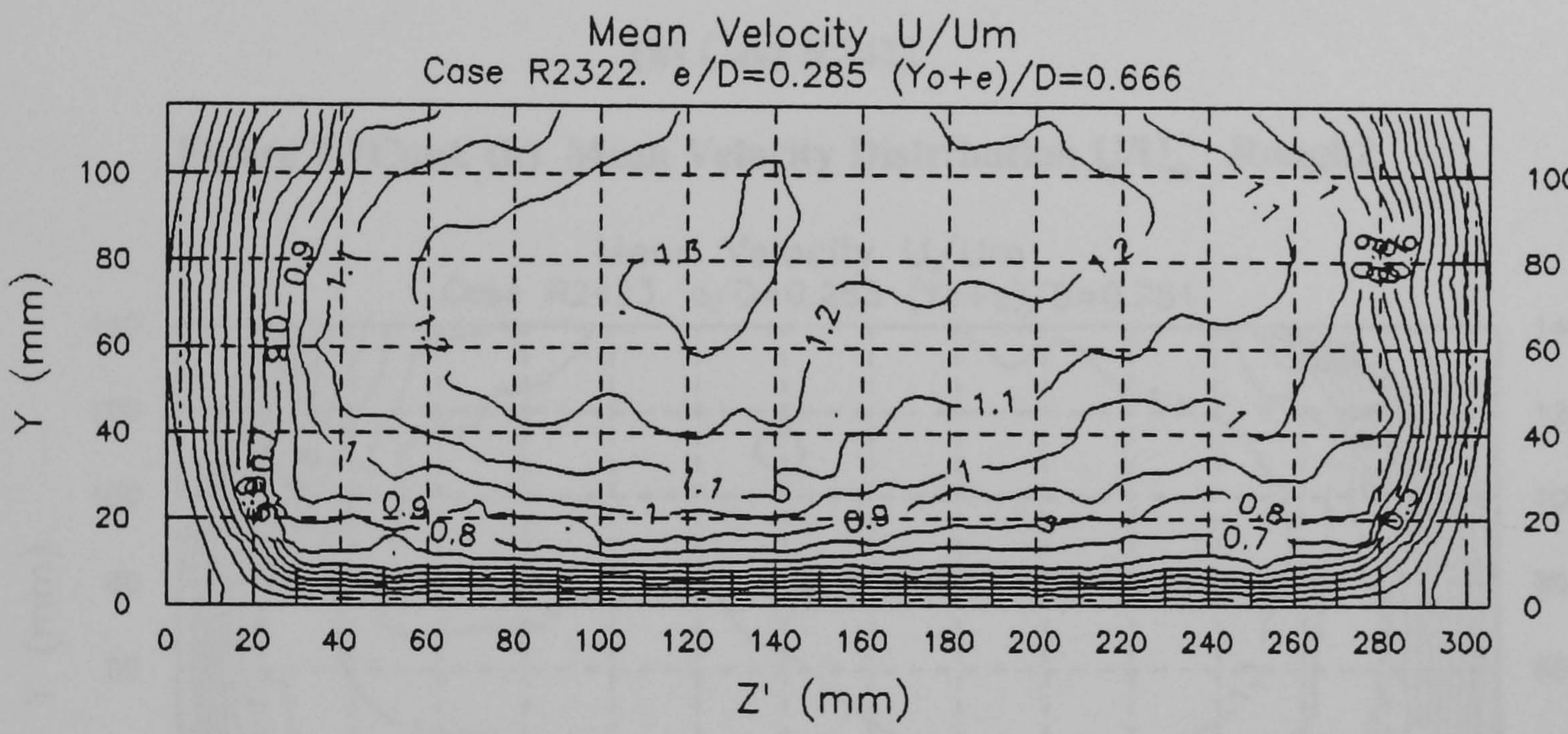

(g) Case R2322

Figure 7.7Cont. (f - g) Mean Velocity Distribution U/U_m : Rough2

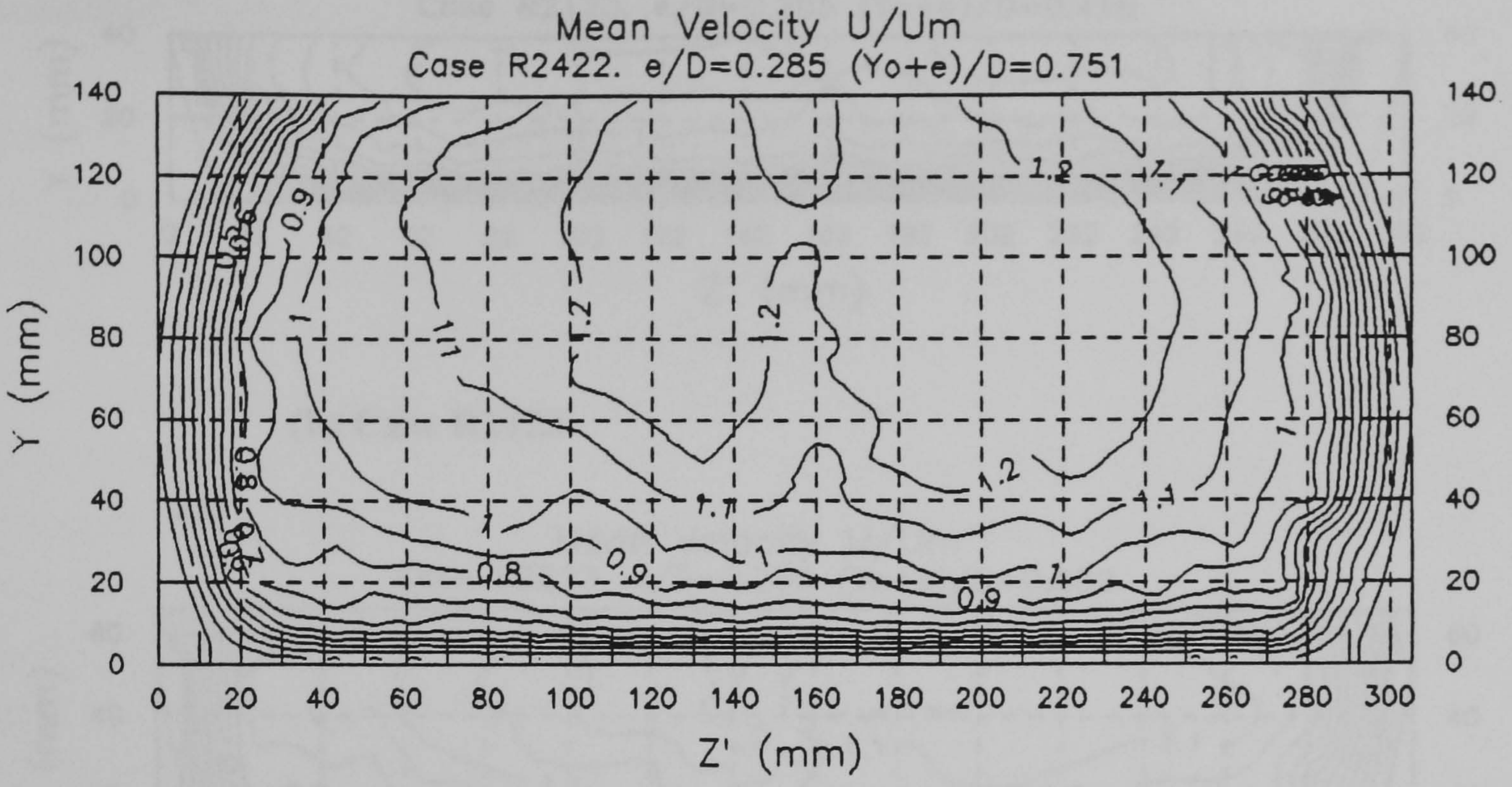

(h) Case R2422

Figure 7.7Cont. (h) Mean Velocity Distribution U/U_m : Rough2

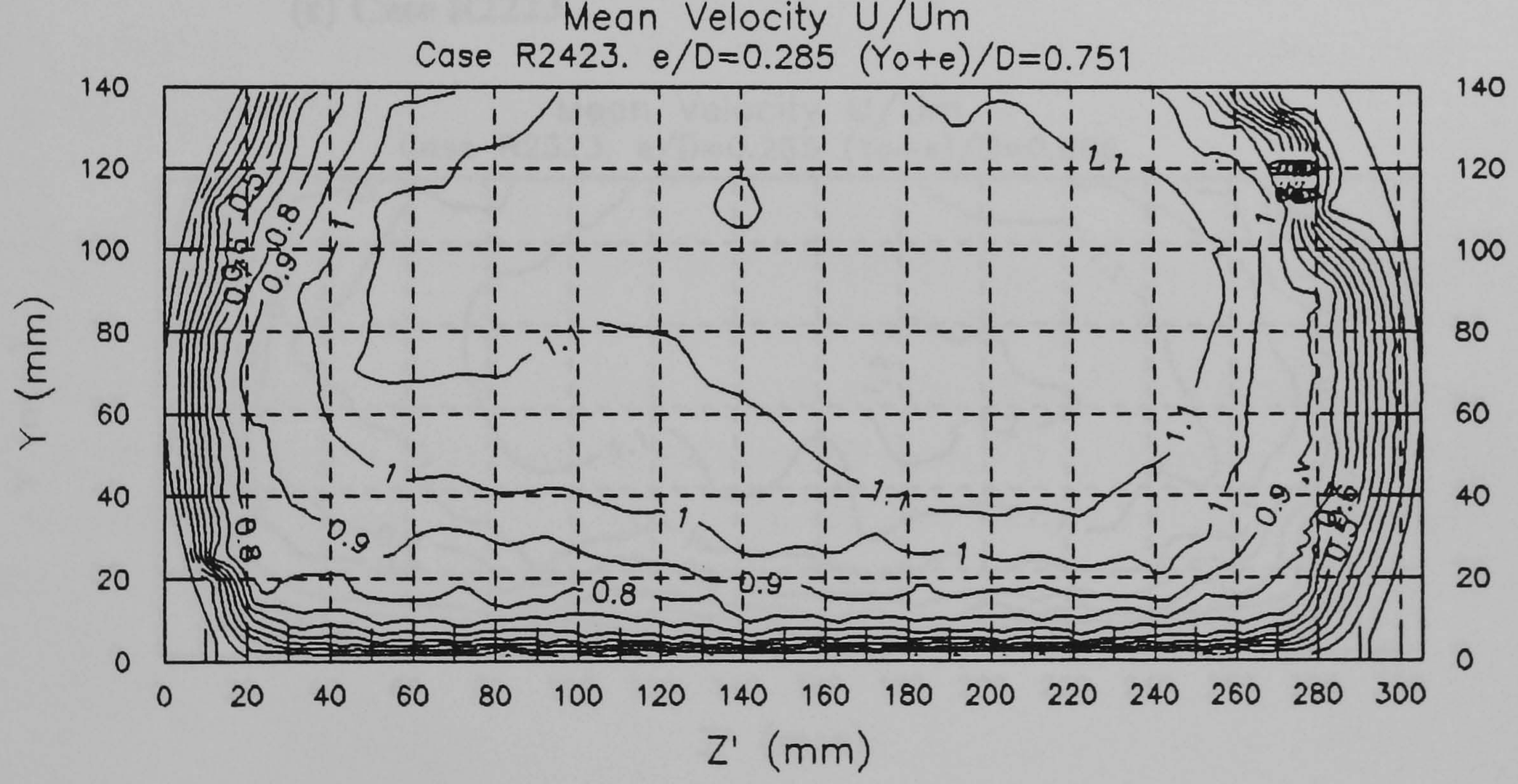

(a) Case R2423

Figure 7.8 (a) Mean Velocity Distribution U/U_m : Rough3

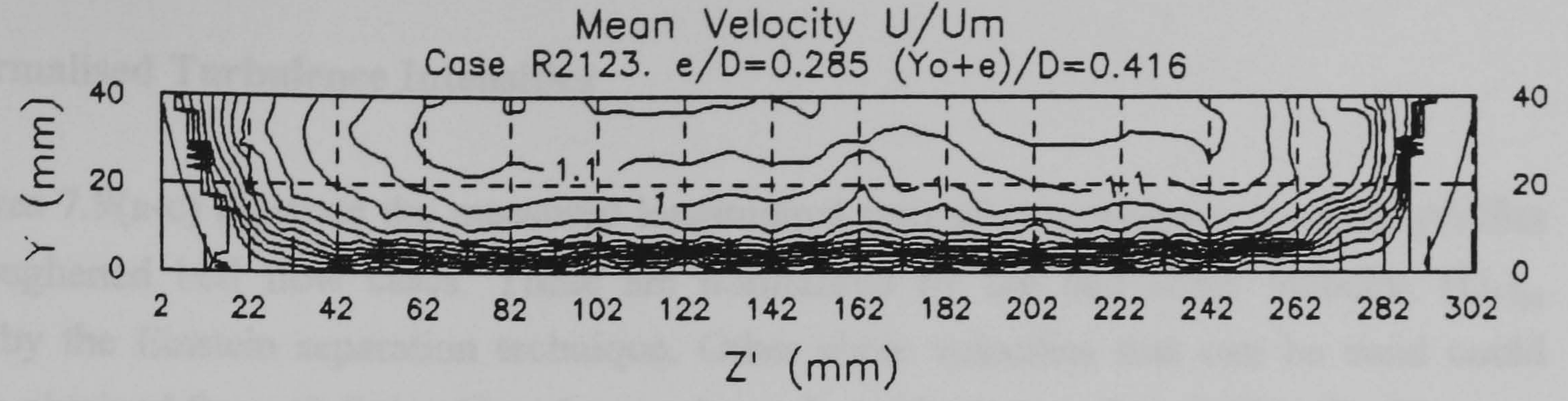

(b) Case R2123

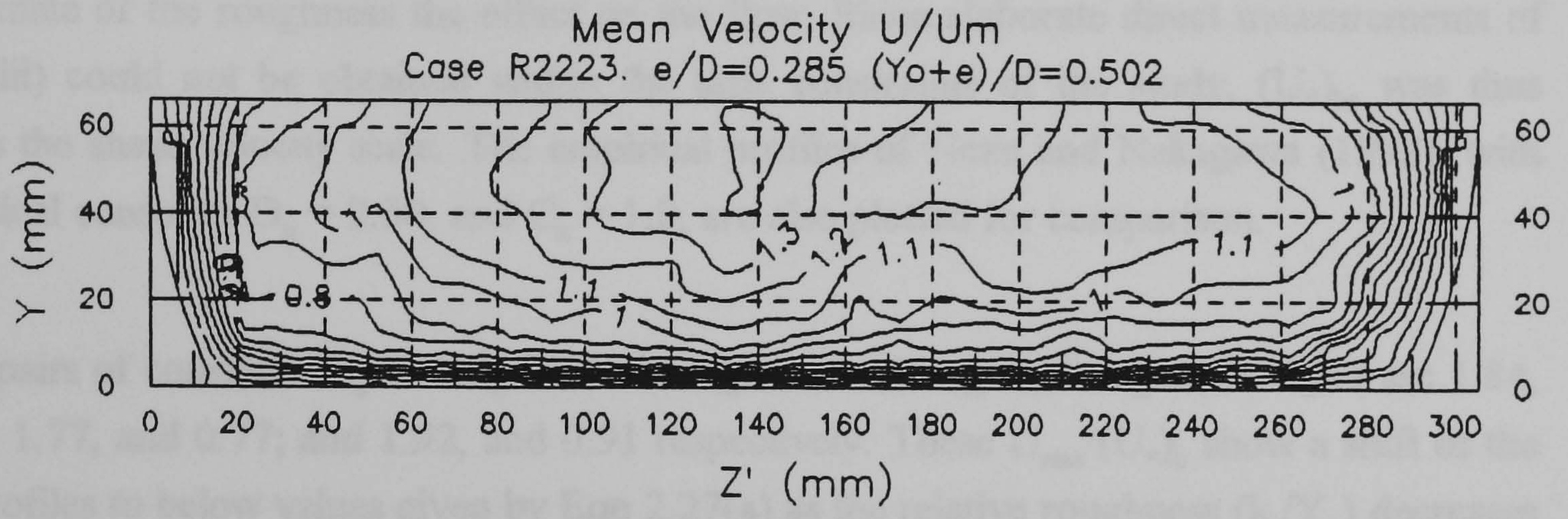

(c) Case R2223

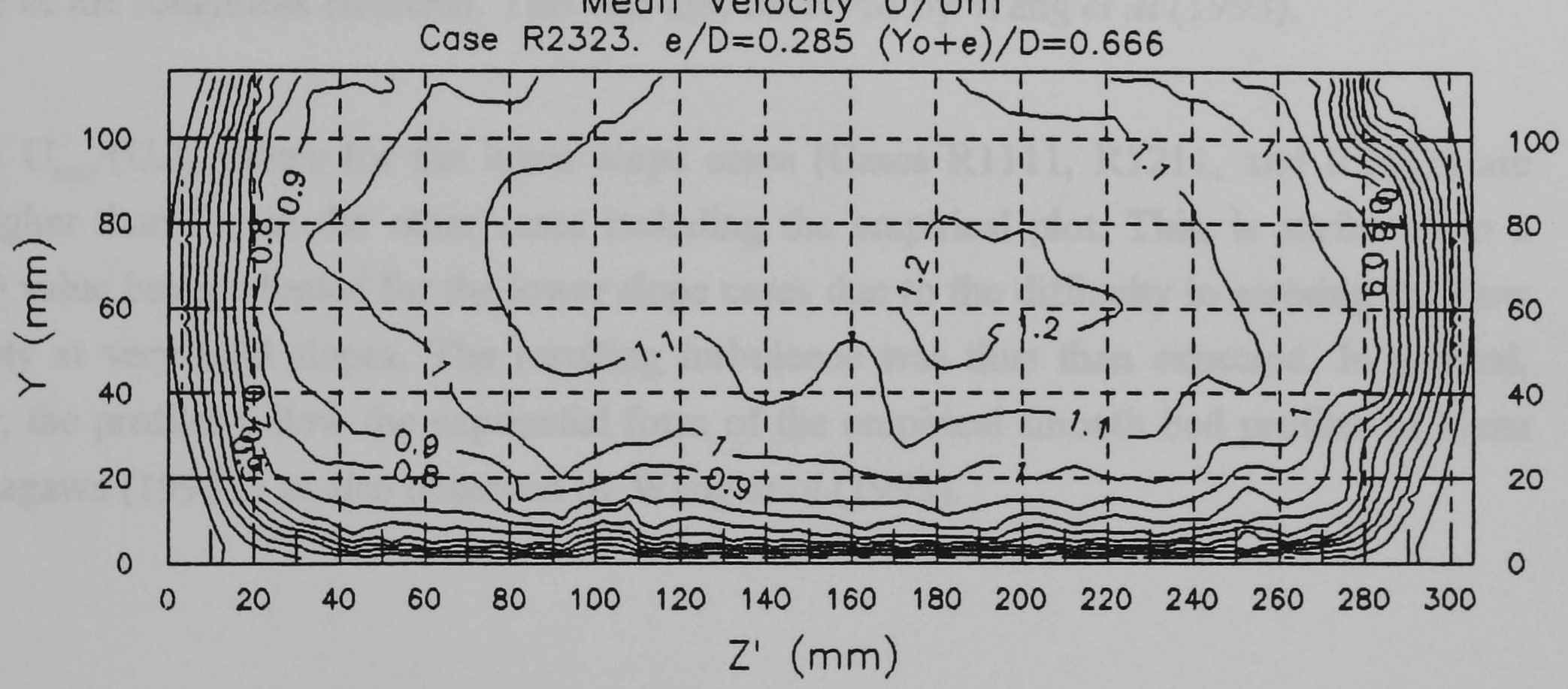

(d) Case R2323

Figure 7.8Cont. (b - d) Mean Velocity Distribution U/U_m : Rough3

7.4.3 Normalised Turbulence Intensities

Figures 7.9(a-c) illustrate the measured longitudinal centreline turbulence intensity profiles in the roughened bed flow cases. These are normalised by the bed shear velocity, $(U_*)_b$, obtained by the Einstein separation technique. Other shear velocities that can be used could have been obtained from (i) fitting U to the roughness logarithmic law (Eqn 2.21); (ii) $(U_*)_{ave} = \sqrt{(gRS_o)}$; or (iii) direct Preston tube measurements. Method (i) was excluded due to its unreliability (Hoohlo 1991). Table 7.2 shows that $(U_*)_{ave}$ is lower than $(U_*)_b$, and as such an underestimate of the roughness the effect on the flow. Since elaborate direct measurements of method (iii) could not be obtained within the time constraints of the study, $(U_*)_b$, was thus chosen as the shear velocity scale. The empirical profiles of Nezu and Nakagawa (1993), with the empirical constants $D_u = 2.30$, and $C_k = 1.0$, are also plotted for comparison.

The pairs of constants D_u and C_k for bed roughnesses Rough1, Rough2, Rough3 are 1.84, and 0.55; 1.77, and 0.77; and 1.92, and 0.91 respectively. These $U_{rms}/(U_*)_b$ show a shift of the plotted profiles to below values given by Eqn 2.27(a) as the relative roughness (k_s/Y_o) decreases - i.e. $Y_o/k_s > 15$. There is a slight reduction of the magnitude of these intensities in the wall zone $y/Y_o < 0.2$, reflecting the transfer of turbulence energy into the vertical component in the presence of the roughness elements. This was also observed by Wang *et al* (1993).

The $U_{rms}/(U_*)_b$ values for the lower slope cases (Cases R1111, R1211, and R1411) are much higher than for all the other cases including the empirical plot. This, is attributed to a higher Q value being adopted for the lower slope cases due to the difficulty in assesing the flow uniformity at very mild slopes. The resulting turbulence was thus than expected. In general, however, the profiles follow the exponetial form of the empirical smooth bed profiles of Nezu and Nakagawa (1993) - as also observed by Wang *et al* (1993).

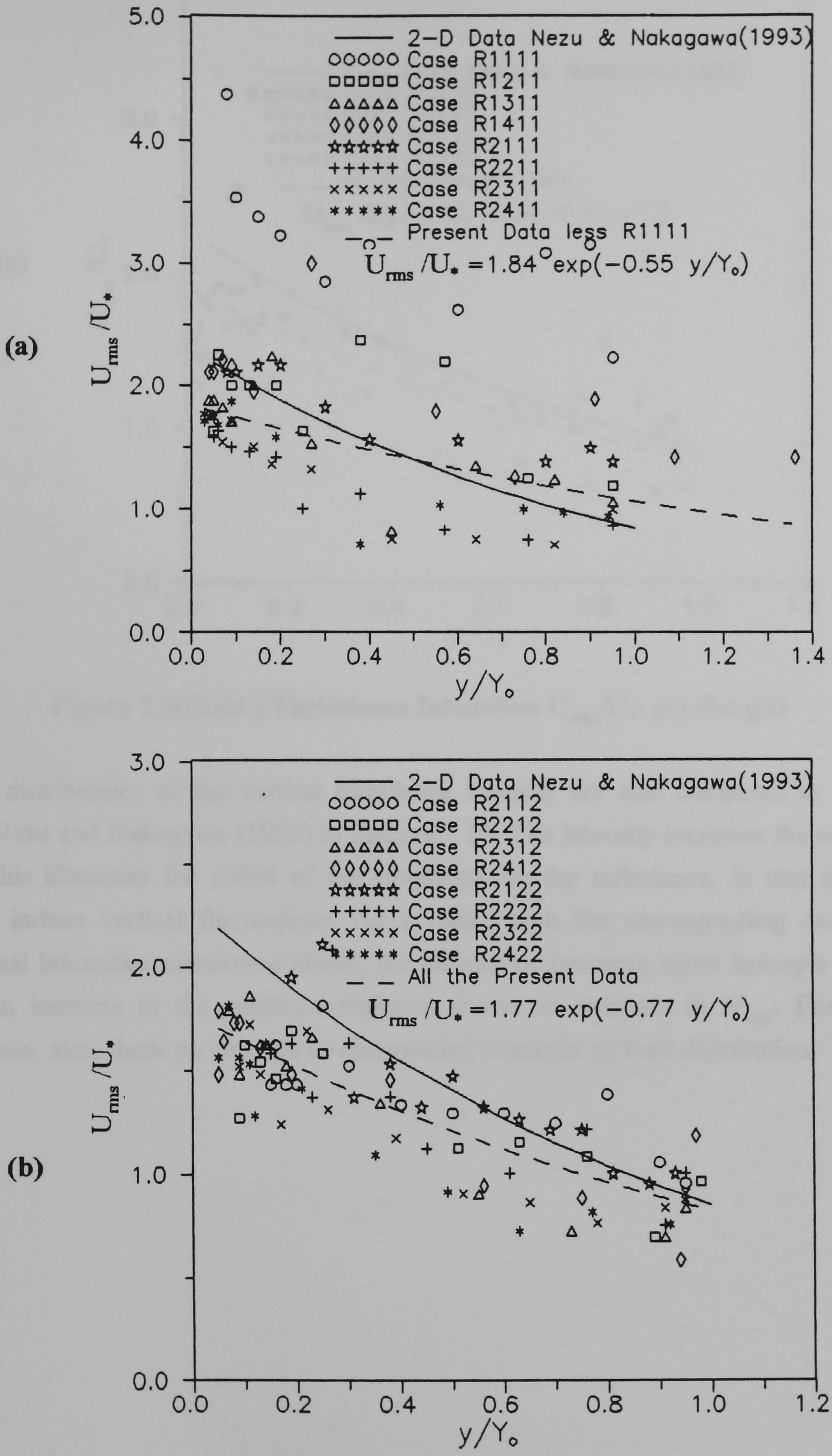

Figure 7.9 Turbulence Intensities U_{rms}/U_*: (a) Rough1 and (b) Rough2

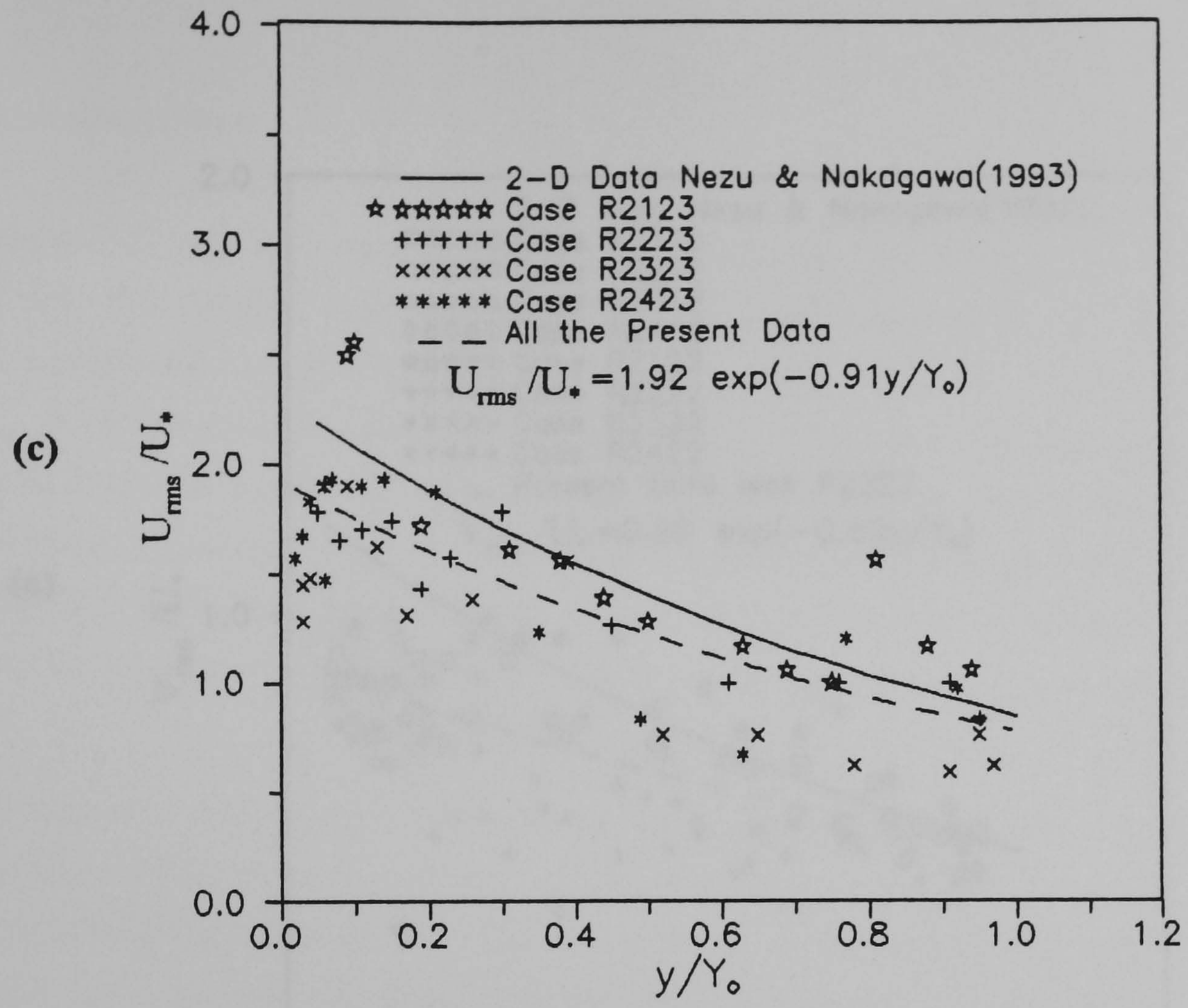

Figure 7.9(Cont.) Turbulence Intensities U_{rms}/U_*: (c) Rough3

The distributions of the vertical turbulence intensity are also compared to the empirical plots of Nezu and Nakagawa (1993) in Figures 7.10. The intensity increases the near bed, $y/Y_o < 0.3$. This illustrates the effect of the roughness on the turbulence, in that the roughness elements induce vertical fluctuations. As a result, with the corresponding decrease in the longitudinal intensities mentioned above, the turbulence becomes more isotropic in this zone. Indeed an increase in the relative roughness shows an increase in V_{rms}. For the vertical components, also, there no clear three-dimensional character of their distribution.

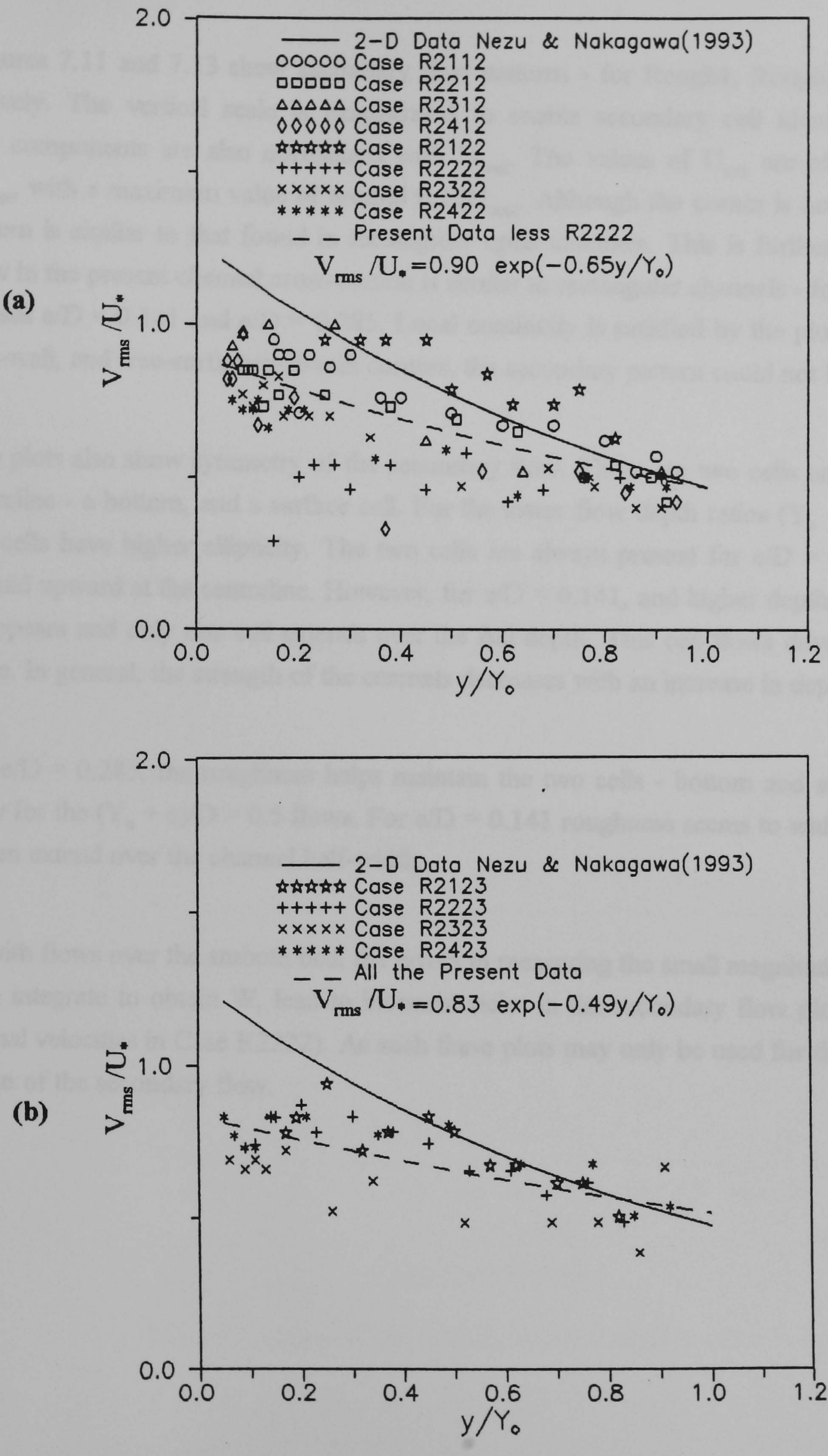

Figure 7.10 Turbulence Intensities V_{rms}/U_*: (a) Rough2 and (b) Rough3

7.4.4 Secondary Flow

Figures 7.11 and 7.13 show secondary flow patterns - for Rough1, Rough2 and Rough3 respectively. The vertical scale is exaggerated to enable secondary cell identification. The velocity components are also normalised with U_{max}. The values of U_{sec} are of the order of $0.05U_{max}$, with a maximum value of around $0.15U_{max}$. Although the corner is not right-angled, the pattern is similar to that found in rectangular open channels. This is further confirmation that flow in the present channel cross-section is similar to rectangular channels - for the two bed thicknesses e/D = 0.141 and e/D = 0.285. Local continuity is satisfied by the plots. Nearer the bed/side-wall, and free-surface/side-wall corners, the secondary pattern could not be resolved.

The plots also show symmetry of the secondary flow. There are two cells on each side of the centreline - a bottom, and a surface cell. For the lower flow depth ratios $(Y_o + e)/D \leq 0.5$, the two cells have higher ellipticity. The two cells are always present for e/D = 0.285. These sweep fluid upward at the centreline. However, for e/D = 0.141, and higher depths, the surface cell disappears and only one cell extends over the full depth. This cell flows downward at the centreline. In general, the strength of the currents decreases with an increase in depth.

For e/D = 0.285, the roughness helps maintain the two cells - bottom and surface cells - especially for the $(Y_o + e)/D > 0.5$ flows. For e/D = 0.141 roughness seems to widen the cells - which then extend over the channel half-width.

As with flows over the smooth bed, the errors in measuring the small magnitudes of V, and having to integrate to obtain W, lead to inconsistencies in the secondary flow plots (e.g. high wall-normal velocities in Case R2222). As such these plots may only be used for the qualitative description of the secondary flow.

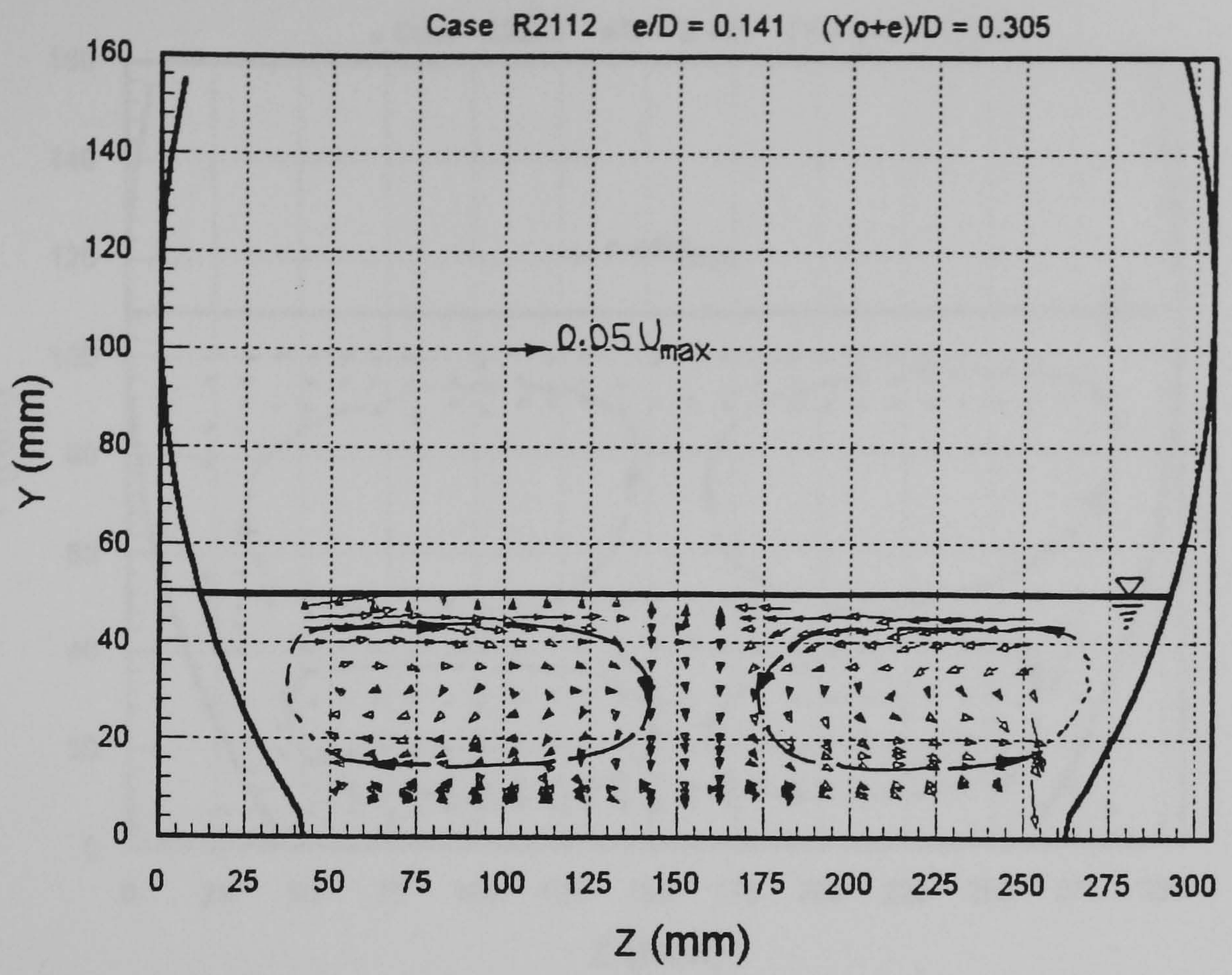

(a) Case R2112

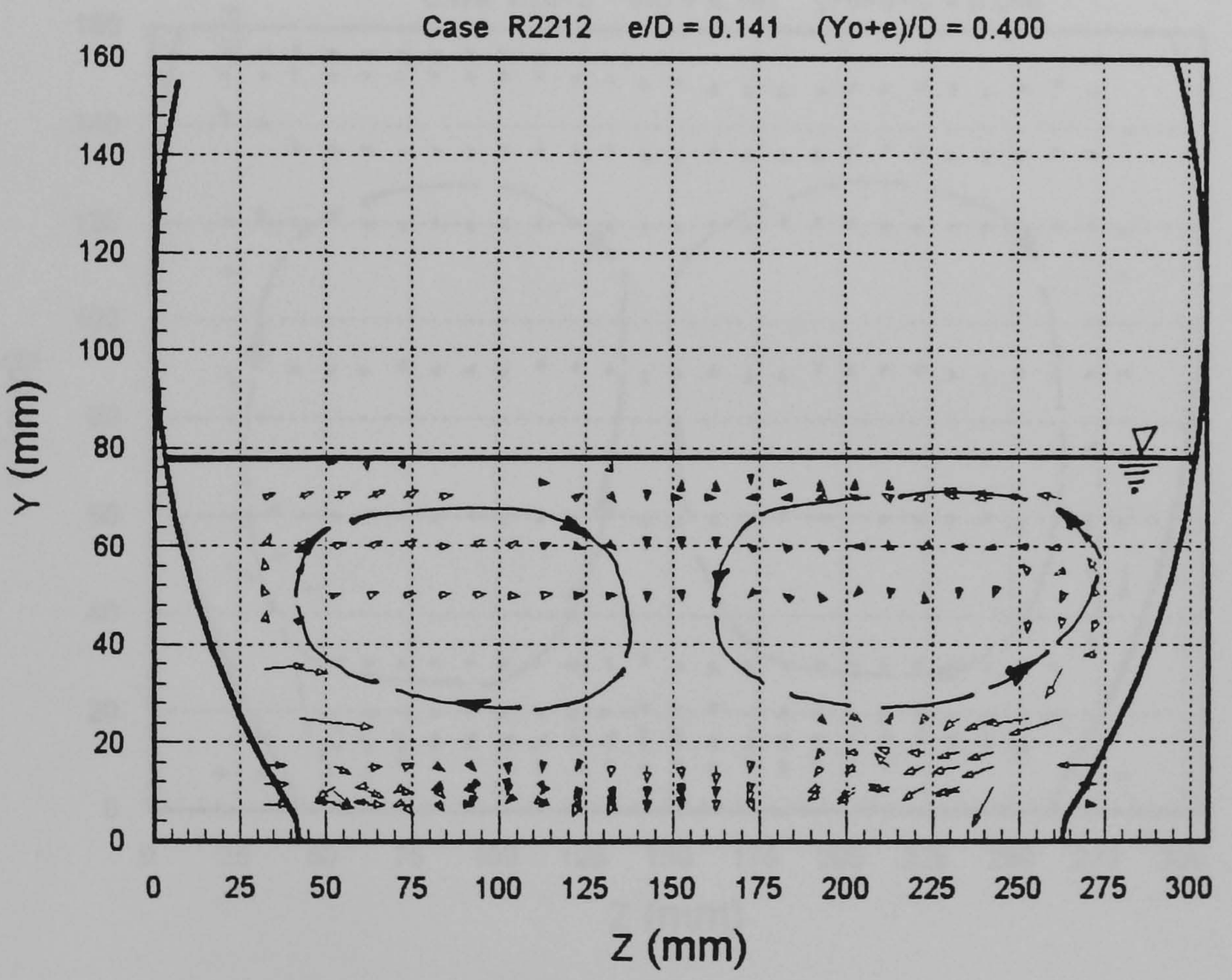

(b) Case R2212

Figure 7.11 (a - b) Secondary Flow: Rough2; e/D = 0.141

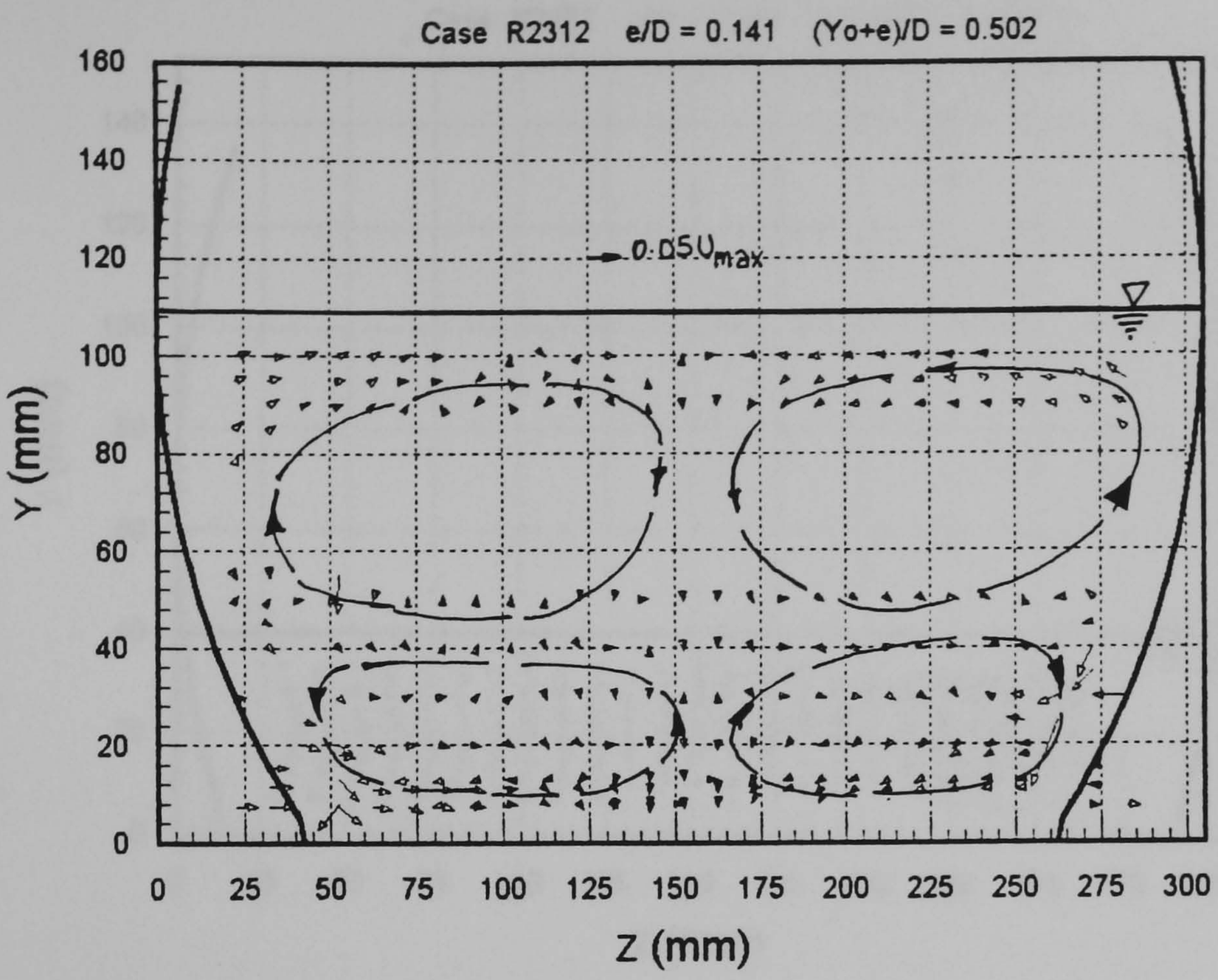

(c) Case R2312

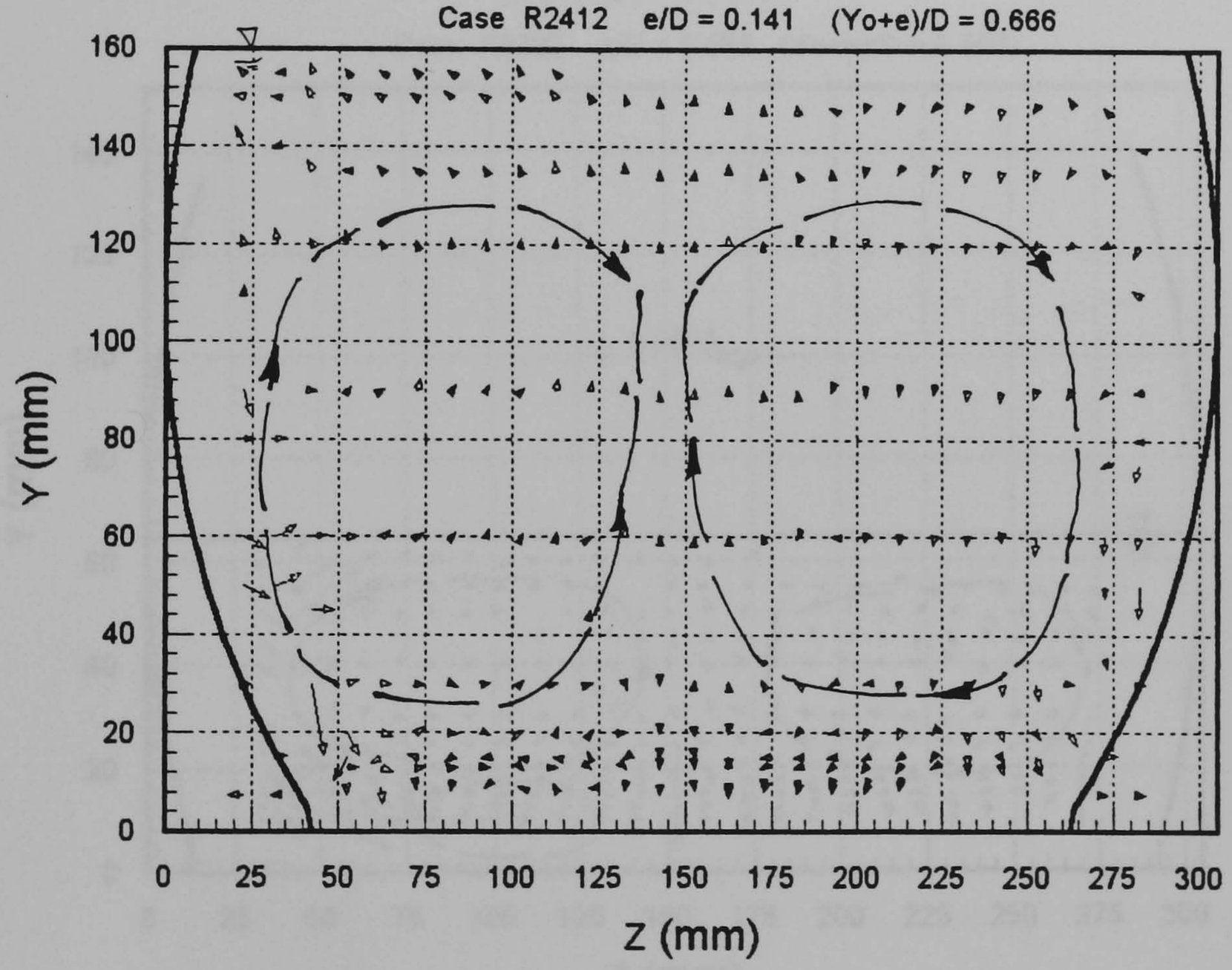

(d) Case R2412

Figure 7.11Cont. (c - d) Secondary Flow: Rough2; e/D = 0.141

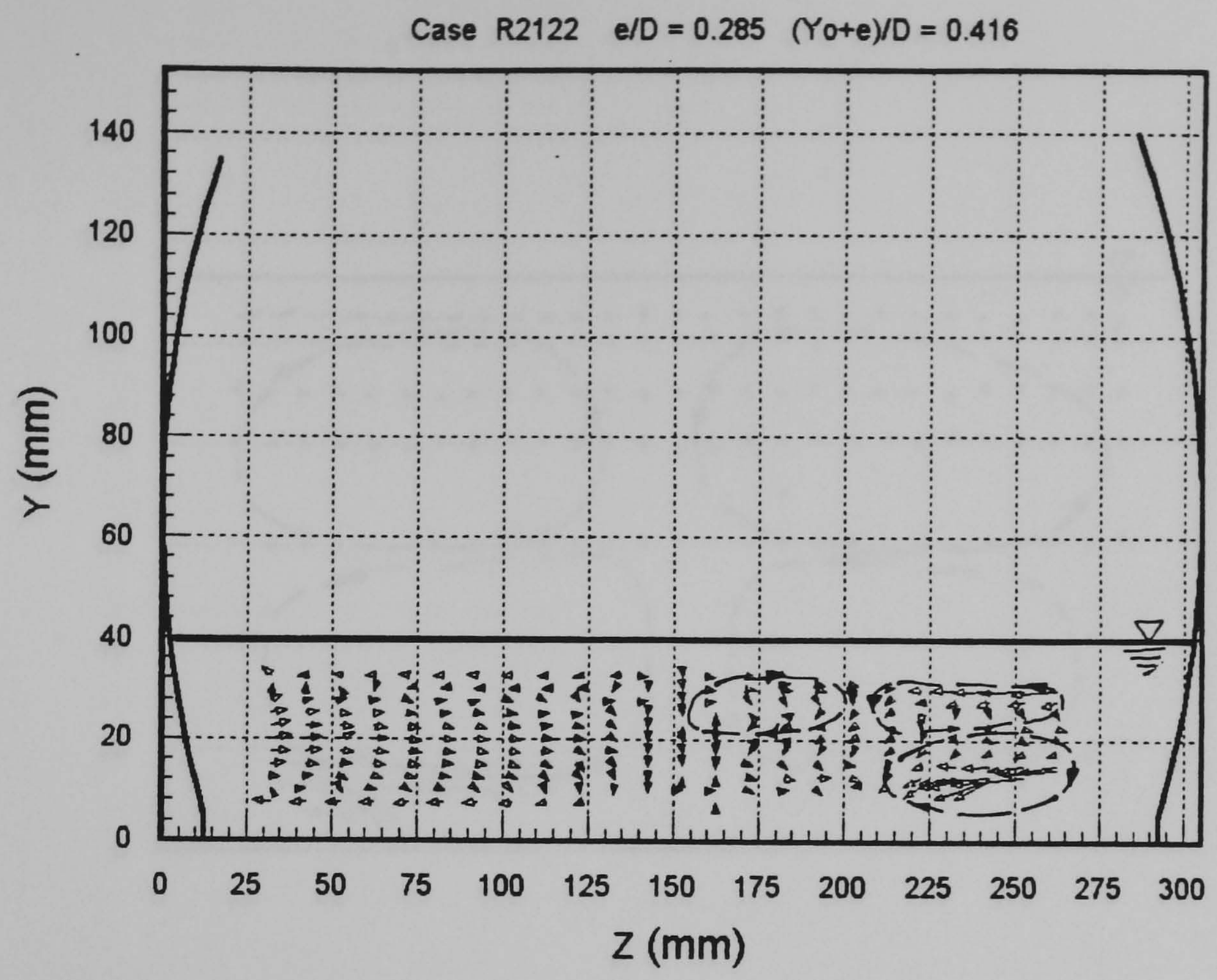

(a) Case R2122

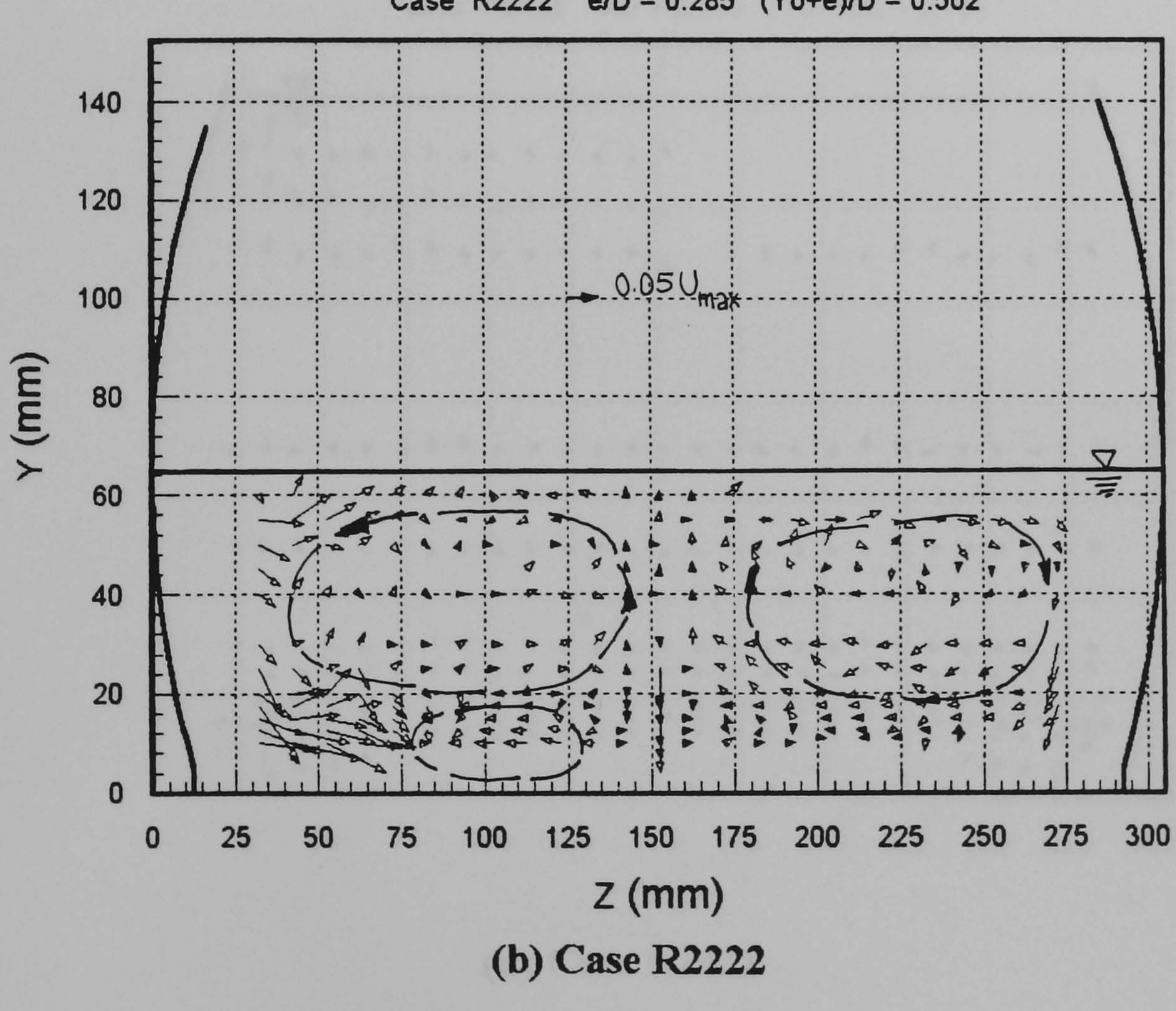

(b) Case R2222

Figure 7.12 (a - b) Secondary Flow: Rough2; e/D = 0.285

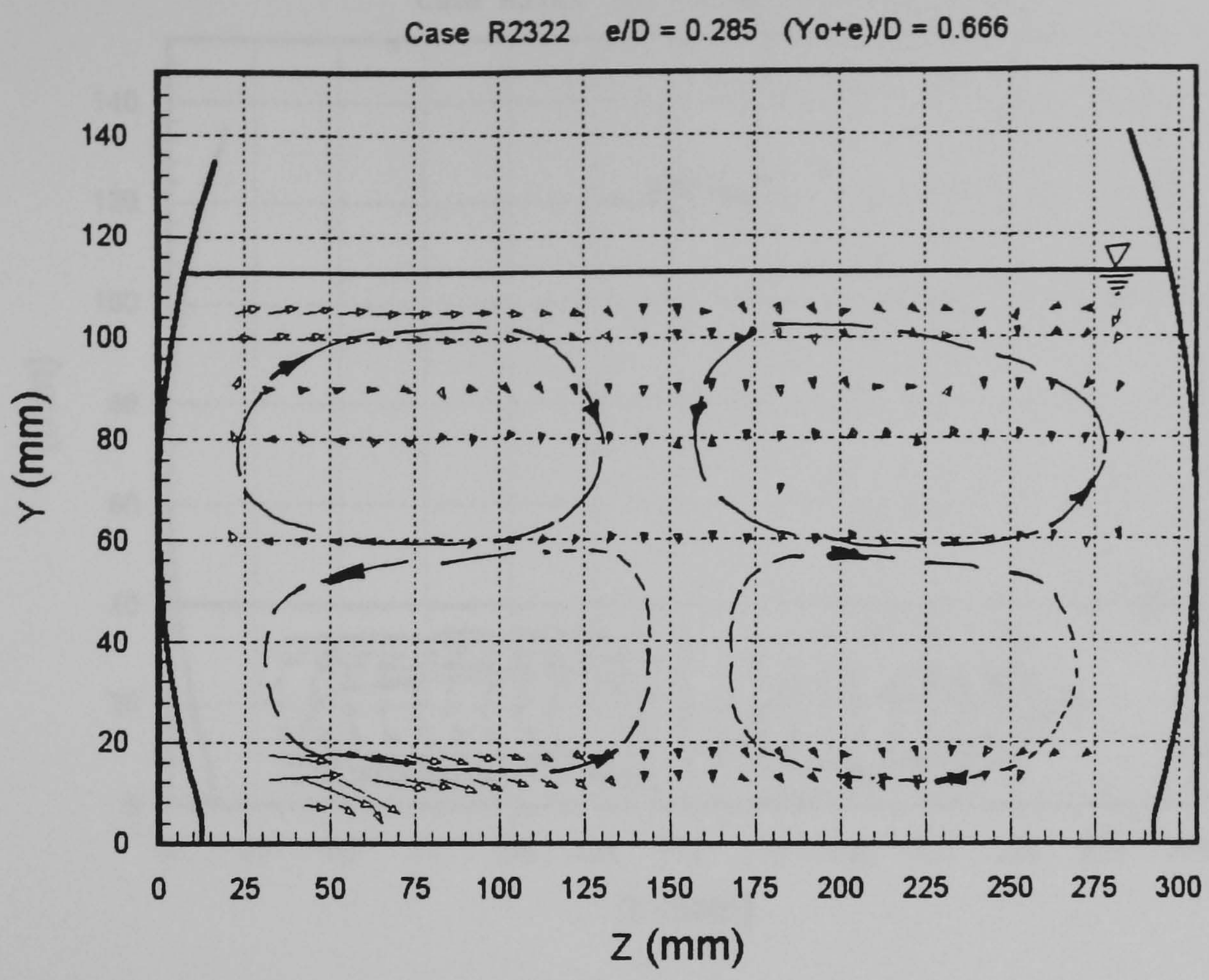

(c) Case R2322

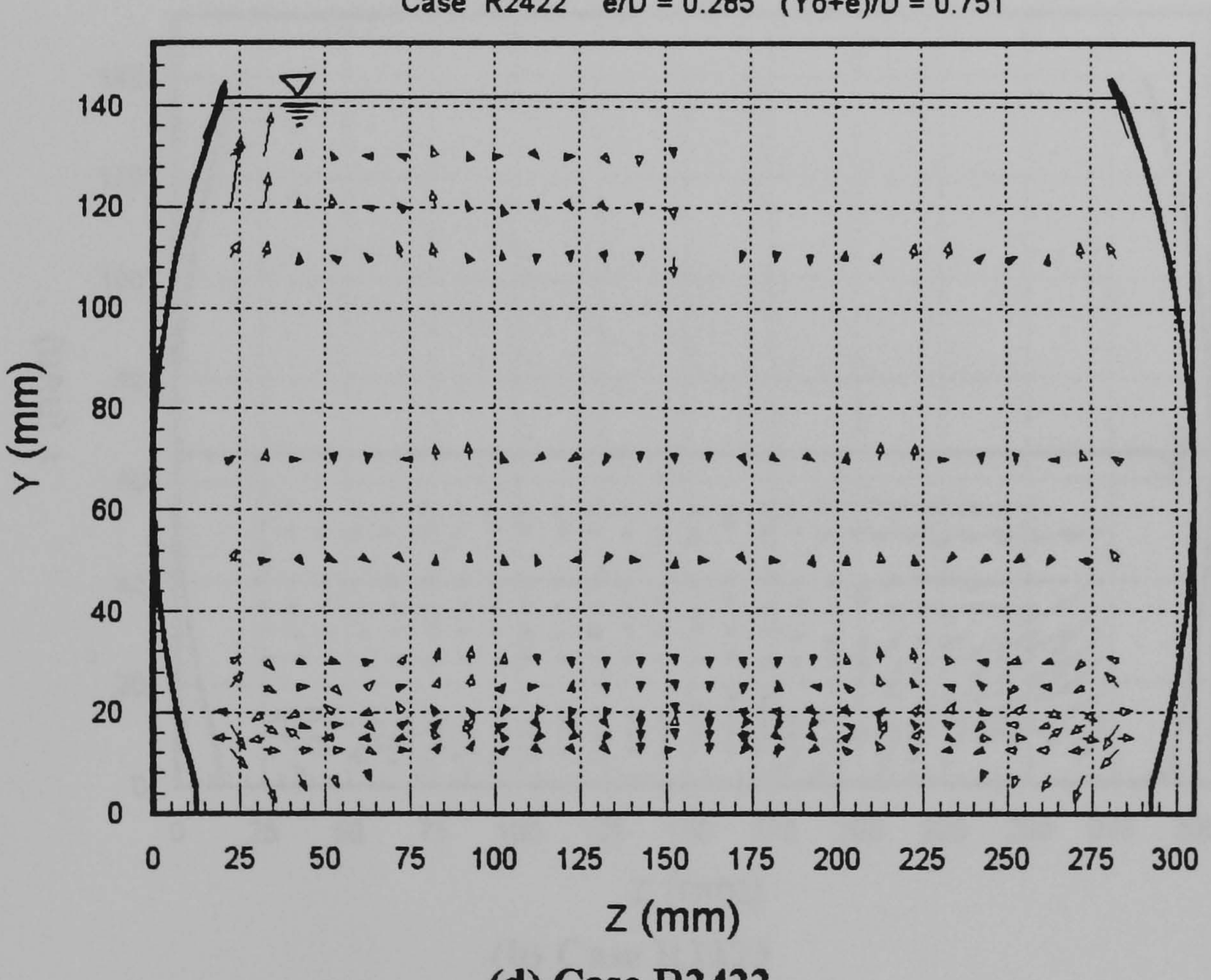

(d) Case R2422

Figure 7.12Cont. (c - d) Secondary Flow: Rough2; e/D = 0.285

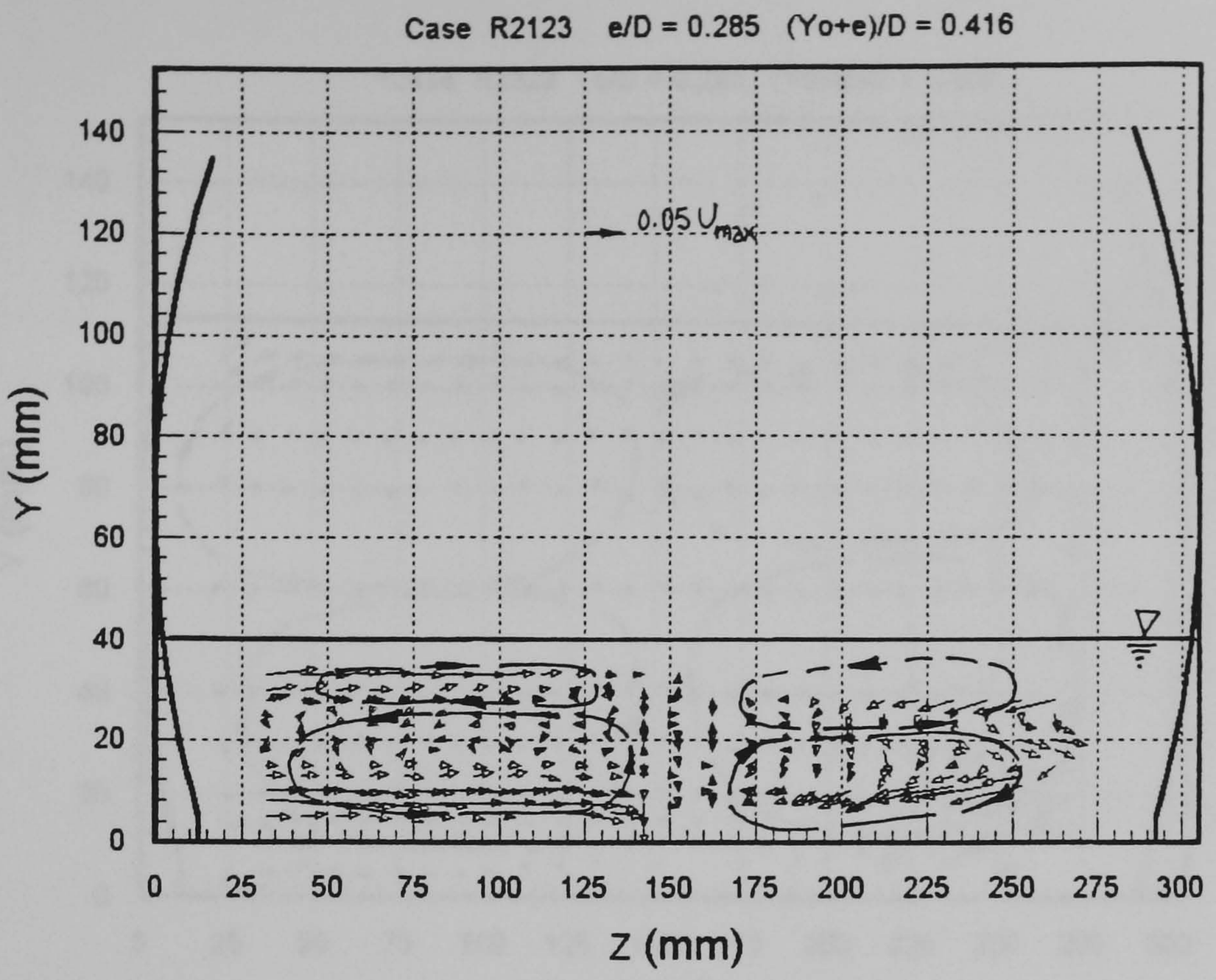

(a) Case R2123

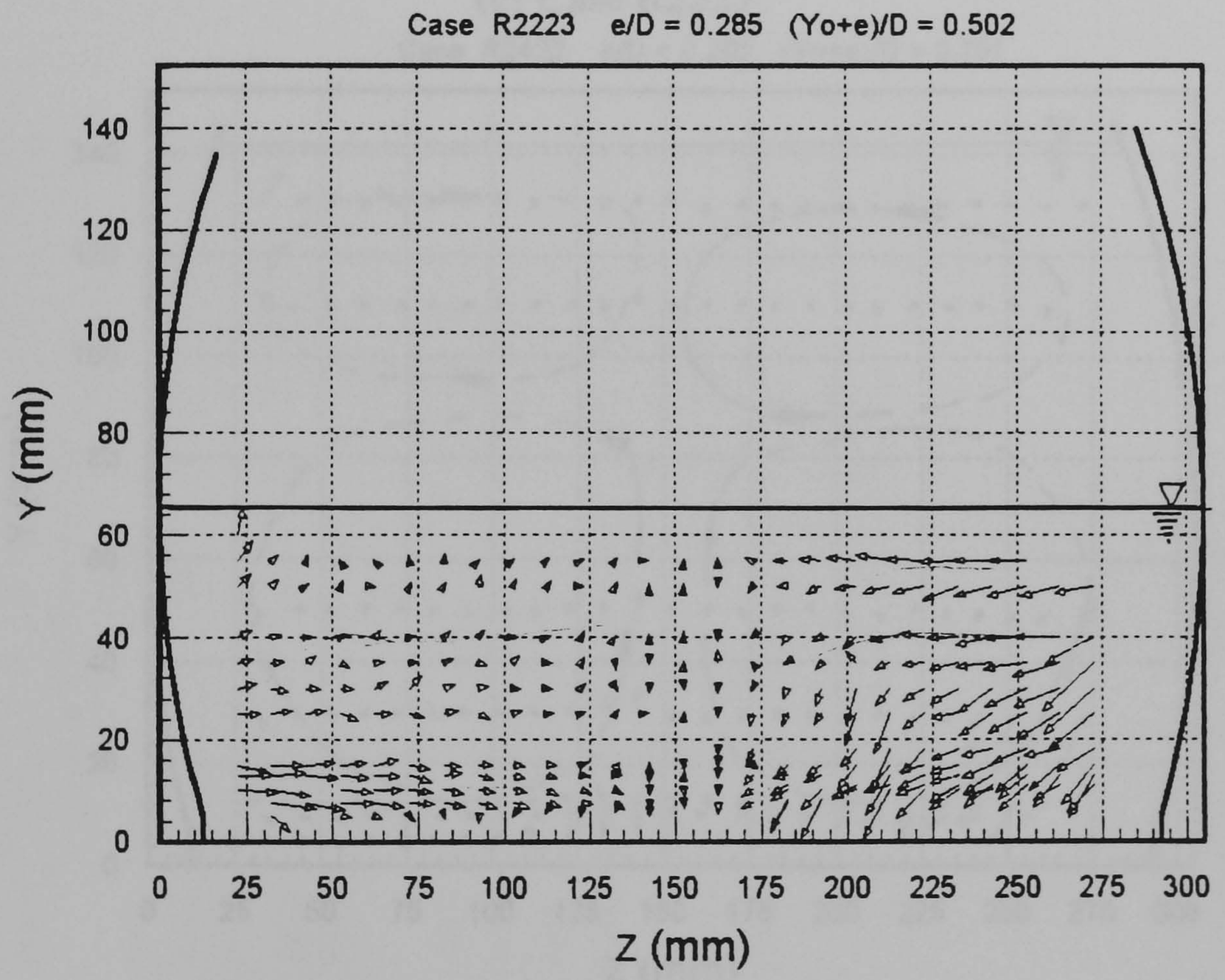

(b) Case R2223

Figure 7.13 (a - b) Secondary Flow: Rough3; e/D = 0.285

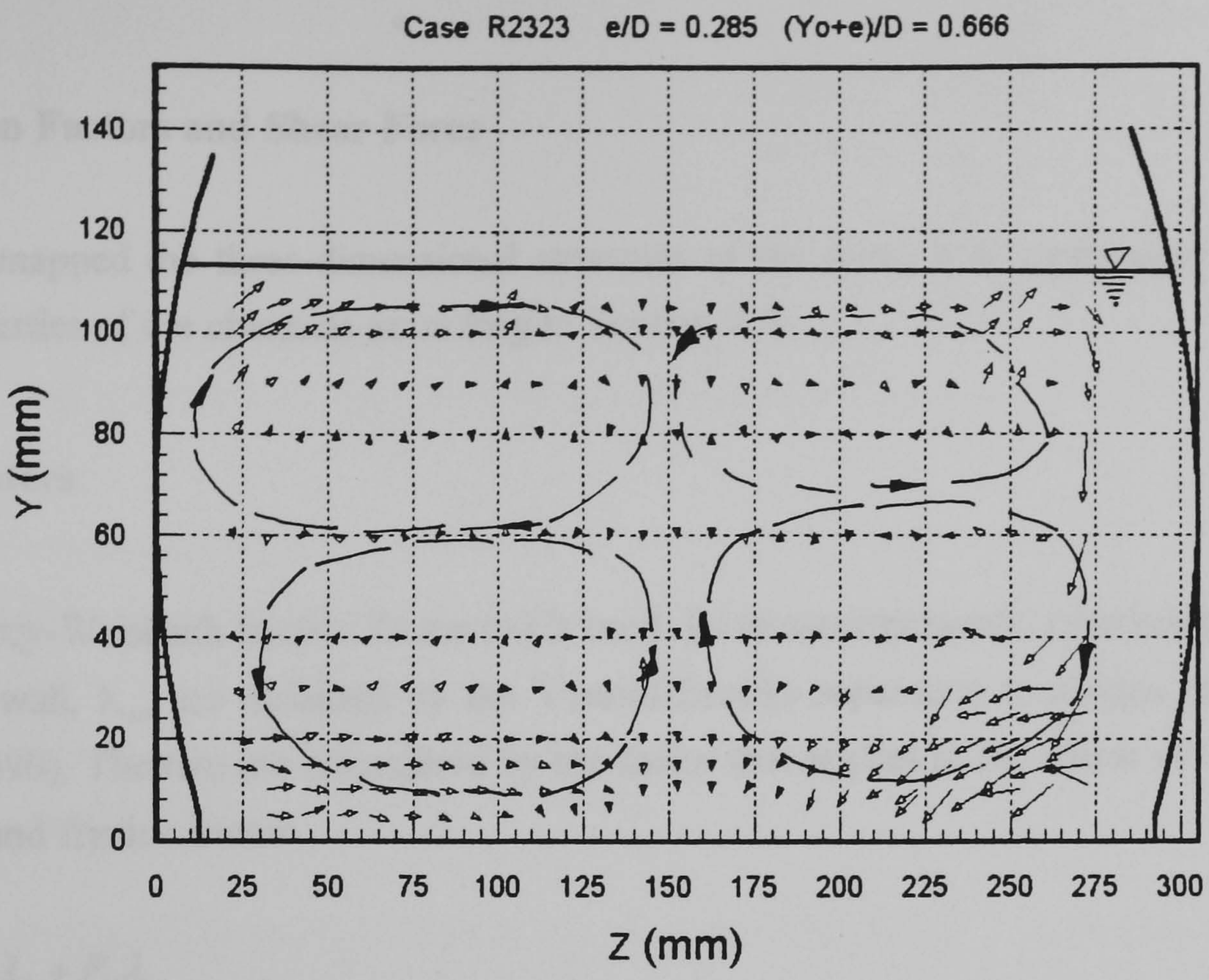

(c) Case R2323

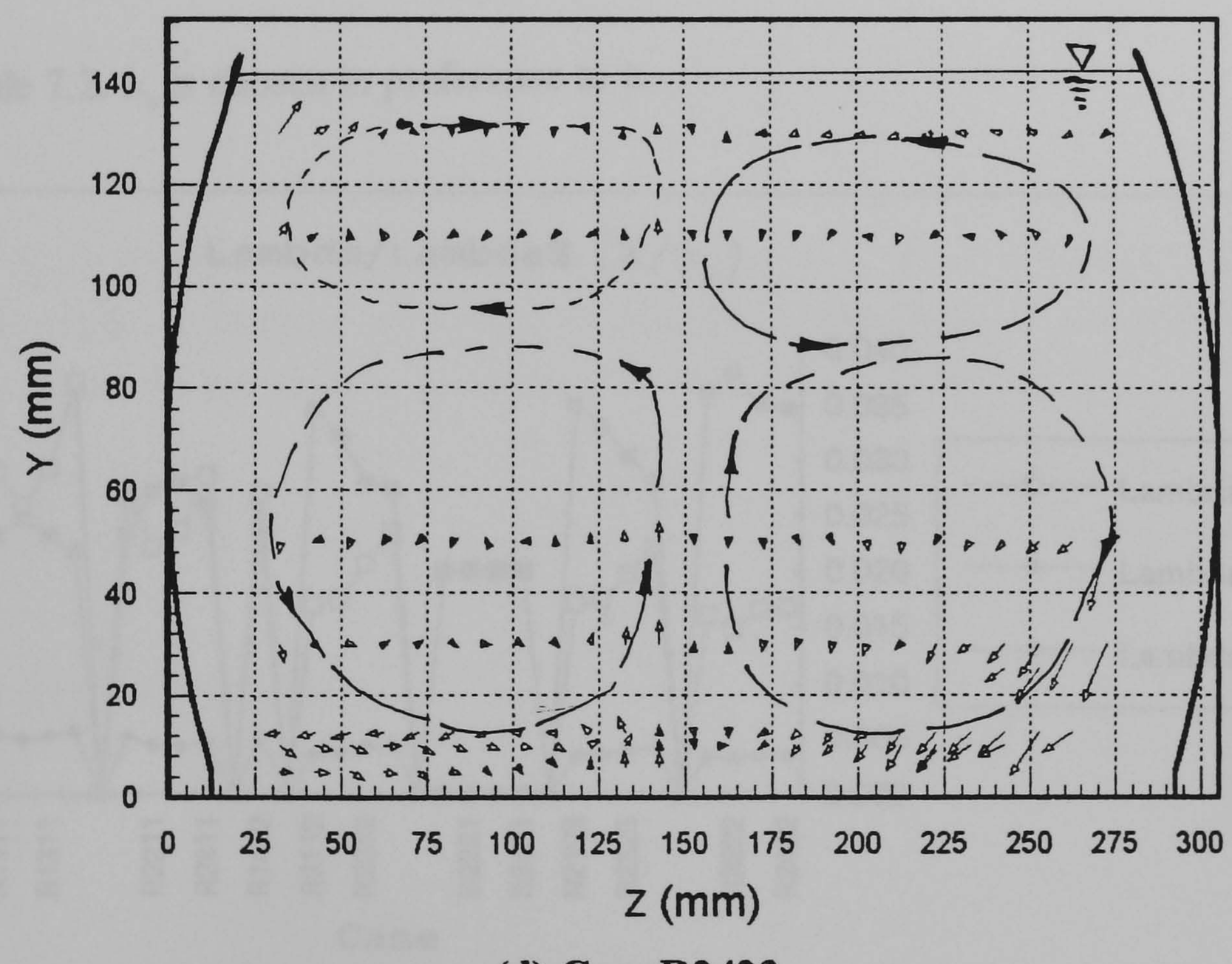

(d) Case R2423

Figure 7.13Cont. (c - d) Secondary Flow: Rough3; e/D = 0.285

7.4.5 Friction Factors and Shear Force

Having mapped the three-dimensional structure of the flow, it is appropriate to note the friction properties of the channels according to Section 2.5.

Friction Factors

The Darcy-Weisbach friction factor (λ) is used. Its two-components, pertaining to the bed, λ_b, and the wall, λ_w, are obtained by the Vanoni-Brooks separation technique (see Alvarez-Hernadez 1990). The two are normalised by the factor that applies to the whole channel, λ_s, the equivalent sand friction factor

$$\lambda_s = \frac{P_b\lambda_b + P_w\lambda_w}{P_b + P_w}, \qquad (2.37)$$

given in Table 7.2. λ_s is chosen in preference to λ

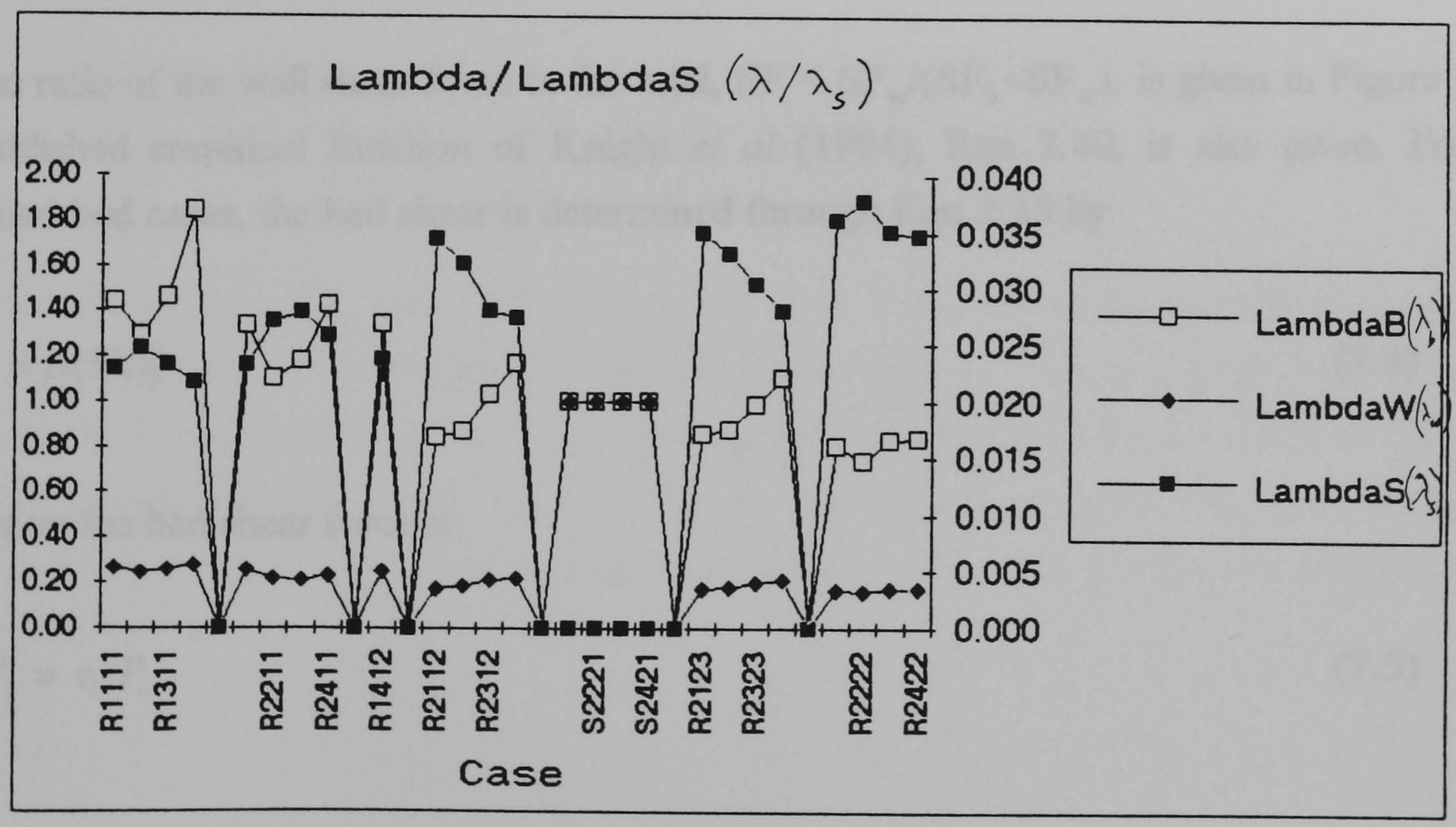

Figure 7.14 Friction Factors (see Table 7.2)

$$\lambda_s = \frac{8\,g\,R\,S_f}{U_m^2} \tag{2.36}$$

due to its independence from the bulk mean velocity U_m which has been shown to be too large in some of the flow cases. Using Eqn 2.36 would lead to exaggerated values of λ_b/λ_s and λ_w/λ_s.

Figure 7.14 shows the ratios λ_b/λ_s and λ_w/λ_s. For the lower bed slope, e/D = 0.141, and roughness Rough1, (cases of transitional roughness R1111 - R1411) the values of λ_b/λ_s are approximately equal to 1.5. On the other hand, for the bed thickness e/D = 0.285, and S_o = 9.27 x 10^{-4}, (fully rough cases R2122 - R2422) the λ_b/λ_s ratio lies in the vicinity of 0.8. This shows that the relative effect of the bed roughness in the low roughness, low slope flows is more pronounced than in the higher roughnesses. The reason for this is that the tractive effect of the roughness is reduced as the wetted wall perimeter increases. It is overwhelms even the effect of the increased bed roughness. In general, λ_s values rise with increasing roughness: from $\lambda_s \sim 0.020$ for low roughness R1411, to $\lambda_s \sim 0.035$ for the high roughness case R2422.

Shear Forces

The ratio of the wall shear force to the total, SF = $SF_w/(SF_b+SF_w)$, is given in Figure 7.15. The published empirical function of Knight *et al* (1984), Eqn 2.40, is also given. For the roughened bed cases, the bed shear is determined through Eqn 2.35 by

$$\tau_b = \rho(U_*)_b^2 \tag{7.4}$$

whereupon the bed shear force is

$$SF_b = \tau_b\, P_b\,. \tag{7.5}$$

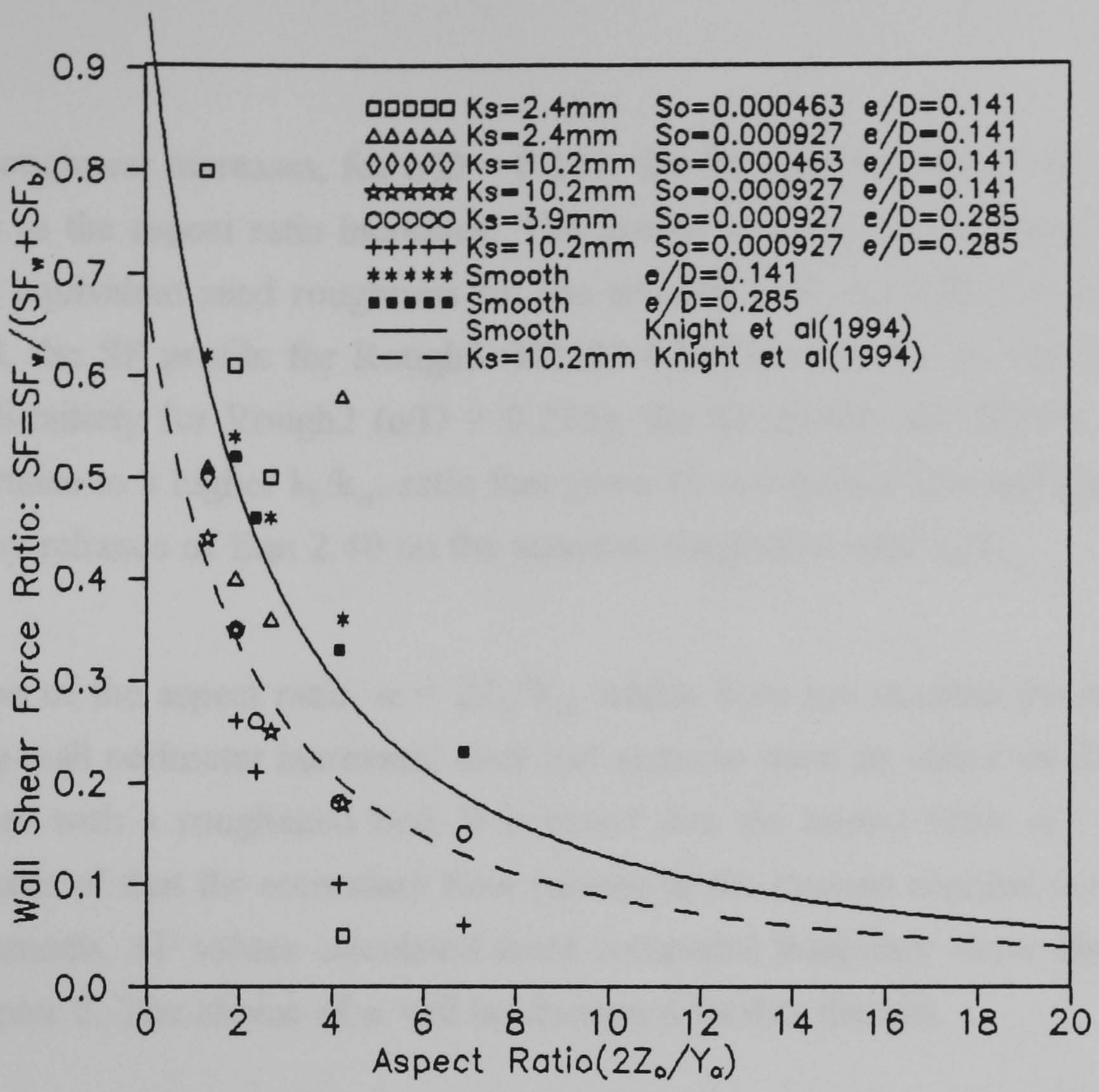

Figure 7.15 Wall Shear Force Ratio (SF): Smooth and Roughened Beds

The wall shear force ratio (SF) is then given by

$$SF = \frac{SF_w}{SF_T} = \frac{SF_T - SF_b}{(\rho g R S_f)P}. \qquad (7.6)$$

For the smooth bed cases, SF follows the Eqn 2.40, the present channel shape gives slightly higher values. This is expected since the aspect ratio, $\alpha = 2Z_o/Y_o$, is an underestimate as it uses the bed width and neglects the greater channel width caused by the side-wall curvature. The wall perimeter is also greater than that for an equivalent rectangular channel. As such, the wall shear force ratio is higher than that given by the Eqn 2.40. The profiles are similar for both bed thicknesses.

As the bed roughness increases, for e/D = 0.141, the SF profile follows Eqn 2.40 closely - i.e. SF decreases as the aspect ratio increases. The profile is, however, strongly dependent on the values of the equivalent sand roughness for the smooth wall, (k_w) used to calculate k_b/k_w. For e/D = 0.285, the SF profile for Rough3 (R2123-R2423) is similar to Eqn 2.40 although slightly steeper. Similarly for Rough2 (e/D = 0.285), the SF profile still follows the shape of Eqn 2.40 but pertains to a higher k_b/k_w. ratio that given by the dashed line in Figure 7.15. This is due to the heavy reliance of Eqn 2.40 on the sensitive roughness ratio k_b/k_w.

The definition of the aspect ratio, $\alpha = 2Z_o/Y_o$, which does not account for the increase in SF as the curving wall perimeter increases, does not seem to have an effect on the distribution of SF in the cases with a roughened bed. It is noted that the aspect ratio, $\alpha = 2Z_o/Y_o$, was adopted on the basis of that the secondary flow pattern in the present channel is similar to that in rectangular channels. SF values calculated from computed boundary shear distributions are presented in Chapter 8. The choice of α will be discussed further therein.

7.5 Similarity Laws

The mean longitudinal velocity distributions are used to derive similarity laws at the channel centreline, and within the wall/bed symmetry zone - the corner zone. The centreline profiles are for both the smooth and the rough-bed cases. Since velocity measurements could not be taken very close to the side-wall, local curvature effects expressed by Rao's law, Eqn 6.26, could not be investigated.

7.5.3 Similarity Laws at the Centreline

Figures 7.16 and 7.17 show the inner logarithmic law of $U(y^+)$, non-dimensionalised by a friction velocity, as a function of the non-dimensional distance y^+. The wake function

$$\zeta(y/h) = \frac{2\Pi}{\kappa}\sin^2\left(\frac{\pi y}{2h}\right) \qquad (2.26b)$$

is added to the standard Log-law, Eqn 2.21 and plotted for comparison.

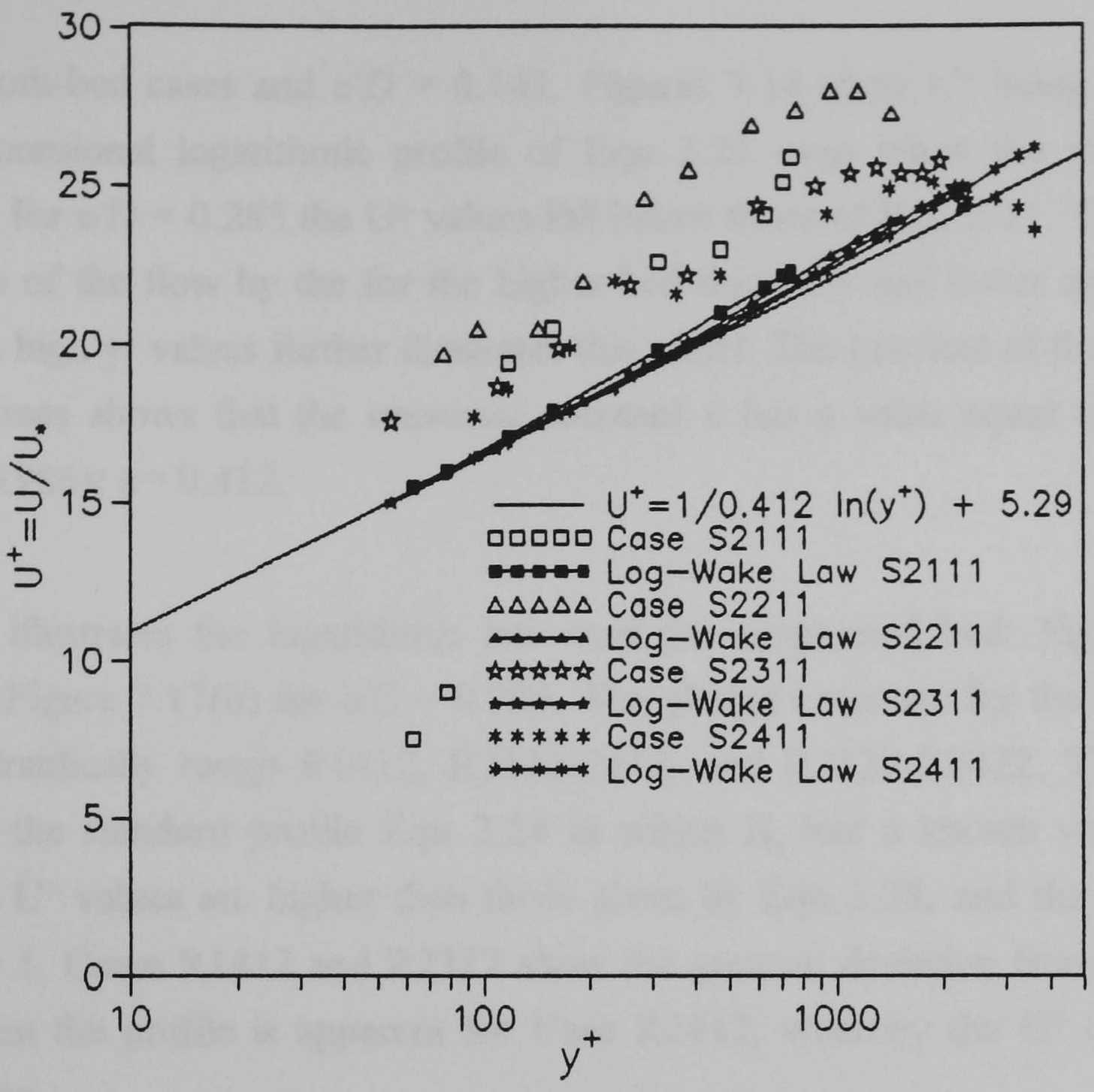

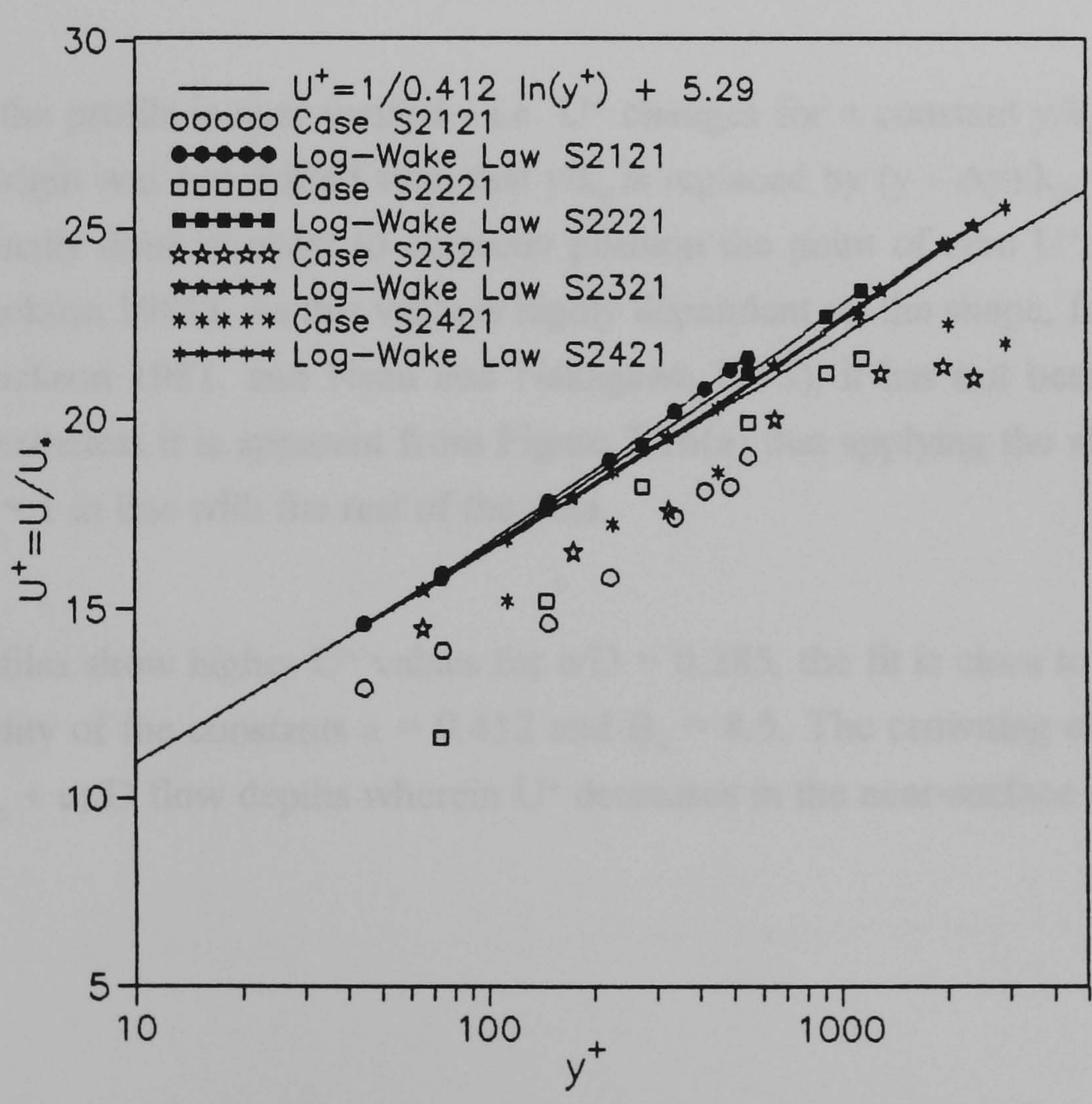

Figure 7.16 U Scaling at Channel Centreline: Smooth Bed. (a) e/D = 0.141; (b) e/D = 0.285

For the smooth-bed cases and e/D = 0.141, Figures 7.16 show U^+ being higher than the standard two-dimensional logarithmic profile of Eqn 2.21 even when the wake function is added. However, for e/D = 0.285 the U^+ values fall below those of Eqn 2.21. This is due to the higher retardation of the flow by the for the higher bed thickness and lower aspect ratios. The lowering of U^+ at high y^+ values further illustrates this effect. The gradient of the U^+ profiles for both bed thicknesses shows that the universal constant κ has a value equal to that found by Nezu and Rodi (1986): κ= 0.412.

Figure 7.17 illustrates the logarithmic law over the roughened bed: Figure 7.17(a) for e/D = 0.141 and Figure 7.17(b) for e/D = 0.285. The plotted cases are for the cases where the flow is fully hydraulically rough R1412, R2112-2412, and R2122-R2422. This is to enable comparison with the standard profile Eqn 2.28 in which B_s has a known value of 8.5. For e/D = 0.141, the U^+ values are higher than those given by Eqn 2.28, and the profile is much steeper for $y/k_s > 1$. Cases R1412 and R2312 show the greatest deviation from Eqn 2.28. The crowning effect on the profile is apparent for Case R2412, whereby the U^+ decreases in the near-surface region.

At $y/k_s \sim 1$, the profile is near vertical - i.e. U^+ changes for a constant y/k_s. This is due to the fact that the origin was not shifted such that y/k_s is replaced by $(y - \Delta y)/k_s$. where Δy is the shift. This is normally done in order to correctly position the point of zero U^+. Δy is normally taken as $0.7k_s$ (Jackson 1981). As this value is highly dependent on the shape, form, and size of the roughness (Jackson 1981, and Nezu and Nakagawa 1993), it has not been applied to the present data. Nonetheless it is apparent from Figure 7.16(a) that applying the shift would place the points at $y/k_s \sim 1$ in line with the rest of the data.

Although the profiles show higher U^+ values for e/D = 0.285, the fit is close to Eqn 2.28. This confirms the validity of the constants κ = 0.412 and B_s = 8.5. The crowning effect is apparent for the higher $(Y_o + e)/D$ flow depths wherein U^+ decreases in the near-surface region.

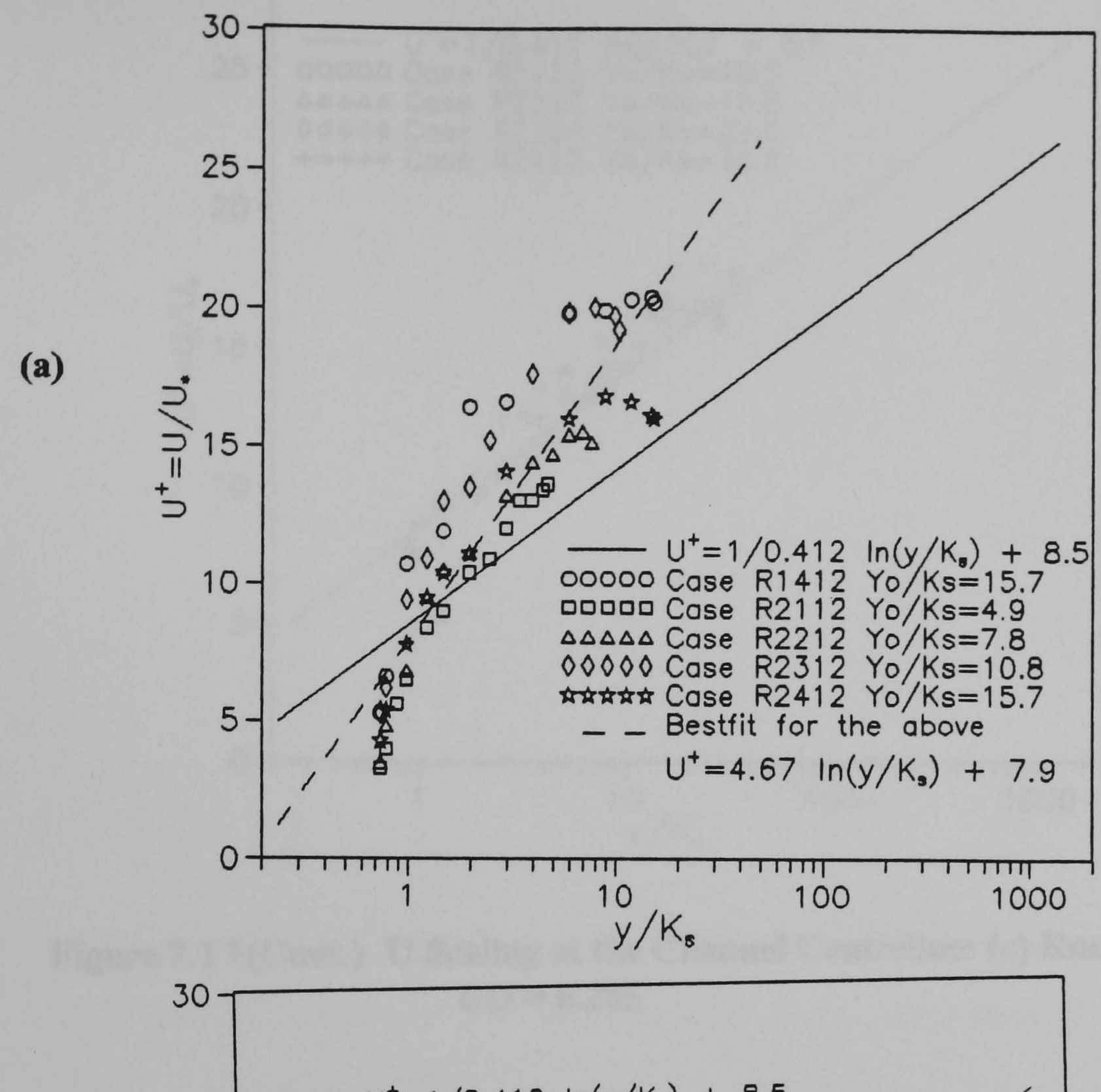

Figure 7.1 7 U Scaling at the Channel Centreline: Rough2. (a) e/D = 0.141; (b) e/D = 0.285

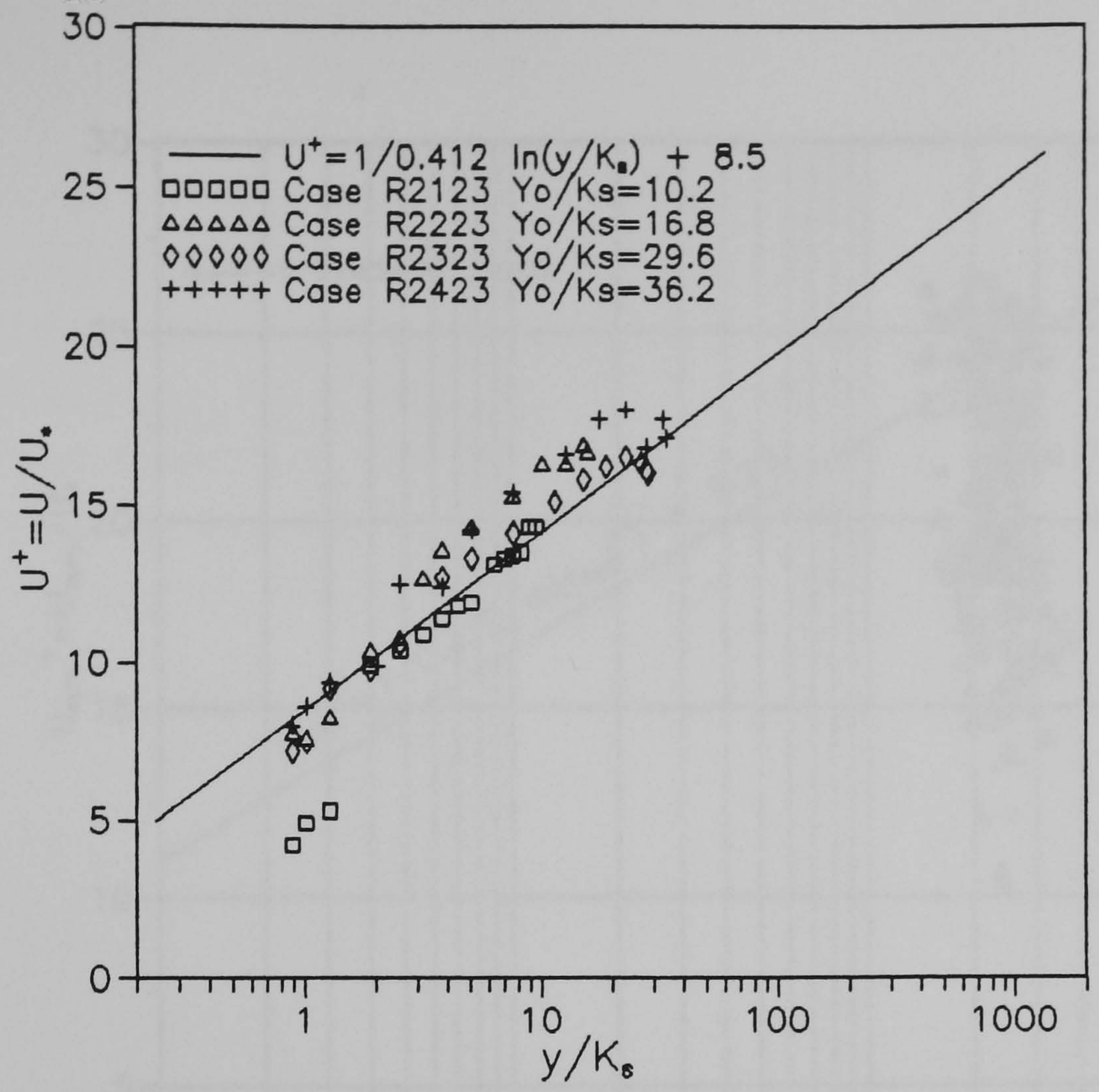

Figure 7.17(Cont.) U Scaling at the Channel Centreline: (c) Rough3. e/D = 0.285

7.5.4 Similarity Laws in the Corner Zone

Scaling of U in the corner zone is examined. The symmetry zone is as defined in Chapter 6 - illustrated in Figures 7.2(b and f). Figure 7.18 shows normalised U in the symmetry zone, $U_{sym}/(U_*)_{ave}$, as a function of the inner non-dimensional wall distance, $r_{sym}(U_*)_{ave}/\nu$ in smooth bed flows and both bed thicknesses. It shows that $U_{sym}/(U_*)_{ave}$ is not a function of $r_{sym}(U_*)_{ave}/\nu$. Instead, $r_{sym}(U_*)_{ave}/\nu$ is constant with an approximate value of 2500. This value is roughly equal to the non-dimensional distance from the right-angled corner at which the effect of the corner on the bed shear stops, as given by Bragg (1969), and Eqn 6.31. This shows that the measured velocity points are not scaled by the inner scales U_* and U_*/ν and thus belong to the outer zone.

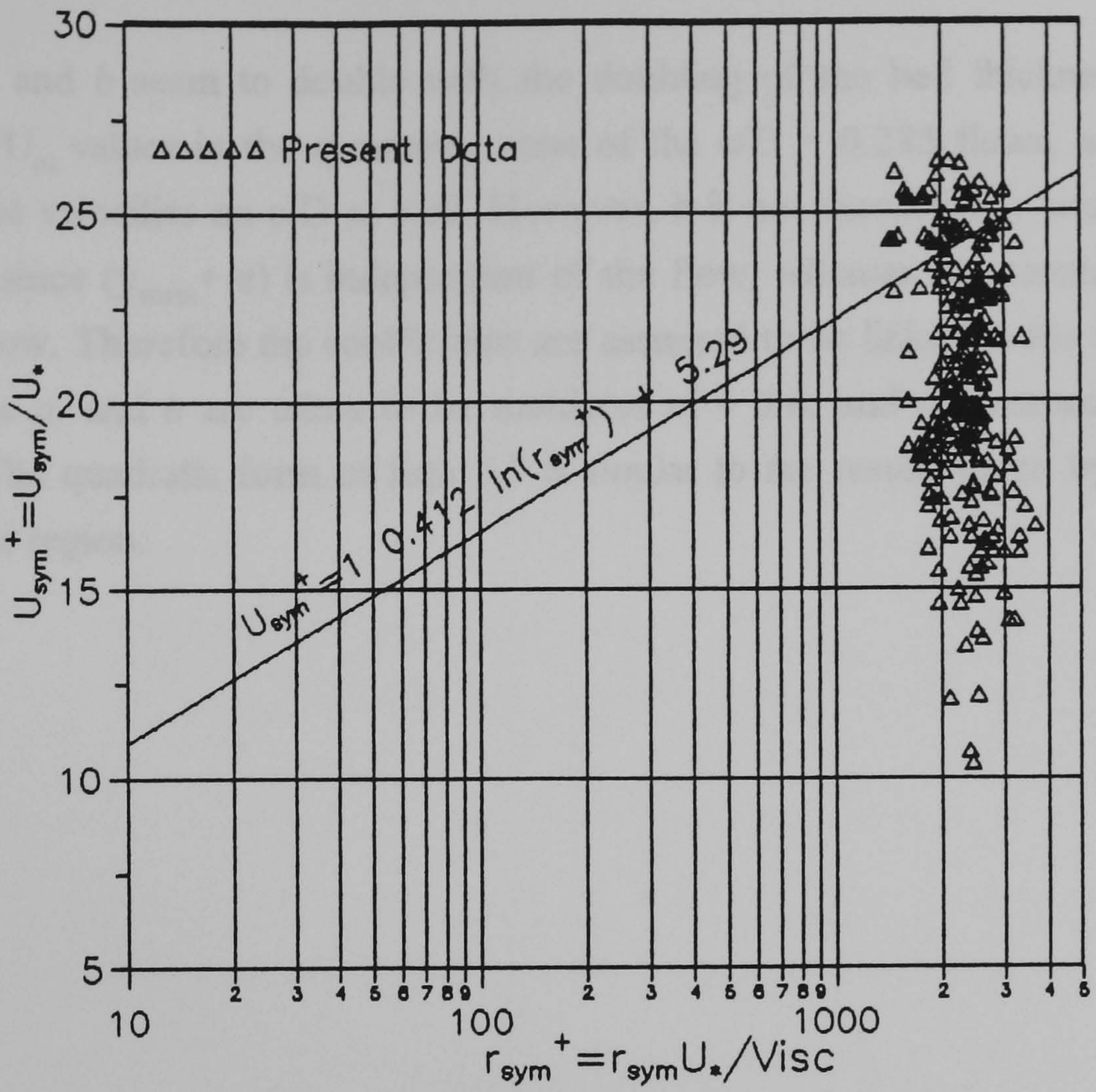

Figure 7.18 U Scaling in the Symmetry -zone: Inner Variables
$r_{sym}^+ U_*/\nu$ *versus* U_{sym}/U_*

Figures 7.19 (a and b) show the velocity scaled using outer-zone parameters - pertaining to the bed thicknesses e/D = 0.141, and e/D = 0.285 respectively. The normalised velocity, U_{sym}/U_m, is plotted against the non-dimensional distance y_{norm}/Y_o. y_{norm} is the norm of the perpendicular distances to the bed and wall respectively, and equals $\sqrt{(y \bullet y_w)}$. A combined plot of U_{sym}/U_m, for all the cases at each bed thickness, shows it to be a quadratic function of y_{norm}/Y_o:

$$\frac{U_{sym}}{U_m} = a\left[\frac{y_{norm}}{Y_o}\right]^2 + b\frac{y_{norm}}{Y_o} + c. \qquad (7.7)$$

For e/D = 0.141, $a \sim -0.6$, $b \sim 0.7$, and $c \sim 0.75$. For e/D = 0.285, $a \sim -1.3$, $b \sim 1.4$, and $c \sim 0.75$. The coefficient c (~ 0.75) stays constant for both bed thicknesses. This indicates that nearest the corner, the flows are similar and the corner affects the distribution of U_{sym}/U_m in a similar manner for the bed thicknesses.

Coefficients *a* and *b* seem to double with the doubling of the bed thickness ratio. This shows higher U_{sym}/U_m values in the symmetry zone of the e/D = 0.285 flows, and suggests a dependence of these velocities on e/D as well. However, it is not theoretically sound to replace y_{norm} by $(y_{norm}+ e)$ since $(y_{norm}+ e)$ is independent of the flow, whereas the normalising Y_o is a dimension of the flow. Therefore the coefficients are assumed to be linked to the ratio e/D. For each given e/D, the *a*, and *b* are taken to be multiples of - 0.6, and 0.7 respectively, with *c* constant at 0.75. The quadratic form of Eqn 7.7 is similar to the results given by Sarma *et al* (1983) for the outer region.

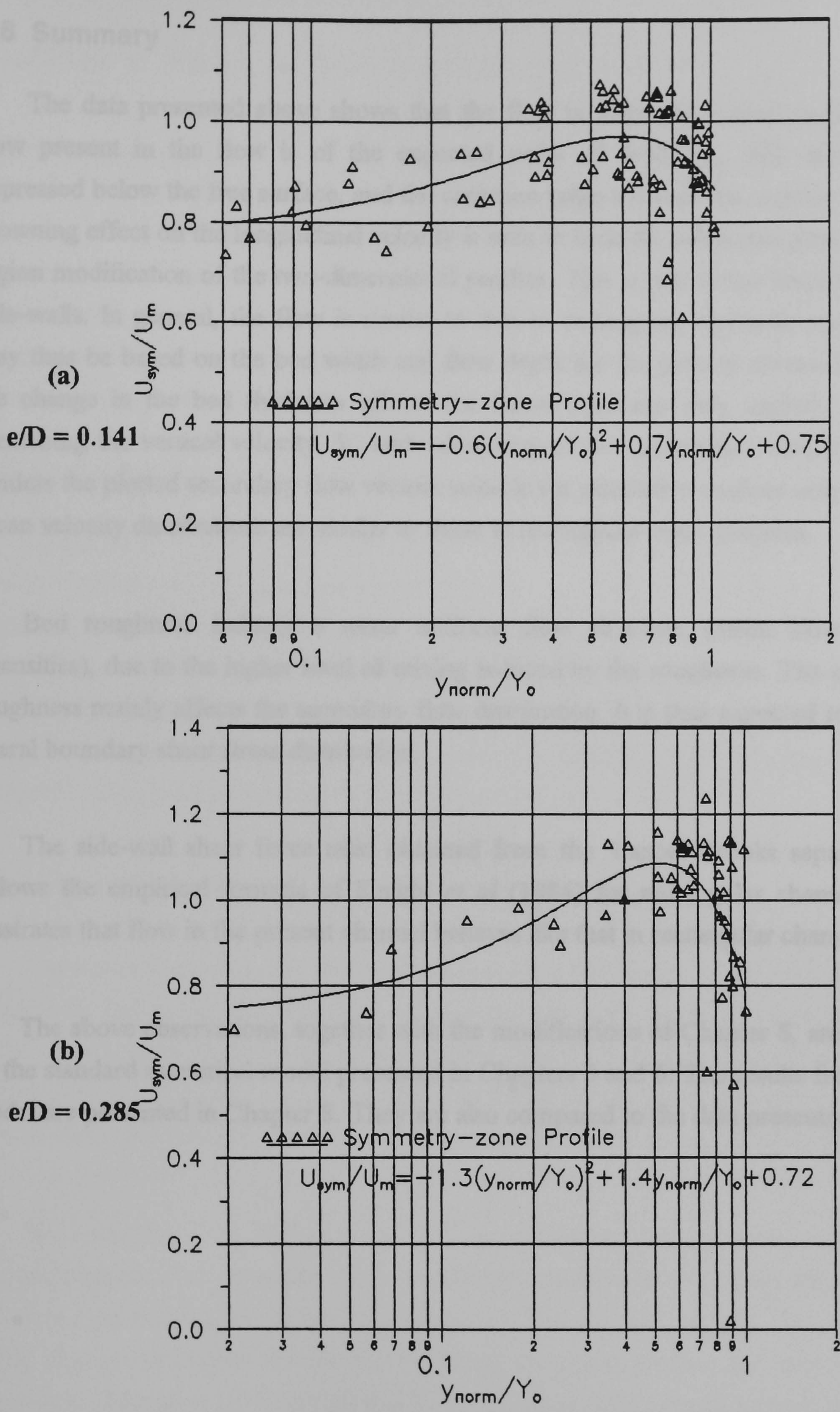

Figure 7.19 U Scaling in the Symmetry -zone: Outer Variables
y_{norm}/Y_o *versus* U_{sym}/U_m

7.6 Summary

The data presented above shows that the flow is truly three-dimensional. The secondary flow present in the flow is of the expected order of $0.05U_{max}$. The velocity maxima are depressed below the free surface, and the contours bulge towards the corners. Furthermore, the crowning effect on the longitudinal velocity is seen in both the full isovel plots, and the surface-region modification of the two-dimensional profiles. This is due to the inward curvature of the side-walls. In general, the flow is similar to that in rectangular channels, and the aspect ratio may thus be based on the bed width and flow depth for the present cross-section. As a result, the change in the bed thickness affects the flows structures only slightly. The difficulty in measuring the vertical velocity, V, and calculating of the transverse velocity (W) from these, renders the plotted secondary flow vectors suitable for qualitative analysis only. Nonetheless the mean velocity distributions are similar to those in rectangular open channels.

Bed roughness induces a more uniform flow structure (mean flow and turbulence intensities), due to the higher level of mixing induced by the roughness. The change in the bed roughness mainly affects the secondary flow distribution. It is thus expected to indirectly affect lateral boundary shear stress distribution.

The side-wall shear force ratio obtained from the Vanoni-Brooks separation technique, follows the empirical formula of Knight *et al* (1984) for rectangular channels. This further illustrates that flow in the present channel behaves like that in rectangular channels.

The above observations, together with the modifications of Chapter 6, are used to improve on the standard numerical model presented in Chapters 3 and 6. The results from this improved model are presented in Chapter 8. They are also compared to the data presented above.

CHAPTER 8: RESULTS OF THE NUMERICAL INVESTIGATION

8.1 Introduction

The results of the numerical modelling are presented in this chapter. The format of the presented data is laid-out in Section 8.2. The numerical stability and convergence of the method is also discussed in this section. The computed flow fields for flow cases presented in Chapter 7 are presented in Sections 8.3 and 8.4 - for the smooth and rough beds respectively. Additional cases are investigated. The boundary shear stresses are also presented in these two sections.

8.2 Data Presentation and Analysis

Cases of S_o = 9.27 x 10^{-4} are treated and the results are compared to the experimental results of Chapter 7. Three bed thicknesses e/D = 0.020, 0.141, and 0.285, and. five flow depths, $(Y_o+e)/D$ = 0.305, 0.4 (or 0.416), 0.502, 0.667, and 0.751, were studied. The bed roughnesses used in the experimental study k_s = 3.92, and 10.2 mm are also used. The k_s/Y_o ratios lie in the range 4 - 30. These cases are summarised in Table 8.1. For both the smooth and rough bed computations, the case references (e.g. S2411C, R2323C) follow the notation of Chapter 7. The additional letter 'C' denotes the 'computed' cases.

8.2.1 Computed Variables

The computational model uses the non-linear k-ε turbulence model with the wall curvature, roughness, and corner modifications. The model computes the six flow parameters: velocities U, V, W; pressure P; turbulent kinetic energy k; and the energy dissipation rate ε. The three turbulence intensities U_{rms}, V_{rms}, and W_{rms} are calculated as the square roots of their respective normal Reynolds stresses. All these variables characterise the mean turbulent flow.

The contours of the primary velocity U, normalised by the computed cross-sectional mean U_m, are plotted. The secondary flow vectors (normalised by U_{max}) are also plotted. For the turbulence parameters, normalised distributions k/U_*^2, $\varepsilon Y_o/U_*^3$, U_{rms}/U_*, V_{rms}/U_*, and W_{rms}/U_*, at the channel centreline are given. For these, empirical profiles for two-dimensional flows (Nezu and Nakagawa 1993) are plotted for comparison. The boundary shear stress distributions for these flows are also given.

Case	2	3	4	5	6	7	8	9	10	11	12
	Equiv.	e/D	(Yo+e)/D	Aspect	ks	Um	Um	Ave. Wall	Integrtd	Shear Force	Shear
	Experiment			Ratio		Experiment	Model	Stress	Stress	Wall (SFw)	Force Ratio
	Case			(2Zo/Yo)	(mm)	(m/s)	(m/s)	Ratio	Ratio	(N/m^2)	Wall (SF)
S2111C	S2111	0.141	0.305	4.25	-	0.454	0.523	1.49	1.25	0.06	0.54
S2311C	S2311	0.141	0.502	1.93	-	0.599	0.704	1.50	1.12	0.22	0.80
S2411C	S2411	0.141	0.666	1.33	-	0.709	0.787	1.46	1.18	0.37	0.91
S2221C	S2221	0.285	0.502	4.17	-	0.361	0.618	1.48	1.20	0.09	0.49
S2321C	S2321	0.285	0.666	2.37	-	0.468	0.726	1.47	1.25	0.21	0.68
S2421C	S2421	0.285	0.751	1.94	-	0.526	0.681	1.48	1.13	0.29	0.77
S2331C	-	0.020	0.502	0.58	-	-	0.707	1.45	1.32	0.39	1.19
S2431C	-	0.020	0.666	0.43	-	-	0.777	1.42	1.25	0.57	1.21
R2112C	R2112	0.141	0.305	4.25	10.2	0.250	0.410	1.50	1.23	0.06	0.55
R2312C	R2312	0.141	0.502	1.93	10.2	0.422	0.654	1.50	1.50	0.22	0.80
R2412C	R2412	0.141	0.666	1.33	10.2	0.490	0.677	1.15	1.21	0.29	0.71
R2122C	R2122	0.285	0.416	6.89	10.2	0.199	0.367	1.02	1.00	0.03	0.24
R2222C	R2222	0.285	0.502	4.17	10.2	0.245	0.490	1.50	1.17	0.09	0.50
R2422C	R2422	0.285	0.751	1.94	10.2	0.364	0.665	1.25	1.18	0.25	0.65
R2332C	-	0.020	0.502	0.58	10.2	-	0.627	1.25	1.18	0.34	1.03
R2432C	-	0.020	0.666	0.43	10.2	-	0.688	1.25	1.15	0.50	1.07
R2123C	R2123	0.285	0.416	6.89	3.92	0.214	0.370	1.25	1.00	0.03	0.29
R2223C	R2223	0.285	0.502	4.17	3.92	0.288	0.477	1.25	1.03	0.07	0.41
R2323C	R2323	0.285	0.666	2.37	3.92	0.398	0.610	1.25	1.00	0.18	0.58
R2423C	R2423	0.285	0.751	1.94	3.92	0.457	0.645	1.28		0.25	0.66
So =	9.27E-04		D =	305	mm						

Table 8.1 Computed Flow Cases

8.2.2 Convergence and Stability

The computer code was written in FORTRAN computer language using single precision arithmetic. Figure 8.1 shows the convergence criterion of Eqn 4.74 applied to the calculation of the pressure correction P', and the actual computed pressure distribution for a typical case - Case 2411C. The ratio of the initial-to-present residuals, $\|r_P\|^k / \|r_P\|^0$, decreases to below the cut-off value of 0.25. This criterion is met during each iteration of the SIMPLE algorithm.

For all the computations, the stability of the method was guaranteed by the use of mesh dimensions $dx = 0.5Y_o$, $dy = 0.05Y_o$, and $dz = 3\ dy$. The size of dz was sufficient to accommodate the roughness step at the corner as stipulated in Chapter 6. Further refinement of the grid was limited by the use of single precision arithmetic in the programming. As such, grid sizes smaller than those quoted lead to solution divergence due to rounding-off errors.

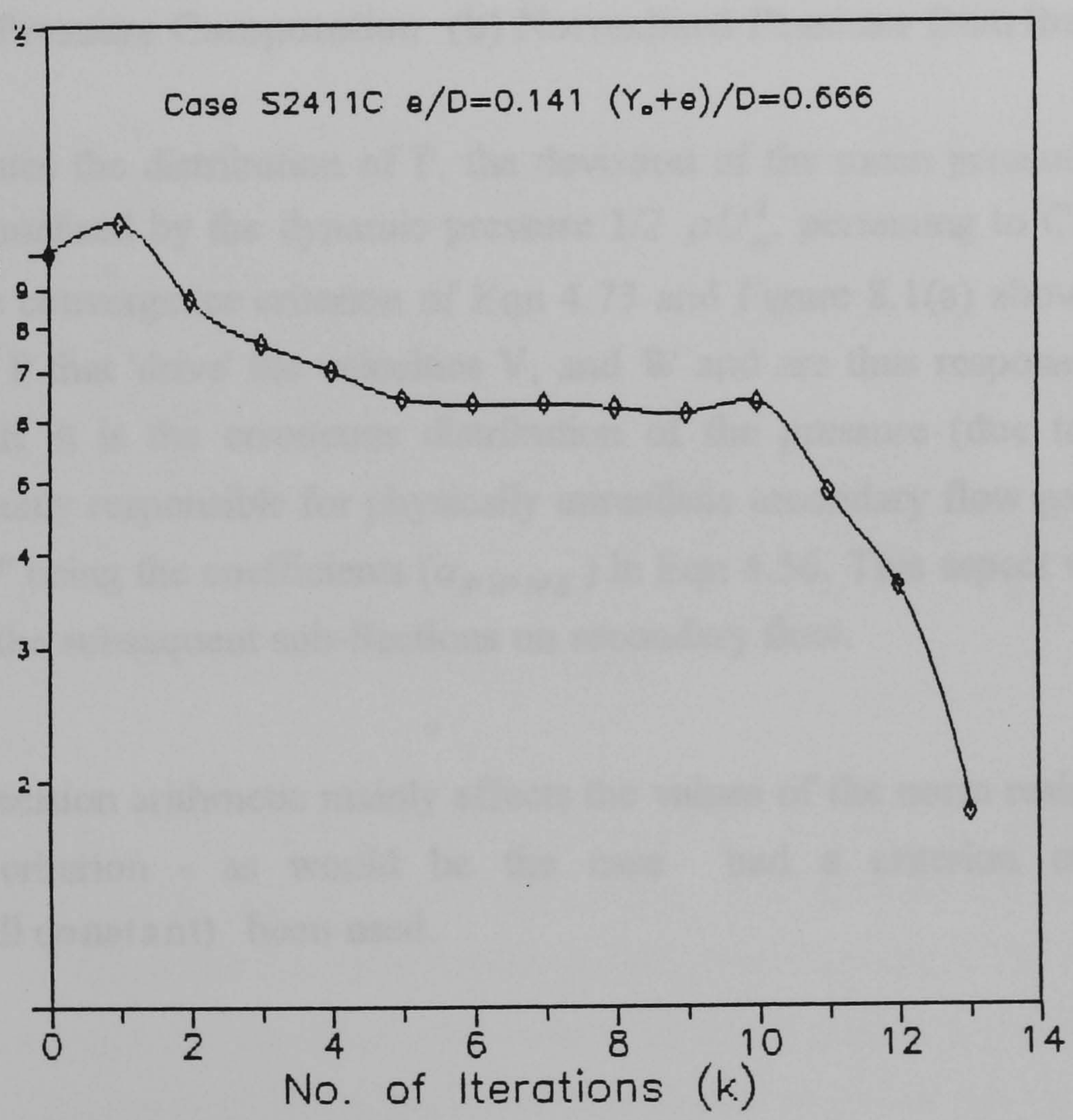

Figure 8.1 Pressure Computation (a) Convergence of Pressure-Correction

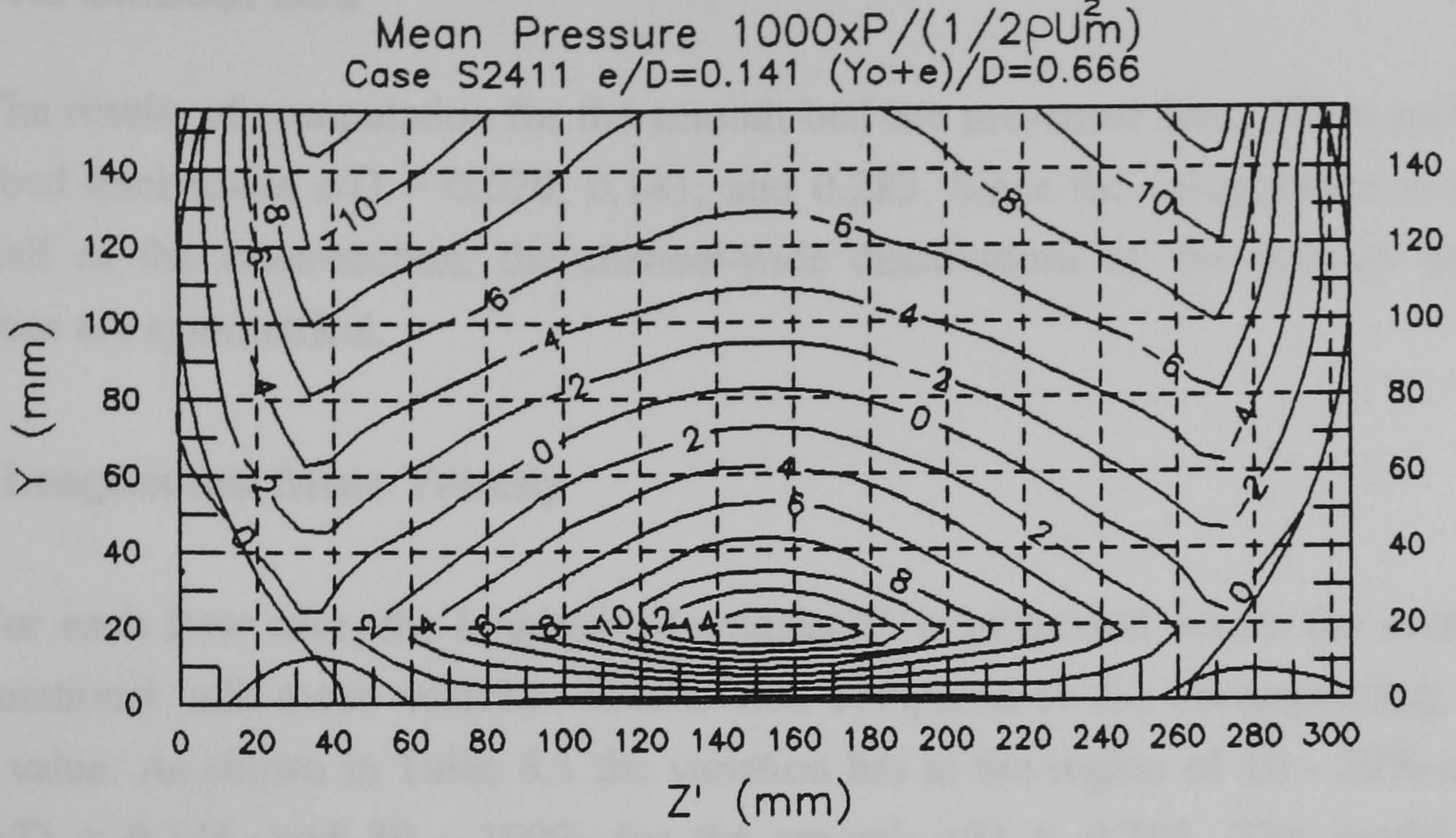

Figure 8.1 Cont. Pressure Computation (b) Normalised Pressure Distribution

Figure 8.1(b) illustrates the distribution of P, the deviation of the mean pressure from the hydrostatic pressure, normalised by the dynamic pressure 1/2 ρU_m^2. pertaining to Case S2411. This is obtained after the convergence criterion of Eqn 4.73 and Figure 8.1(a) above was met. It shows the gradients in P that 'drive' the velocities V, and W and are thus responsible for the secondary flow. As such, it is the erroneous distribution of the pressure (due to improper corrections, P') that is mainly responsible for physically unrealistic secondary flow patterns - the main source of error in P' being the coefficients ($a_{E,W,N,S}$) in Eqn 4.56. This aspect will be seen and further discussed in the subsequent sub-Sections on secondary flow.

The use of single precision arithmetic mainly affects the values of the norm residuals rather than the convergence criterion - as would be the case had a criterion of the type $| \|r_P\|^k - \|r_P\|^0 | \leq$ (small constant) been used.

8.3 The Smooth Bed

The results of computation for the smooth bed are presented first. These pertain to all the three bed thicknesses e/D = 0.020, 0.141, and 0.285. Since the computation is carried-out in one half of the cross-section, the channel-wide distributions of the primary and secondary velocities are symmetrical.

8.3.1 Longitudinal Mean Velocity

For each flow case, the longitudinal velocity U is integrated across the section to obtain computational bulk mean velocity. This is then compared to the corresponding experimental mean value. As shown in Table 8.1 the variation lies in the region of 10 - 20% in the smooth bed e/D = 0.141, and 30 - 100% for the smooth e/D = 0.285. The model predicts the longitudinal velocity in smooth beds to within acceptable limits. The larger discrepancies are due to the errors both in the experimental flows and the model as will be discussed below.

The velocities normalised by the integrated mean velocity, U/U_m, are plotted in Figures 8.2(a-h). They are generally smoother than the equivalent plots of Figures 7.2. This is expected and is due to numerical smoothing whereby the jaggedness of profiles is removed. Nonetheless the plots show (i) a large area within which the velocity maximum lies, similar to the two maxima of Chapter 7; (ii) the velocity dip in the higher flow depths; and (iii) slight upward curvature near the channel centreline, and outwards in the wall/corner region. This illustrates the three-dimensionality of the flow. Effects (ii) and (iii) are more apparent for flows where $(Y_o+e)/D \geq 0.5$, of the bed thickness ratios e/D = 0.141 and 0.285. The computed mean velocity distributions are similar to those found by experiment.

Two flows were investigated for the low bed thickness e/D = 0.020, $(Y_o+e)/D = 0.5$ and $(Y_o+e)/D = 0.666$ - Cases S2331C and S2431C respectively. The predominant effect of the walls is seen in Case 2131C where the contours follow the side-wall curvature. The velocity dip is not present. This is due to the fact that the open corner does not exert the same anisotropic effect as in the higher bed thicknesses. The section is similar to that of a clear pipe running part-full (Nalluri and Novak 1973). However, for $(Y_o+e)/D = 0.666$, velocity dip re-appears and the maximum occurs near the half-depth. This flow is similar to that of a full pipe flow. In both cases the three-dimensionality of the flow is minimal.

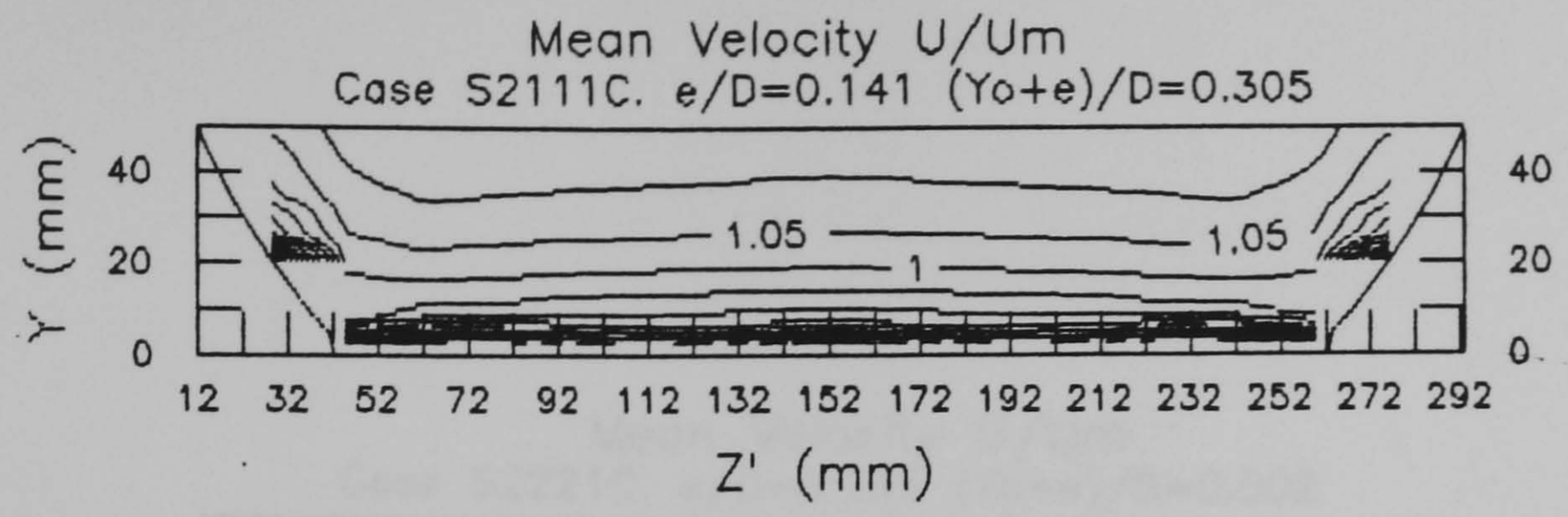

(a) Case S2111C

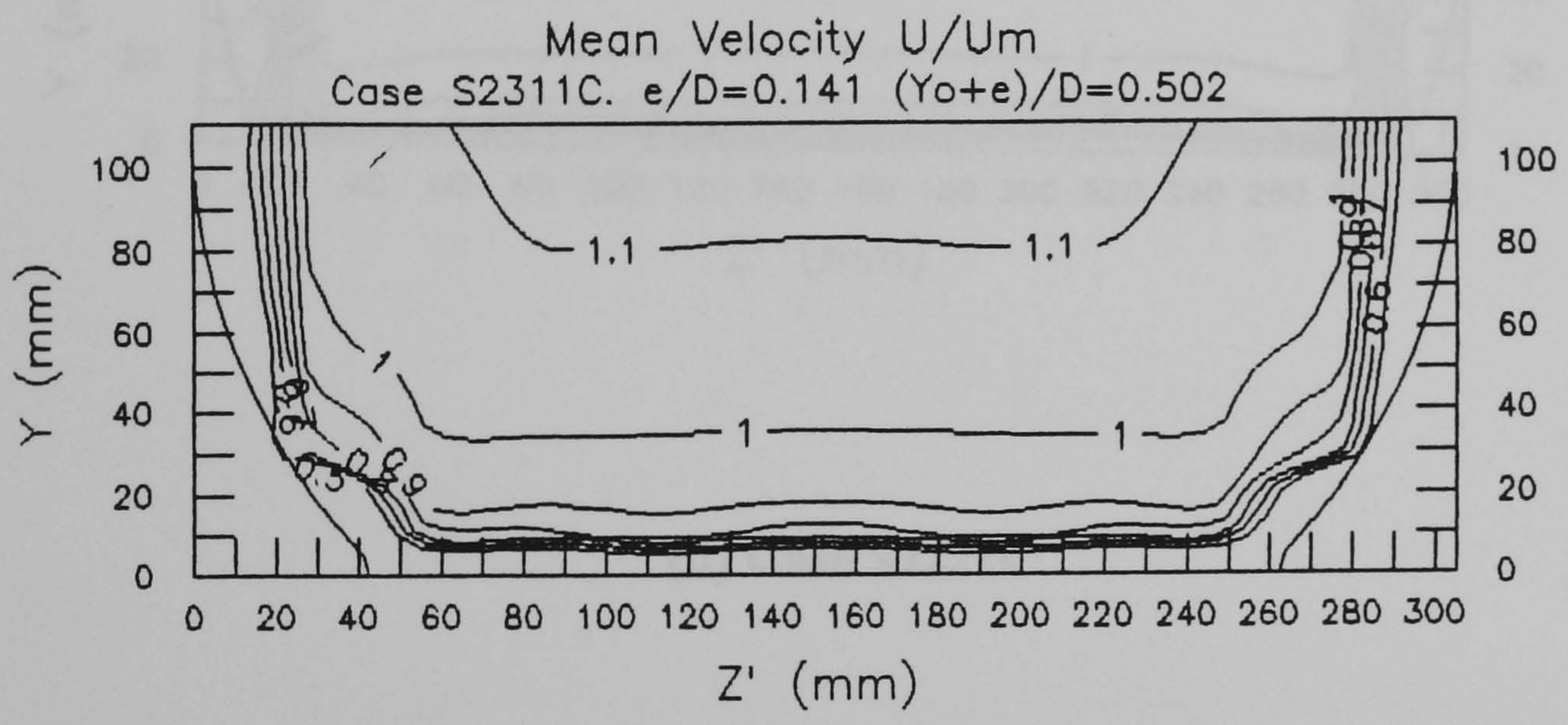

(b) Case S2311C

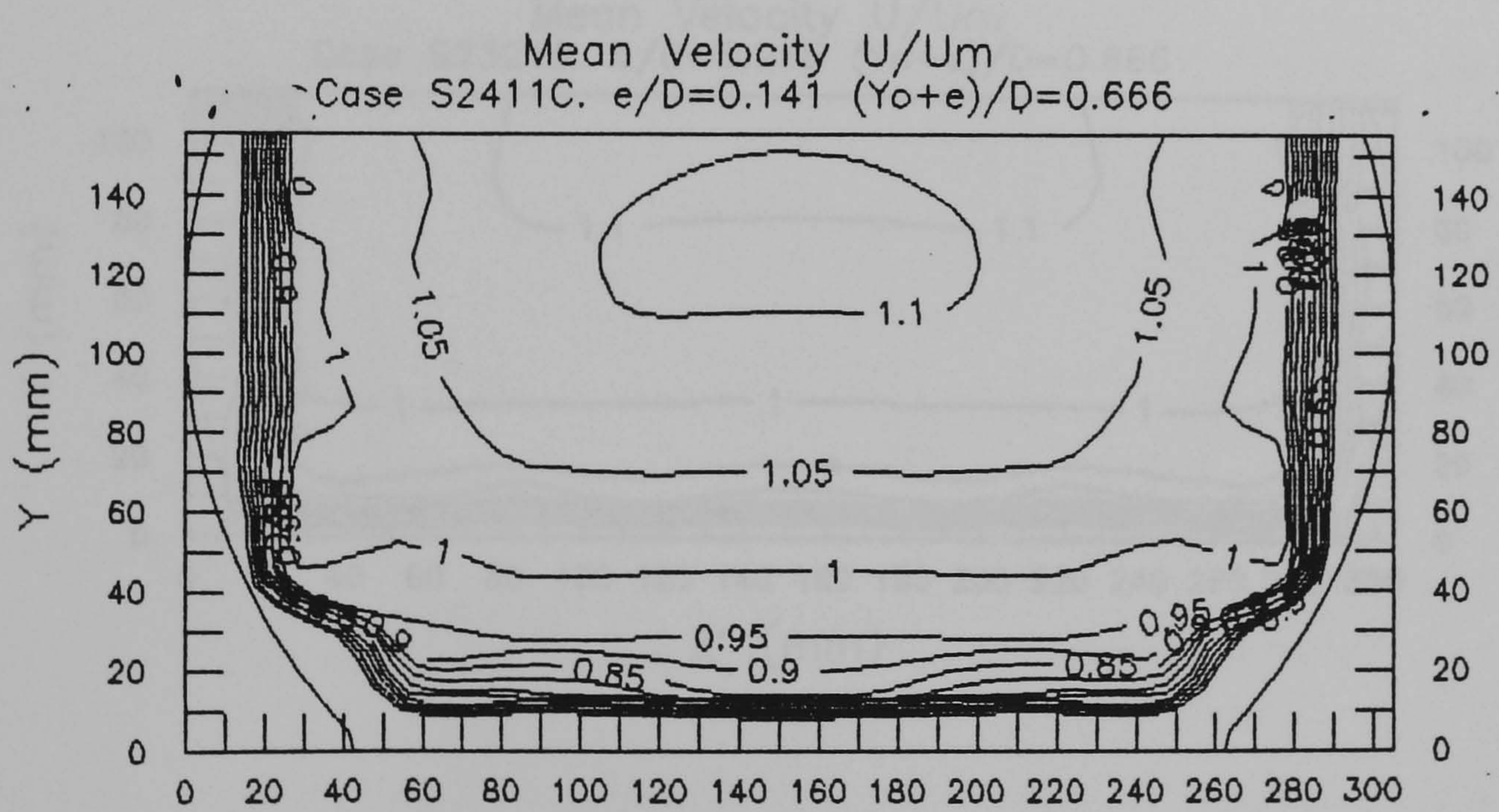

(c) Case S2411C

Figure 8.2 (a - c) Computed Mean Velocity Distribution U/U_m : Smooth Bed

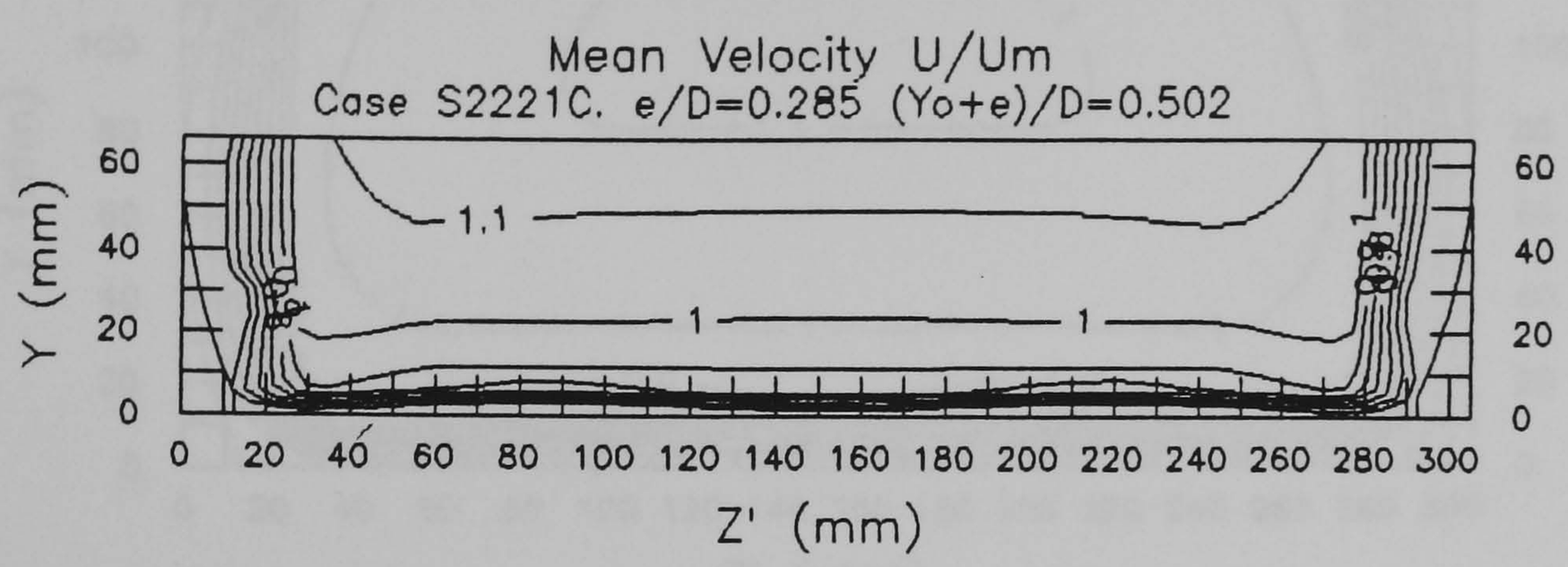

(d) Case S2221C

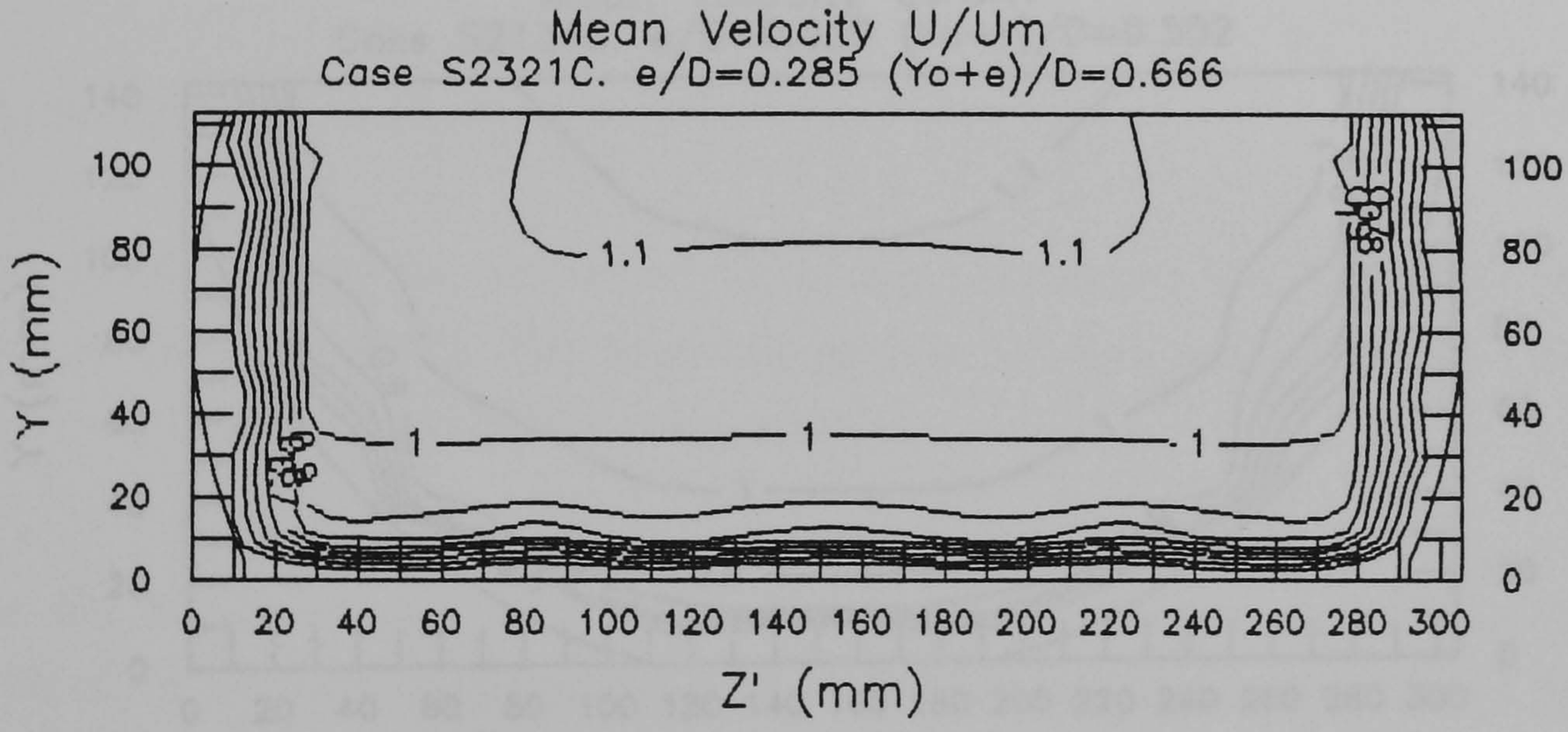

(e) Case S2321C

Figure 8.2 Cont. (d -e) Computed Mean Velocity Distribution U/U_m : Smooth Bed

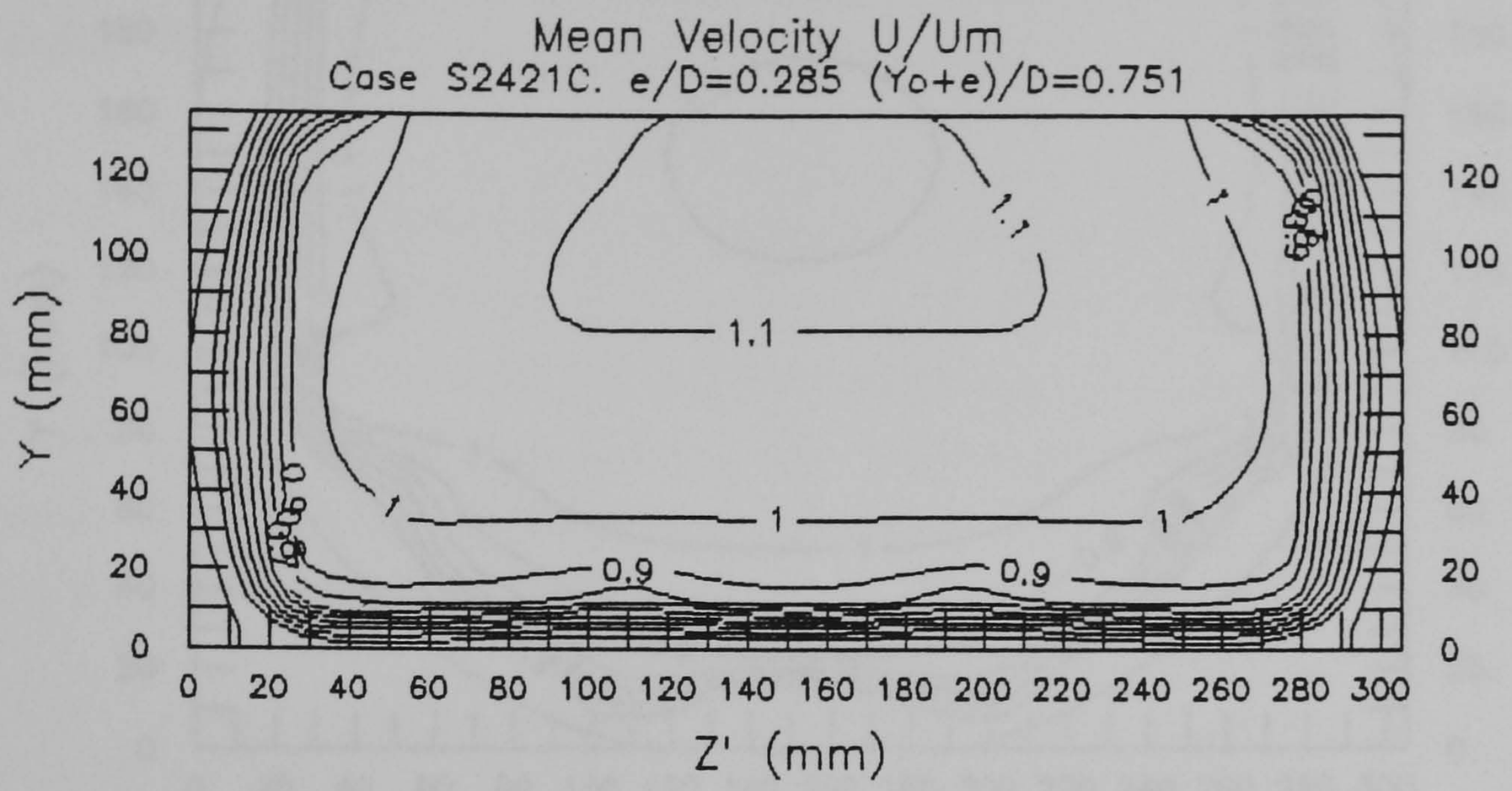

(f) Case S2421C

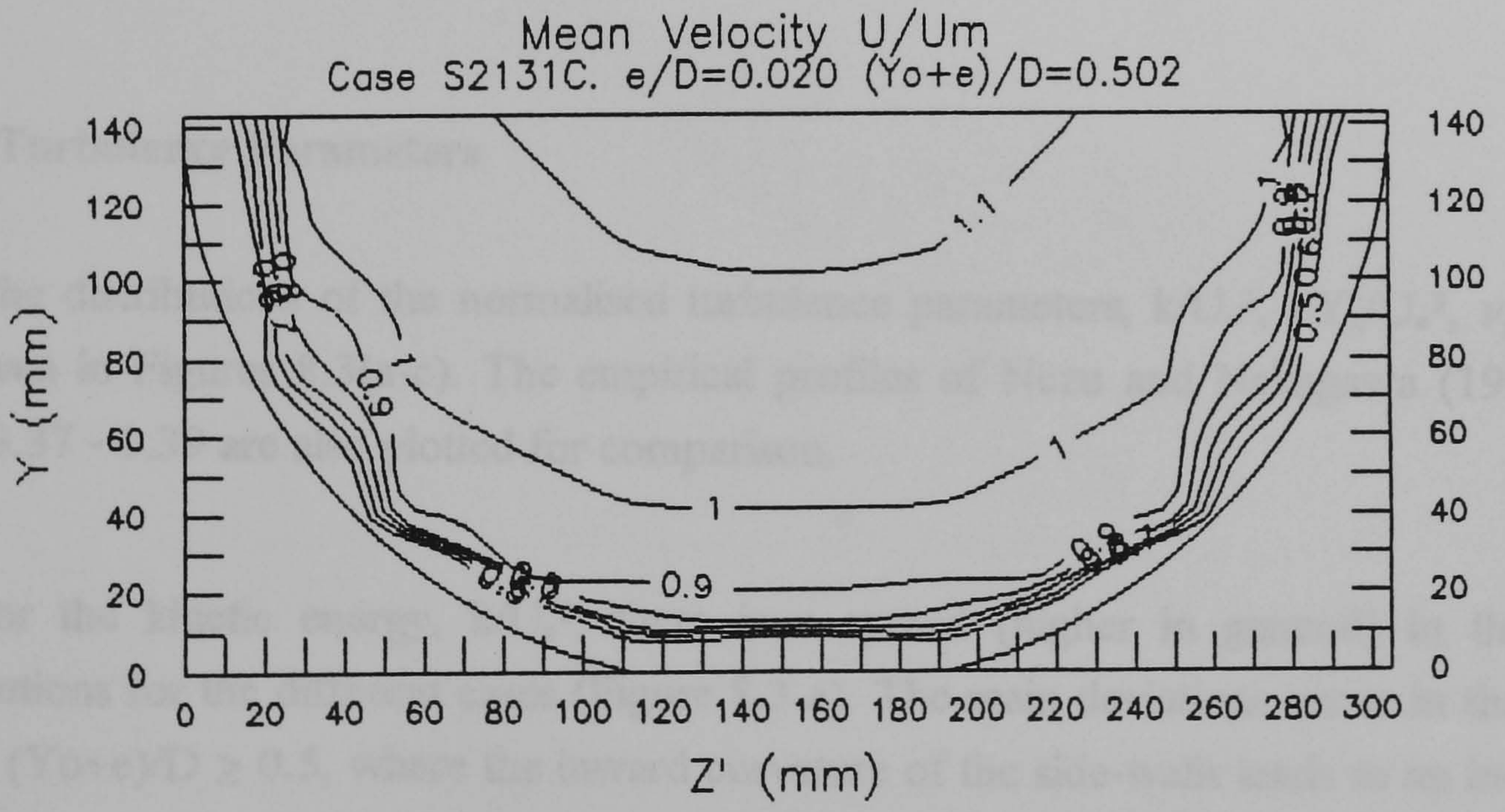

(g) Case S2331C

Figure 8.2 Cont. (f - g) Computed Mean Velocity Distribution U/U_m : Smooth Bed

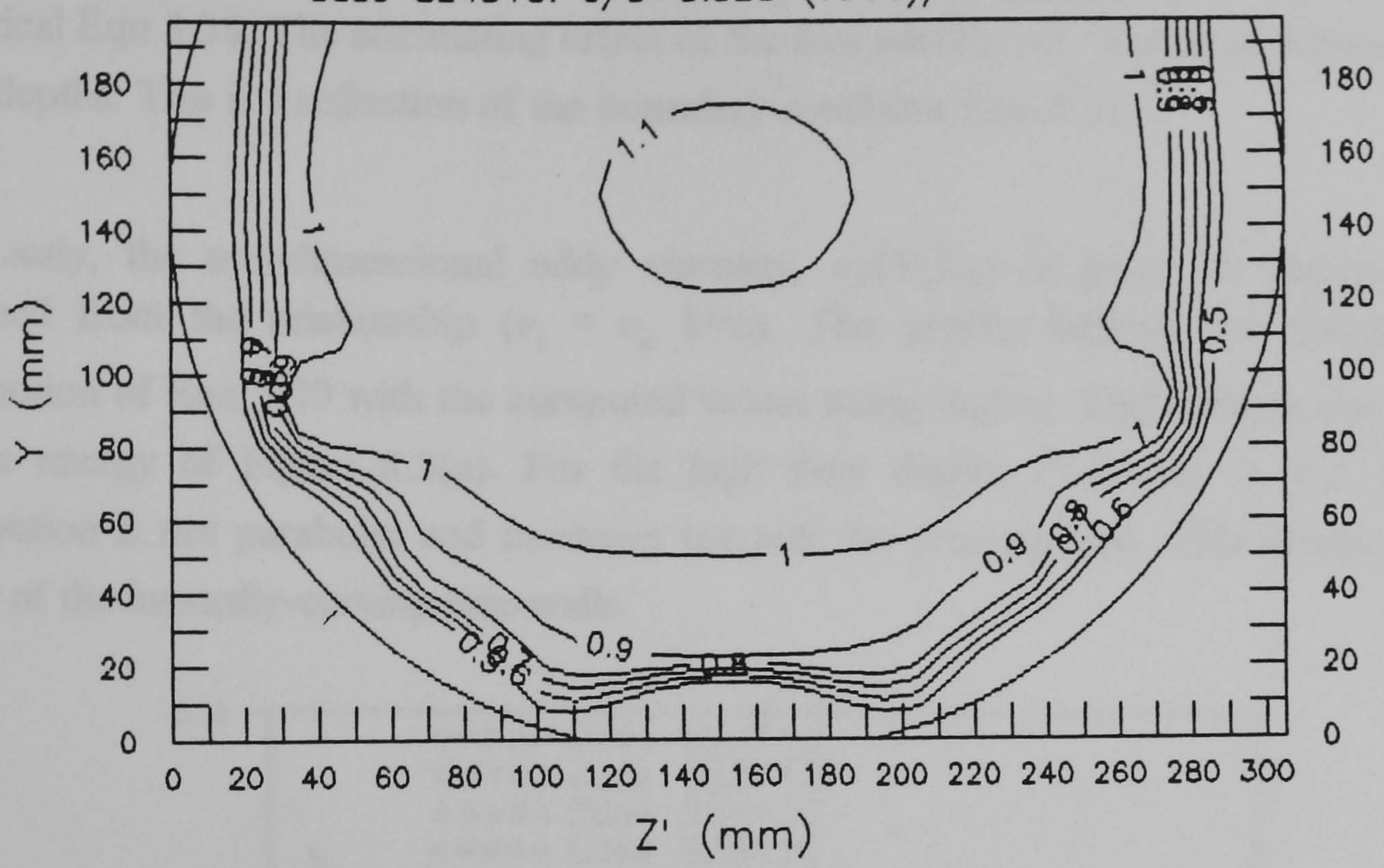

(h) Case S2431C

Figure 8.2 Cont. (h) Computed Mean Velocity Distribution U/U_m : Smooth Bed

8.3.2 Turbulence Parameters

The distributions of the normalised turbulence parameters, k/U_*^2, $\varepsilon Y_o/U_*^3$, $\nu_t/(Y_o U_*)$ and are given in Figures 8.3(a-c). The empirical profiles of Nezu and Nakagawa (1993) given in Eqns 3.37 - 3.39 are also plotted for comparison.

For the kinetic energy, k/U_*^2, there is a spread (higher in general) in the computed distributions for the different cases (Figure 8.3 a). The main deviations occur in the high depth flows, $(Yo+e)/D \geq 0.5$, where the inward curvature of the side-walls leads to an increase in the kinetic energy. The distributions are no longer two-dimensional. Also, the rate of kinetic energy decrease increases closer to the free surface - unlike the exponential decay of Eqn 3.37. This is due to the discretisation of the domain which leads to finite (lower) values at the free surface. However, in summary, the computed profiles are close to the empirical profile.

The dissipation rates in Figure 8.3(b) all collapse to one profile which lies very close to the empirical Eqn 3.38. The attenuating effect of the free surface on $\varepsilon Y_o/U_*^3$ is shown in the higher flow depths. This is a reflection of the boundary condition Eqn 3.35.

Lastly, the non-dimensional eddy viscosity, $\nu_t/(Y_o U_*)$ is given in Figure 8.3(c). It is obtained from the relationship ($\nu_t = c_\mu \, k^2/\varepsilon$). The profile follows the standard parabolic distribution of Eqn 3.39 with the computed values being higher. This reflects the scatter of the kinetic energy of Figure 8.3(a). For the high flow depths (Yo+e)/D $\geq$ 0.5, the $\nu_t/(Y_o U_*)$ distribution is not parabolic and increases towards the free surface. This shows the retarding effect of the inwardly-curving side-walls.

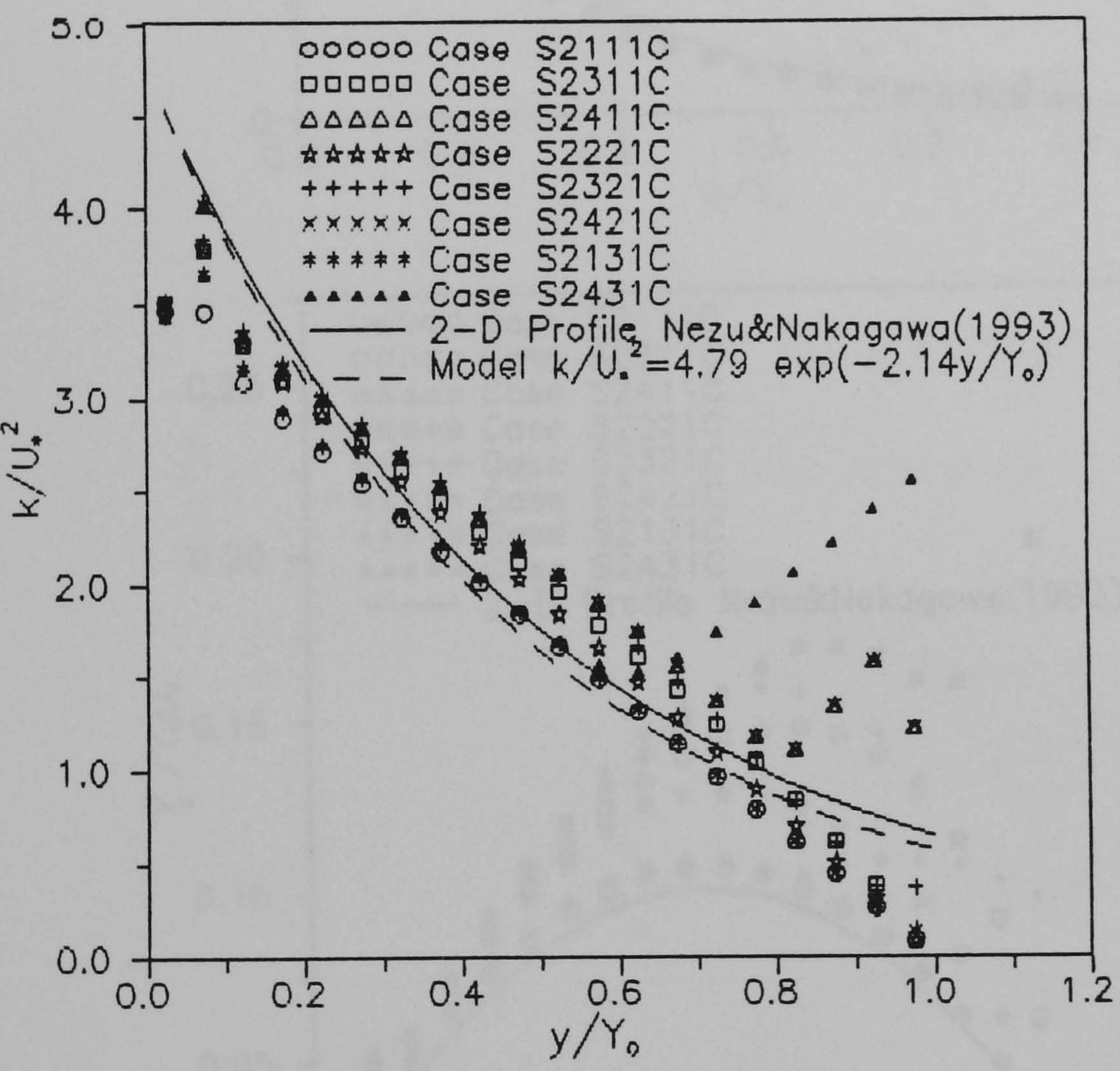

Figure 8.3 Normalised Turbulence Parameters. (a) Turbulent Kinetic Energy (k/U_*^2)

(b)

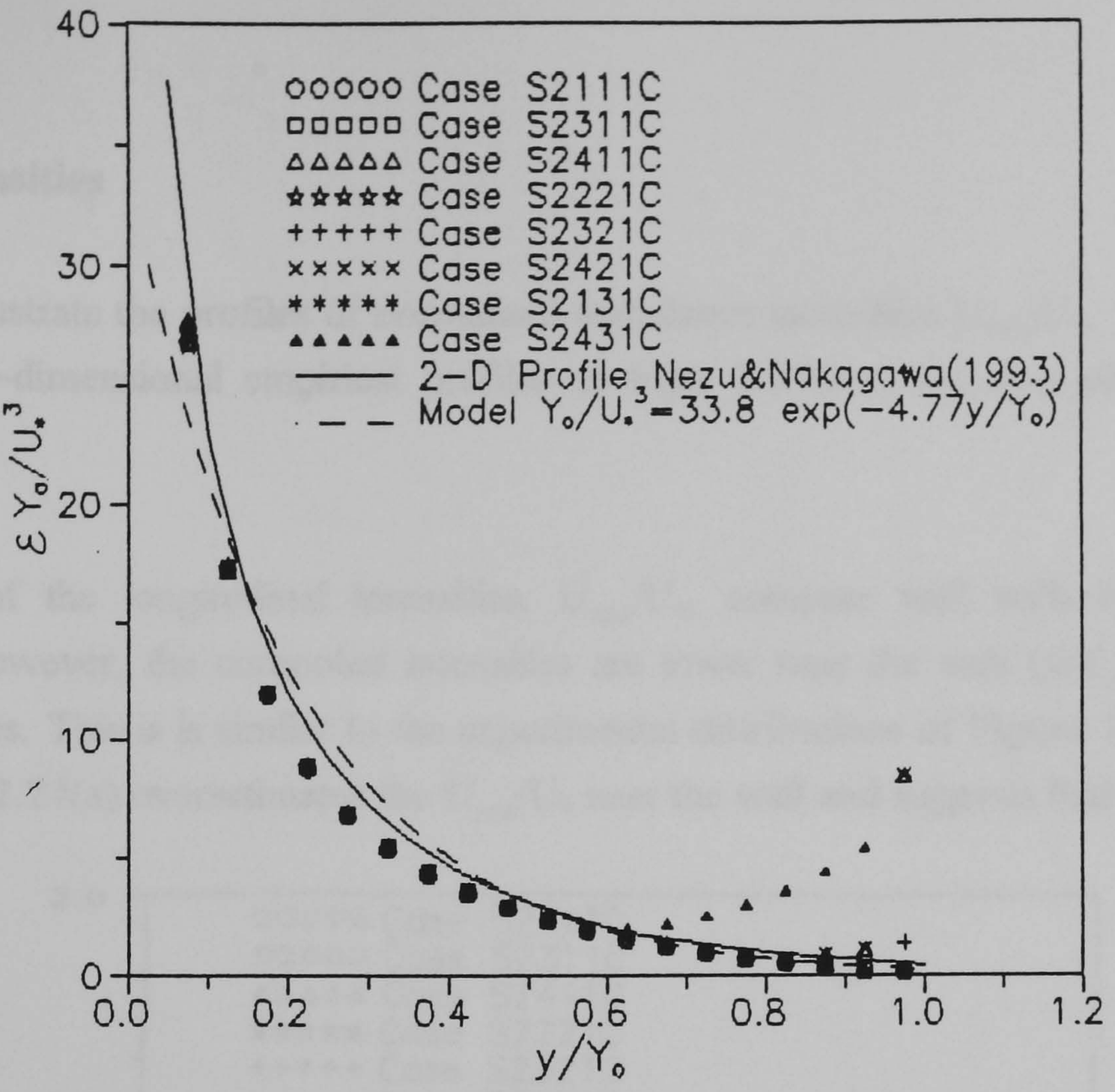

(c)

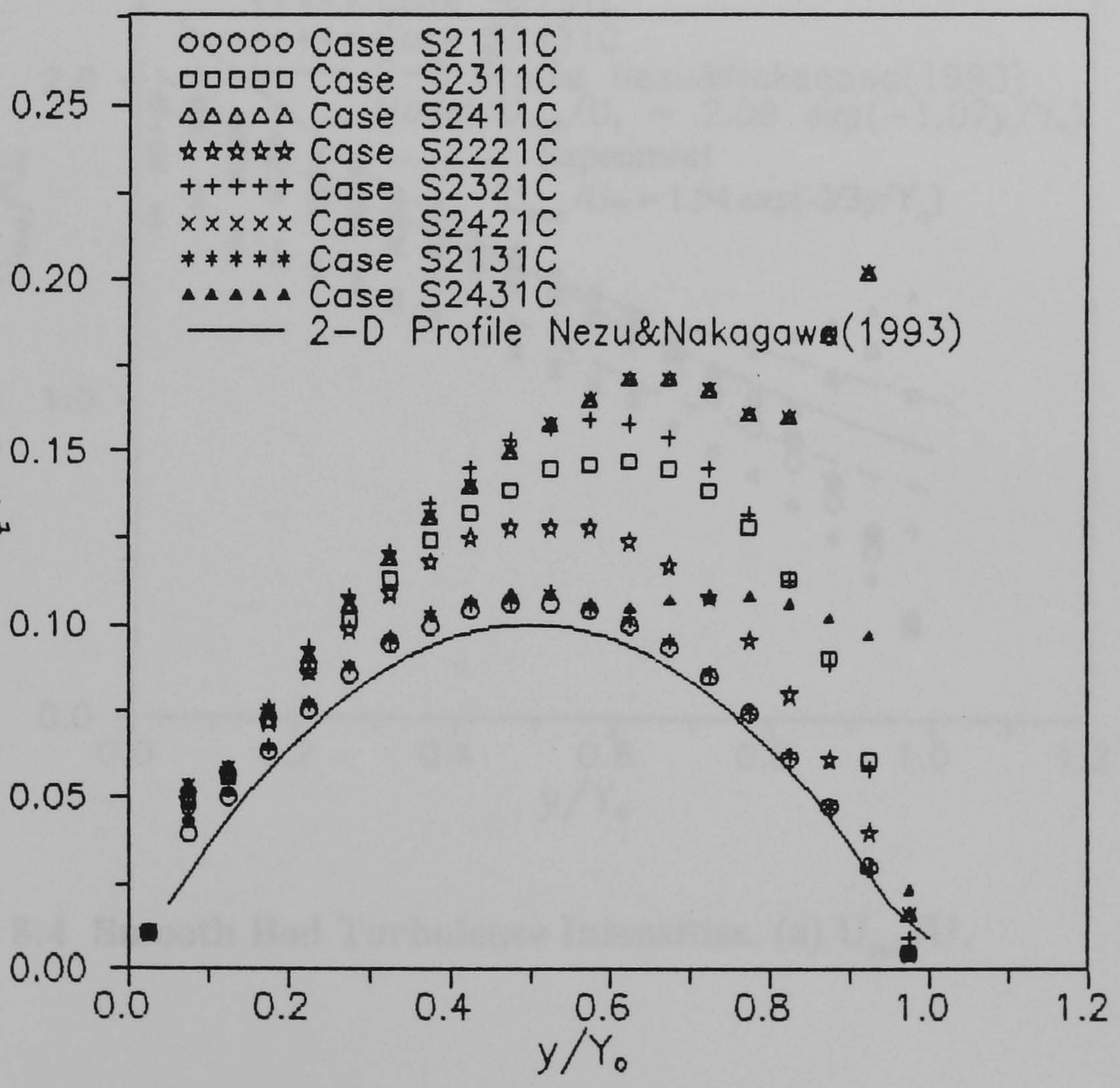

Figure 8.3Cont. Normalised Turbulence Parameters. (b) Rate of Dissipation ($\varepsilon Y_o/U_*^3$); (c) Eddy Viscosity (ν_t/Y_oU_*)

8.3.3 Turbulence Intensities

Figures 8.4(a-c) illustrate the profiles of normalised turbulence intensities U_{rms}/U_*, V_{rms}/U_*, and W_{rms}/U_*. The two-dimensional empirical profiles of Eqns 2.27(a-c) are also added for comparison.

The magnitudes of the longitudinal intensities, U_{rms}/U_*, compare well with the two-dimensional profile. However, the computed intensities are lower near the wall ($y/Y_o < 0.2$) than the empirical values. This is is similar to the experimental distributions of Figure 7.3. This thus indicates that Eqn 2.27(a) overestimates the U_{rms}/U_* near the wall and suggests that the

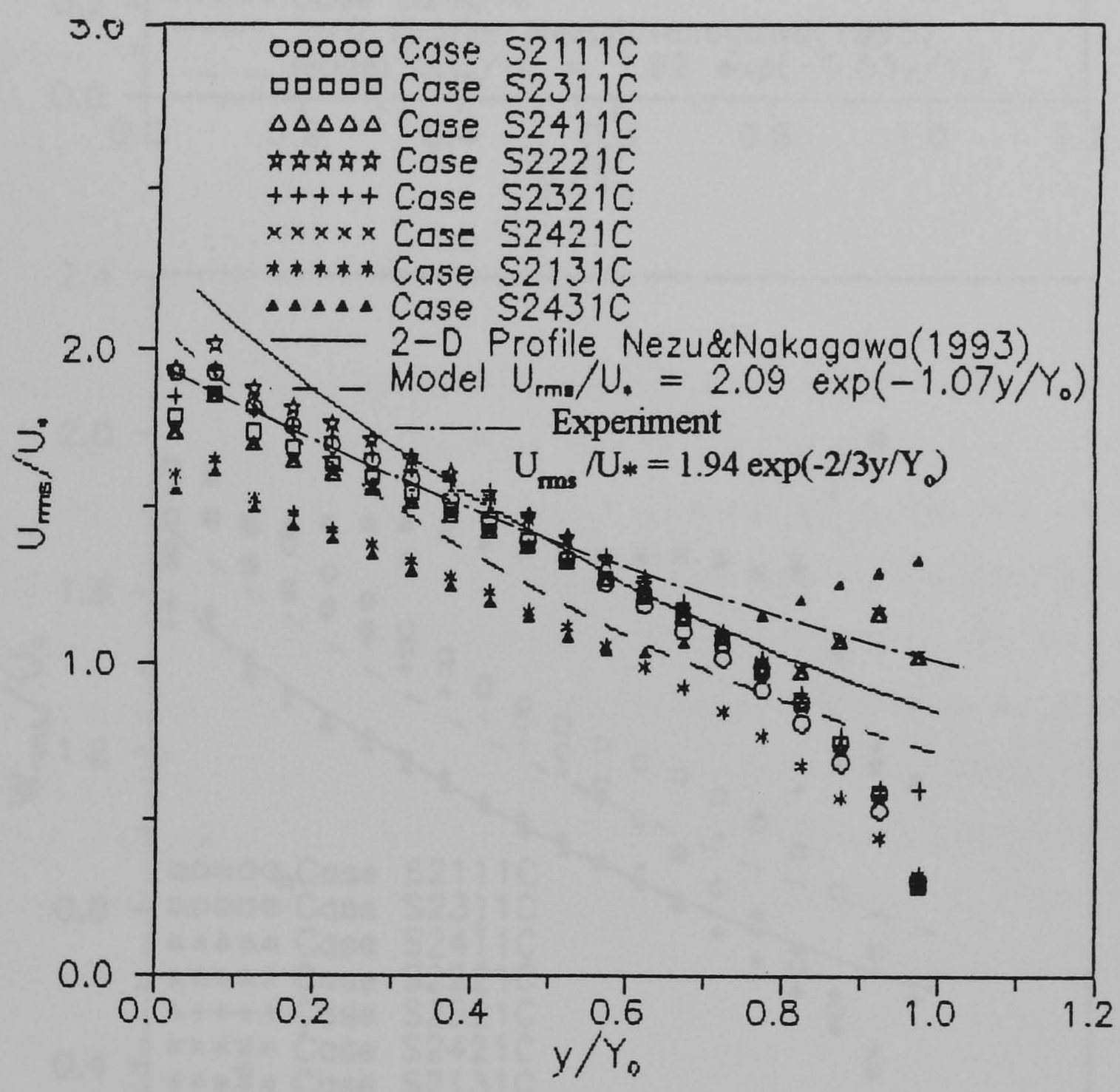

Figure 8.4 Smooth Bed Turbulence Intensities. (a) U_{rms}/U_*

(b)

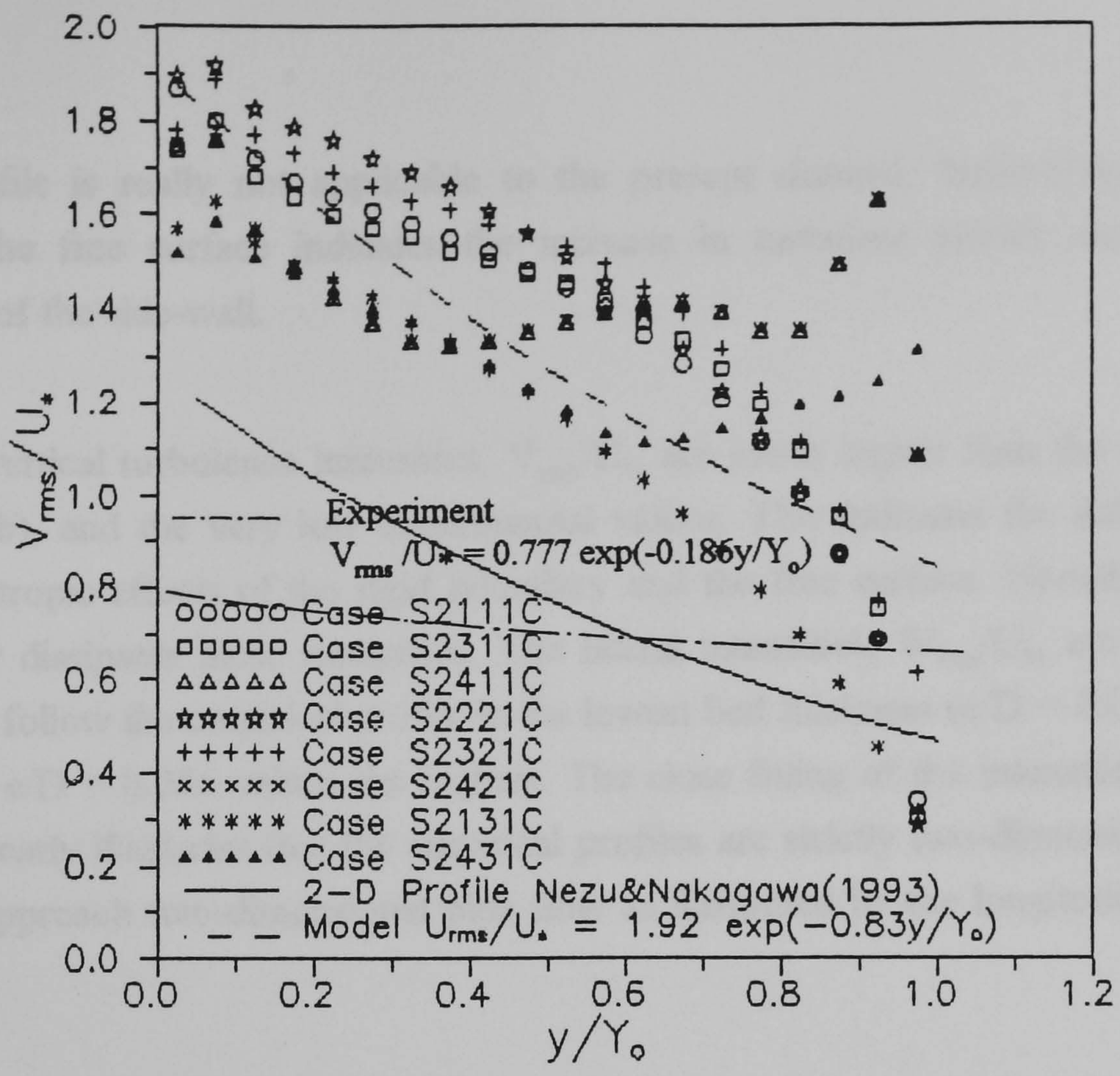

(c)

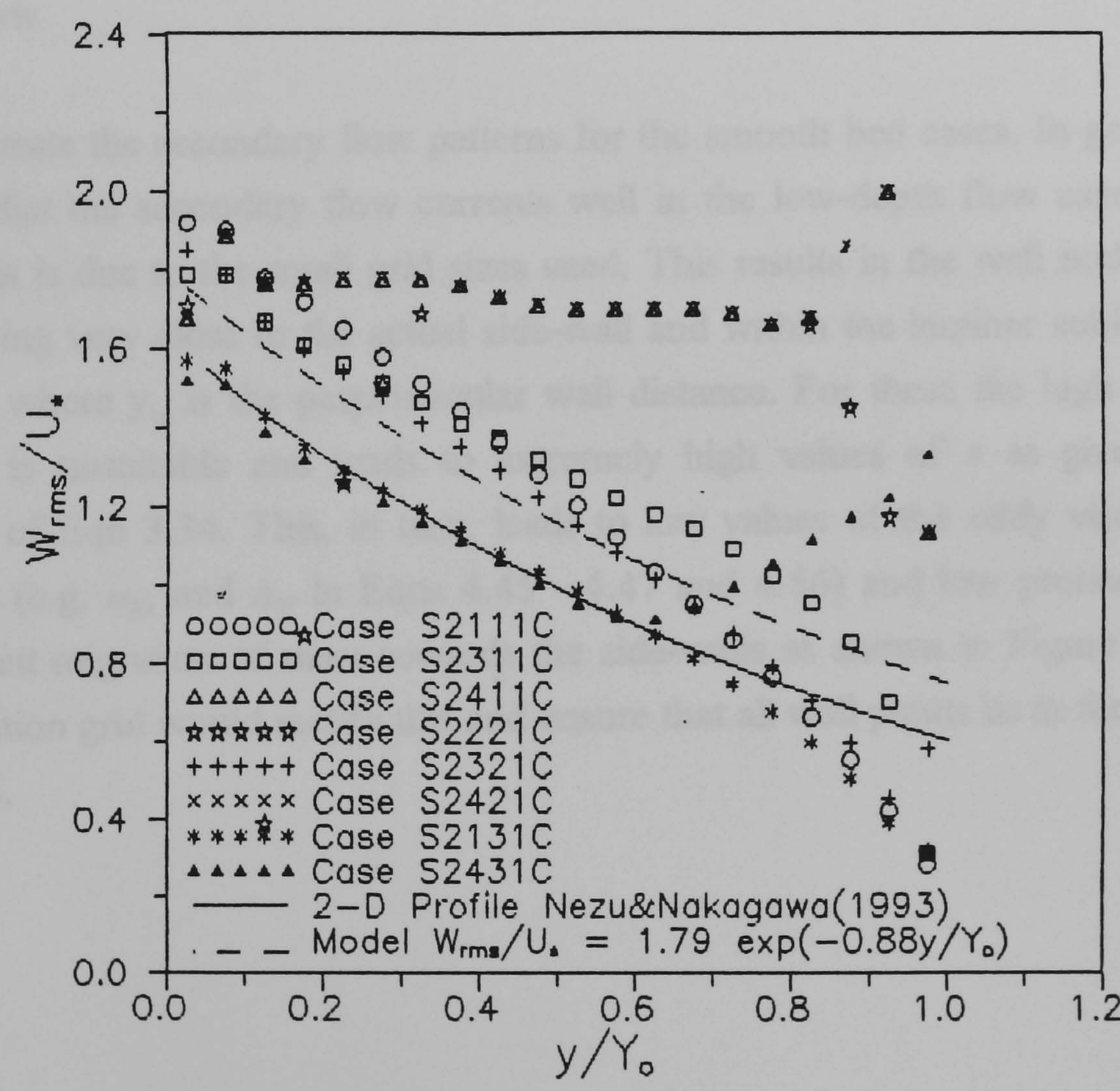

Figure 8.4 Cont. Smooth Bed Turbulence Intensities. (b) V_{rms}/U_* and (c) W_{rms}/U_*

two-dimensional profile is really not applicable to the present channel. Indeed the rise of intensities towards the free surface indicates the increase in turbulent activity due to the increasing proximity of the side-wall.

The computed vertical turbulence intensities, V_{rms}/U_*, are much higher than the empirical values of Eqn 2.27(b), and the very low experimental values. This indicates the difficulty in prescribing the anisotropic effects of the rigid boundary and the free surface. Nonetheless the free surface severely dissipates these intensities. The lateral intensities, W_{rms}/U_*, are given in Figure 8.4(c). These follow the empirical profile in the lowest bed thickness (e/D = 0.020). The rest are higher, with e/D = 0.285 values the highest. The close fitting of the intensities for the e/D = 0.020 cases clearly illustrates that the empirical profiles are strictly two-dimensional, and that the said flows approach two-dimensional pipe flow as illustrated by the longitudinal mean velocity plots.

8.3.4 Secondary Flow

Figures 8.5 illustrate the secondary flow patterns for the smooth bed cases. In general, the model does not predict the secondary flow currents well in the low-depth flow cases - when $(Y_o+e)/D < 0.5$. This is due to the small grid sizes used. This results in the wall nodes on the stepped side-wall being very close to the actual side-wall and within the laminar sublayer such that $y_w U_*/\nu < 11.6$, where y_w is the perpendicular wall distance. For these the high Reynolds number k-ε model is unsuitable and leads to extremely high values of ε as given by the boundary condition of Eqn 3.34. This, in turn, leads to low values of the eddy viscosity and variable coefficients (e.g. a_E, and a_W in Eqns 4.45 - 4.47 and 4.56) and low pressures at the wall, and hence a nett migration of mass towards the side-walls as shown in Figure 8.5(a). A body-fitted computation grid would rectify this and ensure that all wall points lie in the turbulent zone: $y_w U_*/\nu > 11.6$.

For the rest of the flows, there are two secondary flow cells on either side of the channel centreline - a top and a bottom cell. This is similar to the patterns detected by experiment (see Figures 7.2). The top cell covers most of the flow depth and is centred at (y+e)/D ~ 0.35. These currents are weak and of the order of U_{sec}/U_{max} ~ 0.01. They carry high momentum fluid towards the side-walls away from the channel centreline - causing the upward bulging of the primary velocity contours.

The bottom cell lies on the bed and carries high momentum fluid away from the channel centreline towards the corner. This was shown by the bulging of the primary velocity contours upwards at the channel centreline, and towards the corner, and similar to the slight bulging in experimental Cases S2211 and S2121. It has much stronger currents with a magnitude of the order U_{sec}/U_{max} ~ 0.1. The small region of action of the bottom currents means that the effect on the primary velocity is limited and the contour bulging in mild.

It is, therefore, clear that the non-linear k-ε model allows the model to predict the turbulence anisotropy which leads to the secondary flow. This is illustrated in Figure 2.6. Indeed Eqns 6.8 - 6.13 show that the momentum source terms for the vertical and transverse directions are present when the standard k-ε model would have set them to zero. The said normal stress anisotropy is an expression of the pressure distribution as expressed by the stress tensor of Eqn 2.7.

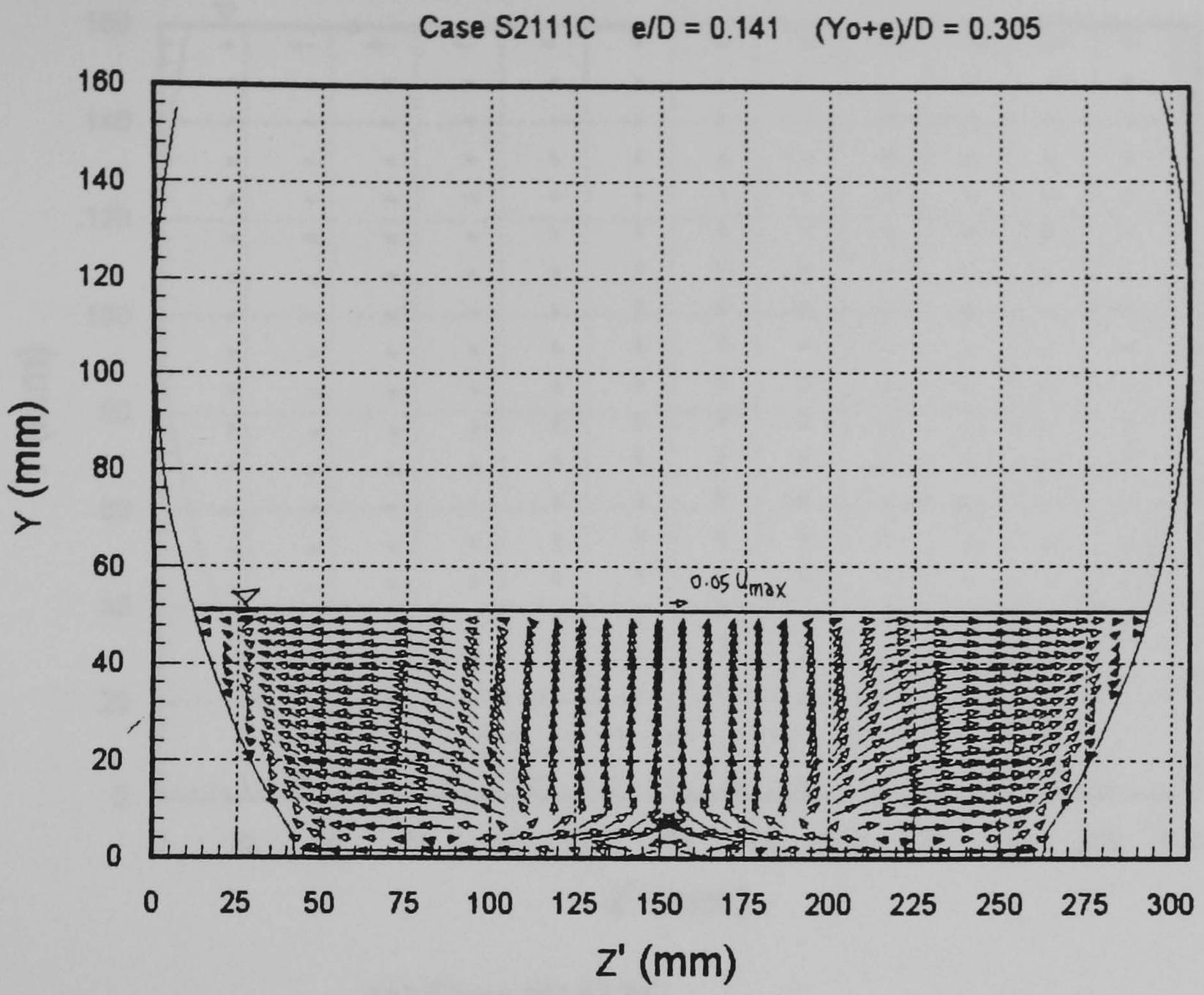

(a) Case S2111C

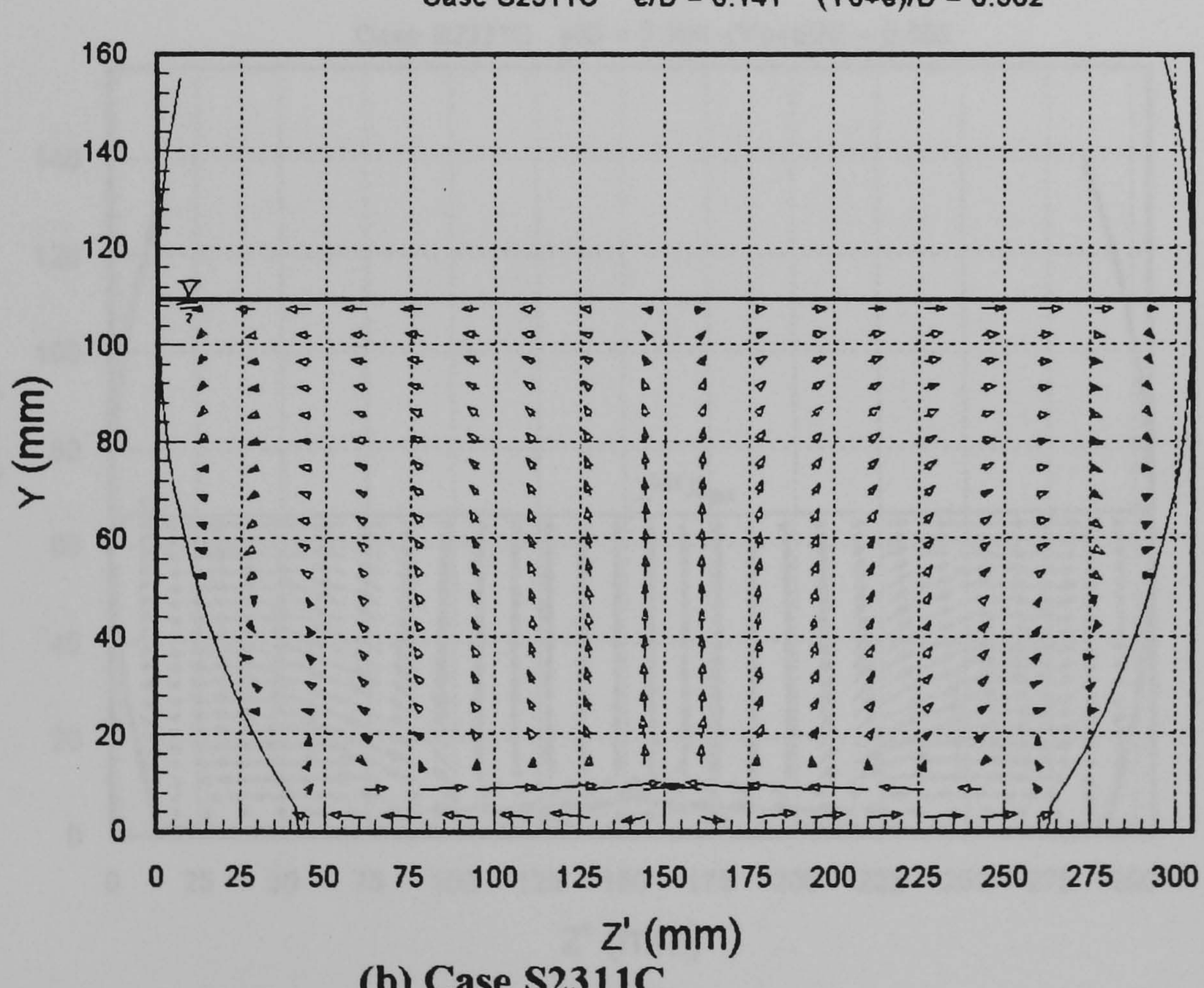

(b) Case S2311C

Figure 8.5 (a - b) Computed Secondary Flow: Smooth Bed

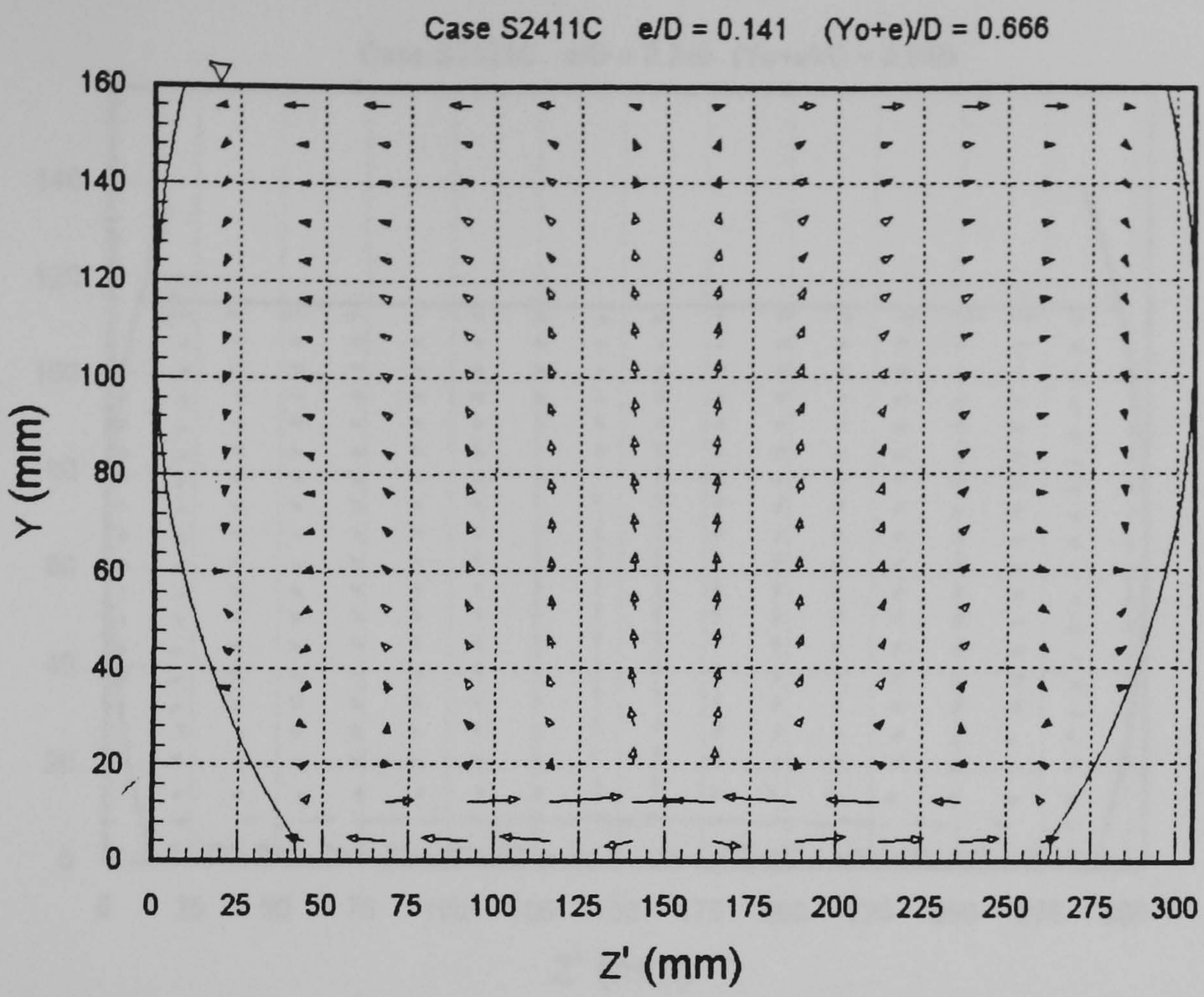

(c) Case S2411C

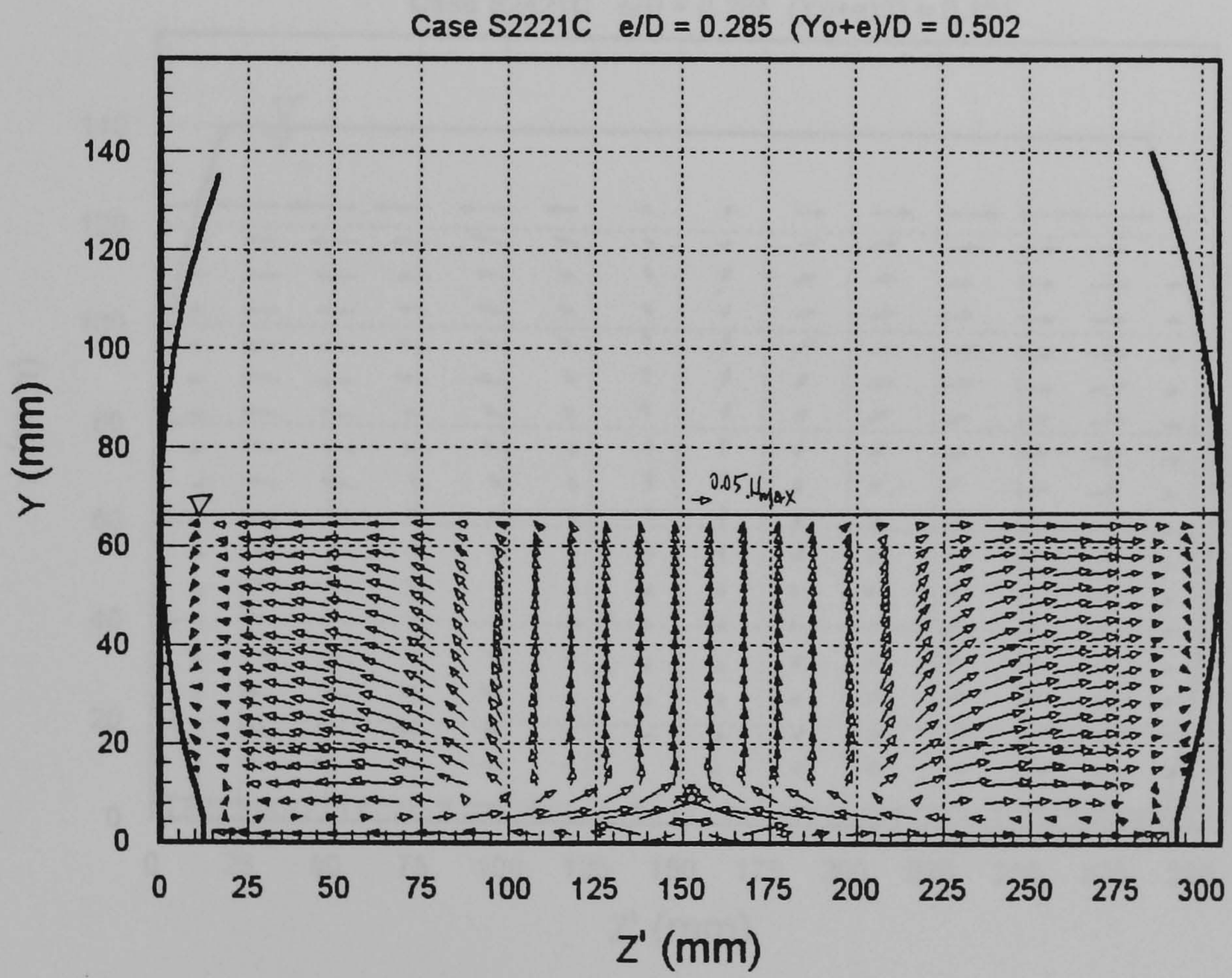

(d) Case S2221C

Figure 8.5 Cont. (c - d) Computed Secondary Flow: Smooth Bed

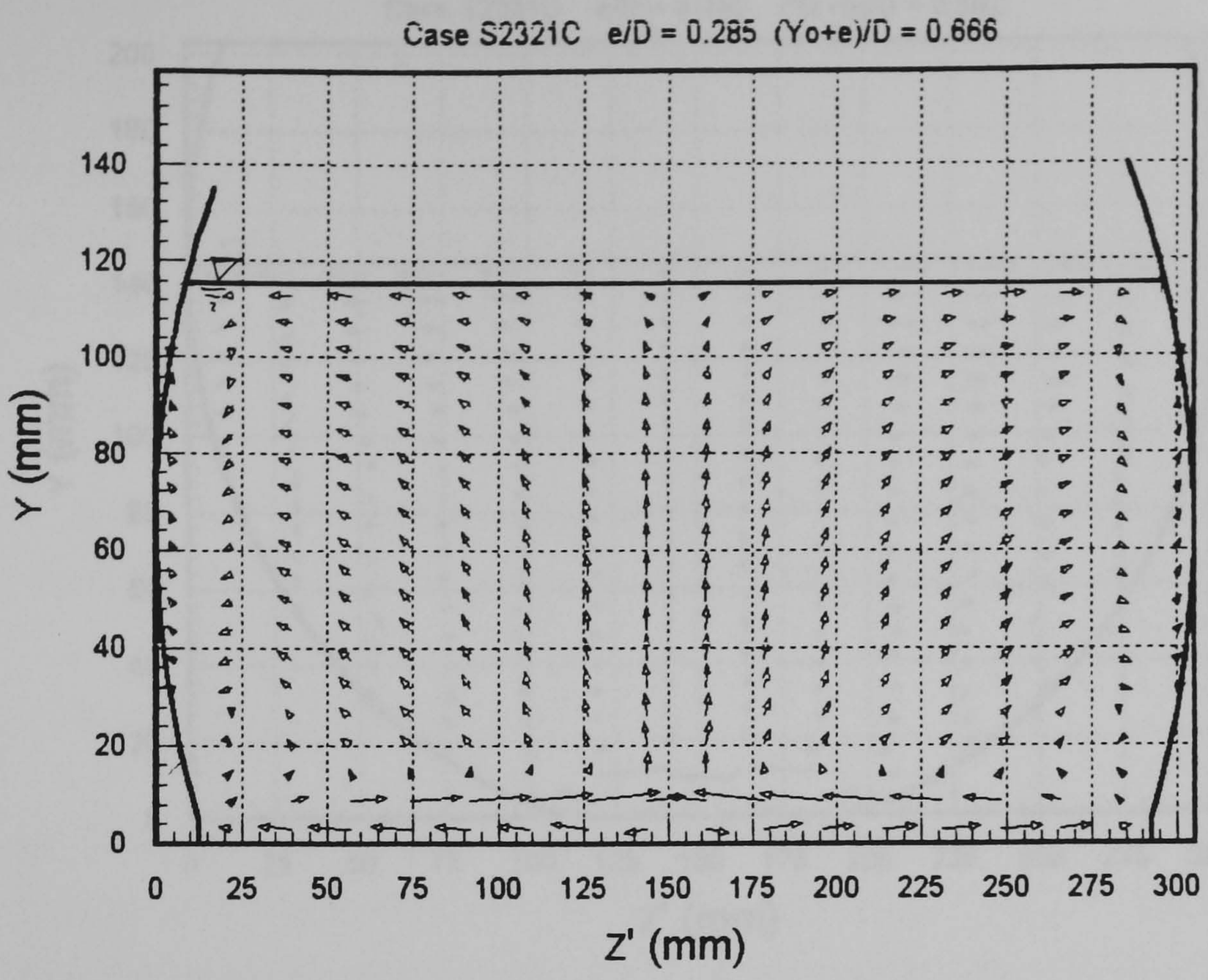

(e) Case S2321C

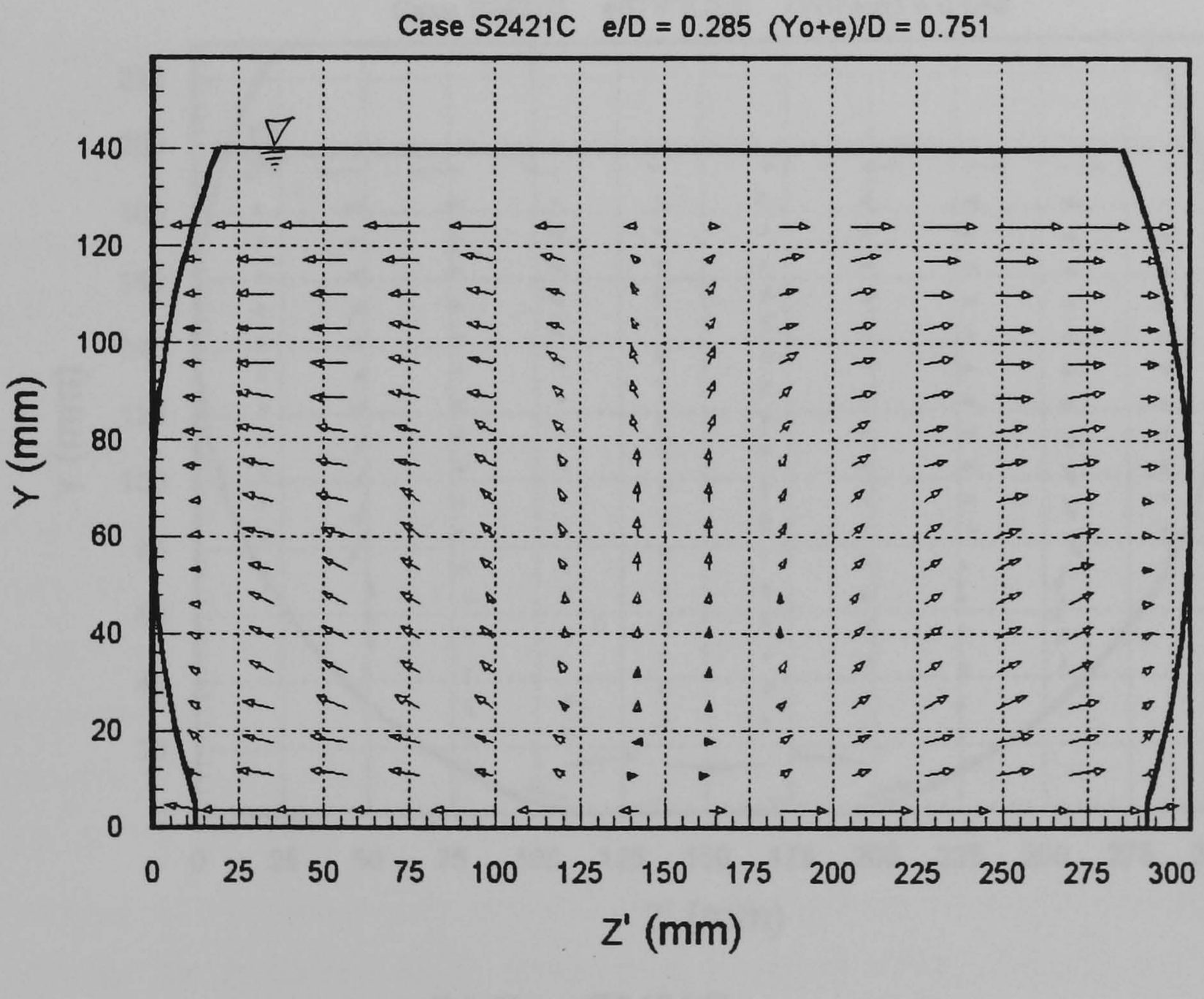

(f) Case S2421C

Figure 8.5 Cont. (e - f) Computed Secondary Flow: Smooth Bed

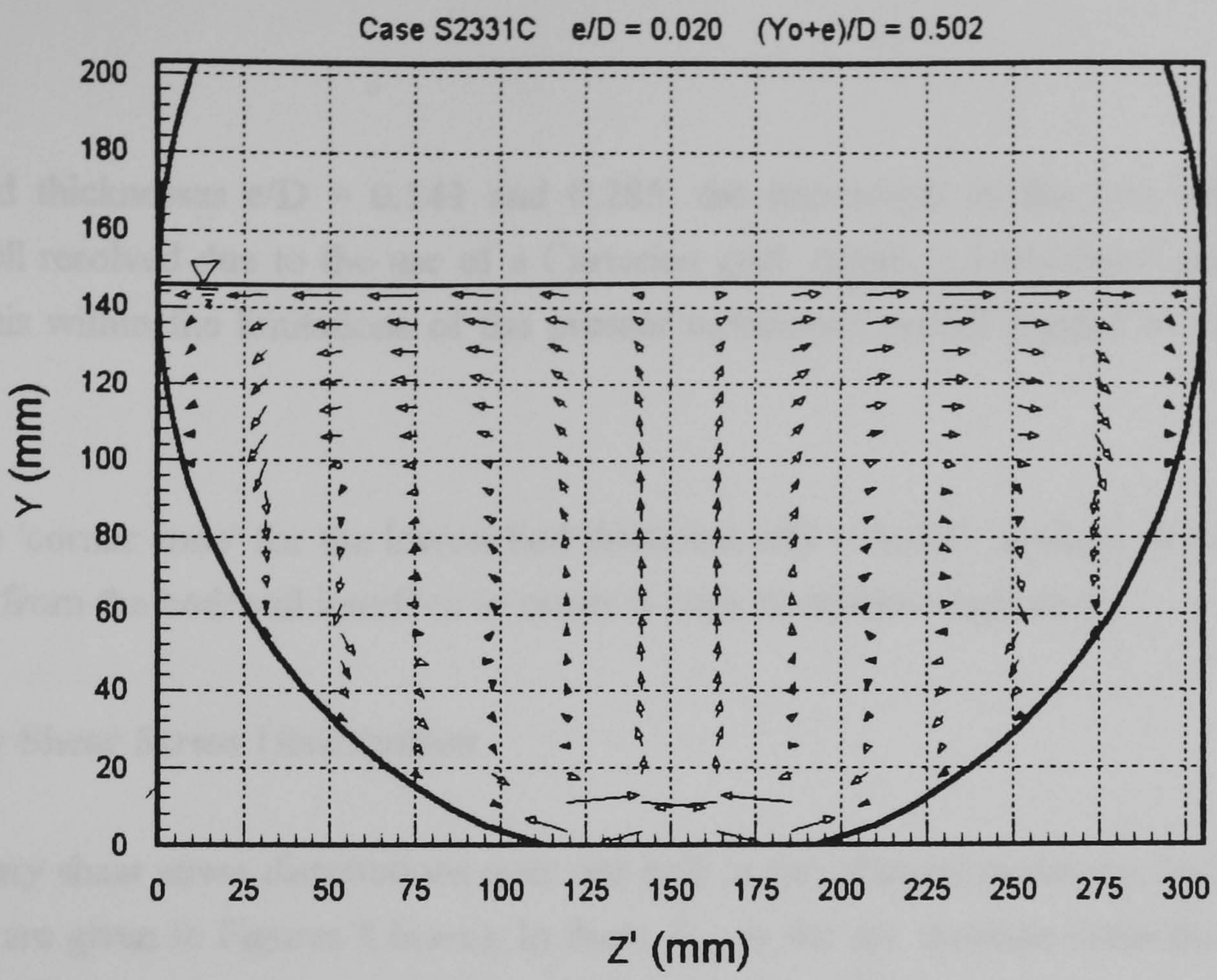

(g) Case S2331C

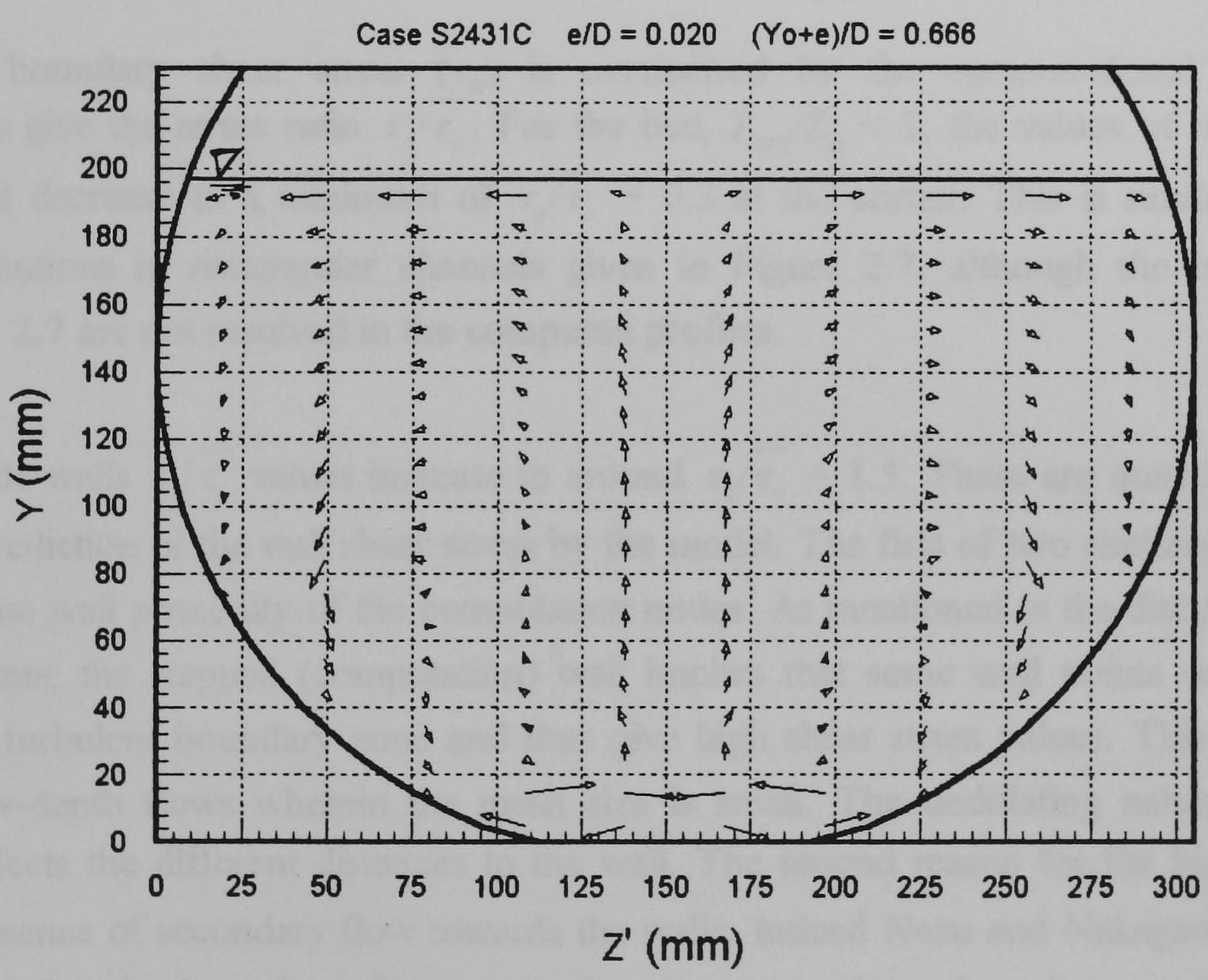

(h) Case S2431C

Figure 8.5 Cont. (g - h) Computed Secondary Flow: Smooth Bed

For the bed thicknesses e/D = 0.141 and 0.285, the interaction of the two cells at the corner is not well resolved due to the use of a Cartesian grid. Again, a body-fitted grid system might resolve this within the limitations of the present turbulence model applied in the corner zone.

There is no 'corner zone' for the lowest bed thickness e/D = 0.020. Instead, the two cells meet farther up from the bed/wall interface to create a zone of relative stagnation.

8.3.4 Boundary Shear Stress Distribution

The boundary shear stress distributions over one half of the channel perimeter for the three bed thicknesses are given in Figures 8.6(a-c). In these Z_{arc} is the arc distance from the channel centreline ALONG the perimeter, and Z_o is the half bed width. The corner is thus represented by $Z_{arc}/Z_o = 1$.

The local boundary shear stress (τ_o) is normalised by the cross-sectional average $\overline{\tau_o} = \rho g R S_f$ to give the stress ratio $\tau_o/\overline{\tau_o}$. For the bed, $Z_{arc}/Z_o < 1$, the values of $\tau_o/\overline{\tau_o}$ are nearer unity and decrease to a minimum of $\tau_o/\overline{\tau_o} \sim 0.3$ at the corner. This is similar to the measured distributions in rectangular channels given in Figure 2.7, although the inflexions shown in Figure 2.7 are not resolved in the computed profiles.

Over the side-walls $\tau_o/\overline{\tau_o}$ values increase to around $\tau_o/\overline{\tau_o} = 1.5$. These are quite high and reflect an overprediction of the wall shear stress by the model. The first of two explanations for this is the extreme wall proximity of the computation nodes. As mentioned in the discussion on secondary currents, the stepped (computation) wall implies that some wall points do not lie within the fully turbulent boundary zone and thus give high shear stress values. This is more acute in the low-depth flows wherein the mesh size is small. The undulating nature of the distributions reflects the different distances to the wall. The second reason for the high $\tau_o/\overline{\tau_o}$ values is the presence of secondary flow towards the walls. Indeed Nezu and Nakagawa(1993) have pointed out that the boundary shear stress rises in zones where there is secondary flow towards the boundary.

Table 8.1 (Column 10) gives values of the stress ratio averages integrated over the whole channel perimeter. These are given by

$$[\frac{\tau_o}{\overline{\tau_o}}]_{\text{integrated}} = \frac{1}{1/2P} \int_0^{1/2\,P} \frac{\tau_o}{\overline{\tau_o}} \; dZ_{arc} \qquad (8.1)$$

where P is the total wetted perimeter. The integration of $\tau_o/\overline{\tau_o}$ is performed numerically. These values are high and represent an over prediction. As illustrated by Figures 8.6, the bulk of this overprediction arises from the high $\tau_o/\overline{\tau_o}$ values over the side-walls.

The shear force on the side-walls is given by integrating the shear distributions only over the side-walls in the manner of Eqn 8.1. This integrated mean value is then multiplied by $\overline{\tau_o}$ to yield the wall shear force SF_w - given in Column 12 of Table 8.1. The wall shear force ratio (SF) is given by

$$SF = \frac{SF_w}{SF_T} = \frac{SF_w}{\overline{\tau_o}\,(1/2\,P)}. \qquad (8.2)$$

These are given in Column 13 of Table 8.1.

The values of SF are of the order of 0.5 - 0.8 for bed thicknesses e/D = 0.141 and 0.285. These are as expected although slightly higher than those predicted by Knight *et al*'s (1994) empirical profile of Eqns 2.40 - 2.42. This is similar to the SF values of Chapter 7, and arises as a result of the difficulty of defining the aspect ratio in the present channel. SF values of 1.19 and 1.21 are given for the two cases of bed thickness e/D = 0.020. These are spurious values as the wall shear force is greater than the total shear force! They indicate the seriousness of the overprediction of the side-wall shear stress mentioned above. It should also be noted that these large values are a result of the relatively large side-wall perimeter which strongly influences the SF values.

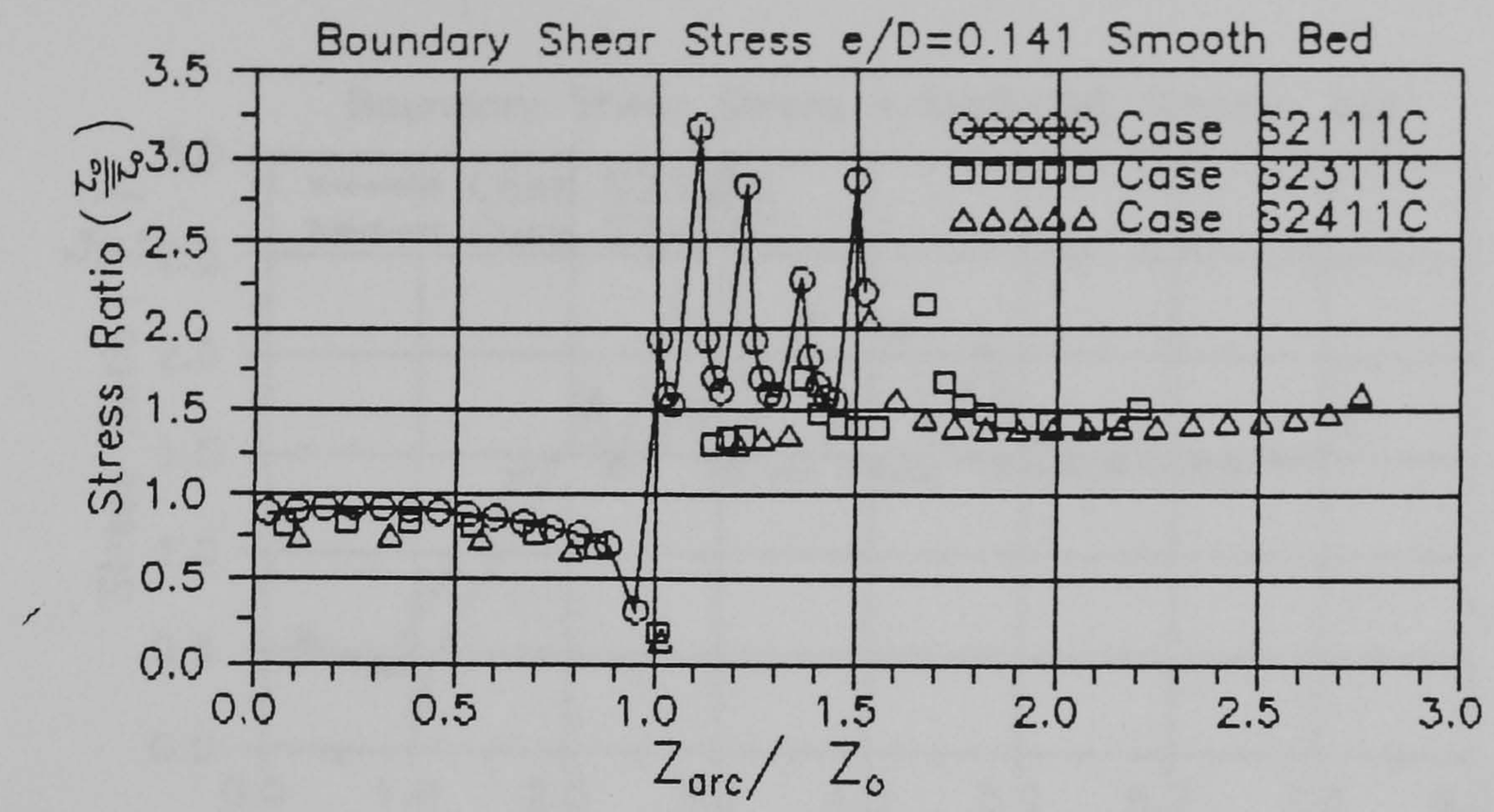

(a) Bed Thickness e/D = 0.141

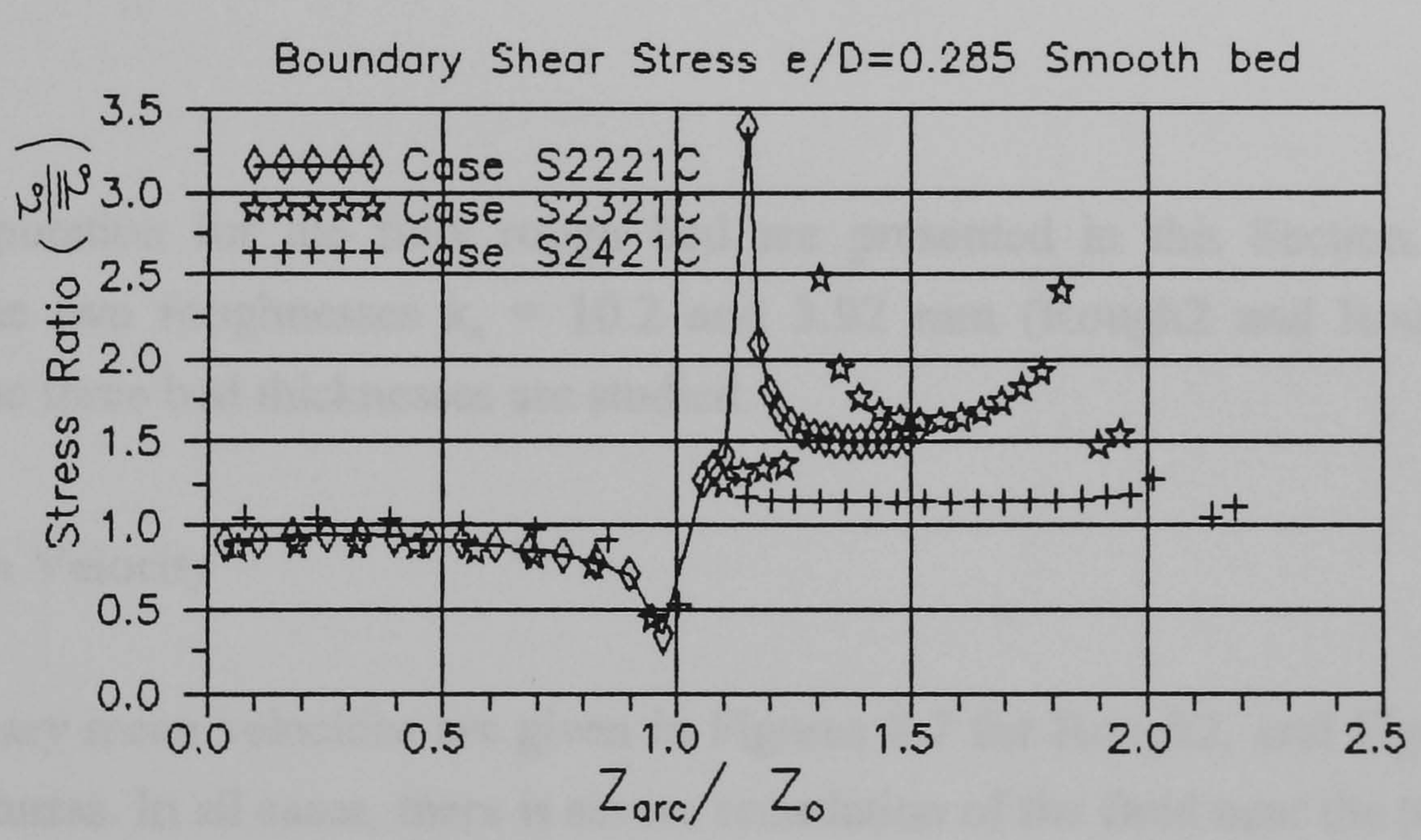

(b) Bed Thickness e/D = 0.285

Figure 8.6 (a - b) Computed Boundary Shear Stress: Smooth Bed

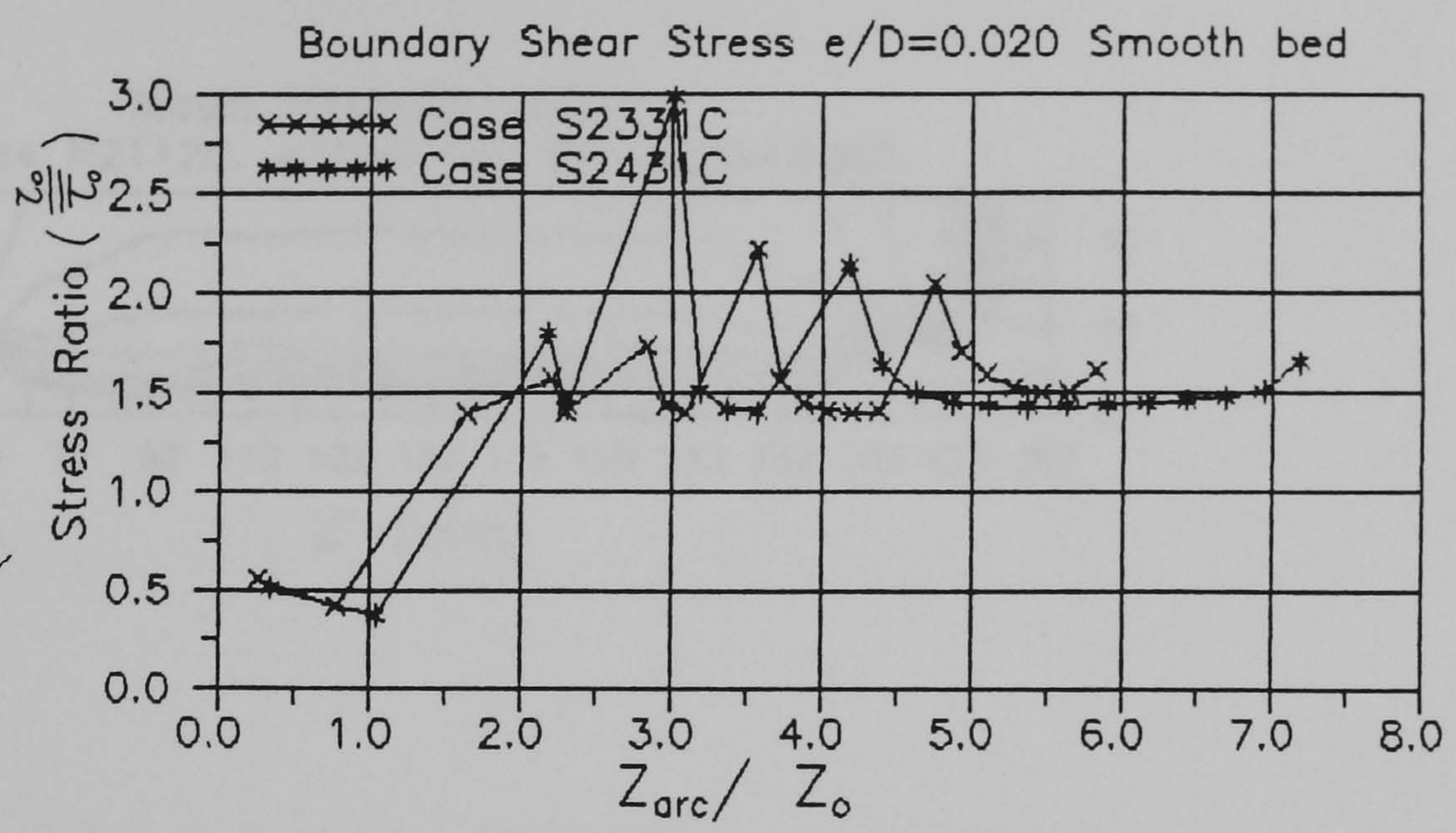

(c) Bed Thickness e/D = 0.020

Figure 8.6 Cont. (c) Computed Boundary Shear Stress: Smooth Bed

8.4 The Rough Bed

The results of computation for the fully rough bed are presented in this Section. As detailed in Table 8.1, the two roughnesses k_s = 10.2 and 3.92 mm (Rough2 and Rough3 respectively) are used. The three bed thicknesses are studied.

8.4.1 Longitudinal Mean Velocity

The normalised primary mean velocities are given in Figures 8.7 for Rough2, and Figures 8.8 for Rough3 bed roughness. In all cases, there is severe retardation of the fluid near the bed - as with previous studies (e.g. Hinze 1973, and Naot 1984). This leads to raised contours which bulge upwards towards the free surface. In low-depth flows the velocity maxima are dipped and occur near the side-walls away from the influence of the bed roughness - at a depth of y/Y_o= 0.7. As the flow depth is increased, the maxima move towards the channel centreline. In these flows, the velocities bulge towards the corner along the geometric bed/wall symmetry line.

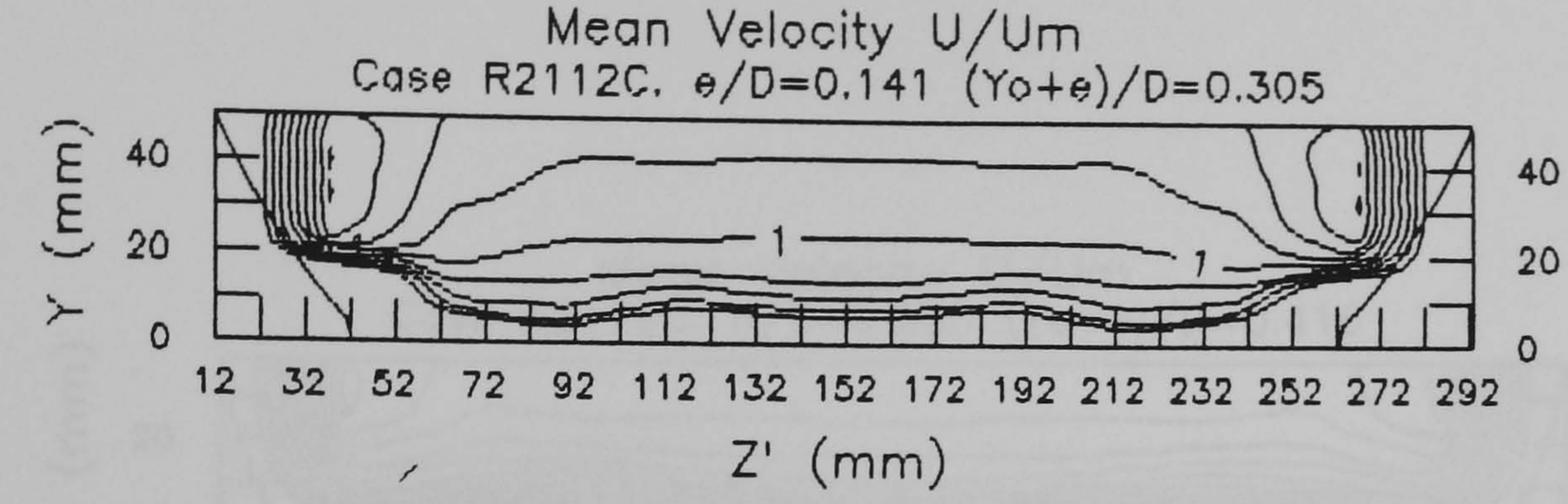

(a) Case R2112C

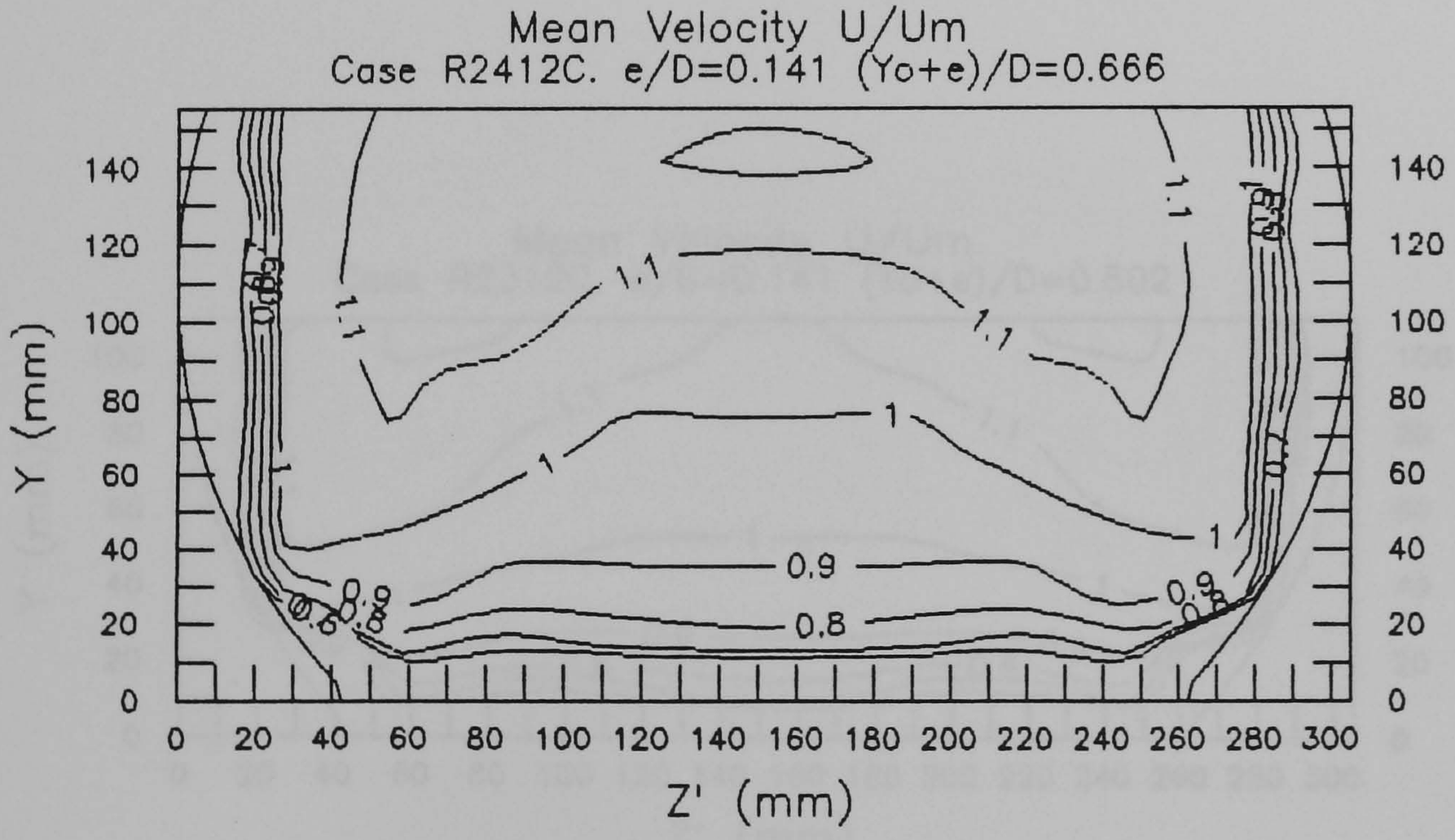

(b) Case R2412C

Figure 8.7 (a - b) Computed Mean Velocity Distribution U/U_m : Rough2

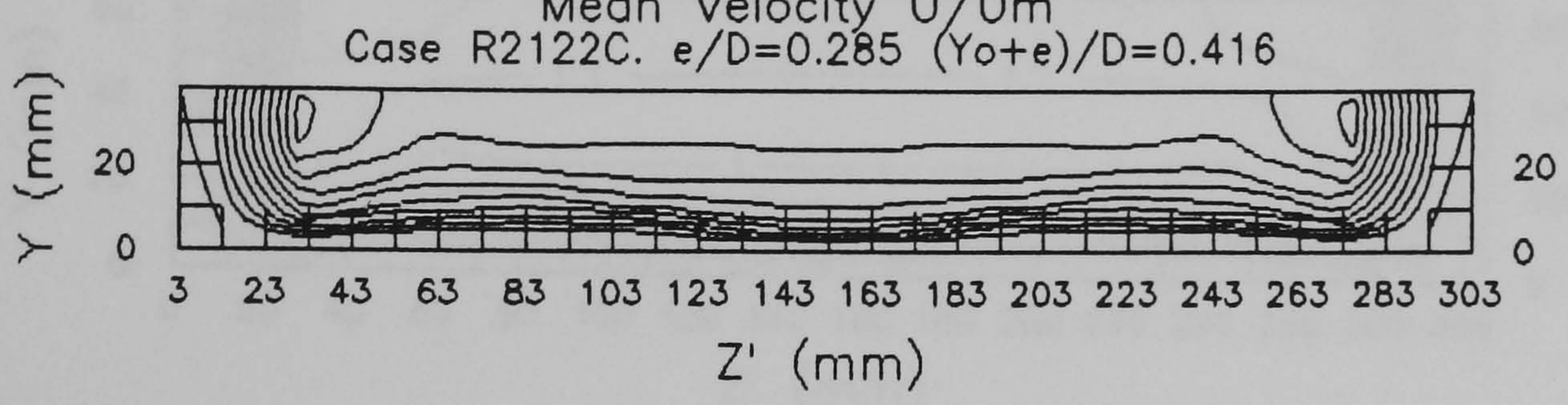

(c) Case R2122C

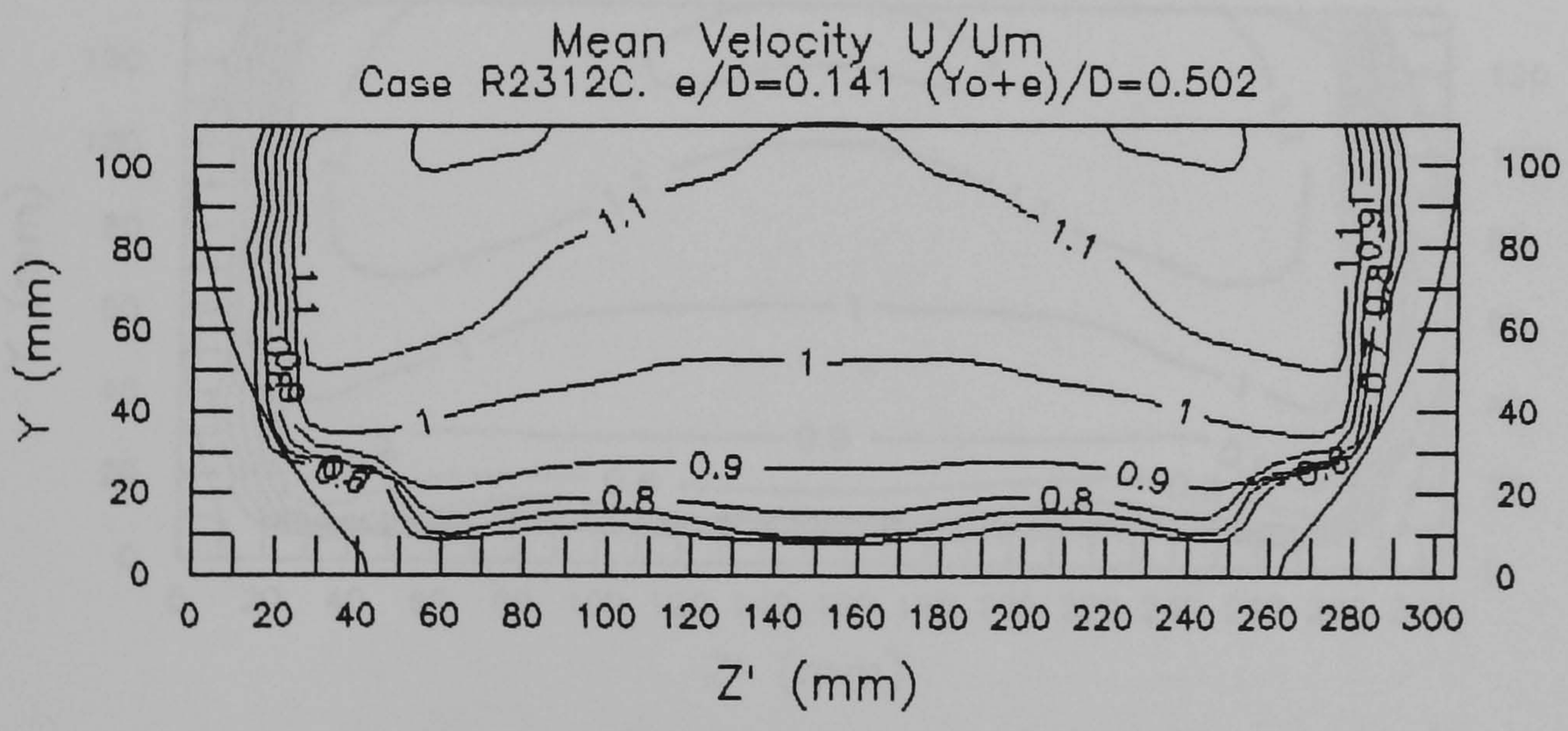

(d) Case R2312C

Figure 8.7 Cont. (c - d) Computed Mean Velocity Distribution U/U_m : Rough2

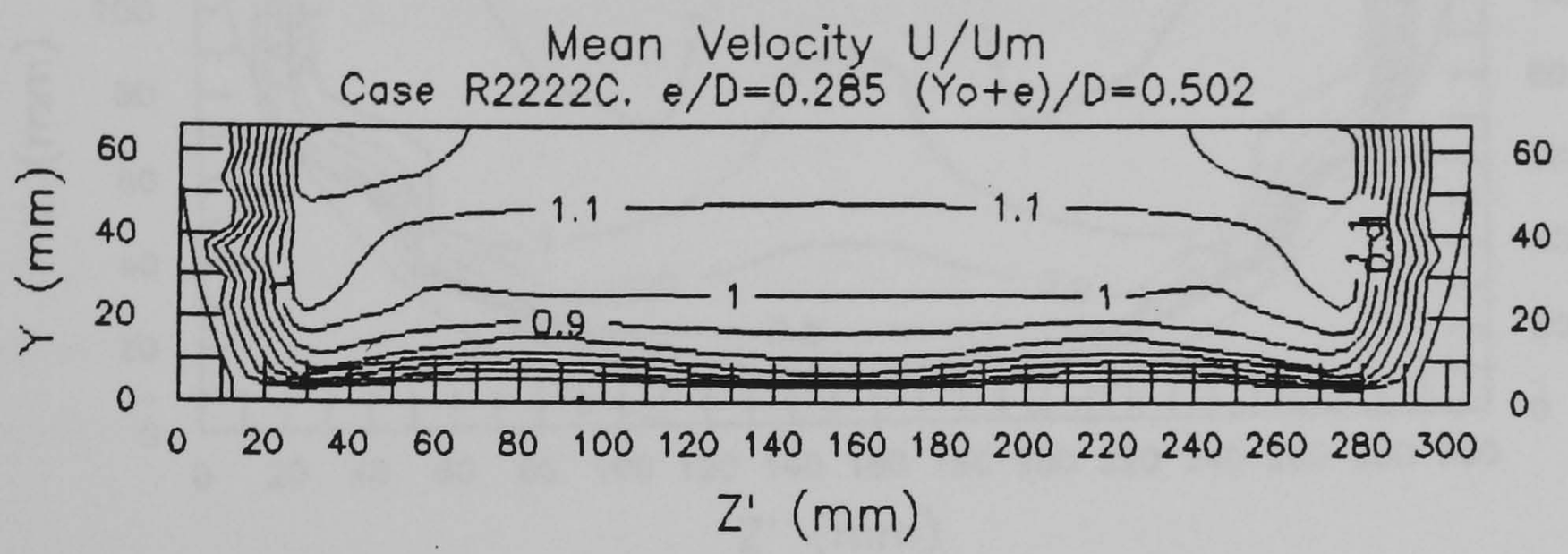

(e) Case R2222C

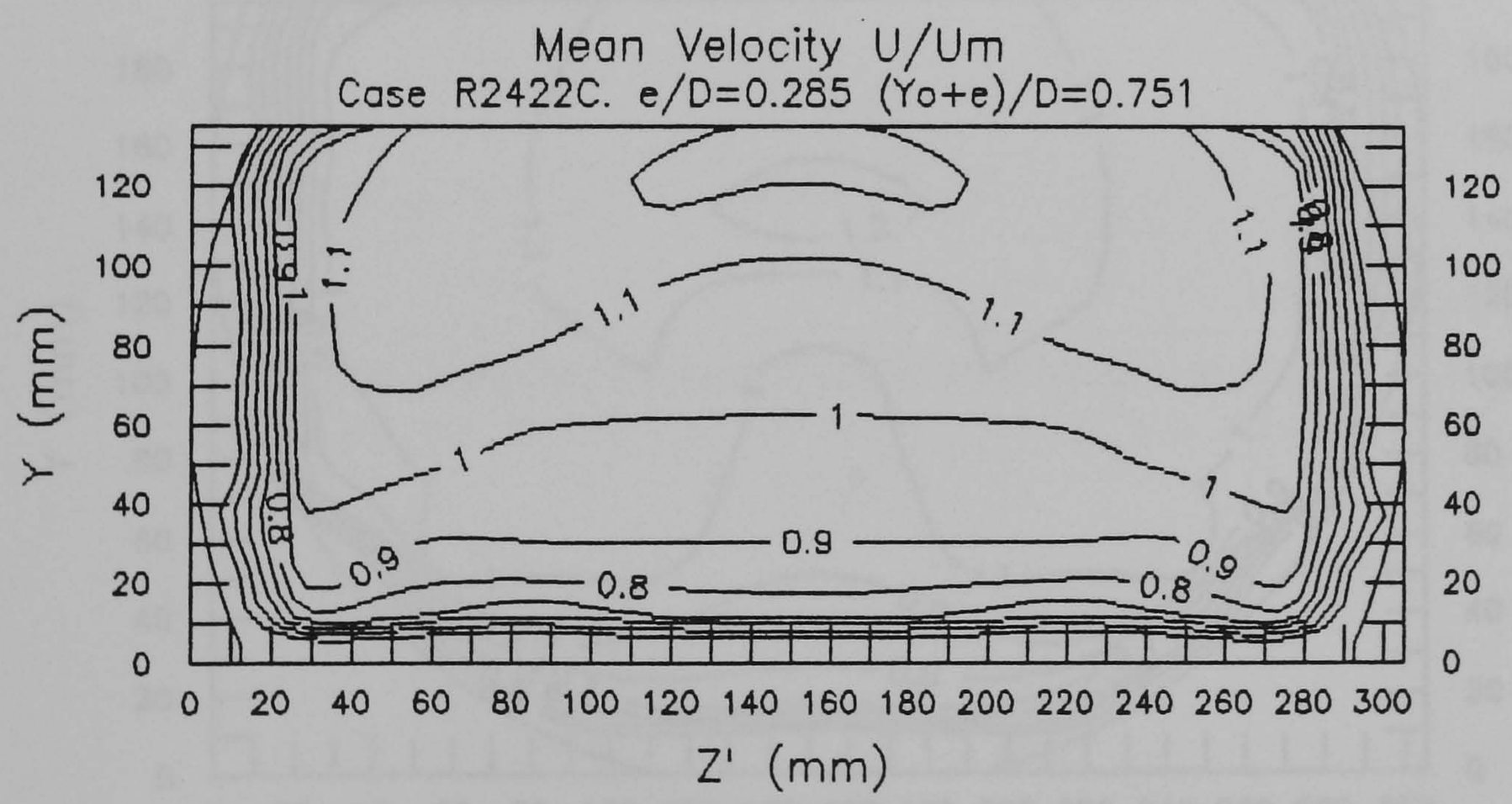

(f) Case R2422C

Figure 8.7Cont. (e - f) Computed Mean Velocity Distribution U/U_m : Rough2

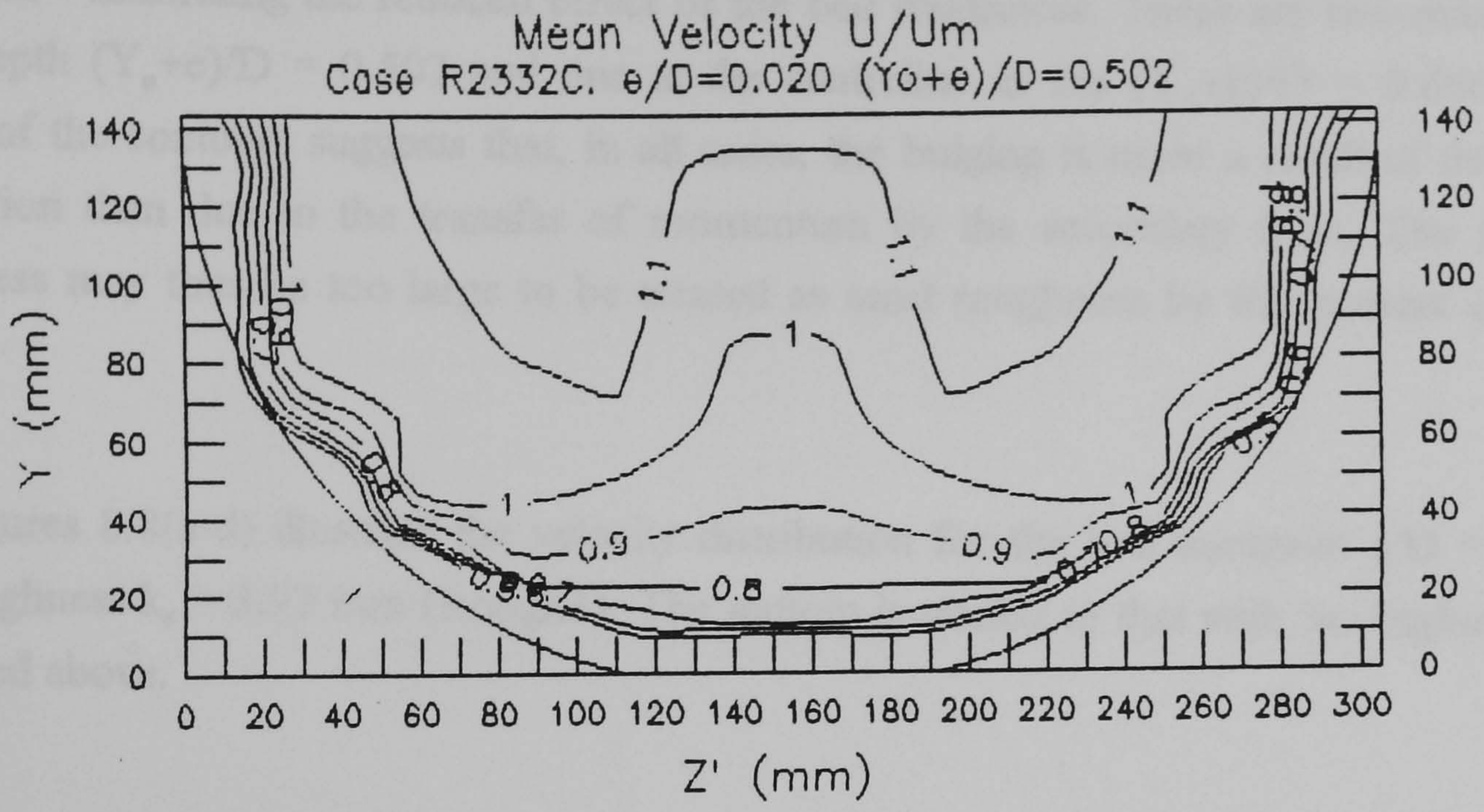

(g) Case R2332C

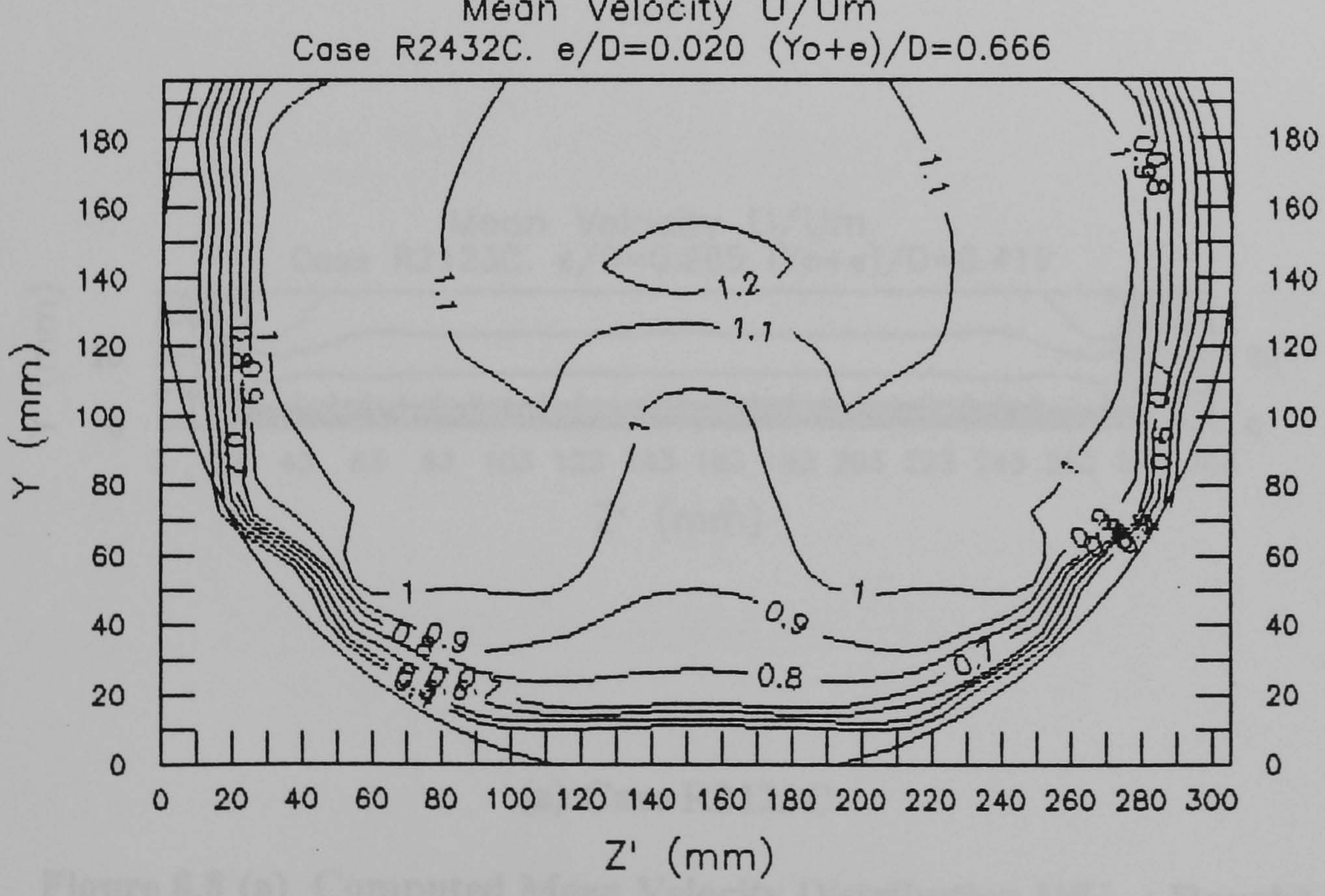

(h) Case R2432C

Figure 8.7 Cont. (g - h) Computed Mean Velocity Distribution U/U_m : Rough2

For the low bed thickness e/D = 0.020, the velocity maxima occur nearer the channel centreline - illustrating the reduced effect of the bed roughness. There are two maxima for the flow depth $(Y_o+e)/D = 0.502$ and one at the centreline in the $(Y_o+e)/D = 0.666$ flow. The nature of the contours suggests that, in all cases, the bulging is more a result of the direct bed retardation than due to the transfer of momentum by the secondary flow. The relative bed roughness may thus be too large to be treated as sand roughness by the present computation model.

Figures 8.8(a-d) illustrate the velocity distribution for the bed thickness e/D = 0.285 and bed roughness k_s = 3.92 mm (Rough3). The pattern is similar to that with the higher roughness described above.

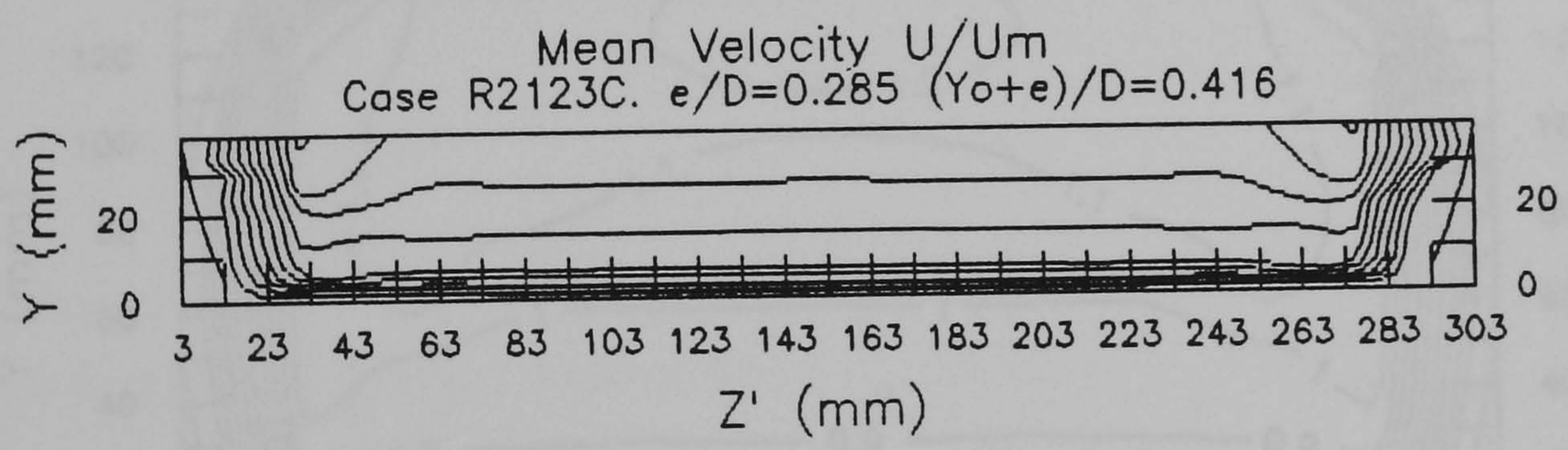

(a) Case R2123C

Figure 8.8 (a) Computed Mean Velocity Distribution U/U_m : Rough3

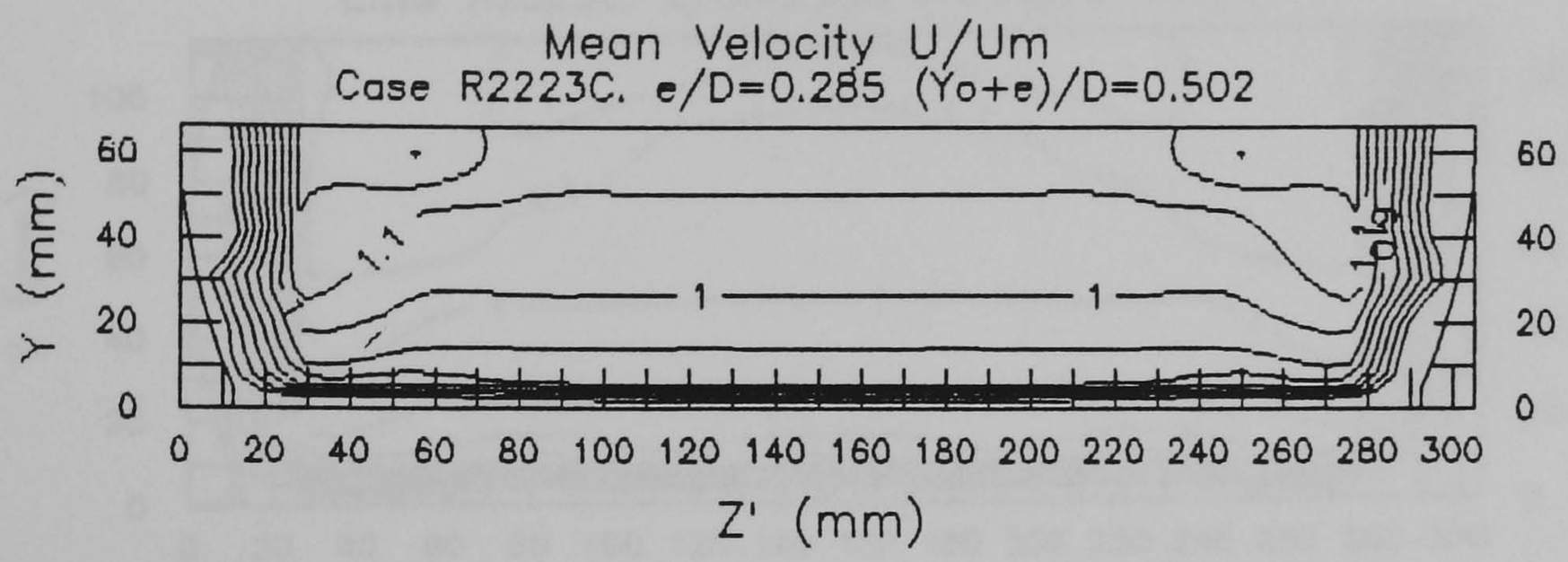

(b) Case R2223C

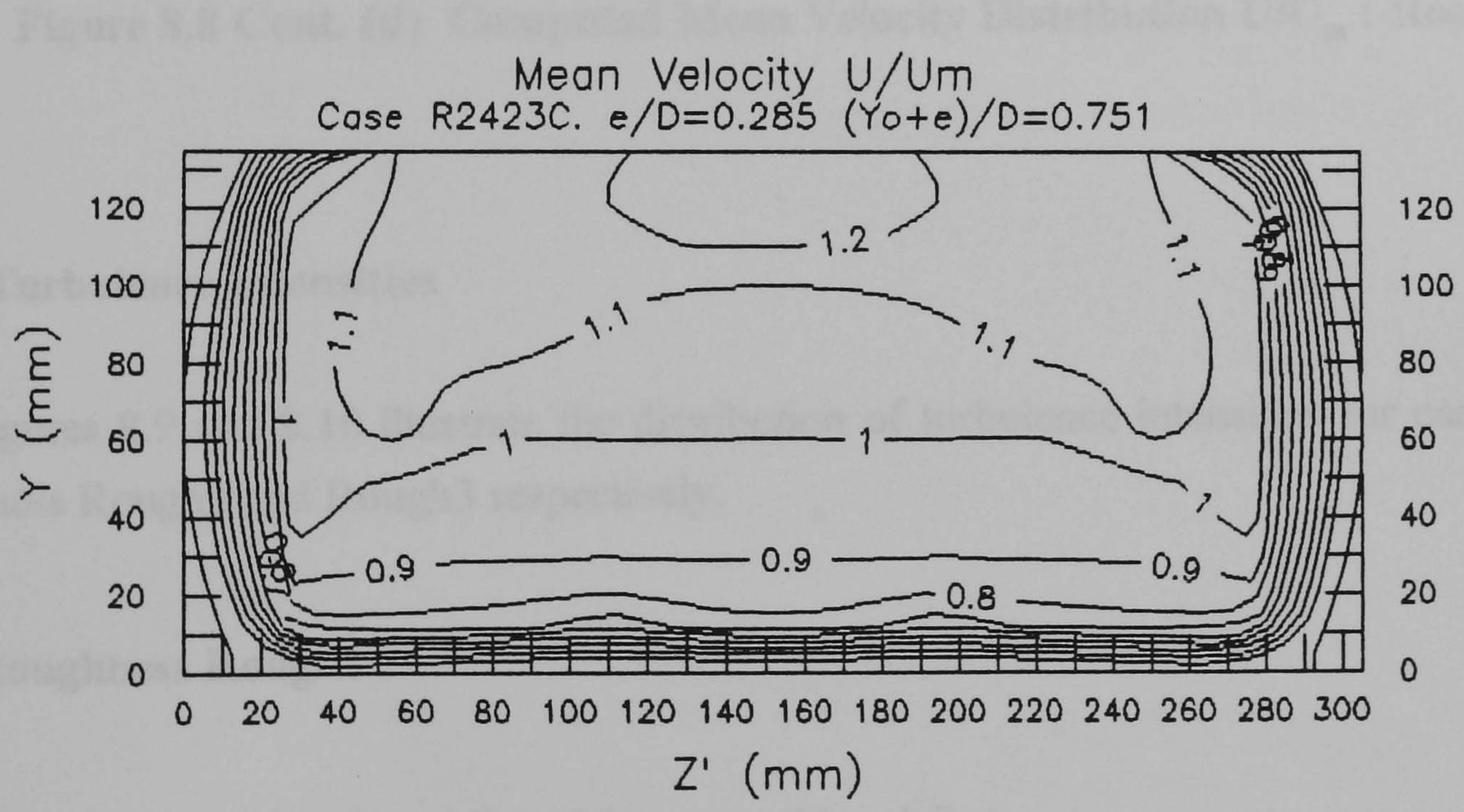

(c) Case R2423C

Figure 8.8Cont. (b - c) Computed Mean Velocity Distribution U/U_m : Rough3

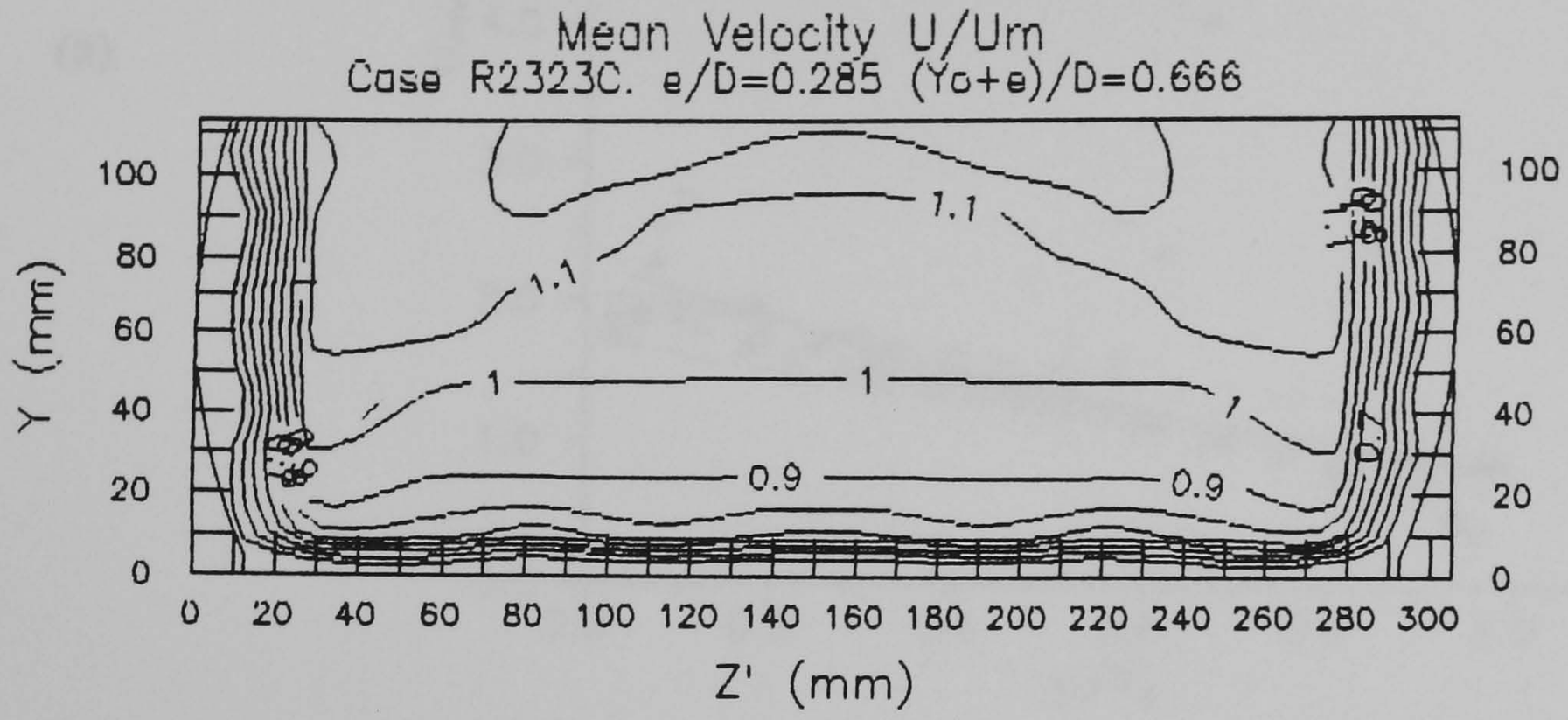

(d) Case R2423C

Figure 8.8 Cont. (d) Computed Mean Velocity Distribution U/U_m : Rough3

8.4.2 Turbulence Intensities

Figures 8.9 and 8.10 illustrate the distribution of turbulence intensities for cases with bed roughness Rough2 and Rough3 respectively.

Bed Roughness Rough2

Cases with bed roughness Rough2 are considered first.

(a)

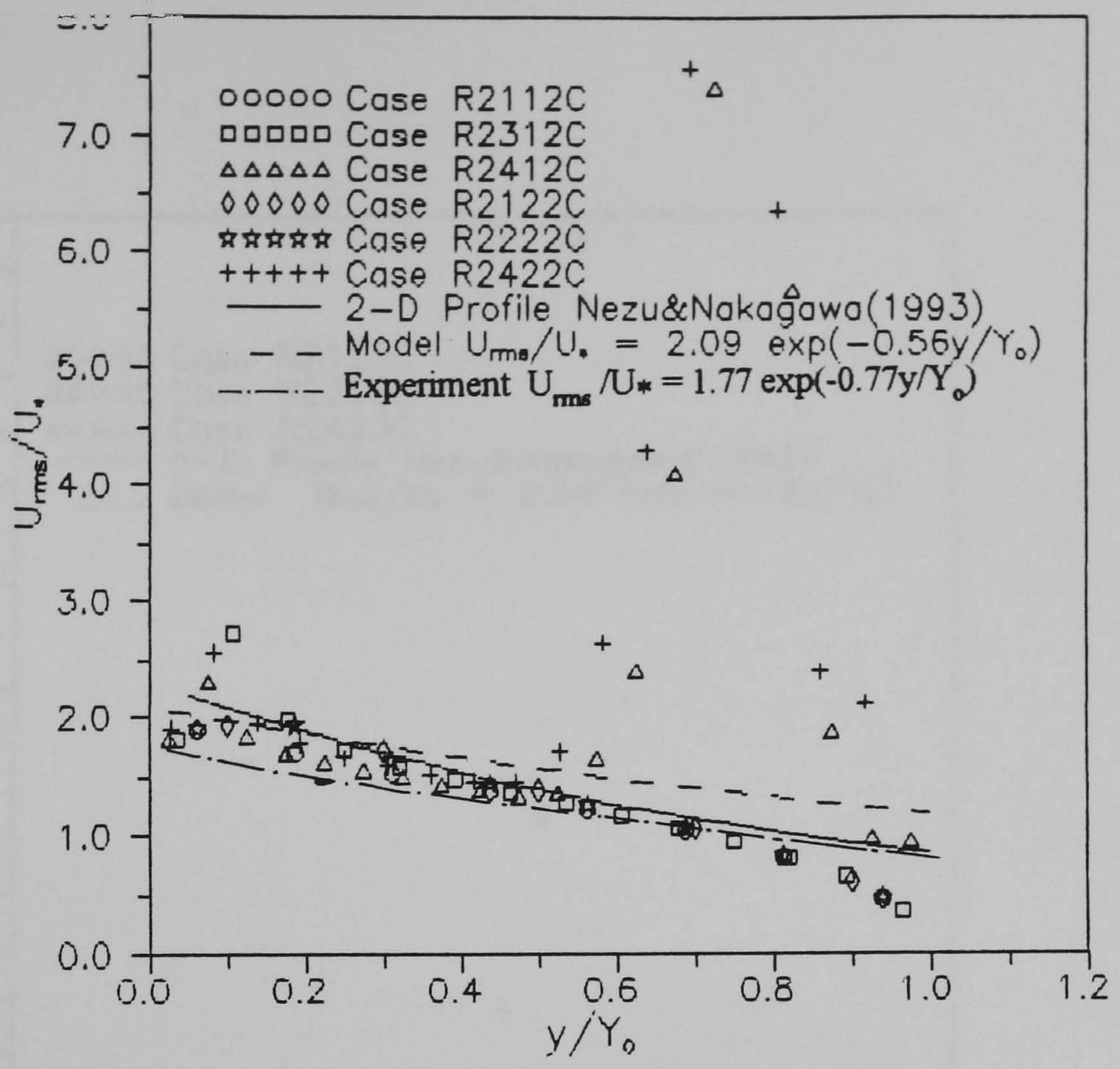

(b)

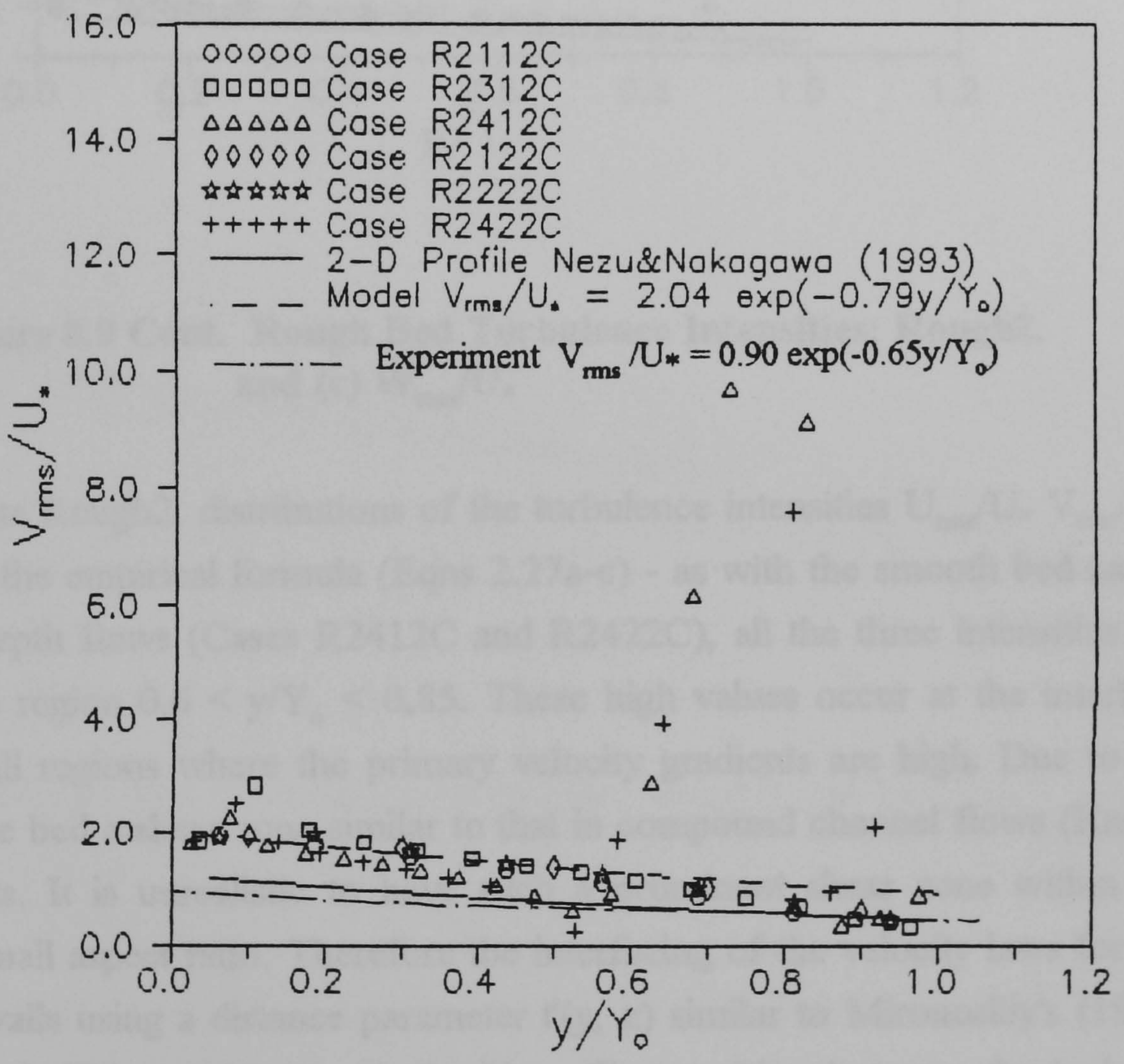

Figure 8.9 Rough Bed Turbulence Intensities: Rough2 (a) U_{rms}/U_*; and (b) V_{rms}/U_*

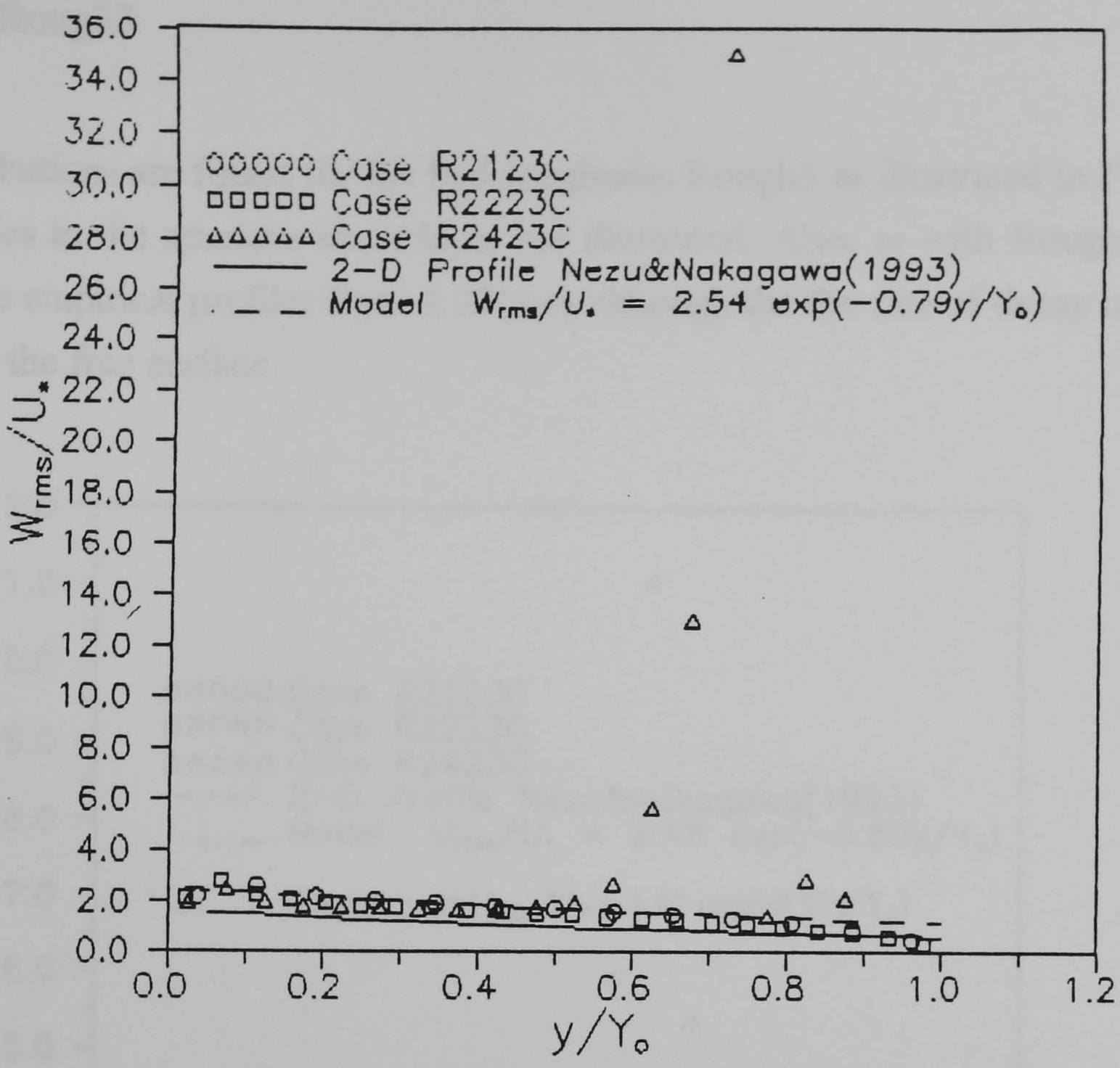

Figure 8.9 Cont. Rough Bed Turbulence Intensities: Rough2. and (c) W_{rms}/U_*

For the bed roughness Rough2, distributions of the turbulence intensities U_{rms}/U_* V_{rms}/U_*, and W_{rms}/U_* are close to the empirical formula (Eqns 2.27a-c) - as with the smooth bed cases. However, for the high-depth flows (Cases R2412C and R2422C), all the three intensities are unrealistically high in the region $0.6 < y/Y_o < 0.85$. These high values occur at the interface between the bed and wall regions where the primary velocity gradients are high. Due to the lower velocities nearer the bed a shear zone similar to that in compound channel flows (Knight and Shiono 1990) results. It is unrealistic to have such a prominent shear zone within the present channel with a small aspect ratio. Therefore the interfacing of the velocity laws for the rough bed and smooth walls using a distance parameter t'(y, z) similar to Mironoskiy's (1991) (see Eqn 6.31) is required. This would smooth the U-profile transition between the bed and wall zones.

Bed Roughness Rough3

Similar distributions are found for the bed roughness Rough3 as illustrated in Figures 8.10. The high intensities in the spurious shear layer are illustrated. Also, as with Rough2 cases, the profiles follow the empirical profiles Eqns 2.27(a-c) although the the rate of decay of the profile increases close to the free surface.

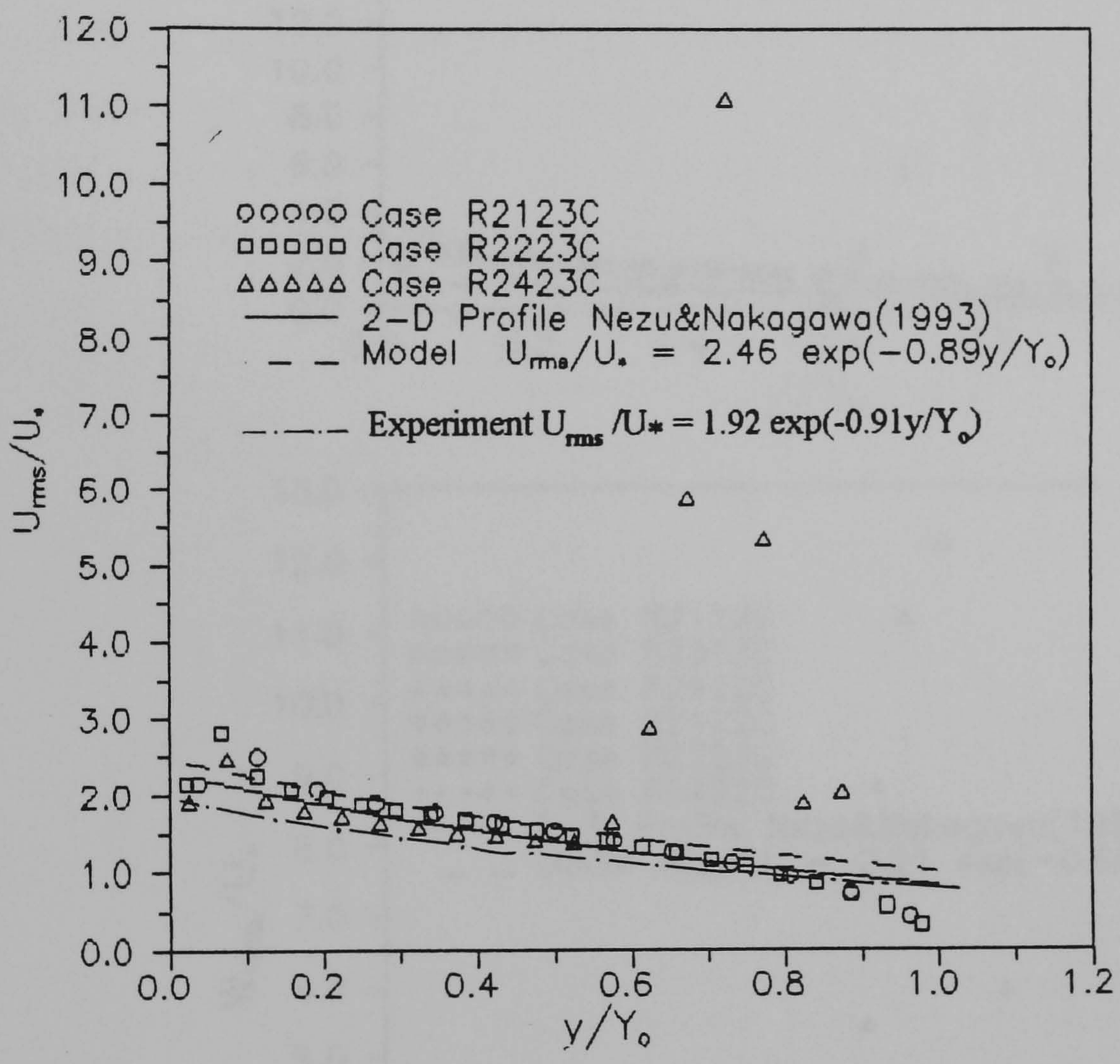

Figure 8.10 Rough Bed Turbulence Intensities: Rough3. (a) U_{rms}/U_*

(b)

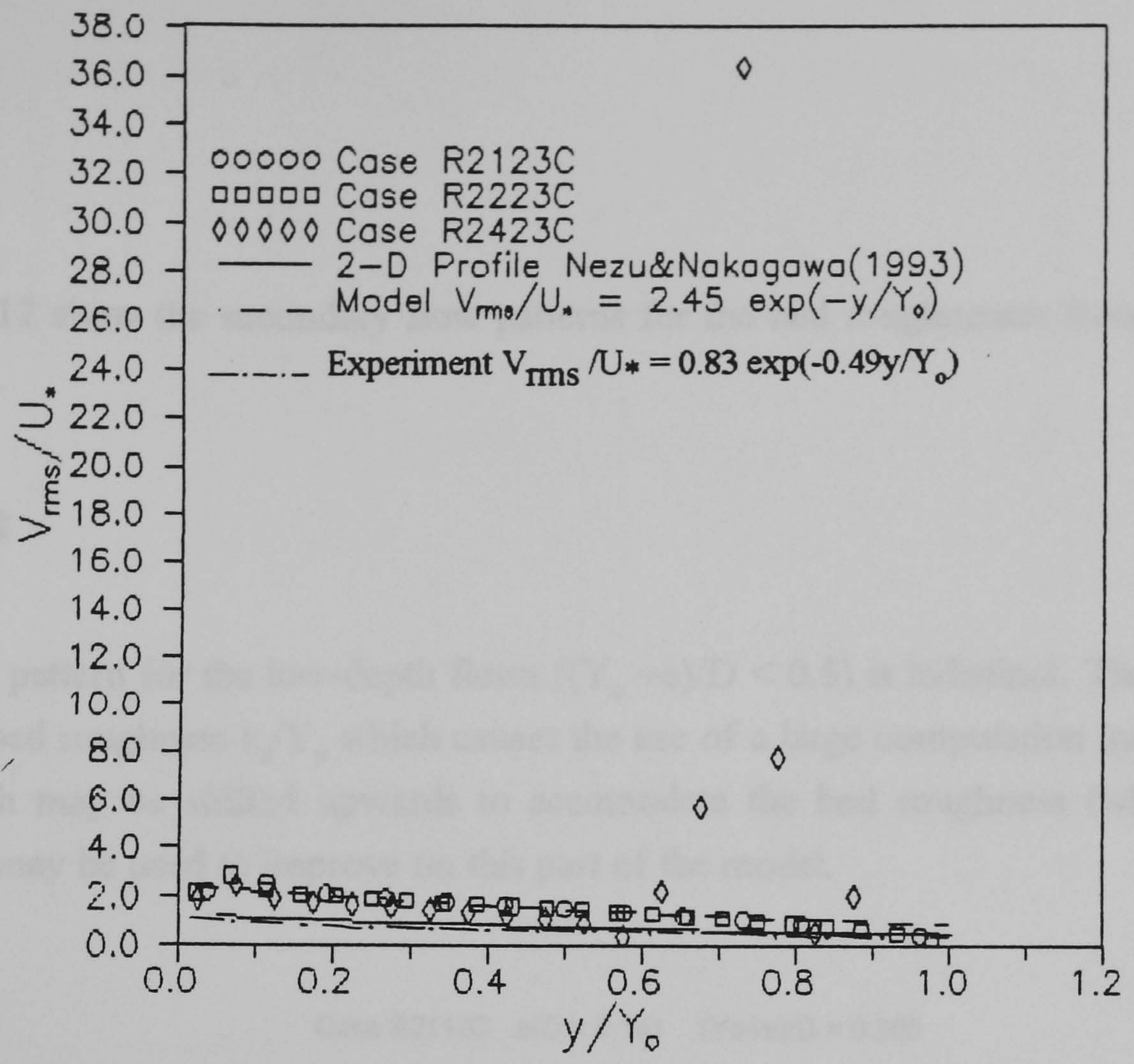

(c)

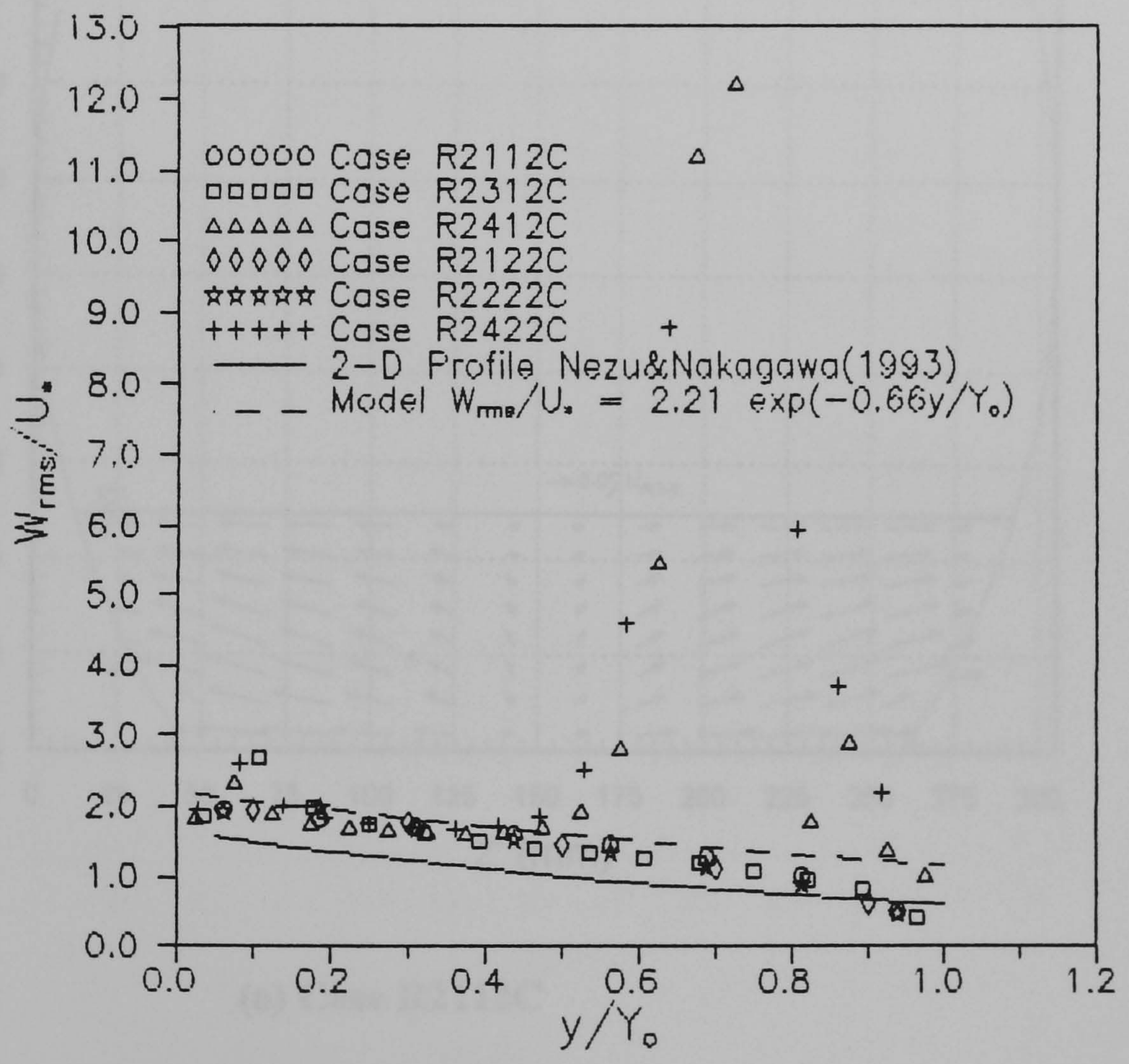

Figure 8.10 Cont. Rough Bed Turbulence Intensities: Rough3
(b) V_{rms}/U_*; and (c) W_{rms}/U_*

8.4.3 Secondary Flow

Figures 8.11 and 8.12 show the secondary flow patterns for the bed roughnesses Rough2 and Rough3 respectively.

Bed Roughness Rough2

The secondary flow pattern for the low-depth flows ($(Y_o + e)/D < 0.5$) is indistinct. This is due to the large relative bed roughness k_s/Y_o which causes the use of a large computation mesh. The use of a grid which may be shifted upwards to accomodate the bed roughness (whilst maintaining refinement) may be used to improve on this part of the model.

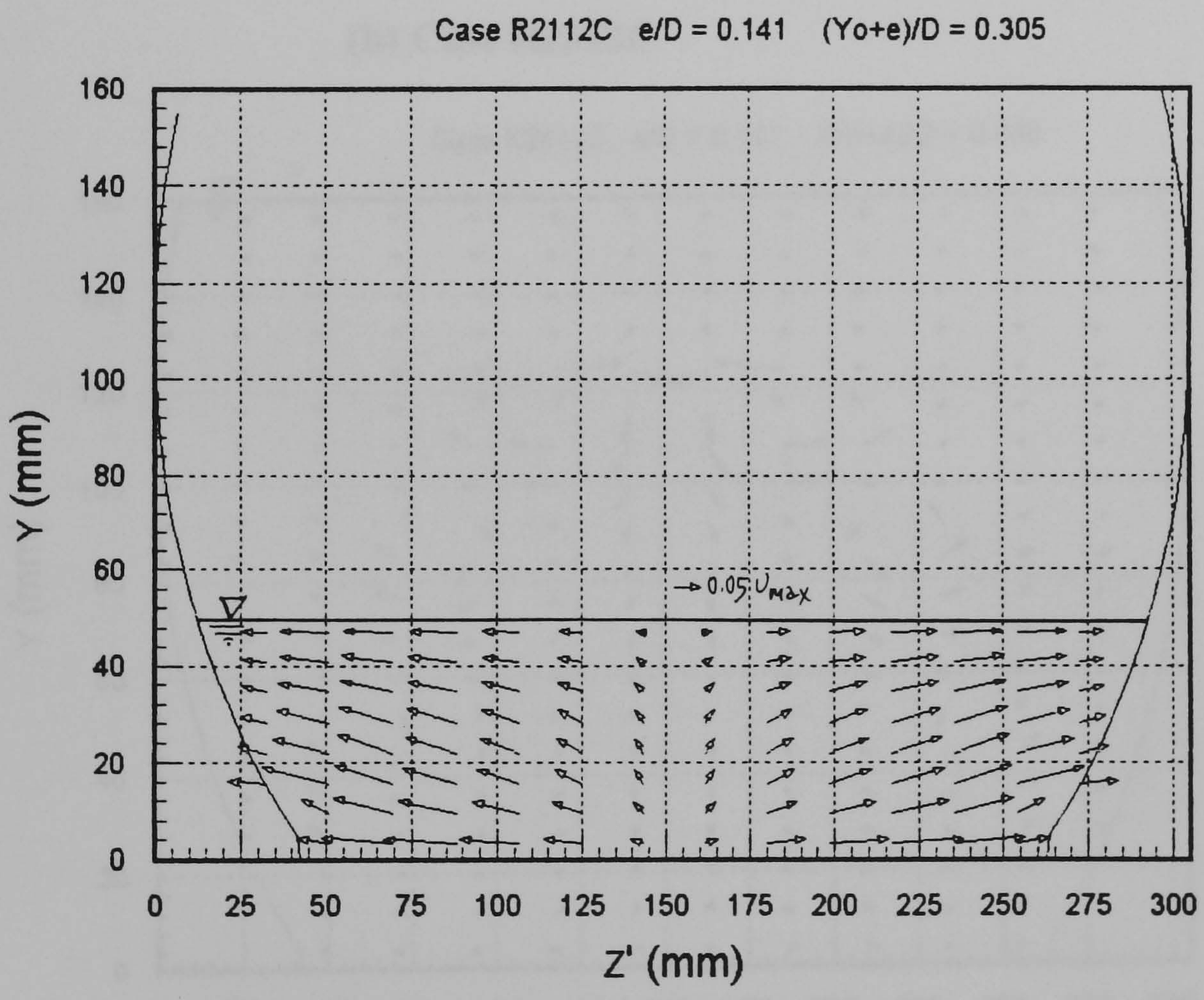

(a) Case R2112C

Figure 8.11 (a) Computed Secondary Flow: Bed Roughness Rough2

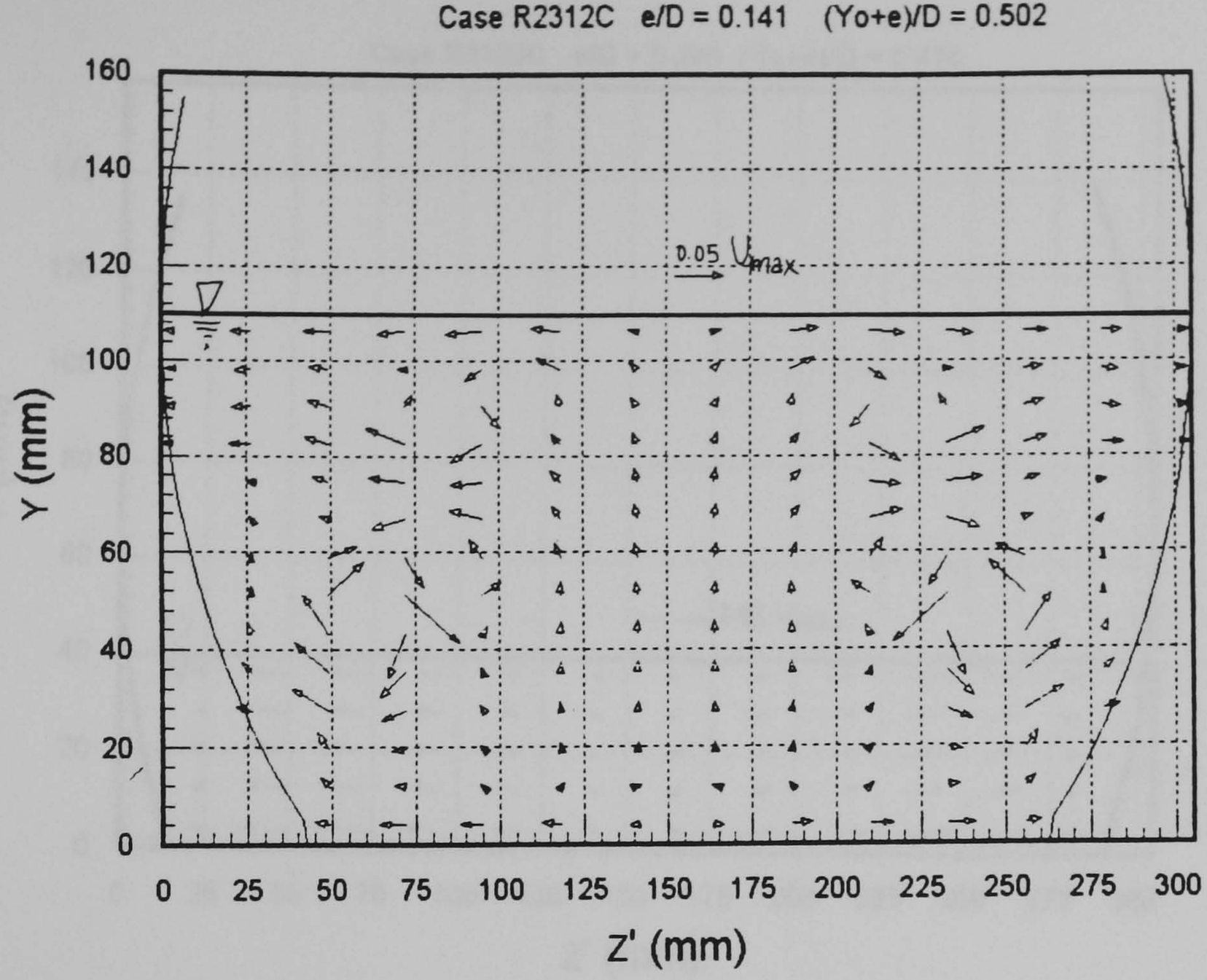

(b) Case R2312C

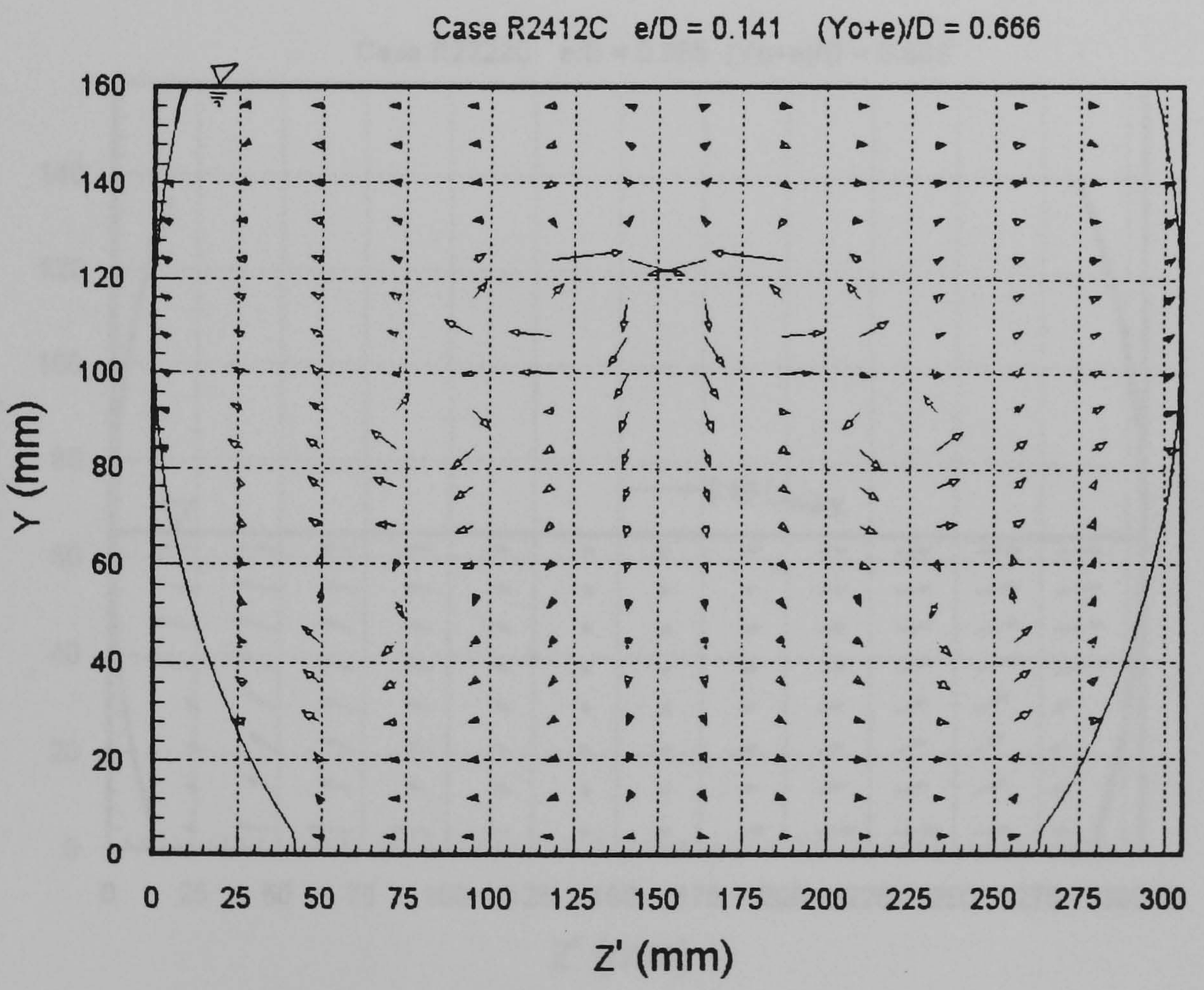

(c) Case R2412C

Figure 8.11 Cont. (b - c) Computed Secondary Flow: Bed Roughness Rough2

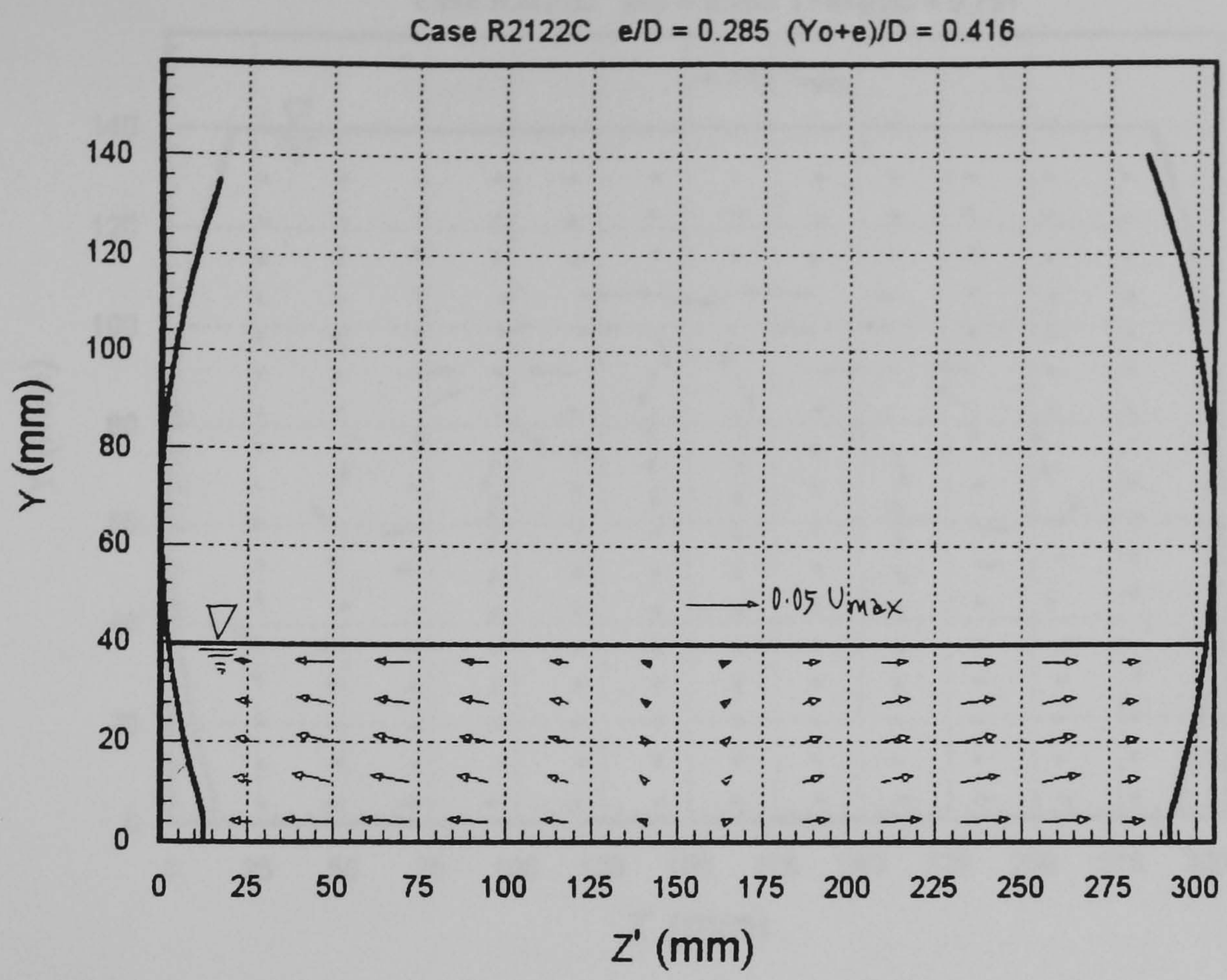

(d) Case R2122C

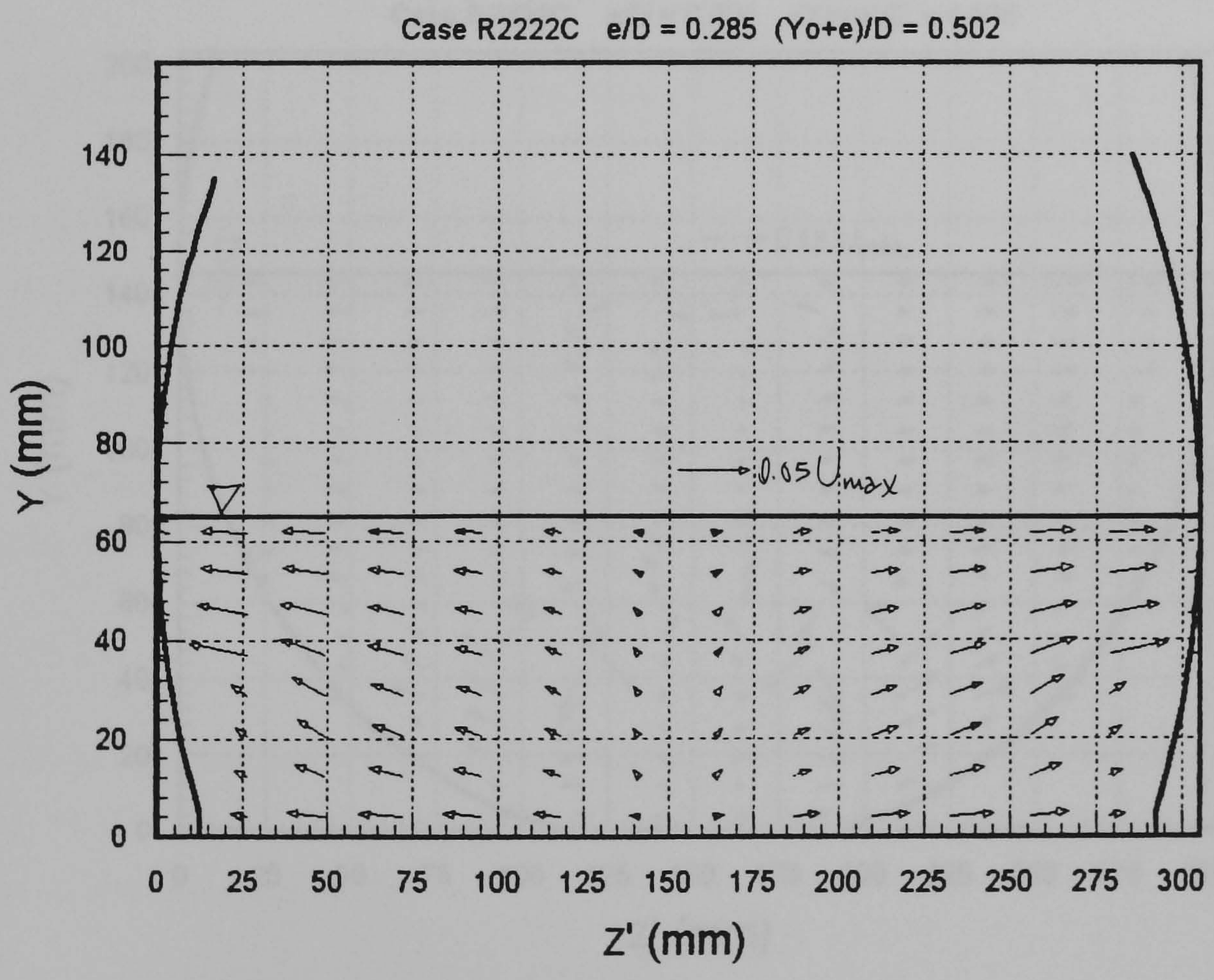

(e) Case R2222C

Figure 8.11 Cont. (d - e) Computed Secondary Flow: Bed Roughness Rough2

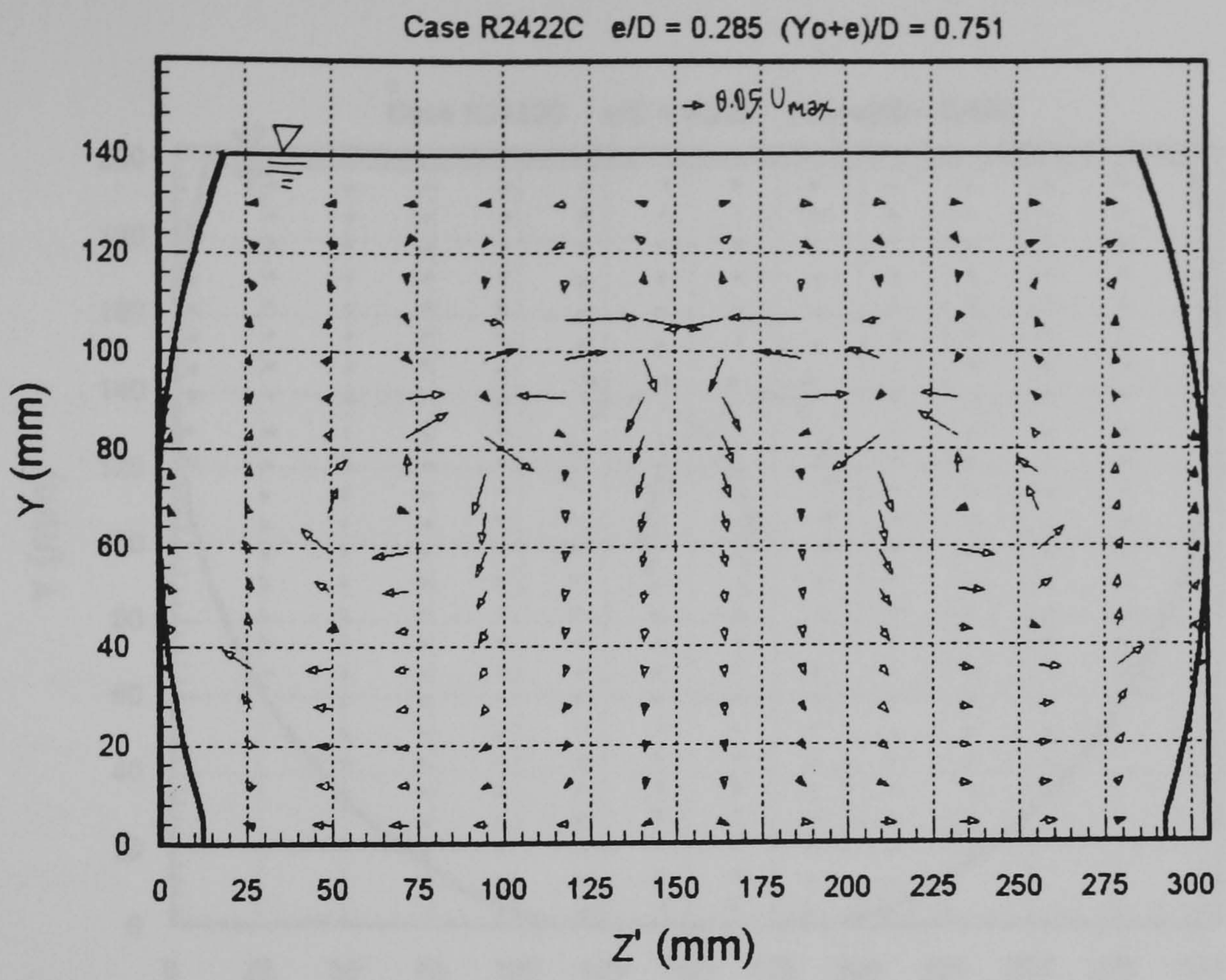

(f) Case R2422C

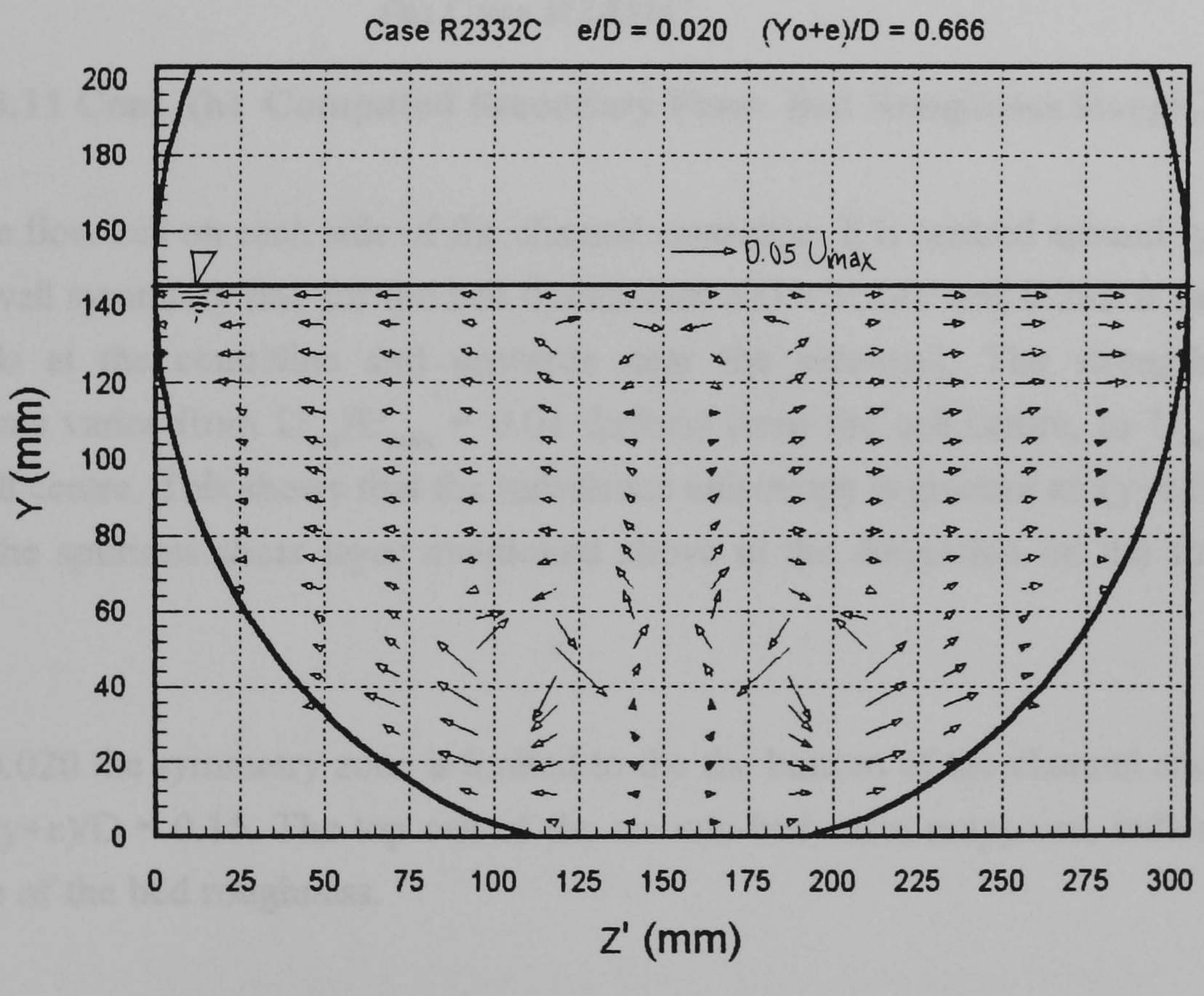

(g) Case R2332C

Figure 8.11 Cont. (f - g) Computed Secondary Flow: Bed Roughness Rough2

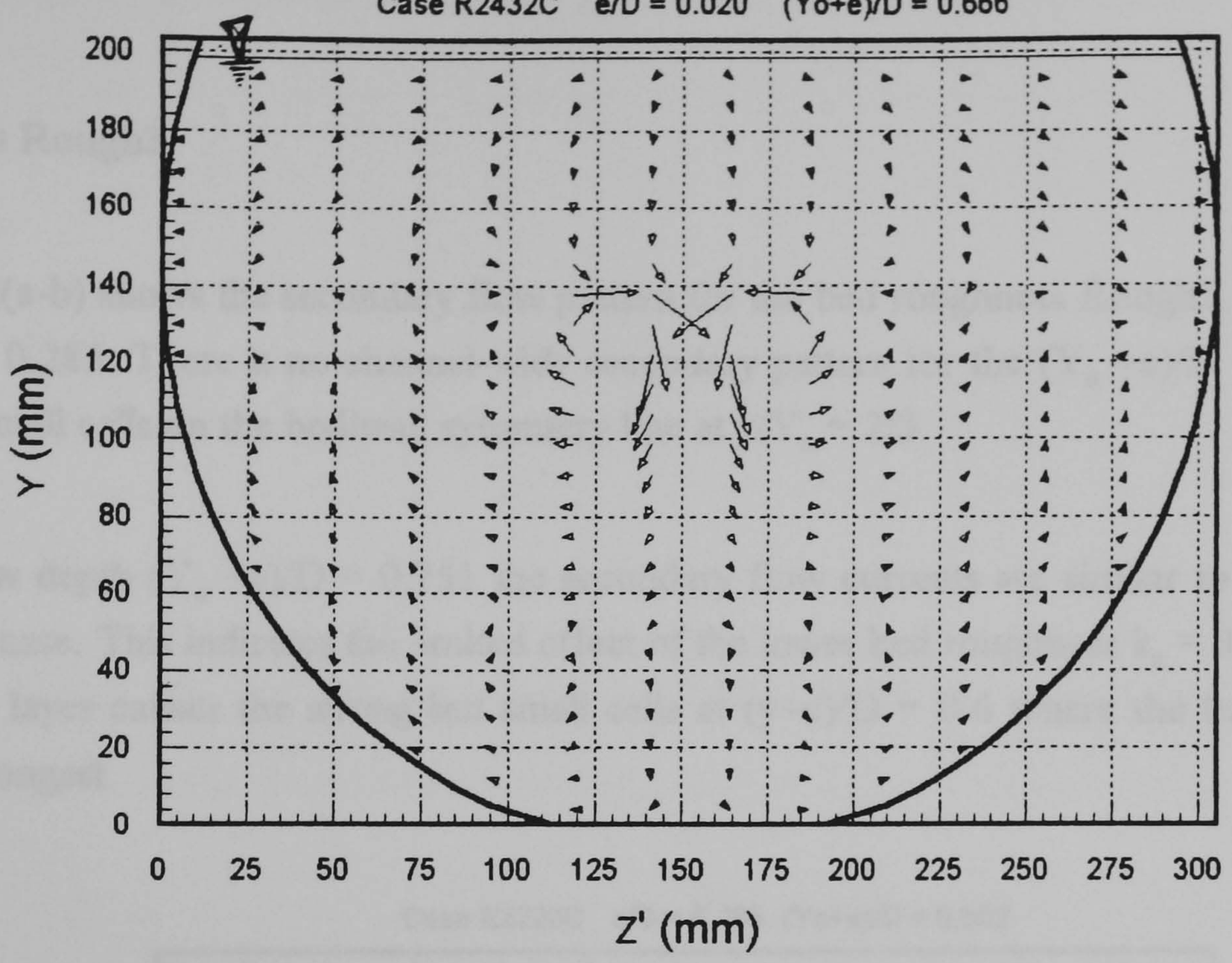

(h) Case R2432C

Figure 8.11 Cont. (h) Computed Secondary Flow: Bed Roughness Rough2

There is one flow cell on each side of the channel centreline. It is centred around (y+e)/D ~ 0.5 on the bed/wall symmtery line for the bed thicknesses e/D = 0.141 and 0.285 It carries the fluid downwards at the centreline and upwards near the side-wall. The strength of the secondary currents varies from U_{sec}/U_{max} ~ 0.01 farthest from the cell centre, to U_{sec}/U_{max} ~ 0.15 near the cell centre. This shows that the turbulence anisotropy is greatest at (y+e)/D ~ 0.5. This is due to the spurious shear layer mentioned above in the discussion on the turbulence intensities.

For e/D = 0.020 the symmetry zone is limited to the the bottom of the channel and the cell is centred near (y+e)/D ~ 0.15. The top cell of the smooth-bed cases reappears, indicating this limited influence of the bed roughness.

Bed Roughness Rough3

Figure 8.12(a-b) shows the secondary flow pattern for the bed roughness Rough3, and bed thickness e/D = 0.285. There is no channel-wide secondary pattern for the $(Y_o + e)/D = 0.502$. There are two small cells on the bed/wall symmtery line at $y/Y_o \sim 2/3$.

For the flow depth $(Y_o + e)/D = 0.751$ the secondary flow currents are similar to those in the smooth bed case. This indicates the limited effect of the lower bed roughness $k_s = 3.92$ mm. Again the shear layer causes the strong but small cells at $(y+e)/D \sim 0.6$ where the turbulence anisotropy is strongest.

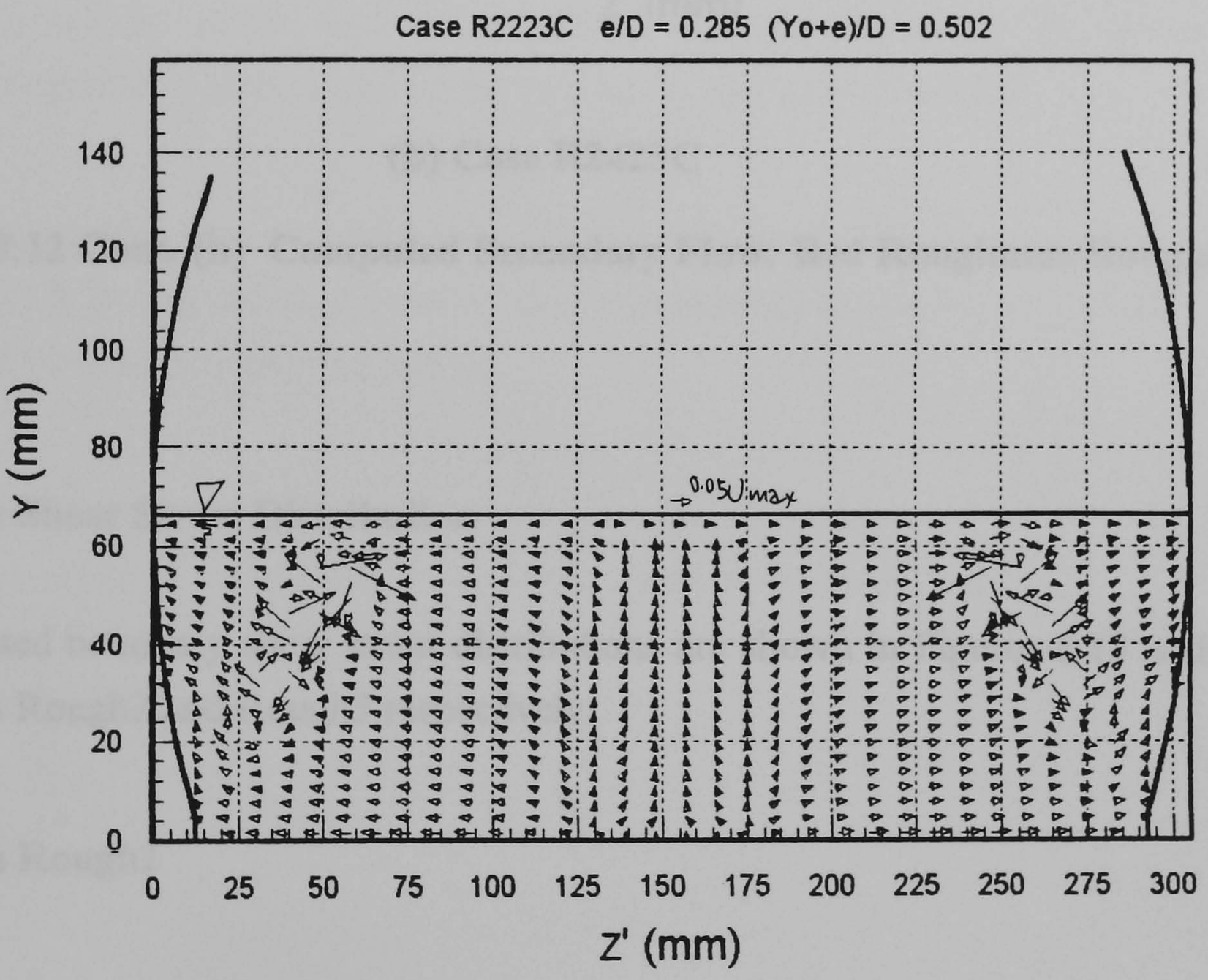

(a) Case R2223C

Figure 8.12 (a) Computed Secondary Flow: Bed Roughness Rough3

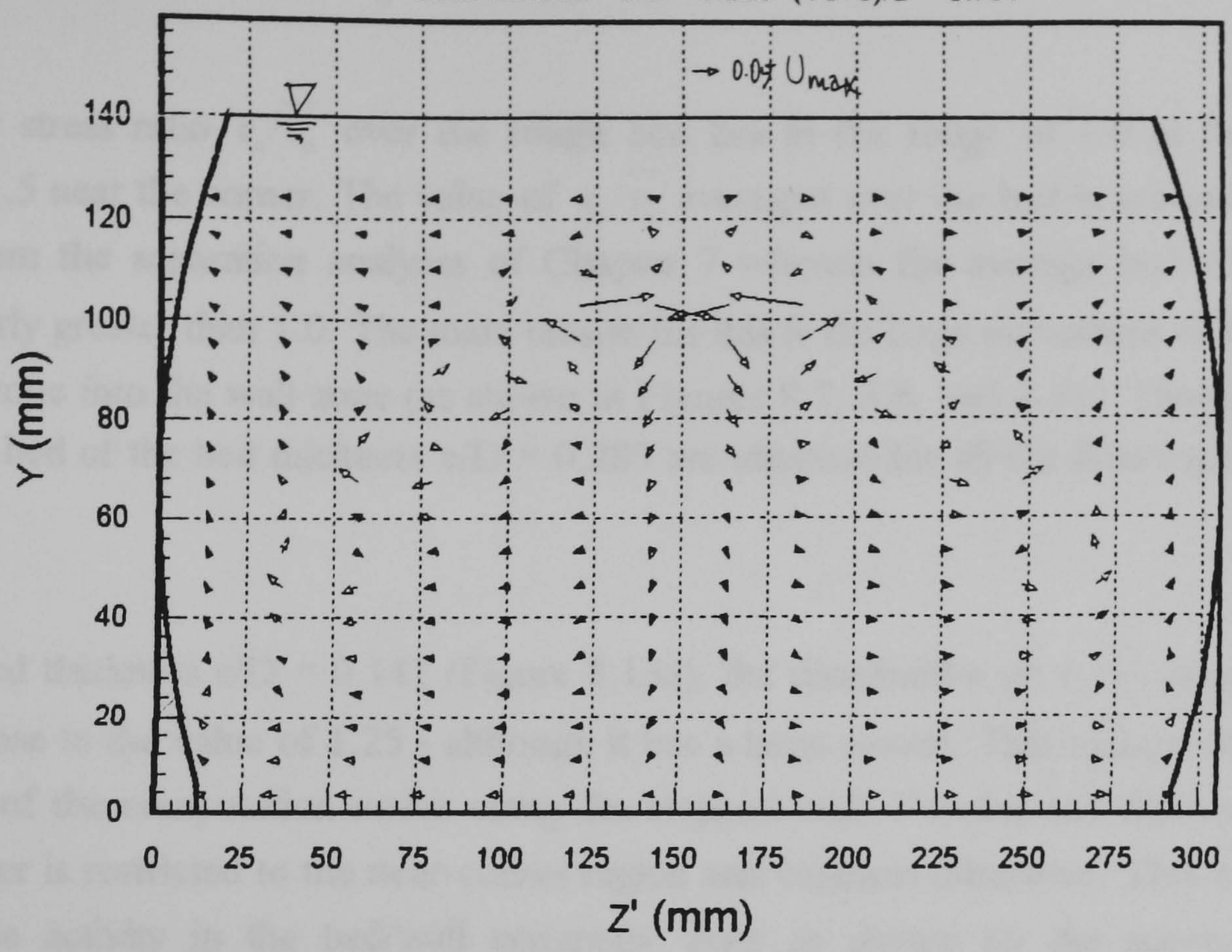

(b) Case R2423C

Figure 8.12 Cont. (b) Computed Secondary Flow: Bed Roughness Rough3

8.4.4 Boundary Shear Stress Distribution

The computed boundary shear stress distributions are shown in Figures 8.13 and 8.14 for bed roughnesses Rough2 and Rough3 respectively.

Bed Roughness Rough2

The cases with bed roughness Rough2 are presesented first.

The shear stress ratio $\tau_o/\overline{\tau_o}$ over the rough bed lies in the range of 1.0 at the channel centreline, to 1.5 near the corner. The value of $\tau_o/\overline{\tau_o}$ averaged over the bed is around 1.0. This is different from the separation analyses of Chapter 7 wherein the average bed shear $\tau_o/\overline{\tau_o}$ values are clearly greater than 1.0. The main reason for this is the large movement of fluid away from the bed zone into the wall zone (as shown in Figures 8.7, 8.8, and 8.11). Distributions of $\tau_o/\overline{\tau_o}$ over the bed of the bed thickness e/D = 0.285 are identical for all the flow cases - Figure 8.13(a-b).

For the bed thickness e/D = 0.141 (Figure 8.13a), the distribution of $\tau_o/\overline{\tau_o}$ over the side-wall the lies close to the value of 1.25 - although it has a large scatter. This reflects the varying wall distances of the computation nodes along the stepped wall. For the bed thickness e/D = 0.285 the scatter is restricted to the near-corner region and uniform otherwise. This reflects the high turbulence activity in the bed/wall symmetry zone as shown by the secondary flow patterns. The integrated average shear stress ratio lies in the range 1.0 - 1.5.

Over the side-walls of the bed thickness e/D = 0.020, the distribution is uniform - although with sharp peaks reflecting the descretisation problems mentioned above. As given in Table 8.1, the integrated mean shear stress ratio is 1.25.

In general the high bed roughness serves to level the shear stress on the bed and side-walls. There is no clear effect of the bed thickness on the shear stress distribution.

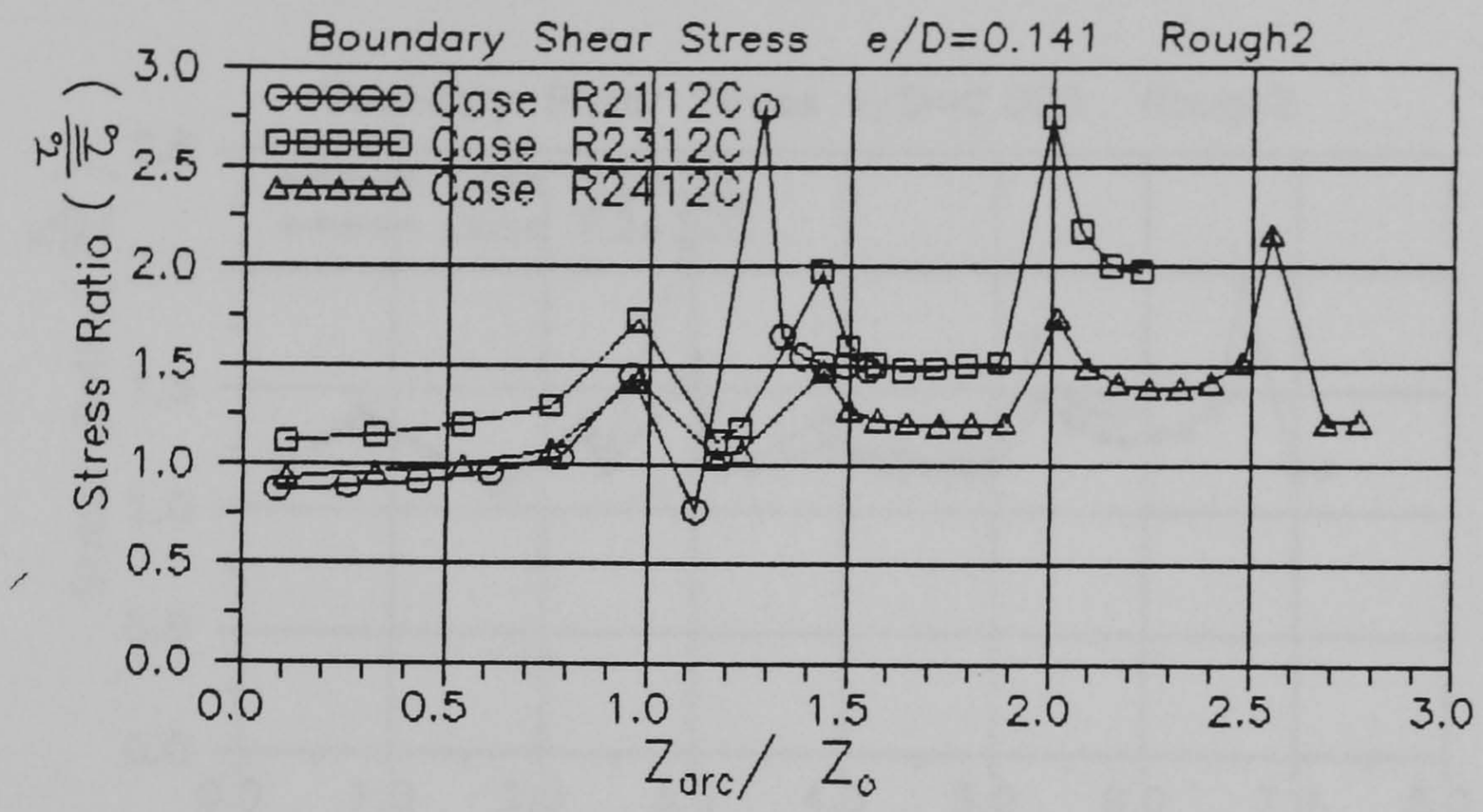

(a) Bed Thickness e/D = 0.141

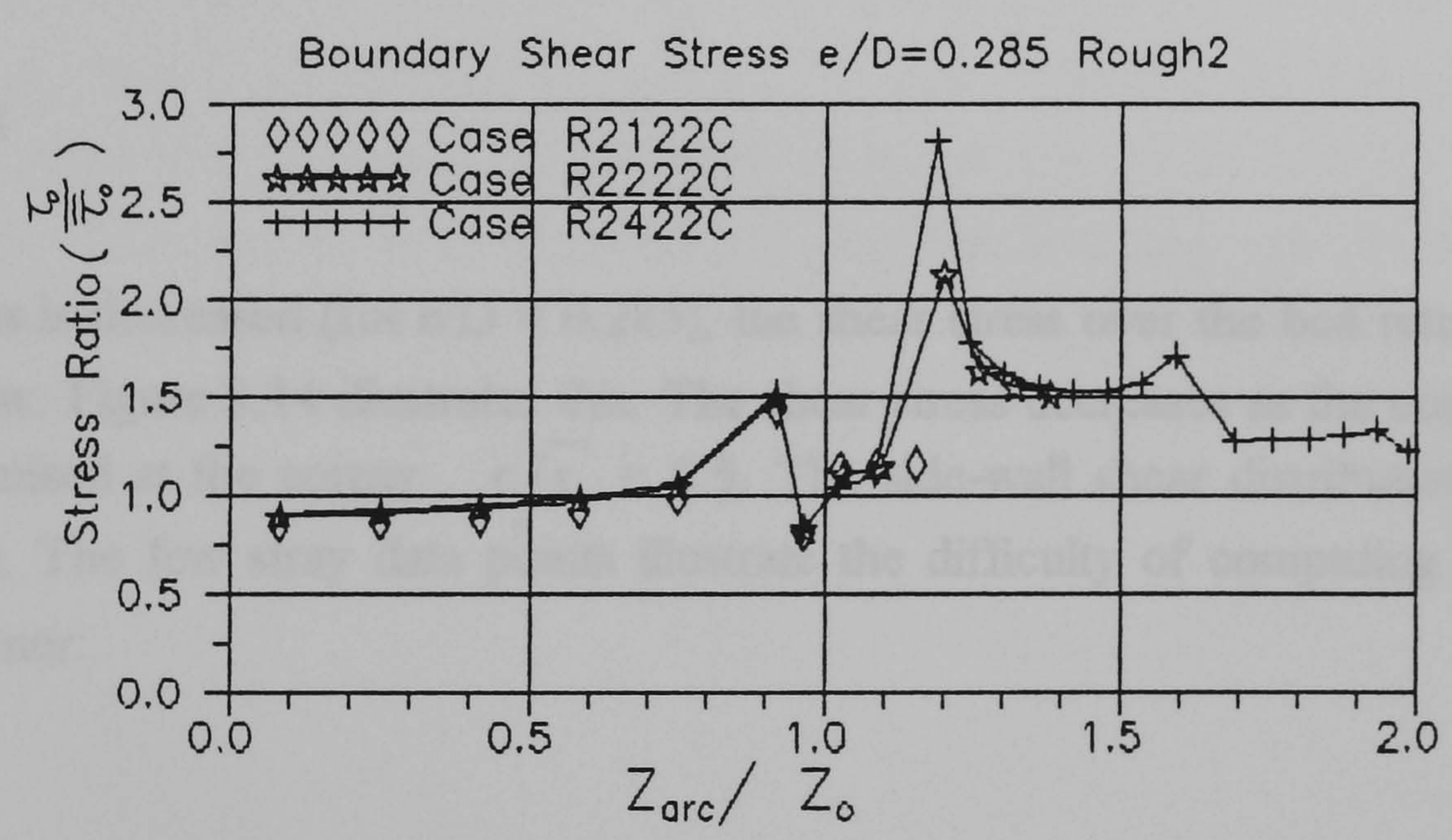

(b) Bed Thickness e/D = 0.285

Figure 8.13 (a - b) Computed Boundary Shear Stress: Bed Roughness Rough2

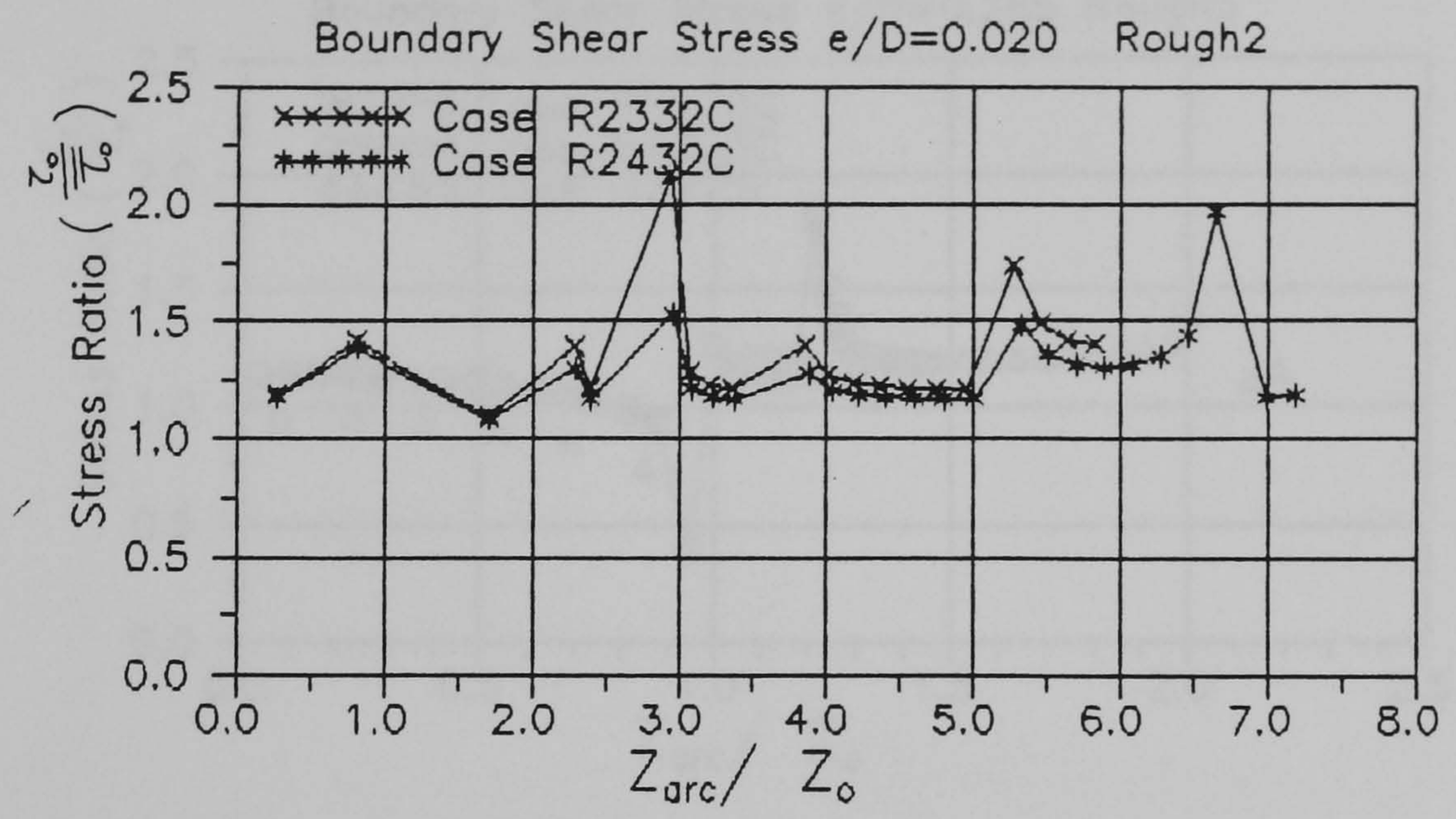

(c) Bed Thickness e/D = 0.020

Figure 8.13 Cont. (c) Computed Boundary Shear Stress: Bed Roughness Rough2

Bed Roughness Rough3

As the bed roughness is decreased (for e/D = 0.285), the shear stress over the bed returns to that of smooth-bed flow. Figure 8.14 illustrates this. The shear stress decreases as the corner is approached, and minimised at the corner $\tau_o/\overline{\tau_o}$ = 0.5. The side-wall shear distribution is uniform at $\tau_o/\overline{\tau_o}$ = 1.20. The few stray data points illustrate the difficulty of computing the boundary shear at the corner.

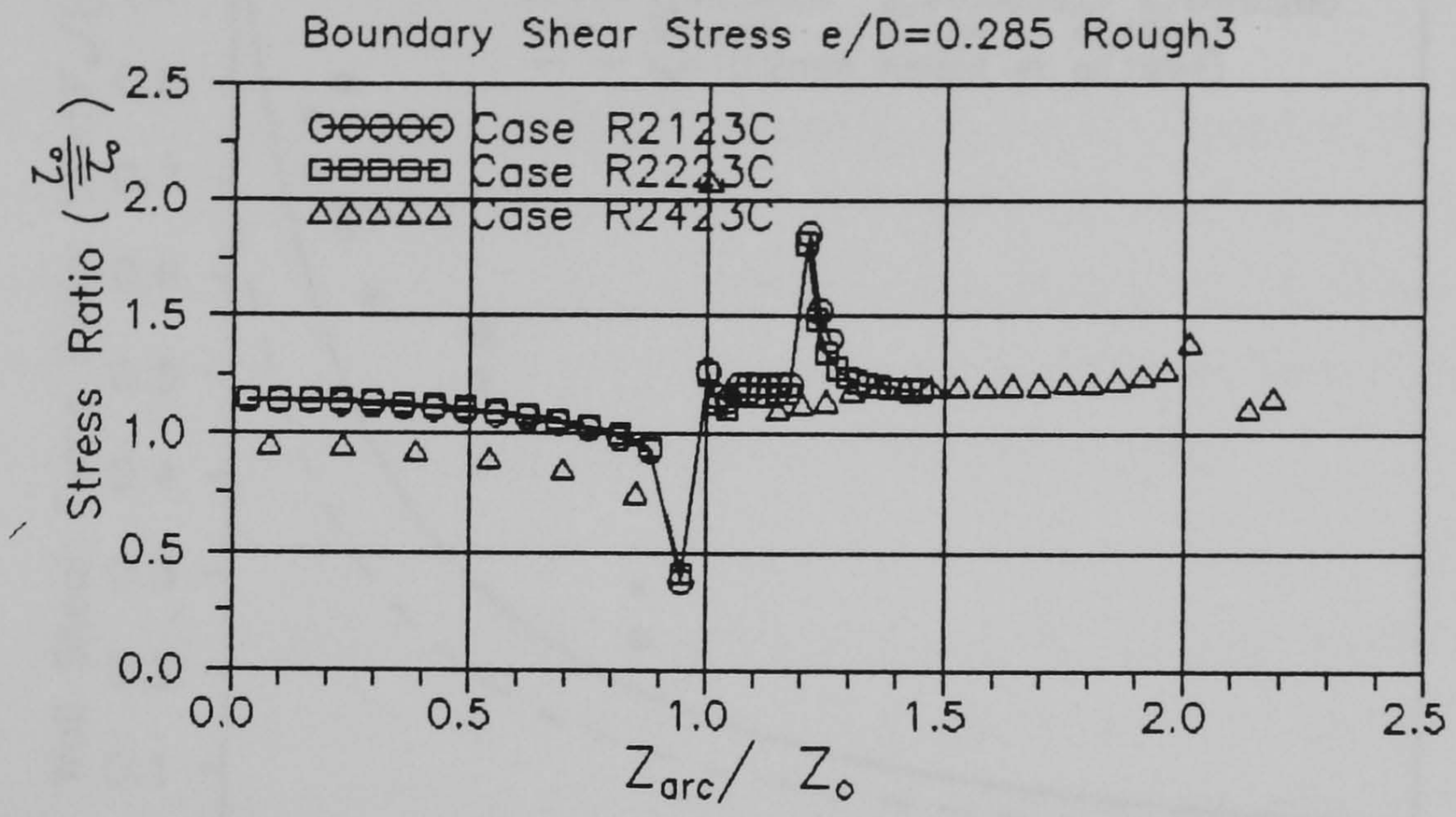

(a) Bed Thickness e/D = 0.285

Figure 8.14 Computed Boundary Shear Stress: Bed Roughness Rough3

The wall shear force ratios (SF) for the rough-bed cases are extracted from the data of Figure 8.6, 8.13 and 8.14. This is summarised in Figure 8.15, and computed SF values are compared to the empirical profiles of Knight *et al* (1994) given in Eqns 2.40 - 2.42. The computed values are larger than those given by the empirical plot. This is in line with the over-predictions of the wall shear stress discussed in the foregoing. For the bed thickness e/D = 0.020 the SF > 1 values are also plotted and seem to follow the pattern of the computed values. This thus calls into question the validity of Eqns 2.40 - 2.42 in describing the wall shear force in the present channel shape.

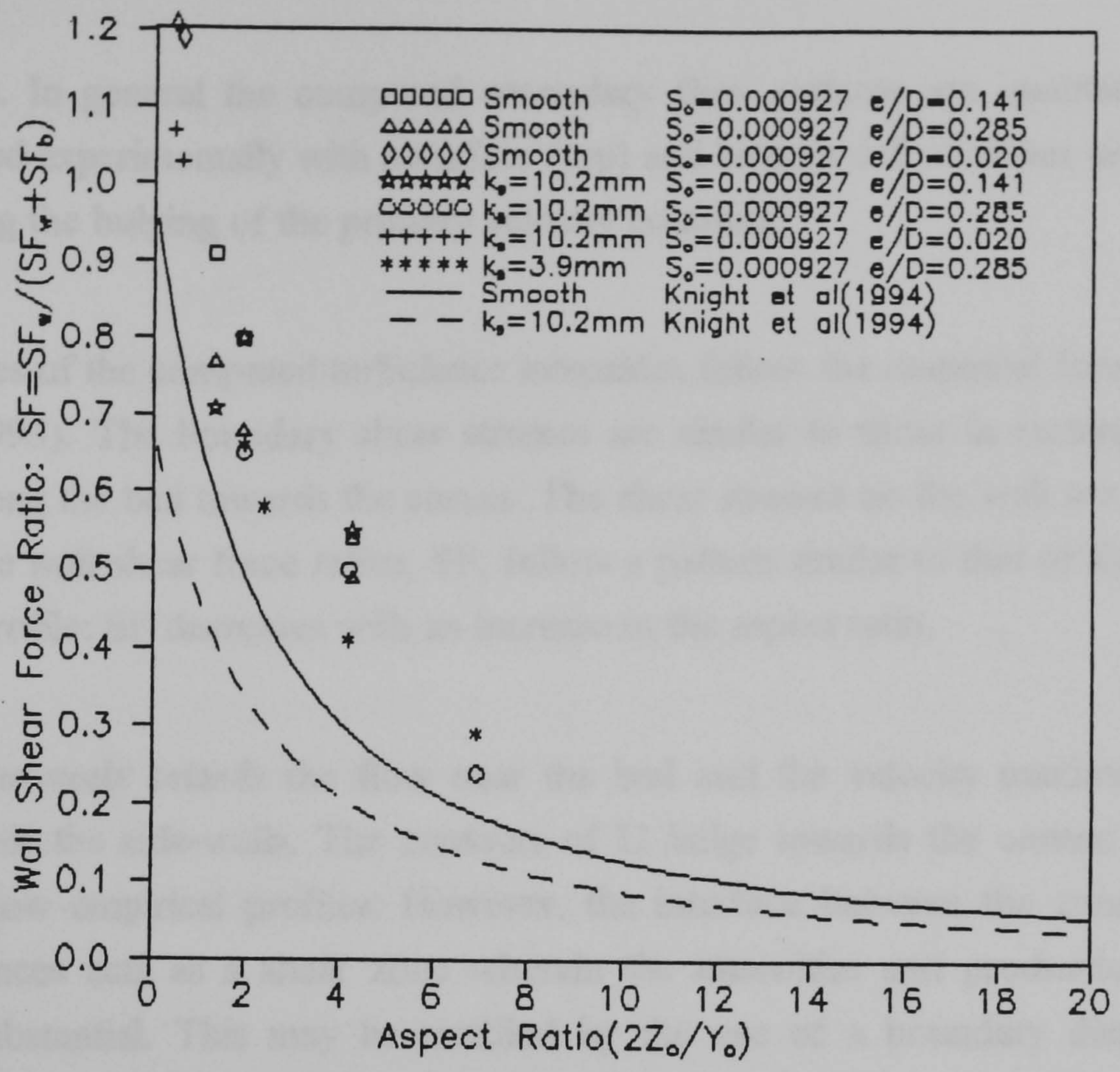

Figure 8.15 Computed Wall Shear Force Ratio (SF)

8.5 Summary

The computed distributions of the longitudinal (primary) and secondary mean velocities (U and U_{sec}), the turbulent quantities k and ε, and the turbulence intensities U_{rms}, V_{rms}, and W_{rms} were presented in the foregoing. The computer program written to carry-out the computation used single precision arithmetic.

For the smooth bed, the computed and experimental primary velocity distributions compare well. Secondary flow is computed in the higher flow depths $(Y_o+e)/D > 0.5$, and shows the presence of a surface and a bottom cell. For the low-depth flows $(Y_o+e)/D < 0.5$ the small grid cell sizes and the stepped side-wall lead to some wall nodes lying within the laminar sublayer. This invalidates the use of the turbulence model (whose usage leads to erroneous turbulence parameter and pressure distributions). The resulting low pressures at the side-wall causes a nett flow into the wall region which does not satisfy the continuity equation in the yz-plane. The use of a boundary-fitted grid system is suggested to guarantee that the wall nodes lie within the fully

turbulent boundary zone. In general the computed secondary flow patterns are qualitatively similar to those determined experimentally with a surface (top) and bottom cell on either side of the centreline, and causing the bulging of the primary velocity contours.

The centreline profiles of the computed turbulence intensities follow the empirical forms of Nezu and Nakagawa (1993). The boundary shear stresses are similar to those in rectangular channels and decrease along the bed towards the corner. The shear stresses on the wall are over predicted. Nonetheless the wall shear force ratios, SF, follow a pattern similar to that of Knight *et al*'s (1994) empirical profile: SF decreases with an increase in the aspect ratio.

The bed roughness severely retards the flow near the bed and the velocity maxima are dipped and shifted towards the side-walls. The contours of U bulge towards the corner. The turbulence intensities follow empirical profiles. However, the interface between the zones of bed and side-wall influences acts as a shear zone wherein the intensities and production of kinetic energy (k) are substantial. This may be rectified by the use of a boundary distance parameter t'(y, z) to reflect the effects of the wall and bed velocity laws in their zone of interaction. Additionally for rough-bed flows, the secondary flow is weak and indistinct due to the gridding problems mentioned above. Nonetheless, on the basis of the primary and secondary velocity distributions, the present channel, with $e/D \geq 0.14$, behaves like a rectangular channel.

The effect of the bed roughness on the boundary shear stress is apparent in the higher bed roughnesses k_s = 10.2 mm. The boundary shear stress is uniform over the bed, although the wall shear is unexpectedly greater than the shear stress at the bed. As the bed roughness decreases, the boundary shear recovers the form found in the smooth bed cases. Only very high roughnesses affect the flow; although the use of the present model in flows with $k_s/Y_o > 0.02$ is not recommended. This is because a large mesh size is required in order to position the bed boundary point above the roughness elements, and does not resolve the rest of the domain.

The wall shear force ratios (SF) are dependent on the length of the side-wall perimeter, with high wall perimeter leading to unrealistically high SF values. For both the smooth and rough bed cases the effect of the bed thickness on the boundary shear stress distribution is minimal.

CHAPTER 9: CONCLUSIONS AND SUGGESTIONS FOR FURTHER STUDY

9.1 Main Conclusions

Thirty-one uniform flow cases were studied experimentally, and twenty-one were numerically modelled. The numerical results of Chapter 8 are compared to the experimental results of Chapter 7.

A pipe of diameter D = 305 mm was used. Two bed thicknesses (e) were studied experimentally and numerically e/D = 0.141 and 0.285. Five flow depths, $(Y_o+e)/D$ = 0.3, 0.4, 0.5, 0.667, and 0.75, were studied. The bed roughnesses used in the experimental study k_s = 1.71, 10.2, and 3.92 mm are also used. The k_s/Y_o ratios lie in the range 4 - 30. A third bed thickness e/D = 0.020 is investigated numerically for comparison with a clear pipe flowing part-full.

9.1.1 Experimental Investigation

The velocity dip and bulging of the mean contours towards the corner indicates the three-dimensionality of the flow. However, some of the contour plots showed asymmetry. This was due to the asymmetry at the flume entrance, and the sensitivity of the contours to slight asymmetry as noted by Melling (1975). On the basis of the mean longitudinal and secondary flow patterns, the present channel behaves like a rectangular channel. The inward side-wall curvature introduces the crowning (retarding) effect on the mean flow. Measured longitudinal and vertical turbulence intensity distributions follow the empirical two-dimensional distributions of Nezu and Nakagawa (1993). The bed roughness causes an expected flattening of the turbulence intensity profiles.

The side-wall shear force ratios (SF) were computed using the friction factors calculated by the Vanoni-Brooks separation technique. Despite being higher, these values follow the trend determined from various channel shapes when the aspect ratio $2Z_o/Y_o$ (= bed width/flow depth) is used.

Similarity laws based on the outer flow parameters Y_o and U_m (cross-sectional mean) were derived in order to modify the boundary conditions for the model.

9.1.2 Numerical Modelling

The non-linear k-ε model, based on the SIMPLE computation technique computes the six flow parameters U, V, W, P, k, and ε on a Cartesian grid using wall functions and the rigid-lid assumption. The three turbulent intensities U_{rms}, V_{rms}, and W_{rms} are also produced. These characterise the turbulent flow in the open channel.

The longitudinal (primary) mean velocity, U, distribution is similar to that determined experimentally. The model over-predicts the cross-sectional mean velocity. For high bed roughness, a spurious shear zone between the bed- and corner-influenced zones appears. This is due to the definition of the boundary distance which leads to high primary velocity gradients at the interface zone. A smooth function of the bed and wall distances, akin to Eqn 6.31, would eliminate this shear zone.

The non-linear k-ε turbulence representation predicts two secondary flow cells on each side of the channel centreline, a bottom and a top cell. The top cell covers most of the flow depth and carries high momentum fluid upwards at the channel centreline. The bottom cell is stronger and is restricted to the bed zone. The magnitude of these currents lie in the reasonable range of $0.01U_{max}$ - $0.15U_{max}$. The model does not predict the secondary flow pattern for the low flow depth cases $(Y_o+e)/D < 0.5$ due to the small mesh size needed. The small grid size leads to side-wall points lying within the laminar sub-layer wherein the k-ε model is not applicable. A body-fitted grid would ensure that side-wall nodes lie within the turbulent wall zone. Nonetheless the wall-function approach used works well.

The calculated turbulence parameters follow empirical profiles available in the literature. The dissipation rate, ε, is increased at the free surface as expected.

The bed boundary shear stress distributions in the smooth bed cases are similar to those in rectangular channels. Along the bed, the distributions are uniform, and reduce gradually to a

minimum $\tau/\overline{\tau_o}$ ~ 0.5 - 0.7 at the corner. However, due coarseness of the grid, the inflexion of the shear distribution experimentally observed in rectangular channels is absent. As the roughness increases the levels of shear stress become uniform along the channel perimeter. In general the integrated mean shear stress ratio ($\tau/\overline{\tau_o}$) ~1.2 for all roughnesses. The present model is, however, not suitable for cases with high relative bed roughnesses $k_s/Y_o > 0.02$. This is due to the unrealistically high grid size that is required for high bed roughness cases. The bed thickness does not have an effect of the pattern of the boundary shear stress distribution. The wall shear force ratios, while dependent on the length of the wall perimeter, follow the empirical trend.

9.2 Suggestions for Further Study

Further study of the flow in the present channel may be undertaken in two distinct fields (i) improvement of the understanding of the physics of the fluid flow, and (ii) improvement of the numerical model.

The Physics of the Flow

(a) The development of non-equilibrium similarity laws for use in deriving the boundary conditions for the flow parameters of the non-linear k-ε model. This also involves the derivation laws wherein the boundary distance is based on the distances to the two boundaries in the corner zone.

(b) The application of the coherent structure approach in detecting and modelling the flow structure in the corner zone. This would lead to a better understanding of the dynamical effect of the wall geometry on the flow.

The Numerical Model

(a) The use of a boundary-fitted computation grid in order to refine the near-corner zone, and ensure that the wall nodes lie within the fully turbulent zones of the wall.

(b) The use of subsequent and more advanced variations of the SIMPLE technique in order to speed-up the convergence of the computation (e.g. non-staggered grid).

BIBLIOGRAPHY

Alfrink, B.J and van Rijn, L.C. (1983). "Two-Equation Turbulence Model for Flow in Trenches", **Journal of Hydraulics Division**, ASCE, 109(HY7), 941-958.

Alvarez-Hernandez, E.M. (1990). "Influence of Cohesion on Sediment Movement in Channels of Circular Cross-Section", **Unpublished PhD Thesis**, University of Newcastle upon Tyne.

Ames, W.F. (1977). **Numerical Methods for Partial Differential Equations**. Toronto: Academic Press.

Baker, A.J. and Orzechowski, J.A. (1983). "An Interaction Algorithm for Three-Dimensional Turbulent Subsonic Aerodynamic Juncture Region Flow", **AIAA Journal**, 21(4), 524-533.

Bernard, P.S. (1986). "Limitations of the Near-Wall k-ε Model", **AIAA Journal**, 24(4), 619-622.

Bradshaw, P. (1965). "The Effect of Wind-Tunnel Screens on Nominally Two-Dimensional Boundary Layers", **Journal of Fluid Mechanics**, 22(4), 679-687.

Bradshaw, P. (1974). **Topics in Applied Physics: Turbulence**. Ed. Bradshaw, New York: Springer Verlag.

Bradshaw, P. (1987). "Turbulent Secondary Flows", **Annual Review of Fluid Mechanics**, 19, 53-74.

Bradshaw, P. and Patel, V.C. (1973). "Comment on 'Mean Velocity Profile of a Thick Turbulent Boundary Layer along a Circular Cylinder'", **AIAA Journal**, 11(6), 894-895.

Bradshaw, P. and Perot, J.B. (1993). "A Note on Turbulent Energy Dissipation in the Viscous Wall Region", **The Physics of Fluids A**, 5, (12), 3305-3306.

Bradshaw, P. and Huang, G.P. (1994). "The Law of the Wall in Turbulent Flow", **Proceedings Osborne Reynolds Centenary Symposium**, UMIST, Manchester.

Bragg, G.M. (1969). "Turbulent Boundary Layer in a Corner", **Journal of Fluid Mechanics**, 36(4), 485-503.

British Standards Institution (1981). **Liquid Flow in Open Channels: Part 4A Classification Tests**, BS 3680: Part 4A. BSI.

British Standards Institution (1990). **Soils for Civil Engineering Purposes: Part 2. Classification Tests**, BS 1377: Part 2. BSI.

Brundrette, E. and Baines, W.D. (1964). "The Production and Diffusion of Vorticity in Duct Flow", **Journal of Fluid Mechanics**, 39(3), 375-396.

Buchhave, P., George, W.K. Jnr and Lumley, J.L. (1979). "The Measurement of Turbulence with the Laser-Doppler Anemometer", **Annual Review of Fluid Mechanics**, 11, 443-503.

Cardoso, A.H., Graf, W.H. and Gust, G. (1989). "Uniform Flow in a Smooth Open Channel", **Journal of Hydraulic Research**, IAHR, 27, 603-616.

Cazalbou, J.B. and Bradshaw, P. (1993). "Turbulent Transport in Wall-bounded Flows. Evaluation of Model Coefficients Using Direct Numerical Simulation", **The Physics of Fluids A**, 5(12), 3233-3239.

Cebeci, T. and Smith, A.M.O. (1974). **Analysis of Turbulent Boundary Layers**. New York: Academic Press.

Celik, I. and Rodi, W. (1984) "Simulation of Free-Surface Effects in Turbulent Channel Flows", **Physicochemical Hydrodynamics**, 5, 217-227.

Chan, R. and Street, R.L. (1970). "A Computer Study of Finite-Amplitude Water Waves",**Journal of Computational Physics**, 6, 68-94.

Chow, V.T. (1959). **Open-Channel Hydraulics**. London: MacGraw-Hill.

Chung, T.J. (1988). **Continuum Mechanics**, London: Prentice-Hall.

Clark, J.A. (1968). "A Study of Incompressible Turbulent Boundary Layers in Channel Flow, **Journal of Basic Engineering**, ASME, 90, 455-468.

Coles, D. (1956). "The Law of the wake in the Turbulent Boundary Layer", **Journal of Fluid Mechanics**, 1, 191-226.

Colombini, M. (1993). "Turbulence-driven Secondary Flows and Formation of Sand Ridges", **Journal of Fluid Mechanics**, 254, 701-719.

Daly, B.J. and Harlow, F.H. (1970). "Transport Equations in Turbulence", **The Physics of Fluids**, 13(11), 2634-2649.

Demuren, A.O. (1991). "Calculation of Turbulence-Driven Secondary Motion in Ducts with Arbitrary Cross Section", **AIAA Journal**, 29(4), 531-537.

Demuren, A.O. and Rodi, W. (1984). "Calculation of Turbulence-driven Secondary Motion in Non-Circular Ducts", **Journal of Fluid Mechanics**, 140, 189-222.

Drain, L.E. (1980). **The Laser Doppler Technique**. Chichester: John Wiley and Sons.

Durbin, P.A. (1991). "Near-Wall Turbulence Closure Modeling Without 'Damping Functions'", **Theoretical and Computational Fluid Dynamics**, 3, 1-13.

Durst, F., Melling, A. and Whitelaw, J.H. (1976). **Principles and Practice of Laser-Doppler Anemometry**. London: Academic Press.

Einstein, H.A. and Li, H. (1958). "Secondary Currents in Straight Channels", **Transactions of the American Geophysical Union**, 39, 1085-1088.

El-Zaemey, A.K.S. (1991). "Sediment Transport Over Deposited Beds in Sewers", **Unpublished PhD Thesis**, University of Newcastle upon Tyne.

Featherstone, R.E. and Nalluri, C. (1988). **Civil Engineering Hydraulics**. London: Professional Books.

Finlayson, B.A. (1972). **The Method of Weighted Residuals and Variational Principles**. New York: Academic Press.

Gerard, R. (1978). "Secondary Flow in Noncircular Conduits", **Journal of the Hydraulic Division**, ASCE,104(HY5), 603-616.

Gessner, F.B. (1973). "The Origin of Secondary Flow in Turbulent Flow Along a Corner", **Journal of Fluid Mechanics**, 58, 1-25.

Ghani, A. Ab (1993). "Sediment Transport in Sewers", **Unpublished PhD Thesis**, University of Newcastle upon Tyne.

Ghosh, S.N. and Roy, N. (1970). "Boundary Shear Distribution in Open Channel Flow" **Journal of the Hydraulic Division**, ASCE, 96(HY4), 689-713.

Gibson, M.M. and Rodi, W. (1989). "Simulation of Free Surface Effects on the Turbulence with a Reynolds Stress Model", **Journal of Hydraulic Research**, IAHR, 27(2), 233-244.

Grass, A.J. (1967). "The Structure of the Turbulent Boundary Layer ", **Unpublished PhD Thesis**, University of London.

Grass, A.J. (1971). "Structural Features of Turbulent Flow Over Smooth and Rough Boundaries", **Journal of Fluid Mechanics**, 50, 233-255.

Harlow, F.H. and Welch, J.E. (1965). "Numerical Calculation of Time-Dependent Viscous Incompressible Flow of Fluid with Free Surface", **The Physics of Fluids**, 8(11), 2182.

Henderson, F.M. (1966). **Open-Channel Flow**. London: Collier-Macmillan.

Hinze, J.O. (1973). "Experimental Investigation on Secondary Currents in the Turbulent Flow Through a Straight Conduit", **Applied Science Research**, 28, 453-465.

Hinze, J.O. (1975). **Turbulence**. London: MacGraw-Hill.

Hoohlo, C. (1991). "Velocity, Turbulence and Boundary Shear Didtributions in Channels of Circular Cross-Section with Flat Beds", **Unpublished Msc Thesis**, University of Newcastle upon Tyne.

Hoohlo, C., and Nalluri, C. (1993). "Velocity, Turbulence and Boundary Shear Distributions in Pipes of Circular Cross-Section with a Flat Bed: Turbulent Flow", **Numerical Methods in Laminar and Turbulent Flow: Proceedings of the 8th International Conference,** (Ed. C. Taylor), Swansea: Pineridge Press, Pt. 1(2), 230 - 240.

Hussain, A.K.M.F. and Reynolds, W.C. (1975). "Measurements in Fully-developed Turbulent Channel Flow", **Journal of Fluids Engineering**, ASME, 97, 568-580.

Ideriah, F.J.K. (1978). "On Turbulent Forced Convection in a Square Cavity", **Numerical Methods in Laminar and Turbulent Flow: Proceedings of the 1st International Conference,** (Eds. C. Taylor, K. Morgan, and C.A. Brebbia), Swansea: University College Swansea, 257-269.

Jackson, P.S. (1981). "On the Displacement Height in the Logarithmic Velocity Profile", **Journal of Fluid Mechanics**, 111, 15-25.

Jenson, L., Menon, R.K., and Fingerson, L.M. (1988). "An Automatic Signal Processor for LDV systems", **Fourth International Symposium on Applications of Laser Anemometry,** Lisbon:

Kamphuis, J.W. (1974). "Determination of Sand Roughness for Fixed Beds", **Journal of Hydraulic Research**, IAHR, 12(2), 193-203.

Kline, S.J. (1965). **Similitude and Approximation Theory**. London: McGraw-Hill.

Kline, S.J., Reynolds, W.C., Schraub, F.A. and Runstadler, P.W. (1967). "The Structure of Turbulent Boundary Layers", **Journal of Fluid Mechanics**, 30, 741-773.

Knight, D.W. (1981). "Boundary Shear in Smooth and Rough Channels", **Journal of Hydraulic Division**, ASCE, 107(HY7), 839-851.

Knight, D.W., Demetriou, J.D. and Hamed, M.E. (1984). "Boundary Shear in Smooth Rectangular Channels", **Journal of Hydraulic Engineering**, ASCE, 110, 405-422.

Knight, D.W. and Patel, H.S. (1985). "Boundary shear in Smooth Rectangular Ducts", **Journal of Hydraulic Engineering**, ASCE, 111, 29-47.

Knight, D.W. and Shiono, K. (1990). "Turbulence Measurements in a Shear Layer Region of a Compound Channel", **Journal of Hydraulic Research**, IAHR, 28(2), 175-196.

Knight, D.W. Yuen, K.W.H. and Al-Hamid, A.A.I. (1994). "Boundary Shear Stress Distributions in Open Channel Flow", **Mixing and Transport in the Environment**, ed. K.J. Beven, P.C. Chatwin, and J.H. Millbank. 51-87. London: John Wiley and Sons Ltd.

Krishnappan B.G. and Lau Y.L. (1986). "Turbulence Modelling of Flood Plain Flows", **Journal of Hydraulic Engineering**, ASCE, 112, 251-266.

Laufer, J. (1951). "Investigation of Turbulent Flow in a Two-dimensional Channel", **Report 1053**. New York: NACA.

Laufer, J. (1954). "The Structure of Turbulence in Fully Developed Pipe Flow", **Report 1174**. New York: NACA.

Launder, B.E. (1981). "Turbulence Modelling in the Vicinity of a Wall", in **Proceedings of the 1980-81 AFOSR-HTTM-Stanford Conference on Complex Turbulent Flows**. Stanford, Calif.: Stanford University Press.

Launder, B.E. and Spalding, D.B. (1972). **Mathematical Models of Turbulence**. New York: Academic Press.

Launder, B.E. and Ying, W.M. (1972). "Secondary Flow in Ducts of Square Cross-Section", **Journal of Fluid Mechanics**, 54(2), 289-295.

Launder, B.E. and Spalding, D.B. (1974). "The Numerical Computation of Turbulent Flows", **Computer Methods in Applied Mechanics and Engineering**, 3, 269-289.

Launder, B.E., Reece, G.J. and Rodi, W. (1975). "Progress in the Development of a Reynolds Stress Turbulence Closure", **Journal of Fluid Mechanics**, 68, 537-566.

Launder, B.E. and Tselepidakis, D.P. (1988) "Contribution to the Second-Moment Modelling of Sublayer Turbulent Transport", in **Near-Wall Turbulence: 1988 Zoran Zaric Memorial Conference**. Eds. S.J. Kline and N.H. Afgan. 818-833. London: Hemisphere.

Launder, B.E., Li, S-P. (1994). "Elimination of Wall-topography Parameters for Second Moment Closure", **The Physics of Fluids A**, 6, 2(II), 999-1006.

Leutheuesser, H.J. (1963). "Turbulent Flow in Rectangular Ducts", **Journal of the Hydraulics Division**, ASCE, 89(HY3), 1-19.

Leschziner, M.A. and Rodi, W. (1979). "Strongly Curved Open Channel Flow", **Journal of the Hydraulics Division**, ASCE, 105(HY10), 1297-1314.

Lumley, J.L. (1970). "Toward a Turbulent Constitutive Relation", **Journal of Fluid Mechanics**, 41(2), 413-434.

Mansour, N.N., Kim, J. and Moin, P. (1989). "Near-Wall k-ε Turbulence Modeling", **AIAA Journal**, 27(8), 1068-1073.

McComb, W.D. (1990). **The Physics of Fluid Turbulence**. Oxford: Clarendon Press.

McQuivey, R.S. and Richardson, E.V. (1969). "Some Turbulence Measurements in Open-Channel Flow", **Journal of the Hydraulic Division**, ASCE, 95(HY1), 209-223.

Melling, A. (1975). "Investigation of Flow in Non-circular Ducts and Other Configurations by Laser Doppler Anemometry", **Unpublished PhD Thesis**, University of London.

Melling, A. and Whitelaw, J.H. (1976). "Turbulent Flow in a Rectangular Duct", **Journal of Fluid Mechanics**, 37(2), 289-315.

Mironovskiy, A.L. (1991). "Extension of the Generalized Logarithmic Velocity Distribution to the Case of Flow Ducts with Corners", **Heat Transfer-Soviet Research**, 23(4), 503-509.

Nalluri, C., and Novak, P. (1973). "Turbulence Characteristics in a Smooth Open Channel of Circular Cross-section", **Journal of Hydraulic Research**, IAHR, 11(4).

Naot, D. (1984). "Response of Channel Flow to Roughness Heterogeneity", **Journal of Hydraulic Engineering**, ASCE, 110(11), 1568-1587.

Naot, D. and Rodi, W. (1982). "Calculation of Secondary Currents in Channel Flow", **Journal of Hydraulic Engineering**, ASCE, 108, 948-968.

Nezu, I. and Nakagawa, H. (1984). "Cellular Secondary Currents in Straight Conduits", **Journal of Hydraulic Engineering**, ASCE, 110, 173-193.

Nezu, I. (1977). "Turbulent Structure in Open-Channel Flows", **Unpublished PhD Thesis**, University of Kyoto, Japan.

Nezu, I and Nakagawa, H. (1987). "Numerical Calculation of Turbulent Open-Channel Flows in Consideration of Free-Surface Effect", **Memoirs, Faculty of Engineering**. University of Kyoto, 49(2), 111-145.

Nezu, I. and Rodi, W. (1985). "Experimental Study on Secondary Currents in Open Channel Flow". **Proceedings of the 21st IAHR Congress**, IAHR. 115-119.

Nezu, I. and Rodi, W. (1986). "Open-Channel Flow Measurements with a Laser Doppler Anemometer", **Journal of Hydraulic Engineering**, ASCE, 112(5), 335-355.

Nezu, I and Nakagawa, H. (1993). **Turbulence in Open-Channel Flows**. Delft: A.A. Balkema.

Patankar, S.V. (1980). **Numerical Heat Transfer and Fluid Flow**. London: Hemisphere.

Patankar, S.V. (1981). "A Calculation Procedure for Two-dimensional Elliptic Situations", **Numerical Heat Transfer**, 4, 409-425.

Patankar, S.V. (1988). "Recent Developments in Computational Heat Transfer", **Journal of Heat Transfer**, 110, 1037-1045.

Patankar, S.V. and Spalding, D.B. (1972). "A Calculation Procedure for Heat, Mass and Momentum Transfer in Three-dimensional Parabolic Flows", **International Journal of Heat and Mass Transfer**, 15, 1787-1806.

Patel, V.C. (1974). "External Flows", in **Topics in Applied Physics: Turbulence**. Ed. Bradshaw, New York: Springer Verlag.

Patel, V.C, Rodi, W. and Scheueurer, G. (1985) "Turbulence Models for Near-Wall and Low Reynolds Number Flows: A Review", **AIAA Journal**, 23(9), 1308-1319.

Pender, G. and Manson, J.R. (1994). "Developments in Three-Dimensional Numerical Modelling of River Flows", in **Proceedings of the Second International Conference on River and Flood Hydraulics**, York, England, 371-377. Chichester: John Wiley.

Peric, M. (1985). "A Finite Volume Method for the Prediction of Three-dimensional Fluid Flow in Complex Ducts", **Unpublished PhD Thesis**, University of London.

Perkins, H.J. (1970). "The Formation of Streamwise Vorticity in Turbulent Flow", **Journal of Fluid Mechanics**, 44(4), 721-740.

Perry, A.E., Schofield, W.H., and Joubert, P.N. (1969). "Rough Wall Turbulent Boundary Layers", **Journal of Fluid Mechanics**, 37(2), 383-413.

Perry, A.E., and Chong, M.S. (1982). "On the Mechanism of Wall Turbulence", **Journal of Fluid Mechanics**, 119, 173-217.

Perry, A.E., Henbest, S., and Chong, M.S. (1986). "A Theoretical and Experimental Study of Wall Turbulence", **Journal of Fluid Mechanics**, 165, 163-199.

Perry, A.E., Li, J.D., and Marusic, I. (1991). "Towards a Closure Scheme for Turbulent Boundary Layers Using the Attached Eddy Hypothesis", **Journal of Fluid Mechanics**, 336, 67-79.

Rao, G.N.V. (1967). "The Law of the Wall in a Thick Axisymmetric Turbulent Boundary Layer", **Journal of Applied Mechanics**, ASME, 237-238.

Raithby, G.D. (1976). "A Critical Evaluationof Upstream Differencing Applied to Problems Involving Fluid Flow", **Computer Methods in Applied Mechanics and Engineering**, 9, 75-81.

Replogle, J.A. (1964). "Tractive-force Distribution in Sewers and Channels", **Unpublished PhD Thesis**, University of Illinois.

Reynolds, O. (1894). "On the Dynamical Theory of Incompressible Viscous Fluids and the Determination of the Criterion", in **Proceedings Osborne Reynolds Centenary Symposium**, UMIST, Manchester.

Rhie, C.M. and Chow, W.L. (1983). "A Numerical Study of the Turbulent Flow Past an Isolated Airfoil With Trailing Edge Separation", **AIAA Journal**, 21(6), 1525-1532.

Roache, P.T. (1976). **Computational Fluid Dynamics**. Alburqueque, New Mexico: Hermosa Publishers.

Robinson, S.K. (1991). "Coherent Motions in the Turbulent Boundary Layer", **Annual Review of Fluid Mechanics**, 23, 601-639.

Rodi, W. (1972). "The Prediction of Free Turbulent Boundary Layers by use of a two-equation model of Turbulence", **Unpublished PhD Thesis**, University of London.

Rodi, W. (1976). "A New Algebraic Relation for calculating the Reynolds Stresses", ZAMM, 56: T219-21

Rodi, W. (1980). **Turbulence Models and Their Applications in Hydraulics**. Delft: IAHR Secretariat.

Saga, T., Ohnari, H. Watanabe, K., and Saitou, T. (1991). "Coherent Structure in Turbulent Open Channel Flow in Corners", in **FLUCOME '91**, ASME, New York.

Sarma, K.N.V., Lakshminarayana, P., and Rao, N.S.L. (1983). "Velocity Distribution in Smooth Rectangular Open Channels", **Journal of Hydraulic Engineering**, ASCE, 109, 270-289.

Schlichting, H. (1968). **Boundary-Layer Theory**. London: MacGraw-Hill.

Smith, C.R., Walker, J.D.A., Haidari, A.H., and Sobrun, U. (1991). "On the Dynamics of Near-Wall Turbulence", **Philosophical Transactions of the Royal Society:London**, A336, 131-175.

Smith, G.D. (1988). **Numerical Solution of Partial Differential Equations: Finite Difference Methods**, 3rd Edition. Oxford: Clarendon.

Spalding, D.B. (1991). "Kolmogorov's Two-equation Model of Tubulence", **Proceedings of the Royal Society:London**, A434, 101.

Speziale, C.G. (1982). "On Turbulent Secondary Flows in Pipes of Non-circular Cross-section", **International Journal of Engineering Science**, 20(7), 863-872.

Speziale, C.G. (1987). "On Non-Linear k-l and k-ε models of Turbulence", **Journal of Fluid Mechanics**, 178, 459-475.

Speziale, C.G. (1991). "Analytical Methods for the Development of Reynolds-Stress Closures in Turbulence", **Annual Review of Fluid Mechanics**, 23, 107-157.

Steffler, P.M., Rajaratnam, N. and Peterson, A.W. (1985). "LDA Measurements in Open Channels", **Journal of Hydraulic Engineering**, ASCE, 111, 119-130.

Tennekes, H. and Lumley, J.L. (1972). **A First Course in Turbulence**. London: MIT Press.

Thiart, G.D. (1990) "An Improved Finite Difference Scheme for the Solution of Convection-Diffusion Problems with SIMPLEN Algorithm", **Numerical Heat Transfer**, 18(B), 81-95.

Thermo-Systems Inc. (1986). **Instruction Manual - 900 Series Laser Optics.** St. Paul, USA. Thermo-Systems Inc.(TSI).

Thermo-Systems Inc. (1988). **Instruction Manual - Model IFA 550 Signal Processor**, St. Paul, USA. Thermo-Systems Inc.(TSI)

Thompson, J.F., Warsi, Z.U.A., and Mastin, W.C. (1985). **Numerical Grid Generation: Foundations and Applications**. Oxford: North-Holland.

Tominaga, A., Nezu, I. and Nakagawa, H. (1989). "Three-Dimensional Turbulent Structure in Straight Open-Channel Flows", **Journal of Hydraulic Research**, IAHR, 27, 149-173.

Townsend, A.A. (1961). "Equilibrium Layers and Wall Turbulence", **Journal of Fluid Mechanics**, 11, 97-120.

Tritton, D.J. (1988). **Physical Fluid Dynamics**. Oxford: Clarendon Press.

Truesdell, C. and Noll, W. (1965). "The Nonlinear Field Theories of Mechanics". In **Handbuch der Physik**(In English), Vol. III/3. New York: Springer-Verlag.

Van Doormal, J.P. and Raithby, G.D. (1984) "Enhancements of the SIMPLE Method for Predicting Incompressible Fluid Flows", **Numerical Heat Transfer**, 7, 147-163.

Vanka, S.P. (1985). "Block-implicit Calculation of Steady Turbulent Recirculating Flows", **International Journal of Heat and Mass Transfer**, 28(11), 2093-2103.

Vichenevetsky, R. (1981). **Computer Methods for Partial Differential Equations**. London: Prentice-Hall.

Wang, J., Dong, Z., Chen, C., and Xia, Z. (1993). "The Effects of Bed Roughness on the Distribution of Turbulent Intensities in Open-channel Flow", **Journal of Hydraulic Research**. IAHR, 31(1), 89-98.

Yaglom, A.M. (1979) "Similarity Laws for Constant-Pressure and Pressure-Gradient Turbulent Wall Flows", **Annual Review of Fluid Mechanics**, 11, 505-540.

Yalin, M.S. (1979). **The Theory of Hydraulic Models**, London: John Wiley and Sons.

APPENDICES

APPENDIX A: CUSTOMISATION OF LDA TRAVERSING TABLE

A.1 Traversing Table Specification

This Appendix describes the customisation of a computer-controlled traversing table for the LDA optics.

The traversing table was custom-made by Optimage Ltd., Edinbugh, UK. Plate A.1 shows the basic features of this model: McLennan 34HS-311. The arm on which the LDA receiving optics are placed is fixed to the table platform and extends over the flow area. This is such that the transmitting and receiving optics are level.

The table is moved vertically by a stepper motor placed on the underside of the platform. The motor provides). 1.3 Nm of torque at 1000 full (2000half) steps per second. The number of full steps per second can be increased to 2000 with a corresponding decrease in torque (to 0.5 Nm). To half the table in place when not traversing, the motor has a rest torque of 3.0 Nm.

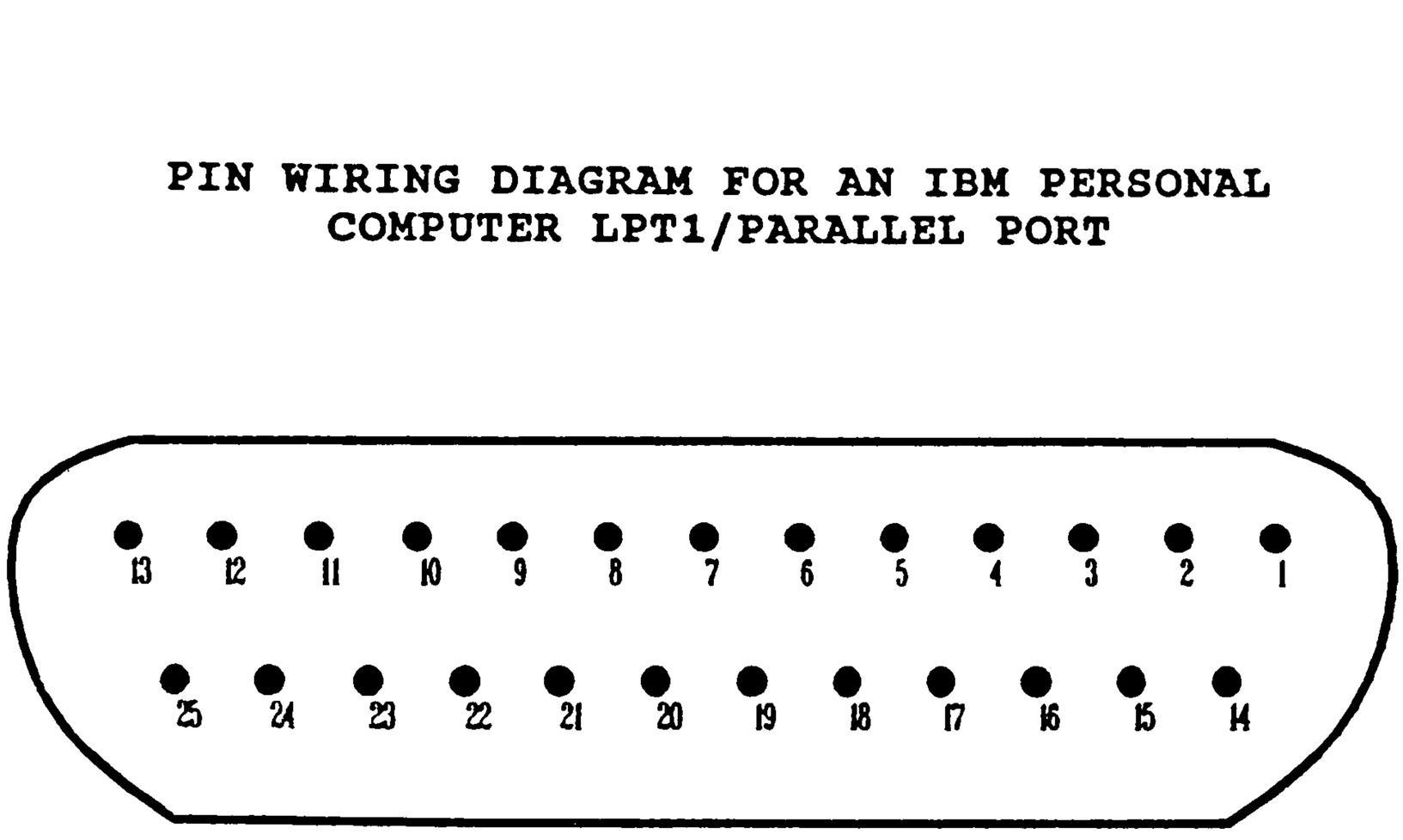

Figure A.1 Wiring Diagram for the LPT1 Port

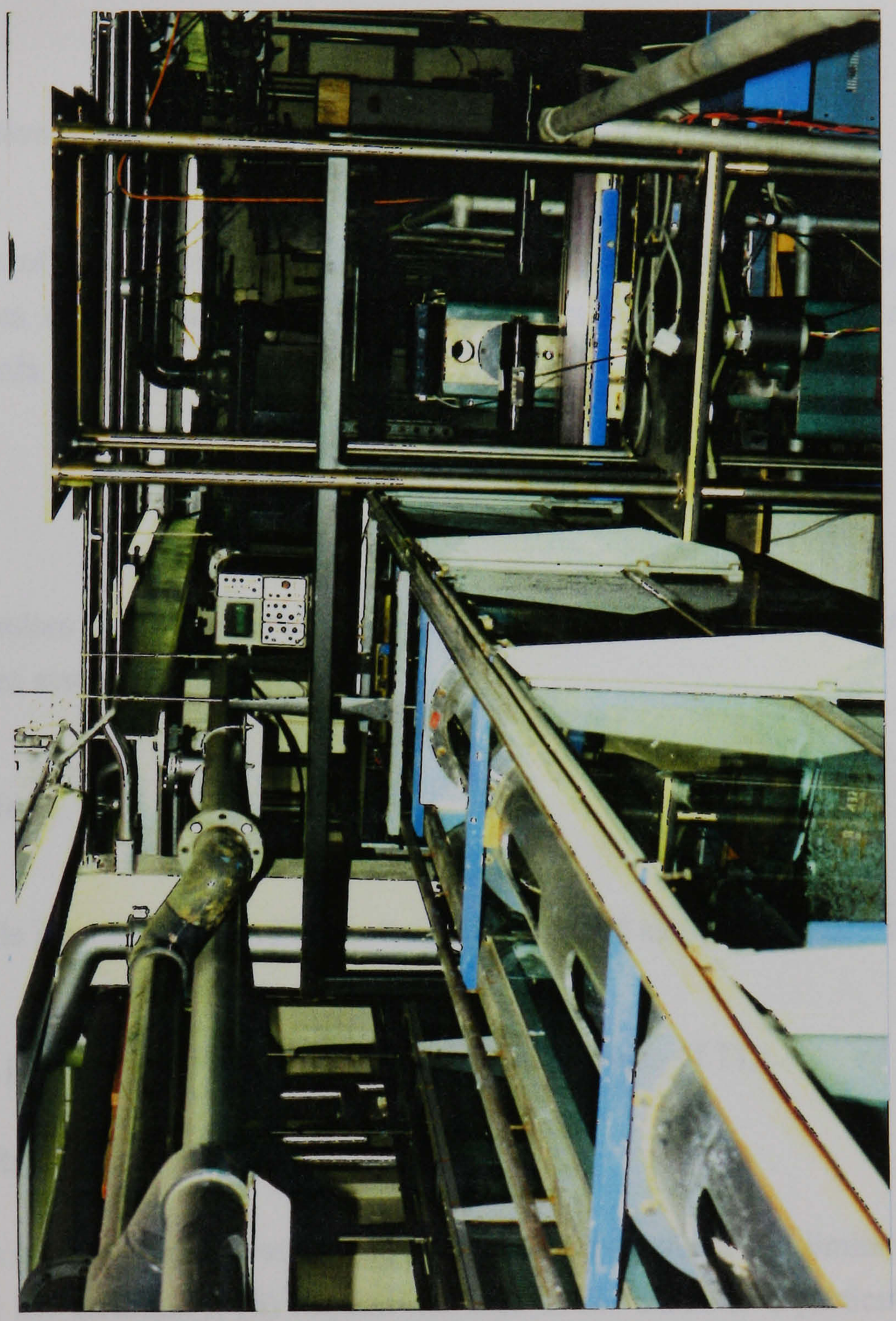

Plate A.1 The Automated Traversing Table at Measurement Section

One full revolution of the motor is achieved by 200 steps. 400 half-steps will thus produce the one revolution. Each step is caused by an electric pulse sent through the LPT1 port of the IBM compatible Personal Computer (PC) via the manufacturer's control unit. The wiring diagram for this port is shown in Figure A.1. Zero voltage at a pin is denoted by 0, and a pulse, is denoted by 1.

Control of Direction

The direction of motor rotation and hence of the vertical traverse, is controlled through PIN 2. A 0 causes upward movement (clockwise motor rotation), whilst 1 moves the table platform downwards.

Drive Pulse

The driving pulses for the motor are supplied though PIN 3. The platform moves by 1 mm for each 100 pulses sent.

Full/Half Step Mode

The step mode is controlled via PIN 4. 0 signifies the full step, and 1 the half step mode.

The required pulses are 5 Volts Transistor-Transistor Logic (TTL).

A.2 Control Program

The program seeks to (i) request the user to set universal traversing limits set by the space constraints within the laboratory; (ii) request the user to set limits of a particular traverse; (iii) request the user to set the step mode; and (iv) to ask for the direction and magnitude of the traverse. Figure A.2 gives the flow chart for the program.

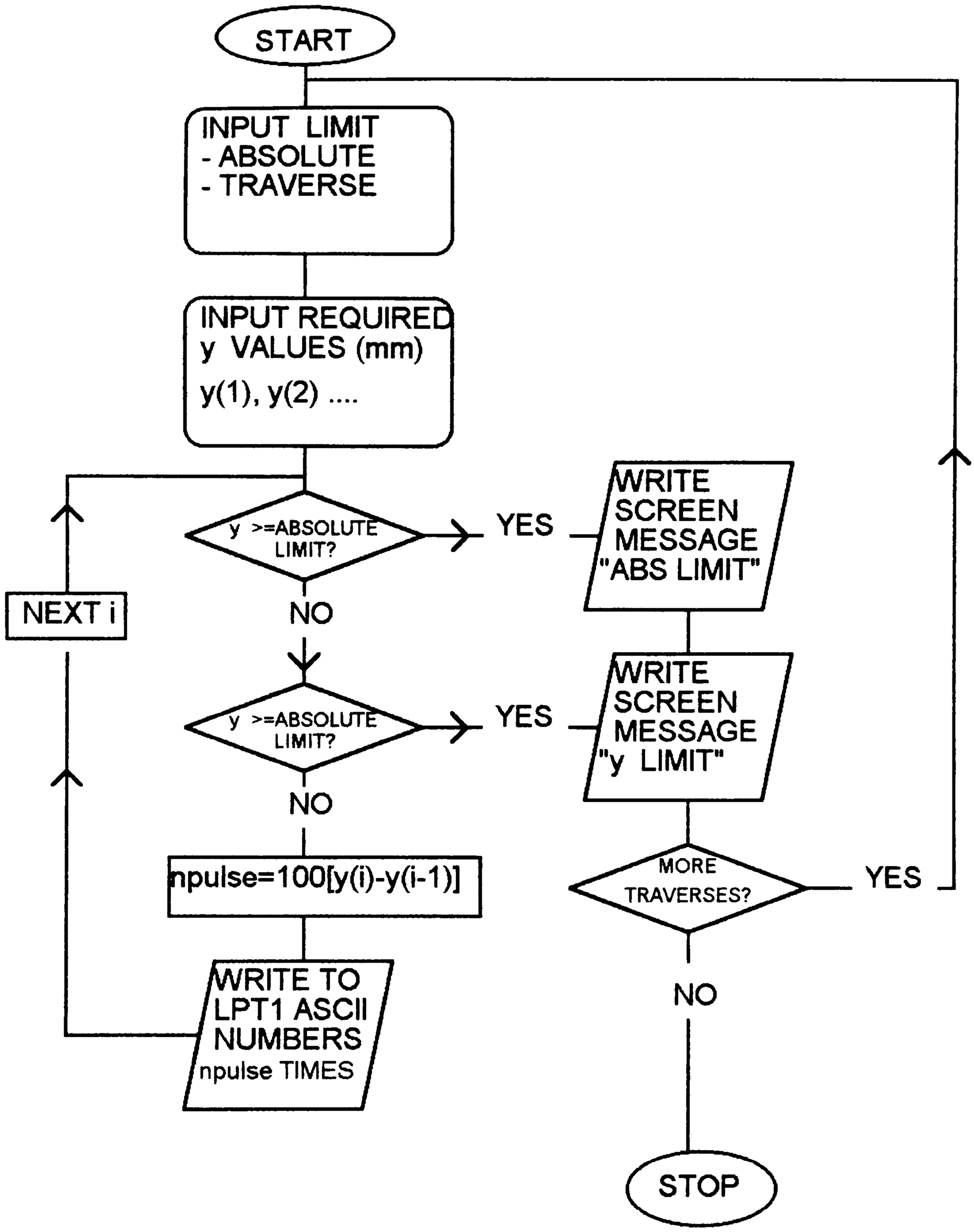

Figure A.2 Control Program Flow Chart

A.2.1 Program Performance

The driving computer program was written in FORTRAN. The WRITE statement is used to send ASCII characters in 8-bit (binary) form depending on what pins were required to have high voltage (1) or low voltage (0). (For example, ASCII character 211 is denoted in binary form by 11010011). For the control combination 0, 1, 1, 0 for pins 1, 2, 3, and 4 respectively, ASCII character 6 is chosen.

The PC was shown to give a high voltage (1) of 4.6 Volts and not the 5 Volts required by the control unit This lead to the stepper motor stuttering and shaky intermittent movement of the table. This was true for all pin voltage combinations.

A.2.2 Rectification of Low Pin Voltage

The low pin voltages were augmented by an external voltage source. This 5 Volt source is attached via 470 mΩ (milli Ohm) resistors to each of the three pins (PINs 2, 3, and 4) used. This is illustrated in Figure A.3. To enable switching of the power source for each pin-line, switches were added to the circuitry.

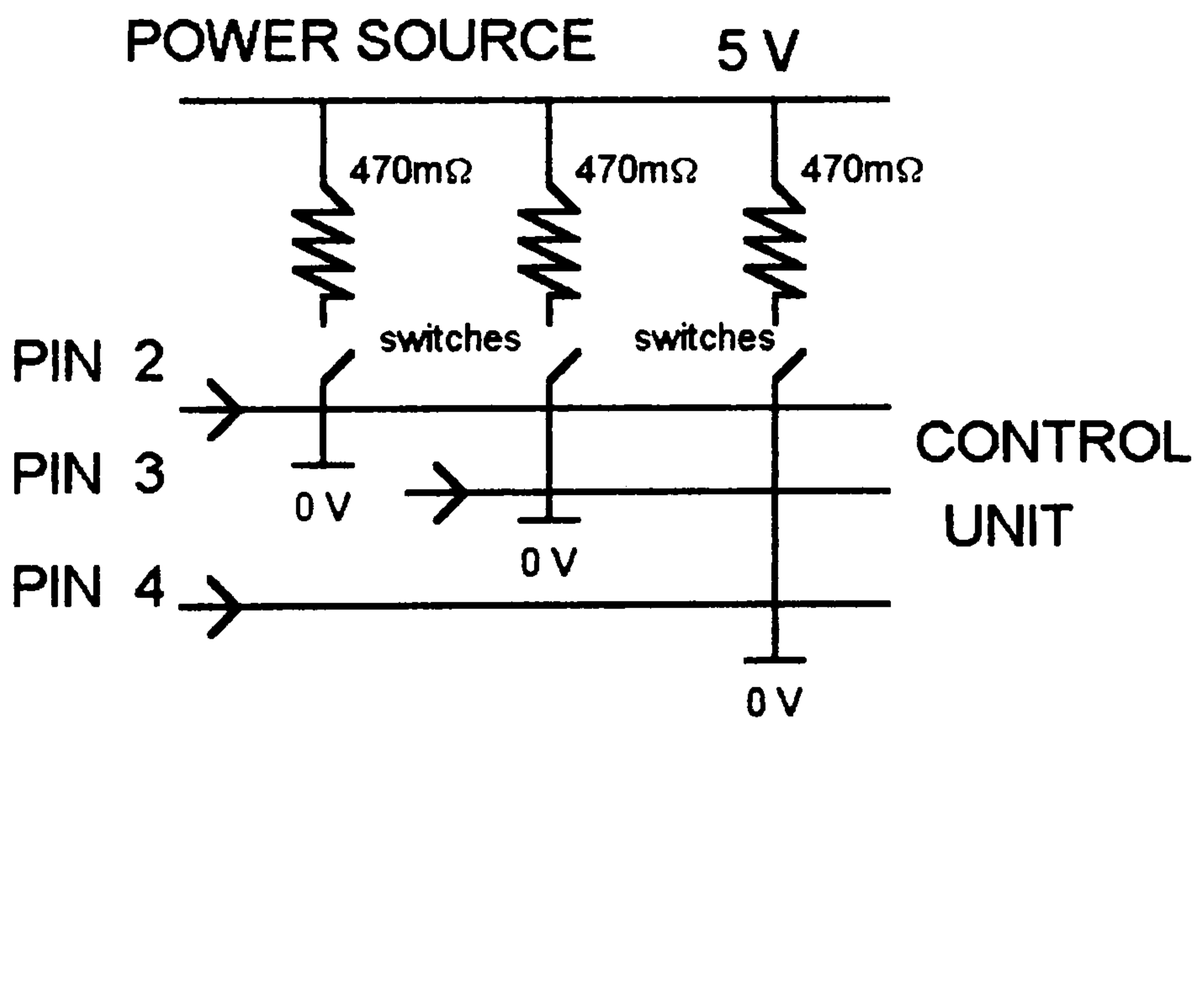

Figure A.3 Pin Voltage Augmentation

The program control of the motor was thus enhanced. The platform traversed as expected. Further (future) improvement would be for the power source to be incorporated within the motor control unit itself.

APPENDIX B: HYDRAULIC PARAMETERS FOR EXPERIMENTAL FLOWS

This Appendix gives all the hydraulic parameters calculated for the experimental study. It is a summation of Tables 7.1 and 7.2.

Table B.1 Summary of Hydraulic Parameters

1	2	3	4	5	6	7	8
Case	So	Yo/D	e/D	(Yo+e)/D	Q (Eqn 3.9) (cumecs)	Q Integrtd (cumecs)	Q Error
S1111	4.63E-04	0.164	0.141	0.305	0.00442	0.00256	42.12%
S1211	4.63E-04	0.259	0.141	0.400	0.00904	0.00492	45.59%
S1311	4.63E-04	0.361	0.141	0.502	0.01350	0.01339	0.85%
S1411	4.63E-04	0.525	0.141	0.666	0.02281	0.02635	-15.50%
S2111	9.27E-04	0.164	0.141	0.305	0.00570	0.00396	30.57%
S2211	9.27E-04	0.259	0.141	0.400	0.01148	0.00918	20.02%
S2311	9.27E-04	0.361	0.141	0.502	0.01821	0.01491	18.11%
S2411	9.27E-04	0.525	0.141	0.666	0.03218	0.02386	25.85%
R1111	4.63E-04	0.164	0.141	0.305	0.00635	0.00451	28.95%
R1211	4.63E-04	0.259	0.141	0.400	0.00724	0.00550	24.06%
R1311	4.63E-04	0.361	0.141	0.502	0.01263	0.00995	21.22%
R1411	4.63E-04	0.525	0.141	0.666	0.02408	0.01939	19.48%
R2111	9.27E-04	0.164	0.141	0.305	0.00669	0.00311	53.52%
R2211	9.27E-04	0.259	0.141	0.400	0.00847	0.00631	25.52%
R2311	9.27E-04	0.361	0.141	0.502	0.01376	0.01141	17.07%
R2411	9.27E-04	0.525	0.141	0.666	0.02521	0.02047	18.81%
R1412	4.63E-04	0.525	0.141	0.666	0.01796	0.01488	17.16%
R2112	9.27E-04	0.164	0.141	0.305	0.00314	0.00185	41.15%
R2212	9.27E-04	0.259	0.141	0.400	0.00679	0.00511	24.75%
R2312	9.27E-04	0.361	0.141	0.502	0.01282	0.01011	21.12%
R2412	9.27E-04	0.525	0.141	0.666	0.02225	0.01803	18.95%
S2121	9.27E-04	0.131	0.285	0.416	0.00322	0.00251	22.06%
S2221	9.27E-04	0.216	0.285	0.502	0.00704	0.00584	17.05%
S2321	9.27E-04	0.380	0.285	0.666	0.01611	0.01358	15.72%
S2421	9.27E-04	0.466	0.285	0.751	0.02191	0.01797	17.97%
R2123	9.27E-04	0.131	0.285	0.416	0.00248	0.00190	23.44%
R2223	9.27E-04	0.216	0.285	0.502	0.00561	0.00462	17.65%
R2323	9.27E-04	0.380	0.285	0.666	0.01373	0.01168	14.91%
R2423	9.27E-04	0.466	0.285	0.751	0.01906	0.01606	15.72%
R2122	9.27E-04	0.131	0.285	0.416	0.00231	0.00157	31.96%
R2222	9.27E-04	0.216	0.285	0.502	0.00477	0.00395	17.21%
R2322	9.27E-04	0.380	0.285	0.666	0.01175	0.00961	18.19%
R2422	9.27E-04	0.466	0.285	0.751	0.01518	0.01281	15.62%
D=	305	mm					
r=	152.5	mm					
Length=	9.105	m					

Table B.1(Cont) Summary of Hydraulic Parameters

9	10	11	12	13	14	15	16
A	A_i	A Error	Pb	Pw	P	R	T
(Eqn 3.3)	Integrtd		(m)	(m)	(Eqn 3.5)	(Eqn 3.8)	(Eqn 3.4)
(m^2)	(m^2)				(m)	(m)	(m)
0.0125741	0.0076502	39.16%	0.2123	0.1220	0.3343	0.0376	0.2808
0.0210100	0.0152651	27.34%	0.2123	0.1829	0.3952	0.0532	0.2988
0.0304026	0.0246102	19.05%	0.2123	0.2453	0.4576	0.0664	0.3050
0.0453663	0.0377505	16.79%	0.2123	0.3472	0.5595	0.0811	0.2878
0.0125741	0.0104402	16.97%	0.2123	0.1220	0.3343	0.0376	0.2808
0.0210100	0.0177502	15.52%	0.2123	0.1829	0.3952	0.0532	0.2988
0.0304026	0.0266504	12.34%	0.2123	0.2453	0.4576	0.0664	0.3050
0.0453663	0.0392603	13.46%	0.2123	0.3472	0.5595	0.0811	0.2878
0.0125741	0.0095702	23.89%	0.2123	0.1220	0.3343	0.0376	0.2808
0.0210100	0.0176401	16.04%	0.2123	0.1829	0.3952	0.0532	0.2988
0.0304026	0.0262602	13.63%	0.2123	0.2453	0.4576	0.0664	0.3050
0.0453663	0.0379606	16.32%	0.2123	0.3472	0.5595	0.0811	0.2878
0.0125741	0.0095701	23.89%	0.2123	0.1220	0.3343	0.0376	0.2808
0.0210100	0.0170396	18.90%	0.2123	0.1829	0.3952	0.0532	0.2988
0.0304026	0.0262604	13.62%	0.2123	0.2453	0.4576	0.0664	0.3050
0.0453663	0.0379544	16.34%	0.2123	0.3472	0.5595	0.0811	0.2878
0.0453663	0.0383805	15.40%	0.2123	0.3472	0.5595	0.0811	0.2878
0.0125741	0.0088003	30.01%	0.2123	0.1220	0.3343	0.0376	0.2808
0.0210100	0.0181990	13.38%	0.2123	0.1829	0.3952	0.0532	0.2988
0.0304026	0.0253506	16.62%	0.2123	0.2453	0.4576	0.0664	0.3050
0.0453663	0.0383507	15.46%	0.2123	0.3472	0.5595	0.0811	0.2878
0.0116039	0.0098021	15.53%	0.2754	0.0842	0.3596	0.0323	0.3007
0.0194975	0.0159902	17.99%	0.2754	0.1364	0.4118	0.0473	0.3050
0.0344612	0.0286003	17.01%	0.2754	0.2383	0.5138	0.0671	0.2878
0.0416582	0.0345804	16.99%	0.2754	0.2957	0.5711	0.0729	0.2638
0.0116039	0.0091252	21.36%	0.2754	0.0842	0.3596	0.0323	0.3007
0.0194975	0.0153403	21.32%	0.2754	0.1364	0.4118	0.0473	0.3050
0.0344612	0.0292504	15.12%	0.2754	0.2383	0.5138	0.0671	0.2878
0.0416582	0.0355057	14.77%	0.2754	0.2957	0.5711	0.0729	0.2638
0.0116039	0.0069001	40.54%	0.2754	0.0842	0.3596	0.0323	0.3007
0.0194975	0.0149501	23.32%	0.2754	0.1364	0.4118	0.0473	0.3050
0.0344612	0.0266502	22.67%	0.2754	0.2383	0.5138	0.0671	0.2878
0.0416582	0.0331503	20.42%	0.2754	0.2957	0.5711	0.0729	0.2638

Table B.1(Cont) Summary of Hydraulic Parameters

17	18	19	20	21	22	23	24	25
Um	Umax	Viscosity	Re	Re	Re	Fr	Fr	d50
		(m^2/s)	4RUm/vi	YoUm/vi	TUm/vi	Um/(gYo)	Um/(gA/T)	
(m/s)	(m/s)							(mm)
0.352	0.413	1.15E-06	46209	15358	86259	0.502	0.531	-
0.430	0.376	1.15E-06	79918	29687	112299	0.489	0.518	-
0.444	0.628	1.15E-06	103082	42665	118298	0.428	0.449	-
0.503	0.837	1.15E-06	142410	70256	126369	0.401	0.404	-
0.454	0.487	1.15E-06	59583	19803	111224	0.648	0.685	-
0.546	0.631	1.15E-06	101448	37685	142552	0.621	0.658	-
0.599	0.655	1.15E-06	138977	57522	159491	0.577	0.606	-
0.709	0.689	1.15E-06	200874	99099	178248	0.566	0.570	-
0.505	0.618	1.15E-06	66314	22040	123790	0.721	0.762	0.93
0.345	0.397	1.15E-06	64019	23781	89957	0.392	0.415	0.93
0.415	0.465	1.15E-06	96411	39904	110642	0.400	0.420	0.93
0.531	0.609	1.15E-06	150316	74156	133385	0.424	0.427	0.93
0.532	0.410	1.15E-06	69901	23232	130485	0.760	0.803	0.93
0.403	0.467	1.15E-06	74879	27815	105217	0.458	0.486	0.93
0.453	0.521	1.15E-06	105017	43466	120518	0.436	0.458	0.93
0.556	0.636	1.15E-06	157389	77646	139661	0.444	0.447	0.93
0.396	0.473	1.15E-06	112126	55316	99497	0.316	0.318	4.2
0.250	0.306	1.15E-06	32841	10915	61306	0.357	0.377	4.2
0.323	0.407	1.15E-06	60017	22294	84334	0.367	0.389	4.2
0.422	0.520	1.15E-06	97828	40490	112268	0.406	0.426	4.2
0.490	0.593	1.15E-06	138867	68508	123226	0.391	0.394	4.2
0.278	0.335	1.15E-06	31279	9693	72871	0.443	0.451	-
0.361	0.469	1.15E-06	59710	20810	96168	0.449	0.456	-
0.468	0.548	1.15E-06	109533	47358	117493	0.438	0.431	-
0.526	0.600	1.15E-06	133981	65207	121160	0.446	0.423	-
0.214	0.272	1.15E-06	24106	7470	56159	0.341	0.348	1.71
0.288	0.415	1.16E-06	47086	16411	75837	0.358	0.363	1.71
0.398	0.487	1.14E-06	93796	40554	100612	0.373	0.368	1.71
0.457	0.560	1.16E-06	114738	55842	103759	0.388	0.368	1.71
0.199	0.287	1.23E-06	20816	6451	48495	0.318	0.323	4.2
0.245	0.359	1.19E-06	38806	13525	62500	0.304	0.309	4.2
0.341	0.453	1.20E-06	75979	32850	81500	0.320	0.315	4.2
0.364	0.473	1.21E-06	87628	42647	79242	0.309	0.293	4.2

Table B.1(Cont) Summary of Hydraulic Parameters

26	27	28	29	30	31	32	33	34
d90	Yo/d90	ks	Sublayer Thickness	Yo/ks	ks/Yo	$\overline{U^*}$	(U*)b Einstein	Re* KsU*/vi
(mm)		(mm)	(mm)			(m/s)	(m/s)	
-	-	-	4.83	-	0	0.013	-	-
-	-	-	2.99	-	0	0.016	-	-
-	-	-	2.39	-	0	0.017	-	-
-	-	-	1.80	-	0	0.019	-	-
-	-	-	3.87	-	0	0.018	-	-
-	-	-	2.43	-	0	0.022	-	-
-	-	-	1.84	-	0	0.025	-	-
-	-	-	1.34	-	0	0.027	-	-
1.18	42.37	2.36	4.83	21.19	0.047	0.013	0.016	27
1.18	66.95	2.36	2.99	33.47	0.030	0.016	0.015	32
1.18	93.22	2.36	2.39	46.61	0.021	0.017	0.016	36
1.18	135.59	2.36	1.80	67.80	0.015	0.019	0.014	40
1.18	42.37	2.36	3.87	21.19	0.047	0.018	0.015	38
1.18	66.95	2.36	2.43	33.47	0.030	0.022	0.024	45
1.18	93.22	2.36	1.84	46.61	0.021	0.025	0.028	51
1.18	135.59	2.36	1.34	67.80	0.015	0.027	0.031	56
5.1	31.37	10.2	1.80	15.69	0.064	0.019	0.022	171
5.1	9.80	10.2	3.87	4.90	0.204	0.018	0.021	165
5.1	15.49	10.2	2.43	7.75	0.129	0.022	0.026	196
5.1	21.57	10.2	1.84	10.78	0.093	0.025	0.029	219
5.1	31.37	10.2	1.34	15.69	0.064	0.027	0.033	242
-	-	-	6.80	-	0	0.017	-	-
-	-	-	3.86	-	0	0.021	-	-
-	-	-	2.27	-	0	0.025	-	-
-	-	-	1.90	-	0	0.026	-	-
1.96	20.41	3.92	6.80	10.20	0.098	0.017	0.018	59
1.96	33.67	3.92	3.86	16.84	0.059	0.021	0.023	70
1.96	59.18	3.92	2.27	29.59	0.034	0.025	0.029	85
1.96	72.45	3.92	1.90	36.22	0.028	0.026	0.030	87
5.1	7.84	10.2	6.80	3.92	0.255	0.017	0.019	142
5.1	12.94	10.2	3.86	6.47	0.155	0.021	0.024	177
5.1	22.75	10.2	2.27	11.37	0.088	0.025	0.030	209
5.1	27.84	10.2	1.90	13.92	0.072	0.026	0.032	216

Table B.1(Cont) Summary of Hydraulic Parameters

35	36	37	38	39	40	41	42	43
(Re*)b	Equivn	Lambda	Lambda	Lambda	Cf	Lambda	Lambda	Lambda
Ks(U*)b/vi	n	Total	Bed	Wall		Smooth	Smooth	Smooth
						(Blasuis)	(Moody)	(Barr)
-	0.007	0.022	-	-	0.003	0.022	0.021	0.023
-	0.007	0.019	-	-	0.005	0.019	0.018	0.020
-	0.008	0.018	-	-	0.006	0.018	0.017	0.019
-	0.008	0.016	-	-	0.006	0.016	0.016	0.018
-	0.008	0.020	-	-	0.007	0.020	0.020	0.022
-	0.008	0.018	-	-	0.006	0.018	0.017	0.019
-	0.008	0.016	-	-	0.007	0.016	0.016	0.018
-	0.008	0.015	-	-	0.006	0.015	0.015	0.017
33	0.005	0.005	0.033	0.006	0.003	-	-	-
31	0.009	0.016	0.032	0.006	0.008	-	-	-
33	0.008	0.014	0.034	0.006	0.007	-	-	-
29	0.008	0.010	0.04	0.006	0.005	-	-	-
31	0.006	0.010	0.031	0.006	0.005	-	-	-
49	0.011	0.024	0.03	0.006	0.012	-	-	-
58	0.011	0.024	0.033	0.006	0.012	-	-	-
64	0.010	0.019	0.037	0.006	0.010	-	-	-
196	0.010	0.019	0.032	0.006	0.009	-	-	-
187	0.014	0.044	0.029	0.006	0.022	-	-	-
232	0.013	0.037	0.028	0.006	0.019	-	-	-
258	0.012	0.027	0.029	0.006	0.014	-	-	-
294	0.012	0.025	0.032	0.006	0.012	-	-	-
-	0.011	0.024	-	-	0.015	0.024	0.023	0.025
-	0.011	0.020	-	-	0.013	0.020	0.020	0.022
-	0.011	0.017	-	-	0.011	0.017	0.017	0.019
-	0.010	0.017	-	-	0.010	0.017	0.016	0.018
62	0.014	0.051	0.03	0.006	0.026	-	-	-
78	0.014	0.042	0.029	0.006	0.021	-	-	-
100	0.013	0.031	0.03	0.006	0.015	-	-	-
101	0.012	0.025	0.031	0.006	0.013	-	-	-
157	0.016	0.059	0.029	0.006	0.030	-	-	-
205	0.016	0.057	0.028	0.006	0.029	-	-	-
254	0.015	0.042	0.029	0.006	0.021	-	-	-
269	0.015	0.040	0.029	0.006	0.020	-	-	-

Table B.1(Cont) Summary of Hydraulic Parameters

44	45	46	47	48	49	50
$\bar{\tau}_o$	Bed Shear	Bed Shear	$\bar{\tau}_b / \bar{\tau}_o$	$\bar{\tau}_b / \bar{\tau}_o$	Shear	Shear
	Einstein	Vanoni-B	Vanoni-B	Einstein	Force Ratio	Force Ratio
(N/m^2)	(N/m^2)	(N/m^2)			Wall	Bed
0.1708	-	-	-	-	0.37	0.63
0.2414	-	-	-	-	0.46	0.54
0.3017	-	-	-	-	0.54	0.46
0.3681	-	-	-	-	0.62	0.38
0.3419	-	-	-	-	0.37	0.63
0.4833	-	-	-	-	0.46	0.54
0.6040	-	-	-	-	0.54	0.46
0.7371	-	-	-	-	0.62	0.38
0.1708	0.256	1.024	6.00	1.50	0.05	0.95
0.2414	0.225	0.484	2.00	0.93	0.50	0.50
0.3017	0.256	0.729	2.42	0.85	0.61	0.39
0.3681	0.196	1.296	3.52	0.53	0.80	0.20
0.3419	0.225	1.089	3.19	0.66	0.58	0.42
0.4833	0.576	0.625	1.29	1.19	0.36	0.64
0.6040	0.784	0.841	1.39	1.30	0.40	0.60
0.7371	0.961	1.369	1.86	1.30	0.51	0.49
0.3681	0.484	0.729	1.98	1.31	0.50	0.50
0.3419	0.441	0.256	0.75	1.29	0.18	0.82
0.4833	0.676	0.4	0.83	1.40	0.25	0.75
0.6040	0.841	0.729	1.21	1.39	0.35	0.65
0.7371	1.089	1.024	1.39	1.48	0.44	0.56
0.2934	-	-	-	-	0.23	0.77
0.4304	-	-	-	-	0.33	0.67
0.6098	-	-	-	-	0.46	0.54
0.6631	-	-	-	-	0.52	0.48
0.2934	0.324	0.169	0.58	1.10	0.85	0.85
0.4304	0.526	0.324	0.75	1.22	0.82	0.82
0.6098	0.841	0.576	0.94	1.38	0.74	0.74
0.6631	0.9	0.784	1.18	1.36	0.65	0.65
0.2934	0.361	0.144	0.49	1.23	0.94	0.94
0.4304	0.576	0.225	0.52	1.34	0.90	0.90
0.6098	0.9	0.441	0.72	1.48	0.79	0.79
0.6631	1.024	0.529	0.80	1.54	0.74	0.74

Table B.1(Cont) Summary of Hydraulic Parameters

51 (z') Corner Influence zone (m)	52 Delta (b-layer) z'/2 (m)	54 LHS of Roughness Equation	55 Aspect Ratio (Bed/Yo)	56 Aspect Ratio (T/Yo)	57 Xm/4R
0.1975	0.0988	-	4.25	5.62	-
0.1661	0.0831	-	2.69	3.78	-
0.1486	0.0743	-	1.93	2.77	-
0.1345	0.0673	-	1.33	1.80	-
0.1396	0.0698	-	4.25	5.62	-
0.1174	0.0587	-	2.69	3.78	-
0.1050	0.0525	-	1.93	2.77	-
0.0951	0.0475	-	1.33	1.80	-
0.1975	0.0988	12.88840985	4.25	5.62	-
0.1661	0.0831	4.065386962	2.69	3.78	-
0.1486	0.0743	4.543739548	1.93	2.77	-
0.1345	0.0673	6.07028546	1.33	1.80	-
0.1396	0.0698	7.961936608	4.25	5.62	-
0.1174	0.0587	2.141839766	2.69	3.78	-
0.1050	0.0525	1.790708273	1.93	2.77	-
0.0951	0.0475	2.473680884	1.33	1.80	-
0.1345	0.0673	5.175189707	1.33	1.80	-
0.1396	0.0698	2.952241391	4.25	5.62	41.64
0.1174	0.0587	2.94078431	2.69	3.78	29.46
0.1050	0.0525	3.779524244	1.93	2.77	23.57
0.0951	0.0475	3.888211634	1.33	1.80	19.32
0.1507	0.0754	-	6.89	7.52	48.54
0.1244	0.0622	-	4.17	4.62	33.08
0.1045	0.0523	-	2.37	2.48	23.35
0.1002	0.0501	-	1.94	1.86	21.47
0.1507	0.0754	1.140605825	6.89	7.52	-
0.1257	0.0629	1.165630286	4.17	4.62	-
0.1040	0.0520	1.691051793	2.37	2.48	-
0.1018	0.0509	2.362092156	1.94	1.86	-
					-
0.1623	0.0811	2.263297816	6.89	7.52	-
0.1297	0.0649	1.689917807	4.17	4.62	-
0.1099	0.0549	2.089261101	2.37	2.48	-
0.1062	0.0531	2.11710186	1.94	1.86	-

APPENDIX C: COMPUTER PROGRAM MASTER FLOW CHARTS

C.1 Main Program

The structure of the main program is shown in the flowchart of Figure C.1. The program first calls the INPUT subroutine to enable the input of channel specifications. The uniform Cartesian grid is then generated by the simple division of the pipe into a mesh of Δz x Δy rectangular cells - indexed by (i, j) as in Figure 4.2. The U(0,y,z), V(0,y,z), W(0,y,z), P(0,x,y,z), k(0,y,z), and ε(0,y,z) values are also set by a subroutine nested within INPUT. The variables are computed in the order U, V, W, P', k, and ε using the subroutine YZSWEEP as the main driving unit. If convergence of the U an d k fields (using criteria of Eqn 4.74) has not been achieved after each call to YZSWEEP the recently computed values are adopted as the previuos iteration values and computation proceeds. The marching procedure of sub-Section 6.2.3 is used in subroutine RESTART. When U and k convergence are reached, the OUTPUT subroutine is used to output data into a disk file.

C.2 INPUT Subroutine

Figure C.2 illustrates the input subroutine. The program asks whether a new section is to be used or an initialisation file already exists for a section previously analysed. For a new section the pipe specifications are requested, namely the diameter (D), bed thickness (e), flow depth (Y_o), bed slope (S_o), the equivalent sand roughness for the bed (k_s) (side-walls assumed smooth), and the vertical number of cells (*idy*; maximum 30). The inputted data is operator-verified before the program proceeds to the grid generation.

Generation of the Cartesian grid is carried-out by the division of the half-section into rectangular mesh cells of size Δz x Δy in the subroutine PARAM. The curved side-wall means the number of horizontal steps (*izw*) varies with j such that *izw* is indexed: *izw(j)*. For the y-sweep, the number of vertical steps (*jys*) differ from *idy* in the wall region such that *jys* is also indexed: *jys(i)*. The starting j value too is indexed: *jstart(i)*.

The initial variable values are then set.in the subroutine INITIALISE. U follows the log-Rao law. V and W are set to zero. k and ε are set according to Eqns 3.24 and 3.25. P = 2/3k. The boundary conditions are also set by calling the subroutine BOUND.

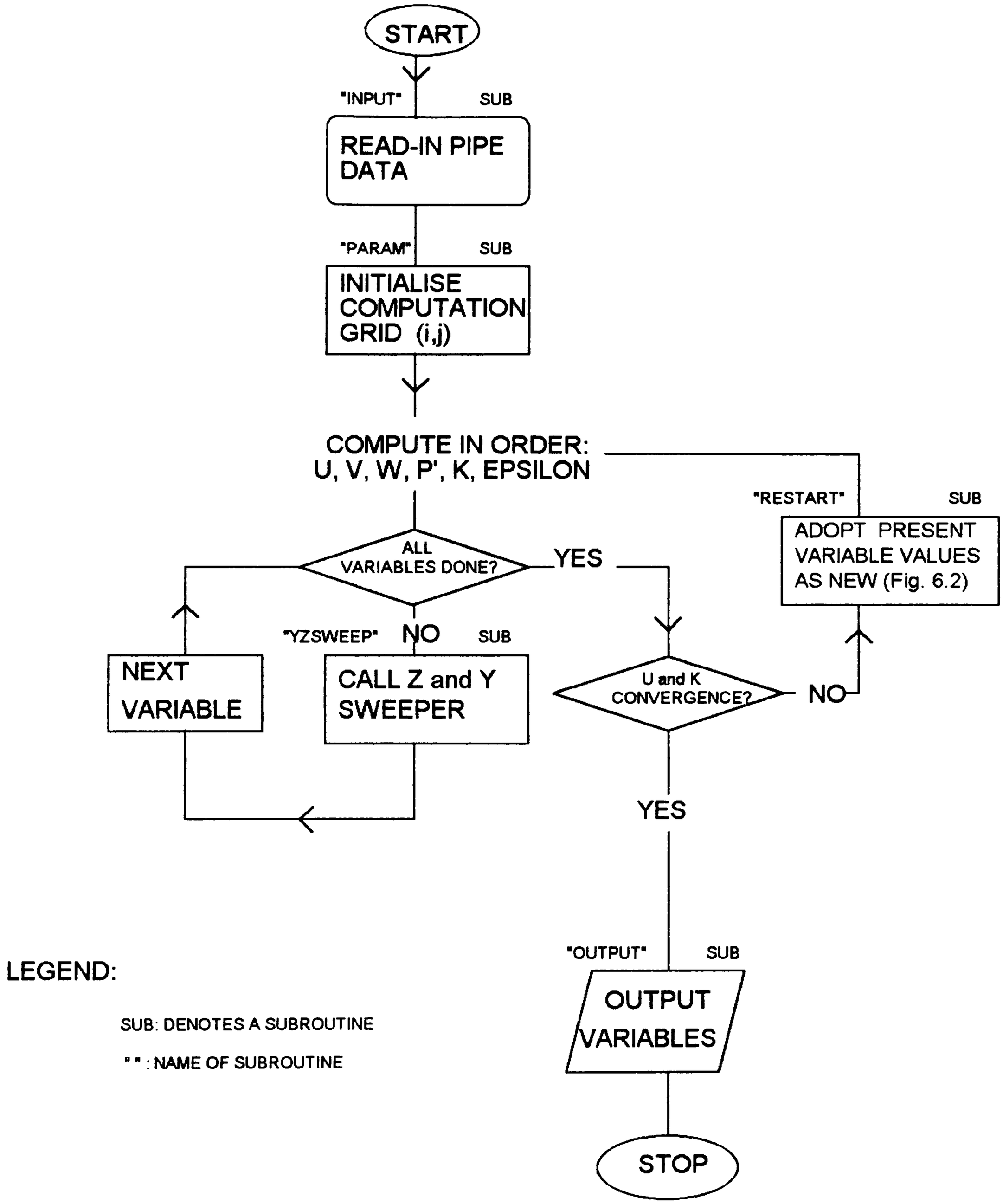

Figure C.1 The Main Program

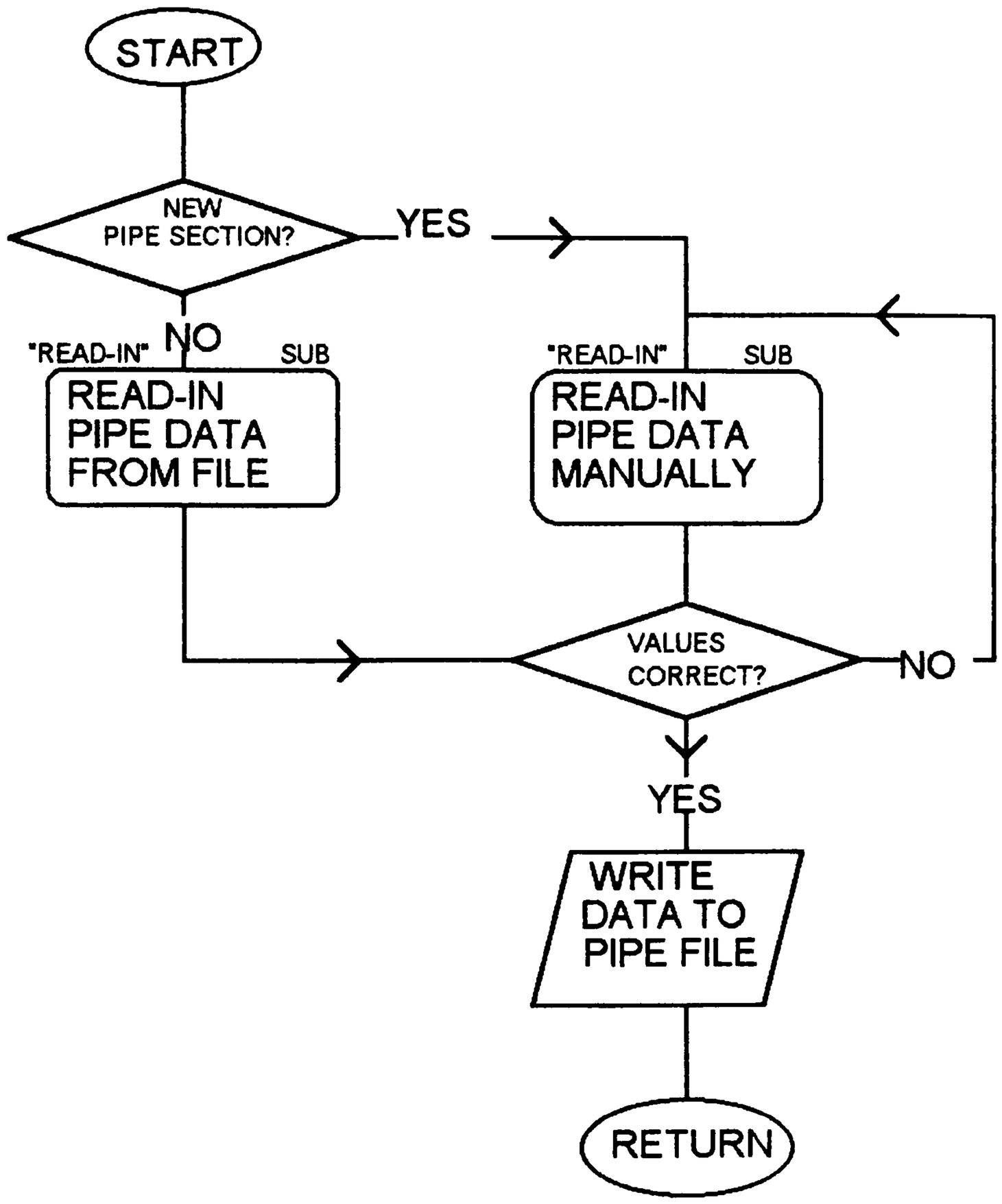

Figure C.2 Input Subroutine ("INPUT")

C.3 Z and Y Sweeping Subroutine: YZSWEEP

The variables are solved according to the SIMPLE procedure in the order of U, V,W, P', k and ε. For each of U, V,W, k and ε, YZSWEEP is called once from the main program. Figure C.3 illustrates this. For the pressure correction P', it is called from the PCORRCT subroutine as many times as is necessary for the convergence criterion (Eqn 4.67) to be met.

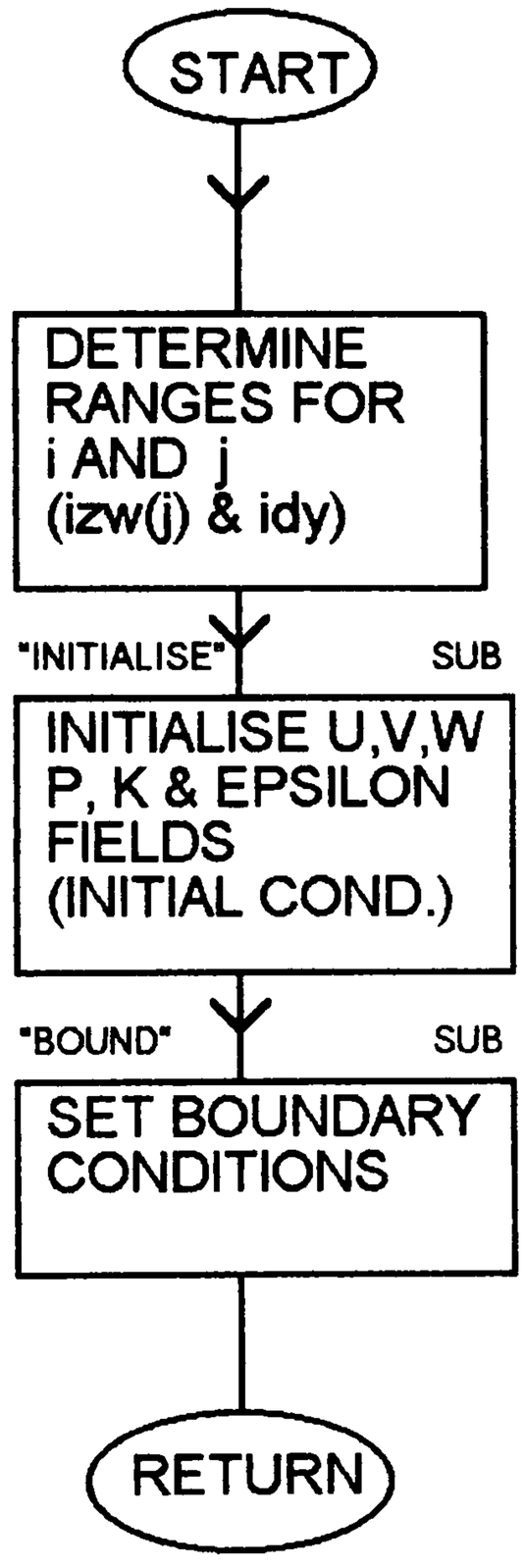

Figure C.3 Grid Generation and Variable Initialisation Subroutine

The z-sweep is implemented by initiating the loop for j = 1 to j= *idy*. For each j, the cells in the range i = 1 to i = *izw(j)* are visitied one at a time. For each cell the SWEEP routine is called to calculate the coefficient matrix [A], and the source-and-constant matrix [B] of Eqn 4.68. When all the cells along the line of constant j have been visited and the matices [A] and [B] have been derived, the STDMA subroutine is called to solve for the variable matrix [ϕ] using the TDMA routine. The generalised solution matrix [ϕ] is converted into the specific values of the variable being solved in SOLUTIONZ. For variables U, V, W, k, and ε, the boundary conditions subroutine BOUND is called to update the boundary conditions before moving to the next j.

Similarly for the y-sweep, the main loop is the is in the i = 1 to i = imax range. The cells in the range *jstart(i)* to *jstart(i)* + *jys(i)* -1 range are each visited to derive matrices [A] and [B]. The general solution matrix [ϕ] is converted into specific variable values in the SOLUTIONY subroutine. For variables U, V, W, k, and ε, BOUND is called before the computation at the next i.

At the end of the sweeps the convergence test is made on U. During the calculation of P', the residuals of Eqn 4.67 are computed and the program control returns to subroutine PCORRCT. If the convergence criterion is not met, the YZSWEEP is called reapeatedly (about 5 times) until convergence. The velocities are then corrected using Eqns 4.53 - 4.55. The Main Program then re-assumes control and YZSWEEP is called to solve for k and ε.

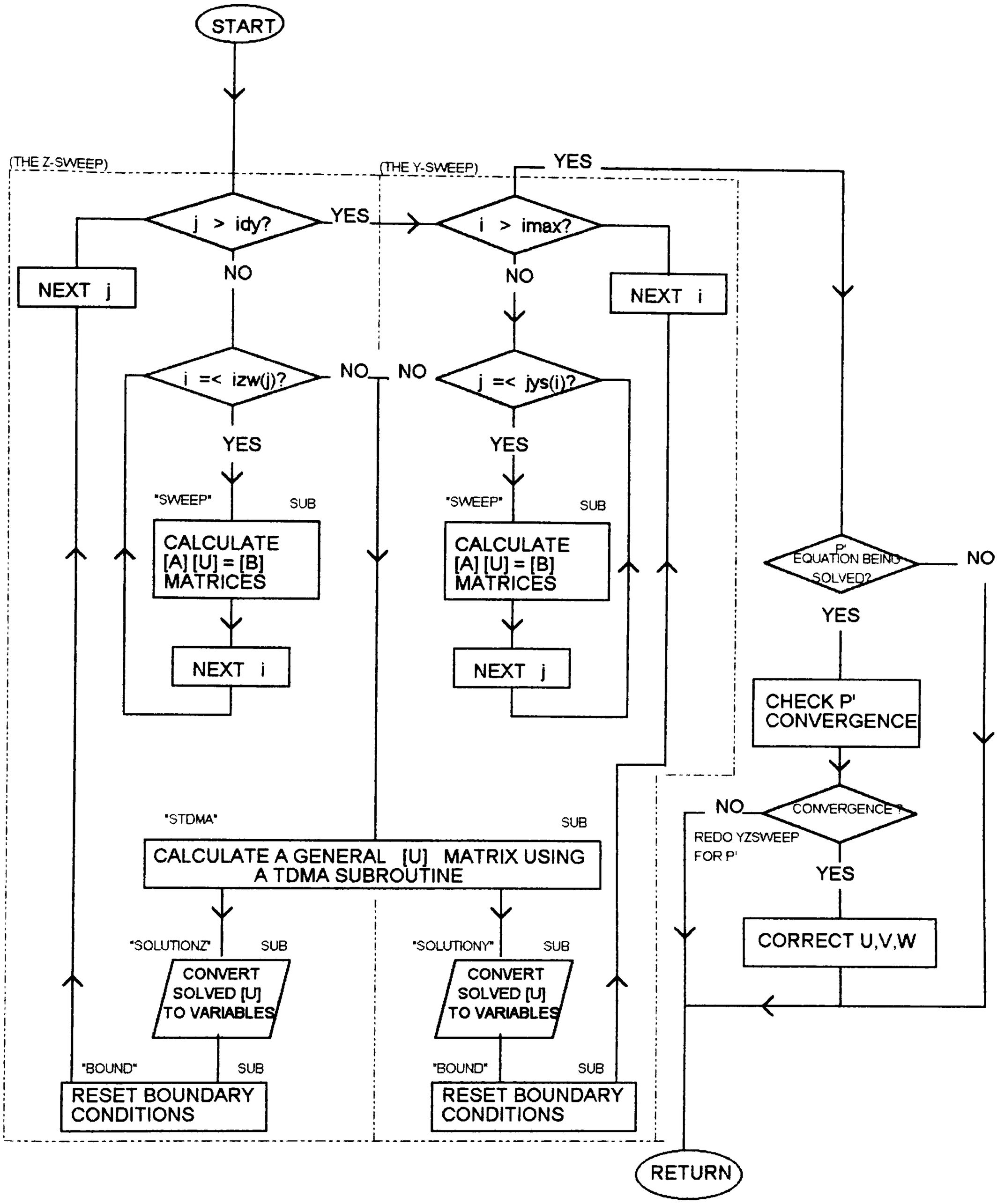

Figure C.4 'Sweeping' Subroutine ("YZSWEEP")

C.4 The SWEEP Subroutine for Matrices [A] and [B]

Figure C.5 illustrates the flow of the SWEEP subroutine for evaluating matrices [A] and [B] of Eqn 4.68. SWEEP is called from the YZSWEEP subroutine for each grid node (i, j). The variable-dependent convection and diffusion coefficients are calculated according to Eqns 4.33 - 4.43, and 4.56. Several gradient 'functions' (not subroutines) are used to evaluate the effective viscosity/diffusion terms according to Eqns 6.2 to 6.13. The coefficients are evaluated for the boundary cells using Eqns 4.58 - 4.65. The source terms are evaluated using Eqns 4.20 and 4.21.

For the z-sweep, coefficients a_P, a_E, and a_W form elements of matrix [A]. Coefficients a_S, a_N, and a_T and the source terms are used to derive elements of [B] using Eqns 4.33 - 4.43. Conversely a_P, a_N, and a_S form elements of matrix [A], and a_E, a_W, and a_T (together with the source terms) are used to derive elements of [B] during the y-sweep.

C.5 Miscellany

The converged data is outputted using subroutine OUTPUT. The data is presented in the non-dimensional forms presented in Chapter 8.

The source code was compiled with the Jumbo Model of the Prospero FORTRAN running on IBM-compatible personal computer.

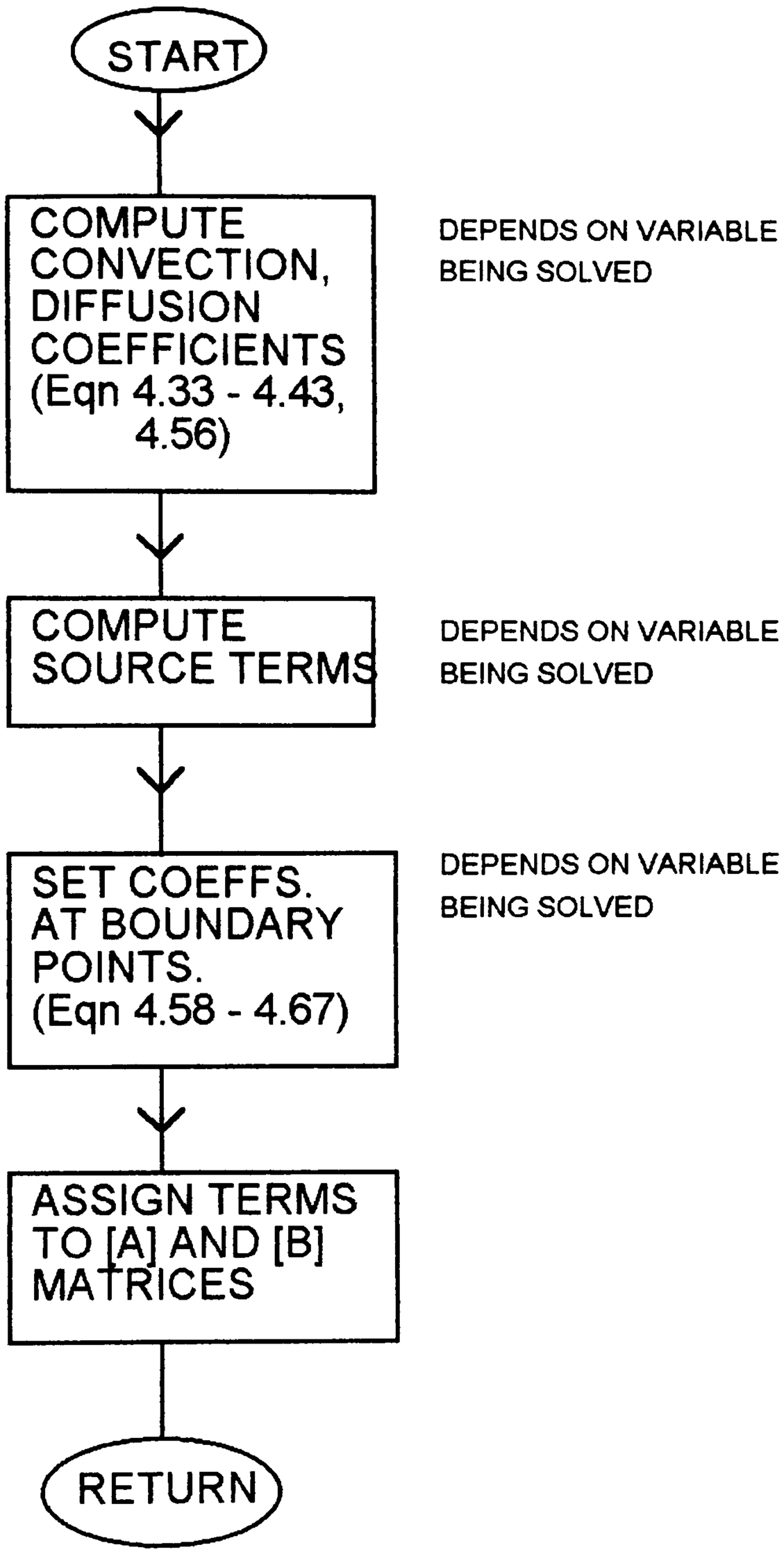

Figure C.5 Coefficient Matrix Subrouitne ("SWEEP")